annual progress

ADVANCED POWER ELECTRONICS TECHNOLOGY AREA

FREEDOMCAR AND VEHICLE TECHNOLOGIES PROGRAM

Less dependence on foreign oil today, and transition to a petroleum-free, emissions-free vehicle tomorrow.

U.S. Department of Energy
Energy Efficiency and Renewable Energy
Bringing you a prosperous future where energy is clean, abundant, reliable, and affordable

FreedomCAR & Fuel Partnership

21st CENTURY TRUCK PARTNERSHIP

U.S. Department of Energy
FreedomCAR and Vehicle Technologies, EE-2G
1000 Independence Avenue, S.W.
Washington, D.C. 20585-0121

FY 2006

FreedomCAR and Vehicle Technologies Annual Progress Report for the Advanced Power Electronics Technology Area

Energy Efficiency and Renewable Energy
FreedomCAR and Vehicle Technologies
Vehicle Systems Team

Edward J. Wall,
FreedomCAR and Vehicle Technologies

Susan A. Rogers,
Technology Development Manager
Advanced Power Electronics

December 2006

Contents

Acronyms and Abbreviations iii

1. Introduction 1

2. Thermal Control for Power Electronics and Motors 7
   - 2.1 Thermal Control for Inverters and Motors 7
   - 2.2 Identifying the Barriers and Approaches to Achieving High-Temperature Coolants 31
   - 2.3 Direct Cooling Options: An Assessment of Air Cooling for Use with Automotive Power Electronics Applications 43
   - 2.4 Modeling Two-Phase Spray and Jet Impingement Cooling 55
   - 2.5 Low Thermal Resistance IGBT Structure 86
   - 2.6 Dynamic and Steady State Modeling to Identify, over Various Drive Cycles, Component and System Performance Efficiency and Thermal Loads 102
   - 2.7 Advanced Thermal Interface Materials to Reduce Thermal Resistance 122

3. Electric Machinery Research and Technology Development 141
   - 3.1 Uncluttered CVT Machine 141
   - 3.2 Interior Permanent Magnet Reluctance Machines 151
     - 3.2.1 Interior Permanent Magnet Reluctance Machines with Brushless Field Excitation—16,000 rpm 151
     - 3.2.2 High-Power-Density Reluctance Interior Permanent Magnet Machines—6,000 rpm 162
   - 3.3 Control of Fractional-Slot Surface Mounted Permanent Magnet Motors with Concentrated Windings 168
   - 3.4 Extending the CPSR of Synchronous Reluctance Motors 219
   - 3.5 Advanced Traction Motor Development 237
   - 3.6 Development of Improved Powder for Bonded Permanent Magnets 249

4. Power electronics Research and Technology Development 264
   - 4.1 Wide Bandgap Materials 264
   - 4.2 Integrated dc-dc Converter for Multi-Voltage Bus Systems 288
   - 4.3 Cascaded Multilevel Inverter 304
   - 4.4 Advanced Converter Systems for High-Temperature HEV Environments 322
   - 4.5 dc/dc Converter for Fuel Cell and Hybrid Vehicle 337
   - 4.6 High Temperature Film Capacitors 347
   - 4.7 Embedded Capacitors for (P)HEV Power Electronic Systems 356
   - 4.8 Glass Ceramic Dielectrics for DC Bus Capacitors 361

5. Systems Research and Technology Development 368
   - 5.1 Fully Integrated HEV Traction Motor Drive Development Using Thermoelectrics and Film Capacitor Innovations 368
   - 5.2 Studies of Competitive Products 394
     - 5.2.1 Benchmarking of Competitive Technologies 394
     - 5.2.2 Component Characterization 410

Acronyms and Abbreviations

A	ampere
A_{RMS} or A_{rms}	ampere rms
AC	air-conditioning
ac	alternating current
AIPM	automotive integrated power module
AMES	Ames Laboratory
ANL	Argonne National Laboratory
BCD	bipolar CMOS DMOS
BDCM	brushless direct current motor
BFE	brushless field excitation
CAD	computer-aided drafting
CAN	controller area network
CFC	chlorofluorocarbon
COP	coefficient of performance
CPA	conventional phase advance
CPSR	constant power speed range
CSI	current-source inverter
CTE	coefficient of thermal expansion
DAC/DAQ	data acquisition system
d-axis	direct-axis
DF	dissipation factor
DMIC	dual-mode inverter control
DOE	U.S. Department of Energy
DSP	digital signal processor
EERE	Energy Efficiency and Renewable Energy
emf	electromotive force
EMI	electromagnetic interference
ESL	effective series inductance
ESR	equivalent series resistance
FC	fuel cell
FCV	fuel cell vehicle
FCVT	FreedomCAR and Vehicle Technologies
FEA	finite-element analysis
FreedomCAR	Freedom Cooperative Automotive Research
FSCW	fractional slot concentrated windings
GaN	gallium nitride
GT	Georgia Institute of Technology
GWP	global warming potential
HC	hydrocarbon
HCFC	hydrochlorofluorocarbon
HEV	hybrid electric vehicle
HFC	hydrofluorocarbon
HFE	hydrofluoroether
HSUPM	hybrid-secondary-uncluttered permanent magnet
HV	high voltage
HVAC	heating, ventilating, and air-conditioning
ICE	internal combustion engine
ID	inner diameter

IGBT	insulated gate bipolar transistor
IM	induction motor
IMA	integrated motor assist
IPM	integrated power module
IPM	interior permanent magnet
I-source	current-source
ISR	Isothermal Systems Research
JFET	junction field-effect transistor
JIC	jet impingement cooling
MLCC	multilayer ceramic capacitor
MMCCC	multilevel modular clamped dc/dc converter
mmf	magneto-motive force
MOSFET	metal oxide semiconductor field-effect transistor
MS	methylsiloxane
MSU	Michigan State University
NASA	National Aeronautics and Space Adminstration
NMOS	negative-channel MOS
NTRC	National Transportation Research Center
OD	outer diameter
ODP	ozone-depleting potential
OFCVTs	Office of FreedomCAR and Vehicle Technologies
ORNL	Oak Ridge National Laboratory
PEEM	Power Electronics and Electric Machines
PEEMRC	Power Electronics and Electric Machinery Research Center
Penn State	Pennsylvania State University
PFC	perfluorocarbon
PHEV	plug-in HEV
PM	permanent magnet
PMDC	permanent magnet brushless dc
PMDC	permanent magnet direct current
PMOS	positive-channel MOS
PMSM	permanent magnet synchronous motor
PWM	pulse-width modulation
q-axis	quadrature-axis
R&D	research and development
rad/s	rotational speed
RFP	request for proposals
RIPM	reluctance interior permanent magnet
rms	root-mean-square
RSC	Rockwell Scientific Company
RTFC	real time flux control
SCR	silicon-controlled rectifier
SDPR	switching device power rating
Si	silicon
SiC	silicon carbide
SKAI	Semikron Advanced Integration
SMPM	surface mounted permanent magnet
SOC	state-of-charge
SOI	silicon on insulator
SPM	surface permanent magnet
SUV	sport utility vehicle

TE	thermoelectrics
THS II	Toyota hybrid system (2004)
toff	turn-off times
ton	turn-on
UT	University of Tennessee
UWM	University of Wisconsin–Madison
V	volt
VIBE	vibration-induced bubble ejection
V-source	voltage-source
VSI	voltage source inverter
W	watt
WBG	wide bandgap
WEG	water–ethylene glycol
ZSC	zero-sequence circuit
ZVS	zero-voltage-switching

Introduction

The U.S. Department of Energy (DOE) and the U.S. Council for Automotive Research (composed of automakers Ford, General Motors, and DaimlerChrysler) announced in January 2002 a new cooperative research effort. Known as FreedomCAR (derived from "Freedom" and "Cooperative Automotive Research"), it represents DOE's commitment to developing public/private partnerships to fund high-risk, high-payoff research into advanced automotive technologies. Efficient fuel cell technology, which uses hydrogen to power automobiles without air pollution, is a very promising pathway to achieve the ultimate vision. The new partnership replaces and builds upon the Partnership for a New Generation of Vehicles initiative that ran from 1993 through 2001.

The Vehicle Systems subprogram within the FreedomCAR and Vehicle Technologies Program provides support and guidance for many cutting-edge automotive and heavy truck technologies now under development. Research is focused on understanding and improving the way the various new components of tomorrow's automobiles and heavy trucks will function as a unified system to improve fuel efficiency. This work also supports the development of advanced automotive accessories and the reduction of parasitic losses (e.g., aerodynamic drag, thermal management, friction and wear, and rolling resistance).

In supporting the development of hybrid propulsion systems, the Vehicle Systems subprogram has enabled the development of technologies that will significantly improve fuel economy, comply with projected emissions and safety regulations, and use fuels produced domestically.

The Vehicle Systems subprogram supports the efforts of the FreedomCAR and Fuel Partnership and the 21st Century Truck Partnership through a three-phase approach intended to

- Identify overall propulsion and vehicle-related needs by analyzing programmatic goals and reviewing industry's recommendations and requirements and then develop the appropriate technical targets for systems, subsystems, and component research and development activities;
- Develop and validate individual subsystems and components, including electric motors, emission control devices, battery systems, power electronics, accessories, and devices to reduce parasitic losses; and
- Determine how well the components and subsystems work together in a vehicle environment or as a complete propulsion system and whether the efficiency and performance targets at the vehicle level have been achieved.

The research performed under the Vehicle Systems subprogram will help remove technical and cost barriers to enable the development of technology for use in such advanced vehicles as hybrid and fuel-cell-powered automobiles that meet the goals of the FreedomCAR Program.

A key element in making hybrid electric vehicles practical is providing an affordable electric traction drive system. This will require attaining weight, volume, and cost targets for the power electronics and electrical machines subsystems of the traction drive system. Areas of development include these:

- Novel traction motor designs that result in increased power density and lower cost;
- Inverter technologies involving new topologies to achieve higher efficiency and the ability to accommodate higher-temperature environments;
- Converter concepts that employ means of reducing the component count and integrating functionality to decrease size, weight, and cost;
- More effective thermal control and packaging technologies; and
- Integrated motor/inverter concepts.

This report highlights the activites and progress achieved in the Advanced Power Electronics Research and Development Effort during FY 2006. We are pleased with the progress made during the year and look forward to continued work with our industrial, government, and scientific partners to

overcome the challenges that remain to delivering advanced power electronics and electric machines for vehicle applications.

Below are summaries of major accomplishments for each technical project.

Thermal Control for Inverters and Motors

- An oil spray cooling system for a 6000-rpm drive motor was designed, fabricated, and tested. The cooling was significantly improved from similar motors that incorporate oil-sling cooling systems.
- ORNL has designed, built, and tested an inverter half the size of a commercially available module of the same power rating. The dc test reached 600-A capability (200 A per leg) and the ac switching test achieved 250 Arms for a 3-phase output.

Identifying the Barriers and Approaches to Achieving High-Temperature Coolants

- The study was performed to identify practical approaches, technical barriers, and cost impacts for achieving high-temperature coolant operation for certain traction drive subassemblies and components of hybrid electric vehicles (HEVs). The results of the study showed it to be evident that a few formidable technical and cost barriers exist, and no effective approach for mitigating the barriers was evident in the near term.
- All significant barriers that pertain to the inverter, dc link capacitor, and motor were identified.
- Approaches for resolving many of the barriers were discussed in the study.
- Component-level issues were addressed in the study for operation at a significantly higher coolant temperature. These issues generally pertained to the cost and reliability of existing or near-term components that would be suitable for use with 105°C coolant. The assessed components included power electronic devices/modules such as diodes and insulated gate bipolar transistors (IGBTs), inverter-grade high-temperature capacitors, permanent magnets (PMs), and motor-grade wire insulation. The need for potentially modifying/resizing subassemblies such as inverters, motors, and heat exchangers was also addressed in the study.

Advance Thermal Interface Materials to Reduce Thermal Resistance

- Several CNT growth processes have been investigated and initial thermal resistance measurements on two-sided carbon nanotube TIM were conducted

Modeling Two-Phase Spray and Jet Impingement Cooling

- Completed and published results on 2 phase jet model
- Transferred results from single phase jet impingement modeling to low R IGBT structure
- CRADA with Bowles Fluidics to evaluate self-oscillating jets

Direct Cooling Options: An Assessment of Air Cooling for Use with Automotive Power Electronics Applications

- Developed thermal subsystem model for forced air and compressed air cooling
- Performed investigations of air cooling potential and system requirements

Thermal subsystem simulations

- Thermal resistance model developed to evaluate cooling potential of thermal control technologies
- Performed initial investigations into the impact of PHEVs on component thermal loads

Uncluttered CVT Machine

- The design of the proof-of-concept uncluttered rotor without windings and a half stator wound core to couple to the uncluttered rotor was completed. The uncluttered rotor and its half stator were fabricated,

and the uncluttered rotor teeth were machined out of solid steel instead of laminations in order to lower costs for the proof-of-concept prototype. The uncluttered rotor concept for the brushless rotating stator (or armature) was proved through tests conducted on the prototype.

Interior Permanent Magnet Reluctance Machines with Brushless Field Excitation—16,000 rpm

- The 16,000-rpm motor design was completed and the prototype fabricated. Initial testing was performed and a dimensional and cost analysis was made based upon the Toyota Prius motor. This motor design enables better motor performance with system cost savings. Also, if used in a vehicle architecture requiring a boost converter, this motor can produce 250-kW output at 16,000 rpm. This significantly widens the possible applications for this type of motor.

High-Power-Density Reluctance Interior Permanent Magnet Machines—6000 rpm

- The new technology derived from this project shows that the air-gap flux density produced by the new PM arrangement can be doubled compared with that of the Toyota/Prius motor. The PM torque component is proportional to the product of the PM fundamental air-gap flux density and the current of the motor. Therefore, the higher PM fundamental air-gap flux density produces higher toque at a given current of the motor and hence a higher power density of the motor.

Control of Fractional-slot Surface-mounted PM Motors with Concentrated Windings

- Two 55-kW surface permanent magnets (SPMs) with fractional slot concentrated windings (FSCW) incorporating FreedomCAR targets were designed and studied. SPM1 was selected for developing an analytical model to accurately predict the stator tooth and yoke iron losses in FSCW-SPM machines. SPM2 was selected for an analytical model comparison study.
- The SPM2 motor was modeled with SPEED software, and ORNL collaborated with the University of Wisconsin at Madison (UWM) to compare design parameters calculated using SPEED's PC-BDC module with those calculated by UWM.
- A closed-form analytical model was successfully developed that can accurately predict the stator tooth and yoke iron losses in FSCW-SPM machines during open-circuit operation.
- A detailed point-by-point finite-element analysis (FEA) of FSCW-SPM machines was completed and is proving very useful in identifying the relative contributions of hysteresis and eddy-current losses in different parts of the machine as a function of rotor speed.
- Three control schemes were developed.
  - — The UWM scheme controls to ensure maximum motor efficiency and shows how motor losses under load may be sufficiently reduced by field weakening, which increases total current, to offset the additional I2R losses and thereby improve motor efficiency.
  - — The first ORNL scheme is a low-cost scheme because it eliminates current sensors. The ORNL simulator assumes losses that increase with the square of the speed.
  - — The second ORNL scheme uses a set of antiparallel silicon controlled rectifiers in each phase to ensure that any load is accommodated with minimum current, which ensures that it is a maximum overall efficiency scheme.

- ORNL evaluated its first control scheme with the simulator for two constraints, first so that rated current is not exceeded and second so that rated power is not exceeded. The limiting current constraint allows considerably more power to be delivered over a large part of the power speed curve.

Extending the CPSR of Synchronous Reluctance Motors

- FLUX2D software was applied to a model of a PM motor that was created by ORNL to determine the phase advance, which is the angle between the center of a rotor pole and the stator current orientation

that will produce maximum torque. The model of the PM motor was created with inset magnets, and the magnets were turned off to simulate a synchronous reluctance motor with doubly salient poles. The torque produced was then calculated for a fixed rotor as the current in the stator was varied over one pole, and for current fixed in the stator with the rotor turned through one pole angle. Definite maxima were found with only rough agreement between the two approaches. A similar exercise with COMSOL demonstrated good agreement between the two approaches for estimating the phase advance for maximum torque.

- Using SPEED as a design tool, two synchronous reluctance motors were modeled to attempt to meet FreedomCAR targets. The first model with four turns per pole could not deliver maximum power at 2000 rpm. Adequate power at 2000 rpm required eight turns per pole, which doubled the amount of copper to increase both cost and weight. The motor was too heavy and too expensive to meet FreedomCAR goals.
- A per-phase model was designed by applying a winding function to a synchronous reluctance motor with salient rotor and stator poles to determine the inductance that should be used. This approach yielded direct and quadrature inductances, which had to be added for use in the model. Unfortunately, flux fringing, verified by a COMSOL analysis, indicated that use of the winding function was clearly an approximation. Later work showed that a reliable model should include not only flux fringing but also saturation.

Advanced Traction Motor Development

- The technical report entitled *FreedomCAR Advanced Traction Drive Motor Development Phase 1* was issued in September 2006. The report documents the design effort and conclusions reached by UQM Technologies, Inc. during the Phase 1 task. A 6 pole-pair machine with 36 slots in a 3-slot-per-pole configuration was determined to be the final design choice. The final design met or exceeded most of the 2010 FreedomCAR goals and traction motor technical targets.

Wide Bandgap Materials

- Several silicon carbide (SiC) Schottky diodes, junction field effect transistors (JFETs) and gallium nitride (GaN) Schottky diodes were acquired.
- SiC Schottky diodes, JFETs, and GaN Schottky diodes were tested, characterized, and modeled.
- A 55-kW all-SiC inverter was modeled and its performance was compared with that of similarly rated all-Si and Si-SiC hybrid inverters.
- High-temperature packages were built for SiC power devices to operate at 200°C.
- All-Si and Si-SiC (Si IGBTs and SiC Schottky diodes) hybrid inverters were built and tested and the results compared.

Integrated dc/dc Converter for Multi-Voltage Bus Systems

- Topology development
  - — A half-bridge–based dc/dc converter was developed that can interconnect the 14-V, 42-V and high-voltage buses and can reduce the component count by 50% over the conventional full-bridge–based technologies. Further refinements have eliminated the inductor capacitor (LC) filter for the 14-V bus.
  - — Interleaved modular configurations using the half-bridge as building blocks share the capacitor legs and provide a greater degree of component count reduction as the number of modules increases when scaling up the power level.
  - — The capacitor leg current in the interleaved configurations can be significantly reduced, thus decreasing the capacitance.
  - — A novel control scheme was also devised that can control the power flow among the three buses and reduce the flux density of the transformers.

- Prototype demonstration
  - A 4-kW prototype was designed and built using two 2-kW modules.
  - The prototype was successfully tested at load power levels of up to 4.6 kW.
  - Efficiencies were measured between 93.0 and 95.8% over a wide power range of 0.5 to 4.6 kW.
  - Evaluation of the prototype indicates that it exceeds the 2015 FreedomCAR targets for specific power and power density and the 2010 cost target.

Cascaded Multilevel Inverter

- A control algorithm was developed to keep the capacitors charged.
- The inverter/converter was simulated in PSpice and Simulink.
- A design simulation of an electrical drive system with the inverter/converter was developed.
- A 1.2-kW prototype was designed.

Advanced Converter Systems for High-Temperature HEV Environments

- Michigan State University designed and fabricated a 10-kW dc/dc converter module based on one of its earlier topologies.
- The University of Tennessee (UT) and ORNL devised an alternative dc/dc converter topology and fabricated a low-power proof-of-concept circuit to demonstrate its feasibility.
- UT and ORNL designed a high-temperature gate drive using a new silicon-on-insulator process by Atmel.
- Pennsylvania State University evaluated capacitors for high-temperature applications.

dc/dc Converter for Fuel Cell and Hybrid Vehicle

- Ballard focused on the production beta design to address differences between the DOE goals and the Alpha design results. The major achievement in FY 2006 was the design and verification of the final beta unit to meet the targets. Tasks included
  - Electrical improvements over the Alpha design
  - Cost reduction
  - Volume reduction
  - Weight reduction
  - Thermal design improvement
  - Manufacturing process improvements

Fully Integrated HEV Traction Motor Drive Development Using Thermoelectrics and Film Capacitor Innovations

- The thermoelectrics (TE) research that was performed was used to produce a comparison chart of commercially available TE devices. Many manufacturers' products were evaluated, and the data have been pulled together for comparison of costs and capabilities. Informative results were obtained that provide good insight into how the available TEs perform, and how some emerging TE technologies are improving performance in some helpful areas.
- A motor type was chosen in order to provide a tangible basis for design concepts and packaging innovations. The design chosen was a commercially available General Electric 5-kW induction motor.

Benchmarking of Competitive Technologies

- The efficiency mapping tests of the Prius PM synchronous motor (PMSM) and inverter were completed in a specially prepared test cell using an ORNL controller system developed for this project.
- The benchmarking design and packaging evaluation was completed for the Accord subsystems.

- The Accord motor was prepared with a new rotor shaft design and motor end plates, and the inverter was prepared through analysis of the circuit and the construction of auxiliary circuitry.
- Tests were completed on the Accord subsystems that included back–electromotive force, locked rotor, and efficiency mapping.
- Prius and Accord technical evaluations and test results were documented, and technical reports were issued for both during the year.

Component Characterization

- Commercial film and ceramic capacitor benchmarks were defined and characterized.
- Capacitor test samples were tested in two modes, statically and dynamically. Capacitor testing in the static mode requires a thermal cycling process that must continue uninterrupted for extended periods of time. Capacitor testing in the dynamic mode requires testing at thermal extremes and requires ripple current and bias voltage input from the operator.
- Magnet benchmarks for bonded and sintered magnets were defined and characterized.
- Magnet test samples were tested over a temperature range from 20 to 235°C.
- The development of a data acquisition system using LABView was completed to control the environmental chamber and to log data from the measuring instruments for capacitor evaluations.

High Temperature Film Capacitors

- Invented chemical synthesis procedures for three different polymer film families: (1) low cost polyphenylated polyethylene dielectrics, (2) polyaryl ether dielectrics, and (3) Norbornene based purified product.
- Developed a chemical synthesis route that resulted in lower cost polyphenylated polyphenylene product that should reduce cost of these polymer films by more than a factor of ten compared to previous synthesis routes.
- Demonstrated excellent high temperature electrical performance for low cost polyphenylated polyphenylene polymer dielectrics spin deposited on Al Coated Si wafers (dissipation factor less than 0.01 at 150^{o}C).

Embedded Capacitors for (P)HEV Power Electronic Systems

- Refined $LaNiO_3$ (LNO) buffer layers to avoid deleterious effects of a parasitic low capacitance interfacial oxide layer.
- Developed a core technology of PLZT/ LNO/ Ni capacitor foils with dielectric constants > 1150 (1.5 $\mu F/cm^2$) and loss $\leq$ 0.06.
- Developed PLZT/LNO/Ni capacitor foils reaching 580 V with breakdown fields $\geq$ 1.2 MV/cm.

Glass Ceramic Dielectrics for DC Bus Capacitors

- In FY2006 we evaluated flat panel display glass from Schott North America. The dielectric constant of 7 is triple that of conventional polymers, which will decrease the capacitor size by over 60%. In addition the permittivity is constant up to 400°C which far exceeds the DOE FreedomCAR goal of 140°C.

Susan Rogers
Advanced Power Electronics
FreedomCAR and Vehicle Technologies Program

2. Thermal Control for Power Electronics and Motors

2.1 Thermal Control for Inverters and Motors

Principal Investigator: John Hsu, Curtis Ayers, Chester Coomer
Oak Ridge National Laboratory
National Transportation Research Center
2360 Cherahala Boulevard
Knoxville, TN 37932
Voice: 865-946-1325; Fax: 865-946-1210; E-mail hsujs@ornl.gov

DOE Technology Development Manager: Susan A. Rogers
Voice: 202-586-8997; Fax: 202-586-1600; E-mail: Susan.Rogers@ee.doe.gov

ORNL Program Manager: Mitch Olszewski
Voice: 865-946-1350; Fax: 865-946-1262; E-mail: olszewskim@ornl.gov

---

Objectives

The objective of the Thermal Control for Inverters and Motors project is to reduce the size of the inverter by 50% in FY 2006 (based on the current size of the SemiKron 400-A, 160-kW inverter) and then reduce it to one-third of the original size in FY 2007 without negatively impacting the cost, life expectancy, and performance of the entire system.

Motor cooling is also addressed in this project. A cooler motor is particularly needed for plug-in hybrid vehicles because the demand on the motor is higher for providing sufficient torque and power without constantly relying on the help of the engine.

Approach

Much effort has been exerted within the electronics research community to improve semi-conductor die cooling, but little or no attention has been given to improving cooling for dc-link bus capacitors. Oak Ridge National Laboratory (ORNL) has recognized the importance of cooling all the components in the traction drive system, especially the dc-link capacitor. In this project, ORNL uses the passenger air conditioning (AC) coolant to aid in the cooling of the power electronics circuitry. Tapping into the AC system can enable cooling of the insulated gate bipolar transistors (IGBTs), diodes, dc-link capacitor, digital signal processors (DSPs), gate drives, and control power supply without relying on the AC compressor. Note that not all the components need to be submerged in the liquid refrigerant, because the refrigerant vapor and the hermetic housing of the refrigerant provide separate cooling environments for the different components of the inverter/motor drive system.

As part of this project, an oil-spray cooling method was investigated to improve motor cooling.

Approach in FY 2006

- Design and test motor heat exchanger with oil spray
- Design and fabricate hermetic container
- Fabricate film capacitor with tapered metal distribution and bare metal end connections
- Mount silicon dies in prototype cascade inverter
- Assemble and test inverter
- Perform initial integration of floating loop, inverter, and motor

Major Accomplishments

1. An oil spray cooling system for the drive motor was designed, fabricated, and tested. The cooling was significantly improved compared with oil-sling cooling systems.
2. ORNL designed, built, and tested a half-size, full-power inverter. The dc test reached 600-A capability (200 A per leg), and the ac switching test achieved 250 A_{RMS} for 3-phase output.

Technical Discussion for Motor Cooling

Motor windings will heat up in operation because of the finite resistance of the wire and the amperage load. Two primary motor cooling strategies have been used in the Power Electronics and Electric Machinery Research Center laboratory. The first, the "slinger" method, is patterned after the mechanism used in the Toyota Prius electric traction motor. The second method, the "pumped-spray" method, uses an external pump to spray cooled lubricant directly on the electric windings of the motor.

The "slinger" mechanism places a disk with a few slots cut radially into the outer edge adjacent to and rotating with the motor rotor. A portion of the disk periphery is immersed into cooling lubricant in the motor lower internals (the sump) so that during motor/disk rotation, the lubricant is picked up in the slots and hurled by centrifugal force onto the other motor internals, hence the name "slinger." This slinger arrangement has the advantage of simplicity and low cost. An obvious disadvantage is that the lubricant flow is not spread uniformly on the motor windings around the periphery of the motor internals. (However, this simple, inexpensive method may be better in some sense under low loads or short transients than a more complicated method.) A test apparatus was assembled to mirror as closely as possible the configuration of the Prius traction motor, and then operated at load to evaluate the performance of the simple slinger cooling method. The tests were conducted in 2004.

An external pump was used to spray cooling lubricant directly onto the motor windings to evaluate this more direct spray cooling method. This pumped-spray cooling method uses a dedicated external pump that takes coolant from the motor sump, passes it through a heat exchanger, and sprays the coolant through 18 nozzles distributed uniformly over the top half of the motor casing. The sprayed coolant impinges directly onto the motor stator windings, where the coolant drips off the windings back into the sump. To compare the results of the slinger tests with the pumped spray tests, the results were made as comparable as possible. They are shown in Table 1. The laboratory ambient temperature was approximately 20°C for both test series.

Table 1. Comparison of cooling methods

	Pumped spray	Slinger
Total electrical power (W)	2270	2070
Maximum winding temperature (°C)	59.2	142.0
Lubricant sump temperature (°C)	31.9	65.0
Pumping power (W)	104.0	96.0

The pumping power for the pumped-spray method was measured by the current and voltage draw of the dc motor that powered the rotary gear pump. The pumping power for the slinger method was measured by the load on the motor that powered the rotating slotted disk. Thus even though the pumped-spray method required an independent pump, a power increase of only approximately 8% was required for the increased cooling. The viscous drag and momentum transfer experienced by the rotating disk slinger method is not as effective in pumping cooling fluid as is the rotary gear pump.

Based on an inspection of Table 1, the pumped-spray method clearly reduced the maximum winding temperature by a considerable amount compared with the slinger, while removing approximately 10% more heat. This significant improvement in cooling is no doubt a result of the higher coolant flow rate and more uniform coolant distribution of the pumped-spray method. Although this method is more involved

than the simple slinger method, the results show a distinctly advantageous lower motor winding temperature.

Details of the Pumped-Spray Cooling Method

- It uses hydraulic fluid as the coolant, sprayed directly on windings and adjacent internal structure.
- The cooling subsystem uses commercially available components.
- A stainless steel brazed plate heat exchanger is used.
- Transmission oil is used.
- A gear pump is used.
- Screen filters are used.
- Multiple spray nozzles are aimed at hot spots

The motor cooling subsystem uses spray nozzles, as shown in Figure 1. The electric motor cooling test loop was designed, assembled, debugged, and tested on August 28, 2006. The test loop circulates the coolant through a heat exchanger, pumps the coolant, and sprays the cooled fluid on the motor windings. The cooling fluid is a synthetic hydraulic fluid, manufactured by Amsoil and designated as ATH. There were 12 spray nozzles on each of the two sides of the ORNL 6000-rpm BFE test motor; 3 were horizontally aimed at the excitation coil, and the remaining 9 were radially aimed at the stator windings in the upper half of the motor casing.



Figure 1. Photo of inside of motor housing showing spray nozzle locations.

For the electrical power levels tested, the motor stator windings were cooled well below the temperature limit of ~180°C. Test results are presented in Table 2, which reports the measured pressures; Table 3, which reports the measured phase currents, voltages, and total power; and Table 4, which reports the measured temperatures. The motor was wired in a delta configuration. There were three tests at the stated power levels. The loop pressures experienced by the cooling fluid for all power levels are given in Table 2. The pump dc motor was set to an 8-V and 13-A draw.

Table 2. Loop pressures

Place in loop	Gauge pressure (psi)
Pump discharge	26.0
HX inlet	26.0
HX outlet	19.5
Motor inlet	19.5

Table 3. Motor winding electrical parameters

Maximum line current (A)	Leg A-B		Leg B-C		Leg A-C		Total power (W)
	Current (A)	Potential (V)	Current (A)	Potential (V)	Current (A)	Potential (V)	
109.0	48.9	16.3	59.5	16.0	57.5	16.4	1535
205.4	86.0	27.9	109.7	27.2	105.3	27.1	6970
266.0	103.9	33.6	138.0	32.3	134.2	33.7	9439

Table 4. Temperatures

Thermocouple location	Test at 1448 W	Test at 5860 W	Test at 7491 W
1. Oil sump	26.0°C	32.8°C	42.0°C
2. Motor front, 1:00 outside stator	42.3°C	91.7°C	133°C
3. Motor back, 10:00 outside stator	34.5°C	60.0°C	81.2°C
4. Motor back, 12:00 inside stator	43.0°C	81.6°C	133°C
5. Motor front, 9:00 inside stator	34.2°C	77.5°C	79.0°C

The tests were conducted by first electrically powering the windings to yield the approximate maximum line current shown in Table 3 with the hydraulic pump off. The maximum line current is seen in the third line for the delta leg configuration given in Table 3. After less than a minute, the winding temperatures started to increase noticeably, and then the hydraulic pump was energized. This heatup procedure was used to decrease the time needed for a steady state to occur. The first trial procedure had the oil flowing before the ac current was initiated, and the elapsed time to a steady-state was much longer than desired. The oil was allowed to flow until no perceived change in the winding temperatures was noticed, approximately 10–15 minutes. The ac motor current was then shut off, and the temperatures decreased quickly. The dc pump motor was shut off after a few more minutes.

Although the power supply had the capability of providing higher power, further testing at higher power was not completed because the winding fibrous insulation external to the motor case started to smoke at currents higher than the maximum reported in Table 3. This smoke was probably from residual cooling fluid on the fibrous insulation. The spray cooling system was designed to cool only the inside of the motor and not the outside. Further tests could be conducted at higher powers if cooling external to the case were provided, such as simply using a fan to blow laboratory ambient air over the external motor leads.

As seen from the data in Table 3, the delta configuration was not perfectly balanced. The total power was calculated by squaring each leg current, multiplying by the leg resistance, and then adding the three leg powers. The measured resistance for Leg A–B is 0.162 ohm, for Leg B-C is 0.154 ohm, and for Leg A–C is 0.156 ohm, all measured at the laboratory ambient temperature of approximately 19°C. The resistance values were calculated based on the average temperature of the windings for the three maximum line-current cases, respectively. Table 1 shows that the coolant pumping power was 104 W for 2270 W total system power. It is important to note that for all total powers shown in Table 3, the coolant pumping power remained at 104 W.

The heat generation rate in the windings should be uniform at any position. Referring to Table 4 data, note that the maximum stator temperature occurred at the topmost positions for all tests. Also note that the winding temperature decreased as the thermocouple position became more horizontal. The spray nozzles, which had the same orifice diameter, were evenly spaced over the top half of the motor and were fed coolant from a common supply tube. This would imply that the coolant flow experienced by the windings increased with an increasingly more horizontal position. In addition, since the lower part of the stator is immersed in the oil sump, thermal conduction through the iron core and copper in the stator transports heat from the upper part of the stator to the oil sump. To lower this maximum winding temperature, it would be advantageous to bias the flow more toward the top of the motor by increasing the orifice size at

the topmost positions, decreasing the orifice size at the more horizontal positions, or perhaps eliminating the most horizontal orifice. This topmost orifice size bias might increase the other temperatures, but the objective of the spray cooling arrangement should be to decrease the maximum temperature no matter where it occurs.

Of particular note is that the temperature rise across the water side of the heat exchanger was on the order of 10°C above laboratory ambient for all tests, and the water pump head pressure was 26 psi for all tests. This low temperature rise might indicate that the heat load on the heat exchanger was low; it might also indicate that there was a fair amount of heat loss to ambient. The heat exchanger was noticeably warm to the touch but not hot, and there may have been a significant heat loss from the bare metal of the heat exchanger to ambient. The heat exchanger was oriented vertically, which might increase any natural convection to the lab ambient.

The ORNL tests described show that the hydraulic fluid motor cooling loop will keep the stator winding temperatures well below the temperature of concern for the power levels listed for these tests, even with the coolant pumping power maintained at a low level. The cost for the ORNL approach will be slightly higher because of the additional pump. However, an effort is ongoing to attempt to modify the exchanger and to incorporate the pump with the shaft to reduce costs.

Technical Discussion for Inverter Size Reduction

The goal for FY 2006 was to reduce the size of the inverter by 50%, using the Semikron inverter (Model 4001GD06) as a baseline (Figure 2).

Data published by Semikron rate this inverter at 160 kW using 25°C coolant, and 82 kW with 70°C coolant, with the *specific power at 9.9 kW/kg* and the *volumetric power density at 9.5 kW/liter*. The derated current for the 70°C condition is about 250 A_{RMS}. For purposes of comparison with the ORNL inverter that is based on a 50–60°C maximum coolant temperature (bulk liquid temp in a 2-phase system), the Semikron rating at 70°C will be used to provide a more even rating comparison. The ORNL inverter is rated at approximately 65 kW (based on dc test results and cooling capabilities), with 19 kW/kg and 21 kW/L power capabilities. Key specifications are compared in a tabular form in Table 5.

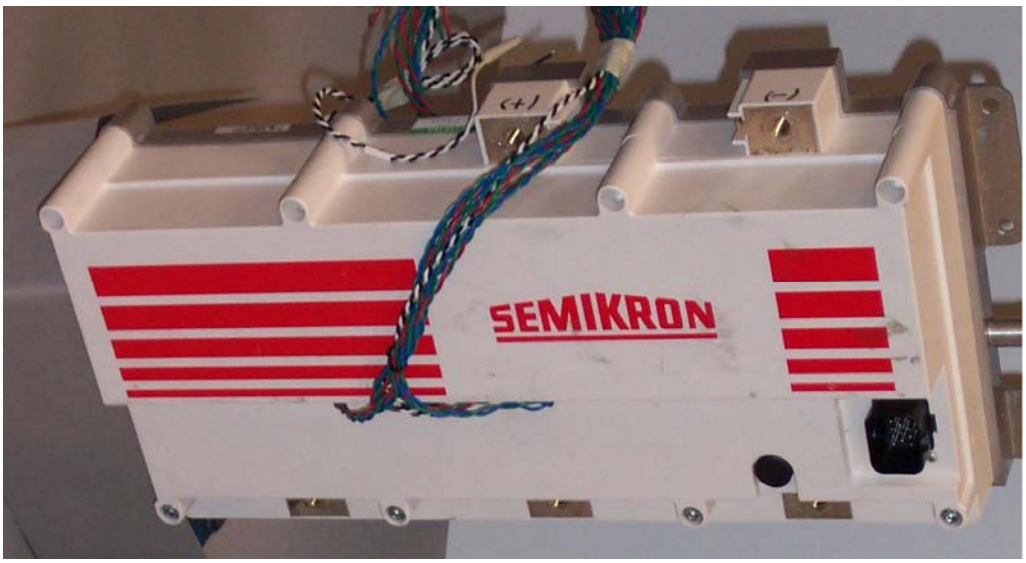


Figure 2. SEMIKRON Model 4001GD06 82-kW inverter.

Table 5. Comparison of key specifications

	Semikron 82 kW	ORNL 65 kW	FreedomCar targets 55 kW
Volume (l)	8.6	3.1	6.1
Full load amps	252	250	
kW/kg	9.9	19	11
kW/liter	9.5	21	9

Approach to Size Reduction

- Direct-contact 2-phase cooling technique (ORNL floating loop)
- Capacitor size reduction through shape innovation and lower-temperature environment
- Shift from conventional power electronics packaging methods

1. Direct two-phase cooling technique

The ORNL floating loop cooling system (refer to Publications section and related patents in the Patents section) is a direct contact 2-phase cooling technique that improves cooling sufficiently to partially enable a reduction in size from existing conventionally cooled inverters (Figure 3). The improved heat transfer coefficient achieved by directly submerging the power electronics devices and conductors in refrigerant (R134a in this research) allows the silicon devices to be pushed to higher current levels than conventional cooling will allow, with the same or reduced junction temperatures.

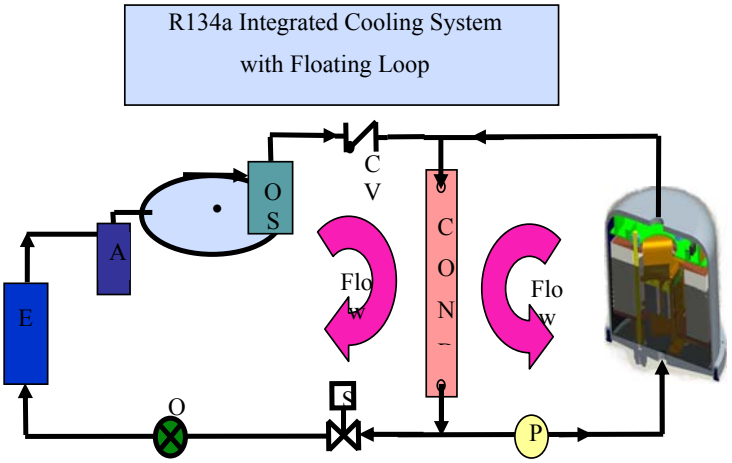


Figure 3. ORNL floating loop schematic diagram.

Conventional design (e.g., the Semikron design) depends on conduction cooling from one side of the silicon power chip to transfer heat through an electrically insulating layer (usually aluminum nitride) into the heat sink. The thermal resistance of this setup is high compared with direct 2-phase liquid cooling, in which the coolant itself completely surrounds the chips and the associated electrical conductors near the chips. Heat fluxes of as much as 95 W/cm^2 (using both sides of the silicon chip as heat transfer areas) have been achieved in the laboratory during testing of the ORNL FY 2006 half-size inverter. This result is based on dc load testing in which up to 167 W has been dissipated from each of 12 IGBT chips at the

peak dc loading. Similar calculations for the Semikron inverter indicate about 42 W per chip of heat dissipated, which equates to less than 50 W/cm^2 (using one side of the chip as conduction heat transfer area). These data indicate that about four times as much heat is being removed from each chip using the direct-cooling technique.

The current test results were limited at this stage by the loading equipment capabilities presently available at ORNL. Testing will continue for higher currents when the loading capability is increased in the near future. The gate driver circuitry, which was designed for a lower-current-capability IGBT, presently exhibits a saturation voltage protection that is too low. This situation is also limiting some of our output current tests. The protection enables around 250 A for a given leg of the 3-phase circuit, which is made up of two IGBT chips. The IGBTs themselves have been tested using a Tektronix high-power curve tracer and do not show any current saturation in this range. The saturation curve in Figure 4 shows that the pair of chips can handle a collector current of 384 A and that the Vce/Ic curve is still linear at the 384-A point. This indicates that the pair of chips can exceed this value by a significant amount, allowing the chips to be pushed to a higher current than previous tests have used.

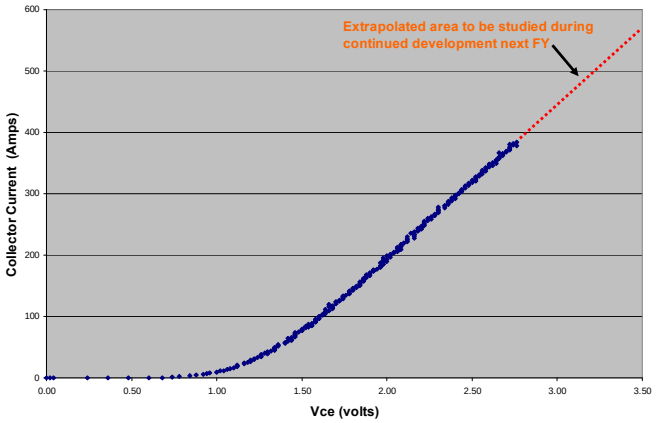


Figure 4. Curve tracer data showing Semikron current capability.

During the next fiscal year, the gate drive circuits will be fully matched to the IGBTs that are chosen for the final 1/3-size prototype. This modification will enable maximum power density to be drawn from that assembly. The loading equipment will be upgraded to handle the needed inverter current and power output to complete the full-power testing.

2. Capacitor size reduction

The dc link capacitor design that was chosen for this project has resulted in a much smaller capacitor for the ORNL cylindrical half-size inverter. The capacitors being used are polypropylene film, 900 V and 500 microfarads (µf). Polypropylene capacitor has been undergoing various types of tests while submerged in R134a over the past 2 years. The actual inverter capacitor being used has been tested in a submerged manner over the past 6 months for ripple current capability and is now being tested in the actual full-power inverter configuration in dc and ac tests. These tests prove the viability of the capacitor for this type of use and thus enable the size and volume of the required dc link capacitance to be significantly reduced. Tests to date indicate we can achieve a 50% size reduction, and ongoing ripple current tests will determine what the maximum reduction in capacitance for inverter usage can be.

Laboratory Capacitor Performance Tests

- Maximum ripple current: 300 A_{RMS}
- Resonance frequency: 8 kHz

Figure 5 shows the Semikron inverter capacitor on the left and the cylindrical inverter capacitor on the right. Not only is the configuration significantly different, but also the volume and thus the mass are very different. The Semikron capacitor depends on conduction heat transfer through the bottom of the package and acceptable ambient conditions around the top of the inverter housing. The ORNL capacitor configuration, along with the design concept, allows the capacitor to be directly surrounded by liquid coolant. This insulates it from ambient conditions to a large degree and maintains the capacitor core temperature close to bulk liquid temperature. The typical operating temperature for the capacitor in this design will be less than 60ºC, as opposed to temperatures under the hood of around 90–125ºC.

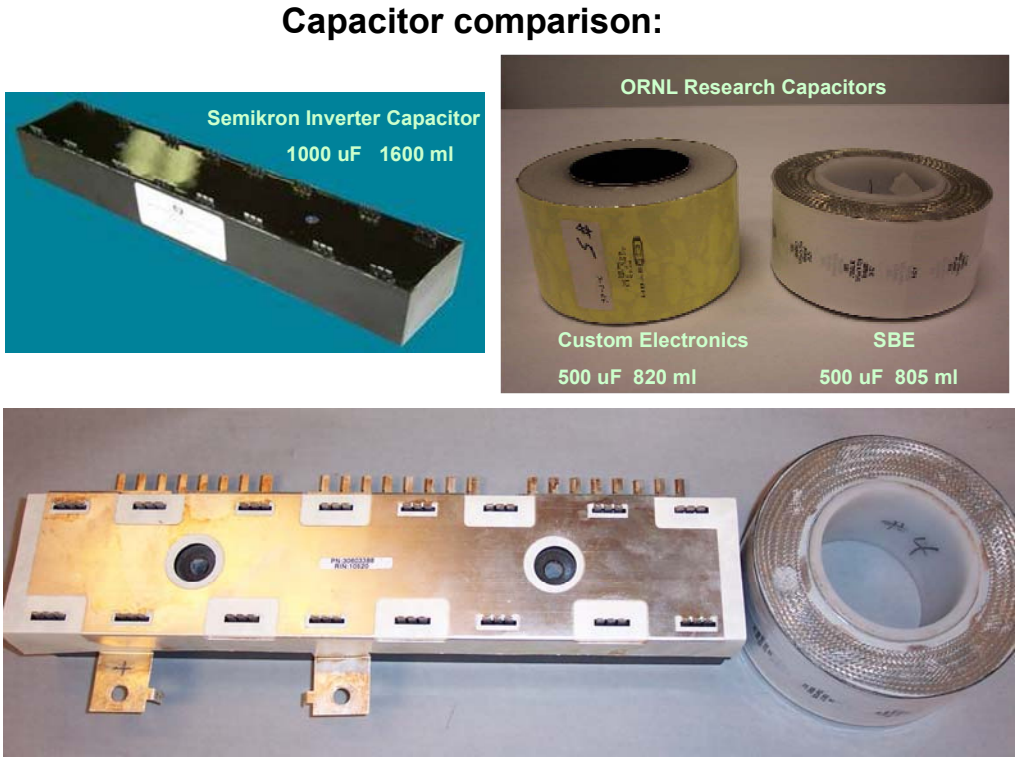


Figure 5. Comparison of Semikron 82-kW dc link capacitor and Custom Electronics and SBE cylindrical capacitors for ORNL half-size inverter. The ORNL design reduces capacitance and volume by 50%.

3. Shift from conventional electronics packaging methods

The long, rectangular block shape of the Semikron capacitor fits the conventional inverter design, which is typically planar and rectangular. Heat removal from the typical inverter is unidirectional through the bottom of the package to a cold plate cooled with water or air. The ORNL approach is to achieve the most volume-efficient shape, which is a sphere or cube. The cylindrical capacitor with a hollow core enables this type of 3-dimensional design.

The first ORNL FY 2006 prototype was developed to perform dc load testing. Figure 6 shows the core of the power section of the inverter, which is built from subsections of the Semikron DBC power electronics cards (Figure 7). The dc link capacitor was not needed for these tests, so it is not installed in this prototype.



Figure 6. Core of first FY 2006 ORNL prototype inverter.

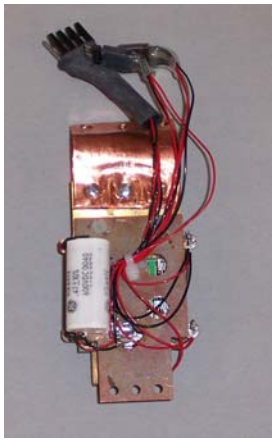


Figure 7. Power IGBT subassembly.

ORNL chose to use the Semikron DBC power board for the FY 2006 half-size inverter prototype for expediency in building and testing the whole inverter geometry to meet the FY 2006 goals. In the meantime, plans and modeling efforts are ongoing to develop the final substrate geometry that will be used to help complete the final 1/3-size inverter. The full board used by Semikron provides power to one of the three phases of the inverter. ORNL was able to cut the full board into three discrete subsections to efficiently turn one board into three boards to serve for all three phases on the new inverter. Figures 8 and 9 show the full board and the subsection used by ORNL. The subsection is the power section used in

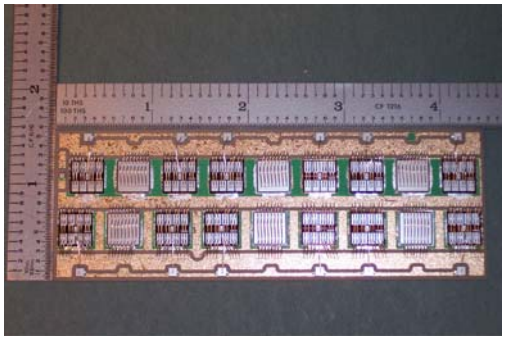


Figure 8. Semikron power IGBT board.

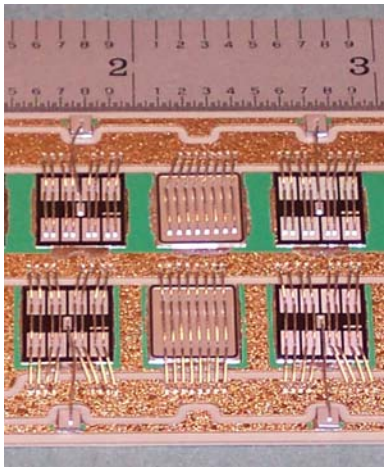


Figure 9. One of three sections of the Semikron board used to produce subassemblies for prototype.

the power subassembly shown in Figure 7. It uses 1/3 of the silicon chips required in the full Semikron board but provides essentially the same current and power performance.

The first row seen in Figure 8 makes up one of the six legs of a full inverter with an IGBT-diode-IGBT arrangement. The second row of chips makes up a second leg in one phase of the inverter—the pair can be represented by A_{upper} and A_{lower}, for example, for the A phase. The 3-dimensional shape that is the core of ORNL's design can begin to be seen in this assembly. It becomes even more evident with the final prototype half-size inverter design seen in the 3-dimensional model shown in Figure 10.

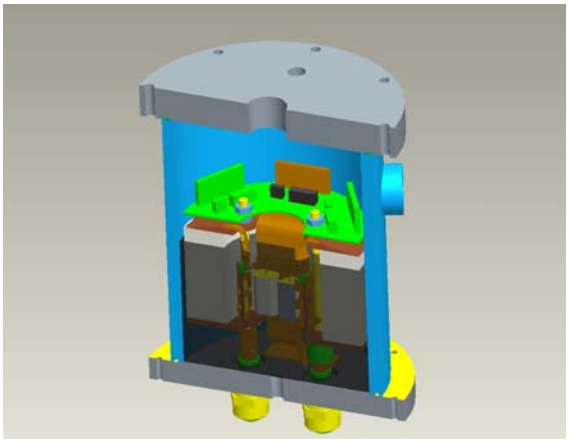


Figure 10. A three-dimensional model of the ORNL prototype showing assembly components.

In the cross-section view in Figure 10 can be seen the dc link cylindrical capacitor; the power electronics subassemblies are packaged in the hollow core of the capacitor. The dc links, disks mounted on the top and bottom ends of the capacitor, feed dc power from the external feed-throughs (seen at bottom) to the power electronics subassemblies in the center. The 3-phase output from the subassemblies exits the housing through the bottom alongside the dc input feeds. The dark shaded area shows an approximate liquid level for the coolant, and the gate driver and interface card can be seen on the top of the assembly.

Liquid feed to the system is through the bottom in the center, and vapor removal (to the condenser) is through the center of the top. This design depicts our test vessel, not a "final" design. A model of a standalone inverter might look like the unit shown in Figure 11. This model has been used to calculate the specific power and volumetric power density, and a plastic vessel/assembly has been built to verify packaging possibilities.

This model was developed with ProEngineer Wildfire software, and materials and densities of each of the parts were supplied to the software. Using this information, the software was used to provide volume and mass information for the whole model.

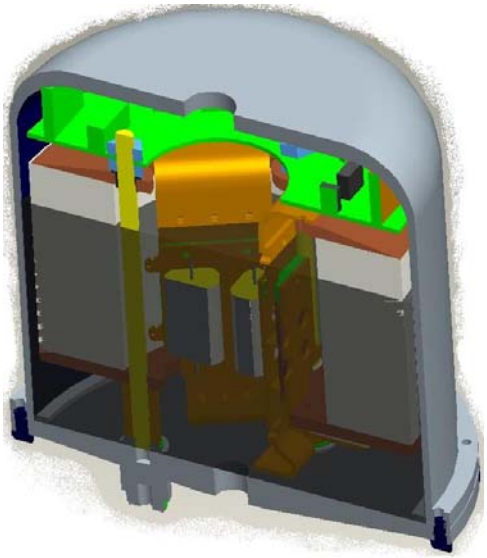


Figure 11. Model showing tighter packaging.

The FY 2006 ORNL model, which is calculated to provide approximately 65 kW of power output, has an estimated volume of 3.1 L and an estimated mass of 3.5 kg. The size and mass calculations include the DSP controller, accessory power supplies, and an interface board, estimated using the solid modeling software. For this phase of the development, these components were placed outside the pressure housing. Future developments can show the feasibility of internal or external mounting for these components. The finished inverter core is shown in Figure 12. The subassembly is complete, ready for insertion into the housing in preparation for full-power ac output. The system power is fed into a dummy R-L load on the 3-phase output to test for maximum current capability.

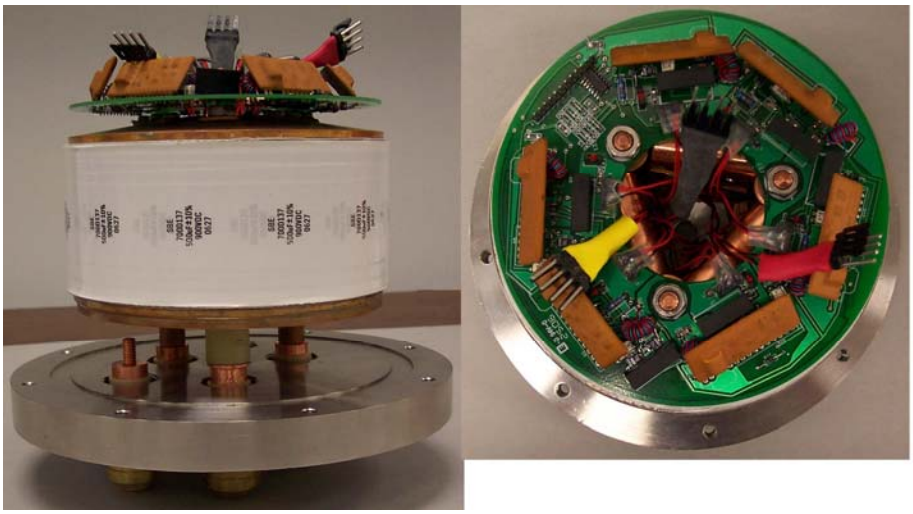


Figure 12. Side view and top view of ORNL prototype internal components.

Laboratory Testing for the ORNL Inverter Prototype

The first prototype was built early in the year to provide testing and data, using the re-sized Semikron boards. This unit primarily served as the dc loading prototype, but lessons learned in construction and mounting of the dies were used to improve the final half-size prototype design built later in the year. dc load testing was performed in the following manner. The inverter was built as a full-fledged 3-phase inverter with individual gate controls as usual. For the dc test, the plus and minus dc link were wired directly into the power supply with no load in between. The phase outputs of the inverter were left open-circuited since no ac output was being created. The gates for all the legs of the inverter were turned fully on for the duration of the test, and the chips themselves served as the load for the test in a short-circuit configuration. This configuration would cause the IGBTs to fail if the current during the test were not controlled, so the power supply was operated in current control mode. The voltage was allowed to float as the current was increased for the dc tests. This method produces heat in the IGBTs without the need to produce controlled ac output currents, and it was appropriate for the initial year's load testing. The IGBTs heated up with increasing dc current, and a temperature-to-current capability was determined. A dc test setup was developed to provide a method of measuring junction temperatures based on forward voltage drops, in order to correlate surface-mounted temperature measurement methods (such as thermistors or thermocouples). We hope to develop this method so that it can be used directly in operating inverters; but at this point, it requires a more steady-state operating condition (dc instead of ac output).

ac load testing was set up in a much more conventional manner: a full-fledged inverter with a DSP controller connected to a 3-phase R-L output load. The power was supplied to the inverter by a dc power supply at voltages up to 350 V_{dc}. The existing load equipment at ORNL at this time prevented full power

(full calculated power is 65 kW), but it reached approximately the full load current required of 250 A. The FreedomCAR inverter output capability was reached (55 kW), but higher values are expected from this inverter design that will produce the high specific power and volumetric power density that were calculated based on dc test results. Some trouble was experienced above 225 A_{RMS}, but only because of a mismatch of the gate driver and the particular IGBTs that were used for this prototype. A false saturation condition was detected, causing the gate drivers to shut down at around 250 A_{RMS}. As seen in the Semikron saturation curve (Figure 4), this value can be increased significantly (hopefully to ~ 400 A_{RMS}) when the gate drive problems are resolved.

The test results for this project year are listed in Table 6. Data sheets from the power analyzer taken at the various test levels are found in Appendix A. These results, along with the calculated specific power and volumetric power densities, show that the goal of a 50% reduction from the baseline for inverter size was reached.

Table 6. One-half size inverter test results

dc OUTPUT TEST (all gates turned on, current controlled):
— used to determine overall cooling capability for the IGBTs, and maximum current capability

dc link (volts)	dc current (A)	Power losses (W)
3.3	400	1430
3.6	500	2000

ac OUTPUT TEST (operated with DSP controller with R-L output load):
— these tests help determine overall operability of the inverter, and maximum power capability

dc link (v)	Modulation index	V_{ac} output	A_{RMS} output	Power out (kW)
350	0.95	255	153	55
150	0.15	25	200	4 (load reconfigured)
104	~0.2	45	225	8.1

Conclusions

- Tests on the oil spray cooling of the motor confirm that oil-spray cooling is a more effective cooling system than oil-sling cooling system in the same motor structure.
- Motor cooling test data are as follows:
  - Maximum power: 9.4 kW @ 266 A, 104 W pump power
  - Maximum temperature: 133°C @7.5 kW
- Coolant pump power can be tailored to the cooling load demand. For lower cooling demand periods, the pump speed (and thus power) can be reduced. When higher system power is needed, and thus more motor cooling, the coolant pump flow rate can be increased as needed.
- There is at least a 4.5 : 1 increase in motor heat removal with no change in the required input coolant pumping power.
- The 500-µf dc link film capacitor functions well while submerged in refrigerant.
- The dc link capacitor tests reveal no limitations so far in handling of ripple current of up to 300 A_{rms}. These tests will continue in order to determine the maximum ripple current capability. Results of the ripple current capability tests will determine the final size for the capacitor. It appears that the capacitor can be reduced in size and volume.

- Tests on the half-size full rated inverter, including dc load and ac tests were conducted. The dc load tests confirmed that the inverter meets the full-load half-size objective. The output capability was successfully tested at up to 55 kW and is expected to be higher based on load calculations from dc test data. Loading capability limitations prevented testing at a higher power for this fiscal year.
- The size of the FY 2006 inverter is calculated at 3.1 L, including the DSP controller, accessory power supplies, interface electronics, and the inverter core itself. This is a reduction of more than 50% from the published Semikron size of 8 L.

ORNL One-half size inverter dc load testing

A_{dc} input	490
A_{RMS} output	347 (calculated)
Max power	110 kW (calculated)
Chip T	70 C
Delta T	38 C
Chip cooling	167 W/chip

ORNL One-half size inverter ac load testing

Maximum A_{RMS} output: 250
Maximum power output: 55 kW (limited only by output loading capability)
Inverter chip temp

- Specific power density for the FY 2006 prototype inverter = 19 kW/kg
  - Semikron baseline is 9.9 kW/kg; improvement is 92%
- Volumetric power density for the FY 2006 prototype inverter = 21 kW/liter
  - Semikron baseline is 9.5 kW/L; improvement is 121%

Future Direction

- Complete prototype design of ORNL substrate/IGBT mounting
- Redesign gate driver to match new IGBTs
- Use double-side die mounting without wire bonds
- Complete capacitor ripple current testing to determine final size/volume
- Integrate suitable components inside inverter shell
- Prototype and test new feedthrough concept for I/O connections

Publications

Curt Ayers and Kirk Lowe, "Fundamentals of a Floating Loop Concept Based on R134a Refrigerant Cooling of High Heat Flux Electronics," presented at SemiTherm22 Conference, Dallas, March 2006.

Kirk Lowe and Curt Ayers, "Operating Controls and Dynamics for Floating Refrigerant Loop for High Heat Flux Electronics," presented at SemiTherm22 Conference, Dallas, March 2006.

Patents

John Hsu, Curtis Ayers, Chester Coomer, and Laura Marlino, "Floating Loop System for Cooling Integrated Motors and Inverters Using Hot Liquid Refrigerant," U.S. Patent 6,993,924 B2, February 7, 2006.

John S. Hsu, Donald J. Adams, Gui-Jia Su, Laura D. Marlino, Curtis W. Ayers, and Chester Coomer, "Cascaded Die Mountings with Spring-Loaded Contact-bond Options," U.S. Patent 6,930,385, August 16, 2005.

John S. Hsu, Donald J. Adams, Gui-Jia Su, Laura D. Marlino, Curtis W. Ayers, and Chester Coomer, "Total Thermal Management System for Hybrid and Full Electric Vehicles," U.S. Patent 6,772,603, August 10,2004.

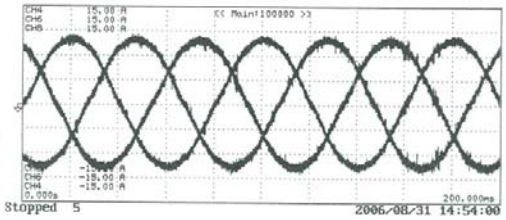
John S. Hsu and William S. Schwenterly, "Superconducting PM Undiffused Machines with Stationary Superconducting Coils," U.S. Patent No. 6,700,297, March 2, 2004.

Appendix A. Power Analyzer Data Sheets from ac Testing of the ORNL Half-size Inverter

DC$_{in}$ Ph A Ph. B Ph. C PWR$_{out}$

YOKOGAWA ◆ Uover:▪ ▪ ▪ ▪ 200ms 500kS/s
CH3 120Vpk Iover:▪ ▪ ▪ ▪ 200ms 500kS/s

	Element1	Element2	Element3	Element4	Σ A	Σ B
Urms[V]	44.98	32.41	32.33	32.30	44.98	32.35
Umn [V]	49.96	27.43	27.31	27.23	49.96	27.32
Udc [V]	44.98	-0.03	-0.18	0.06	44.98	-0.05
Uac [V]	0.14	32.41	32.33	32.30	0.14	32.35
Irms[A]	7.82	6.91	6.92	6.93	7.82	6.92
Imn [A]	8.46	6.87	6.88	6.90	8.46	6.88
Idc [A]	7.52	0.08	0.06	0.14	7.52	0.09
Iac [A]	2.14	6.91	6.92	6.93	2.14	6.92
P [W]	0.338k	0.165k	0.154k	0.010k	0.338k	0.319k
S [VA]	0.352k	0.224k	0.224k	0.224k	0.352k	0.388k
Q [var]	0.096k	-0.152k	0.162k	0.223k	0.096k	0.010k
λ [ ]	0.9621	0.7351	0.6895	0.0440	0.9621	0.8226

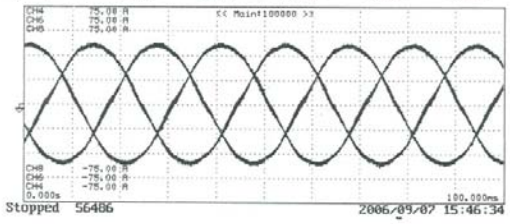


Stopped 5 2006/08/31 14:54:00

9/7/06

YOKOGAWA ◆ Uover:▪ ▪ ▪ ▪ 100ms 1MS/s
CH8 0.1Apk Iover:▪ ▪ ▪ ▪ 100ms 1MS/s

	Element1	Element2	Element3	Element4	Σ A	Σ B
Urms[V]	0.00	0.00	0.00	0.00	0.00	0.00
Umn [V]	0.00	0.00	0.00	0.00	0.00	0.00
Udc [V]	0.00	0.01	0.01	0.03	0.00	0.02
Uac [V]	0.00	0.00	0.00	0.00	0.00	0.00
Irms[A]	35.16	32.01	32.03	31.97	35.16	32.00
Imn [A]	38.92	31.89	31.90	31.84	38.92	31.87
Idc [A]	35.04	0.09	0.06	0.19	35.04	0.11
Iac [A]	2.98	32.01	32.03	31.97	2.98	32.00
P [W]	0.000k	-0.000k	0.000k	-0.000k	0.000k	-0.000k
S [VA]	0.000k	0.000k	0.000k	0.000k	0.000k	0.000k
Q [var]	0.000k	0.000k	0.000k	0.000k	0.000k	0.000k
λ [ ]	Error	Error	Error	Error	Error	Error



32 Amps
205 VDC
~7 kW

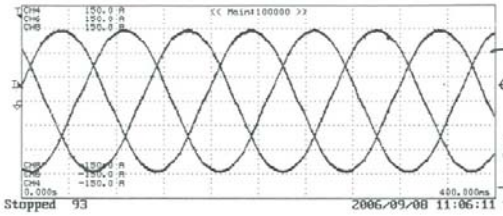
Stopped 56486 2006/09/07 15:46:34

DC = 175 VDC

PWR in ≈ 14 kW

YOKOGAWA ◆ Uover:= = = =
CH1 300Vpk Iover:= = = =
200ms 500kS/s
200ms 500kS/s

	Element1	Element2	Element3	Element4	Σ A	Σ B
Urms[V]	174.47	126.11	126.04	125.76	174.47	125.97
Umn [V]	193.77	103.94	103.82	103.40	193.77	103.72
Udc [V]	174.45	-0.14	-0.22	0.42	174.45	0.02
Uac [V]	2.37	126.11	126.04	125.76	2.37	125.97
Irms[A]	82.47	77.47	77.53	77.62	82.47	77.54 → 77.30
Imn [A]	89.09	77.18	77.23	77.51	89.09	77.30
Idc [A]	80.20	0.11	-0.01	0.23	80.20	0.11
Iac [A]	19.20	77.47	77.53	77.62	19.20	77.54
P [W]	13.99k	7.417k	6.132k	1.284k	13.99k	13.549k → 13.549k
S [VA]	14.39k	9.769k	9.772k	9.762k	14.39k	16.918k
Q [var]	3.38k	-6.358k	7.608k	-9.677k	3.38k	1.250k
λ [ ]	0.9720	0.7592	0.6275	0.1315	0.9720	0.8009



Stopped 93 2006/09/08 11:06:11

pf = 1

eff ≈ 97%

pwm 2kHz

f_{elec} = 25 hz

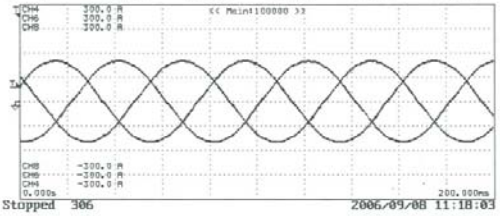
MI = 0.9

DC = 200 VDC

PWR_{in}

YOKOGAWA ◆ Uover:= = = =
CH1 300Vpk Iover:= = = =
200ms 500kS/s
200ms 500kS/s

	Element1	Element2	Element3	Element4	Σ A	Σ B
Urms[V]	200.16	144.68	144.69	144.67	200.16	144.68
Umn [V]	222.30	119.06	119.06	119.12	222.30	119.08
Udc [V]	200.14	-0.36	-0.40	0.04	200.14	-0.24
Uac [V]	2.71	144.68	144.69	144.67	2.71	144.68
Irms[A]	94.35	88.89	88.73	88.69	94.35	88.77 → 88.47
Imn [A]	101.94	88.67	88.37	88.36	101.94	88.47
Idc [A]	91.76	-0.01	-0.07	0.58	91.76	0.16
Iac [A]	21.96	88.89	88.73	88.69	21.96	88.77
P [W]	18.36k	9.773k	8.056k	1.668k	18.36k	17.829k → 17.829k
S [VA]	18.89k	12.860k	12.837k	12.831k	18.89k	22.245k
Q [var]	4.44k	-8.359k	9.995k	-12.722k	4.44k	1.636k
λ [ ]	0.9720	0.7599	0.6275	0.1300	0.9720	0.8015



Stopped 306 2006/09/08 11:18:03

pf

eff = 97.1%

pwm 2khz

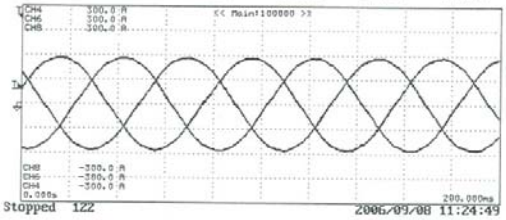
f_{elec} = 25hz

MI = 0.9

DC = 225 VDC

YOKOGAWA ◆ Uover:▪ ▪ ▪ ▪ 200ms 500kS/s
CH1 300Vpk Iover:▪ ▪ ▪ ▪ 200ms 500kS/s

	Element1	Element2	Element3	Element4	Σ A	Σ B
Urms[V]	225.06	163.32	162.87	162.63	225.06	162.94
Umn [V]	249.96	134.63	133.96	133.68	249.96	134.09
Udc [V]	225.04	0.10	-0.29	0.75	225.04	0.19
Uac [V]	3.15	163.32	162.87	162.63	3.15	162.94
Irms[A]	105.86	99.96	99.58	99.80	105.86	99.78
Imn [A]	114.41	99.79	99.25	99.58	114.41	99.54
Idc [A]	103.00	0.14	-0.13	0.19	103.00	0.07
Iac [A]	24.45	99.96	99.58	99.80	24.45	99.28
P [W]	23.17k	12.419k	10.189k	2.093k	23.17k	22.607k
S [VA]	23.83k	16.326k	16.218k	16.230k	23.83k	28.160k
Q [var]	5.55k	-10.598k	12.618k	-16.094k	5.55k	2.419k
λ [ ]	0.9724	0.7607	0.6282	0.1290	0.9724	0.8028



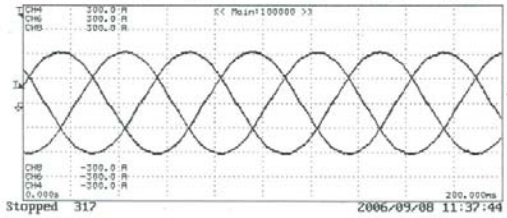
Stopped 122 2006/09/08 11:24:49

PWR in
I_{out}
P_{out}
pf
eff = 97.6%

DC = 250 VDC

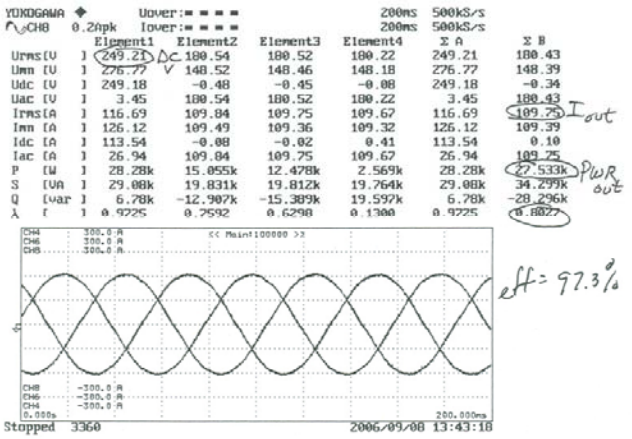
YOKOGAWA ◆ Uover:▪ ▪ ▪ ▪ 200ms 500kS/s
CH8 0.4Apk Iover:▪ ▪ ▪ ▪ 200ms 500kS/s

	Element1	Element2	Element3	Element4	Σ A	Σ B
Urms[V]	249.56	181.20	180.66	180.45	249.56	180.77
Umn [V]	277.16	149.19	148.50	148.21	277.16	148.64
Udc [V]	249.53	0.19	0.06	0.24	249.53	0.16
Uac [V]	3.49	181.20	180.66	180.45	3.49	180.77
Irms[A]	117.06	110.65	109.96	110.09	117.06	110.23
Imn [A]	126.51	110.37	109.48	109.68	126.51	109.84
Idc [A]	113.89	0.28	0.11	0.22	113.89	0.20
Iac [A]	27.06	110.64	109.96	110.09	27.06	110.23
P [W]	28.41k	15.255k	12.471k	2.49k	28.41k	27.73k
S [VA]	29.21k	20.049k	19.864k	19.87k	29.21k	34.51k
Q [var]	6.82k	-13.009k	15.462k	-19.71k	6.82k	2.45k
λ [ ]	0.9724	0.7609	0.6278	0.1251	0.9724	0.8034



Stopped 317 2006/09/08 11:37:44

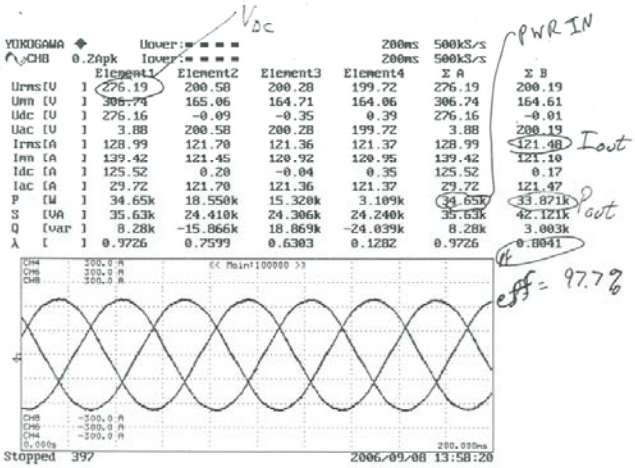
PWR in
I_{out}
P_{out}
pf
eff = 97.6%



I_{out}

PWR_{out}

$eff = 97.3\%$



V_{DC}

PWR_{IN}

I_{out}

P_{out}

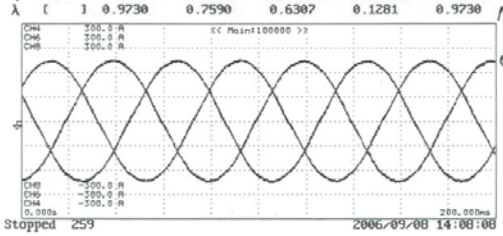
$eff = 97.7\%$

300Vdc

YOKOGAWA ◆ Uover:▪ ▪ ▪ ▪ 200ms 500kS/s
CH8 0.2Apk Iover:▪ ▪ ▪ ▪ 200ms 500kS/s

	Element1	Element2	Element3	Element4	Σ A	Σ B
Urms[V]	300.25	217.45	217.49	217.32	300.25	217.42
Umn [V]	333.46	178.68	178.72	178.55	333.46	178.65
Udc [V]	300.22	-0.21	-0.13	-0.48	300.22	-0.27
Uac [V]	4.23	217.45	217.49	217.32	4.23	217.42
Irms[A]	139.62	131.58	131.57	131.47	139.62	131.54
Imn [A]	150.98	131.21	131.25	130.99	150.98	131.15
Idc [A]	135.92	-0.16	0.49	0.25	135.92	0.19
Iac [A]	31.94	131.58	131.57	131.47	31.94	131.54
P [W]	40.79k	21.717k	18.046k	3.659k	40.79k	39.763k
S [VA]	41.92k	28.611k	28.614k	28.570k	41.92k	49.534k
Q [var]	9.68k	-18.627k	-22.207k	28.335k	9.68k	-40.834k
λ [ ]	0.9730	0.7590	0.6307	0.1281	0.9730	0.8027

pwr IN
Iout
Pout
pf
eff = 97.5%



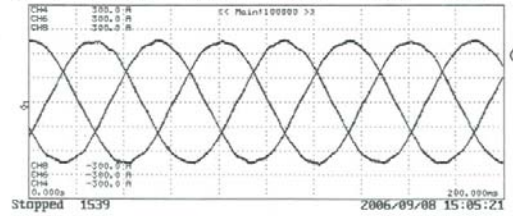
Stopped 259 2006/09/08 14:08:08

VDC = 300 V Robicon

YOKOGAWA ◆ Uover:▪ ▪ ▪ ▪ 200ms 500kS/s
CH6 0.2Apk Iover:▪ ▪ ▪ ▪ 200ms 500kS/s

	Element1	Element2	Element3	Element4	Σ A	Σ B
Urms[V]	304.13	220.33	220.64	220.05	304.13	220.34
Umn [V]	337.73	180.98	181.31	180.67	337.73	180.99
Udc [V]	304.06	-0.32	-0.40	0.26	304.06	-0.15
Uac [V]	6.50	220.33	220.64	220.05	6.50	220.34
Irms[A]	138.03	133.15	133.01	133.01	138.03	133.06
Imn [A]	152.83	132.79	132.52	132.61	152.83	132.64
Idc [A]	137.59	0.11	-0.13	0.51	137.59	0.17
Iac [A]	11.07	133.15	133.01	133.01	11.07	133.06
P [W]	41.84k	22.268k	18.491k	3.74k	41.84k	40.76k
S [VA]	41.98k	29.337k	29.346k	29.27k	41.98k	50.78k
Q [var]	-3.47k	19.100k	-22.788k	29.03k	-3.47k	-3.69k
λ [ ]	0.9966	0.7590	0.6301	0.1279	0.9966	0.8027

Approx pwr IN
Iout
Pout
pf =
eff = 97.4%



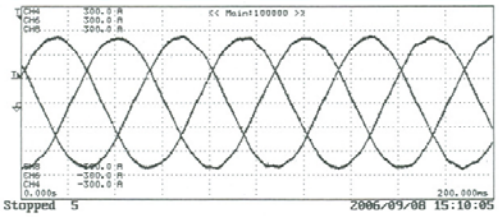
Stopped 1539 2006/09/08 15:05:21

325 Vdc Robicon

YOKOGAWA ◆ Uover:= = = = 200ms 500kS/s
CH1 600Vpk Iover:= = = = 200ms 500kS/s

	Element1	Element2	Element3	Element4	Σ A	Σ B
Urms[V]	327.62	237.35	237.41	237.02	327.62	237.26
Umn [V]	363.82	194.92	194.96	194.58	363.82	194.82
Udc [V]	327.55	-0.38	-0.54	0.22	327.55	-0.23
Uac [V]	6.66	237.35	237.41	237.02	6.66	237.26
Irms[A]	148.41	143.09	143.16	143.15	148.41	143.13
Imn [A]	164.33	142.70	142.72	142.72	164.33	142.72
Idc [A]	147.95	0.13	-0.18	0.49	147.95	0.14
Iac [A]	11.69	143.09	143.16	143.15	11.69	143.13
P [W]	48.46k	25.775k	21.422k	4.40k	48.46k	47.20k
S [VA]	48.62k	33.962k	33.988k	33.93k	48.62k	58.82k
Q [var]	3.95k	-22.115k	26.387k	-33.64k	3.95k	4.27k
λ [ ]	0.9967	0.7589	0.6303	0.1296	0.9967	0.8024

PWRIN PWR OUT



Stopped 5 2006/09/08 15:10:05

pf=

eff = 97.4%

R134a ⇒ 1.26kW

Vdc

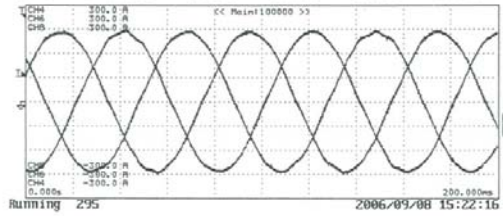
YOKOGAWA ◆ Uover:= = = = 200ms 500kS/s
CH1 600Vpk Iover:= = = = 200ms 500kS/s

	Element1	Element2	Element3	Element4	Σ A	Σ B
Urms[V]	351.70	254.64	254.71	254.29	351.70	254.55
Umn [V]	390.58	209.11	209.17	208.69	390.58	208.99
Udc [V]	351.64	-0.41	-0.48	-0.01	351.64	-0.30
Uac [V]	6.52	254.64	254.71	254.29	6.52	254.55
Irms[A]	159.26	153.56	153.74	153.45	159.26	153.58
Imn [A]	176.36	153.14	153.25	152.99	176.36	153.13
Idc [A]	158.77	0.00	-0.09	0.52	158.77	0.14
Iac [A]	12.40	153.56	153.74	153.45	12.40	153.58
P [W]	55.83k	29.675k	24.695k	5.05k	55.83k	54.37k
S [VA]	56.01k	39.103k	39.158k	39.02k	56.01k	67.71k
Q [var]	4.47k	-25.465k	30.390k	-38.69k	4.47k	4.93k
λ [ ]	0.9968	0.7589	0.6306	0.1295	0.9968	0.8030

Iout

Pout

pf



Running 295 2006/09/08 15:22:16

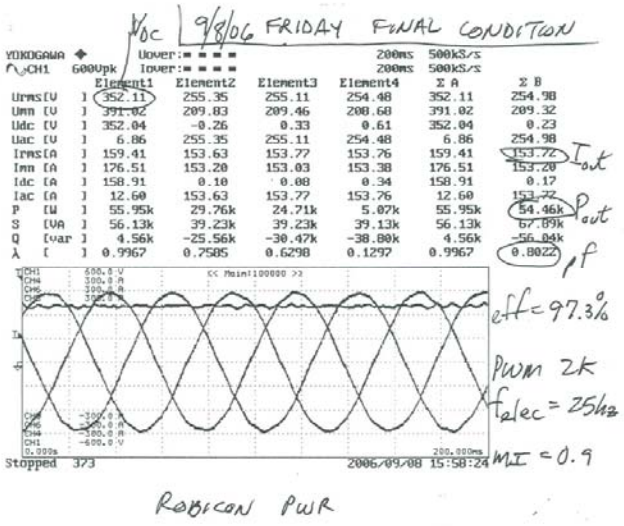
eff = 97.4%

Pwm 2kHz

25 fdec

MI (0.9)

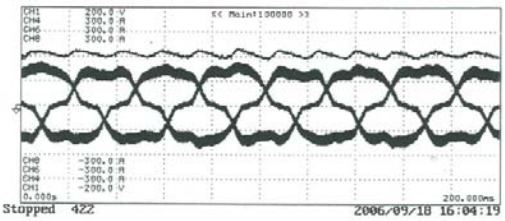
1.5 kW internal cooling


Voc 9/8/06 FRIDAY FINAL CONDITION
YOKOGAWA
CH1 600Vpk
Uover:
Iover:
200ms 500kS/s
200ms 500kS/s
Element1 Element2 Element3 Element4 Σ A Σ B
Urms[V] 352.11 255.35 255.11 254.48 352.11 254.98
Umn [V] 391.02 209.83 209.46 208.68 391.02 209.32
Udc [V] 352.04 -0.26 0.33 0.61 352.04 0.23
Uac [V] 6.86 255.35 255.11 254.48 6.86 254.98
Irms[A] 159.41 153.63 153.77 153.76 159.41 153.72
Imn [A] 176.51 153.20 153.03 153.38 176.51 153.20
Idc [A] 158.91 0.10 0.08 0.34 158.91 0.17
Iac [A] 12.60 153.63 153.77 153.76 12.60 153.72
P [W] 55.95k 29.76k 24.71k 5.07k 55.95k 54.46k
S [VA] 56.13k 39.23k 39.23k 39.13k 56.13k 67.09k
Q [var] 4.56k -25.56k -30.47k -38.80k 4.56k -56.04k
λ [ ] 0.9967 0.7585 0.6298 0.1297 0.9967 0.8022
Stopped 373
2006/09/08 15:58:24
Iout
Pout
pf
eff=97.3%
PWM 2k
felec = 25Hz
MI = 0.9
ROBICON PWR

Y-Y txfmr, delta load

YOKOGAWA ◆ Uover:▪ ▪ ▪ ▪ 200ms 500kS/s
CH8 0.2Apk Iover:▪ ▪ ▪ ▪ 200ms 500kS/s

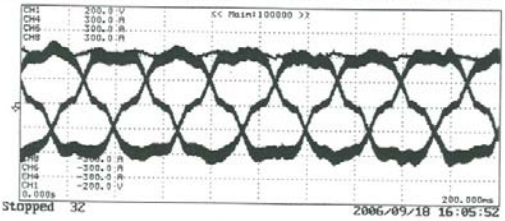
	Element1	Element2	Element3	Element4	Σ A	Σ B
Urms[V]	104.13	27.35	27.37	26.96	104.13	27.23
Umn [V]	115.56	10.61	10.58	10.32	115.56	10.50
Udc [V]	104.04	0.04	0.04	0.05	104.04	0.04
Uac [V]	4.29	27.35	27.37	26.96	4.29	27.23
Irms[A]	13.74	77.57	75.41	77.26	13.74	26.75 Iout
Imn [A]	14.06	74.46	72.11	75.45	14.06	74.01
Idc [A]	12.30	3.27	-3.75	23.36	12.30	7.63
Iac [A]	6.11	77.50	75.31	73.65	6.11	75.49
P [W]	1.282k	0.491k	0.434k	0.021k	1.282k	0.925k Pout
S [VA]	1.431k	2.122k	2.064k	2.083k	1.431k	3.619k
Q [var]	-0.634k	-2.064k	2.017k	2.083k	-0.634k	-0.047k
λ [ ]	0.8963	0.2315	0.2102	0.0103	0.8963	0.2556



Stopped 422 2006/09/18 16:04:19

YOKOGAWA ◆ Uover:▪ ▪ ▪ ▪ 200ms 500kS/s
CH8 0.2Apk Iover:▪ ▪ ▪ ▪ 200ms 500kS/s

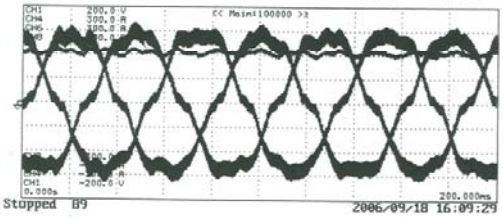
	Element1	Element2	Element3	Element4	Σ A	Σ B
Urms[V]	104.02	32.60	32.56	32.56	104.02	32.57
Umn [V]	115.45	14.15	14.11	14.18	115.45	14.15
Udc [V]	103.94	0.12	0.06	0.26	103.94	0.15
Uac [V]	4.07	32.60	32.56	32.56	4.07	32.57
Irms[A]	26.23	112.69	110.63	109.71	26.23	111.01 Iout
Imn [A]	27.78	108.85	106.77	105.40	27.78	107.01
Idc [A]	24.71	3.60	-4.27	1.36	24.71	0.23
Iac [A]	8.81	112.63	110.55	109.71	8.81	110.96
P [W]	2.570k	1.031k	0.933k	0.047k	2.570k	1.964k Pout
S [VA]	2.729k	3.674k	3.602k	3.572k	2.729k	6.263k
Q [var]	0.915k	-3.526k	3.479k	-3.572k	0.915k	-0.047k
λ [ ]	0.9420	0.2807	0.2589	0.0132	0.9420	0.3136



Stopped 32 2006/09/18 16:05:52

YOKOGAWA ◆ Uover:= = = = 200ms 500kS/s
CH8 0.2Apk Iover:= = = = 200ms 500kS/s

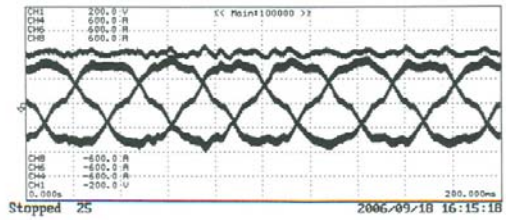
		Element1	Element2	Element3	Element4	Σ A	Σ B
Urms	[V]	104.03	37.47	37.47	37.60	104.03	37.51
Umn	[V]	115.44	18.12	18.09	18.25	115.44	18.15
Udc	[V]	103.94	0.16	2.04	-0.32	103.94	0.63
Uac	[V]	4.49	37.47	37.41	37.60	4.49	37.49
Irms	[A]	45.56	152.61	151.17	149.29	45.56	151.02 Iout
Imn	[A]	48.84	148.17	147.67	144.28	48.84	146.71
Idc	[A]	43.78	3.77	21.66	1.95	43.78	9.13
Iac	[A]	12.64	152.57	149.61	149.28	12.64	150.48
P	[W]	4.553k	1.892k	1.752k	0.086k	4.553k	3.644k Pout
S	[VA]	4.740k	5.719k	5.664k	5.613k	4.740k	9.813k
Q	[var]	1.318k	-5.397k	5.386k	5.612k	1.318k	-0.010k
λ	[ ]	0.9606	0.3308	0.3094	0.0152	0.9606	0.3714



Stopped 89 2006/09/18 16:09:29

YOKOGAWA ◆ Uover:= = = = 200ms 500kS/s
CH8 0.4Apk Iover:= = = = 200ms 500kS/s

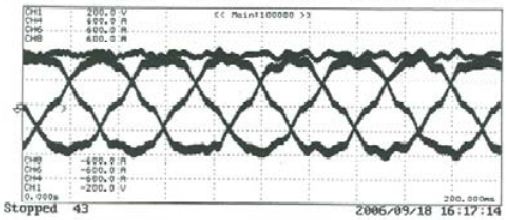
		Element1	Element2	Element3	Element4	Σ A	Σ B
Urms	[V]	103.98	40.14	39.98	39.96	103.98	40.03
Umn	[V]	115.36	20.53	20.38	20.44	115.36	20.45
Udc	[V]	103.86	4.17	-0.06	-0.16	103.86	1.32
Uac	[V]	4.99	39.92	39.98	39.96	4.99	39.95
Irms	[A]	59.71	179.19	174.36	173.05	59.71	175.53 Iout
Imn	[A]	64.18	176.57	170.51	168.22	64.18	171.77
Idc	[A]	57.68	55.77	-4.85	2.41	57.68	17.78
Iac	[A]	15.44	170.29	174.29	173.04	15.44	172.54
P	[W]	5.995k	2.60k	2.33k	0.11k	5.995k	4.94k Pout
S	[VA]	6.208k	7.19k	6.97k	6.91k	6.208k	12.17k
Q	[var]	1.614k	6.70k	-6.57k	6.91k	1.614k	0.13k
λ	[ ]	0.9656	0.3622	0.3343	0.0159	0.9656	0.4056



Stopped 25 2006/09/18 16:15:18

YOKOGAWA ✦ Uover:▪ ▪ ▪ ▪ 200ms 500kS/s
CH0 0.4Apk Iover:▪ ▪ ▪ ▪ 200ms 500kS/s

	Element1	Element2	Element3	Element4	Σ A	Σ B	
Urms[V]	103.96	42.59	42.59	42.59	103.96	42.59	
Umn [V]	115.32	22.92	22.90	22.92	115.32	22.92	
Udc [V]	103.82	0.15	0.03	-0.02	103.82	0.05	
Uac [V]	5.38	42.59	42.59	42.59	5.38	42.59	
Irms[A]	77.55	202.02	199.92	199.26	77.55	200.40	I_{out}
Imn [A]	83.62	197.35	195.63	194.73	83.62	195.90	
Idc [A]	75.23	3.14	-5.09	2.69	75.23	0.24	
Iac [A]	18.86	202.00	199.86	199.24	18.86	200.36	
P [W]	7.813k	3.32k	3.07k	0.15k	7.813k	6.38k	P_{out}
S [VA]	8.063k	8.60k	8.51k	8.49k	8.063k	14.78k	
Q [var]	1.989k	-7.94k	7.94k	8.48k	1.989k	0.00k	
λ [ ]	0.9691	0.3855	0.3603	0.0173	0.9691	0.4319	

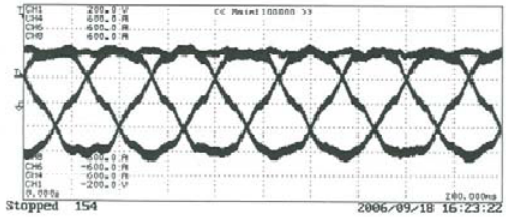


Stopped 43 2006/09/18 16:17:14

DC Link

YOKOGAWA ✦ Uover:▪ ▪ ▪ ▪ 200ms 500kS/s
CH8 0.4Apk Iover:▪ ▪ ▪ ▪ 200ms 500kS/s

	Element1	Element2	Element3	Element4	Σ A	Σ B	
Urms[V]	103.81	44.88	44.84	44.83	103.81	44.85	
Umn [V]	115.17	25.37	25.28	25.39	115.17	25.35	
Udc [V]	103.69	0.14	-0.13	-0.23	103.69	-0.07	
Uac [V]	5.04	44.88	44.84	44.83	5.04	44.85	
Irms[A]	97.19	226.85	224.59	223.33	97.19	224.92	I_{out}
Imn [A]	105.09	222.00	220.33	218.38	105.09	220.24	
Idc [A]	94.58	2.75	-4.36	2.38	94.58	0.26	
Iac [A]	22.38	226.83	224.54	223.32	22.38	224.90	
P [W]	9.80k	4.20k	3.88k	0.17k	9.80k	8.08k	P_{out}
S [VA]	10.09k	10.18k	10.07k	10.01k	10.09k	17.47k	
Q [var]	2.39k	-9.27k	-9.29k	10.01k	2.39k	-18.57k	
λ [ ]	0.9715	0.4125	0.3850	0.0171	0.9715	0.4623	



Stopped 154 2006/09/18 16:23:22

2.2 Identifying the Barriers and Approaches to Achieving High-Temperature Coolants

Principal Investigator: John Hsu
Oak Ridge National Laboratory
National Transportation Research Center
2360 Cherahala Boulevard
Knoxville, TN 37932
Voice: 865-946-1325; Fax: 865-946-1262; E-mail: hsujs@ornl.gov

DOE Technology Development Manager: Susan A. Rogers
Voice: 202-586-8997; Fax: 202-586-1600; E-mail: Susan.Rogers@ee.doe.gov

ORNL Program Manager: Mitch Olszewski
Voice: 865-946-1350; Fax: 865-946-1262; E-mail: olszewskim@ornl.gov

---

Objectives

The goal of this project is to identify the barriers and approaches to achieving high-temperature coolant operation for the traction drive components of a hybrid vehicle and to identify the cost benefits/penalties when moving from a dedicated cooling loop at 65°C to the use of 105°C coolant from the engine radiator.

This assessment is important because automotive manufacturers are interested in utilizing the existing water/glycol engine cooling loop to cool hybrid electric vehicle (HEV) subassemblies to eliminate an additional coolant loop with its associated reliability, space, and cost requirements. In addition, the cooling of power electronic devices, traction motors, and generators is critical in meeting the FreedomCAR and Vehicle Technology (FCVT) goals for power rating, volume, weight, efficiency, reliability, and cost.

System tradeoffs will be taken into account in studying the use of high-temperature coolants. Corresponding radiator size, electronics packaging issues, motor housing size, pumps, hoses, power electronics, reliability of components, and meeting the 15-year FreedomCAR lifetime goal will be assessed against cost. The result of this effort will be a definitive analysis of the issues and tradeoffs involved with increasing the coolant temperature so as to ascertain the feasibility of moving ahead with 105°C coolant in hybrid vehicles.

Approach

The approach in this project is to review available literature and data to identify the barriers and approaches to achieving high-temperature coolants. A 50/50 water/glycol mixture will be used as a baseline coolant at 105°C in this investigation. Information will be collected from technical literature and industry.

Because heat flux is proportional to the temperature difference between the device's hot surface and the coolant, a device that can tolerate higher temperatures enables the device to be smaller while dissipating the same amount of heat. Trench insulated gate bipolar transistors (IGBTs) with higher-junction-temperature (175°C) silicon dies are gradually emerging into the market. This is an option that could provide more cooling margin in using 105°C coolant. Additionally, the permissible ripple current of various types of dc bus capacitors decreases rapidly as temperatures increase. New film dc-bus capacitors with higher-temperature capabilities are also emerging in the market. Necessary modifications to the existing cooling loop will be studied; cost, size, volume and weight tradeoffs assessed; and the results of the study reported.

The cooling of the power electronic devices, traction motors, and generators is critical in meeting the FreedomCAR goals for volume, weight, efficiency, reliability, and cost. Currently, the most commonly used coolant in automotive applications is a 50/50 water/glycol liquid mixture. The combustion engine is normally cooled by <100°C n reach 105ºC or higher. Commercially available automotive-grade silicon electronic components have maximum junction temperature limits of 125°C. Therefore, the temperature difference between the junction and the 50/50 mix coolant of these devices is 20ºC (i.e., 125°C – 105°C). The less temperature difference that exists between the coolant and the dies' permissible junction temperature, the less margin there is to dissipate heat to the coolant environment.

This investigation focuses on identifying the barriers and approaches to achieving high-temperature coolants by analyzing the benefits and tradeoffs to using high-temperature coolants from the component, module, and system level perspectives.

Major Accomplishments

This study was performed by Oak Ridge National Laboratory (ORNL) to identify practical approaches, technical barriers, and cost impacts to achieving high-temperature coolant operation for certain traction drive subassemblies and components of HEVs. HEVs are unique in their need for the cooling of certain dedicated-traction drive subassemblies/components that include the electric motor(s), generators(s), inverter, dc converter (where applicable), and dc link capacitors. The new coolant system under study would abandon the dedicated 65°C coolant loop, such as used in the Prius, and instead rely on a 105°C engine cooling loop.

Because there is high interest by original equipment manufacturers (OEMs) in reducing manufacturing cost to enhance their competitive standing, the approach taken in this analysis was designed to be a positive, "can-do" approach that would be most successful in demonstrating the potential or opportunity of relying entirely on a high-temperature coolant system. Nevertheless, it proved to be clearly evident that a few formidable technical and cost barriers exist, and no effective approach for mitigating the barriers was evident in the near term.

The goals of the project were fully met by the identification of all significant barriers that pertain to the inverter, dc link capacitor, and motor. Approaches for resolving many of the barriers were also discussed; however, the full range of solutions will only come from additional R&D.

For operation at a significantly higher coolant temperature, component-level issues had to be addressed in this study. These issues generally pertained to the cost and reliability of existing or near-term components that would be suitable for use with the 105°C coolant. The assessed components include power electronic devices/modules such as diodes and IGBTs, inverter-grade high-temperature capacitors, permanent magnets (PMs), and motor-grade wire insulation. The need for potentially modifying/resizing subassemblies, such as inverters, motors, and heat exchangers, was also addressed in the study.

To obtain pertinent information to assist ORNL researchers to address the thermal issues at the component, module, subassembly, and system levels, preexisting laboratory test data obtained at varying temperatures were analyzed in conjunction with information obtained from technical literature searches and industry sources.

Technical Discussion

This project considers the potential temperature-related impacts on the performance of materials, components, and subsystems used in a Prius-like HEV traction system based on increasing the cooling loop temperature from 65°C to 105°C. The sections below focus on (1) the inverter power electronic devices, (2) inverter dc link capacitors, and (3) selected PM synchronous motor (PMSM) components that have the highest vulnerability to operation at elevated temperatures. The barriers that will be identified in each of these three main subsections will be those barriers that may prevent the components and subsystems from operating reliably during a 15-year service life when cooled by a 105°C cooling loop.

Note: The potential need for resizing the radiator was assessed, and it was determined that (1) the HEV heat load is small compared with that of the engine and (2) the air-to-coolant differential

temperature would be much higher, improving heat dissipation. Therefore, the need for a size change is considered minor or nonexistent.

Inverter/Converter Power Electronics Circuitry

This section considers what barriers may exist to operating the inverter and converter packages at 105°C. The analysis will consider inverter bus voltages of up to 500 Vdc for meeting peak power operation. Similarly, the Prius uses a 500-V boost converter, and the short-duration peak current in each leg of the inverter is ~200 A_{RMS}.

Conventional silicon-based materials and power device packaging designs are clearly challenging barriers to the use of a high-temperature coolant because junction temperatures will need to increase in high-temperature-coolant-based inverters to ~150°C. For this reason, currently marketed but not fully life-tested devices will be considered in this analysis: silicon-based trench IGBTs and high-temperature diodes, both with junction temperature ratings of up to 175°C. These IGBTs and diodes are presently available from several manufacturers.

Although device specifications list "175°C" maximum junction temperatures, the technology for these trench IGBTs and diodes is not mature; consequently, many design details must be considered that would normally have less importance. These include the determination of ratings for the actual parallel-device module packaging, observing current-dependent thermal deratings, observing temperature ratings for switching vs conductance, and the need to consider exactly how the module will be cooled in the final design.

On a positive note, Semikron's recent efforts at developing a 133-kW high-temperature inverter system show the high potential of using even presently available power electronic devices. Their analysis showed[1] that the 40°C coolant rise did not require an increase in inverter size or in the number of power electronic devices. This was based on (1) using new high-temperature devices, (2) using devices with lower losses, (3) increasing the power density, and (4) improving the heat sink. Only a modest cost increase was projected for the power electronics.

This assessment of high-temperature power electronics did not identify any serious barriers, except for the use of conventional silicon-based power electronics. Instead, a listing was developed of what might best be characterized as weak barriers for the cooling of the inverter and converter subsystems at 105°C. This is based on individual assessments of the thermal performance of trench IGBTs and the potential for thermal fatigue and wire bonding failures in the power electronics device packaging.

The following describes both *potential* barriers for the inverter/converter and certain design considerations that merit mentioning:

1. As expected, conventional silicon-based materials and power device packaging cannot support the use of a high-temperature coolant because junction temperatures will need to increase to ~150°C.
2. Recent literature[2] indicates that new 600-V IGBTs, using a trench metal oxide semiconductor top cell with ultra-thin 70-µm wafer technology, may be qualified for 175°C junction temperature, but the maximum operating temperature under switching conditions is reduced to 150°C. Because 150°C is much better than 125°C and most likely adequate based on development efforts, the thermal derating issue is a design consideration. More recently and subsequent to this study, Infineon Technologies announced 200°C junction temperature trench IGBTs.
3. There appears to be a significant potential for a solder-related fatigue issue that would limit the lifetime of IGBTs below 15 years if the use of a high-temperature coolant is implemented. This must be further investigated so that appropriate high-temperature solders, sintering, or other known technologies are employed.
4. The cooling requirements of the inverter driver board must be thoroughly evaluated and/or certain driver circuit components may have to be upgraded to maintain reliability/expected life at elevated temperatures.

Thermal Assessment of High-Temperature dc Link Capacitors

The capacitors used at the high-voltage dc-link-to-inverter interface are of interest because, within the bounds of current technology, it is very challenging to manufacture capacitors that provide adequate ripple current at the elevated temperatures. Even in a 65°C system, the present technology can barely meet this high-temperature application with acceptable volume, mass, cost, and reliability/lifetime. Highlighting this fact, the Prius capacitor module has a mass of 3.1 kg (almost 7 lb). In the case of the Prius, the modular polymer film capacitor takes up a significant portion of the volume inside the inverter/converter housing, as indicated in Figure 1.

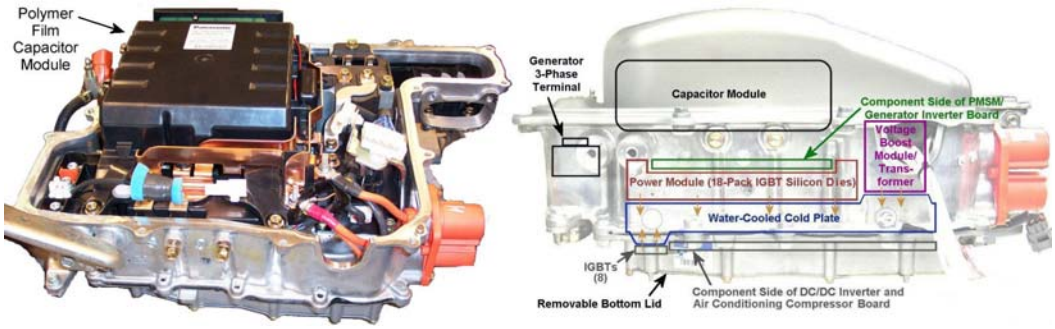


Figure 1. Modular capacitor position and size in the Prius inverter/converter casing.

The above concerns are certainly less of an issue for inverters placed in the much cooler passenger compartment as Honda does in its HEV line; however, that is outside the scope of this assessment, which considers only the use of a 105°C coolant for cooling of the HEV components and subsystems.

An engine compartment temperature of 140°C is considered applicable in the inverter design where a coolant-filled "cold plate" covers the base of a fully enclosed aluminum case in which the dc link capacitor is housed. Adopting a 105°C inverter coolant loop will increase the temperature of all the components in the casing, including the capacitor. There is also the potential for active capacitor cooling in some future HEV design.

Although many types of dielectrics exist, polymer film capacitors are generally produced with polypropylene, polyester, polycarbonate, or polystyrene. The temperature effects of these dielectrics result in changes in the capacitance, dissipation factor, and lifetime of film capacitors. High temperatures limit the available ripple current levels. Alterations in capacitance and dissipation factor play a large role in the amount of power dissipated and ultimately in the efficiency of the capacitor.
The amount of power dissipated across a capacitor is given as

$$P = V_{AC}{}^2 * 2\pi f * C * DF = \frac{I_{AC}{}^2}{2\pi f * C} * DF \quad . \tag{1}$$

The maximum heat removal capacity is

$$P = \frac{\Delta T}{R_{th}} \quad . \tag{2}$$

Solving these two equations for the current ripple yield

$$I_{AC} = \sqrt{\frac{(T_R - T_A) * 2\pi f * C}{R_{th} * DF}} \quad . \tag{3}$$

Assuming that a 500-µF capacitor has a case thermal resistance, R_{th}, of 130W/°C and that the capacitor is operated at a 5-kHz inverter switching frequency at rated temperature, the plots in Figure 2 show the maximum available ripple current of the capacitor vs temperature for polymer film and ceramic capacitors.

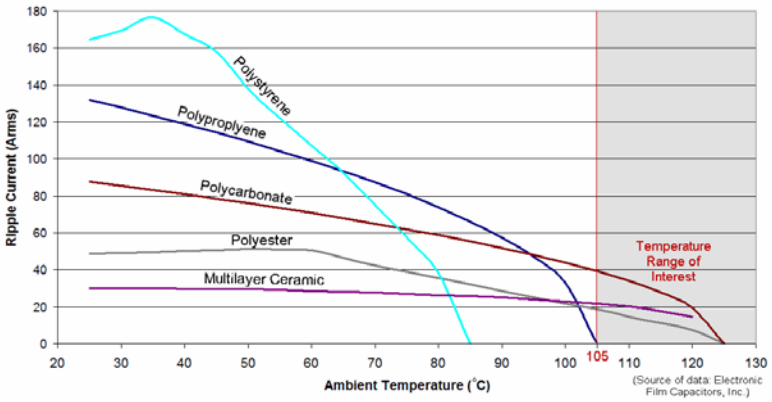


Figure 2. Ripple current vs ambient temperature for high-temperature capacitors.

Clearly, the adverse affect of temperature on ripple current is a serious issue. Even the polycarbonate, polyester, and ceramic capacitors do not appear to be of any potential use within the shaded range of interest. This leads to the question of what capacitors are being developed in laboratories or in the process of entering into production. Unfortunately, products in development are shrouded in secrecy, and details are considered to be proprietary. This has provided a serious obstacle to the assessment of high-temperature capacitors.

ORNL is able to report that a leading ceramic capacitor manufacturer produces a high-temperature capacitor for which the specifications are reportedly: 16 µF per module, 400-V continuous, I_{ripple} = 25A @ 125°C maximum, and the cost is $20/module. Based on the required ripple current in an inverter, ~7 modules would be needed in parallel at a total cost of $140 in large-quantity purchases. However, the 400-V limit is problematic because a 600-V rating for an appropriate margin in HEV systems includes a 500-V boost converter.

Other, higher-cost 400-V capacitors were reported, but there were no reports of newly developed 600-V, high-temperature, inverter-grade capacitors being available other than prohibitively expensive Teflon capacitors. However, Semikron[3] reports that in the process of their development of a high-temperature inverter, they reached the conclusion that commonly available, 600-V capacitors can be used if three are placed in parallel. Using this approach instead of utilizing a high-temperature capacitor increases the volume, mass, and cost by a factor of 3; this is considered a serious penalty.

New capacitors with improved specifications and significantly lower cost are expected in 1 to 2 years—or in 10 years—depending on which technical or industry source is consulted.

The design barriers for dc-link capacitors include the following:

1. Temperature increases in the dc-link capacitor application have a strong and detrimental effect on the ripple current specification for many types of polymer capacitors.

2. High-temperature (125°C or higher) capacitors with adequate ripple current and a 600-V continuous rating can be found today by taking existing capacitors and using three in parallel. This approach triples cost and size, which is a serious penalty and a major barrier. There is a need for low-cost, high-temperature capacitors, and it is important that these be brought to the market soon.
3. The reliability and lifetime of any newly released, high-temperature capacitors must be well established through testing before they are introduced into vehicles.
4. Ceramic capacitors have superior high-temperature performance compared with polymer film capacitors; however, presently the cost is high, and an unacceptable energetic and flammable failure mode exists.
5. Teflon capacitors have excellent high-temperature performance, but cost is clearly prohibitive.

Thermal Characterization of Magnets

Neodymium-iron-boron (NdFeB) magnets are the most powerful of all the magnets commonly used in industry and are made of advanced rare-earth materials. They provide high performance and resilience against demagnetization. However, these magnets are extremely sensitive to temperature and susceptible to oxidation if not properly coated.[4,5]

NdFeB magnets are frequently selected for HEV applications, including the Prius, because of their high magnetic strength and acceptable cost. Unique Mobility (UQM), a major manufacturer and researcher of PM motors, also uses NdFeB PMs.[6–10]

An increase in temperature of NdFeB PMs reduces the magnetic strength linearly up to 100°C as follows:[11]

$$B_r = B_{rA} + s(T - T_A) \quad ,$$

where B_{rA} is the residual flux density at normal ambient temperature T_A, and s is the slope of the B_r temperature characteristic (for NdFeB this tends to be –0.1% per °C). Above 100°C, the magnetic field strength begins to fall more rapidly as indicated in Table 1.[7,12]

Table 1. Characteristic of Delco Remy MQ2[a] NdFeB magnets

Residual induction	0.8T
Intrinsic coercive force	1.43 ma/m
Temperature coefficient of bromine to 100°C	–0.10%
Temperature coefficient of bromine to 125°C	–0.11%
Temperature coefficient of bromine to 175°C	–0.15%

[a]MQ2—Delco Remy Magnequench Division

For an NdFeB PM with the above characteristics, Figure 3 shows the reduced strength of the magnet in per unit form vs temperature. It is estimated that there will be a 20–30% reduction in flux strength for motor operation at the higher coolant temperature as PM temperature approaches 200°C. This temperature-induced effect represents a very significant barrier. This reduction in magnetic field strength due to temperature is reversible because the magnetization will return to the original value once the temperature is decreased.

If the operating temperature of the motor exceeds a certain critical temperature, irreversible demagnetization of the magnet will result.[9] This critical temperature is ~150°C for many types of NdFeB magnets, but 220°C for the particular type of NdFeB PM selected for the Prius.[13] However, the reversible, temperature-induced reduction in field strength is more significant because the motor performance (i.e., shaft power) will be significantly reduced at temperatures that will be frequently reached during vehicle operation (assuming a 105°C coolant).

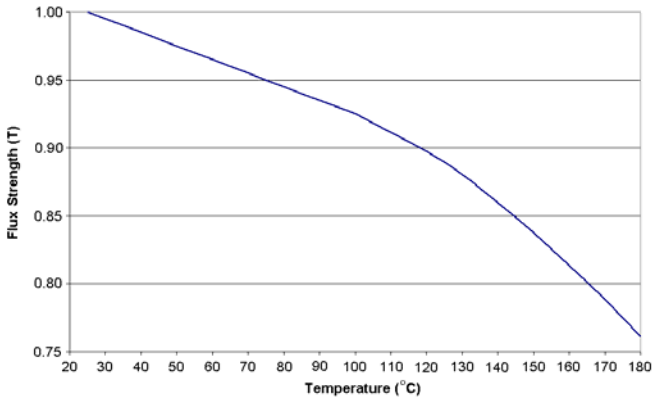


Figure 3. Flux strength of a selected NdFeB magnet vs temperature.

Stator Winding Insulation

Magnet wire used in many applications today is inverter spike resistant (ISR). This Class H wire has excellent resistance to damage from high-voltage spikes that commonly result from rapidly changing pulse-width modulated (PWM) currents in inductive circuits.

Motor wire insulation is a well-developed technology that is not expected to change significantly in the next several years. That is not to imply that major strides have not been made in the last 25 years. Today's motors operate at significantly higher temperatures while meeting 20,000-h lives or greater. The most common types of insulation, in order of increasing quality, are Class A, Class B, Class F, and Class H. These insulations are rated for maximum temperature in 25°C increments as indicated in Figure 4. Less common insulations are available such as Class S (240°C) and Class C (over 240°C); however, the use of these would create a cost increase, which may be avoidable.

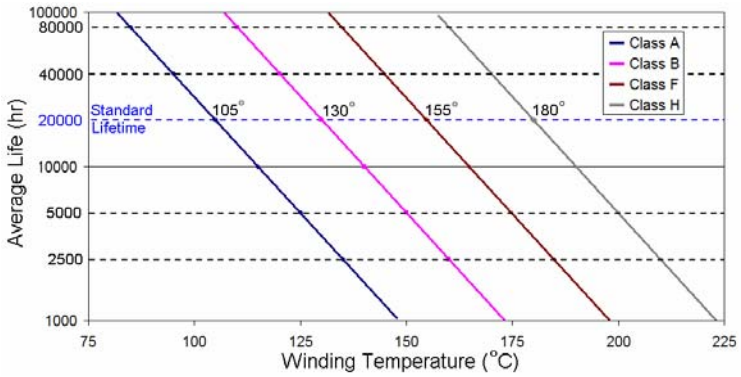


Figure 4. Average motor insulation life vs winding temperature for four insulation types.

For HEV applications, it is essential to fully understand the duty cycle and rate of accrued time on the motor when estimating motor insulation life. For instance, the Prius is considered to be a "strong hybrid" since the motor is relied upon 100% for accelerations from a full stop. It is also used to assist the engine for accelerations and high torque demands such as passing vehicles at highway speeds and for driving up a grade. Table 2 shows an estimate of the required number of hours that may be expected from the motor during a 15-year period. The example numbers reflect heavy usage of the vehicle with an accrued

Table 2. Estimate of life-shortening hours accrued during 15 years of city driving

Daily vehicle operation (h/day)	Days in a year	Number of years	Fraction of vehicle-operation time when the stator insulation is at a life-shortening temperature	Accrued life-shortening hours in 15 years	Accrued miles in the 15 years @ 35 mph
1.25	365	15	0.75	5,100	240,000

240,000 miles. If one assumes the fraction of time when the motor temperature is hot (near or above 180°C) to be 0.75, then the number of life-shortening hours on the insulation is 5,100 h. This high fraction would reflect stop-and-go city driving rather than highway usage where the motor may be seldom used. The 5,100 h is far below the 20,000-h standard for motor insulation life. Referring to Figure 4, this would necessitate the use of Class H insulation at 200°C instead of the 180°C standard.

PMSM Barriers

Before identifying design barriers, the following observations are made concerning an unmodified PMSM that is cooled with a 105°C cooling loop:

1. Heat will not be removed from the casing as effectively as in the case of a 65°C coolant design.
2. Because of (1), the oil temperature, stator temperature, and rotor temperatures will be higher.
3. There will be significant time periods when the 105°C coolant will be *heating* the motor casing.
4. There will also be times when the 105°C coolant will provide *cooling* due to (a) the temperature floor of the PMSM being raised and (b) motor operation in engine compartment temperatures of up to 140°C.

Figure 5 shows the general design approach for a PMSM cooled by 105°C coolant. Because the temperature floor is raised substantially, a design response is needed to lower and stiffen the temperature ceiling by making the heat exchanger, and possibly other components, more effective in responding to thermal excursions that occur during vehicle operation.

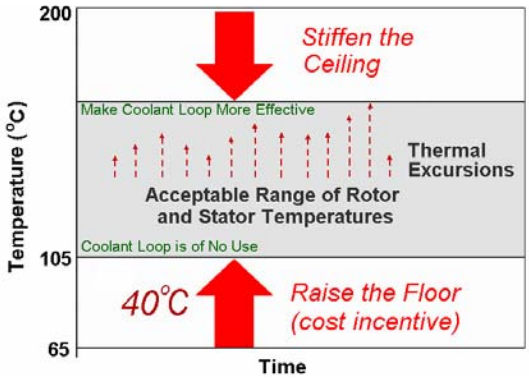


Figure 5. General PMSM design approach applicable for high-temperature cooling.

The following are the PMSM barriers:

1. The primary barrier for the PMSM is that the flux strength of the PMs will decrease 20–30% whenever the PMs are at elevated temperatures consistent with operation based on a high-temperature coolant. This will reduce PMSM/vehicle performance and/or require higher, compensating motor current. Higher motor current will compound the thermal control problem.

2. As determined in the electrical assessment, higher temperatures result in a very substantial 29% increase in losses due to temperature-induced changes in back-emf and stator winding copper losses. This will result in unacceptable temperatures for the stator insulation and PMs unless the cooling system is significantly improved and/or the size of the motor is increased to facilitate heat transfer. Detailed thermal studies will be required to produce a high-temperature motor design.
3. During those times when heat flows from the motor to the coolant, the temperature gradient between the coolant and casing will be low, reducing the effectiveness of the heat exchanger.
4. Because of increased stator winding operating temperatures, Class H insulation will be operated beyond its conventional limits. This may be acceptable based on total hours of operation at high temperatures, but some level of detailed verification/study may be needed.
5. Higher-temperature stator insulation (Class C) can be used but at higher cost.
6. One design approach to better controlling PM temperature entails the design of a more effective water/glycol-coolant-to-oil heat exchanger. Increasing the size of the heat exchanger and locating it at the bottom of the PMSM are desirable approaches but will increase volume, mass, and cost. Encircling the stator with a cooling jacket is another option. These approaches are considered to be "a beginning" that must be followed by other, yet-undefined improvements.
7. The acceptability of raising coolant temperature can only be fully verified by selecting detailed candidate designs and performing thermal analysis and performance modeling. This will involve developmental costs.

System-Level Assessment

In considering numerous design changes that must be or could be pursued to eliminate a dedicated, low-temperature cooling loop, it is important to weigh the cost requirements of each proposed design against the cost savings of eliminating the dedicated cooling loop.

The Prius uses a $480 radiator (2.05 g and 4.19 L) that is partitioned to provide a low-temperature, 1.14-L, dedicated coolant loop radiator. This loop also uses a $142 12-Vdc electric pump (344 g) and miscellaneous hoses. The elimination of this system may entail simply eliminating the partitioning in the radiator, eliminating the pump, and reconfiguring a few hoses. Table 3 shows the predicted cost savings. Using an unpartitioned radiator would save ~$80 and, with the elimination of the pump and two hoses, the total savings would be ~$250, based on the retail prices of new components. The wholesale cost would be ~$187.50.

Table 3. Itemized listing of costs of eliminated components

Eliminated components or features	Cost savings ($)	Source used as basis of estimation
Electric pump	142	Toyota of Knoxville
Partitioning of the radiator	80	–
Hoses (2) associated with eliminated components (pump and partitioned radiator)	28	toyotapartscheap.com
Total retail	250	
Minus 25% retail store profit	–62.5	
Wholesale	187.50	

Conclusion

This study consisted of a technical/engineering evaluation and literature search designed to investigate the feasibility of raising the coolant temperature of a Prius-like HEV system from 65°C to 105°C. The study focused on subsystems and components that were deemed most vulnerable to operation at higher temperatures. These included the inverter power electronics, the dc link capacitor for the inverter, and stator insulation and PMs in the PMSM.

There is high interest among the OEMs in reducing manufacturing cost to enhance their competitive standing. One candidate means of accomplishing this is eliminating the HEV-dedicated coolant loop. In

light of this high interest, a positive, "can-do" approach was used in this study to the fullest extent possible to fairly assess the potential or opportunity of relying entirely on a high-temperature coolant system. Nevertheless, it proved to be clearly evident that a few formidable technical and cost barriers exist, and no effective approach for mitigating the barriers was identifiable in the near term.

The major barriers encountered in this study are

1. Inverter dc link—High-temperature (125°C or higher) capacitors with adequate ripple current and a 600-V continuous rating can be found today only by taking existing capacitors and using three in parallel or by using prohibitively expensive Teflon film capacitors. The first approach triples cost and size, which is a serious penalty and a major barrier. There is a need for low-cost, high-temperature capacitors, and it is important that these be brought to the market soon.
2. PMSM1—The primary barrier for the PMSM is that the flux strength of the PMs will decrease by 20–30% whenever the PMs are at elevated temperatures consistent with operation based on a high-temperature coolant. This will reduce PMSM/vehicle performance and/or require higher, compensating motor current. Higher motor current will compound the thermal control problem.
3. PMSM2—Higher temperatures result in a very substantial 29% increase in losses due to temperature-induced changes in back-emf and stator winding copper losses. This will result in unacceptable temperatures for the stator insulation and PMs unless the cooling system is significantly improved and/or the size of the motor is increased to facilitate heat transfer. Detailed thermal studies will be required to produce a high-temperature motor design.

Although there were no "major barriers" for the inverter/converter power electronics, one issue remains. New 600-V IGBTs, using a trench MOS top cell with ultra-thin 70-μm wafer technology, may be qualified for 175°C junction temperature, but the maximum operating temperature under switching conditions is reduced to 150°C. Because 150°C is much better than 125°C and most likely adequate, the thermal derating issue is mainly a design consideration. Furthermore, very recently, Infineon Technologies released new devices that can reportedly operate with a 200°C junction temperature without the need for current derating.

Table 4 lists the potential cost increases that would result from resolving the barriers for the major critical subsystems/components identified in this assessment. Other costs may be incurred for such things as inverter driver circuit improvements, the buck/boost converter high-temperature capacitor, improved oil spray design for stator cooling, etc. However, the costs of the items listed in Table 4 already exceed the $188 cost savings of eliminating the dedicated coolant loop by a substantial amount. Even the summation of the *minimum* estimated costs exceeds the cost savings.

Table 4. Estimations of additional costs to resolve barriers in components/subsystems

Subsystem or component	Constraints specified by the assessment	Estimates of additional cost
Inverter power electronics	The *future* cost increase for high-temperature power electronic modules when they become available for full rated switching current without thermal derating.	$25–125/inverter $4–21/converter
dc link capacitors	The cost increase of using three times the capacitance prior to new products becoming available with adequate ripple current and a 600-Vdc continuous rating.	$210–250[a]
PMSM (protecting PM and stator insulation)	The cost increase for additional casting in the heat exchanger and other as-yet unknown improvements necessary for control of PM temperatures and dissipating higher losses.	$30–200
Total		**$269–596**

[a]This assumes the cost of a low-temperature capacitor, similar to that used in the Prius, is ~$100.

Table 5 is a qualitative comparison matrix of various parameters of interest for each of the critical components and subsystems. The parameters of interest include availability of components, mass, volume, performance, reliability, lifetime, and cost. For temperatures lower and higher than the 65°C base case, the potential thermal effect is designated as either being positive (+) or negative (−), where applicable. Major barriers are designated with double negatives. As an example using stator insulation, adopting a 105°C coolant would have negative impacts on mass, volume, and cost *if* it were necessary to use a different type of insulation, such as Class C. This assessment considered remaining with Class H to be potentially feasible, depending on whether heat transfer can be significantly improved, in which case those negatives would not apply. This illustrates how some designations in the table are only *potentially* applicable.

Table 5. Multiparameter, temperature-based qualitative comparison

Parameter	50°C	65°C	105°C
Elimination of HEV-dedicated cooling system			
Cost		Base case	+
Inverter power electronics			
Availability of components		Base case	
Mass		Base case	
Volume		Base case	
Vehicle performance		Base case	
Reliability	+	Base case	−
Attaining a 15-year life		Base case	−
Cost		Base case	
dc link capacitor			
Availability of components		Base case	− −
Mass		Base case	−
Volume		Base case	−
Vehicle performance		Base case	
Reliability	+	Base case	−
Attaining a 15-year life	+	Base case	−
Cost	+	Base case	− −
PMSM PMs			
Availability of components	+	Base case	−
Mass		Base case	
Volume		Base case	
Vehicle performance	+	Base case	− −
Reliability	+	Base case	−
Attaining a 15-year life	+	Base case	−
Lack of a new PMSM design[a]		Base case	− −
Cost	+	Base case	−
PMSM stator insulation			
Availability of components		Base case	
Mass		Base case	−
Volume		Base case	−
Vehicle performance		Base case	−
Reliability		Base case	
Attaining a 15-year life		Base case	−
Lack of a new PMSM design[a]		Base case	− −
Cost		Base case	−

[a]A new design is needed for significantly improved heat dissipation.

Future Direction

The high-temperature barrier study is complete as of the end of FY 2006. The study served to highlight a number of areas needing attention, and there are potential areas in which the FCVT program may see a new (or renewed) need to support development. These areas include the development of low-cost, high-temperature components and packaging concepts that meet all the required specifications. The components include IGBTs, diodes, inverter-grade capacitors, and PMs. Innovations in cooling systems, such as oil-spray cooling of the rotor/stator, are also needed for the development of a viable high-temperature PMSM.

Publications

R. H. Staunton, J. S. Hsu, and M. R. Starke, *Barriers to the Application of High-Temperature Coolants in Hybrid Electric Vehicles*, ORNL/TM-2006-514, Oak Ridge National Laboratory, 2006.

References

1. Communication from J. Mookken, Semikron, to R. H. Staunton (ORNL) via email, *Inverters for High Temperature*, and phone on August 7, 2006.
2. P. Kanschat, H. Ruthing, et al., "600V-IGBT: A Detailed Analysis of Outstanding Static and Dynamic Properties," presentation at PCIM Europe Conference, 2004.
3. John Mookken, Semikron, "High-Temperature (105°C) Inverter Development," presentation at DOE FreedomCAR Vehicle Technology Program Annual Review, Oak Ridge, Tennessee, August 2006.
4. R. H. Staunton, S. C. Nelson, P. J. Otaduy et al., *PM Motor Parametric Design Analyses for a Hybrid Electric Vehicle Traction Drive Application*, ORNL/TM-2004/217, Oak Ridge National Laboratory, Oak Ridge, Tennessee, September 2004.
5. Anil Naji, "High Performance Permanent Magnets 7," Catalog, Magnet Sales and Manufacturing Inc, 1995.
6. Arnold Technologies, "TechNotes: How to Select the Appropriate Permanent Magnet Material," December 2002.
7. J. G. West, "Propulsion Systems for Hybrid Electric Vehicles," *Electrical Machine Design for All-Electric and Hybrid-Electric Vehicles (Ref. No. 1999/196), IEE Colloquium*, pp.1/1–1/9, 1999.
8. *Annual Report 2005*, UQM Technologies, Frederick, Colorado, 2005.
9. T. Sebastion "Temperature Effects on Torque Production and Efficiency of PM Motors Using NdFeB Magnets," *IEEE Transactions on Industrial Applications*, **31**(2), April 1995.
10. F. Crescimbini, A. D. Napoli, L. Solero, and F. Caricchi, "Compact Permanent-Magnet Generator for Hybrid Vehicle Applications," *IEEE Transactions on Industrial Applications*, **41**(5), October 2005.
11. Akira Kawahashi, "A New Generation Hybrid Electric Vehicle and Its Supporting Power Semiconductor Devices," Toyota Motor Corporation, *Proceedings of 2004 International Symposium on Power Semiconductor Devices and ICs*, 2004.
12. J. F Gieras and M. Wing, *Permanent Magnet Motor Technology*, Marcel Dekker, 2002.
13. Verbal communication from Dr. Hitoshi Yamamoto, Neomax America, Inc., to J. S. Hsu, ORNL, during the 2005 Permanent Magnet Conference, 2005.

2.3 Direct Cooling Options: An Assessment of Air Cooling for Use with Automotive Power Electronics Applications

Principal Investigator: Desikan Bharathan
National Renewable Energy Laboratory
1617 Cole Blvd.
Golden, CO 80401 USA
Voice: 303-887-4215; Fax: 312-235-3703; E-mail: Desikan_bharathan@nrel.gov

DOE Technology Development Manager: Susan A. Rogers
Voice: 202-586-8997; Fax: 202-586-1600; E-mail: Susan.Rogers@ee.doe.gov

---

Abstract

Air cooling of electronic components using high-speed airflow that is in direct contact with hot electronic components is assessed. Strict requirements for power conversion devices as needed for automotive applications are addressed. Continuing work in air cooling in FY07 is outlined. Recommendations for future course of research in this area for thermal control of power electronics are suggested.

Objectives

The overall effort in this area falls under the general program for thermal control of the Advanced Power Electronics and Electrical Machines (APEEM) program. The National Renewable Energy Laboratory (NREL) leads research and development activities in thermal control related in the APEEM program. We provide an overview of the activities that fall under the thermal control activities.

The overall objective of the thermal control activities is to develop advanced technologies and effective integrated thermal control systems, aimed to meet U.S. Department of Energy (DOE) FreedomCAR program goals. The FreedomCAR goals address key requirements for power electronics, such as target values for volumes, cost, and weight of various subcomponents. The barriers for thermal control technologies are affected by the overall specifications related to these quantities. These limitations are:

- Volume and temperature limits. Existing systems are bulky and difficult to accommodate for automotive applications. Existing thermal control techniques are inadequate to dissipate high-heat fluxes (~250 W/cm2) while limiting the operation of silicon-based electronic components to a temperature of less that 125°C.
- Cost. Material and processing technologies remain costly for use in automotive industry, which is highly cost competitive.
- Weight. Current components are generally considered heavy resulting in needs for additional structural support and increased use of parasitic power.

To achieve the specific FreedomCAR goals for 2010, significant advancement in thermal control of both the power electronics and motors for electric propulsion system must be achieved. Through optimization of existing technologies and their extension to new pioneering cooling methods, we intend to achieve higher power densities, smaller volumes, weights, and increased reliabilities for the drivetrain components. Detailed investigations into thermal issues can provide viable paths to bridge gaps to achieve of FreedomCAR technical targets. It is intended that these paths will also lead to lowering the costs for such new technologies to allow their applications in the automotive industry.

The thermal control and management of electronics, and electronic systems represent major technical barriers to achieving specific FreedomCAR goals in 2010. Electronic chips used as switches in power conversion devices operate at high currents and extreme heat loads resulting in hot spots. Thermal performance of a power module containing such switches may be measured by the maximum temperature rise in the switching die at a given power dissipation level with a fixed heat-sink temperature. The lower the die temperature, the better its electric performance and reliability will be. As the thermal resistance from junction of the die to the heat sink is reduced, higher power densities can be achieved for the same temperature rise, or for the same power density, lower junction temperature can be attained. It is also important to reduce thermal excursions to improve the life and reliability of the dies.

The problem areas of concern in thermal control of power electronics are many including: operating temperature of insulated gate bi-polar transistors (IGBTs); thermal contact resistance between various layers of a power module; low thermal conductivity of the thermal paste; maximum heat flux that can be removed (ideally faster IGBTs would reject heat at a rate of about 250 W/cm^2); limitations on the inlet cooling fluid temperature (it is desirable to use the ICE coolant at 105^{o}C); cost of the cooling technology in terms of its complexity, weight, and volume.

The existing cooling technologies are depicted in Figure 1. This figure shows that conventional cooling techniques, such as forced convection and simple 2-phase boiling techniques, are not capable of removing target level of heat fluxes (in the range of 250 W/cm^2) at low temperature differences (20^{o}C). However, this figure shows clearly that enabling technologies—such as spray cooling and jet impingement, along with innovative packaging improvements—can help meet the goals of the FreedomCAR program. It is, therefore, our objective to investigate and establish, through modeling and testing, the potentials for these enabling technologies to achieve the desired goals.

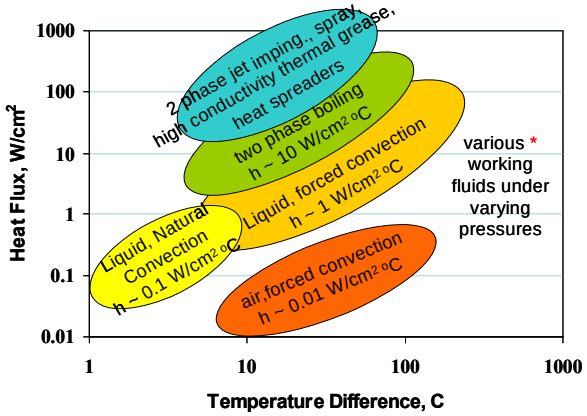


Figure 1: Capabilities of existing cooling technologies

Ideally, it would be more beneficial if the IGBTs could be designed to operate at higher temperatures. Through use of silicon carbide and other innovative materials, DOE's APEEM program is also pursuing parallel, longer-term research projects to evaluate and achieve that objective. However, to meet today's needs of the U.S. industry, the existing silicon-based IGBTs should be operated at temperatures below 125^{o}C.

Existing inverter power modules are constructed by bonding die, copper layers, and a substrate together; and these layers then are mounted on a base plate with an intervening thermal grease layer to

accommodate thermal stresses. Figure 2 shows the structure of the mounted die on a cold plate with the heat being removed by a coolant supplied to one side of the die. Various layers of the construction are indicated. A major contributor to the thermal resistance is the thermal grease. While thermal interface materials are used to promote heat transfer between the DBC and cold plate by filling in voids with conductive material, the thermal interface material layer remains a significant thermal resistance. In addition, the thermal grease is used to reduce thermal stress that may result from differential thermal expansions amongst the various layers. These greases can withstand high temperatures, but have very low thermal conductivities of about 0.3 W/mK to 0.5 W/mK. As a result of this low thermal conductivity, the thermal grease constitutes about 30% to 40% of the total thermal resistance between the silicon die and the heat sink. It is also crucial to reduce or even eliminate this resistance by increasing the thermal conductivity of the thermal grease.

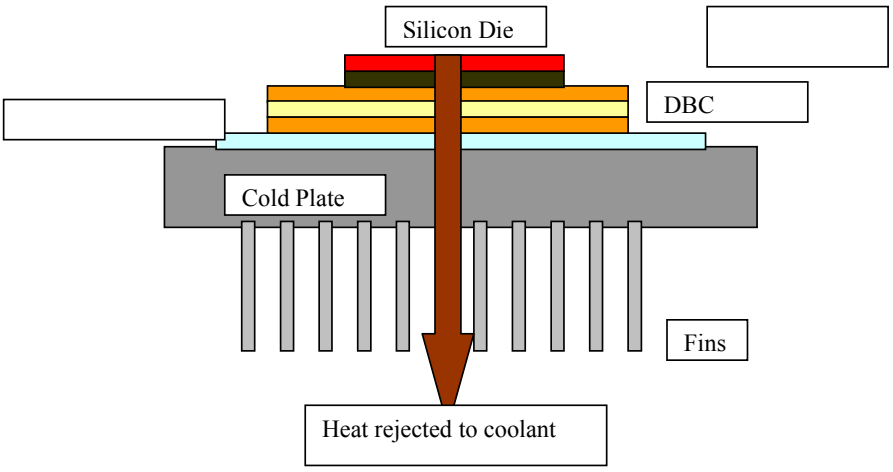


Figure 2. Schematic diagram of the cooling path for removing heat from a silicon die

Another approach for removing higher heat fluxes from the IGBTs is to spread out their heat flux over a larger surface. Currently, copper or aluminum base plates spread the heat over an increased area of about 20% to 30%, thus reducing the maximum heat flux at the coolant-to-heat-transfer-surface interface. Use of more effective heat spreaders—such as highly conductive layers, mini-heat pipes, and/or phase change materials embedded within the cold plate—can spread out the heat flux over larger areas and reduce the maximum heat flux by as much as 40%. With such a reduction in the maximum heat flux, the removal rate may be met by one of the enabling cooling technologies, such as jet impingement and spray cooling.

Another approach to maintaining the power module's temperature at 125°C or below is to provide a separate cooling loop where the coolant can enter the heat sink at lower temperatures, hence providing a larger temperature difference to maintain the IGBT's temperature at the desired value, while removing high-heat fluxes.

A last approach is the use of air on both sides of the silicon switches. Use of air for cooling has many advantages. Air is the ultimate heat sink for all heat rejection from an automobile. All the heat that is to be rejected, either directly or through the use of an intermediate coolant loop must end up in air. Direct use of air can eliminate many components of the cooling loop and the necessity for carrying a secondary coolant. Ambient air is assumed to be available at a nominal 30°C for all the vehicle cooling strategies.

Use of such air increases the overall temperature-driving potential available to reject the heat. Air, as the cooling medium, is benign, nontoxic, and free when compared to many other fluids. Airflow is also amenable to be modulated in a transient manner to suit the needs the system, as the system load varies during operation.

Despite the many advantages, air cooling has many drawbacks as well. Air remains a poor heat transfer medium, with low thermal conductivity and low density. A fan or a compressor must move the airstream to the required hot spots that result in additional parasitic power loads. The coefficient of performance for such a system may turn out to be low.

Cooling with air may not resolve problems related to the current generation of silicon-based devices. But as technology changes, the trench IGBTs can operate at 175°C, and the more advanced Si-C based devices are projected to operate at even higher temperatures. It is with these devices, that air cooling may become a practical option.

To address these thermal control issues, NREL has undertaken many distinct areas of research and development. Multiple avenues of research are expected to ultimately result in significant advancement in thermal control of power electronics to meet the target goals and objectives of the FreedomCAR initiative. The following describes progress made toward evaluating air cooling as a viable option for power electronic components in FY2006 under the FreedomCAR program.

Overall Objective

The objective of the present task is to assess the potential for reducing the cost and complexity for the cooling system for power electronics using air. This study and assessment are aimed to result in quantifying the relative merits for the use of air for cooling power electronic devices to achieve high-heat flux removal rates under steady-state and transient conditions. The cooling system could also be modulated to match both the base line and the transient cooling needs, and thus perhaps needs to be sized to handle only the peak transients for short periods of time. The parasitic load for running such a cooling system can be minimized by a proper approach to optimize the system weight and cost.

In conjunction with utilizing an air-cooling system, NREL evaluated a compressed air system as well. This system is similar in concept to the Brayton air cycle; it is run as a heat pump rather than a power cycle. A compressed air system might achieve a coefficient of performance of the order of 2 to 3. An air volume of 1 liter, compressed to a pressure of 5 bars, when expanded to atmospheric pressure, can reach temperatures as low as –50°C or lower. Such a pulse of air can remove a quantity of heat on the order of 40 to 80 J using pulses lasting 1 to 2s.

This project assessed air cooling of power electronics over a range of outside air temperatures; air velocities; degrees of mixing of outside air and engine compartment air; and other parameters. The goal is to determine under what conditions air cooling would be acceptable.

Use of compressed air for cooling power electronic systems that result in hot spots with high-heat fluxes warrants a closer look. The load on the power electronic systems is highly transient with large peaks occurring over very short durations (with peak to average ratio of 20 or larger, lasting over 1 to 3s time frame). Depending on how the electronic device may be constructed, the heat capacity of the device may be low to cause large temperature swings on the device over the duration of peak demand. Pulsed compressed air jets may be used to effectively remove the high-heat fluxes during such transients. During normal demands, a conventional system may carry the base load for heat removal.

To evaluate such a system using compressed air, we needed to generate a detailed load profile for the power electronic system for various standard driving cycles. The detailed transient model for the compressed air system may then be developed using standard thermodynamic principles. The system can be evaluated with models for transient heat transfer occurring over the hot spots. Once the sizes for various components can be arrived at, the overall system cost can be evaluated and assessed as to their viability for use. Use of a compressed air tank in the vehicle that can be refilled at a gas station offers an alternative approach to this evaluation. Infrastructure for such compressed air already exists. Temperature monitoring circuitry can be used to activate air pulses as and when necessary to minimize the airflow requirements for the system.

This effort was carried out as part of the thermal management tasks under the DOE APEEM program under the Office of Energy Efficiency and Renewable Energy.

Detailed Objective

The overall objective is to assess the suitability of air cooling for heat removal from power electronic components being developed as part of the FreedomCAR effort under DOE.

The overall mission of the FreedomCAR program addresses many components of the vehicle. Achieving the FreedomCAR goals will require the development of new technologies for power electronics and electric machinery. The new technologies must be compatible with high-volume manufacturing; ensure high reliability, efficiency, and ruggedness; and simultaneously reduce cost, weight, and volume. Key components for fuel cell and hybrid-electric vehicles include motors, inverters/converters, sensors, control systems, and other interface electronics.

One of the specific objectives related to power electronics is to develop automotive integrated modular power modules for power conversion and control. Building blocks to be developed include power switch stages optimized to run newly developed motors, drives, DC/DC converters, and advanced controllers and sensors.

The technical targets as specified by the Energy Efficiency Technology Team (EE Tech Team) are summarized below. The FreedomCAR goals and technical targets for 2010 for the electric-propulsion system, as given in Table 1, include the motor, inverter, gearbox, and controller.

Table 1. Electric Propulsion System Goals and Technical Targets for 2010

FreedomCAR Goals	
Peak power	55 kW for 18 seconds
Continuous power	30 kW
Lifetime	>15 years (150,000 miles)
Cost	<$12/peak [<$660][a]
Technical Targets	
Specific power at peak load	>1.2 kW/kg [<46 kg][a]

Volumetric power density	>3.5 kW/l [<16 l][a]
Efficiency (10 to 100% speed, 20% rated torque)	90%

Numbers in square brackets are equivalents for a 55 kW peak-power system.

Of specific interest to this study is the inverter/converter where the electronic chips are expected to generate heat fluxes of up to 250 W per square centimeter of the silicon-based external chip contact surface. Current technology based on silicon chips requires that the chip maximum temperature not exceed 125°C to assure their reliable performance over the required life of 15 years. To reduce the complexity and perhaps the overall cost for the electronic cooling system, the technology team also set other system requirements such as: the coolant to be used will be the same water-ethylene glycol mixture that cools the internal combustion engine, and that this coolant will be available at a return temperature of 105°C.

These requirements, as set by the EE Tech Team, dictate the use of a particular fluid and limit the choices of methods that can be adopted to achieve high heat removal capabilities. However, parallel activities within the APEEM program generated additional tasks to look into technologies that might have the potential to yield substantially higher heat removal capabilities, and/or reduce the complexity of the cooling system, or both.

Use of air for heat removal falls under the category of technologies that could potentially meet the heat removal requirements with greater ease and lower cost.

Approach

Our overall approach to investigating air cooling as an option for power electronics included a review of literature, and an investigation of high-heat flux air cooling used in mission-critical applications, such as turbine blade cooling, and other similar applications that occur in hot-wire anemometry. We attempted to assess the hardware options that may be available in the industry for varied air-cooling devices. We conducted system level analyses to identify areas of critical needs. We also conducted computational analyses of fluid flow and heat transfer for promising devices and geometry. Based on the collective information of all these efforts we arrived at recommendations for future activities in this area.

Our attempt aims to enhance the three key parameters that affect the overall heat transfer rate, namely the air-side heat transfer coefficient, area that is in contact with air, and the overall temperature driving potential. The approach to enhancing the heat transfer coefficient is to attempt to establish high-speed airflow with thin boundary layers that may be interrupted often to capture an entrance-region type of flow. Use of pins and other types of fins is to be investigated for increasing the area of contact. Air refrigeration is also attempted to increase the temperature-driving potential. Details of the various approaches are summarized in the following sections.

Major Accomplishments

Initial assessment for air cooling focuses on a simple heat transfer that occurs on a single chip. We assume a chip frontal area of nominal 1 cm^2 with the chip generating a heat load of 200 W. Air at ambient pressure and a temperature of 30°C is used in arrangement with a jet schematically shown in Figure 3.

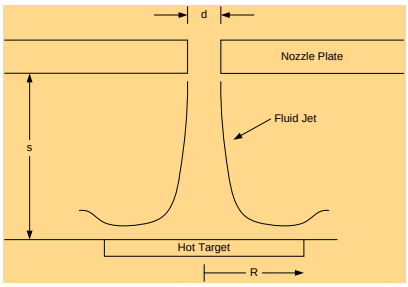


Figure 3. Schematic diagram of an air jet impinging on a hot surface

Use of Ambient Air with Conventional Devices

Figure 4 shows a flow sheet for cooling with air developed using the commercially available software ASPEN. The chip shown as a block is maintained at a temperature of 125°C (using steam for the purposes of the simulation).

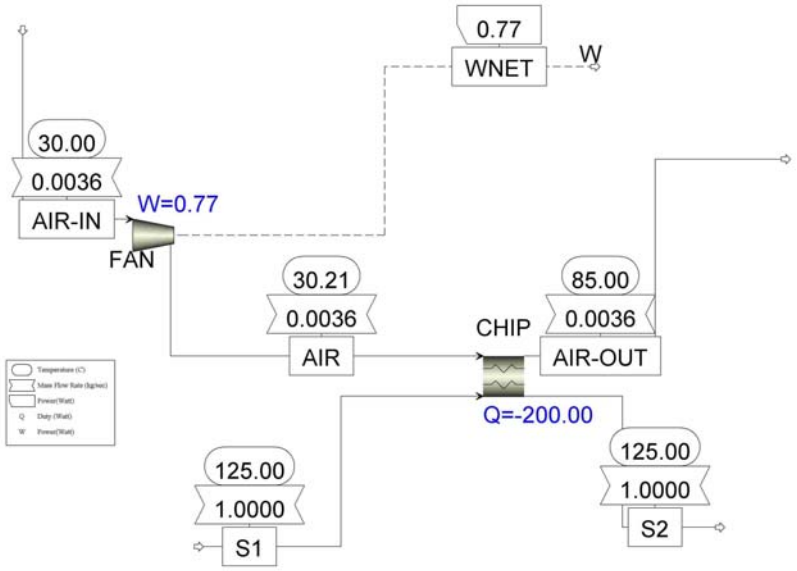


Figure 4. Flow sheet for air cooling with a target chip generating 200W heat load

Only key parameters are shown in this figure. The air approach temperature is fixed at 40°C below that of the target hot surface, a value typical for airflow applications. The fan operates with an efficiency of 56 %, once again typical for airflow.

Based on this simulation, we find that the airflow requirement per chip is about 3.6 g/s (or 2 ACFM), and the required (UA) product, that is the product of the heat-transfer coefficient and the available area for heat transfer, is 3.15 W/K. Typical industrial airflow applications nominally achieve a heat transfer coefficient of about 40 W/m^2K. If we use this value, the required area for achieving the above stated conditions is about 800 fold. That is, the area must be enhanced by a factor of 800 through the use of fins or other means. We find that nominal heat transfer coefficient falls well below the needs to accomplish the task at hand.

Use of refrigerated air with conventional devices:

Compressed, cooled air can be expanded to yield even lower temperatures. Figure 5 shows a schematic arrangement for such a system. The general consensus is that such a refrigerated system is perhaps too complicated to be of use in automotive applications. The system consists of a compressor that is coupled with an expander and heat rejection system in between. Power from expansion is used in the compressor to offset the required work input. Nominal values for the efficiencies for the various components were used in evaluating this system, such as setting the turbine at 90%, the compressor at 80%, and all air-cooler approach temperatures at 40°C.

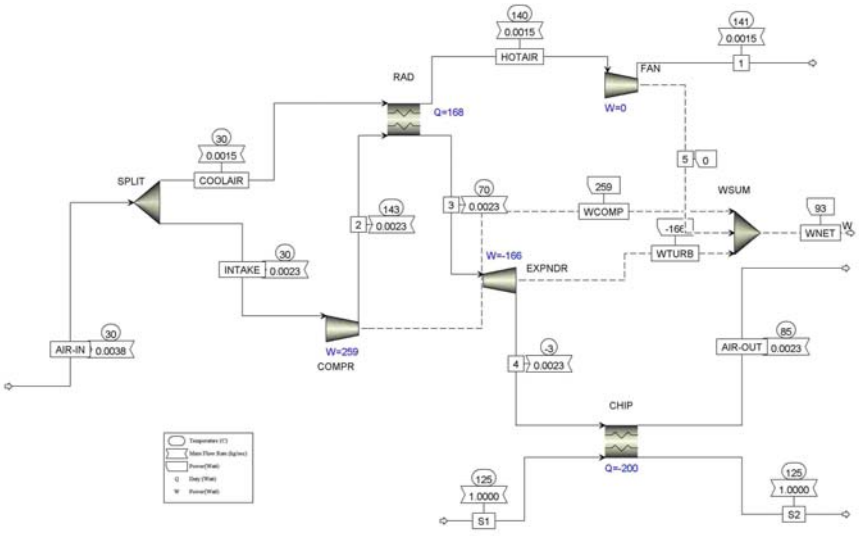


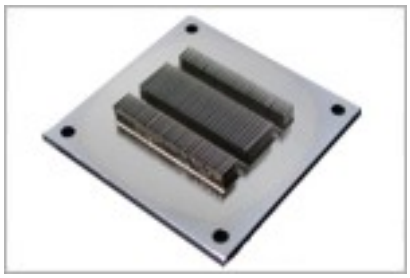
Figure 5. Schematic arrangement and flow conditions for a refrigerated air cooler to remove nominal 200 W of heat load

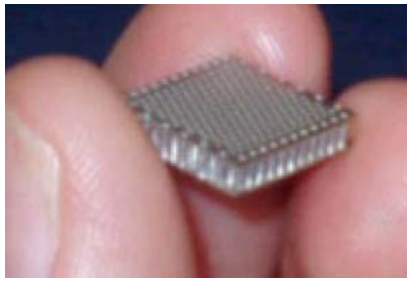
The conclusion from this simulation is that the effective coefficient of performance for this system is approximately 2. That is, a parasitic power of 93 W must be expended to remove the 200 W heat load, with an overall increase in the temperature-driving potential by a factor of 2 (from that for the previous case discussed). The improvement in the heat exchanger requirement is not substantial to offset the increase in parasitic power and the complexity for this system.

Microchannels and Microjet Arrays

We attempted to find hardware suitable for use with air cooling. We found two types of devices that are currently being offered as cooling devices for personal computer CPUs. These are microchannel devices

and microjet arrays. Figure 6 (a) shows a CPU cooler internals with microchannels and 6 (b) shows a micro jet array. (Courtesy Preytek, Co, Inc, and International Mezzo Technologies, Inc., respectively).





6(a) 6(b)

Figure 6. Photographs of microchannel and microjet devices

Microchannels have been studied and many results are available in the literature. We attempted to look into the micro jet arrays in detail for this task. The manufacturer's literature provided experimentally measured data for the microjet devices as shown in Figure 7.

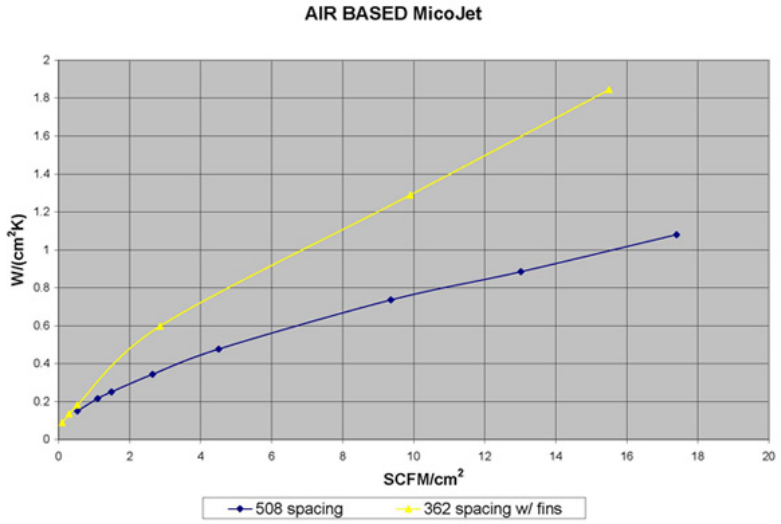


Figure 7. Variation of heat transfer coefficient with air flux (Courtesy: International Mezzo Technologies, Inc.)

An effective heat transfer coefficient is plotted as a function of air flux rate for these jets with differing jet-to-jet spacing. The abscissa can be converted to an effective superficial impingement velocity. The quantity 1 SCFM/cm^2 refers to a superficial impingement velocity of 4.72 m/s. Because the jets occupy only a fraction of the total area and the actual volumetric flow might be different from the standard volume flow quoted, the actual impingement velocity is likely to be a lot higher. The heat transfer coefficient from this device is a factor of 250 higher than typical values nominally encountered in industrial applications. If such high heat transfer coefficient can be verified, this device might have the

potential to fill the need for use with power electronics. Based on this assessment, we attempted to model the flow and heat transfer using this device.

CFD Analyses of Microjets

Simple axisymmetric airflow analysis of a microjet is shown in Figure 8. The jet diameter is fixed at 300 μm and the target diameter is 500 μm. Airflow rate is 5 CFM/cm^2. Figure 8 shows the airflow pattern at an air impingement velocity of 270 m/s.

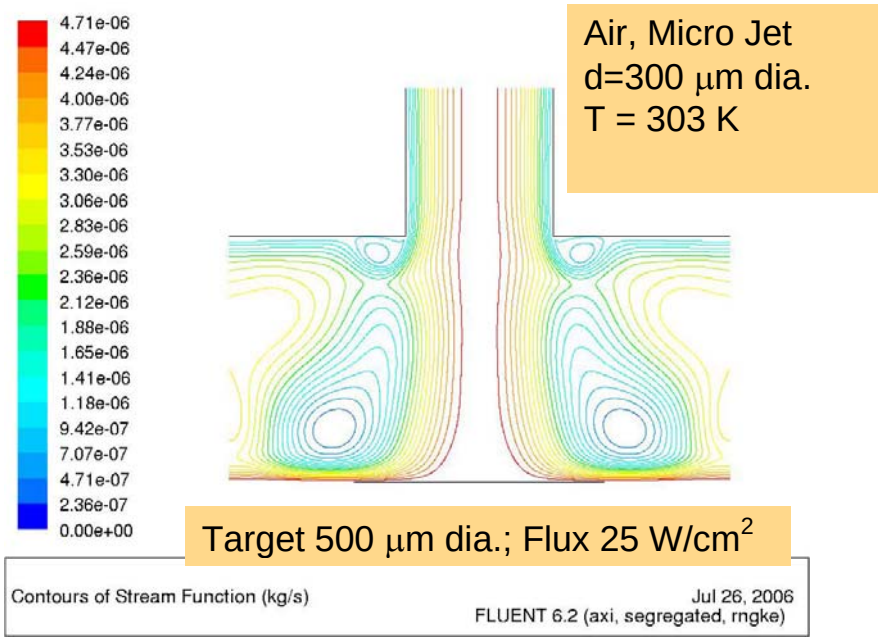


Figure 8. Streamline flow pattern for an impinging air jet

Figure 9 shows the temperature contours. Temperatures are indicated in Kelvin. Based on the heat flux of 25 W/cm^2, and an overall maximum temperature difference of 15 K between the target hot surface and the inlet air, we arrive at a nominal heat transfer coefficient of 1.33 W/m^{2}K. With an average target temperature of 51.25°C and inlet air temperature of 26.85°C, the average heat transfer coefficient is 1.07 W/cm^{2}K.

Based on this simulation, it appears that these types of microjets at high air velocities have the potential to yield high heat transfer coefficients. Our work in FY07 will investigate these devices both analytically and experimentally to assess the potential.

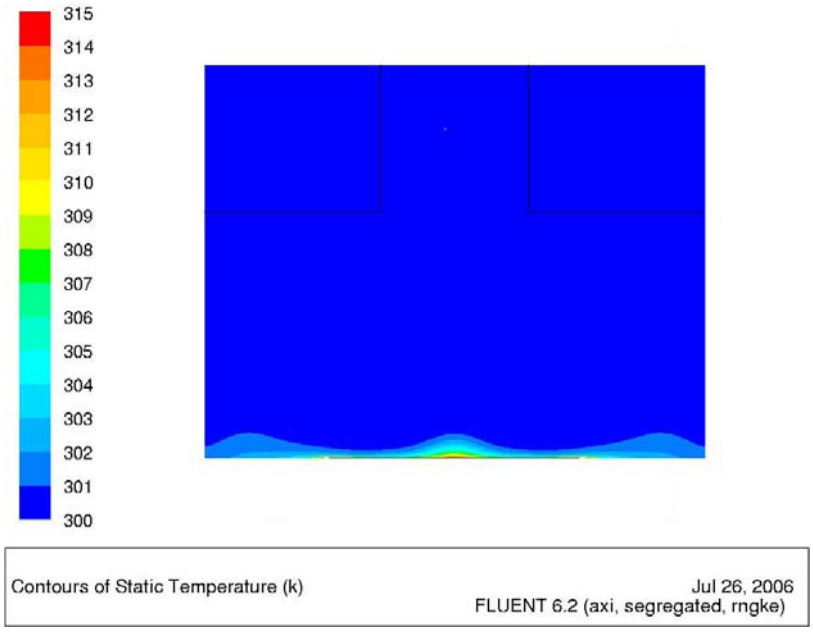


Figure 9. Temperature contours for the air jet impinging on a hot surface

Further analyses of the jet array as shown in Fig. 6b were carried out to assess their potential. Table 2 summarizes the results.

Table 2. Results of the CFD Analyses to Assess Heat Transfer Performance of Air Microjet Arrays

Configuration	Air Pressure Drop (kPa)	Wall Maximum Temperature (^oC)	Effective Heat Transfer Coefficient (W/cm^2K)
1 CFM/cm2 1.5 mm pitch	24	114	0.36
5 CFM/cm2 0.6 mm pitch	11	124	0.27
5 CFM/cm2 1.5 mm pitch	417	59	0.97

Based on these analyses we find that a heat transfer coefficient of 0.5 W/cm^2K is readily achieved with these devices. We, however, need to verify this performance based on experiments scheduled in the future.

Scope and Limitations

Reported results in this paper are confined to data obtained from the literature and CFD analyses conducted at NREL. We will attempt to get relevant data for validation of these results when our laboratory will be in full operation during the next fiscal year.

Technical Discussion

Critical applications for air cooling occur in applications related to gas turbine blade cooling. Extremely high-heat fluxes must be removed to maintain a lower temperature at the turbine blades. There is a significant effort going on in the gas turbine industry, federal labs, and universities. Cooling for power electronic components can benefit from many of these studies related to blade cooling.

As an example of such application, Marques and Kelly [2004] report on fabrication and performance of micro pin fin arrays. Their studies use 500μm diameter fins in air passages that is 500μm apart. Air-side heat transfer coefficients of up to 0.8 W/cm^2K have been reported. They also provide correlations for Nusselt numbers and friction factors that can be used to optimize the geometry for a particular application. Many other cooling strategies for blade cooling are found in Hans et. al [2001] and Shen et. al. [1996]. We believe a thorough literature review and an extended experimental study will result in viable options for cooling power electronic chips with air.

Conclusions

Air cooling is likely to meet the program goal for heat flux removal at a rate of 200 W/cm^2 with relatively low cost and complexity. While air cooling may not be appropriate for the current generation of silicon-based devices, it remains an attractive option for devices that can operate at higher temperatures. Use of air helps avoid the need for a secondary cooling fluid in vehicles. Improving chip manufacturing technologies continue to push the envelope on the highest temperature environment that these chips may see during operation.

Air cooling remains a viable option for power electronics. Continued research in this area will result substantive progress in this cooling technology. We recommend maintaining an effective R&D effort in this area.

References

Hans, J.C.; Dutta, S.; Ekkad, S., Gas Turbine Heat Transfer and Cooling Technology, Taylor and Francis, 2001.

Marques, C.; Kelly, K.W.,"Fabrication and Performance of a Pin Fin Micro Heat Exchanger," J. Heat Transfer, v126, pp 434-444, June 2004.

Shen, J.R.; Wang, Z.; Ireland, P.T.; Jones, T.V.; Byerley, A.R. "Heat Transfer Enhancement Within a Turbine Blade Cooling Passage Using Ribs and Combinations of Ribs With Film Cooling Holes," ASME J. of Turbomachinery, v118, pp 428-434, 1996.

2.4 Modeling Two-Phase Spray and Jet Impingement Cooling

Principal Investigator: *Sreekant Narumanchi*
National Renewable Energy Laboratory
MS 1633
1617 Cole Blvd
Golden, CO 80401-3393
Voice: 303-275-4062; Fax: 303-275-4415; E-mail: sreekant_narumanchi@nrel.go v

DOE Technology Development Manager: *Susan A. Rogers*
Voice: 202-586-8997; Fax: 202-586-1600; E-mail: Susan.Rogers@ee.doe.go v

---

Abstract

Meeting the FreedomCAR goals of cost, weight, and volume of power electronics components requires efficient thermal control strategies to dissipate the heat generated during the operation of these devices. Several parallel paths are being pursued to achieve the goal of 250 W/cm^2 heat dissipation while keeping the silicon die (in the IGBT package in an inverter) temperature below 125°C. This report describes both modeling and experiments, in single and two-phase jet/spray cooling in the context of cooling power electronics devices such as IGBTs in inverters of hybrid vehicles. Single-phase self-oscillating jets are being investigated experimentally. Significant progress has been made in modeling boiling jet impingement cooling of the IGBT package using R134a. An experimental apparatus has also been fabricated to enable two-phase jet/spray impingement experiments with fluids such as R134a, HFE7100/7200, and a glycol-water mixture.

Objectives

In hybrid vehicles, inverters are used for DC-AC conversion. These inverters involve a number of insulated gate bipolar transistors (IGBTs), which are used as on/off switches. The heat dissipated in these transistors can result in heat fluxes of up to 250 W/cm^2, which makes the thermal management problem quite important. The broad objective of this task is thermal control of automotive power electronics components. The FreedomCAR goal is to dissipate 200–250 W/cm^2 from the silicon die in the IGBT package. It is also desired for the maximum die temperature to be below 125°C. The automotive industry would like to eliminate any additional cooling loops. Hence, it is preferable to use a glycol-water mixture drawn from the engine cooling outlet at 105°C as the coolant for the power electronics components. Accordingly, the specific objectives of this task are to explore liquid jets and sprays, both in the single-phase and two-phase regime for cooling the IGBT package and meeting program goals. With single-phase jets, concepts such as self-oscillating jets are also explored. Jets and sprays in the boiling regime are also investigated.

Approach

NREL is exploring the performance of both single-phase as well as two-phase jets and sprays. The rationale is to characterize the heat transfer performance of these technologies in the context of cooling automotive power electronics and establish a database. Ultimately, this information will be fed into overall system-level modeling in order to ascertain the cooling technologies most suited for automotive applications.

To meet the objectives outlined above, the following approach was adopted in FY 2006:

- **Experiments with steady and self-oscillating single-phase jets**

One of the FreedomCAR goals is to utilize glycol water at 105°C for cooling the automotive power electronics components. Given that it is desired to maintain the silicon die at 125°C, it implies only a 20°C difference between the die and the coolant temperature. This implies that high heat transfer coefficients would be required in conjunction with concepts like enhanced surfaces. There have been some studies in the literature which demonstrate that oscillating jets could enhance heat transfer over steady jets by as much as 50%–70% [1-4]. As a baseline, for a 1.25 mm diameter steady freesurface water jet at a velocity of 10 m/s, a heat transfer coefficient of 40,000 W/m^2K can be obtained. In some of these studies [1-3], the oscillation is induced by mechanical means, while in others [4] the jets are self-oscillating. Self-oscillating jets involve no moving parts and the oscillations are induced strictly by pressure differences in the fluid. This makes them quite attractive. However, there is very limited literature on the heat transfer performance of self-oscillating jets. Hence, we decided to explore the heat transfer potential of self-oscillating jets.

Bowles Fluidics Corporation (BFC) has a long history of fabricating fluidic nozzles for a variety of applications. NREL established a CRADA with BFC to explore the heat transfer performance of different types of fluidic nozzles. We fabricated an apparatus which allows characterization of the heat transfer performance of different types of fluidic nozzles. Different fluidic nozzles have been obtained from BFC and some initial heat transfer experiments have been performed to characterize the performance of these nozzles. Comparable steady jet experiments have also been performed to serve as a baseline against which to compare the performance of the fluidic nozzles. Initially, water is being used as the coolant; however, the ultimate goal is to use a glycol-water mixture at 105°C as the coolant. Results of the heat transfer performance will be fed into our thermal systems model to determine the impact of these technologies at the system level.

- **CFD model of nucleate boiling in impinging jets**

Using glycol-water jets at 105°C inlet temperature implies that in order to keep the silicon die temperature at 125°C, very high heat transfer coefficients may be required (almost 140,000 W/m^2K without any surface area enhancements) in order to dissipate 250 W/cm^2 from the IGBT package. At present, it is not very clear that such heat transfer coefficients can be achieved with the use of glycol-water jets without resorting to very high jet velocities (in excess of 35 m/s). Hence, in parallel, we are also exploring two-phase jet impingement cooling of the IGBT package. In electronics cooling, for jets in the two-phase regime, it is desirable to operate in the nucleate boiling regime [5] since a small increase in the target surface temperature is accompanied by a large increase in the heat flux that can be dissipated from the surface.

Therefore, in FY 2005 NREL employed the Eulerian multiphase model, within the framework of the CFD code FLUENT, to study nucleate boiling in impinging jets. A user-defined function was incorporated into FLUENT to enable these predictions. A mechanistic model of nucleate boiling was used. However, the vapor energy equation was not solved and it was assumed that the vapor is at the saturation temperature. In FY 2006, the model was improved to solve for the energy equation of the vapor. The model was validated with a couple of experimental studies reported in the literature on nucleate boiling in submerged jets. The code was then employed to study the cooling of an IGBT package using impinging R134a jets.

R134a and HFE7100/7200 are fluids that are suitable for use in electronic cooling applications. They have the potential to meet the targets of 250 W/cm^2 heat dissipation from the silicon die while keeping the die temperature below 125°C using jet velocities of the order of 10 m/s.

- **Apparatus for spray and boiling jet experiments**

Concurrent with the numerical simulations of boiling jets, a subcontract was established with Mudawar Thermal Systems in FY 2006 to construct an apparatus which will enable spray and jet experiments in the two-phase regime. Two test vessels are being constructed – one of which will be able to withstand pressures of up to 600 psi. The intent is to perform boiling jet and spray experiments with R134a and HFE7100/7200. As mentioned previously, both R134a and HFE7100/7200 are fluids which are suitable for automotive applications. The experiments with R134a are to be performed at pressures of up to 250 psi, while the experiments with HFE7100/7200 will be performed at atmospheric pressure (~ 15 psi). This is the reason for the fabrication of two separate test vessels.

The vessel that can withstand high pressures requires thicker walls; however, this also means that the experiments would require a longer time to reach steady state. Hence, for low pressure experiments, the test vessel with thinner walls will be used. The fabrication of the test vessels, the target surface, heaters and the rest of the instrumentation is reaching completion. All experiments will be performed on a target surface of area 1cm x 1cm. The intent is to first characterize the heat transfer performance of R134a and HFE7100/7200 sprays and jets on a test surface in a simple configuration and, if promising heat transfer performance is observed, test these cooling schemes on an actual IGBT package.

Major Accomplishments

The main accomplishments of FY 2006 are listed below.

- In FY 2005, we performed extensive CFD modeling of single-phase jets (both freesurface and submerged) and characterized their heat transfer performance. The information acquired from these modeling efforts was utilized to design a jet impingement cooling scheme for a low resistance IGBT package. This will be described in much more detail in another milestone report.

- The high heat flux (HHF) test loop in the Electrical Systems Laboratory at NREL was completed. This loop has all the components necessary to enable single-phase liquid cooling experiments. Broadly, the loop consists of a reservoir, pump, filter, flowmeters, preheater (to heat the working fluid), temperature control units, and several outlets for plugging in thermocouple sensors. All measurements (e.g., pressure, liquid flowrate, temperatures) are made through a data acquisition system via Labview. The laboratory also has a power supply unit (ABC1000) that can supply power for a variety of applications.

- The heat transfer performance of self-oscillating water jets was experimentally explored using fluidic nozzles provided by BFC. Initial results indicated that at a certain flow rate and nozzle-to-target distance, the heat transfer coefficients due to these self-oscillating freesurface jets is almost 30% higher than steady freesurface jets, given the same nozzle exit area and jet velocity. More detailed tests employing concepts from design of experiments are currently underway to evaluate different

fluidic nozzles. The goal is to determine the optimal jet configuration and the subsequent performance.

- In active collaboration with Fluent Inc., a user-defined function was implemented in FLUENT, which enables numerical simulations of impinging jets involving nucleate boiling. The code was applied to study jet impingement cooling, via nucleate boiling, of an IGBT package using R134a jets. Conditions were demonstrated for dissipating 200 W/cm^2 while keeping the silicon die temperature close to 125°C. These are important results because they demonstrate conditions under which R134a can be used to come close to meeting the FreedomCAR goals. Some initial results have been published at the ITherm conference [6] and detailed results will be submitted for possible publication in a journal [7].

- Mudawar Thermal Systems, under subcontract with NREL, has completed fabrication of a test vessel and apparatus that can be used to perform jet and spray cooling experiments in the two-phase regime. These will enable experiments with R134a and HFE7100/7200, two fluids that are particularly suitable for use in automotive applications.

Technical Discussion

The section outlines the progress made in FY 2006. It elaborates on the major accomplishments outlined in the previous section. This section is divided into three parts – one for single-phase jet experiments, one for two-phase jet modeling, and the third for experiments with two-phase sprays/jets.

• Single-phase jets

As mentioned previously, one of the FreedomCAR goals is to use a glycol-water mixture as a coolant at 105°C in the single-phase regime. Hence, we have established a test loop at NREL that will enable experiments with single-phase jets. This loop is shown in Figure 1(a). It consists of a reservoir, pump, filter, mass flowmeters, turbine flowmeters, and valves for regulating flow rate. The loop is also fully instrumented with pressure sensors, thermocouples for monitoring temperatures, and a data acquisition system controlled by LabView.

We also fabricated an apparatus that would enable characterization of the heat transfer performance via single-phase jets. The apparatus is shown in Figure 1(b). It consists of two Teflon plates with a transparent polycarbonate cylinder in between. A copper plug 1-1/2 inches in length and half an inch in diameter fits snugly in the center of the lower Teflon plate. The surface of the copper plate serves as the target surface on which the jet impinges. We are exploring self-oscillating jets to enhance heat transfer coefficients from the target surface. Figure 1(c) shows the sample nozzles obtained from Bowles Fluidics. Six different types of fluidic nozzles are shown. Initial testing has been carried out with two different types of fluidic nozzles and one steady jet. The area of the jet exit of the fluidic nozzles is 1.1 x 1.1 mm^2. The steady jet producing nozzle has the same exit area of 1.21 mm^2 and has a circular opening of 1.24 mm diameter. For the steady jet, a circular opening was chosen to make the steady jet nozzle very efficient. The rationale was that this would provide a fair basis for comparison with the performance of the fluidic nozzles. Figure 1(d) shows a snapshot of one of the experiments

(a) (b)



(c) (d)

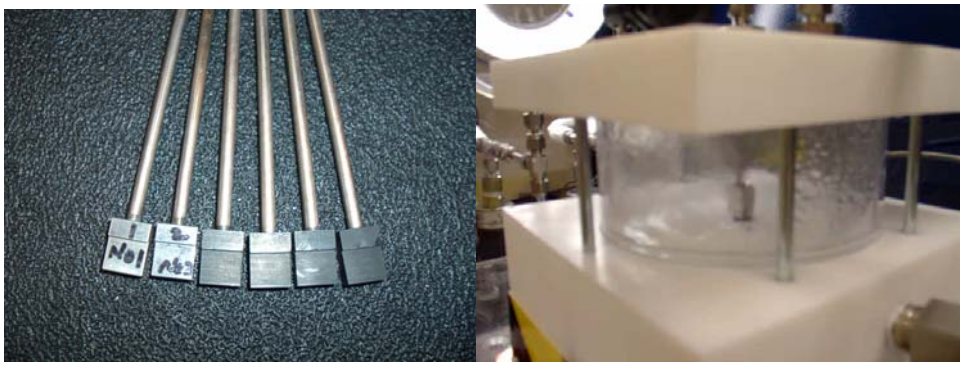


Figure 1. (a) Test loop; (b) experimental apparatus; (c) nozzles; (d) one sample experiment

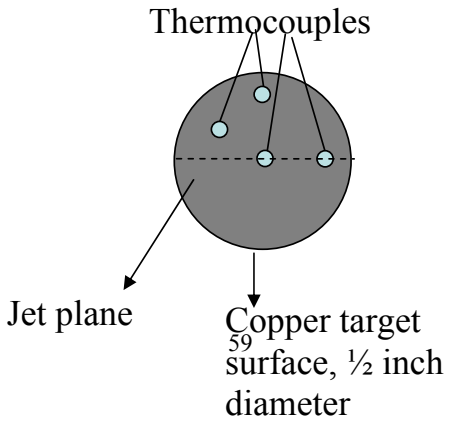


Figure 2. Surface of the copper plug that serves as the target surface

The surface of the copper plug is shown in Figure 2. The jet centerline is aligned with the center point of the target. For self-oscillating jets, the plane of oscillation is also shown in the figure. There are four thermocouples on the surface of the copper plug. The thermocouples are brought out through the backside of the apparatus. The rationale for placing multiple thermocouples is to determine the temperature distribution on the target surface. At the back of the copper plug, a resistive heater from RF Florida Labs is attached via a couple of bolts. Thermal grease is placed between the copper plug and the resistive heater to ensure good contact. A thermocouple is also attached to the heater in order to monitor its temperature. The power is supplied to the heater via ABC 1000 power supply (from Aerovironment Inc.) The maximum operating temperature of the heater is rated at 150°C. Key measurements being made include the jet inlet temperature, the jet outlet temperature, temperatures at four points on the copper target surface, the temperature of the resistive heater, the jet flow rate, the pressure drop across the jet, and the power input to the heater.

A heat transfer analysis was done (in FLUENT) on the lower Teflon plate to gauge the heat loss from the sides and the back of the apparatus when heat is applied to the resistor. A heat transfer coefficient was applied to the top of the copper target surface and the surrounding Teflon block. A wide range of heat transfer coefficients characteristic of impinging jets were applied on the copper surface (about 20,000–50,000 W/m^2K). From the simulations, it is expected that the heat losses from the sides and back of the apparatus should be no more than 3%. The apparatus is placed on an insulating material with a very low conductivity of 0.02 W/mK. The apparatus allows for both freesurface and submerged configurations.

In the literature, the three main categories of jets that have been explored are freesurface, submerged, and confined submerged jets. These are illustrated schematically in Figure 3 (taken from [8]). In a freesurface configuration (Figure 3(a)), the liquid jet issues into a different fluid—usually a gas which is of much lower density than the liquid, while in a submerged jet the liquid jet issues into another fluid of comparable density (Figure 3(b)). In a submerged confined jet (Figure 3(c)), the liquid jet is in a submerged configuration, and in addition there is also a plate/wall confining the liquid after impingement on the target surface.

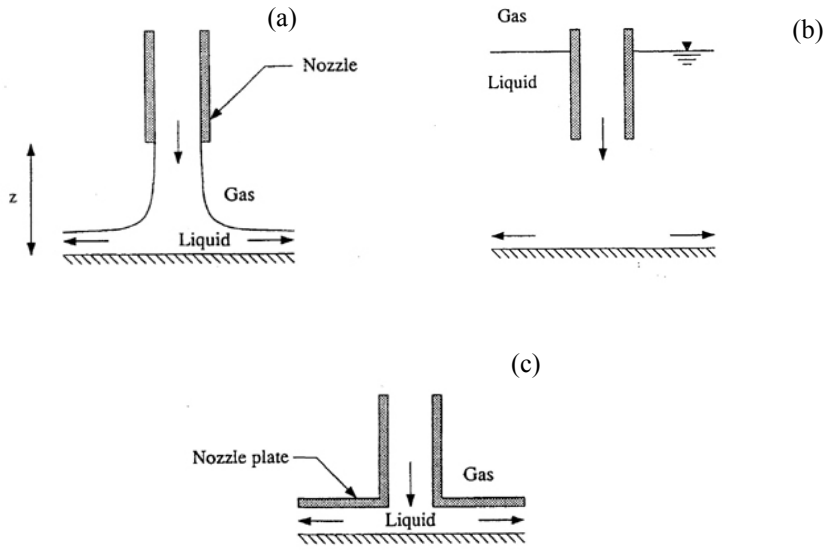


Figure 3. Different jet impingement configurations (taken from [8]): (a) free-surface jet, (b) submerged jet, (c) confined submerged jet

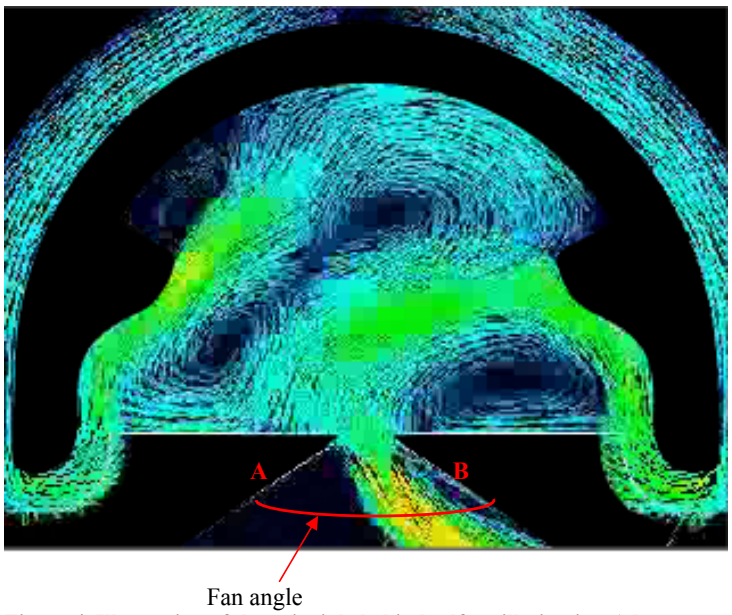


Figure 4. Illustration of the principle behind self-oscillating jets (photo courtesy of BFC)

As mentioned earlier, NREL is exploring the performance of self-oscillating jets. Figure 4 illustrates the concept behind self-oscillating jets. The jet oscillates within the angle depicted in Figure 4. This angle is referred to as the fan angle. The frequency of these oscillations is determined by the time taken for the jet to detach from one wall (wall A in Figure 4), attach to wall B, detach from wall B, and come back and attach to wall A. Essentially, the jet performs a sweeping motion within the fan angle. From a heat transfer viewpoint, this sweeping motion has the potential to disrupt the boundary layer growth and thereby enhance heat transfer between the surface and the liquid.

The initial tests were carried out with two different types of fluidic nozzles: one with a Strouhal number (defined as St = fd/v, where f is the frequency of oscillation, d is the hydraulic diameter of the jet and v is the velocity of the jet) of 0.1 and the other with St of 0.02. As mentioned before, both these jets have an opening of dimensions 1.1 x 1.1 mm. The baseline steady jet has a diameter of 1.24 mm and the same area of 1.21 mm^2 as the fluidic nozzles. The frequency vs. jet velocity and the fan angle vs. velocity characteristics for fluidic1 are shown in Figure 5, while the frequency vs. velocity characteristic for fluidic2 is shown in Figure 6. The frequency vs. velocity characteristic is almost a linear curve for both fluidic nozzles within the velocity range of interest of 3–10 m/s.

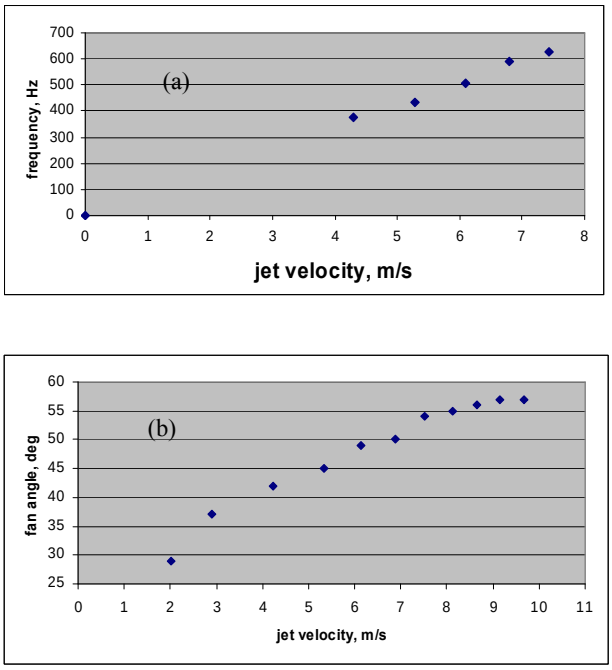


Figure 5. (a) Frequency versus velocity characteristics for nozzle 1 (called fluidic1) with St ~ 0.1; (b) fan angle versus velocity characteristic

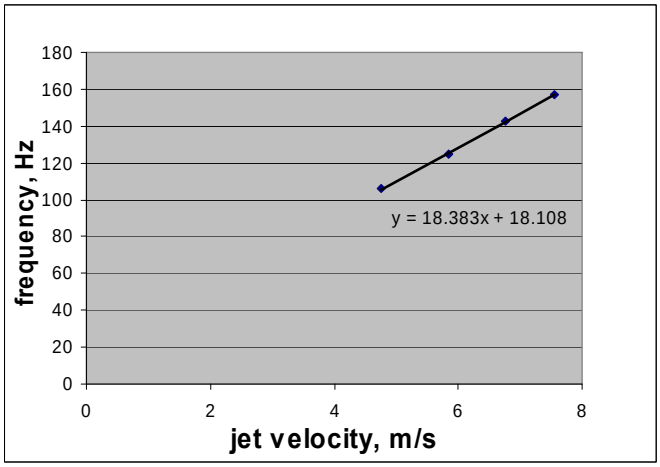


Figure 6. Frequency versus jet velocity characteristic for nozzle 2 (fluidic2) with St ~ 0.02

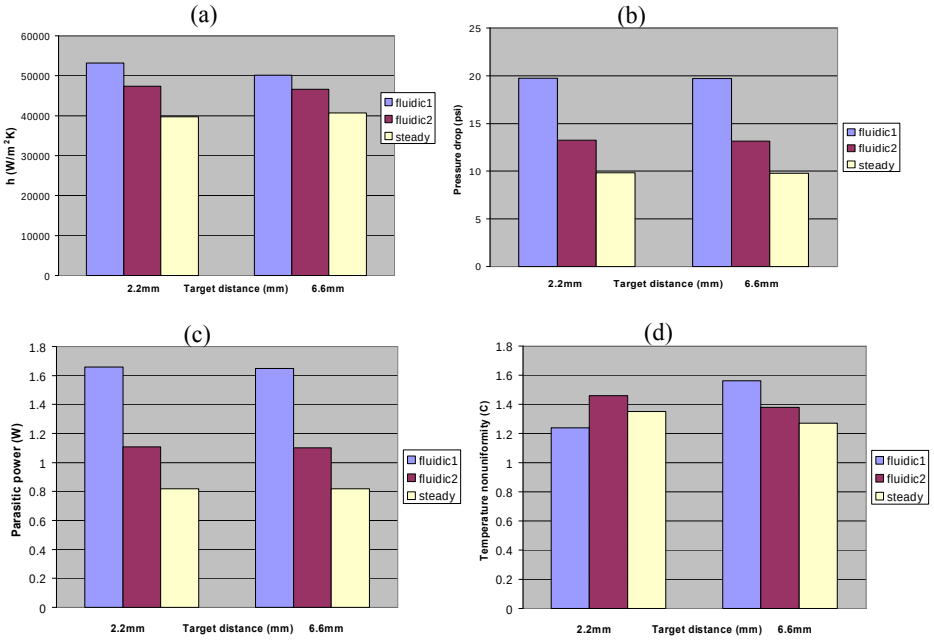


Figure 7. Results for the different nozzles at two target distances of 2.2 mm and 6.6 mm at a velocity of 10 m/s (0.73 lpm). (a) heat transfer coefficients; (b) pressure drop; (c) parasitic power; (d) temperature nonuniformity

Table 1. Summary of the Freesurface Jet Experimental Results With the Three Different Nozzles, Including the Steady Jet Nozzle

Nozzle	Snp (mm)	Q (lpm)	ΔP (psi)	Power, P(W)	h (W/m^2K)	$\Delta T_{nonunif}$ (C)	h/P ($1/m^2K$)
fluidic1	2.2	0.733	19.76	1.66	53,162	1.24	32,025
fluidic1	6.6	0.732	19.7	1.65	50,133	1.56	30,384
fluidic2	2.2	0.735	13.24	1.11	47,362	1.46	42,669
fluidic2	6.6	0.731	13.17	1.1	46,672	1.38	42,429
steady	2.2	0.73	9.83	0.82	39,681	1.35	48,391
steady	6.6	0.73	9.79	0.82	40,674	1.27	49,602

Table 1 shows a summary of the preliminary freesurface jet experiments performed with fluidic nozzles and the steady jet. Two different nozzle-exit-to-target distances were considered—2.2 mm and 6.6 mm at a velocity of 10 m/s (corresponding to 0.73 lpm). In the table, Snp denotes the nozzle exit-to-target distance, Q is the jet flow rate in lpm, ΔP is the pressure drop across the jet (psi), P is the parasitic power consumption (product of Q and ΔP), h is the heat transfer coefficient, $\Delta T_{nonunif}$ is the nonuniformity in the temperature on the copper surface (i.e., the maximum temperature difference among the four thermocouple readings), and h/P is a measure of the performance of the jet. The last column in Table 1 indicates the type of nozzle being used. Figure 7 is basically a visual representation of the results presented in Table 1. It shows the heat transfer coefficients (Figure 7(a)), the pressure drop across the jet

(Figure 7(b)), the parasitic power consumption (Figure 7(c)), and the temperature nonuniformity (Figure 7(d)) on the target surface. The heat transfer coefficient is defined as follows:

$$h = \frac{q}{A(T - T_{ref})} \quad (1)$$

where h is the heat transfer coefficient, q is the power applied to the resistive heater, A is the area of the surface of the copper plug (1.267 cm^2), T is the surface temperature of the copper surface (average of the four thermocouple readings on the copper target surface), and T_{ref} is the jet inlet temperature. For the initial experiments reported here, T_{ref} is at 25°C.

Figure 7(a) shows the heat transfer coefficients at the two target distances of 2.2 and 6.6 mm, and a jet velocity of 10 m/s (flowrate of 0.73 lpm). Figure 7(a) shows that fluidic1 performs better than the steady jet for both target distances. At the smaller target distance of 2.2 mm, the enhancement in heat transfer due to fluidic1 is about 30%. At a velocity of 10 m/s, the frequency of fluidic1 is about 910 Hz, while the frequency of fluidic2 is 272 Hz. It is postulated that at the close target distances, the high frequency of fluidic1 combined with the elevated velocity is sufficient to disrupt the boundary layer growth on the target surface.

The time-averaged boundary layer for this case is different from that of the time-averaged boundary layer for the steady jet at similar velocities. This could possibly explain the enhancements observed. The heat transfer performance of fluidic2 lies between fluidic1 and the steady jet. Figure 7(b) shows that the pressure drop associated with fluidic1 is quite high—almost twice that of the steady jet. Accordingly, Figure 7(c) shows that the parasitic power consumption (product of the flow rate and the pressure drop across the jet) of fluidic1 is highest (twice that of the steady jet). Figure 7(d) shows the temperature nonuniformity on the copper surface. There is no specific trend, and all the non-uniformities range between 1.2°C and 1.5°C. The center point (stagnation point) temperature is the lowest—in line with trends reported in the literature [9-11], and the remaining three thermocouples are bunched together within 0.5°C of one another.

The goal is to increase the heat transfer coefficient at a given flow rate, but the goal is also to reduce the parasitic power. Hence, the goal is to increase the metric h/P, which is tabulated in Table 1. Interestingly, the numbers for h/P reveal that the steady jet still has the highest h/P, which suggests that the pressure drop for fludic1 is very high. Fluidic2 again lies between fluidic1 and the steady jet. At a velocity of 10 m/s, we have been able to achieve heat transfer coefficients of the order of 55,000 W/m^2K with freesurface self-oscillating jets. Currently, we are in the process of testing fluidic nozzles, which have much lower pressure drop while maintaining the frequency characteristics of fluidic1.

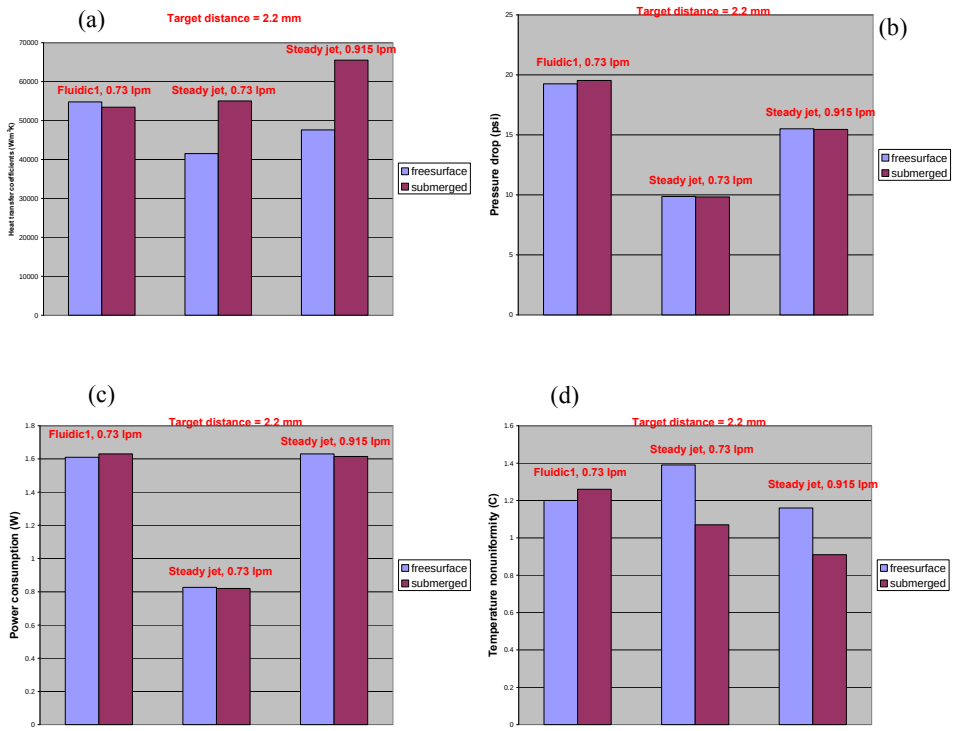


Figure 8. Comparison between freesurface and submerged jets for fluidic1 and the steady jet nozzle, (a) heat transfer coefficient; (b) pressure drop; (c) power consumption; (d) temperature nonuniformity

Table 2. Comparison Between Freesurface and Submerged Jets for Fluidic1 and the Steady Jet at 2.2 mm Target Distance and 10 m/s Velocity (Flowrate ~ 0.73 lpm)

Snp (mm)	Q (lpm)	ΔP (psi)	power (W)	h (W/m^2K)	$\Delta T_{nonunif}$ (C)	h/P ($1/m^2K$)	Nozzle
2.2	0.73	19.25	1.61	54,797	1.2	34,035	fluidic1-freesurface
2.2	0.732	9.87	0.827	41,513	1.39	50,197	steady-freesurface
2.2	0.919	15.5	1.63	47,583	1.16	29,192	steady-freesurface
2.2	0.73	19.53	1.63	53,448	1.26	32,790	fluidic1-submerged
2.2	0.73	9.83	0.82	55,022	1.07	67,100	steady-submerged
2.2	0.913	15.45	1.615	65,529	0.91	40,575	steady-submerged

In addition to freesurface jets, some submerged jet experiments have also been performed. The experiments performed and the results are summarized in Table 2. The experiments were performed with the steady jet and fluidic1 at a target distance of 2.2 mm and a velocity of 10 m/s (flowrate of 0.73 lpm). The various quantities listed in Table 2 are similar to those in Table 1. Figure 8 shows the heat transfer coefficients (Figure 8(a)), pressure drop (Figure 8(b)), parasitic power consumption (Figure 8(c)), and temperature nonuniformity (Figure 8(d)). With the steady jet, in an attempt to make the parasitic power consumption identical to that of fluidic1, the flow rate was increased to 0.915 lpm and experiments were performed for both freesurface and submerged configurations—everything else remaining the same. The freesurface results are the same as shown in Figure 7 and Table 1.

Interestingly, for the freesurface configuration, when the flow rate for the steady jet is increased to 0.915 lpm in order to make the power consumption the same as that of fluidic1, the steady jet still gives about 14% lower heat transfer coefficient than fluidic1. However, the situation for submerged jets is quite different. The submerged steady jet gives comparable heat transfer coefficients to the submerged fluidic1 jet at the same flow rate of 0.73 lpm. When the flow rate of the steady submerged jet was increased to 0.915 lpm in order to make the power consumption the same as the submerged fluidic1 jet, the heat transfer coefficient of the submerged steady jet is about 20% higher than the fluidic1 submerged jet. The key result is that the heat transfer coefficient due to the steady submerged jet is about 30% higher than the steady freesurface jet.

This result is somewhat in line with trends reported in the literature. A few studies have found that the submerged steady jet yields higher heat transfer coefficients than the freesurface steady jet at elevated flowrates/velocities [12]. One postulated reason is the splashing associated with freesurface jets and the thinning of the fluid on the target surface and the consequent bulk warming of the fluid due to the boundary layer reaching the surface of the fluid [12]. Also, it is worth noting that at very close target distances (2.2 mm), given the shape of the nozzle housing (Figure 1(c)), the submerged steady jet configuration becomes more like a submerged confined jet configuration (Figure 3(c), [13]), which has been found to give higher heat transfer performance than a regular submerged steady or a freesurface steady jet [13].

Table 2 also shows h/P values for the different cases. For the freesurface configuration, when the parasitic power consumption is the same, it can be seen that fluidic1 has a higher h/P value (34,035) than the steady jet (29,192). However, for the submerged configuration, when the parasitic power consumption is the same, fluidic1 has a lower h/P value (32,790) than the steady jet (40,575).

The results reported here are initial results. Additional fluidic nozzles have been acquired from Bowles Fluidics. A more detailed set of experiments is being planned utilizing concepts from design of experiments. A detailed uncertainty analysis will also be performed in order to assign error bands to the heat transfer results as well as all other relevant experimental quantities. Also, these experimental results have been reported with water. If significant benefits are found from the use of self-oscillating jets, experiments will also be performed with glycol-water at a temperature of 105°C.

Impact of fluid heat transfer coefficient and fluid temperature

In this section, we will examine the impact of fluid heat transfer coefficient as well as fluid temperature via an ANSYS 3D conduction model with appropriate boundary conditions. The domain is depicted in Figure 9. Figure 9(a) shows the full domain, which is basically the IGBT half bridge, while Figure 9(b) shows a view of part of the half bridge. Figure 9(b) shows the different layers involved. Figure 9(c) shows the backside of the structure. A portion of the aluminum plate is cut out and heat transfer coefficients (h) are imposed directly on the exposed copper layer. For each cutout, on the surrounding aluminum faces,

half the heat transfer coefficient is imposed (h/2). The choice of h/2 on the aluminum walls is appropriate as shown by detailed CFD modeling [14]. Curves for maximum die temperature vs. the imposed heat flux on the silicon die are obtained with different heat transfer coefficient values (Figure 10).

Figure 10(a) shows that to meet program goals (125°C die temperature with 250 W/cm^2 heat dissipation in the die) with 105°C inlet coolant temperature, very high heat transfer coefficient values will be required. Even a heat transfer coefficient of 140,000 W/m^{2}K brings the die temperature to only 140°C—much above the target temperature of 125°C. However, when the coolant inlet temperature is reduced to 70°C (Figure 10(b)), the program goals can be met with a heat transfer coefficient of 60,000 W/m^{2}K. Figure 10 also gives a sense of what a heat transfer coefficient of 55,000 W/m^{2}K (a number which we got experimentally in an earlier section) implies in the context of the IGBT package cooling. In addition to attempts to increase the heat transfer coefficients, the surface area from which heat transfer takes place can also be enhanced. The challenge of using 105°C glycol-water as a coolant is a formidable one.

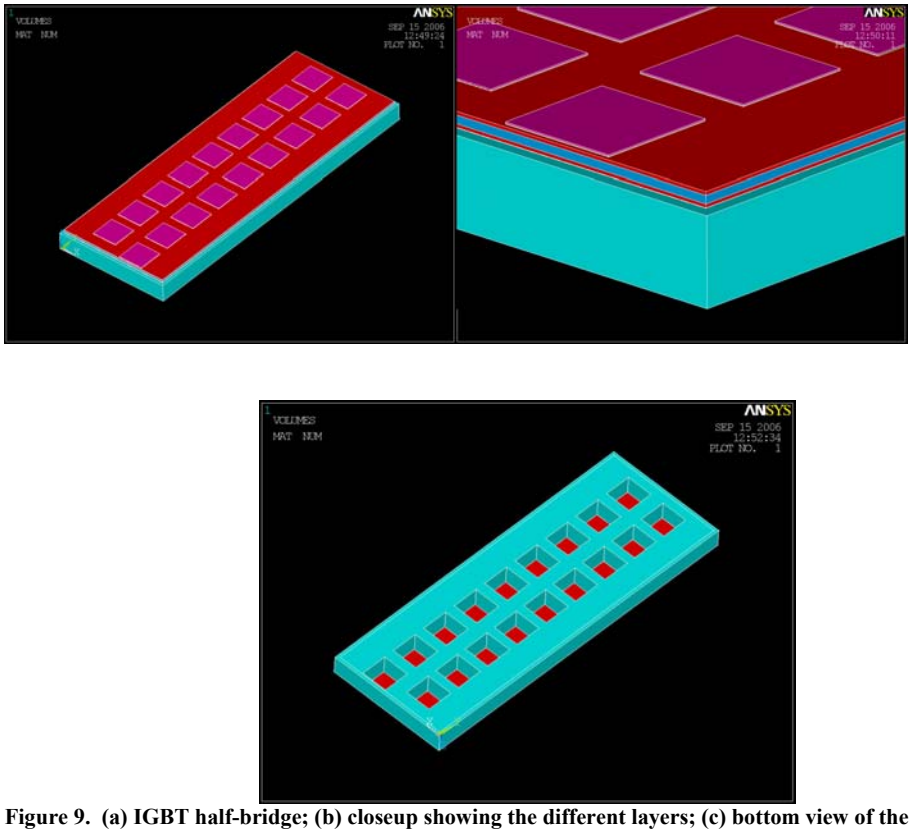


Figure 9. (a) IGBT half-bridge; (b) closeup showing the different layers; (c) bottom view of the IGBT half-bridge showing the cut through the aluminum plate

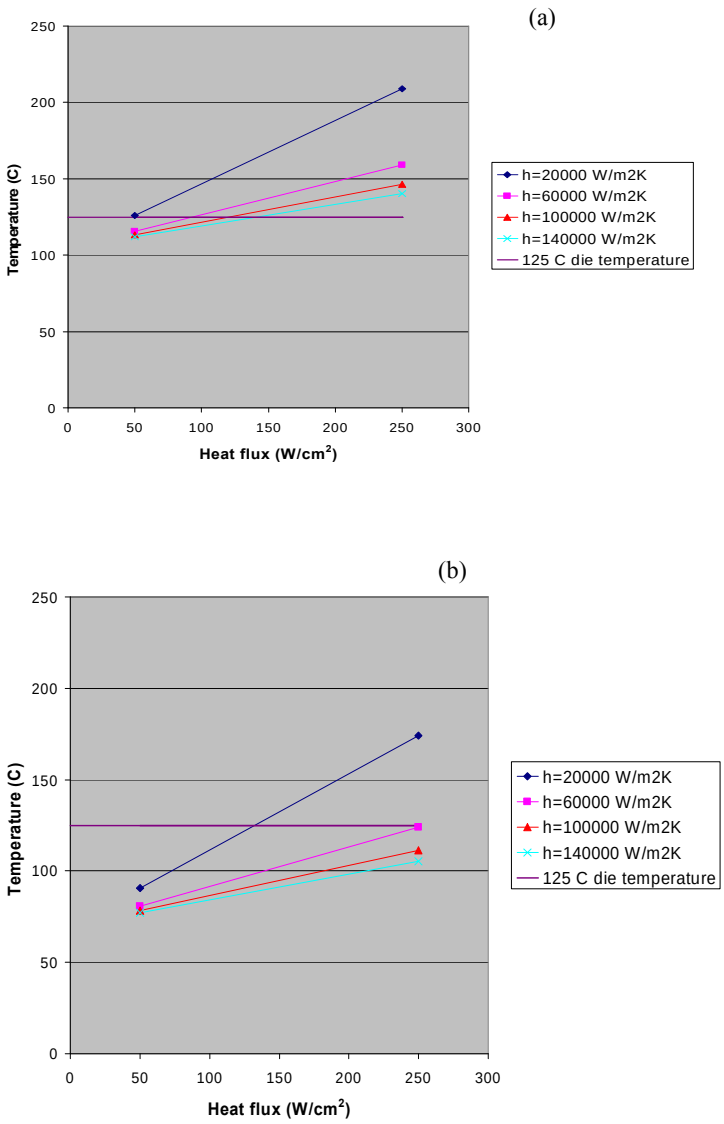


Figure 10. Die temperature versus heat flux for (a) T_{inlet} =105°C; (b) T_{inlet}=70°C

- **Two-phase jets—numerical (CFD) modeling**

As mentioned previously, it is not clear at this point if program goals can be met with 105°C glycol-water coolant. Hence, in parallel with the effort on single-phase jets, in FY 2006 work was also done on boiling jets (nucleate boiling). The rationale is to explore different cooling methodologies that could potentially meet the FreedomCAR goals and create a database of experimental and modeling results. These results can then be incorporated into system level modeling and design in order to ascertain the most feasible cooling solution in the automotive context.

In this section, turbulent jet impingement involving nucleate boiling is explored numerically. The framework for these computations is the CFD code FLUENT. For nucleate boiling, the Eulerian multiphase model is used. A mechanistic model of nucleate boiling is implemented in a user-defined function (UDF) in FLUENT. This effort has involved close collaboration with the staff at Fluent Inc. In the modeling effort in FY 2005 [6], the vapor phase was assumed to be at the saturation temperature, and the vapor energy equation was not solved. In FY 2006, the model was extended to solve the energy equation of the vapor. The model is described in detail in [7]. The numerical results for boiling water and R113 jets (submerged) are validated against existing experimental data in the literature.

R134a is already in use in automotive air-conditioning units. It is also a fluid which is suitable for automotive applications from various viewpoints. Hence, some representative IGBT package simulations that use R134a jets for cooling the package are also presented.

Experimental validations

In the following sections, we present two validations of our numerical modeling approach with experimental data available in the literature. These cases are chosen so as to span different fluid properties (water, R113), saturation temperatures, degree of subcooling, and jet velocities.

Validation With Experimental Study of Katto and Kunihiro [15]. First, we examine the experimental study of Katto and Kunihiro [15]. The domain and the boundary conditions are shown in Figure 11. A water jet with 3°C sub-cooling at atmospheric pressure (i.e., with T_{inlet} = 97°C) impinges on a 10-mm-diameter disk with an inlet velocity of 2 m/s. The baseline nozzle diameter is 1.6 mm, and the distance between the nozzle exit and the heated plate is maintained at 3 mm. A heat flux is imposed on the hotplate surface, as shown in Figure 11. This is a submerged jet configuration. An axisymmetric domain is established. The RNG k-epsilon model with standard wall functions is used. With the use of the standard wall function, the y+ close to the walls should be maintained above 30. All the results presented here are mesh-independent to within 5%. The properties of water at 1 atmosphere pressure are listed in Table 3.

There is ambiguity about the exact temperature measured in the experiments. All indications are that the stagnation point temperature is reported in the experiments. Figure 12 shows the boiling curve, which is a plot of the wall heat flux vs. the stagnation point wall superheat. The wall superheat is defined as $\Delta T_{sat} = T_w - T_{sat}$, where T_w is the wall stagnation point temperature while T_{sat} is the saturation temperature of the fluid at a given pressure. The experimental data are close to the stagnation point superheat (within 20%) from the CFD simulations, which is encouraging. Given the nature of this problem, uncertainties on the order of even 20% are quite common and acceptable. There is temporal fluctuation in all quantities—such as temperature, fluid volume

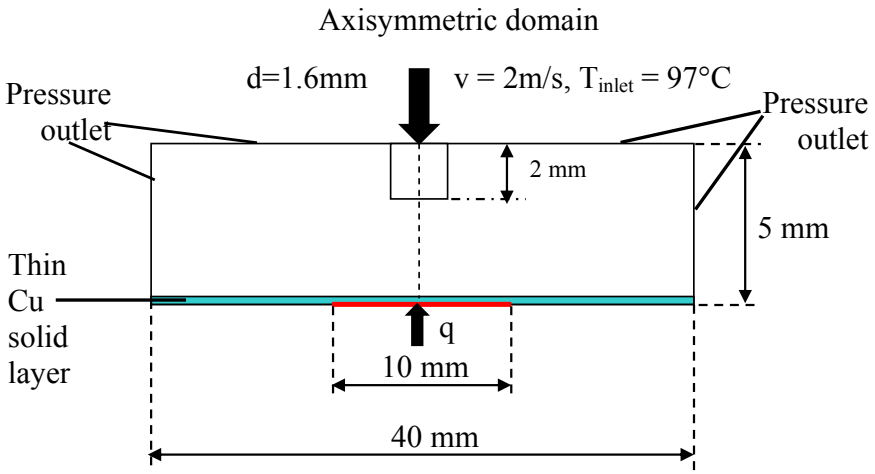


Figure 11. Axisymmetric domain used for the Katto and Kunihiro study (1973) with submerged water jets involving nucleate boiling.

Table 3. Properties of Water and R-113 at 1 Atmosphere Pressure (1.013e+05 Pa)

	Water		**R-113**	
	Liq.	**Vap.**	**Liq.**	**Vap.**
Saturation temperature (°C)	100		47.6	
Surface tension (N/m)	0.059		0.014	
Latent heat (J/kg)	2,257,000		144,000	
Density, kg/m^3	958	0.6	1,507	7.5
Specific heat, J/kg-K	4,219	2,010	980	724
Dynamic viscosity, Ns/m^2	2.83e -04	1.23e -05	5.23e -04	1.08e -05
Thermal conductivity, W/mK	0.68	0.025	0.074	0.01

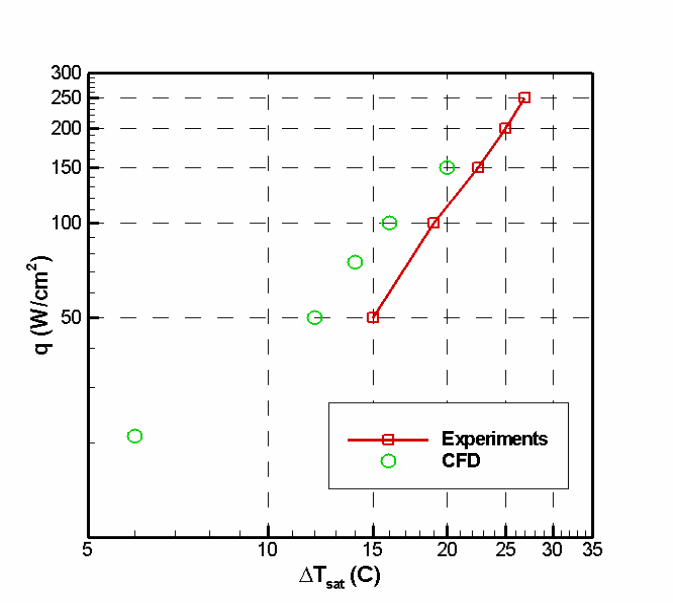


Figure 12. Boiling curve for the Katto and Kunihiro (1973) study

fraction, mass flow rates, and energy transfer rates obtained from the CFD simulations. A temporal average is reported here.

Validation with Zhou and Ma [16] Experimental Study. In this section, we consider another experimental study with submerged boiling jets. This is the study by Zhou and Ma [16] with a submerged R-113 jet. The rationale for choosing this study is that it involves a coolant distinct from water; it involves fluid subcooling and a wide range of jet velocities. The domain is shown in Figure 13. As a simplification, the domain is assumed to be axisymmetric. The nozzle diameter is 1 mm. The target plate (constantan foil) area in the actual experiment is 5 x 5 mm, corresponding to a disk of radius 2.8 mm. A heat flux is applied to the target surface. The distance between the end of the nozzle and the target surface is 5 mm. In the experiments, the stagnation zone temperature is measured with a spatial resolution of about 0.2 mm. Also, the direction of gravity is not the same as in the actual experiment. However, we have confirmed through simulations that the impact of gravity on nucleate boiling in impinging jets is not important. This aspect has also been demonstrated experimentally. Figure 14 shows the results of the validation.

The boiling curves (heat flux vs. stagnation point wall superheat) from both experiments and the CFD predictions are plotted in Figure 14. Figure 14(a) shows the curve for a jet velocity of 0.41 m/s while Figure 14(b) shows results for a jet velocity of 11.36 m/s. The R-113 properties at atmospheric pressure are listed in Table 3. The fluid subcooling is 18.5°C, which means that the jet inlet temperature is 302.3 K. At the elevated velocity, the saturation temperature of the fluid changes along the target wall; this aspect is accounted for in the code. The match between experiments and CFD predictions is good (they are within 10%). At the lower velocity, the wall superheat fluctuates quite a lot; hence, time-averaged quantities are reported. The results for wall superheat presented here are mesh-independent to within 2%. For both the velocities, the fraction of evaporative heat flux is plotted as a function of the applied heat flux. The fraction is simply the heat flux that goes into vaporizing the fluid divided by the total heat flux applied at the wall. As seen in Figure 14(a), at the lower velocity the fraction of evaporative heat flux is

quite high. It touches 75% at a flux of 54 W/cm^2. Basically, as the jet velocity is decreased, we move closer to a pool boiling situation. On the other hand, for the higher velocity case (11.36 m/s), the fraction of evaporative heat flux is only 52% at a heat flux of 250 W/cm^2.

For this higher velocity case, the prediction from a pure single-phase case is also shown, i.e., there is no boiling involved. At lower heat fluxes, it can be seen that there is virtually no difference between the single-phase and boiling predictions. However, as the heat flux is increased, the single-phase case shows higher wall temperatures (superheat) as compared to the boiling case, a pointer to the impact of boiling in reducing the wall temperatures.

Overall, these validations give some confidence in the Eulerian multiphase model implemented in FLUENT. Hence, we look at some IGBT package simulations involving boiling jets in the next section.

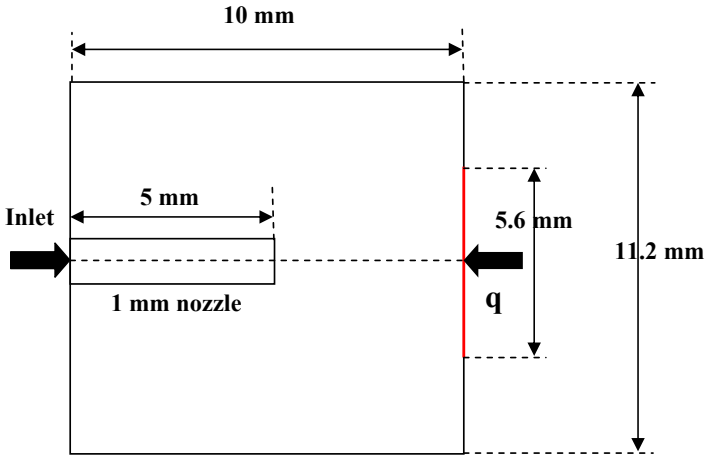
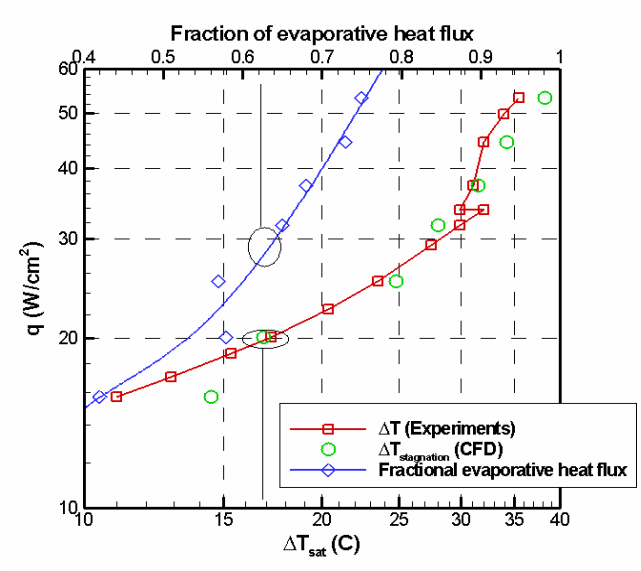
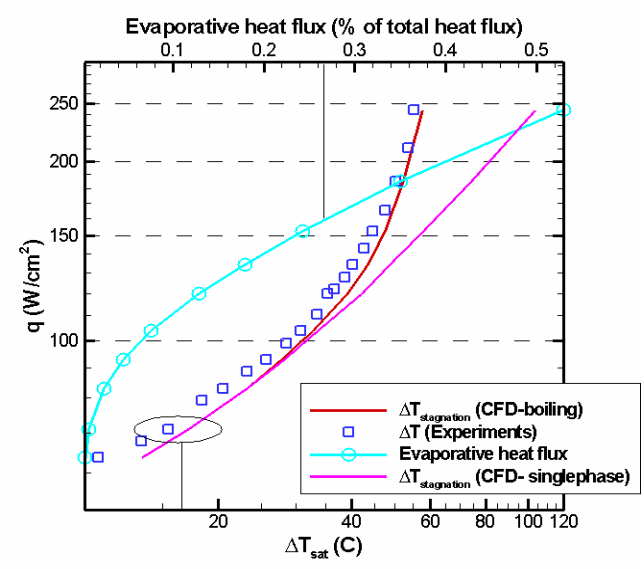


Figure 13. Domain for the Zhou and Ma (2004) study with submerged jets of R113 involving nucleate boiling



(a)



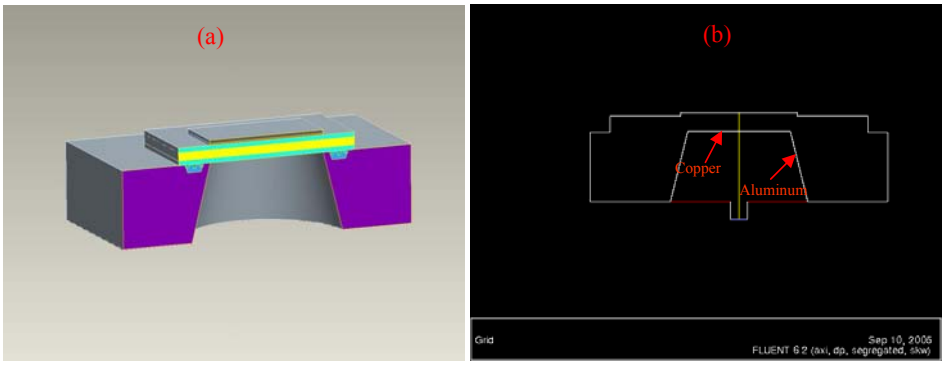
(b)

Figure 14. Boiling curve at different velocities for the Zhou and Ma (2004) study, (a) jet velocity of 0.41 m/s; (b) jet velocity of 11.36 m/s

IGBT package simulations with boiling jets. The previous section established some confidence in the CFD predictions of FLUENT by comparing them with experimental data from the literature. This section explores IGBT package simulations with boiling jets.

The axisymmetric domain used in the simulation is shown in Figure 15. The IGBT package consists of several layers. The silicon die is mounted on a direct bond copper (DBC) stack, which consists of an aluminum nitride layer sandwiched between two copper layers, and the DBC layer is attached to the aluminum baseplate/heat sink. Further details on the IGBT structure can be found in [14]. The boiling simulations are performed on a low resistance IGBT structure as shown in Figure 15(c). This low resistance IGBT structure is described in more detail in another milestone report that describes the development of a jet impingement cooling scheme for the IGBT package. These boiling simulations are fairly intensive and take several hours to converge on 64-bit Linux machines with 1.4 GHz processor speed, even with a small spatial mesh (i.e., small number of cells).

In the automotive industry, R134a is the working fluid used in the air-conditioning units. Here we explore the possible use of R134a as the cooling fluid for the IGBTs. The simulations presented here are performed with an R134a (properties given in Table 4) jet inlet temperature of 47°C. For the boiling simulations, the pressure is maintained at 1.32 MPa (i.e. ~ 13 atmospheres), at which the saturation temperature of the R134a is 50°C. So there is a 3°C sub-cooling in the R134a temperature at the inlet. A volumetric heat generation term is included in the silicon layer to simulate heat dissipation. The results for temperatures are mesh-independent to within 2%. The jet inlet velocity is 2 m/s (Figure 16(a)). Figure 16 shows the contours for velocity, vapor phase fraction, and temperature for the case of 75 W/cm^2 heat dissipation in the silicon die, a jet (diameter = 1.5mm) velocity of 2 m/s, a jet inlet temperature of 47°C, and with a saturation temperature of 50°C at a pressure of 1.32 MPa. Table 5 shows two sets of results—one case in which the heat flux dissipation in the silicon die is 75 W/cm^2 with the jet inlet velocity at 2 m/s, while another case in which the heat flux dissipation in the die is 200 W/cm^2 with the jet inlet velocity at 10 m/s. For both cases, jet inlet temperature is 47°C with a saturation temperature of 50°C (at 1.32MPa).



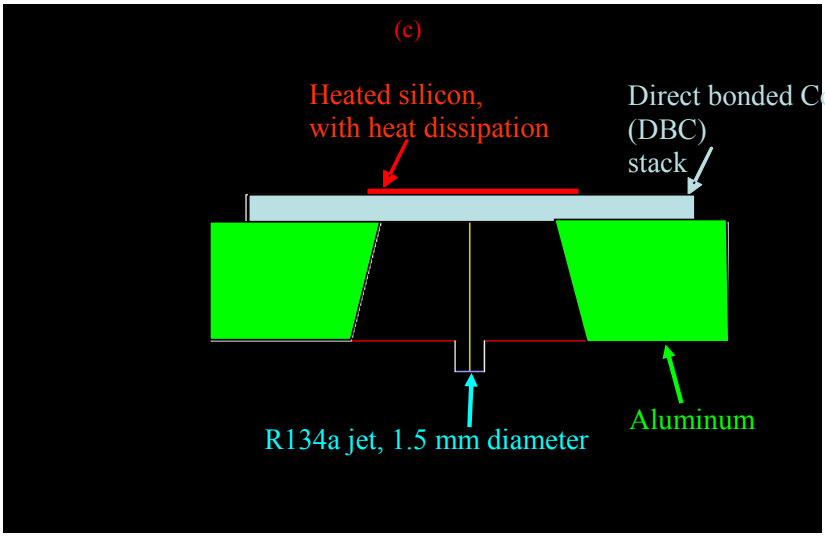
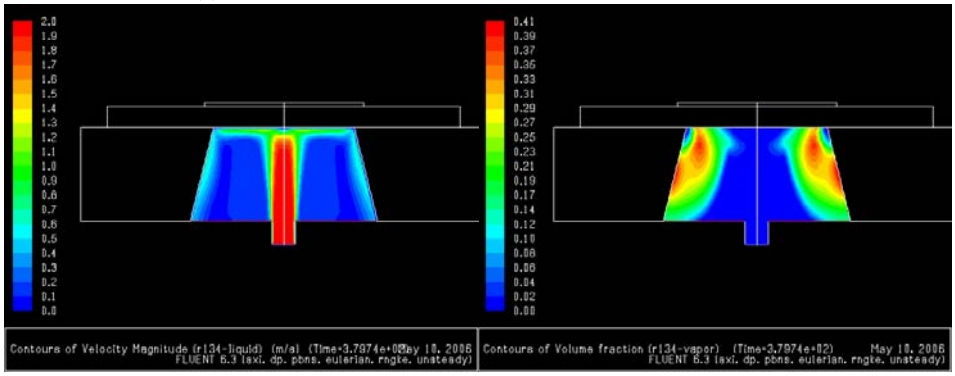


Figure 15. Axisymmetric domain used for the IGBT package simulation; (a) reduced thermal resistance IGBT structure; (b) axisymmetric domain used in the simulations; (c) different layers and some boundary conditions used

Table 4. Properties of R134a at 1.32 MPa, Saturation Temperature = 323.15K

	Liquid	**Vapor**
Density, kg/m^3	1103.4	66.16
Specific heat, J/kgK	1575	1219
Thermal conductivity, W/mK	0.0735	0.018
Dynamic viscosity, kg/ms	0.000167	0.0000138

(a) (b)



(c)

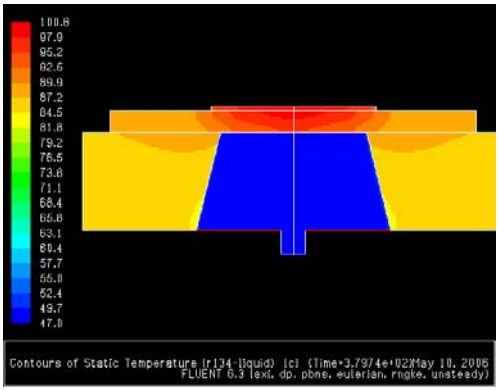


Figure 16. Representative contours of (a) velocity, (b) vapor fraction, (c) temperature in the domain for 75 W/cm^2, T_{inlet} = 47°C, T_{sat} = 50°C at P=1.32 MPa

Table 5. Maximum Die Temperatures for R134a Jet (1.5mm diameter) Impingement Cooling of the IGBT Package Involving Nucleate Boiling, T_{inlet} = 47°C, T_{sat} = 50°C at P=1.32 MPa

	75 W/cm^2, 2 m/s			200 W/cm^2, 10 m/s		
	T_{max} (°C)	h_{Cu} (W/m^{2}K)	h_{Al} (W/m^{2}K)	T_{max} (°C)	h_{Cu} (W/m^{2}K)	h_{Al} (W/m^{2}K)
Boiling	100.5	7,459	4,786	126.3	18,729	9,734
No boiling	115.4	6,088	3,300	110	26,476	14,321

Results are quite interesting. At a heat flux of 75 W/cm^2 and 2 m/s jet velocity, for the case involving boiling, the maximum die temperature is 100.5°C. For comparison purposes, a case is also shown where the boiling is "switched off"; i.e., it simulates single-phase flow. The temperature when there is no boiling is 115.4°C. This clearly demonstrates the impact of boiling in reducing the die temperature.

When the heat flux is increased to 200 W/cm^2 and the jet velocity is increased to 10 m/s, for the case involving boiling, the maximum die temperature is 126.3°C, while for the case when there is no boiling, the maximum temperature is only 110°C. This is an interesting result, and it suggests that boiling is not

beneficial at all jet velocities. The result here suggests that at elevated velocities, boiling may have a detrimental impact upon the heat transfer. We did an analysis that clearly shows why this happens. Basically, the vapor is associated with much smaller heat transfer coefficients than the liquid. So the appearance of vapor hinders heat transfer to some extent. It becomes a tradeoff between two opposing effects—the conversion to vapor aids in heat removal due to latent heat effects; however, the appearance of vapor also hinders heat transfer due to low heat transfer coefficients. These trends can be clearly seen in the overall averaged heat transfer coefficients (Table 5) at the aluminum and copper surfaces (the sides facing the fluid).

For the flux of 75 W/cm^2 and jet velocity of 2m/s, the heat transfer coefficients for the boiling case are higher than for the case where there is no boiling. However, at a flux of 200 W/cm^2 and a velocity of 10 m/s, the heat transfer coefficients for the no-boiling case are higher than the case where there is boiling. Interestingly, this means that at some velocity and heat flux combination in between the two cases we have examined, the boiling and no boiling cases will yield roughly similar maximum die temperatures. From a broader FreedomCAR goal perspective, these simulations demonstrate conditions under which R134a can be used to come close to meeting the program goal of 200 W/cm^2 heat dissipation from the silicon die while maintaining the temperature close to 125°C.

These numerical results need to be validated experimentally. The experimental validations presented give some degree of confidence in the predictions from the code. It would be interesting to see how experimental results from the IGBT package involving boiling would match up with the predictions presented here. Overall, there is evidence of the benefits of boiling from a heat transfer standpoint – though it appears that boiling may not always be beneficial. Although experiments are essential, modeling can yield very useful information when used within their range of applicability. To the best of our knowledge, this is the first time such validations and package simulations are being reported. Tools such as those presented here can be explored for thermal design involving the use of R134a or any other fluid for thermal management in power electronics as well as other electronics cooling applications.

- **Two-Phase Sprays and Jets—Experimental Apparatus Construction**

In parallel with the numerical effort on two-phase jets, a subcontract was also established with Mudawar Thermal Systems in FY 2006 to fabricate a test vessel/experimental apparatus that would enable experiments with jets and sprays in the nucleate boiling regime. R134a and HFE7100/7200 have been identified as fluids which are particularly suitable for use as coolants for automotive applications. HFE7100/7200 can be used at atmospheric pressure; however, R134a has to be under pressure at about 15 atmospheres (~ 220 psi) in order for its saturation temperature to be at about 50°C–60°C. Hence in order to conduct two-phase experiments with both R134a and HFE7100/7200, two different test vessels are being constructed. One of them can withstand high pressures (up to 600 psi) while the other can withstand up to 100 psi. The cross section of the test vessel and the experimental apparatus is shown in Figure 17. The test surface is a square of 10 x 10 mm area. The test surface is the top surface of an oxygen-free copper block. The copper block is surrounded by fiberglass insulation. Heat is supplied to it via cartridge heaters. One thermocouple is embedded into the copper block and the temperature of the center of the copper block close to the target surface is measured. The surface temperature is backed out from a conduction analysis. The liquid inlet temperature, the temperature in the chamber, the pressure in the chamber and the inlet pressure are all measured. A pressure relief valve is also provided. Figure 18(a) shows the assembled test vessel along with the instrumentation (close-up is shown in Figure 18(b)). The cartridge heaters and the oxygen free copper block along with the fiberglass insulation are shown in Figure 18(c). Figure 18(d) shows one sample spray nozzle from Spraying Systems Inc.

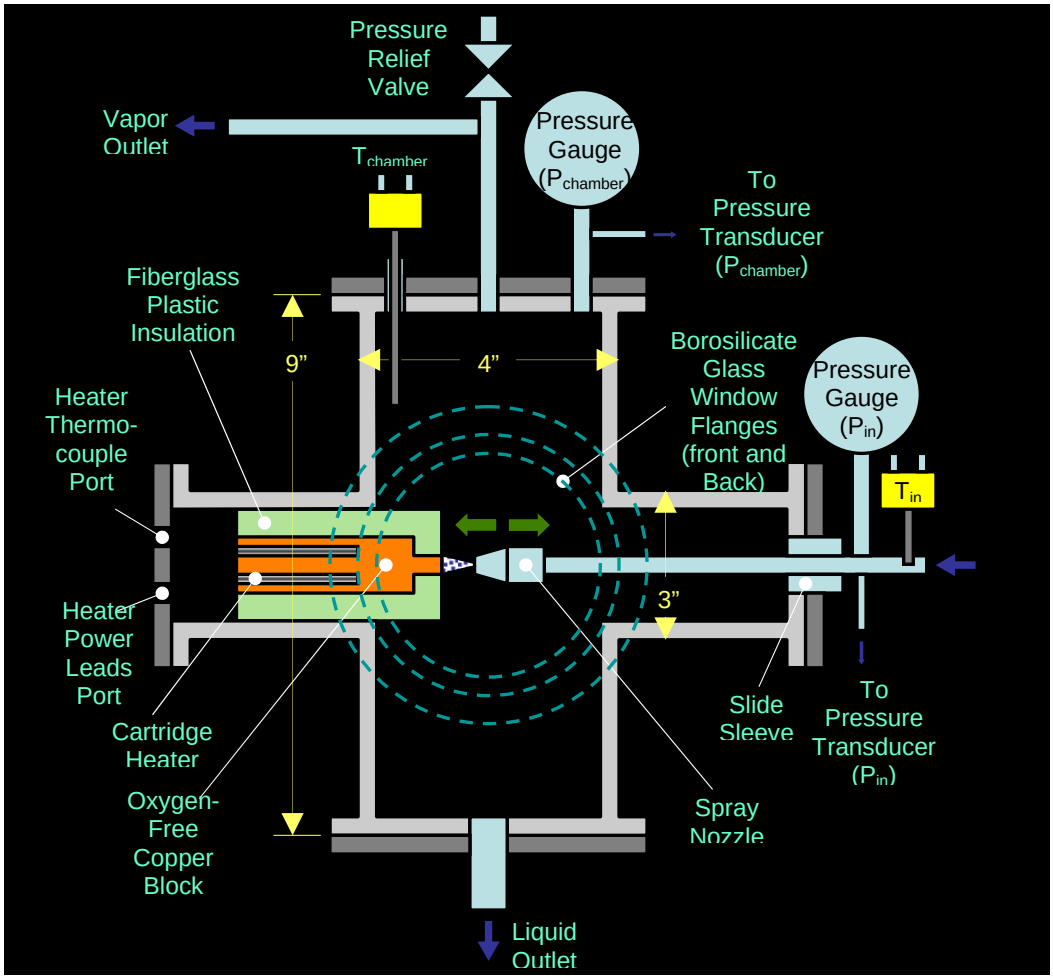
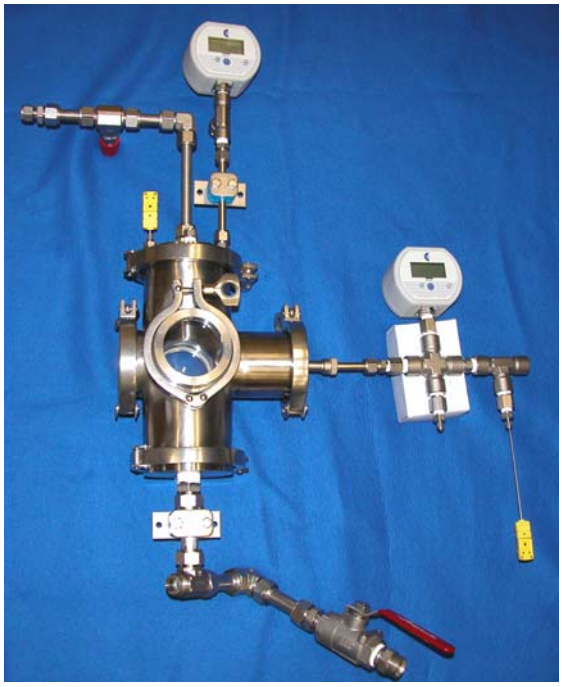


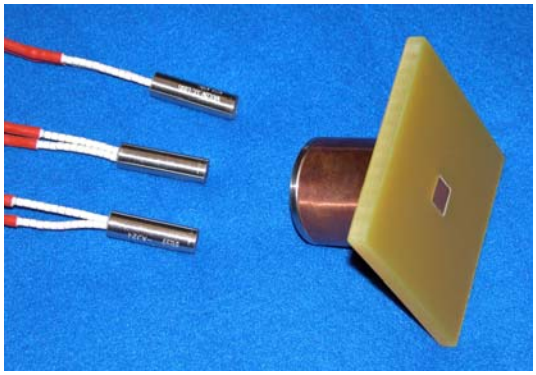
Figure 17. Cross-section of the experimental apparatus for two-phase spray/jet impingement cooling



(a)



(b)



(c)



(d)

Figure 18. Different components of the apparatus/test vessel, (a) test vessel with all the instrumentation; (b) close-up of the test vessel; (c) target surface surrounded by fiberglass insulation; cartridge heaters taken out and shown on the left; (d) spray nozzles from Spraying Systems Inc.

Based on what we have seen thus far in terms of single-phase and two-phase cooling techniques, a comparison between the two approaches is presented in Table 6. In order to achieve program goals with single-phase glycol water jets without using very high velocities, significant heat transfer and surface area enhancements would have to be obtained via concepts like self-oscillating jets and enhanced surfaces. The reliability of the system is yet to be established. With impinging jets, there are concerns related to erosion, corrosion and fouling of the surfaces on which the jet impinges. These aspects need to quantified. The biggest advantage of using single-phase glycol-water jets is that no separate cooling loop would be required. With two-phase jets and sprays, the program goals can be met. However, it would require a separate cooling loop and additional components (e.g., condenser) would be required. For this case also, reliability is yet to be established.

Table 6. Comparison of Single-Phase and Boiling Jets/Sprays as Cooling Options

Single-phase jets (glycol-water)	• Existing cooling loop can be utilized. • With 105°C glycol-water coolant, to avoid very high velocities, heat transfer and surface area enhancements are required. • Reliability needs to be proven (erosion, corrosion, and fouling). • Program goals of 250 W/cm^2 and 125°C die temperature can be met with 70°C glycol-water coolant temperature with a heat transfer coefficient of h=60,000 W/m^{2}K with the low resistance IGBT structure.
Boiling jets or sprays(with R134a or HFE7100/7200)	• A separate cooling loop is required • Some additional components are required (e.g. condenser). For R134a, a high pressure system is required • Reliability needs to be proven • Using R134a, conditions have been demonstrated numerically in this report for dissipating 200 W/cm^2 while keeping the die temperature at 125 C. HFE7100/7200 is also a promising coolant

Conclusions

Based on the results and discussion presented in the previous sections, it can be concluded that both single-phase jets as well as two-phase jets/sprays could potentially be used to meet the program goals of 250 W/cm^2 heat dissipation while maintaining the maximum die temperature of 125°C. Meeting the program goals with glycol-water jets at 105°C will be very challenging. Hence, there is a need to continue exploring concepts like self-oscillating jets as well as enhanced surfaces for improving the heat transfer rates as well as increase the surface area available for heat transfer. Initial results with self-oscillating jets show some promise; however, this technology will have to be thoroughly characterized. The problem is much more tractable with glycol-water jets at 70°C coolant temperature. Results presented in this report suggest that program goals can be met with heat transfer coefficients of the order of 60,000 W/m^{2}K when 70°C glycol-water coolant is used. Conditions have been experimentally demonstrated in the report for achieving these heat transfer coefficients.

With two-phase jets/sprays, it is important to experimentally characterize the performance of fluids such as R134a, HFE7100/7200 and perhaps even glycol-water since there seems to be an interest in using glycol-water even in the two-phase regime. In this report, conditions have been demonstrated for dissipating 200 W/cm^2 while keeping the die temperature close to 125°C using jets of R134a. These numerical simulations show the promise that R134a holds in meeting program goals. HFE7100/7200 are also fluids which potentially could meet the goals. It will also be very critical to look at the system level implications for implementing these cooling technologies in an automotive system. It is important that system-level modeling be done to explore the feasibility of these cooling schemes from an overall systems perspective and also to understand practical aspects such as system complexity and cost.

Next Steps

The goal is to fully characterize the performance of the technologies that have been mentioned in this report; make this information available to industry; and guide the selection of the most promising technology considering performance, reliability, and cost.

Concepts such as single-phase self-oscillating jets to enhance heat transfer from the target surfaces will be fully explored. Surface enhancements may also be beneficial in increasing not only the surface area for heat transfer but also the heat transfer coefficients via changes in the flow. These enhancements may be required in order to meet the program goals with 105°C glycol-water coolant. In the coming year, we plan to shift focus on experiments with glycol-water at 105°C. Once the program goals are met on a test surface (say ½ inch diameter), experiments will be carried out on an actual IGBT package/inverter in order to prove these concepts.

Using glycol-water at 105°C and maintaining the silicon die temperature at 125°C is a challenging problem. As seen in earlier sections, even a heat transfer coefficient of 140,000 W/m^2K on the DBC surface (without any surface enhancements) is not enough to keep the die temperature below 125°C. The problem becomes more tractable if the glycol-water coolant inlet temperature is 70°C.

Given that meeting program goals with 105°C glycol-water coolant may be very challenging, two-phase jet/spray impingement cooling also is being explored. Considerable numerical work has been performed in FY 2005 and FY 2006 relating to nucleate boiling in impinging jets. Hence, in FY 2007, experiments will be performed to characterize the performance of two-phase jets and sprays of coolants such as R134a, HFE7100/7200 and perhaps even glycol-water in the two-phase regime.

Some other aspects that are of concern are erosion, corrosion, and fouling which can all be categozied under issues related to reliability. It is not entirely clear at this point what would be the best cooling option from an overall systems context. Hence, the immediate goal is to characterize the heat transfer performance of these different cooling options and then incorporate all these options into an overall systems level modeling framework.

References

[1] Zumbrunnen, D.A. and Aziz, M., 1993, "Convective heat transfer enhancement due to intermittency in an impinging jet," ASME Journal of Heat Transfer, **115**, pp. 91−98.

[2] Mladin, E.C. and Zumbrunnen, D.A., 1994, "Nonlinear dynamics of laminar boundary layers in pulsatile stagnation flows," Journal of Thermophysics and Heat Transfer, **8**(3), pp. 514−523.

[3] Mladin, E.C. and Zumbrunnen, D.A., 1997, "Local convective heat transfer to submerged pulsating jets," International Journal of Heat and Mass Transfer, **40**(14), pp. 3305−3321.

[4] Camci, C. and Herr, F., 2002, "Forced convection heat transfer enhancement using a self-oscillating impinging planar jet," ASME Journal of Heat Transfer, **124**, pp. 770−782.

[5] Narumanchi, S.V.J., Amon, C.H. and Murthy, J.Y., 2003, "Influence of pulsating submerged liquid jets on chip-level thermal phenomena," ASME Journal of Electronic Packaging, **125**, pp. 354−361.

[6] Narumanchi, S.V.J., Troshko, A., Hassani, V. and Bharathan, D., 2006, "Numerical simulations of boiling jet impingement cooling in power electronics," ITherm conference, San Diego, CA.

[7] Narumanchi, S.V.J., Troshko, A., Bharathan, D. and Hassani, V., 2006, "Numerical simulations of nucleate boiling in impinging jets: applications in power electronics cooling," Int. J. Heat Mass Transfer, **to be submitted**.

[8] Wolf, D.H., Incropera, F.P. and Viskanta, R., 1993, "Jet impingement boiling, Advances in Heat Transfer, **23**, pp. 1−132.

[9] Garimella, S.V., 2000, "Heat Transfer and flow fields in confined jet impingement," in Annual Review of Heat Transfer, pp. 413−494.

[10] Lienhard, J.H., 1995, "Liquid jet impingement," in Annual Review of Heat Transfer, pp. 199-270.

[11] Webb, B.W. and Ma, C.-F., 1995, "Single-phase liquid jet impingement heat transfer," Advances in Heat Transfer, **26**, pp. 105−217.
[12] Womac, D.J., Ramadhyani, S. and Incropera, F.P., 1993, "Correlating equations for impingement cooling of small heat sources with single circular liquid jets," ASME Journal of Heat Transfer, **115**, pp. 106−115.
[13] Garimella, S.V. and Rice, R.A., 1995, "Confined and submerged liquid jet impingement heat transfer," ASME Journal of Heat Transfer, **117**, pp. 871−877.
[14] Narumanchi, S.V.J., Hassani, V. and Bharathan, D., 2005, "Modeling single-phase and boiling liquid jet impingement cooling in power electronics," National Renewable Energy Laboratory, NREL Report No. TP-540-38787. www.nrel.gov/docs/fy06osti/38787.pdf.
[15] Katto, Y. and Kunihiro, M., 1973, "Study of the mechanism of burn-out in boiling system of high burn-out heat flux," Bull. JSME, **16**(99), pp. 1357−1366.
[16] Zhou, D.W. and Ma, C.F., 2004, "Local jet impingement boiling heat transfer with R113," Heat and Mass Transfer, **40**, pp. 539−549.

Publications

The following are the publications and presentations for FY 2006.

Publications

1. Narumanchi, S.V.J.; Troshko, A.; Hassani, V.; and Bharathan, D. 2006, "Numerical simulations of boiling jet impingement cooling in power electronics," Proceedings of the 2006 ITherm conference, May 29-June 2, San Diego, CA.
2. Narumanchi, S.V.J.; Troshko, A.; Hassani, V.; and Bharathan, D. 2006, "Numerical simulations of nucleate boiling in impinging jets: applications in power electronics cooling," to be submitted to the International Journal of Heat and Mass Transfer.

Presentations

1. Narumanchi, S.V.J.; Troshko, A. 2006, "Numerical simulations of boiling jet impingement cooling in power electronics," CFD User's Summit, Monterrey, CA, May 22−24, 2006.

Nomenclature

C_P	Specific heat, J/KgK
d	Jet diameter, m
D	Target equivalent diameter, m
DBC	Direct bonded copper (Copper, aluminium nitride and copper layers bonded together)
f	Frequency, Hz
$\vec{g}$	Gravitational acceleration vector, m/s^2
h	Heat transfer coefficient, W/m^{2}K
IGBT	Insulated-gate bipolar transistor
k	Thermal conductivity, W/mK
p	Pressure, N/m^2
Pr	Prandtl number
q, q''	Heat flux, W/m^2
Re	Reynolds number
u,U	Liquid velocity, m/s

v	Phase velocity, m/s
	Jet velocity at the nozzle exit, m/s

Greek symbols

ΔT	Temperature difference, K
μ	Dynamic viscosity, Ns/m^2
ν	Kinematic viscosity, m^2/s
ρ	Density, Kg/m^3
σ	Surface tension, N/m

Subscripts

avg	Average
CHF	Corresponding to critical heat flux
d	Jet diameter
eff	Effective
f	Corresponding to fluid
l	Corresponding to liquid
q	Corresponding to phase q
sat	Corresponding to saturation
sub	Corresponding to subcooling

2.5 Low Thermal Resistance IGBT Structure

Principal Investigator: *Keith Gawlik*
National Renewable Energy Laboratory
1617 Cole Boulevard
Golden, CO 80401
Voice:303-384-7515; Fax: 303-384-7540; E-mail: keith_gawlik@nrel.gov

DOE Technology Development Manager: *Susan A. Rogers*
Voice: 202-586-8997; Fax: 202-586-1600; E-mail: Susan.Rogers@ee.doe.gov

Abstract

This report summarizes the FY 2006 activities in reducing thermal resistance between the silicon die of the IGBT and the coolant. Activities included simulation and analysis of enhanced IGBT structures, jet impingement experimental studies, and the development of prototype parts. From the jet impingement studies, we were able to conclude that heat transfer increases as jet impingement increases and heat transfer increases as the nozzle-to-target spacing is reduced. Simulation and experiment resulted in a design that allows 105°C coolant at 100 W/cm^2 heat flux and keeps die temperatures at acceptable levels. The structural, fluid, and thermal simulations performed on various geometries for the nozzle plate and base plate have resulted in a design ready for prototype evaluation. Experimental testing and optimization of the design is planned for the coming year.

Objective

The objective of this project is to reduce the thermal resistance between the silicon die of the insulated gate bipolar transistor (IGBT) and the coolant. By reducing the thermal resistance, a target coolant temperature of 105°C can be used to cool the inverter electronics. This project will address one of the important targets of the Advanced Power Electronic and Electric Machines (APEEM) Program, which is the use of coolant at 105°C.

Approach

In previous fiscal years, NREL proposed eliminating several layers in the structure of the IGBT module to assist its effective cooling by a 105°C inlet coolant temperature. In the proposed layout, holes of appropriate dimension are cut through the base plate all the way to the direct bonded copper (DBC) layer of the IGBT. Nozzles are positioned under the DBC direct coolant onto the target surface in high-speed jets. The jets are oriented such that they are directly under the IGBT and diode dies. Therefore, the coolant comes into direct contact with the DBC layer and eliminates the thermal resistances of the base plate and the thermal interface material; the latter causes about 40% to 50% of the total thermal resistance of the IGBT structure. NREL created several thermal and structural models of the proposed low thermal resistance architecture. The numerical modeling shows very promising results and the thermal resistance can be reduced by as much 60%. The weight of the base plate can be reduced by as much as 51% because portions of the base plate are eliminated to allow direct coolant access to the DBC. This structure has

been modeled with various size holes, and structural and thermal analyses have been completed. Currently NREL is conducting fatigue and thermal cycling analysis on the proposed structure.

The idea of a low thermal resistance IGBT structure has been extensively examined with ANSYS, CFX, FLUENT, and other thermal and structural modeling tools. In addition, the actual hardware testing and evaluation are needed for proof of concept. Therefore, NREL has also designed and built small- and full-scale prototypes to validate the modeling results observed through simulation.

This project is strongly aligned with DOE's FreedomCAR objectives. It addresses a major issue facing the industry: the use of coolant at a 105°C inlet temperature. Our analysis shows that a temperature difference as low as 21°C for a heat flux of 90 W/cm^2 is feasible. This is far more than what the current technology can do, which is to remove about 60 W/cm^2 at a temperature difference of about 50°C.

In addition to continuing the refinement of the IGBT nozzle and plenum designs through simulation, in this fiscal year we prepared a simple, small scale, six-jet low thermal resistance IGBT module for laboratory testing and evaluation. We constructed and tested a set of IGBTs with the low thermal resistance structure in the laboratory environment with a die temperature of 125°C and the inlet coolant temperature of 105°C. A water-glycol mixture was used as the coolant and the back of the DBC was cooled by the single phase jet impingement technique. The tests simulated the structure of the Semikron inverter that has been used in our modeling activities.

At the end of this fiscal year NREL worked with Semikron through a CRADA, to build a prototype of the proposed structure in an actual inverter. Prototype nozzle and base plate parts have been machined, and the parts will be sent to Semikron to add its module. Next fiscal year, the whole unit will be tested for various operating conditions and proof of concept.

If successful in long-term testing, the new low thermal resistance design will have a significant impact on the design of the inverter unit. It will allow the industry to eliminate a separate cooling loop and allow use of the coolant exiting the engine at 105°C to cool the power electronics unit directly. It will also reduce the weight of the heat sink by as much as 51%. The project will help DOE achieve one of its major targets of using 105°C coolant inlet temperature for cooling of power electronics. The targets for thermal management of power electronics and electric machines are not firmly set yet. However, based on the current cold plate design, the heat sink constitutes 32% of the weight of a Semikron inverter. This project will reduce that fraction to 16% of the total weight of the inverter. The current technology uses 75°C coolant inlet temperature. This project will meet the target of 105°C inlet coolant temperature. The current technology can remove 60 W/cm^2 heat flux; the proposed structure will remove 90 W/cm^2, or 50% more.

Major Accomplishments

Detailed structural and thermal analyses and experimental testing of conventional and low thermal resistance IGBT structures have been performed with the finite element and finite volume modeling software packages ANSYS, CFX, and FLUENT, and show a reduction in thermal resistance of at least 64%. These results have led to a patent being filed for the cut-through IGBT structure invention, while modeling design refinement continues as subtleties in the flow and thermal fields are understood. Results also indicate that the high heat transfer available through jet impingement cooling can limit the maximum operating temperature of the dies to 125°C with an inlet temperature of 105°C given power densities as high as 100 W/cm^2. This is a 66% higher heat transfer rate than a conventional IGBT structure can handle with 75°C coolant.

- Modeling of next-generation low thermal resistance architecture is complete.
- Experimental evaluation of six-jet structure is complete.
- Results indicate 64% less thermal resistance than the conventional configuration.
- Results indicate viability of 105°C inlet coolant temperature.
- Prototype parts have been machined and will be sent to Semikron for assembly of a complete, functioning unit.

Technical Discussion

Simulation and analysis of enhanced IGBT structures

Implementing this new concept required redesigning the cooling plate to maximize the area exposed to the impinging jets and designing the hardware required to create the jets. The basic concept of this design can be seen in Figure 1 in an exploded format. The aluminum base plate, nozzle plate, and flow channel plate have been designed as individual components to reduce the cost of fabrication. Each component can be directly cast with minimal machine finishing to provide an inexpensive end product to the consumer.

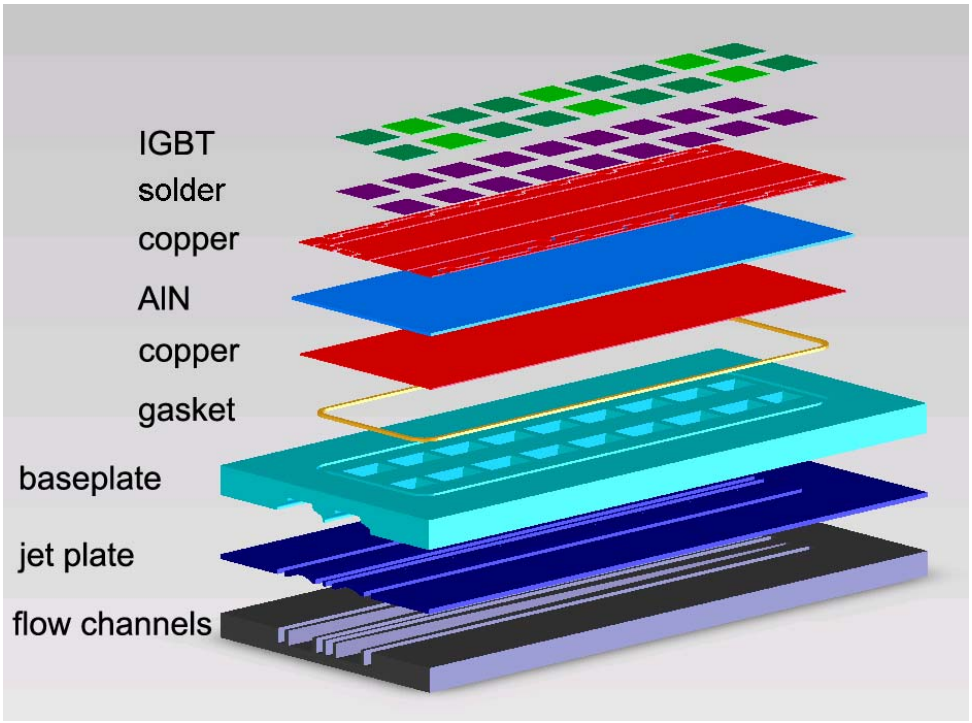


Figure 1. Exploded view of the low thermal resistance IGBT structure

The cut-through design of the aluminum cooling plate for the IGBT structure is an effective solution to the problem of minimizing the thermal resistance to provide maximum cooling. In this layout, the 18 holes lie directly below the respective power electronic dies. In the latest generation of the design, shown in Figures 2 and 3, the individual holes have been merged into open rows, with a bridge between the rows that help distribute the force applied to the electrical contacts. These bridges help to support the phase of the inverter from excessive bending and reduce the risk of cracking. The cut-through allows the jets of coolant fluid to impinge directly on the DBC to which the IGBTs and power diodes are soldered. The benefits of this design are the lack of thermal grease and the ability to have high heat transfer coefficients on the DBC target surfaces.

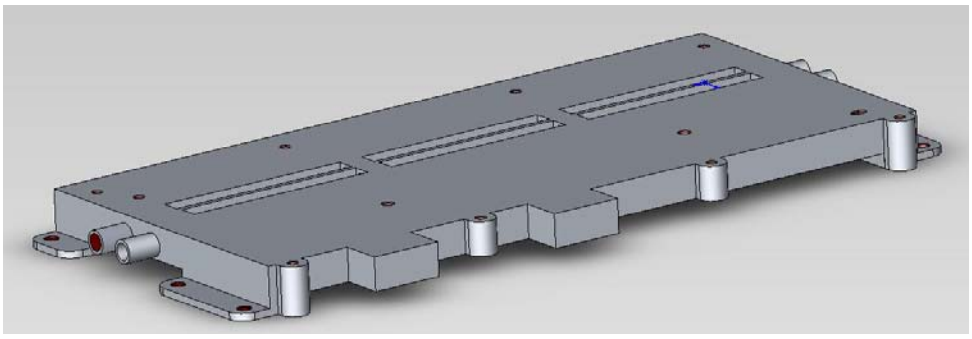


Figure 2. Base plate of the latest design, showing the elongated open holes under the rows of IGBTs and diodes

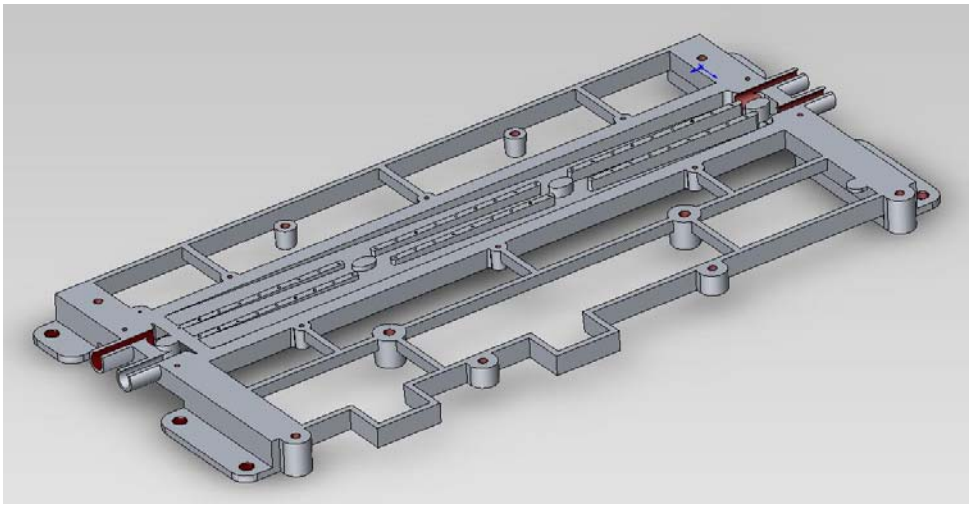


Figure 3. Cutaway view of the nozzle plate located under the DBC

The elongated holes are surrounded by a groove for an O-ring to seal the DBC and the aluminum. An O-ring must be in place to prevent the coolant from penetrating into the electronics side. Using an O-ring allowed us to eliminate any rigid bonding between the heat sink and the DBC. This allows the two surfaces to freely expand and contract as the temperature varies, which decouples the strain and reduces the thermally induced stress. Figure 4 shows the top view of the circuit board, which contains the IGBTs

and diodes, and which is mounted on the elongated holes of the base plate. The opposite side is sealed to the base plate with O-rings.

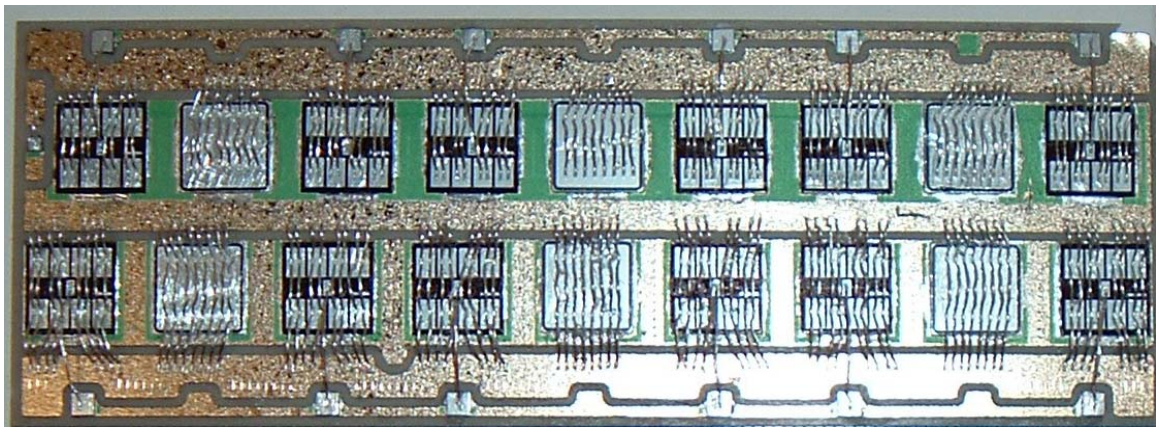


Figure 4. Top view of the circuit board containing IGBTs and diodes, which are mounted to the base plate. The DBC surface on the opposite side is cooled by the impinging jets.

Simulations using structural, heat transfer, and fluid dynamics finite element and finite volume codes have resulted in an advanced design ready for prototyping. Maximum stresses and deflections (Figure 5) were found in the structural simulations of the latest design to be acceptable with Semikron's assembly process, which applies 3000 psi to the DBC assembly. In the thermal and fluid simulations, heat flux was set to 100 W/cm^2, for a total heat load of 3.6 kW. The coolant flow rate was 20.4 lpm. Jet heat transfer coefficients derived from Narumanchi's numerical work showed the maximum temperature to be 125.8°C with a 105°C inlet temperature, as shown in Figure 6. The results showed only a 4°C temperature difference between the DBC target surface and jet inlet temperature.

Fluid flow simulations were performed to obtain uniform flow from all jets (Figure 7) and to explore ways to minimize jet-to-jet interactions and smoothly exhaust spent coolant. Maximum jet speed was 10.6 m/s at the given flow rate and with 1.5-mm diameter nozzles. When the jets are submerged, as is anticipated in actual operation, the impingement velocity at the target decreases somewhat compared to a free surface jet, but the heat transfer coefficient is not adversely affected (Figure 8). The average heat transfer coefficient over the cut-through region is 20,560 W/m^{2}K.

Jet interaction does not substantially decrease the heat transfer coefficient. Pressure drop through the assembly is 7.5 psi, which compares favorably to Semikron's current elliptical fin cold plate design.

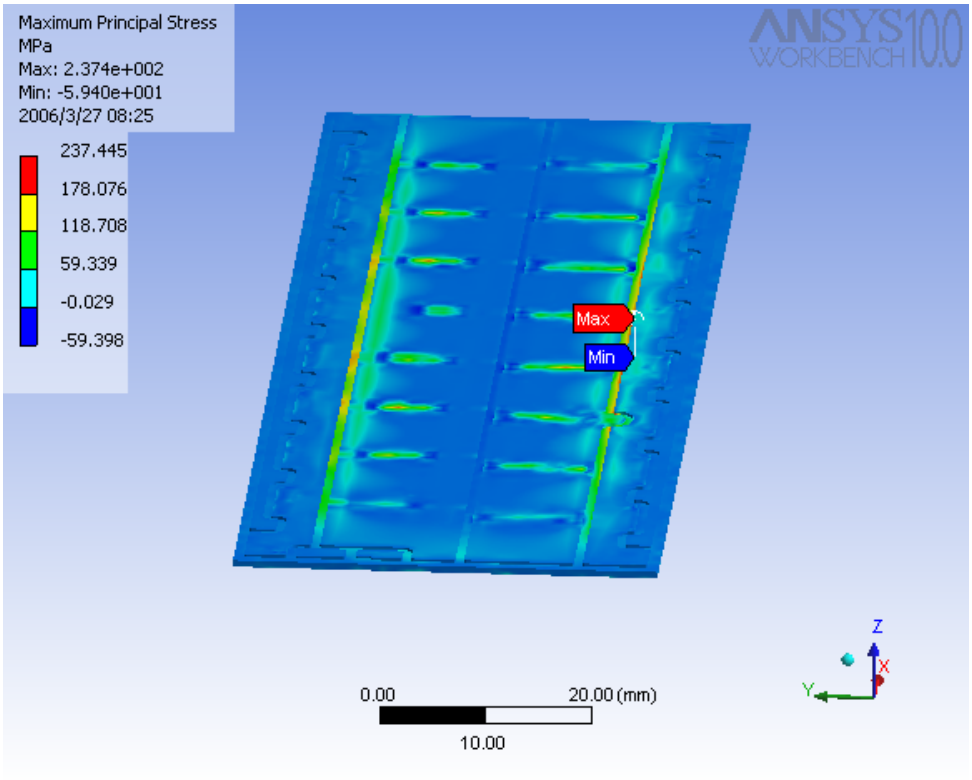


Figure 5. Maximum stresses in the assembly were acceptable to Semikron

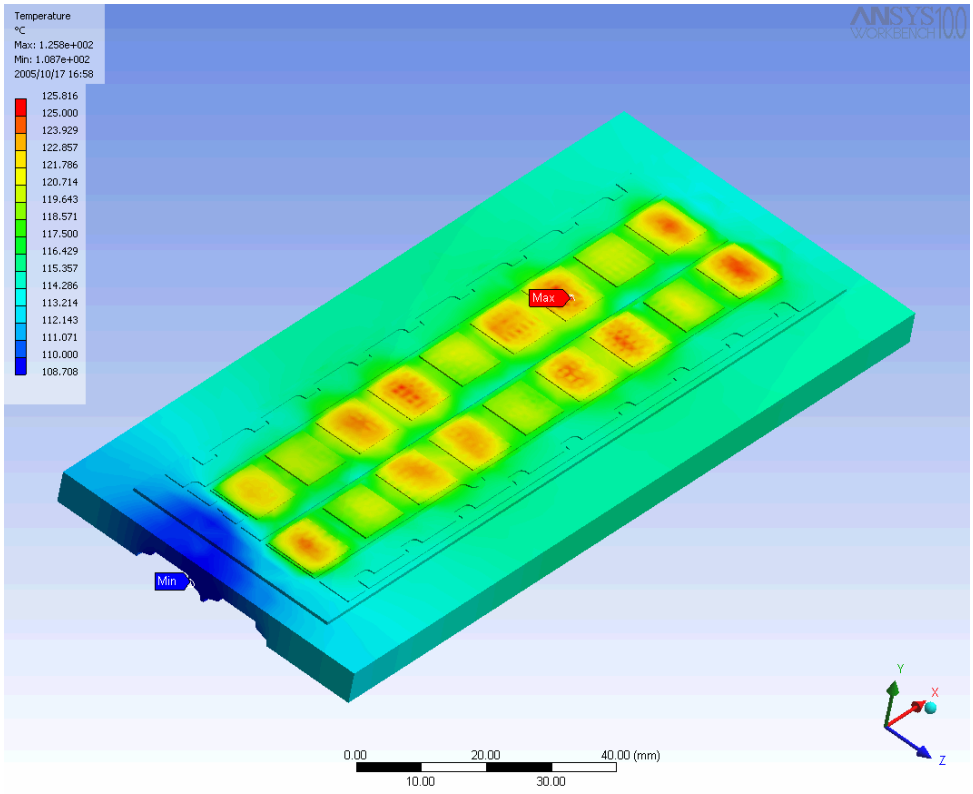


Figure 6. Die temperature contours at 100 W/cm^2, 105°C inlet temperature, 20.4 lpm flow rate

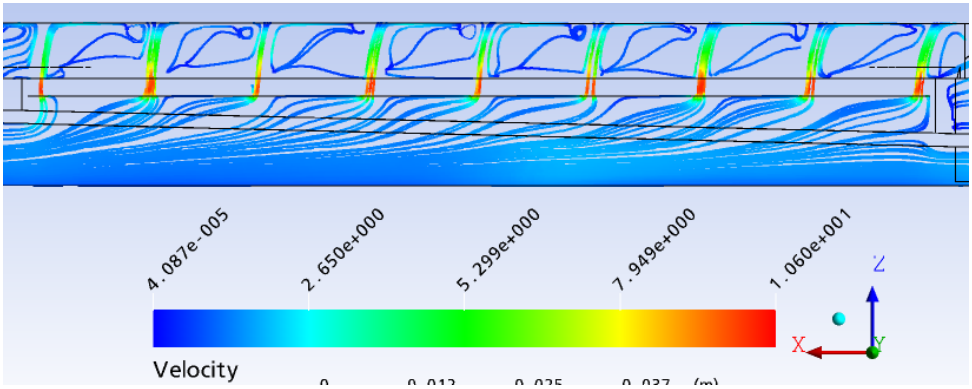


Figure 7. Uniform jet flow is obtained from the latest generation nozzle plate

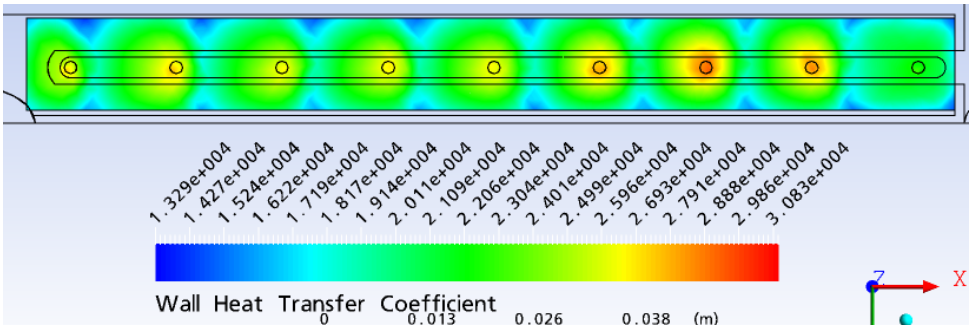


Figure 8. Heat transfer coefficients on target surface, with outline of nozzle plate shown below

Jet impingement experimental study

Jet impingement heat transfer has been studied and documented for its proven ability to attain high heat transfer coefficients. The primary focus of previous studies has been in three classes of impinging jets: submerged, confined, and free surface. Many times in practice, the available topology of the surfaces do not lend themselves to one of these configurations. Structural and other geometric considerations often make the impingement of jets into cavities an attractive solution for those wishing to optimize heat transfer performance with impinging jets.

As power requirements continue to increase in the realm of power electronics, the ability to extract the maximum heat flux is desirable. For that reason, an experimental study was performed on the geometric influences of impinging jets in cavities. This parametric study determined the effect of four variables on the average heat transfer coefficient on a constant given area: nozzle-to-target distance, velocity, chamfer angle, and geometric cavity shape.

Single-phase liquid jets have been studied extensively in the literature, which includes experiments, theoretical analyses, and numerical simulations. Different configurations of impinging jets, including single free-surface jets, multiple free-surface jets, single submerged jets, multiple submerged jets, and confined single submerged jets, have been studied. Planar and circular jets have also been studied. In the field of electronics cooling, many experimental correlations have been developed for the local and average heat transfer coefficients on the surface of the simulated chip. Most of the simulated chips are either 10 × 10 mm or 12.7 × 12.7 mm. Air jets have also been studied extensively. Some of the nondimensional heat transfer correlations developed from studies on air jets can be applied to liquid jets. Researchers have explored the impact of a vast array of parameters such as jet velocity, jet diameter, impact angle, nozzle-to-nozzle spacing, turbulence level, nozzle shape, nozzle length, jet pulsations, jet confinement, chip-surface enhancement, and fluid properties on the chip surface heat transfer coefficients. All these are covered in detail in comprehensive reviews.

In hybrid electric cars, inverters perform the DC/AC conversion. The inverters contain a number of IGBTs, which function as on/off switches. A substantial amount of power is dissipated by the IGBTs. Each IGBT has a silicon die area of 9 × 9 mm, with a thickness of 0.25 mm. One goal of this part of the project was to explore and compare the single-phase jet impingement configurations reported in the literature for cooling IGBTs. Typically, the package consists of the silicon die, copper layer, aluminum nitride, copper layer, aluminum base plate, and heat sink. In automotive applications, a 50:50 mixture of ethylene glycol and water is typically used as a coolant. In this project, we first considered a chip of 10 × 10 mm and looked at the heat transfer performance of single-phase jet impingement configurations such as single and multiple free-surface jets, single and multiple submerged jets, and confined jets. We restricted ourselves to circular jets at this point. Different empirical correlations from the literature were

used to gain insights into the average heat transfer coefficients that can be obtained from the chip surface. Numerical simulations (computational fluid dynamics) were performed for some of the configurations reported in the literature and were used in the simulations described in the preceding section. Simple calculations were also performed to understand the pressure drop associated with some of the jet impingement configurations.

Another practical concern associated with these systems is erosion. High-velocity jets (>5 m/s) have the potential to erode the material onto which they impinge.

IGBT package simulations were also performed with a glycol-water mixture and water as fluids. The jet inlet velocity temperature was maintained at 105°C, and simulations were performed with two heat fluxes of 90 and 200 W/cm^2.

The apparatus used for this experiment comprised several parts and tested two concepts. The first was a simple test to verify that a standard double-seal O-ring could adequately seal the inner chamber from the environment at pressures as high as 100 psi and at elevated temperatures. The second was to verify and determine the effects of flow rate and nozzle-to-target spacing on heat transfer. The first objective was accomplished by completely assembling the apparatus and using compressed air at 150 psi to test for leaks. The system was pressurized and the supply of air was removed while the pressure within the test vessel was monitored. Stable pressure indicated that the assembly was free from leaks and the O-ring provided an adequate seal.

The next focus of the experiment was to determine the effects of nozzle spacing and jet velocity on heat transfer. The experiments were carefully designed and conducted to extract the most information from the data. The apparatus contained six resistors to provide heat fluxes up to 140 W/cm^2, adjustable nozzles and flow rate, and heat transfer coefficients up to 35,000 W/m^2K. Figure 9 shows the array of resistors mounted on the apparatus. Figure 10 shows the apparatus opened up, with the target surfaces under the resistors displayed. Figure 11 shows the set of six nozzles, which can be moved closer or further away from the target surfaces. Figure 11 also shows the O-ring groove.

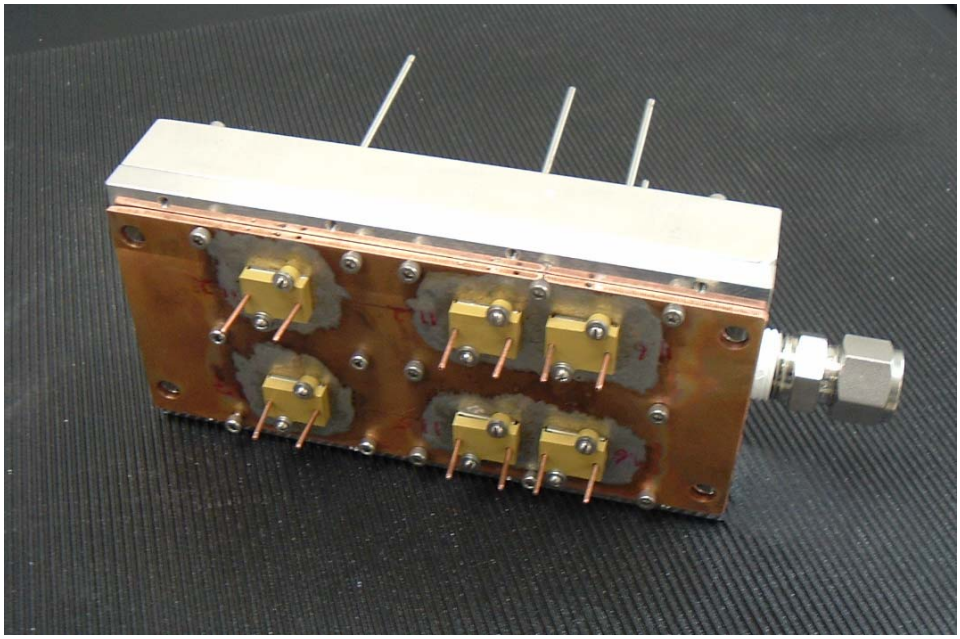


Figure 9. Resistors mounted on experimental apparatus

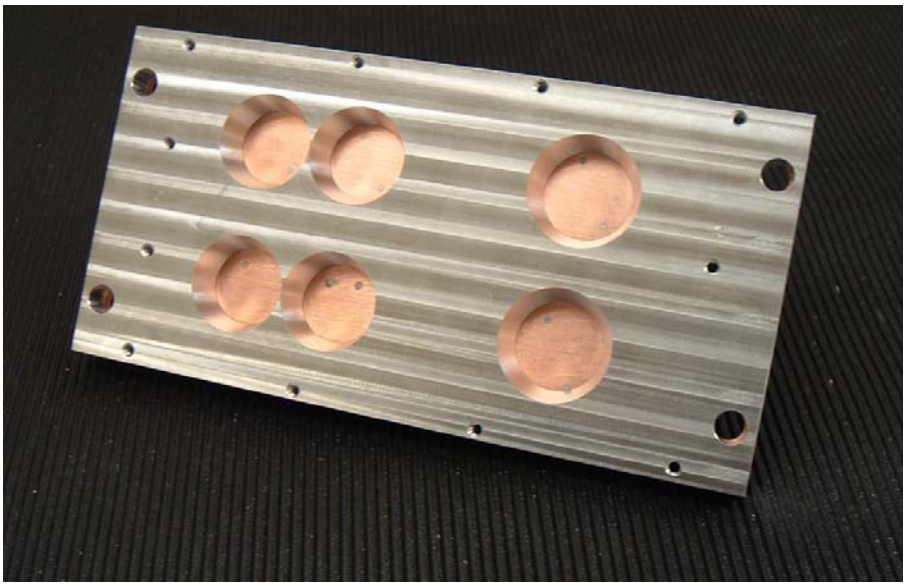


Figure 10. View of target surfaces, under resistors

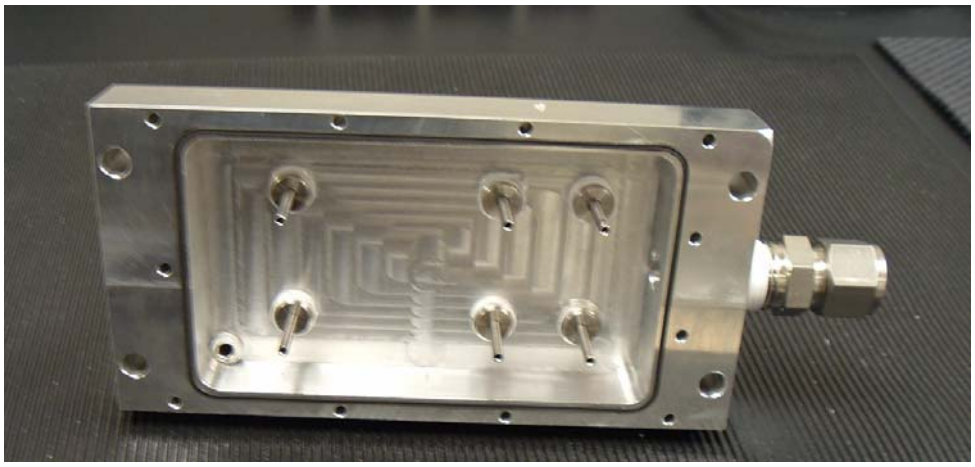


Figure 11. Nozzle array

Matlab's Model Based Calibration toolbox was used to analyze the data collected from the series of experiments. The domain space was mapped onto a homomorphic region through the use of coded values to build a response model and corresponding response surface. Validations of the model and subsequent error distribution were further analyzed.

After evaluating several models for response surfaces, including radial basis functions and polynomials up to fifth order, we chose a third order polynomial with a corresponding $R^2 = 0.9956$.

The coded values were then used in the polynomial expansion of the response surface. The resulting equation for the difference in temperature, *DT*, as a function of the coded nozzle to target spacing, x_1, and the flow rate, x_2, is

$$DT = 9.0579 - 0.65132x^1 - 1.7798x^2 + 1.0206x_1^2 - 1.2349x_1x_2 + 0.90627x_2 + 1.3586x1^3 + 1.8056x_1^2 x_2 - 2.1525x_1x_2^2 - 1.939x_2^3$$

A simple sensitivity analysis of the coefficients in the equation confirmed the high degree of interactions between the two parameters in this study and is confirmed by the convoluted topology exhibited in the response surface.

The use of jet impingement heat transfer has demonstrated that heat transfer can be vastly improved by manipulating the nozzle-to-target spacing of the nozzle and by adjusting the flow rate and consequent velocity of the jet. By constructing and sampling a robust design space, we could analyze the data collected and propose a model. The model described by the equation when compared to the experimental data had a relevance of $R^2 = 0.9956$. Further analysis, validation, and error estimates of the data and resulting model showed that for the data collected and the sampling space, the model is justifiably robust. Error is minimized in regions except where the velocity is extremely high and the nozzle is extremely close to the target surface.

The general trends exhibited in the data are primarily as follows:

- Heat transfer increases as the velocity increases.

- Heat transfer increases as the nozzle-to-target spacing is reduced.

These two generalizations certainly have exceptions, but generally hold true. The equation can be used to optimize jet spacing and velocity given identical geometric layouts specified in this experiment.

Prototype parts

The simulation and experimental work resulted in Generation 13 of the design being chosen as the best one to prototype. The parts were machined in August 2006 and will be sent to Semikron for the addition of the module. Figure 12 shows the base plate and nozzle plate parts. The base plate is shown with the bottom side up. This side will receive the nozzle plate and will be sealed with a cover plate. The inlet and outlet fluid ports are seen on either side of the base plate. The nozzle plate is shown with the jet side up. Figure 13 shows the nozzle plate put into position in the base plate. Figure 14 shows the base plate with the module mounting surface up. The elongated holes, over which the DBC (with the IGBTs and diodes) is mounted, are shown. The nozzles can be seen through the elongated holes. The bridges running between the holes support the assembly. Figure 15 shows a close view of the nozzles, holes, and O-ring grooves. The nozzles are placed directly under the IGBTs and diodes, which are not spaced evenly. The O-ring groove is designed to accept a quad-style ring, which was found in the experimental work to seal the assembly up to 150 psi. Figure 16 is another view of the nozzle plate, showing how the nozzles are placed according to the IGBT and diode locations, and the angled plenums on either side of the plate, which promote uniform flow from each nozzle. Figure 17 shows one end of the nozzle plate in a close view.

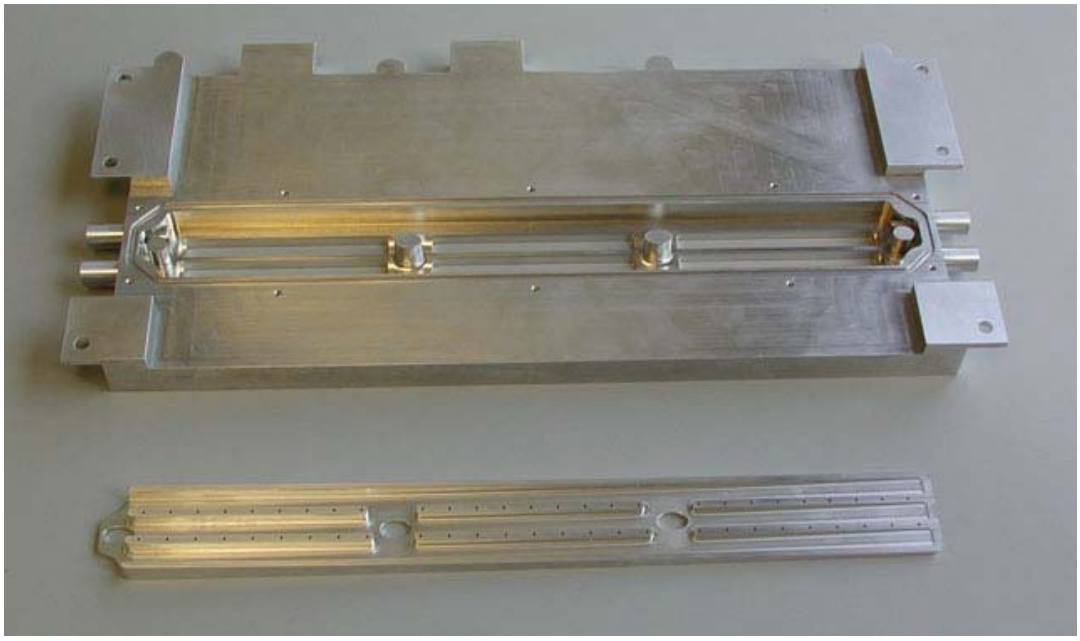


Figure 12. Base plate and nozzle plate parts

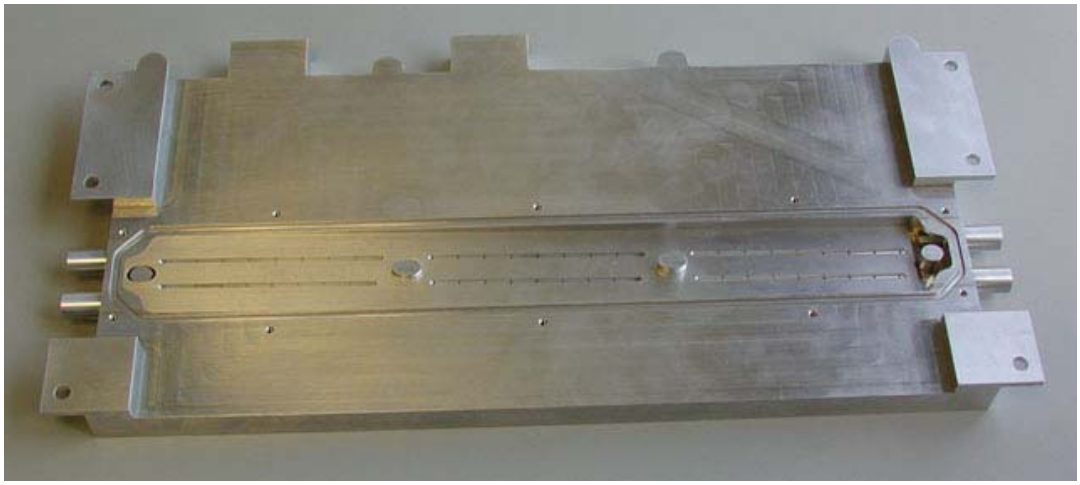


Figure 13. Nozzle plate in position in the base plate

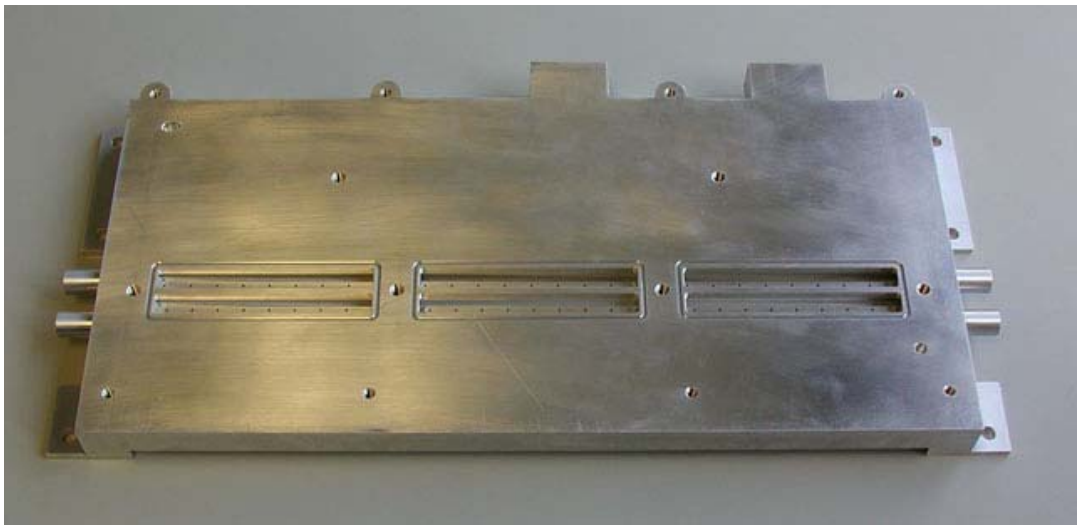


Figure 14. Base plate, with nozzle plate inserted, shown with module mounting surface up



Figure 15. Close view of the nozzles, elongated holes, and O-ring grooves

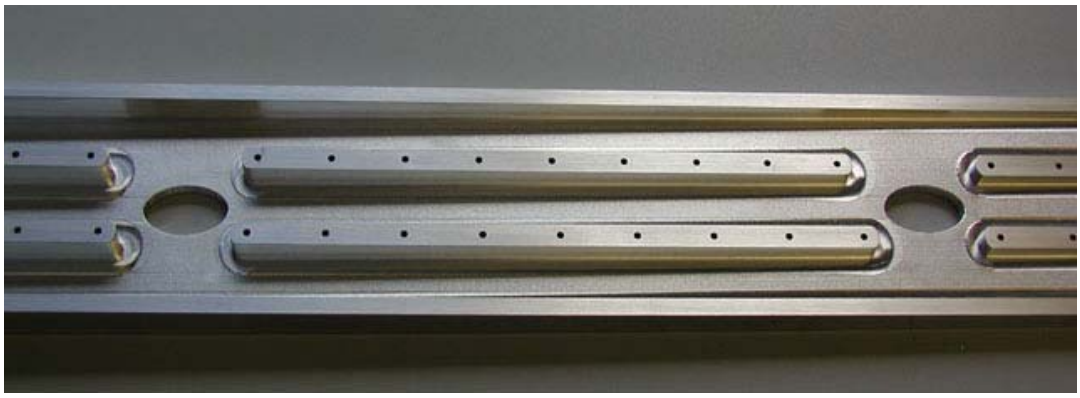


Figure 16. View of the center of the nozzle plate, showing nozzle placements, holes for mounting bosses, and the angled outlet plenum



Figure 17. View of one end of the nozzle plate

Conclusions

A series of structural, fluid, and thermal simulations performed on various geometries for the nozzle plate and base plate has resulted in a design that is ready for prototype evaluation. Experimental analysis of the major influences on thermal performance of the multijet concept showed the effects of nozzle size, distance from the target, and fluid flow rate. Simulation and experiment resulted in a design that allows use of 105°C coolant at 100 W/cm^2 heat flux and keep die temperatures at acceptable levels and pressure drop approximately the same as Semikron's current elliptical fin product.

Next Steps

After Semikron adds the electronics module, the fully functioning prototype will be tested in NREL in a long-term evaluation of thermal, fluid, and structural performance. Further modifications to the nozzle plate and base plate may be necessary as the test progresses. The erosive and corrosive effects of new and old coolant will be explored. Collaboration with Semikron will continue as a design ready for production is developed.

References

D. Benhammou, Jet Impingement Experiment Study, NREL Technical Report, June 2006

Patents

Patent pending.

2.6 Dynamic and Steady State Modeling to Identify, over Various Drive Cycles, Component and System Performance Efficiency and Thermal Loads

Principal Investigator: *Michael P. O'Keefe*
National Renewable Energy Laboratory
1617 Cole Blvd.
Golden, CO 80401 USA
Voice: 303-275-4268; Fax: 303-275-4415; E-mail: michael_okeefe@nrel.gov

DOE Technology Development Manager: *Susan A. Rogers*
Voice: 202-586-8997; Fax: 202-586-1600; E-mail: Susan.Rogers@ee.doe.gov

---

Abstract

This report summarizes the FY 2006 activities in dynamic and steady state modeling applied to Advanced Power Electronics and Electric Machines (APEEM) thermal control technology R&D. It elaborates on two key areas of focus: (1) the development of thermal control requirements by cascading vehicle level requirements and duty cycles down through APEEM components. A survey of the various powertrain technologies of interest to DOE (hybrid electric vehicle, fuel cell vehicle, and plug-in hybrid electric vehicle) has been conducted from a thermal control standpoint; and (2) the valuation of APEEM thermal control technologies in a systems context. A heat transfer model of the inverter power electronics board and assembly is used to compare the various cooling technologies for their performance.

Objective

Guide the Advanced Power Electronics and Electric Machines (APEEM) Program's thermal control technology R&D effort to best meet APEEM program needs by:

- Defining the thermal requirements for advanced automotive powertrain systems of interest to DOE and FreedomCAR: hybrid electric vehicle (HEV), plug-in hybrid electric vehicle (PHEV), and fuel cell vehicle (FCV).
- Evaluating thermal control technologies in a systems context.
- Recommending a thermal control R&D pathway.

Approach

Analyze the thermal control portfolio of R&D projects to:

- Define the Thermal Cooling Requirements for Advanced Powertrains: Use a vehicle system's context to explore the cooling requirements of various powertrain architectures.
- Evaluate Thermal Control Technologies: Work with project principal investigators and use computational analysis to compare and contrast the thermal control technologies under investigation or consideration in the DOE program. These comparisons should fall within logical

and consistent contexts (i.e., tied back to actual component operation and accepted worst-case scenarios) that show an "apples-to-apples" comparison of cooling performance, implications for component life, cost, volume, and weight.

Major Accomplishments

Preliminary identification of the thermal requirements for power electronics and electric machines (PEEMs) in advanced vehicle powertrains such as PHEVs.

Evaluation of the APEEM portfolio of thermal control technologies in a systems context with an inverter assembly thermal model.

Technical Discussion

We focused on two topic areas during FY 2006: preliminary identification of the thermal requirements of advanced powertrains, especially PHEVs; and the evaluation of the APEEM portfolio of thermal control technologies in a systems context.

PEEM System Thermal Requirements

The thermal requirements for PEEMs, especially with emerging technology and new vehicle requirements, are developing. This study yields a preliminary estimate of the additional heat load that must be dissipated for advanced power train systems (HEVs, PHEVs, and FCVs) as a first step in identifying these requirements. Special attention is paid to PHEVs. This section begins with a background on PHEVs and follows with a discussion of the analysis conducted to estimate the heat rejection and cooling requirements for PHEVs, HEVs, and FCVs.

Background on Plug-in Hybrid Electric Vehicles

PHEV is a dual-fuel technology that can transform the transportation energy infrastructure from nonrenewable, high-carbon fuels to more environmentally responsible options. One PHEV fuel is electricity from the electrical utility grid (a secondary energy source generated from one or more primary energy sources such as coal, natural gas, wind, and hydro power). The other fuel could be one of any number of options, although gasoline is most likely. This is in contrast to the conventional HEV, in which all of the motive power ultimately derives from gasoline (electricity is used only to temporarily store energy).

PHEVs can deliver performance equivalent to today's vehicles and offer key advantages related to energy security and transportation sustainability. Compared with other technology options, PHEVs do not have the infrastructure issues (e.g., hydrogen for FCVs) or the limited range issues (e.g., battery electric vehicles [BEVs]) exhibited by other technologies. The energy security and fuel efficiency benefits of PHEVs result from efficient delivery of fuel energy from the tank to the wheels and, more importantly, a transition from conventional transportation fuels to electricity. This is possible because PHEVs exhibit aspects of BEVs and HEVs, namely:

A large energy storage unit that can be recharged from the electrical utility grid and supply net motive energy over a significant distance.

A hybrid powertrain that typically uses an internal combustion engine with an electric motor.

By blending aspects of BEVs with conventional HEVs, we can realize many of the advantages of a BEV and eliminate several disadvantages. Because a PHEV requires fewer batteries than a full BEV, the PHEV comes with a reduced cost penalty versus a BEV for equivalent performance. Furthermore, the PHEV has range equivalent to an HEV or conventional vehicle (CV), and charging times are much shorter than for an equivalent BEV. In contrast to an equivalent HEV, overall fuel consumption (and liquid fuel consumption in particular) is further reduced since fuel energy is supplied from both electricity and liquid fuel as opposed to just liquid fuel, as is the case for conventional HEVs.

Although the general traits mentioned here are true for any PHEV, the specific architecture and optimal configuration of the PHEV is still in flux. Current consensus tends to favor a parallel HEV architecture with increased battery capacity. Other architectures have been proposed, however. For example, a series "range-extending" option (where the engine serves only to generate electricity for batteries) has been successfully built and sold (the Renault Kangoo).

The question of how much electrical capacity to store on-board the PHEV is also still under debate. The PHEV20 appears to be a good choice for a midsize sedan, based on some preliminary work done at NREL (Simpson et al. 2006), though PHEV40 and PHEV60 vehicles are also being considered. (The 20, 40, and 60 refer to the distance that can be driven in miles all-electrically by the PHEV.) The issue of enforcing an all-electric range on the PHEV (a range where the engine would absolutely not operate) is still open, though early analysis indicates that an all-electric range constraint may add significant cost to a PHEV at minimal additional benefit.

PHEVs work well with duty cycles where many relatively short trips comprise the bulk of distance traveled. By recharging between these short trips, a large portion of the motive energy to propel the vehicle can come from the electrical grid instead of gasoline or other fossil fuels. The transition from today's petroleum-based transportation fuels to electricity opens up many opportunities. By recharging the vehicles' batteries overnight, electrical utilities can increase their operating efficiency by increasing their base load. Furthermore, the difference between peak capacity and base-load capacity means that power utilities will typically have enough excess capacity at night to recharge a large number of vehicles before they have to add new generating capacity (new power plants). If done correctly, this can lead to net reductions in total carbon dioxide and other greenhouse gas emissions. Furthermore, if effort is made to transform the power plants on the national electrical grid to use more renewable sources of energy, the benefits of renewable energy can be brought to the transportation sector directly through PHEVs. All of this together will have a positive impact on national energy security, energy sustainability, and environmental stewardship.

However, PHEVs face major challenges to commercialization. Chief among these is increased vehicle cost, which results from the large number of advanced batteries on the vehicle, the life of those batteries, the hybrid-electric drive system (PEEMs), and supporting electrical subsystems. For other recent analyses on PHEVs, see Simpson et al. (2006), O'Keefe and Markel (2006), and Markel and Simpson (2006).

To address the cost issues, engineers and scientists are seeking electric drive solutions that improve in several key areas at once: lower cost, higher efficiency, lower weight, smaller size, higher reliability, and longer life. As higher power demands are forced through smaller surface areas with warmer integrated cooling fluids near temperature-sensitive electronics, thermal control of these systems becomes increasingly critical. To make real progress on systems that advance on all the key metrics, a systems solution will be needed that closely integrates thermal control from the beginning.

In this study, we analyze the electric powertrain components in a vehicle context to determine thermal control requirements for a PHEV and other advanced architectures. This is a first step toward understanding the problem so that we can choose the best solution to solve it.

From Vehicle to APEEM Thermal Requirements

For research to be beneficial, we need to understand the context of the problem that needs to be solved. This is no less true for the research being conducted on thermal systems for PEEMs. Why? Simply because the thermal control technologies we research are subsystems of a larger electric drive system—which itself is a subsystem of the entire vehicle. A thermal control system has meaning only in the context of cooling requirements for given components. Furthermore, we must look not only at our specific context, but must also be aware of how the thermal control subsystem interacts and interfaces with other subsystems (for example, the engine thermal control system).

The FreedomCAR Program has done a good job of identifying research targets for vehicle systems. Many of these research goals have been cascaded down to the subsystem level. In this study, we will use the concept of cascading to relate vehicle-level requirements and duty cycle operation to the subsystem level. This will give us a first look at the thermal control requirements for electric drive system components for whichever powertrain architecture we care to examine.

Let us consider a midsize sedan with performance competitive for the North American market. Reasonable assumptions have been identified for the midsize sedan by NREL researchers in collaboration with the DOE/FreedomCAR Vehicle Systems Technical Team. These performance requirements appear in **Table 1**. The requirements are assembled from a database of present-day vehicle performance requirements and were identified as reasonable by the DOE/FreedomCAR Vehicle Systems Analysis Technical Team.

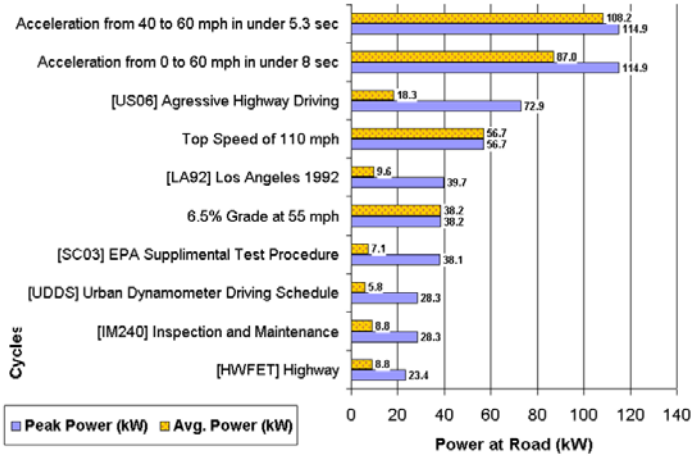
(a) Table 1: Midsize Sedan Performance Requirements and Vehicle Assumptions

1 Attribute	2 Value
Top Speed	110 mph
Full Acceleration time from 0 to 60 mph	≤ 8 s
Passing Acceleration time from 40 to 60 mph	≤ 5.3 s
Hill Climbing road grade (percent rise over roadway run) to climb with engine at 66% of rated power	6.5% at 55 mph
Range maximum distance traveled starting fully fueled	400 miles
Glider Mass the mass of the vehicle minus the powertrain	905 kg (1995 lb)
Accessory Loads accessory loads assumed for the PHEV	0.7 kW electric (average) 4.0 kW electric (peak)
Transmission Efficiency efficiency of the mechanical gearing between the motor/engine and wheels	85%
Electrical Generation Efficiency for Accessories efficiency of generating power to the electric accessories	85%

Figure 1 shows the average and peak power requirements at the road-tire interface to propel a vehicle with the same weight and chassis/body parameters (drag, frontal area, etc.) as the Toyota Prius over several driving events. The Prius was chosen for this study as it has become something of a baseline for HEVs. In addition to the vehicle performance requirements (acceleration, hill climbing, etc.), the power requirements for several standard vehicle duty cycles (vehicle time-speed driving patterns) are also shown. The cycles include the HWFET (highway federal emissions test—nonaggressive highway

driving), US06 (United States Highway 6—aggressive highway driving), UDDS (urban dynamometer driving schedule—nonaggressive urban driving), the IM240 (inspection and maintenance for 240 seconds—a light urban driving cycle), and the LA92 (Los Angeles 1992—aggressive urban driving). Minimum powertrain component sizes can be estimated based on these duty cycles and performance requirements.

Because even a PHEV cannot power a vehicle continuously with electricity over the vehicle's maximum driving range, there is necessarily a distinction between the vehicle's minimum engine power (which can run continuously over the vehicle's range) and minimum motor power (where continuous power is tied to the battery capacity). If we examine the duty cycle and performance constraints in **Figure 1** and apply our assumptions about transmission efficiencies and auxiliary loads from **Table 1**, we can estimate the peak and continuous power required at the engine/motor. This appears in **Table 2**.



(b) Figure 1. Vehicle minimum peak and continuous power requirements

(c) Table 2. Peak and Continuous Power Requirements

$P_{peak,\min} = \frac{114.9\,kW}{0.85} + \frac{4\,kW}{0.85} \approx 140\,kW$ based on acceleration requirement; assumes that top speed is a peak power requirement
$P_{continuous,\min} = \frac{\frac{38.2kW}{0.85} + \frac{4kW}{0.85}}{0.66} \approx 75kW$ based on hill climbing requirement where power can only be 66% of engine peak
$P_{peak} = P_{engine} + P_{motor,peak} \geq 140\,\text{kW}$ $P_{continuous} = P_{engine} \geq 75\,\text{kW}$ $\therefore$ if $P_{motor,peak}$ is 55 kW as per FreedomCAR targets, P_{engine} must be ≥ 85 kW

The performance requirements listed in **Table 1** imply certain minimum continuous and peak power outputs for vehicle powertrain components, which are summarized in **Figure 1**.

According to the conservative analysis given in **Table 2**, an engine of 85 kW or greater power coupled with a 55 kW (peak) motor would be ideal. These power requirements are derived by applying the performance requirements from **Table 1** to a vehicle with the same weight and body parameters (drag coefficient and frontal area) as the Toyota Prius. In actuality, the peak power output from the Toyota Prius powertrain is 82 kW at 53 mph—substantially less than the 140 kW peak predicted here. This means that the actual Toyota Prius does not meet the performance requirements of **Table 2**. A quick search on the Internet for acceleration times of the Prius will confirm this is true. This raises the question of which high-level design requirements we should work toward. Aggressive performance requirements add more cost and system complexity. However, some minimum performance will be needed for consumer acceptance. **Table 1** is indicative of the North American light-duty vehicle market—but is it too aggressive? The Prius, despite meeting less stringent market requirements, has some degree of consumer acceptance.

The previous analysis shows how vehicle requirements and duty cycles relate to component sizes. We have confirmed that the FreedomCAR motor peak power shaft output of 55 kW is reasonable and that an engine size of 85 kW shaft output is in the ballpark for a car the size of a Toyota Prius with North American market performance (assuming a parallel hybrid configuration). Let us shift now to a study of how vehicle duty cycle and performance requirements relate to electric drive component operation.

The ADVISOR™ software results from the simulation of several midsize sedan vehicle models are presented next. The objective of this preliminary study is to have a sense for the heat rejection profiles of components in electric drive subsystems of advanced powertrains over the execution of various vehicle duty cycles and performance requirements. The numerical vehicle models used in this analysis are representative of midsize sedan HEV, PHEV, FCV, and CV architectures. The models were created by NREL's Vehicle Systems Analysis Team for a separate analysis and were useful for our analysis as well. We intend to continue—and expand—the collaboration with the DOE FreedomCAR Vehicle Systems Analysis Team to ensure we are using the best, most accurate, and most relevant vehicle models and data possible.

Each numerical vehicle model in this study uses a different powertrain: CV (manual transmission), HEV (parallel), PHEV (similar to the HEV but with larger size and capacity components), and FCV. By

simulating each vehicle model over several duty cycles (speed-time traces), we can learn how the electric drive duty cycle is influenced by the vehicle-level duty cycle.

An overview of the vehicle models used in this study is given in **Table 3**. Although the performance of each model is similar to that presented in **Table 1**, the FCV model in particular has not been rigorously adjusted for performance parity. Thus, the FCV model has less aggressive performance than that specified by the requirements. NREL intends to continue working with other groups in the DOE program on vehicle systems modeling to improve these models. For now, we present the models we have from the ADVISOR software, which should give some early directional indications for component heat rejection.

(d) Table 3. Parameters for Vehicle Models Used in This Study

3 Attribute	4 CV	5 HEV	6 PHEV20	7 PHEV40	8 FCV
Weight (lb/kg)	3587/ 1627	3384/ 1535	3525/ 1599	3616/ 1640	3706/ 1681
Drag Coefficient	0.30	0.30	0.30	0.30	0.33
Frontal Area (m^2)	2.27	2.27	2.27	2.27	2.00
Accessory Loads (kW) (mechanical/electrical)	0.823/ 0.0	0.0/ 0.7	0.0/ 0.7	0.0/ 0.7	0.0/ 0.7
Rolling Resistance Coefficient	0.009	0.009	0.009	0.009	0.009
Prime Mover Peak Power (kW)	145	82	84	86	58
Motor Power (kW) (Peak/Continuous)	NA	39/ 39	50/ 50	50/ 50	88/ 88
Battery Capacity [usable] (kWh)	NA	0.38	5.67	10.84	0.73
Top Speed (mph)	147.5	137.1	134.4	138.9	97.9
Acceleration Time 0−60 mph (seconds)	8.0	8.1	8.0	8.1	10.9
Fuel Economy over UDDS Cycle (mpg gasoline equivalent) (charge sustaining mode)	22.7	37.4	38.3	37.6	70.1

Each powertrain considered has vastly different thermal performance (see **Figure 2**). Here the average heat rejection by subsystem is listed for the various powertrains over the UDDS cycle. The CV, HEV, PHEV20 (a PHEV with 20 miles of all-electric driving capacity), PHEV40 (a PHEV with 40 miles of all-electric driving capacity), and FCV are shown. The CV, because of its large internal combustion engine, rejects much more heat than the other vehicles. A large portion of this heat is rejected directly to the atmosphere through engine exhaust. Most of the remaining energy is rejected via the engine coolant through the radiator. Thus, despite the large amount of heat rejected by the internal combustion engine in a CV, the engine, which can withstand relatively high temperatures (compared to power electronics) has no major thermal control issues (i.e., the technology adequately cools present designs).

In contrast, the power electronics for HEVs and PHEVs reject much less heat on average than the internal combustion engine; however, it must reject that heat through much smaller thermal masses, within confined spaces, and in the presence of temperature-sensitive electronics. This situation presents a major technical hurdle to technology advancement in PEEM R&D. It also emphasizes the need for focused thermal cooling R&D as a joint effort with the PEEM R&D.

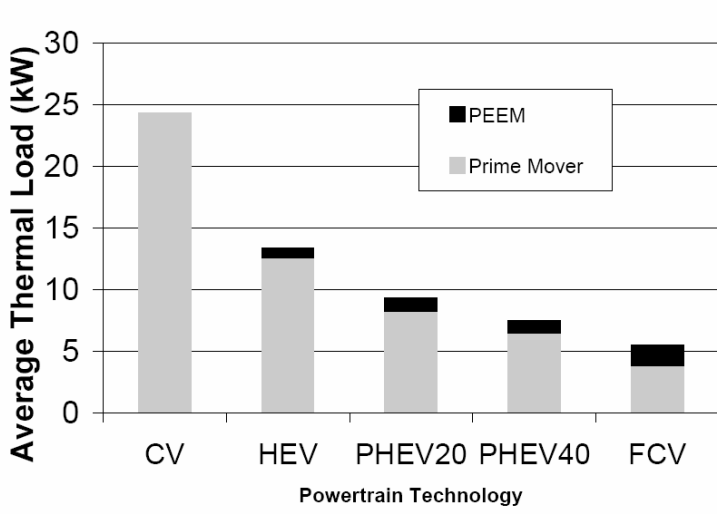
Because PHEVs are of special interest, we will now look more specifically into the cooling requirements for PHEVs in contrast with HEVs. **Table 3** shows that the motor size for the PHEV is 25% larger than that of the HEV. A first approximation of the increase in thermal loads of a PHEV over an HEV would be:

(e) Equation 1: $$PITL = \frac{\overline{ML_{PHEV}}}{\overline{ML_{HEV}}} \cdot \frac{(P_{\max,motor,PHEV} - P_{\max,motor,HEV}) \cdot 100\%}{P_{\max,motor,HEV}}$$

where:

$PITL$ = percentage increase in thermal loads and

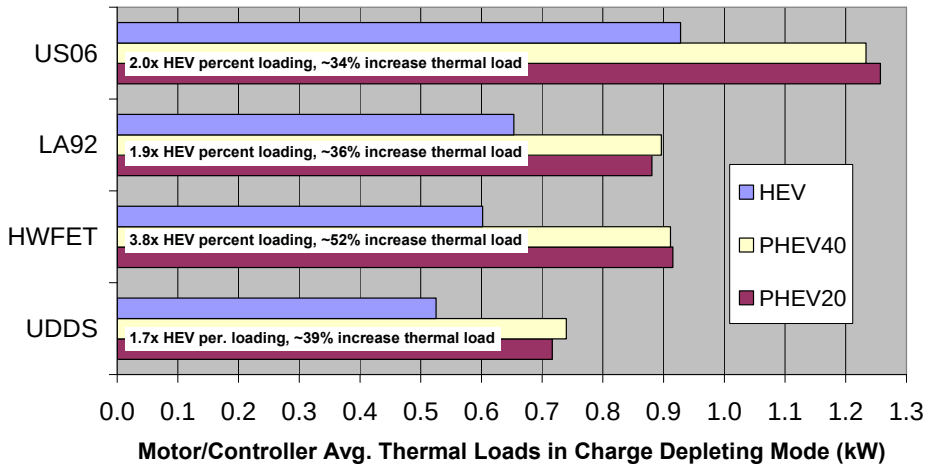
ML = motor loading $= \frac{\overline{P_{motor}}}{P_{\max,motor}}$



(f) Figure 2. Average thermal loads by vehicle subsystem and vehicle powertrain (UDDS cycle)

However, when we apply **Equation 1**, we find that the percentage increase in thermal loading of PEEM systems for the PHEV versus the HEV is overestimated (see **Figure 3**). As noted on the graph, for the US06 aggressive highway driving cycle, the average motor loading of the PHEV is twice that of the HEV. That is, for the PHEV, the average to peak possible power throughput at the motor is twice that of an HEV. Coupled with a 25% increase in motor size for the PHEV versus HEV (given in **Table 3**), we would have expected a 50% increase in thermal loads; however, after running our vehicle system models, we see that there has been only a 36% increase in thermal loads. Why is this?

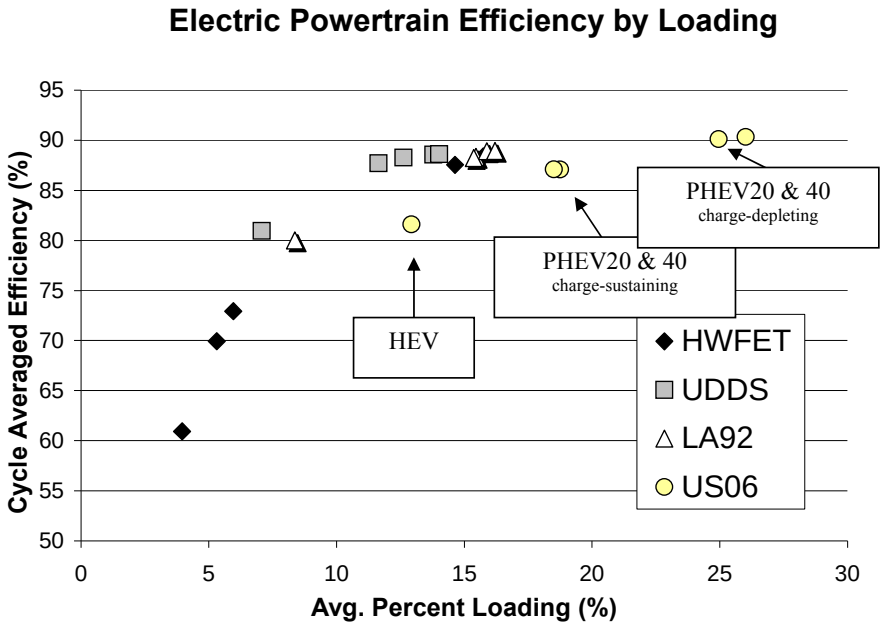
The simple relationship given by **Equation 1** for the increase in thermal loading is linear. However, we are dealing with a nonlinear system. Specifically, we see from **Table 4** that as the PEEM drive system utilization is increased (i.e., as the system reaches higher average loading), the system efficiency increases. This increase in efficiency counteracts the increase in wasted heat that would have been seen otherwise. This is clearly demonstrated in **Figure 4**.



(g) Figure 3. Increase in PEEM thermal loads for PHEVs over HEVs

(h) Table 4. Motor and Inverter Combined Heat Rejection by Duty Cycle

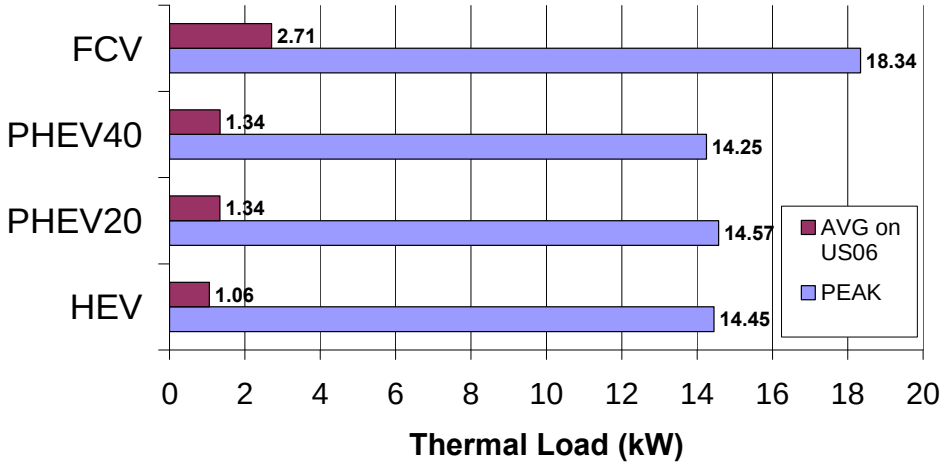
9 Powertrain	10 $\overline{P_{loss}}$	11 $\overline{P_{shaft,out}}$	12 $\overline{P_{electric,in}}$	13 $\frac{E_{shaft}}{D}$	14 $\overline{\eta_{shaft,out}}$
15 –	16 kW	17 kW	18 kW	19 kJ/mile	20 %
UDDS Cycle (1369 s and 7.45 miles per cycle)					
HEV	0.53	2.23	2.76	115.5	81.0
PHEV20 charge-sustaining	0.79	6.11	6.90	420.6	88.6
PHEV20 charge-depleting	0.72	5.11	5.82	595.1	87.7
PHEV40 charge-sustaining	0.80	6.21	7.01	428.6	88.6
PHEV40 charge-depleting	0.74	5.57	6.31	615.9	88.3
HWFET Cycle (765 s and 10.26 miles per cycle)					
HEV	0.60	0.94	1.54	5.8	60.9
PHEV20 charge-sustaining	0.81	2.17	2.98	46.5	72.9
PHEV20 charge-depleting	0.92	6.96	7.87	462.4	88.4
PHEV40 charge-sustaining	0.80	1.86	2.65	35.1	69.9
PHEV40 charge-depleting	0.91	6.41	7.32	415.1	87.5



(i) Figure 4. PEEM cycle averaged efficiency by loading

Figure 4 shows the average percent loading of the HEV, PHEV20, and PHEV40 models simulated over various drive cycles. The average percent loading is the average power output at the motor shaft divided by the maximum possible shaft output power times 100%. The PHEVs are simulated in charge-sustaining mode (where the net energy in the energy storage system is relatively constant over distance) and charge-depleting mode (where there is a net reduction in energy storage system energy with distance). Figure 4 demonstrates a general trend for the increase in cycle averaged efficiency as we move from an HEV to a PHEV. The strength of this trend varies over duty cycle, but is visibly present over all the driving profiles examined. This favorable increase in cycle averaged efficiency decreases the average heat rejection from the PEEM systems for PHEVs compared to HEVs over the various drive cycles. This trend does not hold consistently for PHEV charge-sustaining versus charge-depleting operation. In fact, a PHEV charge-depleting operation is not always more efficient than a PHEV charge-sustaining operation. This depends on the specifics of the given duty cycle (see **Table 4**).

The analyses presented thus far examine cycle averaged thermal loading, which tells us about the anticipated day-to-day average heat rejection of the PEEM components. This can relate to life and daily performance. However, peak—not average thermal loading—must be used to size PEEM thermal control technologies. Peak losses are compared to average losses in **Figure 5**. The peak losses are the maximum thermal load generated over either the US06 or 0−60 mph acceleration test. The average losses correspond to the US06 (the average thermal load per time over the US06). There is a huge disparity between the peak and average loads. This disparity indicates that technologies such as thermal storage technologies (phase change materials and the like) that remove the peak rejection rates and "level the load" may be worthwhile to examine for use in a thermal control system. A thermal storage technology could enable cheaper and smaller thermal control devices sized for average versus peak power rejection.



(j) Figure 5. Average versus peak thermal loading from PEEM components

Analysis of Thermal Control Technologies

The second major effort conducted during FY 2006 was to evaluate some of the current APEEM Thermal Control R&D in a systems context. Specifically, we have estimated the peak silicon device temperature (the IGBT or diodes) in inverter power electronics that are associated with each thermal control technology under various heat rejection scenarios. A one-dimensional (1D) heat-transfer model and a more sophisticated three-dimensional (3D) finite element model (FEA model) of the inverter power electronics are used to simulate the peak silicon device temperatures and to make consistent comparisons of the APEEM thermal control technologies. This next section will present the heat transfer models as well as the results thus far on this effort.

Inverter Power Electronics Heat Transfer Models

Two heat transfer models were used in this study: a 1D heat transfer model and an FEA model. The fundamentals of both models can be understood by considering the 1D electrical-circuit analogy to heat transfer. In the electrical-circuit analogy, the concept of thermal resistance is modeled analogous to "electrical resistors." Temperature is analogous to voltage, and temperature drops analogous to voltage drops. Entropy flow (heat transferred at a given temperature) becomes analogous to current.

Resistance to thermal conduction is given by the relation:

(k) Equation 2: $\theta_{th,conduction} = \frac{L}{k \cdot A}$

(l) Equation 3: $R_{th,conduction} = T \cdot \theta_{th,conduction}$

where θ is "classical thermal resistance," R is an "Ohm's law thermal resistance," L is the thickness of the layer, k is the thermal conductivity (in units of W/(m·K) or similar), T is the temperature of the material, and A is the cross-sectional area for convective heat transfer. In SI, the units are K^2/W for the Ohm's law thermal resistance and K/W for classical thermal resistance. There is a similar relationship for the resistance associated with convective heat transfer:

(m) Equation 4: $\theta_{th,convective} = \frac{1}{h \cdot A}$

(n) Equation 5: $R_{th,convective} = T \cdot \theta_{th,convective}$

where h is the convective heat transfer coefficient in $W/(m^2 \cdot K)$ and A is the corresponding area for heat transfer. Again, T shows up as the bulk temperature associated with the resistance and thermal resistance can be given by either the "classical" form or the Ohm's law form.

Entropy flow is analogous to current:

(o) Equation 6: $\dot{S} = \frac{\dot{Q}}{T}$

where $\dot{Q}$ is the 1D rate of heat transfer trough a material (in W) and T is the bulk representative temperature in Kelvin of the material. $\dot{S}$ is the entropy flow.

To determine temperature drops across a given thermal layer, we can use the analogy of Ohm's law as follows:

(p) Equation 7: $\Delta V = I \cdot R \rightarrow \Delta T = \dot{S} \cdot R_{th}$

which can be simplified to:

(q) Equation 8: $\Delta T = \dot{Q} \cdot \theta_{th}$

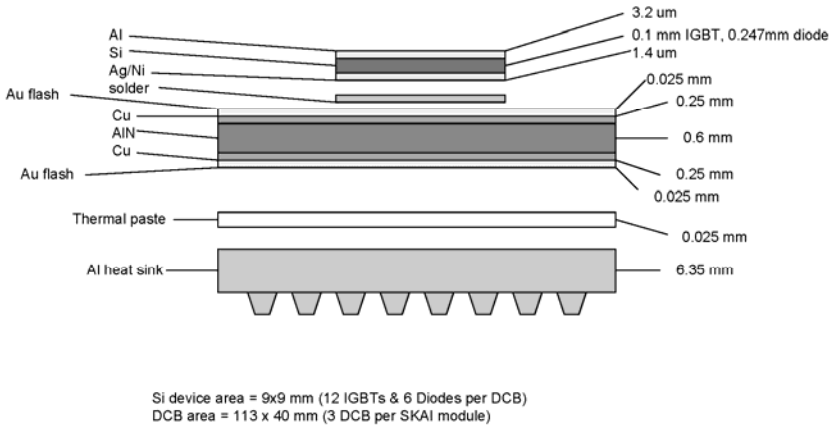
where θ_{th} would correspond to either the convective or conductive version of classical thermal resistance, depending upon the context of where one was measuring the temperature drop.

Similar electrical relationships apply using the variables we've defined. For example, the power attributed to heat rejection through any given layer is:

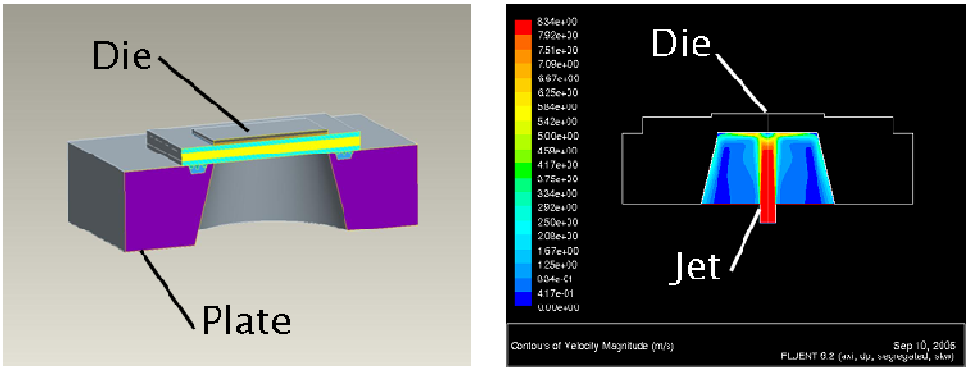
(r) Equation 9: $P = I^2 \cdot R = I \cdot V \rightarrow \dot{Q} = \dot{S}^2 \cdot R_{th} = \dot{S} \cdot T$

The electrical analogy to heat transfer serves as the basis to construct a model of the heat transfer in an inverter. The inverter assembly's various layers and components are modeled as thermal resistors that conduct heat from the silicon devices of the power electronics to the coolant of the thermal control system. The coolant in the thermal control system ultimately convects heat away to the radiator and then to the ambient air. The baseline inverter assembly is modeled after the Semikron SKAI system (see **Figure 6**). The only difference between the models we used and that of **Figure 6** is that the diode thickness is set

the same as the IGBT thickness. Thus, all silicon devices (silicon die) rise to the same peak temperature in our models. Another promising assembly structure is the low thermal resistance assembly, which opens holes in the cold plate to allow cooling via liquid coolant jets that impinge directly on the backside of the direct bonded copper (DBC) layer of the inverter. This assembly dramatically reduces the thermal conduction resistance between heat source and sink. A schematic of this layout is given in **Figure 7**.



(s) Figure 6. Semikron SKAI thermal stack-up (graphic courtesy of Semikron/John Mookken)



(t) Figure 7. Low thermal resistance assembly that allows for direct backside cooling via jets

The physical layers of the inverter form thermal resistances that result in temperature increases to conduct a given amount of heat. Another critical resistance that must be accounted for is "spreading resistance," which is encountered when one cross-sectional area of heat flow interfaces with a different cross-sectional area of heat flow. The heat flow path is thus no longer directly vertical; instead, the heat must spread out from the smaller device to the larger. The temperature rises under these conditions. Several authors (Cullham et al. 2000), (Muzychka, 2004), and (Yovanovich et al. 1999) have introduced analytical methods to simulate spreading resistance with 1D models. The techniques presented by these authors are being investigated for use in our 1D model.

Spreading resistance is defined as follows:

(u) Equation 10: $\theta_{th,total} = \theta_{th,1D} + \theta_{th,spreading}$

where $\theta_{th,\ total}$ is the total thermal resistance, which is composed of the 1D thermal resistance ($\theta_{th,\ 1D}$) and the spreading resistance ($\theta_{th,\ spreading}$).

The spreading resistance is quite large (on the same order as the total 1D resistance) and is thus important to include in the model. However, spreading resistance is a complex function of the geometry and heat transfer boundary conditions of the problem. We currently use a 3D FEA model, which is created with the ANSYS FEA software, to estimate the spreading resistance. We are still interested in the 1D model as well, though methods for including spreading resistance in the 1D model must be developed before we can use it with confidence. The 1D heat transfer model is important for its simplicity and speed. By keeping the model at a high level, we retain the ability to do quick-feedback simulations. We intend to enhance the 1D model by including spreading resistance and transient behavior (i.e., thermal "inductance" and "capacitance") in the coming fiscal year. The objective will be to accurately predict the peak temperature increase of power electronics devices under various conditions and estimate the temperature loading on power electronics over a duty cycle.

For this report, temperatures are being predicted accurately with a model developed with the ANSYS FEA software. This model includes spreading resistance. A comparison of simulations of a baseline pin-fin heat exchanger with a 100 W/cm^2 thermal load on all silicon devices (IGBTs and diodes) for the architecture are shown in Figure 6 and in Table 5. This analysis compares the current predictive capability of the 1D model to the equivalent ANSYS 3D FEA model with and without spreading resistance. The 1D thermal model agrees well with the more advanced ANSYS FEA model when thermal spreading is neglected. In fact, most of the differences between the models are likely due to slight differences in assumptions between the two models. However, when spreading resistance is included, the simulated peak temperature changes significantly from the 1D case, indicating the importance of including the spreading resistance.

(v)

(w) Table 5. 1D Model Results versus ANSYS Model with and without Thermal Spreading Resistance

21	**22 1D Thermal Model**	**23 ANSYS Model without Spreading**	**24 ANSYS Model with Spreading**
$T_{coolant}$ (^{o}C)	70.00	70.00	70.00
$T_{peak,\ IGBT\ \&\ Diodes}$ (^{o}C)	97.30	97.07	114.29
ΔT (^{o}C)	27.30	27.07	44.29
$\dot{Q}''$ (W/cm^2)	100	100	100
$\dot{Q}$ (kW)	1.458	1.458	1.458
$\theta_{th,\ convection}$ (^{o}C/kW)	4.42	4.42	2.96
$\theta_{th,\ 1D}$ (^{o}C/kW)	14.30	14.15	14.15
$\theta_{th,\ spreading}$ (^{o}C/kW)	0.00	0.00	13.27
$\theta_{th,\ Total}$ (^{o}C/kW)	18.72	18.57	30.38

Thermal Cooling Technology Assessment

In this section, we present the results of several thermal control technologies evaluated in the context of a heat transfer model of inverter power electronics. As mentioned at the end of the previous section, the

ANSYS FEA software is being used to accurately include spreading resistance. A list of the technologies investigated appears in **Table 6**.

The total classical thermal resistance from the silicon die to the coolant (bulk temperature) in our inverter assembly follows:

(x) Equation 11: $\theta_{total} = \theta_{th,convective} + \theta_{th,conduct,1D} + \theta_{th,spreading}$

The terms of **Equation 11** are reflected in the columns of **Table 6** and provide some insights into what each cooling technology is doing and where each can be improved. As mentioned earlier, the spreading resistance is nearly equivalent to the 1D resistance for all the technologies. Thus, any of the technologies can benefit from advanced heat spreading technology.

Looking specifically at pin fin technology, we see that, although the resistance at the pin fins is the smallest of the three terms (convective, 1D conductive, and spreading), it is still on the same order of magnitude as the other resistances. Thus, the pin fin technology can benefit from a more advanced mechanism to convect heat away at lower resistance. The jet spray work is an answer to this need to decrease pin-fin convective resistance. Advances to the thermal interface materials (TIMs) used on pin-fin devices have a significant effect on the 1D conduction resistance because the 1D thermal resistance is quite large.

When we compare pin-fin technology to liquid jets, we can see an order of magnitude decrease in the convective resistance. The 1D conductive resistance is also significantly reduced, though this is due to the low thermal resistance assembly (see **Figure 7**). Because little TIM material is used in the low thermal resistance assembly and because of the nature of the geometry, improvements to TIMs do not significantly affect the temperature increase. This can be seen by examining the change in 1D conduction resistance and thermal spreading resistance for the liquid jets when advanced TIMs are applied. The 1D conduction resistance does drop. However, at the same time, the spreading resistance increases. A multipronged approach that uses advanced TIMs to decrease 1D resistance and simultaneously attacks spreading resistance may prove more effective.

Looking at the possibilities with air cooling, we see first of all, that under very optimistic assumptions for future performance, air cooling has nearly doubled the total thermal resistance of the pin fin technology. However, air cooling's saving grace is the coolant temperature—assumed here to be 30°C. Thus, even with the higher resistance, maximum temperature increases are acceptable for air under the optimistic scenario.

We have a long way to go before achieving the highly optimistic air cooling performance given under the "best possible" scenario of **Table 6**. The present day cooling capability of air is listed as "Air Jets (present day)" in the table. The maximum temperature increase is clearly unacceptable. The major challenge with air will be to decrease the cooling resistance to acceptable levels. If levels similar to that given by the "best possible" case can be achieved, other improvements to 1D conductive and spreading resistance may be beneficial.

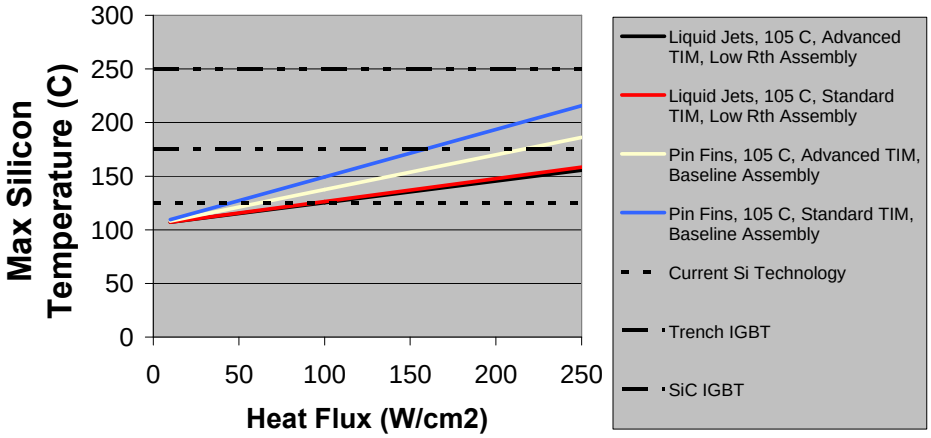
Figure 8 through **Figure 10** show the results as a function of heat rejection rate per unit area ($\dot{Q}''$). These results are given for three coolant temperature assumptions: 30°C, 70°C, and 105°C. These assumptions come from estimated coolant temperatures for air cooling, a single loop (cooling only the PEEM components), and dual loop (a coolant loop for both the engine and PEEM components), respectively. The figures show liquid jets with a low thermal resistance assembly to be the most promising near-term technology. Also, the application of advanced TIMs on pin fin technology makes a significant difference. If the optimistic potential for air cooling can be approached, this technology could be quite promising as well, but there is a long way to go.

The results generated in **Table 6**, **Figure 8**, **Figure 9**, and **Figure 10** are based on numerical models created with the ANSYS FEA software. We will improve these models and do further experimental work to validate the results presented here. Also, the current simulations show only peak temperature increase. Other critical metrics such as weight, volume, cost, and the impact on component life will be addressed as this project progresses.

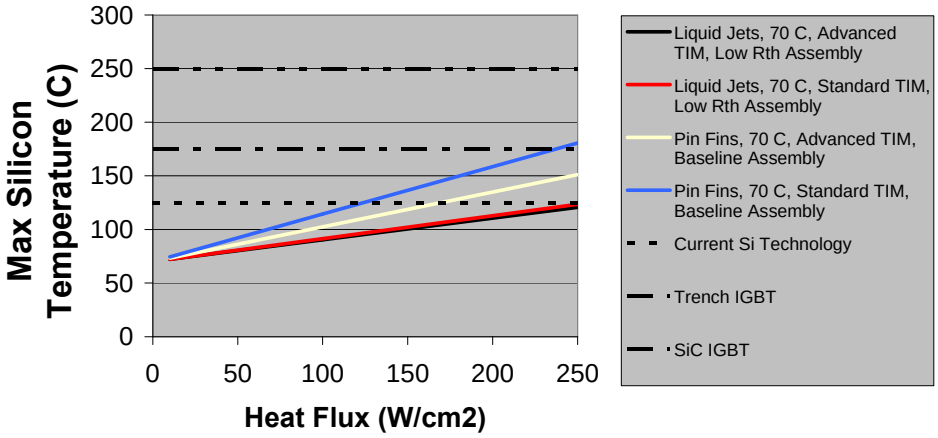
(y) Table 6. APEEM Thermal Control Technologies Evaluated

Cooling Aparatus	TIM Conduction (W/m.K)	Convection Coefficient (W/cm2.K)	Coolant	Coolant Bulk Temperature (C)	Assembly	Silicon Device Max Temperature (C) **	$\theta_{convect}$ C/kW	$\theta_{cond,1D}$ C/kW	θ_{sp} C/kW	θ_{total} C/kW
Pin Fins	1	2	WEG	105	Baseline	149.29	2.96	14.14	13.27	30.38
Pin Fins	1	2	WEG	70	Baseline	114.29	2.96	14.15	13.27	30.38
Pin Fins	7.5	2	WEG	105	Baseline	137.43	2.79	9.35	10.10	22.24
Pin Fins	7.5	2	WEG	70	Baseline	102.43	2.79	9.35	10.10	22.24
Liquid Jets	1	6, 3	WEG	105	Low Rth	126.37	0.45	8.36	5.84	14.65
Liquid Jets	1	6, 3	WEG	70	Low Rth	91.37	0.45	8.36	5.84	14.65
Liquid Jets	7.5	6, 3	WEG	105	Low Rth	125.23	0.58	6.38	6.92	13.88
Liquid Jets	7.5	6, 3	WEG	70	Low Rth	90.23	0.58	6.38	6.92	13.88
Air Jets (best possible)	1	0.50, 0.25	Air	30	Low Rth	114.60	22.45	13.38	22.20	58.02
Air Jets (best possible)	7.5	0.50, 0.25	Air	30	Low Rth	105.69	23.29	8.49	20.14	51.91
Air Jets (present day)	1	0.04, 0.02	Air	30	Low Rth	632.35	367.68	14.24	31.22	413.13
Air Jets (present day)	7.5	0.04, 0.02	Air	30	Low Rth	620.49	368.92	8.78	27.30	405.00

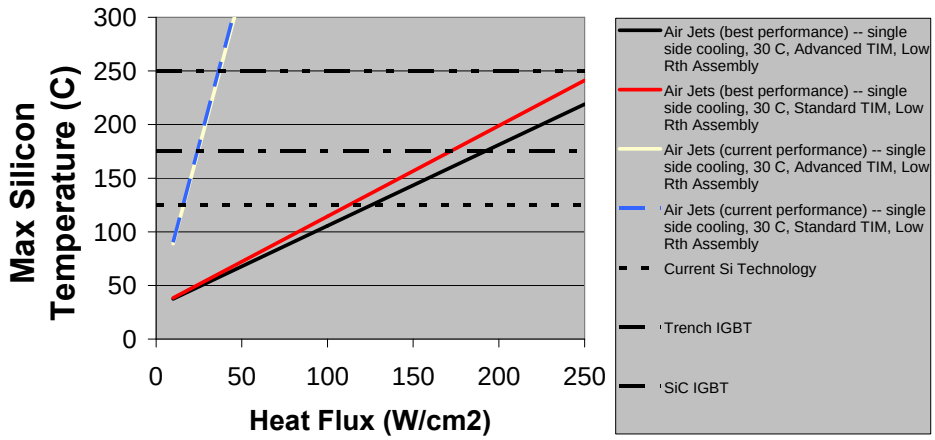
** Maximum temperature for a 100 W/cm2 thermal load (1.458 W of thermal energy input)



(z) Figure 8. Si die max temperature for 105°C coolant APEEM cooling technologies by $\dot{Q}''$



(aa) Figure 9. Si die max temperature for 70°C coolant APEEM cooling technologies by $\dot{Q}''$



(bb)Figure 10. Si die max temperature for 30°C coolant APEEM cooling technologies by $\dot{Q}''$

Conclusions

In conclusion, this report has surveyed the initial work to bring a systems analysis perspective to the thermal cooling R&D effort associated with the DOE APEEM program. Two key areas were discussed:

Determination of thermal cooling requirements and thermal loads by the cascading of vehicle level requirements and duty cycle operations down through the various APEEM drive technologies

Evaluation and application of the thermal control technology portfolio in a systems context using an inverter heat transfer model to show the effectiveness of the various cooling strategies we are evaluating under the APEEM program.

Next Steps

Several next steps have been identified for this thermal subsystem analysis effort:

1. Collaborate with the FreedomCAR vehicle systems analysis team to simulate electric drive subsystems with DOE FreedomCAR-accepted vehicle models for CVs, HEVs, PHEVs, and FCVs. This work should extend into predictions for actual thermal loadings over time from inverters and other APEEM components—ongoing through FY 2007.
2. Improve the 1D thermal model of the inverter power electronics assembly to include thermal spreading. Validate the model with more advanced simulations (e.g., ANSYS) and laboratory testing—December 2006.
3. Include the ability to handle transients in the 1D thermal model of inverter power electronics. Apply this model to thermal cycling analysis—April 2007.
4. Evaluate remaining APEEM thermal control technologies with the inverter thermal model—December 2006.

5. Increase collaboration between the NREL team and other APEEM teams (specifically ORNL) to better couple the thermal design and analysis with current APEEM projects—ongoing through FY 2007.

References

Culham, J., Yovanovich, M., Lemczyk, T. "Thermal Characterization of Electronic Packages Using a Three-Dimensional Fourier Series Solution." Journal of Electronic Packaging., Vol. 122. September 2000.

Markel, T., Simpson, A. "Plug-in Hybrid Electric Vehicle Energy Storage System Design." Presented at the Advanced Automotive Battery Conference in Baltimore, Maryland. May 19, 2006.

Muzychka, Y. "Influence Coefficient Method for Calculating Discrete Heat Source Temperature on Finite Convectively Cooled Substrates." 2004 Inter Society Conference on Thermal Phenomena. 2004.

O'Keefe, M., Markel, T., "Dynamic Programming Applied to Investigate Energy Management Strategies for a Plug-in HEV." To be presented at EVS-22, Friday October 27, 2006.

Simpson, A., Markel, T., Brooker, A. "Cost-Benefit Analysis of Plug-in Hybrid Electric Vehicle Technology." To be presented at EVS-22, Friday October 27, 2006.

Yovanovich, M., Muzychka, Y., Culham, J. "Spreading Resistance of Isoflux Rectangles and Strips on Compound Flux Channels." Journal of Thermophysics and Heat Transfer., Vol. 13, No. 4,. October–December 1999.

2.7 Advanced Thermal Interface Materials to Reduce Thermal Resistance

Principal Investigator: Sreekant Narumanchi
National Renewable Energy Laboratory

MS 1633
1617 Cole Blvd
Golden, CO 80401-3393
Voice: 303-275-4062; Fax: 303-275-4415; E-mail: sreekant_narumanchi@nrel.gov

DOE Technology Development Manager: Susan A. Rogers
Voice: 202-586-8997; Fax: 202-586-1600; E-mail: Susan.Rogers@ee.doe.gov

---

Abstract

In a typical IGBT package in an inverter, the grease layer which attaches the DBC layer to the heat sink has the highest thermal resistance in the package. This report describes our attempt to develop high performance, reliable, and low cost thermal interface materials (TIMs). Three different techniques for growing nanotubes on a copper substrate have been explored. Preliminary thermal resistance measurements have been made. Metal-coated particles embedded in polymer compounds are also being explored for possible use as TIMs. A test stand is being acquired in-house to characterize the thermal resistance of these novel TIMs.

Objectives

Thermal interface materials pose a major bottleneck to heat removal from the IGBT package. In a typical IGBT package, for example, the direct bond copper (DBC) layer is attached to the aluminum heat sink via a thermal grease, which has a thermal conductivity of 0.8 W/mK and is a major contributor to the thermal resistance in the package. Accordingly, a project was undertaken in FY 2006 to explore advanced thermal interface materials for reducing the thermal resistance. These are the objectives of this project:

- Identify and assist in the development of low thermal resistance, low cost, thermal interface materials. We are currently exploring interface materials based on carbon nanotubes (CNTs) and metal coated particles.
- Characterize the thermal performance of these novel interface materials over an extended temperature and pressure range characteristic of automotive applications.
- Characterize the impact of thermal cycling on thermal resistance.

If these advanced materials are suitable for automotive applications and yield enhancements in thermal conductance over the state-of-the-art conventional interface materials by at least a factor of 5, the ultimate objective is to explore the possibility of replacing the grease in IGBT packages with these advanced thermal interface materials.

Approach

NREL's approach for FY 2006 in order to meet the objectives mentioned above is given below.

- We conducted a survey of the existing state-of-the-art thermal interface materials. This includes greases, pastes, filler pads, adhesives, polymer compounds, solders, phase change materials, as well as the state-of-the-art carbon nanotubes research.

- A subcontract was established with the University of Colorado at Boulder to explore carbon nanotubes as thermal interface materials. The idea is to grow CNTs directly on a copper substrate/foil, which could then be used as an interface material. In the literature, some studies have reported enhanced thermal conductance of the grease by up to 100% when nanotubes are embedded in the grease. The concept behind growing nanotubes directly on a substrate is to obtain even higher thermal conductances than can be obtained by enhancing thermal greases.

- After the growth process of nanotubes on the copper foil is optimized, characterize the thermal resistance of the copper foil-CNT-copper foil structure and compare with a copper foil-conventional TIM-copper foil structure.

- By the end of FY 2006, a subcontract with Federal Technology Group (FTG) will be established. FTG is a company that specializes in the metal coated particle technology for various applications. The idea is to embed metal coated particles (example—copper-coated diamond) in a polymer compound in order to enhance the thermal conductance. FTG will also be working with companies such as Honeywell and GE. The idea behind metal coated particles is to reduce the interfacial thermal resistance between the particles and the host matrix. These metal coated particles also have very good wetting properties. Again, the desire is to obtain at least a factor of 5 enhancements over the state-of-the-art thermal interface materials.

- We are close to acquiring in-house at NREL a test stand for performing thermal resistance measurements over the automotive temperature range (-40°C –150°C). This test stand is based on the standard ASTM-D5470 test method for thermal resistance measurements. This test stand will be utilized to perform thermal resistance measurements of the novel as well as conventional thermal interface materials. It is also intended to perform reliability and thermal cycling tests on the novel materials. The test stand will aid in characterizing the impact of thermal cycling on the thermal resistance.

Major Accomplishments

The following are the main accomplishments of this project in FY 2006:

- Under a subcontract, our colleagues at the University of Colorado at Boulder achieved growth of CNTs on a copper foil. Three different growth strategies were investigated. The growth process of CNTs is being optimized in order to get the highest CNT density.

- Some preliminary thermal resistance measurements have been performed and the results are encouraging.

- A subcontract has been established with FTG to explore metal coated particles embedded in polymer compounds.

- We have specified and ordered a test stand for thermal resistance measurements. This should enable characterization of thermal resistance of the novel TIMs that are being developed as part of the project, as well as conventional TIMs, over a wide temperature and pressure range typical of automotive applications.

Technical Discussion

-
- **Importance of Thermal Interface Materials**

In this section, we point out why thermal interface materials are important. Figure 1 shows the different layers constituting a typical IGBT package in an inverter. The silicon die is soldered to the direct bond copper (DBC) layer – which is composed of an aluminum nitride layer sandwiched between two copper layers. This DBC layer is attached to an aluminum base plate/heat sink via thermal grease. This thermal grease is about 25–50 microns in thickness and has a thermal conductivity of 0.8 W/mK. Typically, the inverter has a heat sink in which the coolant flows through pin fins in a channel flow configuration. Figure 3(a) shows the thermal resistance of the different solid layers in the IGBT package except for the aluminum base plate/heat sink. It shows that the grease layer has the highest thermal resistance/impedance (~ 0.1 K/W). The units are more appropriate for thermal impedance, but here thermal resistance and impedance will be used interchangeably. In order to assess the impact of thermal resistance, a 3D ANSYS conduction modeling was performed. The domain used for the simulation is shown in Figure 2 – Figure 2(a) shows the IGBT half-bridge, while Figure 2(b) shows a closeup revealing the different layers constituting the IGBT package. The details of package geometry is provided in [1].

The fluid temperature is fixed at 105°C signifying glycol-water mixture at 105°C. Except for the resistance of the interface material, all other parameter values are fixed as shown in Figure 3(a). These values are based on a typical IGBT package. As shown in Figure 3, the heat flux is fixed at 100 W/cm^2, and the coolant temperature is 105°C and the heat transfer coefficient used on the back of the aluminum baseplate is 50,000 W/m^{2}K. Figure 3(a) shows that when the resistance of the grease is about 0.1 K/W, the maximum die temperature is about 148.5°C. When the resistance of the interface material is reduced to 0.01 K/W (10 times reduction—Figure 3(b)), the die temperature reduces to 136°C. This is a very noticeable difference (~35%) and points to the impact of interface materials. Figure 3(c) shows that impact of the TIM thermal conductivity on the maximum die temperature. Interestingly, increasing the thermal conductivity beyond 6 W/mK does not significantly change the maximum die temperature. This implies that once the thermal resistance of the interface material is not the dominating resistance, it does not matter if its resistance is reduced further. Other layers in the package start dictating the thermal map in the package.

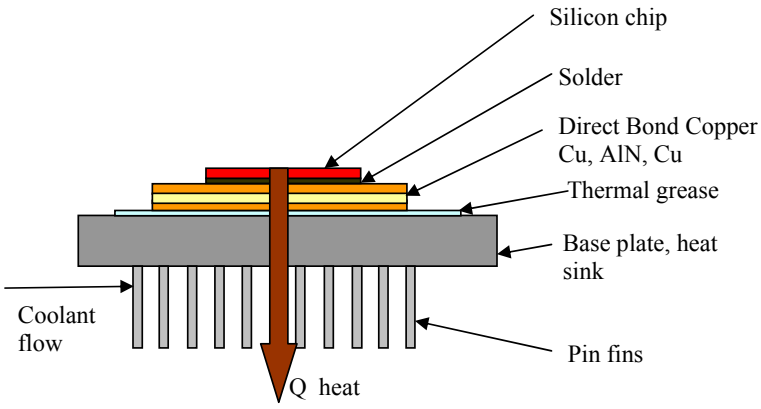


Figure 1. Different layers constituting the IGBT package in an inverter

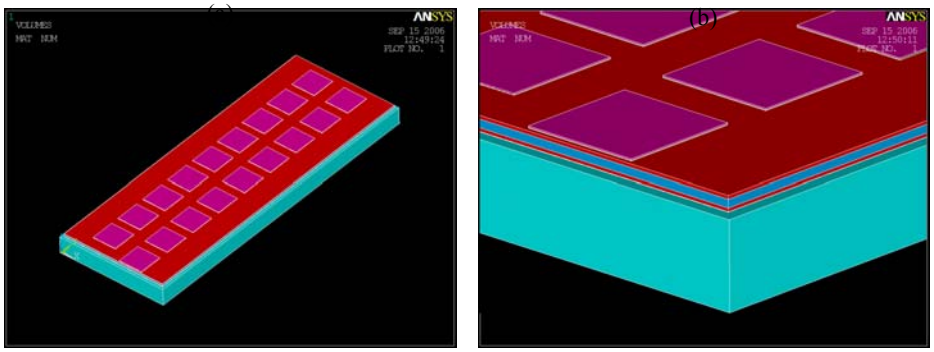


Figure 2. Domain for ANSYS 3D conduction model for illustrating the impact of TIM on the temperature fields; (a) IGBT half-bridge; (b) closeup showing part of the structure and the different layers

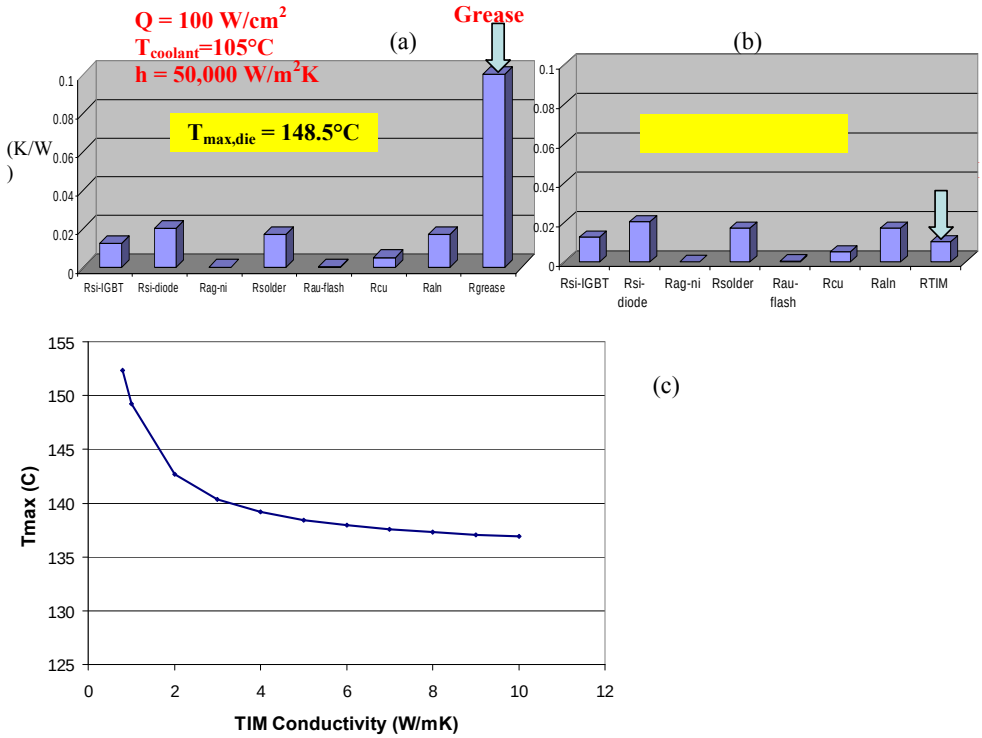


Figure 3. Impact of the thermal resistance of the TIM on the die temperature via ANSYS simulations, (a) case with typical thermal grease; (b) case with improved TIM; (c) impact of TIM thermal conductivity on the maximum temperature in the die

- **State-of-the-Art of Thermal Interface Materials**

In this section, we review the state-of-the-art of thermal interface materials. Figure 4 shows a schematic depiction of what a thermal interface material looks like in a real application. The surfaces of the two layers are uneven as depicted in Figure 4(a). The interface material fills up these irregularities. However, there still may be some pockets of air. Figure 4(b) shows the temperature as a function of the vertical distance. In the bulk of the material as well as in the bulk of the interface material, there is a linear temperature gradient. There is a change in the gradient at the interfaces due to the contact resistance between the interface material and the substrate. The total thermal resistance is composed of the bulk resistance and the contact resistances. Accordingly, the thermal resistance due to an interface material can be written as:

$$R = R_c + BLT/k_{TIM} \quad (1)$$

where Rc is the contact resistance, BLT is the bond-line thickness of the interface material and k_{TIM} is the bulk thermal conductivity of the interface material. A high thermal conductivity can reduce the bulk thermal resistance of the interface material; however, it is very critical that the contact resistance also be minimized. Contact resistance is an area where significant attention has been focused in the literature (e.g. [2-4]).

While the focus here is on the automotive power electronics cooling, it is worth noting that thermal interface materials also play a key role in connecting various components of the thermal solution in the microelectronics industry [4]. The continual increase in cooling demand for microprocessors has led to increased focus on improving the thermal interface materials. Figure 5 shows the state-of-the-art of thermal interface materials. Significant advances have been made in the development of thermal greases/gels, phase change materials, solder, phase change melt alloys, advanced polymers, and carbon nanotubes [4-6]. Figure 5 indicates the state-of-art of the best performing thermal interface materials. Also included is work from Xu and Fisher [5-7] on direct growth of nanotubes on a substrate. By growing nanotubes on both sides of the copper foil, Xu and Fisher [5, 6] have demonstrated thermal resistance of the order of 4 mm^2K/W which is 5 times lower thermal resistance than the best performing greases/gels in the market.

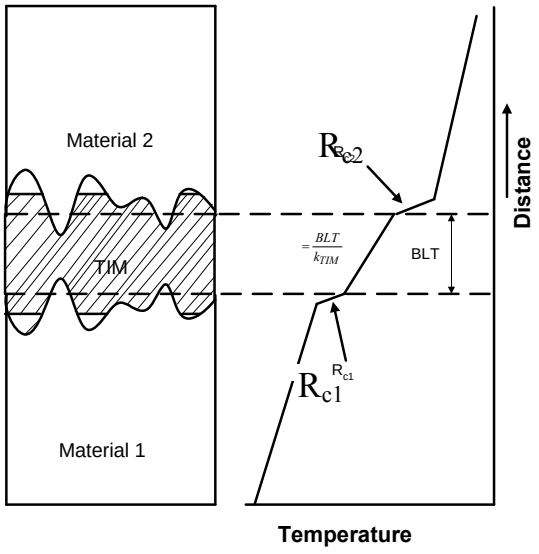


Figure 4. (a) Representation of a TIM in an actual application; (b) The depiction of temperatures as a function of distance in the vertical direction – impact of bulk resistance and the contact resistance (adapted from R. Prasher [4]).

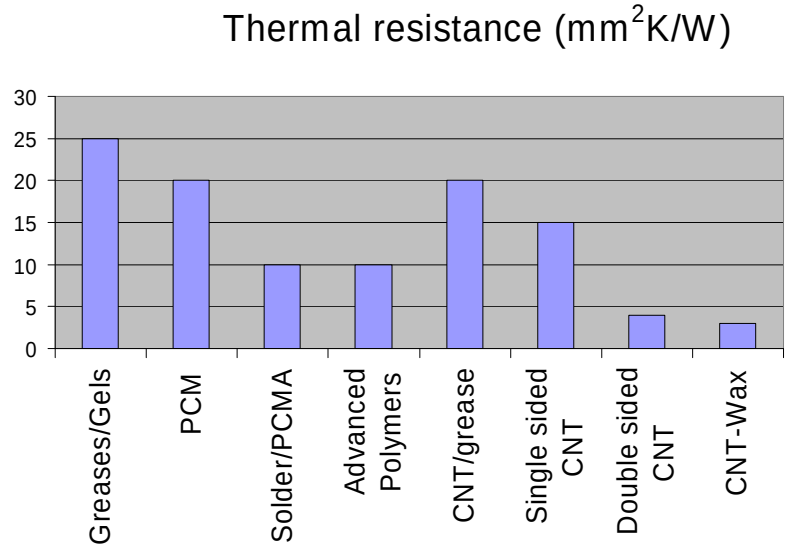


Figure 5. State–of-the-art of thermal interface materials.

Carbon Nanotubes as Thermal Interface Materials

Carbon nanotubes are currently actively being explored as thermal interface materials [5, 6, 8, 9]. Carbon-based materials (diamond and in-plane graphite) display the highest measured thermal conductivity of any known material at moderate temperatures. Their structure is indicated in Figure 6(a). In 1991, Sumio Iijima at NEC, Japan, first noticed carbon nanotubes lying in a smear of soot [10]. Carbon nanotubes (CNTs as they are commonly called) exhibit very high thermal and electrical conductivity. Hone et al. [11] showed that the thermal conductivity of single walled carbon nanotubes (SWCNTs) exceeded 200 W/mK in the direction parallel to the alignment axis of the magnetic field used in the synthesis. Kim et al. [12] measured the thermal conductivity of an individual multi-walled carbon nanotube (MWCNT) to be more than 3000 W/mK at room temperature using a microfabricated suspended device. However, theoretical predictions for the conductivity are as high as 6,600 W/mK as reported by Berber et al. [13]. As a result, CNTs offer an attractive alternative for thermal management of electronic packages.

Biercuk et al. [14] mixed 1 wt % of unpurified SWCNTs in of industrial epoxy and reported a 70% increase in the thermal conductivity of the composite at 40 K rising to a 125% augmentation at room temperature. Liu et al. [15] introduced a mixture of unpurified SWCNTs and MWCNTs into silicone elastomer and reported a 65% enhancement in the thermal conductivity of the composite with 3.8 wt % CNT loading. All these studies have relied on mixing CNTs in a grease/paste. Generally the enahancements have been of the order of 100%. It is desired to increase the thermal performance even further. Hence, researchers turned their attention to direct growth of CNTs on the substrate in the hopes of

further reducing the thermal resistance. As shown in Figure 6(b), the CNTs are directly grown on the two substrates and then the CNTs are either held together under pressure or their ends can be bonded.
Hu et al. [8] characterized vertically oriented CNTs on silicon including the effect of voids and noticed the thermal conductivity to be of the order of 80 W/mK, which is one order higher than that of thermal greases, which are widely used as thermal interface materials (TIMs).

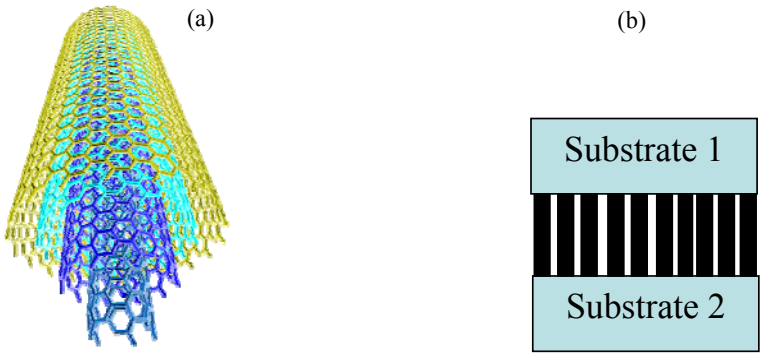


Figure 6. (a) Representation of the structure of multiwalled carbon nanotubes; (b) CNTs grown directly on substrates 1 and 2, the contact between CNTs is either a pressure contact or the CNTs could be bonded.

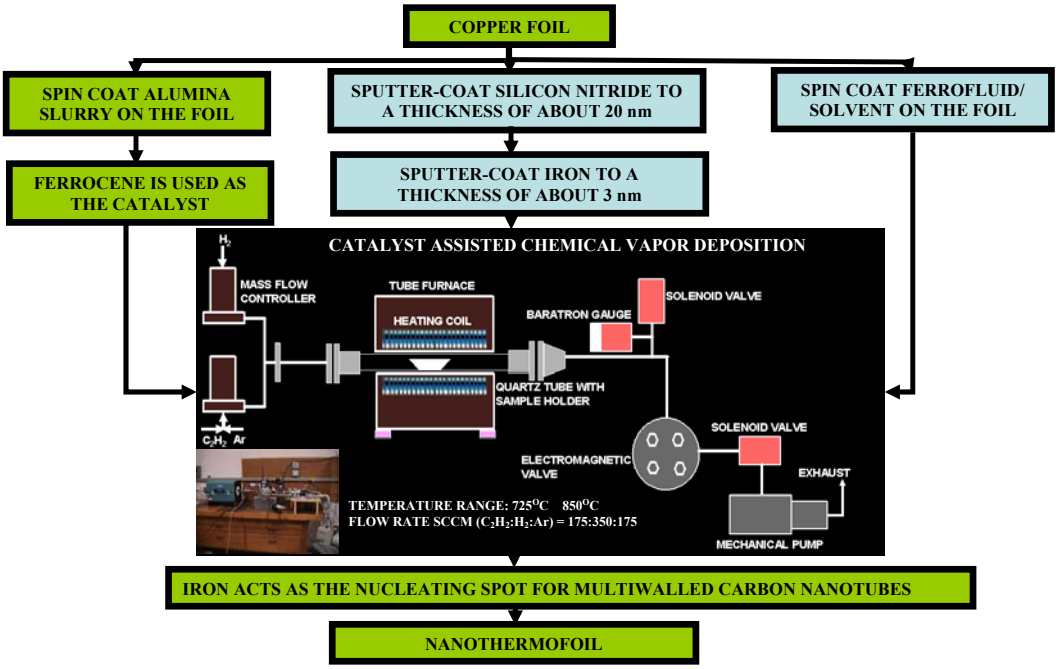


Figure 7. Summary of the growth of CNTs on a copper foil by three different methods.

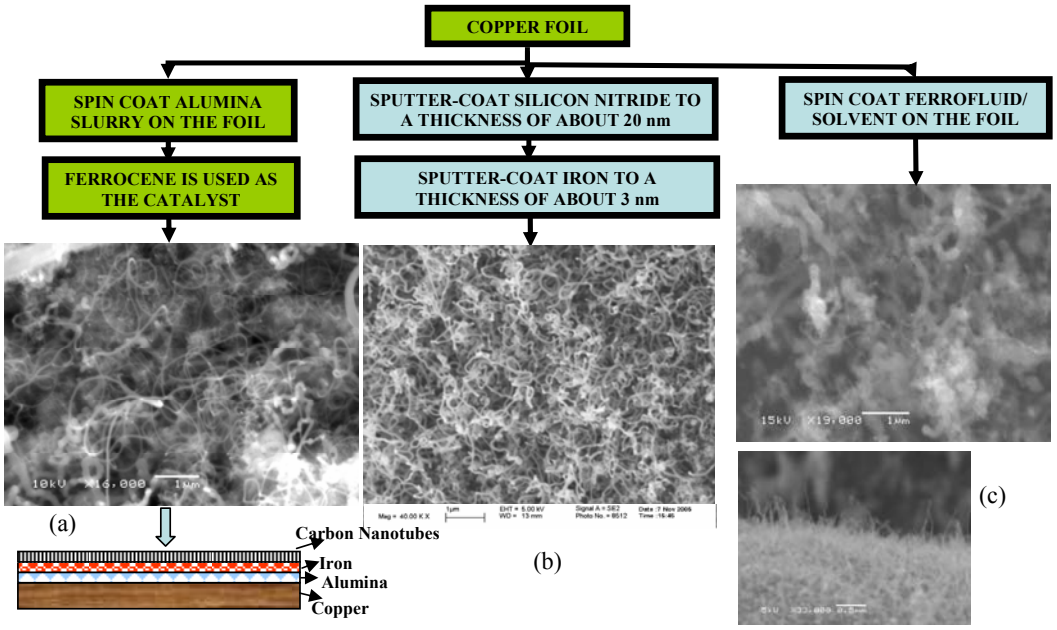


Figure 8. SEM images of growth on a copper foil via three different methods: (a) Ferrocene/alumina, (b) Silicon nitride/iron, (c) Ferrofluid/solvent.

Recently, Xu and Fisher [7] showed that the thermal contact resistance of silicon wafers and copper with a CNT array interface in between could be as low as 23 mm^2K/W. The same authors [6] also reported that free-standing CNT arrays can be very good thermal interface materials compared to phase change TIMs. Furthermore, they observed that a combination of PCM and CNTs produced a minimum thermal resistance of 5.2 mm^2K/W at a pressure of 0.35 MPa, which is nearly five times lower thermal resistance than that of thermal grease.

Growth of Carbon Nanotubes on a Copper Foil

In FY 2006, NREL established a subcontract with the University of Colorado at Boulder to grow nanotubes on a copper foil, characterize the thermal resistance of the foil, and compare the performance with existing thermal interface materials. The growth of CNTs was achieved using a thermal chemical vapor deposition (CVD) reactor shown in Figure 7. Figure 7 outlines the overall process for growing nanotubes on a copper foil via three different methods. The intent in exploring three different methods is to ascertain which method gives the best growth density of CNTs. The assembly consists of mass flow controllers to direct the flow of the gases to the vacuum furnace that houses the sample. The mechanical pump is connected to the quartz tube to pump the reaction chamber down to a low pressure using a series of electromagnetic and solenoid valves.

Three different methods of growing nanotubes were explored as outlined below:

(a) **CVD using ferrocene/alumina**

Electronic-grade copper foil (99.5% purity) of thickness 1.8 mm and a mirror-polish on one side was cut into 19 mm circular blanks. The samples were sonicated in a solution of isopropyl alcohol (IPA) for 10 minutes and rinsed with distilled water to remove residual traces of the alcohol. Alumina powder with a grain size of 1 μm was cold-pressed onto the copper substrate. Then 0.15 gms of Ferrocene, the catalyst source, was taken in a quartz boat and placed near the copper sample. The furnace was then heated to 800°C after being pumped down to 0.18 Torr using a mechanical pump in the presence of Argon. A mixture of acetylene and hydrogen with a flow rate ratio of 250:495 sccm was passed over the sample for a period of 10 minutes. Once the reaction was complete, the gas supplies and the heater were switched off. The sample was then cooled in the presence of Argon. The copper foil was imaged using a Low Vacuum Scanning Electron Microscope (LV-SEM) and the result is shown in Figure 8a. The first image shows bundles of multi-walled carbon nanotubes with a wide range of diameters and chirality on a copper substrate. Along with the nanotubes, the sample also consists of the iron catalyst impurities and amorphous carbon.

(b) **CVD using iron/silicon nitride film**

In this process, the catalyst (iron) is laid down on the copper substrate by sputtering. Since there is a very high possibility of iron diffusing into the copper substrate at the temperatures used for processing nanotubes, a barrier layer of silicon nitride is first sputter-coated on the substrate to a thickness of 3 nm. On top of this layer, iron is sputtered to a thickness of 10 nm. The sample with the sputtered catalyst layer is placed in the furnace and heated at atmospheric pressure, to a temperature of 750°C, in the presence of nitrogen. A mixture of methane, ethylene, and hydrogen with a flow rate ratio of 50:100:500 sccm is passed over the sample for 10 minutes. Then the sample is cooled for a period of 3–4 hrs in the presence of nitrogen and imaged using a scanning electron microscope. The image (Figure 8(b)) shows entangled bundles of carbon nanotubes with small traces of catalyst impurities and amorphous carbon.

(c) **CVD using ferrofluid/solvent**

In this process, the sample is sonicated in a solution of isopropyl alcohol (IPA) for 10 minutes and rinsed with distilled water to remove residual traces of the alcohol. A water-based ferrofluid (EMG-707), obtained from Ferrotec, is used as the catalyst source. The ferrofluid is sonicated for a period of 10 minutes and then spin-coated on the substrate. The furnace is then heated to 750°C after being pumped down to 0.18 Torr using a mechanical pump in the presence of Argon. A mixture of acetylene and hydrogen with a flow rate ratio of 250:495 sccm is passed over the sample for a period of 10 minutes. The sample is then cooled in the presence of Argon. The image in Figure 8(c) shows nanostructures obtained using this method which are in the sub-50 nm regime. The sample also contains traces of catalyst impurities and amorphous carbon in large quantities. Investigation is underway to identify these nano-structures.

Experimental Setup for Measurement

A simple device, constructed at the University of Colorado at Boulder (CU Boulder) for measuring the thermal resistance of these copper foils with CNT growths, is schematically in Figure 9. The specimens and specimen blanks are 1 mm thick copper disks that have a diameter of 19 mm and a surface roughness of 0.13 μm. These are sandwiched between two oxygen-free, high-conductivity (OFHC) copper cylinders that are 19 mm in diameter and 24 mm long. The end of the hot-side cylinder has a heater wound on it. Three thermocouples are attached to each cylinder at known distances from the specimen interfaces. These thermocouples are set into small drilled holes and have additional wire wrapped around the cylinders for thermal anchoring. The specimens and cylinders are clamped between two aluminum plates. By using a torque wrench, specified

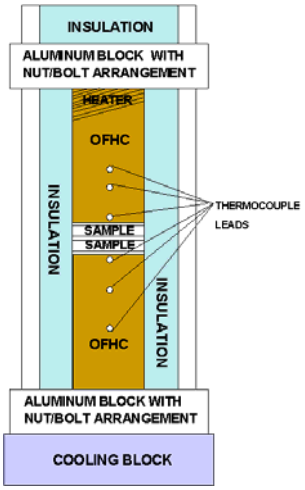


Figure 9. Schematic of experimental setup.

contact pressures can be applied to the specimens. A cooling block is bolted to the cold-end aluminum plate for heat removal, while a ceramic washer (not shown in the schematic) is inserted between the hot-side cylinder and aluminum plate. Since the cylinders and specimen blanks are copper and therefore have very high thermal conductivity, 390 W/mK, heat flows efficiently through the measurement cell.

This experimental setup is similar to that found in the ASTM E 1225 standard test method for thermal conductivity of solids by means of the guarded-comparative-longitudinal heat flow technique [16]. The primary differences between the setup used here and the ASTM E 1225 method are that this method is unguarded and the measurement of interest is the temperature difference across the specimen stack, rather than thermal conductivity. The specimen stack is surrounded, except for the cooling block, by fiber-blanket insulation to minimize heat losses. Calculation of radiative heat losses for the highest measurement power gives about 100 mW, or less than 1% radiative heat loss.

Preliminary Thermal Resistance Measurements

In this section, some preliminary experimental results for thermal resistance are reported. In Figure 10 on the upper left corner, two cases are shown: one in which there is no interface material between the copper foils, and another case in which there are CNTs between the copper foils. The plot on the left shows the temperature difference (between points A and B) vs. the power that is applied for the two cases. The case in which the CNT is between the copper foil shows 5 times smaller temperature difference as opposed to the case where there is no interface material between the copper foils. The pressure applied in the experiments is about 555 psi. The thermal resistance is also plotted in the figure on the right. It can be seen that for the case when there is no interface material between the copper foils, the thermal resistance is about 2.5 K/W, while for the case with CNTs between the copper foils, the thermal resistance drops down to about 0.5 K/W—a factor of 5 lower. This preliminary result demonstrates the impact of CNTs. In the upper right hand corner of Figure 10, the SEM image of the copper foil is shown. As

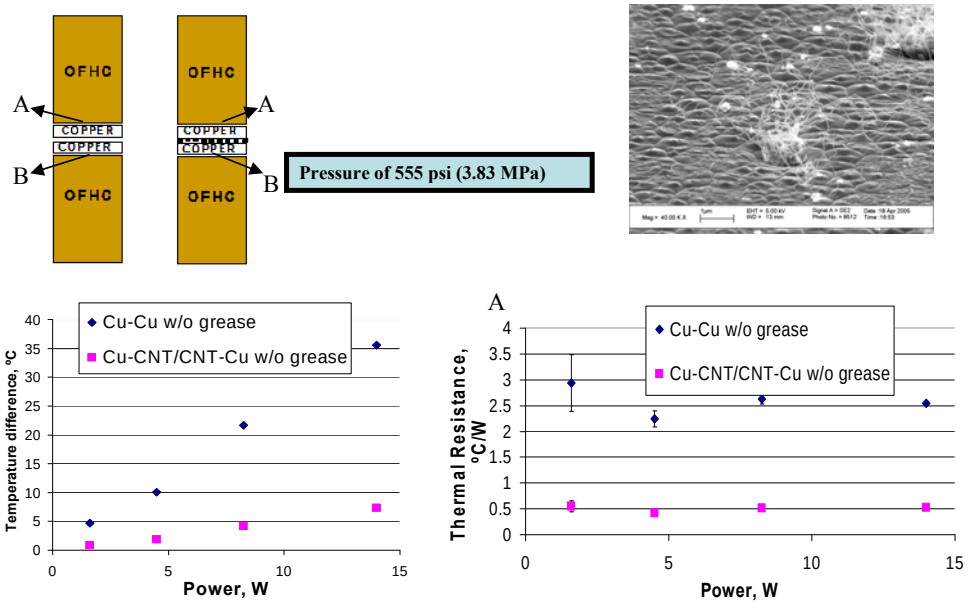


Figure 10. Experimental results demonstrating the impact of CNTs.

can be seen, the CNT growth density is very small. It is postulated that a higher density of CNTs would entail a further decrease in the thermal resistance.
Currently, at CU Boulder, additional samples are being fabricated and the thermal resistances will be characterized very soon.

- **Metal-Coated Particles Utilized in Thermal Interface Materials**

A subcontract is also about to be established with Federal Technology Group (FTG) to explore metal-coated particles embedded in polymer compounds as thermal interface materials. Coating of particles with a metal reduces the thermal resistance between the host matrix and the particles. Figure 11 shows SEM images of copper-coated diamond particles. FTG is also working with Honeywell and GE to develop these novel materials. Initially, the intent is to explore copper-coated diamond, nickel-coated diamond, and copper-nickel-coated diamond particles. Later on, other types of metal coatings and particles will also be explored. The metal coating also improves the wetting characteristics of the particles. All of this contributes towards reducing the contact resistance between the particles and the host matrix. Otherwise, even if the particle has high thermal conductivity, when it is embedded into a polymer compound, the thermal contact resistance between the particles and the host matrix hinders the overall thermal performance of the material. As with CNTs, it has been suggested that metal-coated particles could reduce the thermal resistance of polymer compounds by a factor of 5 or more.

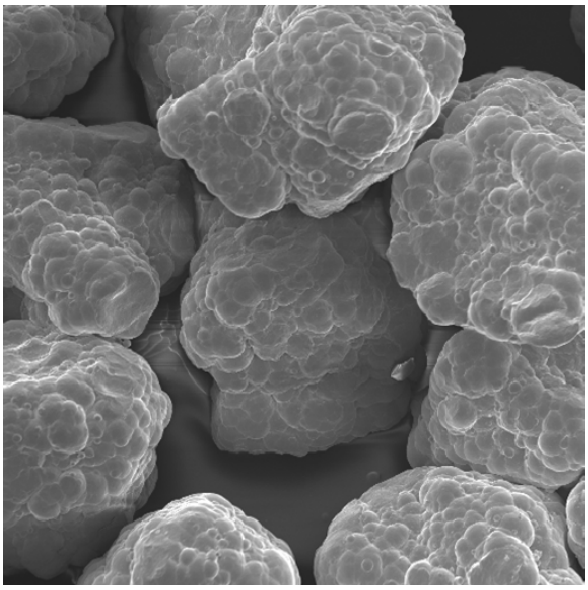


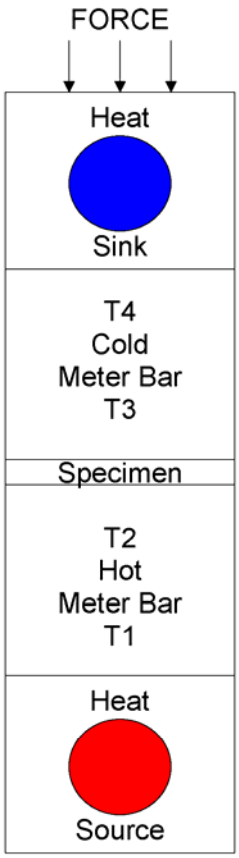
Figure 11.Copper-coated diamond particles (courtesy Federal Technology Group).

- **Test Stand for Thermal Resistance Measurements**

A test stand, based on the ASTM D 5470 test method for measuring thermal resistance, is being acquired by NREL from DS&A LLC. The test stand is expected to be delivered to NREL by the end of FY 2006. The intent of acquiring the test stand is to characterize the thermal performance of the novel interface materials being developed by the subcontractors—CU Boulder and FTG, as well other state-of-the-art thermal interface materials in the market that are suitable for automotive applications. Figure 12 shows the main components of the test apparatus. This equipment is designed to be practical and capable of applying a range of test pressures for different materials. The design for the test stand is intended to meet requirements for operation to temperatures from -40˚C to +200˚C. The extended temperature range requires the use of a higher capacity chiller, for the cold head, and the use of a specialized silicone oil coolant.
DS&A LLC is conducting the fabrication, assembly, and calibration of TIM material test equipment which follows industry standard ASTM D 5470-01.


Chilled liquid Bath
Press, Calorimeter, Load Cell
Power Supply
Data Logger
Air Tank

(a)



(b)

Figure 12. Test stand based on the ASTM D 5470 test method for measuring thermal resistance, (a) the complete apparatus (courtesy: DS&A LLC); (b) ASTM D 5470 measurement principle (ASTM D 5470 standard).

ASTM D 5470 Measurement Principle

The material presented below has been adapted from the ASTM D 5470 test standards document.

(a) *Heat Flow When Using the Meter Bars for Calorimeters:* Calculate the heat flow from the meter bar readings as follows (temperatures are depicted in Figure 12(b)):

$$Q_{12} = \frac{\lambda_{12} \times A}{d} \times \left[T_1 - T_2\right] \qquad (2)$$

$$Q_{34} = \frac{\lambda_{34} \times A}{d} \times [T_3 - T_4] \quad (3)$$

$$Q = \frac{Q_{12} + Q_{34}}{2} \quad (4)$$

where:

Q_{12} = heat flow in hot meter bar, W,

Q_{34} = heat flow in cold meter bar, W,
Q = average heat flow through specimen, W,
λ_{12} = thermal conductivity of the hot meter bar material, W/(m·K),
λ_{34} = thermal conductivity of the cold meter bar material, W/(m·K),

A = area of the reference calorimeter, m^2,
$T_1 - T_2$ = temperature difference between temperature sensors of the hot meter bar, K,
$T_3 - T_4$ = temperature difference between temperature sensors of the cold meter bar, K, and
d = distance between temperature sensors in the meter bars, m.

(b) Derive the temperature of the hot meter bar surface in contact with the specimen from the following:

$$T_H = T_2 - \frac{d_B}{d_A}(T_1 - T_2) \quad (5)$$

where:

T_H = temperature of the hot meter bar surface in contact with the specimen, K,
T_1 = warmer temperature of the hot meter bar, K,
T_2 = cooler temperature of the hot meter bar, K,
d_A = distance between temperature sensors, m, and
d_B = distance from the lower sensor to the surface of the hot meter bar in contact with the specimen, m.

(c) Derive the temperature of the cold meter bar surface in contact with the specimen from the following:

$$T_C = T_3 + \frac{d_D}{d_C}(T_3 - T_4) \quad (6)$$

where:

T_C = temperature of the cold meter bar surface in contact with the specimen,

K,
T_3 = warmer temperature of the cold meter bar, K,
T_4 = cooler temperature of the cold meter bar, K,
d_C = distance between temperature sensors, m, and
d_D = distance from the warmer sensor to the surface of the cold meter bar in contact with the specimen, m.

(d) Calculate the thermal resistance from

$$\theta = (T_A - T_D) \times A/Q \qquad (7)$$

and express it in units of $(K \cdot m^2)/W$.

(e) Obtain apparent thermal conductivity from a plot of thermal resistance for single- and multiple-layered specimens against the respective specimen thickness. Plot values of the specimen thickness on the *x* axis and specimen thermal impedance on the *y* axis.

The curve is a straight line whose slope is the reciprocal of the apparent thermal conductivity. The intercept at zero thickness is the thermal interfacial resistance, R_I, specific to the sample, clamping force used, and the clamping surfaces. As a preferred alternative, compute the slope and the intercept using least mean squares or linear regression analysis.

ASTM D 5470 Model 103 Test Stand and Monitoring Equipment Fabrication, Assembly, and Calibration

(a) ASTM D 5470 [17]is a well-defined test procedure to enable the measurement of the thermal impedance and thermal conductivity of high modulus films. In particular, this procedure is of interest in determining the performance characteristics of thermal interface materials, including films, tapes, phase change materials, and greases. Procedure modifications for the ASTM D 5470 must be incorporated for low modulus materials and for phase-change materials; these modifications are standard practice for experienced users of ASTM D 5470. For testing of phase-change materials and certain other temperature-induced materials, the test temperature should be above the phase change point of the material and physical stops must be incorporated to determine sample thickness. The hardware system proposed will allow the testing of all types of existing thermal interface materials and reveal their thermal performance characteristics for an extended temperature range. In addition, as mentioned previously, this hardware will also be utilized to characterize the thermal resistance of novel interface materials based on CNTs and metal coated particles.

(b) The system (Figure 12) consists of the following:

- A precision air press rated at 990-lb. force at 100 psi, for two-hand operation; with pneumatic regulator. This allows adjustment of the force applied to the ram. Micrometer ram stroke is 8 in. (adjustable in 0.05 mm increments).
- Circulating coolant bath capable of heating and chilling, temperature range -40˚C to +200˚C. The liquid capacity is 20 liters. Chilled coolant bath is complete with digital temperature set point and readouts. The coolant will be specialized silicone oil per recommendation of chiller manufacturer's technical service department.
- Precision laboratory thermometer with 12 channels. Each channel can be programmed to a specific sensor. The thermometer will be furnished with four RTDs for temperature sensing. Each RTD probe is custom fabricated in a stainless steel sheath (6.0” x 1/16”) with a 3-foot

cable. The thermometer will be calibrated with the probes to produce a resolution of +/- 0.001°C and an accuracy of +/- 0.03°C. The data collection software is included.

- Upper and lower metering blocks (Figure 12(b)), precision machined from aluminum alloy (Al7075-0, annealed only) which has a known and documented thermal conductivity. Certifications will accompany each metering block regarding material. The sizes furnished will be one set each of the following: 1" x 1", 2" x 2".
- Agilent Technologies variable DC power supply (200 W, 120 VAC, 1.5 A) to supply power to two resistive cartridge heaters placed in the heater block above the upper metering block. Measurement of the current and voltage determines the power being applied during a test. Digital meters will visually display the volts and amps.
- A cold plate installed under the lower metering block; temperature of the cold plate is determined and regulated by (2) above. Setting this temperature determines the temperature range of the test.
- A load cell (1,000–2,000 lb) installed under the cold plate with digital readout to display the force being applied to the sample under test. The load cell will be calibrated for initial testing.
- Model 103 includes a gauge indicator to determine thickness of material under test.

Conclusion

Carbon nanotubes have been grown on a copper foil via three different techniques. The copper foil fabricated by growing CNTs directly on a copper substrate has demonstrated lower temperature drops across the interface when compared to plain copper substrates. Initial experiments reveal that a factor of 5 improvement was achieved with CNTs incorporated at the copper interface when compared to plain copper substrates at all power levels. More rigorous testing is currently being performed. Metal-coated particles are also being explored for use in thermal interface materials. A test stand is being acquired to characterize the thermal performance of the novel as well as conventional TIMs over temperature and pressure range suitable for automotive applications.

Next Steps

The following activities are planned for FY 2007 and beyond:
a) More detailed thermal resistance measurements will be performed to characterize the performance of CNTs over a range of temperature and pressures. Their performance will be compared against the best possible commercially available thermal interface materials.
b) Via a subcontract to FTG, metal-coated particles embedded in polymer compounds will be explored.
c) The performance of metal-coated particles embedded in polymer compound will also be characterized via thermal resistance measurements over a range of temperature and pressure. Comparisons will be made with commercially available interface materials.
d) Typically carbon nanotubes can be grown by chemical vapor deposition process. Our collaborators at CU Boulder intend to explore a spraying technique for depositing nanotubes on the copper foil which would eliminate the chemical vapor deposition process.
e) The possibility of replacing the grease in the IGBT package with these novel TIMs will be explored. This may involve interaction with OEMs and suppliers to figure out all the practical aspects.
f) The cost impacts of using CNTs and metal coated particles will be examined more closely.

Publications

"Fabrication And Thermal Characterization Of Copper-Carbon Nanotube 'Nano-thermofoil' As An Interface Material," to be presented at IMECE 2006, ASME International Mechanical Engineering Congress and Exposition, Nov. 5-10, 2006, Chicago, IL.

References

[1] Narumanchi, S.V.J., Hassani, V. and Bharathan, D., 2005, "Modeling single phase and boiling liquid jet impingement cooling in power electronics," National Renewable Energy Laboratory, NREL Report No. TP-540-38787. www.nrel.gov/docs/fy06osti/38787.pdf.
[2] Madhusudana, C.V., 1996, "Thermal contact conductance," New York, Springer-Verlag.
[3] Yovanovich, M.M. and Marotta, E.E., 2003, "Thermal spreading and contact resistances," in Heat Transfer Handbook, A. Bejan and A.D. Kraus, Editors, John Wiley & Sons, Hoboken, NJ, pp. 261−395.
[4] Prasher, R., 2006, "Thermal interface materials: historical perspective, status and future directions," to appear in the Proceedings of the IEEE.
[5] Xu, J. and Fisher, T., 2006, "Carbon nanotube array thermal interfaces," Cooling Technologies Research Center, Purdue University, CTRC Report # 2006-01.
[6] Xu, J. and Fisher, T.S., 2006, "Enhancement of thermal interface materials with carbon nanotube arrays," International Journal of Heat and Mass Transfer, 49, pp. 1658−1666.
[7] Xu, J. and Fisher, T.S., 2004, "Enhanced thermal contact conductance using carbon nanotube arrays," Proceedings of the ITherm conference: ninth intersociety conference of thermal and thermomechanical phenomena in electronic systems, Las Vegas, NV.
[8] Hu, X., Padilla, A.A., Xu, J., Fisher, T.S. and Goodson, K.E., 2005, "Thermal characterization of vertically-oriented carbon nanotubes on silicon," Proceedings of the 21st IEEE SemiTherm symposium, San Jose, CA.
[9] Tong, T., Majumdar, A., Zhao, Y., Kashani, A., Delzeit, L. and Meyyappan, M., 2006, "Indium assisted multiwalled carbon nanotube array thermal interface material," IEEE SemiTherm conference, Dallas, TX.
[10] Iijima, S., 1991, "Helical microtubules of a graphite carbon," Nature, 354, pp. 56−58.
[11] Hone, J., Llaguno, M.C. and Nemes, N.M., 2000, "Electrical and thermal transport properties of magnetically aligned single wall carbon nanotube films," Applied Physics Letters, 77(5), pp. 666−668.
[12] Kim, P., Shi, L., Majumdar, A. and Mceuen, P.L., 2001, "Thermal transport measurements of individual multiwalled nanotubes," Physical Review Letters, 87(21), pp. 215502(1−4).
[13] Berber, S., Kwon, Y.-K., and Tomanek, D., 2000, "Unusually high thermal conductivity of carbon nanotubes," Physical Review Letters, 84(20), pp. 4613−4616.
[14] Biercuk, M.J., Llaguno, M.C., Radosavljevic, M., Hyun, J.K., Johnson, A.T. and Fischer, J.E., 2002, "Carbon nanotube composites for thermal management," Applied Physics Letters, 80(15), pp. 2767−2769.
[15] Liu, C.H., Huang, H., Wu, Y. and Fan, S.S., 2004, "Thermal conductivity improvement of silicone elastomer with carbon nanotube loading," Applied Physics Letters, 84(21), pp. 4248−4250.
[16] ASTM, 1986, "Annual Book of ASTM Standards," Vol. 14.02, E 1225, Philadelphia.
[17] ASTM. *ASTM D5470-01 Standard*. 2005.

Nomenclature

A	Area
ASTM	American Society of Testing and Materials
BLT	Bond line thickness
CNTs	Carbon nanotubes

CVD	Chemical vapor deposition
DBC	Direct bonded copper
IGBT	Insulated gate bipolar transistor
k	Thermal conductivity
LVSEM	Low vacuum scanning electron microscopy
OFHC	Oxygen-free high conductivity copper
PCM	Phase change materials
PCMA	Phase change metallic alloys
Q	Heat flow
R	Thermal resistance/impedance
RTD	Resistance temperature detector
T	Temperature
TIM	Thermal interface materials

Greek

λ	Thermal conductivity
θ	Thermal resistance

3. Electric Machinery Research and Technology Development

3.1 Uncluttered CVT Machine

Principal Investigator: John Hsu
Oak Ridge National Laboratory
National Transportation Research Center
2360 Cherahala Boulevard
Knoxville, TN 37932
Voice: 865-946-1325; Fax: 865-946-1210; E-mail: hsujs @ornl.gov

DOE Technology Development Manager: Susan A. Rogers
Voice: 202-586-8997; Fax: 202-586-1600; E-mail: Susan.Rogers@ee.doe.gov

ORNL Program Manager: Mitch Olszewski
Voice: 865-946-1350; Fax: 865-946-1262; E-mail: olszewskim@ornl.gov

---

Objectives

Develop a new machine that combines motor and generator into one unit with a continuously variable transmission (CVT).

- The design enables additional torque coupling between the two rotors for producing more wheel torque.
- The combination of a motor and generator into one machine with only a single permanent magnet rotor has the potential to be simpler and less costly than conventional CVTs.
- The output power of the uncluttered rotor can be doubled.

Approach

- The uncluttered rotor CVT machine project has an ultimate multi-year goal of producing an electric machine with double the power density of current-technology machines at a given rotor speed.
- The principle of the uncluttered rotor was proved in FY 2001 through modification and testing of an induction machine with a specially wound rotor. The FY 2006 effort completed the second step of the proof-of-concept machine and eliminated the windings in the uncluttered rotor.
- The specific FY 2006 goal was to design and build a proof-of-concept uncluttered rotor without windings and a half stator that couples with the uncluttered rotor.

Major Accomplishments

- The design of the proof-of-concept uncluttered rotor without windings and a half stator wound core to couple to the uncluttered rotor was completed. The uncluttered rotor and its half stator were fabricated, and the uncluttered rotor teeth were machined out of solid steel instead of laminations in order to lower costs for the proof-of-concept prototype. The uncluttered rotor concept for the brushless rotating stator (or armature) was proved through tests conducted on the prototype.

Technical Discussion

The physics of the uncluttered CVT can be understood through an examination of a conventional motor. Figure 1 shows that for any conventional motor, the stator sees a counter-torque to the shaft torque. The magnitude of the stator torque is the same as that of the shaft torque. Anchor bolts are used to hold the stator down in practically all motor installations.

Figure 2 shows that the stator counter-torque can be used to double the shaft torque at a given rotor speed by removing the mounting bolts, allowing the stator to rotate on the added bearings, and transferring the stator torque to the shaft through gears, such as a set of planetary gears. Figure 2 also

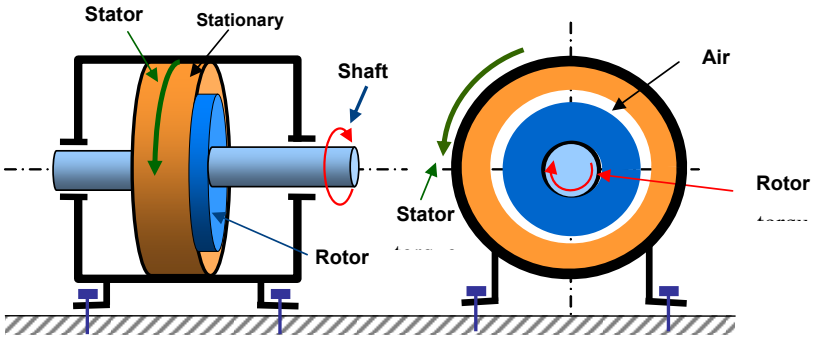


Figure 1. Shaft torque and stator torque of a motor.

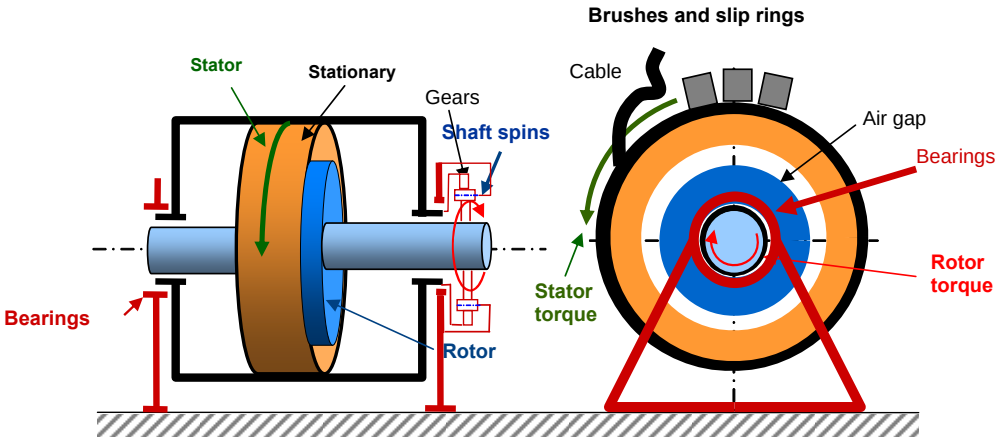


Figure 2. Doubling shaft torque at a given shaft speed.

shows that to harvest the torque of a rotating stator (or armature), brushes and slip rings would normally be required. Oak Ridge National Laboratory's (ORNL's) uncluttered CVT is a novel approach that doubles the torque at a given rotor speed and eliminates the brushes and slip rings. The absence of brushes and slip rings in the ORNL technology is emphasized in Figure 3.

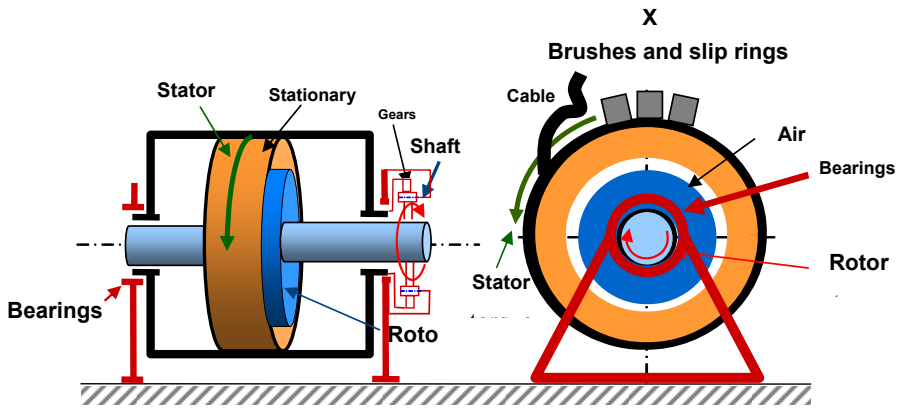


Figure 3. ORNL technology does not have brushes and slip rings.

Uncluttered Rotor

The ORNL technology for eliminating the brushes and slip rings is derived from the uncluttered rotor concept, which is explained through a conventional wound-stator core. When 3-phase currents are fed to the windings of a conventional wound-stator core, a rotating magnetic flux is produced, which goes through the air gap and reaches the rotor to return the rotating flux. The rotating speed of this rotating flux observed from the stator, regardless of whether the stator is stationary or rotating, is determined only by the frequency and number of poles of the winding. Therefore, the function of an uncluttered rotor is to produce a rotating flux. The rotating speed of this flux observed from the uncluttered rotor is determined only by the excitation frequency and by the number of poles of the uncluttered rotor. There are no brushes and slip rings for the excitation of the uncluttered rotor. The excitation wound core for the uncluttered rotor is stationary. The uncluttered rotor has no conductor; hence, no brushes and slip rings are required. The term "uncluttered" arises from the fact that when the current frequency is fed to the stationary excitation coil, the rotor speed does not change the corresponding rotating flux speed viewed from the rotor. The rotor speed influence is totally isolated to prevent a cluttered outcome.

Many variations of the uncluttered rotor and its excitation can be achieved. For example, Figure 4 shows an 18-pole, axial-gap, 2-phase uncluttered rotor that has two sides. The side facing the uncluttered rotor excitation core has rings. The flux has a tangential coupling between the excitation core and the rings. Because the rotation of the rings does not cause a change in the flux entering or leaving the rings, no torque is produced for this tangential magnetic coupling.

The opposite side of the sample axial-gap rotor has conventional teeth. When this side is coupled to a permanent magnet rotor with poles or to a conventional stator with teeth, the radial coupling produces torque. Figure 5 shows the ring side of the actual prototype uncluttered rotor. The opposite side of the rotor with teeth is shown in Figure 6.

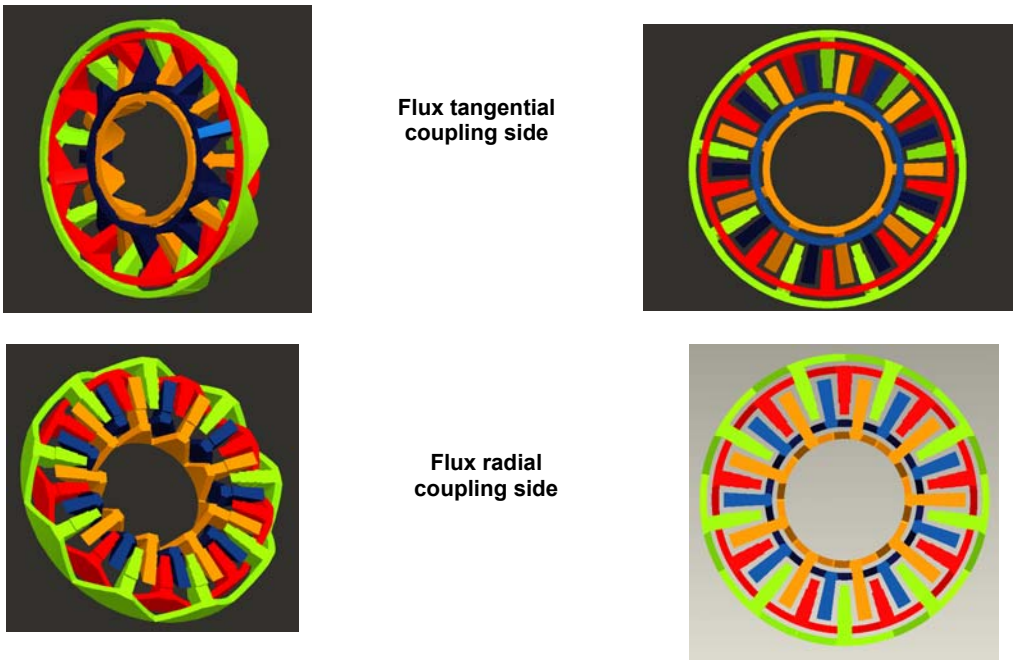


Figure 4. Example of an 18-pole, axial-gap, 2-phase uncluttered rotor.



Figure 5. One side of the proof-of-concept uncluttered rotor with rings.



Figure 6. The opposite side of the proof-of -concept uncluttered rotor with teeth.

The excitation core for the uncluttered rotor is shown in Figure 7. The two circular slots are for the 2-phase excitation coils. The resistance values and the inductance values of these 2-phase coils are designed to be equal for balanced 2-phase operation. The resistance value can be controlled by the wire size and the inductance value by the ring and slot dimensions. For the 3-phase option, three rings would be required, instead of the four rings required for the 2-phase option. In short, the uncluttered rotor made of flux-conducting material produces an equivalent rotating armature without brushes and slip rings.

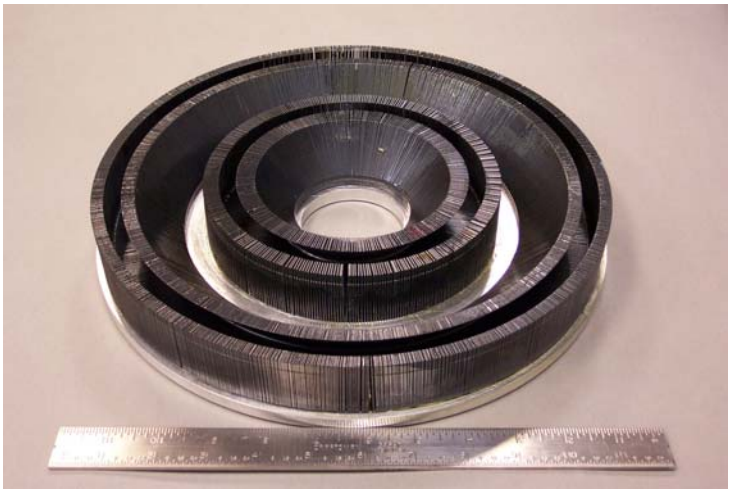


Figure 7. Two-phase excitation core for the uncluttered rotor.

Uncluttered CVT

An uncluttered CVT offers these benefits:

- Rotating stator for harvesting the reaction torque
- Brushless operation
- Combination motor and generator
- Single set of permanent magnets
- Smaller size, lighter weight, and lower cost

Figure 8 shows an example of the uncluttered rotor concept used for a CVT. The portion marked "Completed in FY 06" was to prove the brushless rotating armature concept. Inside this portion, the uncluttered rotor is sandwiched between the uncluttered rotor excitation core on the left and an air gap facing the rotating field of the permanent magnet rotor on the right. The combination of the excitation core and the uncluttered rotor is equivalent to a rotating stator without brushes. The energy going into the stationary excitation core is transferred through the air gap to the uncluttered rotor. Because the magnetic coupling at this air gap is a tangential coupling, no torque is produced during the transfer. The other side of the uncluttered rotor has a radial coupling between the uncluttered rotor and the permanent magnet rotor. Torque would be produced between the uncluttered rotor and the permanent magnet rotor in this air gap.

For the initial concept validation, the permanent magnet rotor was taken out and the wound stator used on the right side was substituted to produce a rotating field.

A possible axial-gap example of an uncluttered CVT is shown in Figure 9. For FY 2006, the experimental setup for using the uncluttered rotor concept to prove the brushless rotating armature concept is shown in Figure 10.

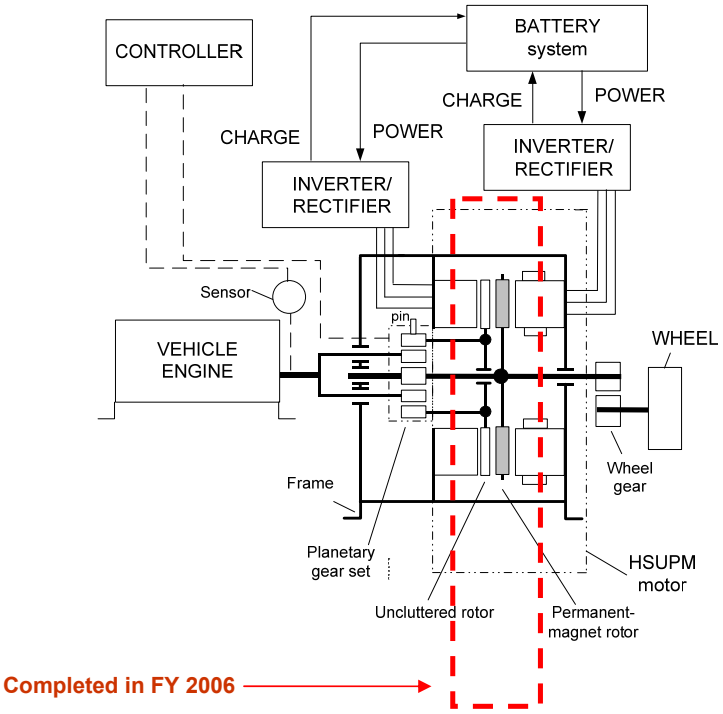


Figure 8. An example of an uncluttered CVT.

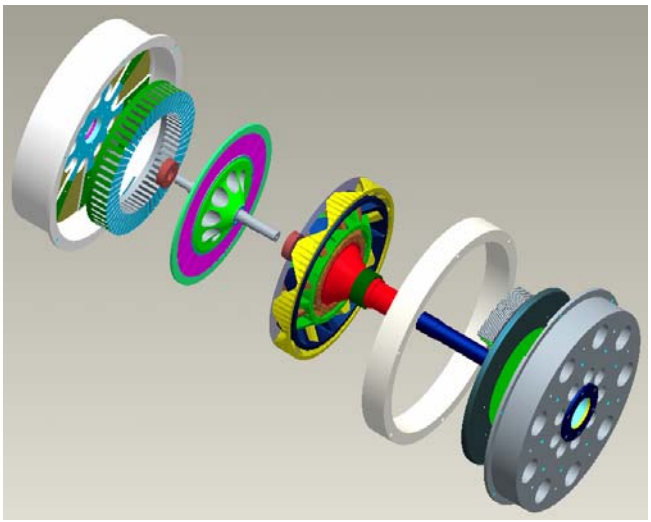


Figure 9. A possible axial-gap example of an uncluttered CVT.

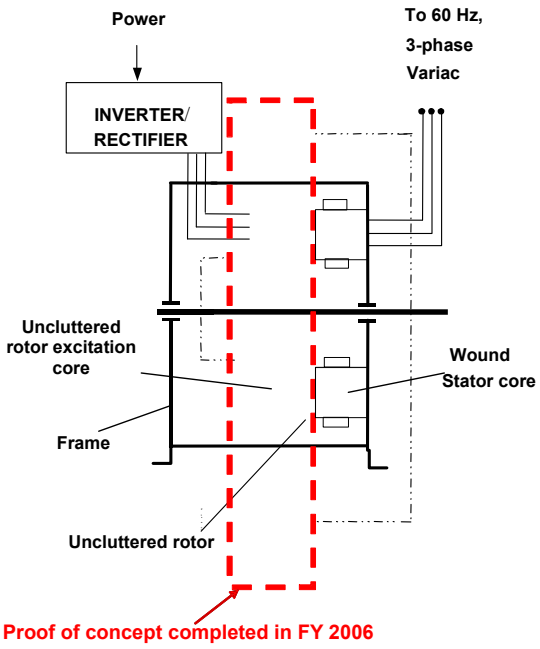


Figure 10. Experimental setup for proving the brushless rotating armature concept.

Figure 11 shows the prototype for the uncluttered rotor proof of concept completed in FY 2006. There are no brushes or slip rings in the machine. The 3-phase wound stator leads are connected to one side of the conventional axial-gap stator that provides a rotating field for the emulation of the rotating permanent magnet rotor. The uncluttered rotor shaft and the uncluttered rotor brushless excitation leads are also shown. The cut view of the proof-of-concept uncluttered rotor prototype is shown in Figure 12.

Tests on the Uncluttered Rotor

The following tests were performed on the prototype.

Induction Mode Test

In this test, the uncluttered rotor and its stator were viewed as a rotating stator or as a rotating wound armature. This rotating wound armature was magnetically coupled to another rotating field produced by the permanent magnet. In this test, the rotating field produced by the permanent magnets was replaced by the rotating field produced by a 3-phase wound core. If the frequency going into the 3-phase wound core is changed, the synchronous speed of the rotating field will be equivalent to the speed of the permanent magnet rotor. Therefore, the rotating wound armature coupled to the rotating field at a synchronous speed will actually be equivalent to an induction motor. In this equivalent setup, the rotating armature will act like a rotor of an induction motor, and the permanent magnet rotor will act like a stator of an induction motor that produces a synchronous magnetic field. The speed of the uncluttered rotor acting as the rotor of an induction motor would have a slip that is lower than the synchronous speed. The speed could be controlled by varying the resistance of the stationary uncluttered- rotor excitation coils. This expectation was clearly confirmed by the test.

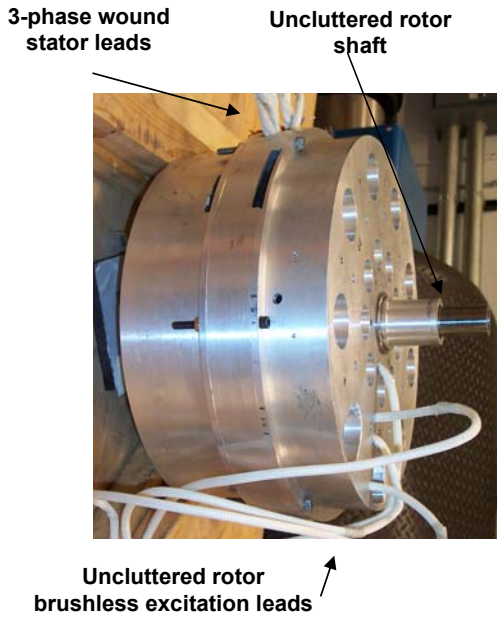


Figure 11. The prototype for the uncluttered rotor proof of concept completed in FY 2006.

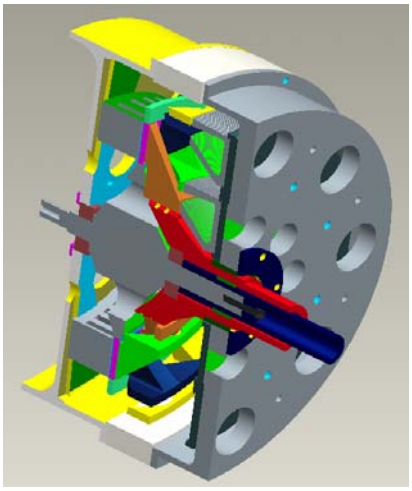


Figure 12. Cut view of the uncluttered rotor proof-of-concept prototype.

dc Mode Test

In this test, a dc current was fed to the stationary uncluttered-rotor excitation coils. The dc flux produced by the dc current went through the flux rings of the uncluttered rotor and turned into 8-pole flux on the other side of the rotor. This 8-pole flux interacted with the rotating flux produced by the 3-phase wound core that resulted in a synchronous motor. The rotor speed should be the synchronous speed of 400 rpm. This expectation was confirmed by the test.

Variable Frequency Mode Test

In this test, a set of variable-frequency two-phase currents was fed to the stationary uncluttered-rotor excitation coils. The variable-frequency flux produced by the variable-frequency currents went through the flux rings of the uncluttered rotor and transformed into an 8-pole rotating flux on the other side of the rotor. The speed of the uncluttered rotor went higher than the synchronous speed of the 3-phase wound core when the 2-phase sequence was opposite to the 3-phase sequence. If the 2-phase sequence is the same as the 3-phase sequence, the speed of the uncluttered rotor would go lower than the synchronous speed of the 3-phase wound core. This expectation was confirmed by the test.
Note that the number of phases of the uncluttered rotor excitation coils can be changed to two, three, or other practical numbers.

Conclusion

The concept of using an uncluttered rotor for the rotating brushless stator armature was proved through induction mode, dc mode, and variable-frequency mode tests. In FY 2006, a prototype was built and the concept for the rotating brushless stator armature was validated.

Future Direction

The next step is to simulate the performance of the uncluttered rotor and subsequently the uncluttered CVT assembly through design iteration and to start work on control of the uncluttered rotor.

Patents

John Hsu, "Hybrid-Secondary Uncluttered Permanent Magnet Machine and Method," U.S. Patent 6,977,454, December 20, 2005.

John Hsu, "Simplified Hybrid-Secondary Uncluttered Machine and Method," U.S. Patent 6,891,301, May 10, 2005.

John Hsu, "Hybrid Secondary Uncluttered Induction Machine," U.S. Patent No. 6,310,417, October 30, 2001.

References

1. J. Hsu, "Hybrid-Secondary Uncluttered Induction (HSUI) Machine," *IEEE Transactions on Energy Conversion* **16**(2), ITCNE4, (ISSN 0885-8969), 192–197 (June 2001).
2. J. Perahia, "Discussion of Hybrid-Secondary-Uncluttered Induction (HSUI) Machine," *IEEE Transactions on Energy Conversion* **17**(1), ITCNE4, (ISSN 0885-8969), 150 (March 2002).
3. J. Hsu, "Closure on Hybrid-Secondary-Uncluttered Induction (HSUI) Machine," *IEEE Transactions on Energy Conversion* **17**(1), ITCNE4, (ISSN 0885-8969), 150 (March 2002).

3.2 Interior Permanent Magnet Reluctance Machines

3.2.1 Interior Permanent Magnet Reluctance Machines with Brushless Field Excitation—16,000 rpm

Principal Investigator: John Hsu
Oak Ridge National Laboratory
National Transportation Research Center
2360 Cherahala Boulevard
Knoxville, TN 37932
Voice: 865-946-1325; Fax: 865-946-1210; E-mail: hsujs @ornl.gov

DOE Technology Development Manager: Susan A. Rogers
Voice: 202-586-8997; Fax: 202-586-1600; E-mail: Susan.Rogers@ee.doe.gov

ORNL Program Manager: Mitch Olszewski
Voice: 865-946-1350; Fax: 865-946-1262; E-mail: olszewskim@ornl.gov

---

Objective

Develop an interior permanent magnet (IPM) reluctance motor with brushless field excitation that offers high torque per ampere per core length by using a brushless excitation coil to enhance the flux. The motor does not require a dc/dc boost converter at medium and high speeds. The core loss is low, because the flux can be weakened by not supplying current to the excitation coil.

Approach

Increase motor speed to reduce size, weight, and cost.

- Achieve field weakening and enhancement by incorporating an additional flux path using external field excitation.
- Improve existing IPM design by adding side magnets without additional brushless field excitation.

Positives

1. The system does not require a dc/dc boost converter, resulting in a reduction in system costs.
2. Sufficiently higher torque per ampere per core length can be attained at low speeds.
3. Lower core losses at low torque regions, especially at high speeds, are attained.
4. Safety and reliability are increased because burning is prevented under the fault condition of a shorted winding.

Negatives

The system has an unconventional rotor structure and unconventional brushless field excitation.

Barriers/Challenges

For 16,000-rpm motors, mechanical stress is a challenge. Thicker bridges that link the rotor punching segments have to be increased. Consequently, the rotor flux leakages significantly lower the motor performance. This barrier can be overcome by the use of external excitation to ensure sufficient rotor flux.

Tasks

- Perform electromagnetic simulations and mechanical analysis.
- Complete fabrication of motor.

- Conduct evaluation tests upon completion of motor assembly.
- Complete testing in FY 2007.

Accomplishments

The assembly of the ORNL 16,000-rpm motor design is shown in Figure 1. Table 1 compares the dimensions of the ORNL 16,000-rpm motor and those of the Toyota/Prius motor.[1,2] The masses and sizes derived from this table provide a basis for a cost comparison with the Prius motor. The extra excitation coils and cores of the ORNL motor are made of copper wires and mild steel. The savings realized by a shorter stator core (1.875 in. compared with 3.3 in. for the Prius) and shorter stator winding compensate for their total cost. The low-current (5 A, maximum) control of the field excitation cost is minimal because of the low-current components required. This motor design enables better motor performance with system cost savings. Additionally, if used in a vehicle architecture requiring a boost converter, this motor can produce 250-kW output at 16,000 rpm. This significantly widens the possible applications for this type of motor.

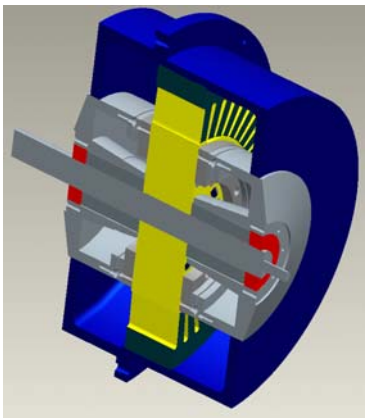


Figure 1. Assembly of ORNL 16,000-rpm motor design.

Table 1. Comparison of dimensions of the ORNL 16,000-rpm motor and the Toyota/Prius motor

	Prius	ORNL
Speed_	6000 rpm	16,000 rpm
Stator Lam. OD_	10.6”	same
Rotor OD_	6.375”	same
Core length_	3.3”	1.88”
Bearing to Bearing outer face_	7.75”	7.45”
Magnet Weight lbs_	2.75	2.57
Estimated field adj. ratio_	none	2.5
Rating_	33/50 kW	same
Boost converter_	yes	No
High speed core loss_	high	low

Technical Discussion

The design for the 16,000-rpm motor not only optimizes torque capability but also incorporates the ability to weaken the air gap flux density by having no excitation coil current. The need for low core losses across a wide range of speeds was also addressed in this design. The design maximizes the thickness of

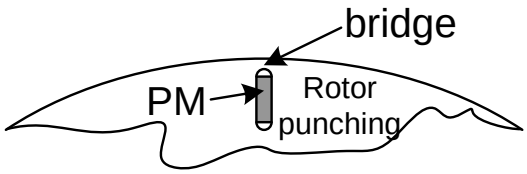


Figure 2. Location of bridge in a rotor punching.

the rotor punching bridges (material between the magnet slots in the rotor) (Figure 2) to satisfy the mechanical stress requirements at the high speeds required of this machine. More leakage flux produced by the PMs can go through these bridges, so the air-gap flux density produced by the PMs will be lower than in other, similar IPM machines such as the lower-speed Prius motor.

The 16,000-rpm motor with brushless field excitation provides flexibility for a drive system design to meet field strength requirements that vary at different loads and speeds. In general, the brushless field excitation approach can provide field enhancement and weakening for strong or weak PMs, as shown in Figure 3.

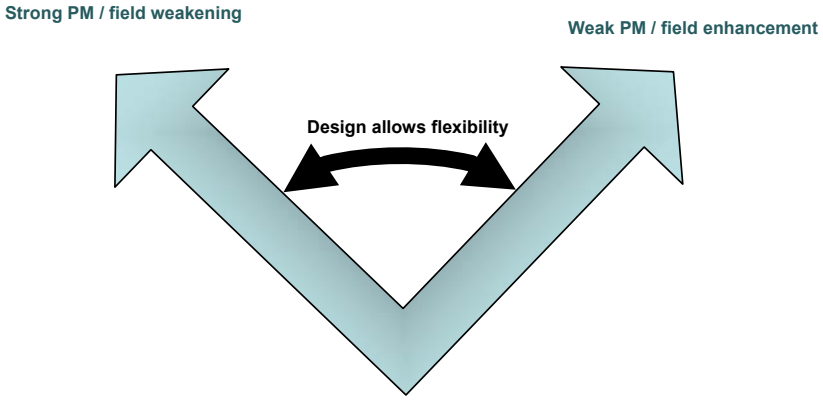


Figure 3. Flexibility provided by adjustable field excitation.

This motor is intentionally designed for low air-gap flux density at high speeds with no field excitation current applied This solves the problem of high core loss seen in existing high-PM-flux-density, high-speed motors of the type used in Prius and Highlander automobiles, which are plagued with both high core and high d-axis current losses necessary for field weakening. Figure 4 shows the rotor punching, the locations of PMs, and the completed rotor.

Figure 5 shows the air-gap flux density distributions at various excitation ampereturns (ATs). The excitation coil has 865 turns. The excitation current is the ATs, divided by the turns (865). The air-gap flux density of this motor can be adjusted with the external excitation coils to tailor the torque output. When high torque is required, the air-gap flux density is enhanced. When low torque and high efficiency are required, the excitation current is reduced to zero.

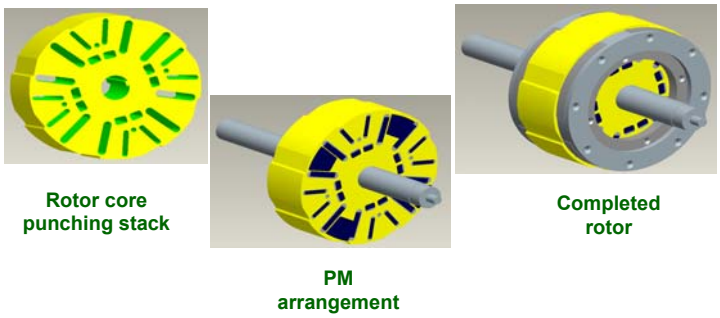


Figure 4. Rotor of ORNL's 16,000-rpm motor.

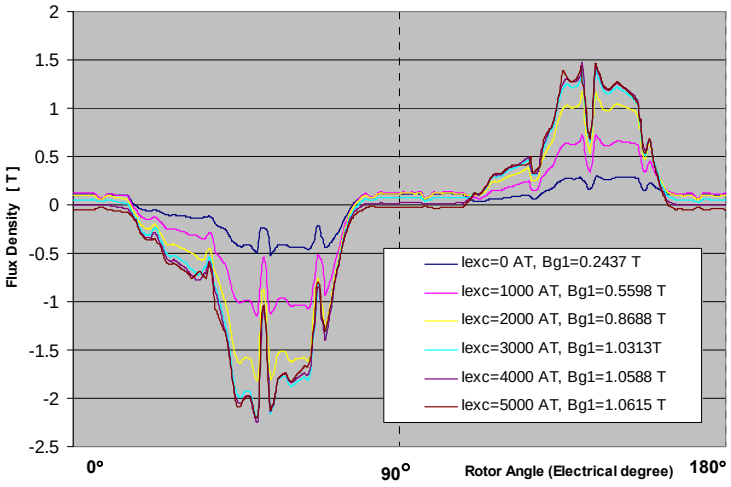
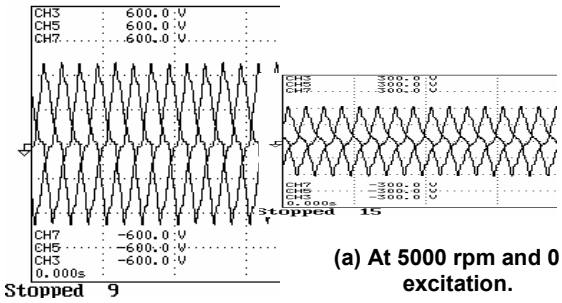


Figure 5. Air-gap flux density distributions with various excitation ampereturns (AT).

Figure 6 shows test results for three-phase, line-to-neutral back-electromotive force (emf) at 5000 rpm with 5-A and 0-A excitation currents, respectively. The asymmetry of the air-gap flux density distribution shown in Figure 5 does not affect the symmetry of the induced back-emf waveform. The expected output torque at 141 A_{RMS} (i.e., 200-A magnitude value) is shown in Figure 7. It clearly shows that the stronger field excitation can enhance the output torque.

The vibration analysis obtained from testing is shown in Figure 8. Vibration analysis will be conducted at each subsequent speed tested.



(a) At 5000 rpm and 0 A excitation.

(b) At 5000 rpm and +5 A excitation.

Figure 6. Three-phase line-to-neutral back-emfs at 5000 rpm with and without field excitation.

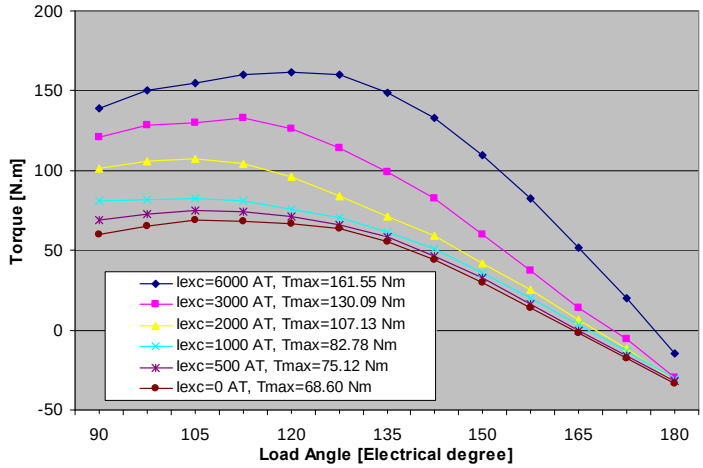


Figure 7. Stronger field excitation that can enhance output torque.

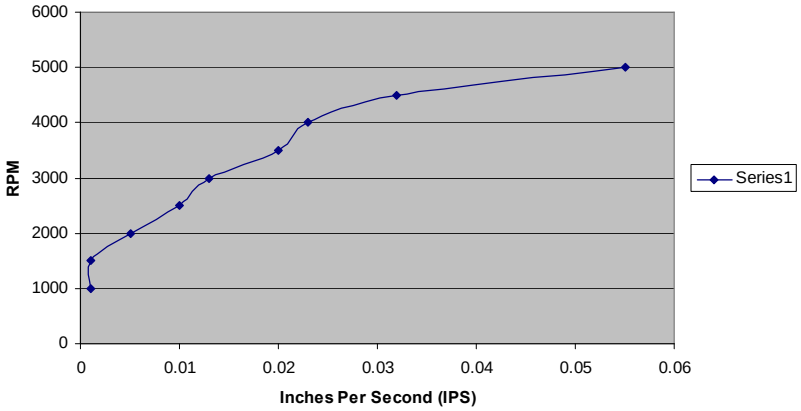


Figure 8. Vibration analysis obtained from test.

Figure 9 shows that the back-emf can be controlled effectively through the external field excitation current with a range of current from 0 to 5 A, thus negating the necessity of using a boost converter to overcome high back-emf. The initial tests show that the air-gap flux density can change up to 2.5 times at a given speed. This enables the motor to have all the advantages of both the existing strong PM reluctance motors (i.e., high power density, high back-emf at high speed, high core loss) and the weak PM reluctance motors (i.e., low power density, low back-emf, lower core loss) without their disadvantages. The additional circuitry necessary to supply the excitation current to the coils should cost less than $10 in production quantities.

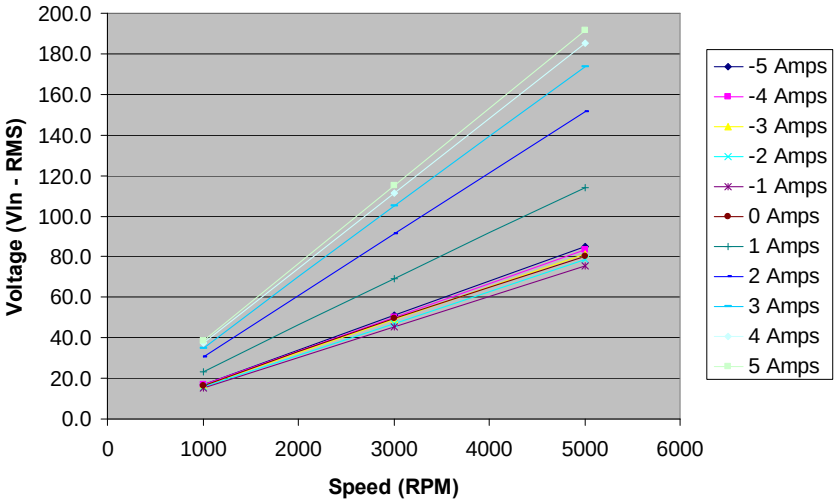


Figure 9. Line-to-neutral back-emf voltage vs speed.

The core and friction loss tests conducted show the benefits of lower air-gap flux density (Figure 10). For example, at 5000 rpm, the core and friction loss is 200 W with zero field excitation, compared with 600 W at high field excitation for a high air-gap flux density. This inherently low air-gap flux density motor design enables significantly lower core losses at high speeds (Figure 11). Yet at low speeds, when high torque is needed, the ability to enhance the field can dramatically boost the torque. The excitation coils coupled with this low air-gap flux design enable the motor to be controlled or "fine tuned" to operate in its highest-efficiency areas across the torque/speed curve.

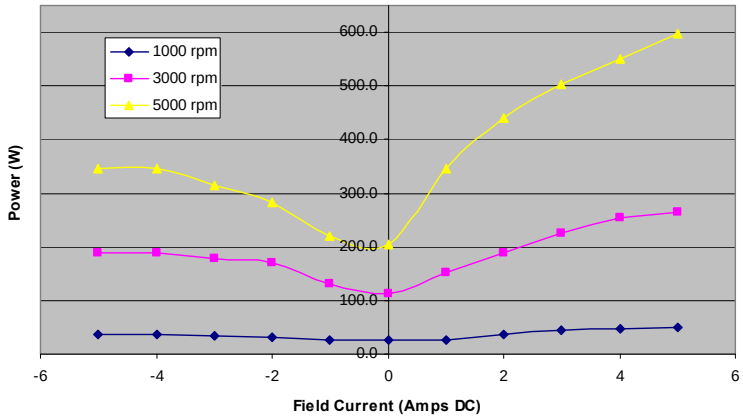


Figure 10. No-load core and friction losses vs field current for each speed.

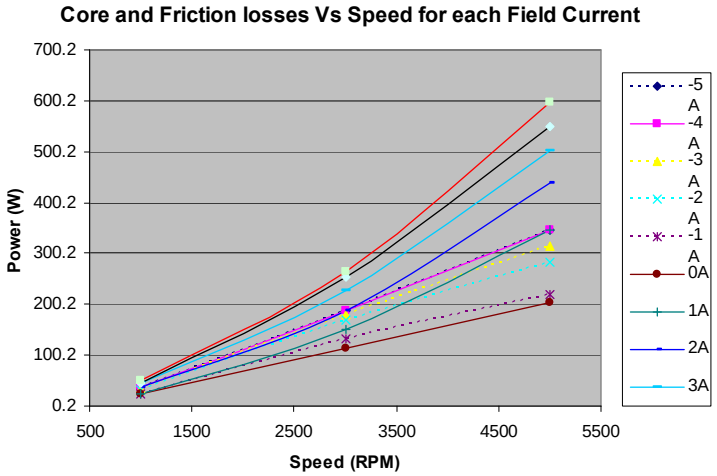


Figure 11. No-load core and friction losses vs speed for each field current.

Mechanical Analyses of 16,000-rpm Rotor

Extensive effort was expended on the high-speed, 16,000-rpm critical speed and three-dimensional (3-D) mechanical stress analyses. A transfer matrix approach was used to estimate the critical speed. The 3-D softwares used for stress analyses were ALGOR, ANSYS, and Pro/E. The analytical results are as follows.

- Estimated critical speed of 16,000-rpm rotors: 24,960 rpm (safety factor = 1.56).
- Stress analyses of rotor:
  - — Figure 12(a) shows the solid models with only a quarter of the PMs having properly defined contact surfaces (i.e., the upper right quarter that shows the gaps between PM and rotor punching).
  - — Figure 12(b) shows that when contact surfaces are bonded to the lamination, the stresses become unrealistically low. This demonstrates the importance of having the contact surfaces properly defined.

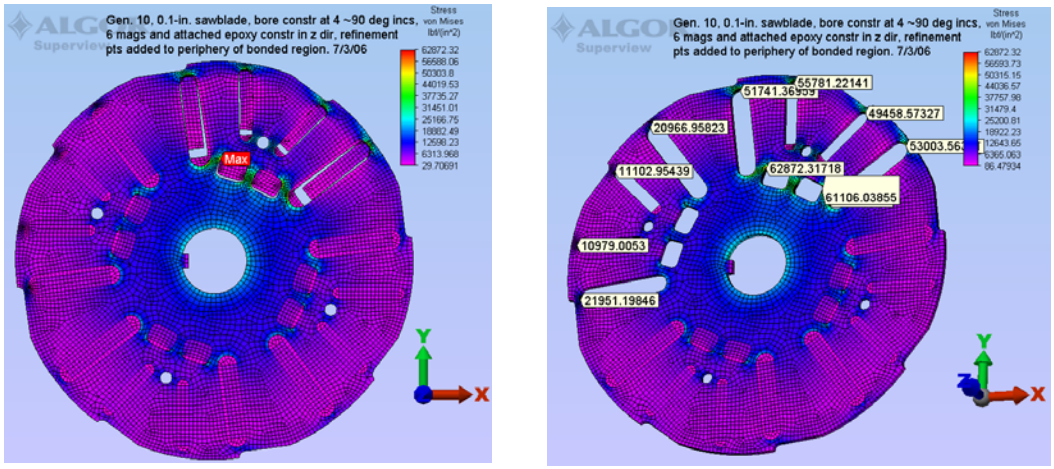


Figure 12. Finite-element stress analysis of 16,000-rpm rotor.

Figure 13 shows that, from the simulation, the radial displacement at the rim of a 0.018-in.-thick 16,000-rpm laminate rotor ranges from 0.00066 to 0.00124 in., which is less than the air gap of 0.029 in. Figure 14 shows that, although acceptable, the shear stresses at the support columns of a 0.018-in.-thick 16,000-rpm laminate rotor are slightly larger because the side of the small magnet nearest to the radial magnet is not along a radius.

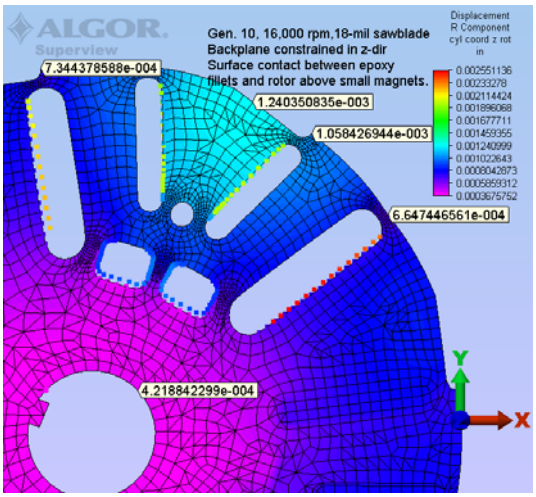


Figure 13. Radial displacement analysis of 16,000-rpm rotor.

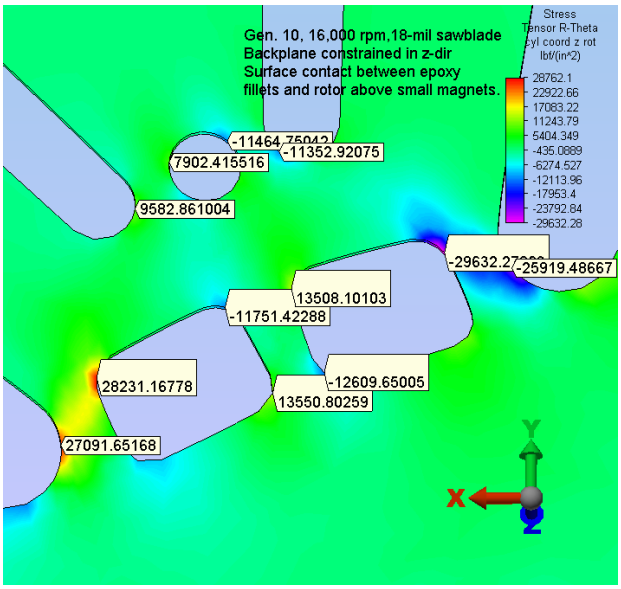


Figure 14. Shear stresses at the support columns of an 0.018-in. thick 16,000-rpm laminate rotor.

Parts fabricated

Figures 15 through 20 show the parts that have been fabricated for the prototype motor.

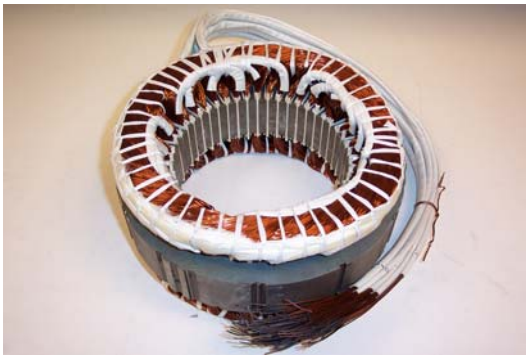


Figure 15. Wound stator core.

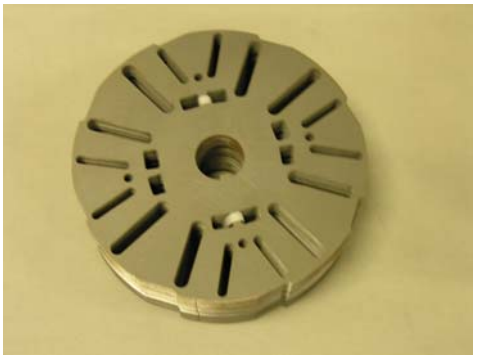


Figure 16. Rotor punching.



Figure 17. Rotor core stack and shaft.

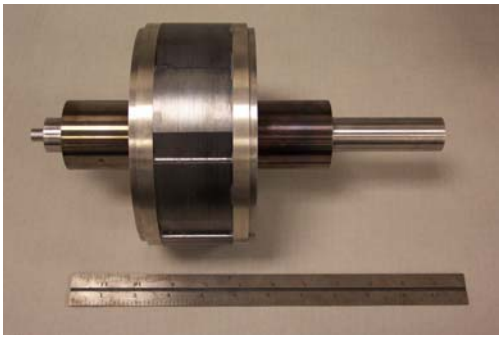


Figure 18. Completed rotor.

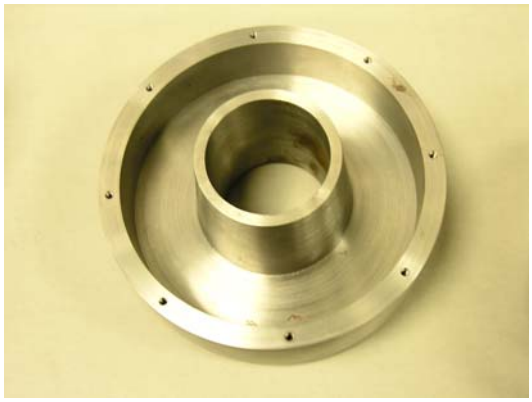


Figure 19. Excitation coil housing.

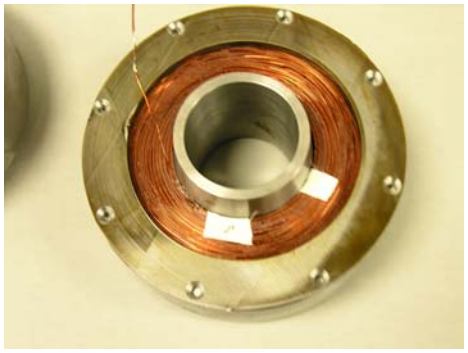


Figure 20. Excitation coil inside the coil housing.

Based on the experience of building the prototype at ORNL, it is anticipated that the motor will not present any complicated manufacturing issues. This is certainly a concern with any design undertaken at ORNL. No issues with added gearbox complexity are expected. We do not foresee a more complex gearbox than the planetary gearbox that is currently used by some automotive manufacturers.

The prototype motor can be further reduced in mass and volume by redesigning the interface between the excitation coils and the motor housing. This improvement will reduce the cost to manufacture the motor by eliminating some machining steps as well as raw materials.

Conclusion

The design of the 16,000-rpm motor not only optimizes torque capability but also incorporates the ability to weaken the air-gap flux density. It also addresses the need for low core losses across a wide range of speeds.

This design maximizes the thickness of the rotor punching bridges (material between the magnet slots in the rotor) to satisfy the mechanical stress requirements at the high speeds required of this machine. More leakage flux produced by the PMs can go through these bridges, so the air-gap flux density produced by the PMs will be lower than in other, similar IPM machines such as the lower-speed Prius motor.

Our motor is intentionally designed for low air-gap flux density at high speeds with no field excitation current applied. This solves the problem of high core losses seen in existing high-PM-flux-density, high-speed motors of the type used in the Prius and Highlander automobiles, which are plagued with both high core and high d-axis current losses necessary for field weakening.

This motor is still in the development stage. Validation data will be available after initial testing is completed this year. Initial test results show the following:

- The back-emf can be controlled effectively through the external field excitation current with a range of current from 0 to 5 A, thus negating the necessity of using a boost converter to overcome high back-emf. The air-gap flux density can change up to 2.5 times at a given speed. This enables the motor to have all the advantages of both existing strong PM reluctance motors (i.e., high power density, high back-emf at high speed, high core loss) and weak PM reluctance motors (i.e., low power density, low back-emf, lower core loss) without their disadvantages. The additional circuitry necessary to supply the excitation current to the coils should cost less than $10 in production quantities.
- The core and friction loss tests conducted show the benefits of lower air-gap flux density. For example, at 5000 rpm, the core and friction loss is 200 W with zero field excitation, compared with 600 W at high field excitation for a high air-gap flux density.

This inherently low air-gap flux density motor design enables significantly lower core losses at high speeds. Yet at low speeds, when high torque is needed, the ability to enhance the field can dramatically boost the torque. The excitation coils, coupled with this low air-gap flux design, enable the motor to be controlled or fine tuned to operate in its highest-efficiency areas across the torque/speed curve.

It is not anticipated that the motor will present any complicated manufacturing issues. Redesigning the interface between the excitation coils and the motor housing will further reduce the mass and volume of the prototype motor, reducing the manufacturing cost.

In addition to the low loss performance improvement, this motor design eliminates the requirement for a boost converter, simplifying the power electronics and enabling cost savings in the total drive system. Comparing mass and size provides a basis for a cost comparison with the Prius motor. The extra excitation coils and cores of the 16,000-rpm motor are made of copper wires and mild steel. The savings realized by a shorter stator core (1.875 in. compared with the 3.3 in. of Prius) and shorter stator winding compensate for their total cost. The low-current (5-A, maximum) control circuit for the field excitation coils cost is minimal because of the low-current components required. This motor design enables better performance with system cost savings. Additionally, if used in a vehicle architecture requiring a boost

converter, this motor can produce 250-kW output at 16,000 rpm, significantly widening possible applications.

Future Direction

In FY 2007 the research goal is to produce a motor with significantly reduced size, weight, and volume from that of current technology. The higher power density and lower system cost will provide industry with a greater cost vs performance ratio. A dramatic system cost savings will be realized by eliminating the dc/dc boost converter as well. Through reductions in core losses at high speeds by using the field weakening capability improvements in vehicle fuel efficiency will also be realized.

In FY 2007 performance testing will be completed. Performance calculations for the 3-D RIPM-BFE motors will be verified and adjustments made in the models depending on testing results. These tests will include the back-emf data with no field excitation as well as with enhancement and weakening of the field. Locked rotor testing will be completed with the same conditions as the back-emf tests (no field excitation and enhancement/weakening of the field). Performance and efficiency mapping will also be completed during FY 2007. Testing will take place at various voltage increments, and speed and torque ranges, similar to the benchmarking tests performed on the Prius motor at ORNL. This motor will be driven by a dynamometer system to facilitate data measurements. Revisions to the motor, due to unforeseen issues, will be resolved, and the motor will be retested as necessary.

Patents

J. S. Hsu et al., "Rotor Apparatus for High Strength Undiffused Brushless Electric Machine," U.S. Patent 6,989,619, January 24, 2006.

J. S. Hsu et al., "Hybrid-Secondary Uncluttered Permanent Magnet Machine and Method," U.S. Patent 6,977,454, December 20, 2005.

J. S. Hsu et al., "Permanent Magnet Machine and Method with Reluctance Poles for High Strength Undiffused Brushless Operation," U.S. Patent 6,972,504, December 6, 2005.

J. S. Hsu et al., "Simplified Hybrid-Secondary Uncluttered Machine and Method," U.S. Patent 6,891,301, May 10, 2005.

J. S. Hsu et al., "High Strength Undiffused Brushless (HSUB) Machine," U.S. Patent 6,573,634, June 3, 2003.

J. S. Hsu et al., "Hybrid Secondary Uncluttered Induction Machine," U.S. Patent 6,310,417, October 30, 2001.

J. S. Hsu et al., "Permanent Magnet Energy Conversion Machine," U.S. Patent 5,952,756, September 14, 1999.

References

1. M. Kamiya, "Development of Traction Drive Motors for the Toyota Hybrid System," Toyota Motor Corporation, 1, Toyota-cho, Toyota, Aichi, Japan.
2. M. Okamura, E. Sato, and S. Sasaki, "Development of Hybrid Electric Drive System Using a Boost Converter," Toyota Motor Corporation, 1, Toyota-cho, Toyota, Aichi, Japan.

3.2.2 High-Power-Density Reluctance Interior Permanent Magnet Machines—6,000 rpm

Principal Investigator: John Hsu
Oak Ridge National Laboratory
National Transportation Research Center
2360 Cherahala Boulevard
Knoxville, TN 37932
Voice: 865-946-1325; Fax: 865-946-1210; E-mail: hsujs@ornl.gov

DOE Technology Development Manager: Susan A. Rogers
Voice: 202-586-8997; Fax: 202-586-1600; E-mail: Susan.Rogers@ee.doe.gov

ORNL Program Manager: Mitch Olszewski
Voice: 865-946-1350; Fax: 865-946-1262; E-mail: olszewskim@ornl.gov

---

Objective

- The objective is development of a high-power-density motor technology for reluctance interior permanent magnet (RIPM) motors, using side magnets located at the motor's end turns.

Approach

- To improve the power density of existing RIPM motors, the rotor of this new design was modified to have additional side magnets. Because this new motor does not use any additional external field excitation, it is more in line with conventional motor structures than other recent Oak Ridge National Laboratory (ORNL) motor projects. This project involved the development of a 6000-rpm motor. However, the new technology resulting from this project can be used for either higher- or lower-speed motors. A dc/dc boost converter and/or a strong direct-axis current for field weakening might be needed for this motor at high speeds because of the high back–electromotive force (emf) produced by the strong permanent magnet (PM) air-gap flux density.
- The unique design of this motor necessitated highly intensive, time-consuming computational modeling. Traditional two-dimensional finite element analyses could not be used effectively in the simulations, so three-dimensional simulations had to be performed.

Major Accomplishments

- The new technology derived from this project shows that the air-gap flux density produced by the new PM arrangement can be doubled compared with that of the Toyota Prius motor. The PM torque component is proportional to the product of the PM fundamental air-gap flux density and the current of the motor. Therefore, higher PM fundamental air-gap flux density produces higher toque at a given current and hence a higher power density of the motor.

Future Direction

This project was completed in FY 2006.

Technical Discussion

The power input of an RIPM motor is shown in Equation (1). The output power of the motor is the input power minus the losses of the motor. If the losses that include the copper loss, core loss, stray loss, and mechanical loss of the motor are neglected for simplification, the output power is represented by the input power.

$$P_{in} = \frac{3}{2}\left[\frac{EV}{X_d}\sin\delta - \frac{V^2}{2}\left(\frac{1}{X_q} - \frac{1}{X_d}\right)\sin 2\delta\right] \quad (1)$$

In Equation (1), E is the back-emf that is proportional to the no-load air-gap flux density. V is the phase voltage, δ is the load angle, and X_d and X_q are the direct and quadrature inductances, respectively. Based on this equation, power can be increased by raising the E value.

Because E is produced by the PMs without excitation from the stator currents, the higher the air-gap flux density is at no load, the higher the E value is. The target for this investigation is to find practical ways to increase the air-gap flux density produced by the PMs. Various novel PM arrangements are compared with the arrangement of the Toyota Prius PM rotor, which is shown in Figure 1. The PMs are situated inside the V-shaped grooves [1–2]. There is an air gap between the rotor and the stator. The air-gap flux density of this motor is used as the base value for the normalized comparison for various novel PM arrangements.

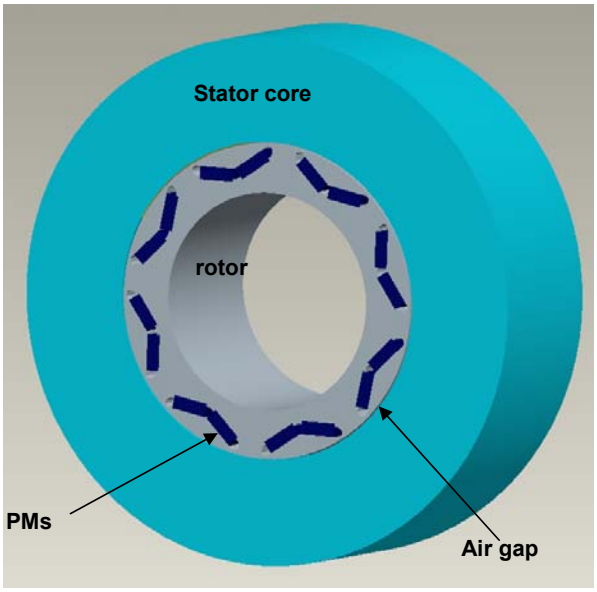


Figure 1. PM arrangement of Toyota Prius rotor.

Figure 2 shows various PM arrangements of an RIPM motor that has no additional field excitation. Figure 2(a) shows the U-shaped PMs that are symmetrically arranged for the north and south poles of the rotor. There is no side PM for this arrangement. Figure 2(b) shows that in addition to the U-shaped PMs, there can be either partial side PMs (represented by the blue magnets) or full side PMs (represented by both the blue and brown magnets). For the partial side-PM arrangement, the side PM and side pole piece are alternately located at the ends of the rotor poles. For the full side-PM arrangement, PMs are located at the ends of the rotor poles. A soft magnetic end ring (not shown) is attached to the ends of the side PMs to provide a flux return path for the side PMs.

Figure 3 shows the locations of the side poles and side PMs of a partial side-PM prototype motor. The magnetic end rings are not shown in this figure. For a full side-PMs arrangement, the side poles are replaced by side PMs. The prototype uses an aluminum non-magnetic spacer to mechanically secure the side poles and side PMs.

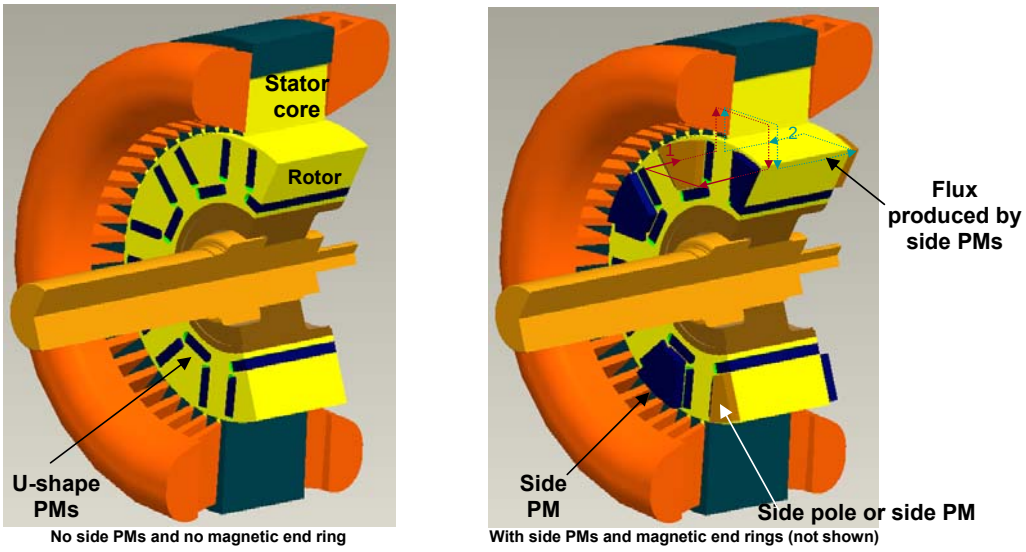


Figure 2. Various PM arrangements for increasing air-gap flux density.

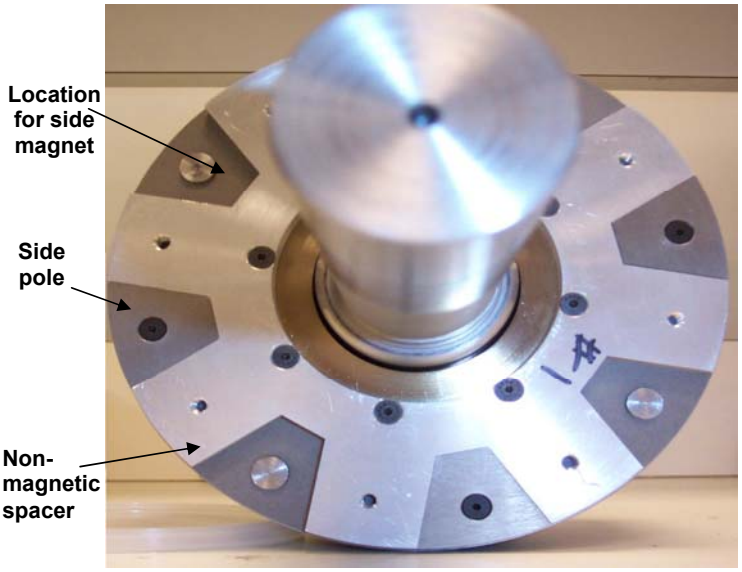


Figure 3. Prototype motor showing locations of side poles and side magnets.

Figure 4 shows the 3-dimensional finite element simulation results for the rotor flux density distributions produced by PMs only for the Toyota Prius; it shows no side-PM, partial side-PM, and full side-PM arrangements. Note that the very high flux density of the rotor is located in the narrow punching bridges on top of the PM grooves. The bridges magnetically short-circuit the PMs and become very saturated. These magnetically saturated bridges limit the flux that leaks from a rotor pole to its adjacent

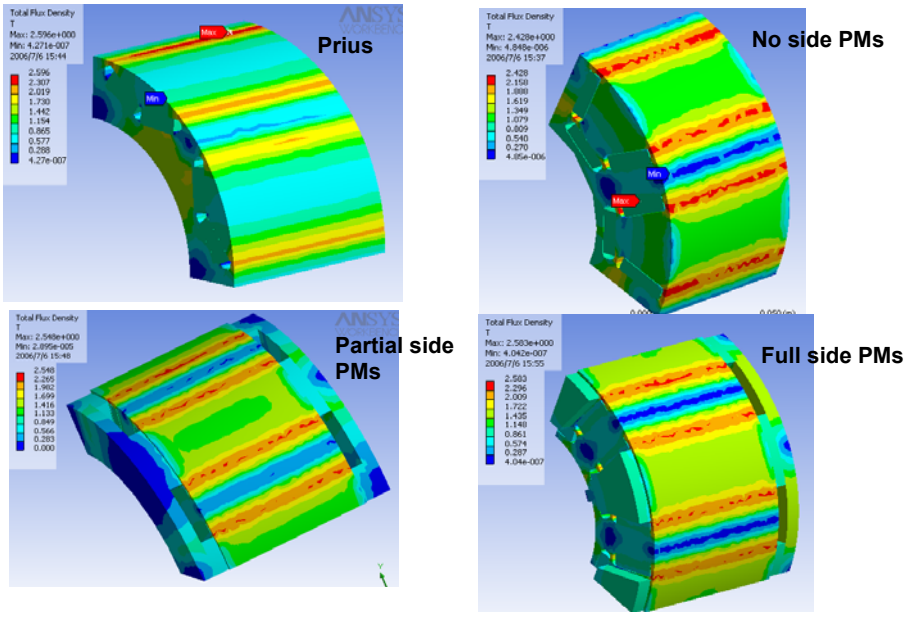


Figure 4. Three-dimensional simulation results for rotor flux density distributions.

pole. Because the bridge flux inside the bridge is mainly in the rotor peripheral direction, the radial air-gap fluxes at the bridge locations are relatively lower.

Figure 5 shows the radial air-gap flux distributions produced by the PMs for the four cases shown in Figure 4. The air-gap no-load flux density for the case of the U-shaped magnets plus full side PMs can reach double the value of the Prius air-gap no-load flux density.

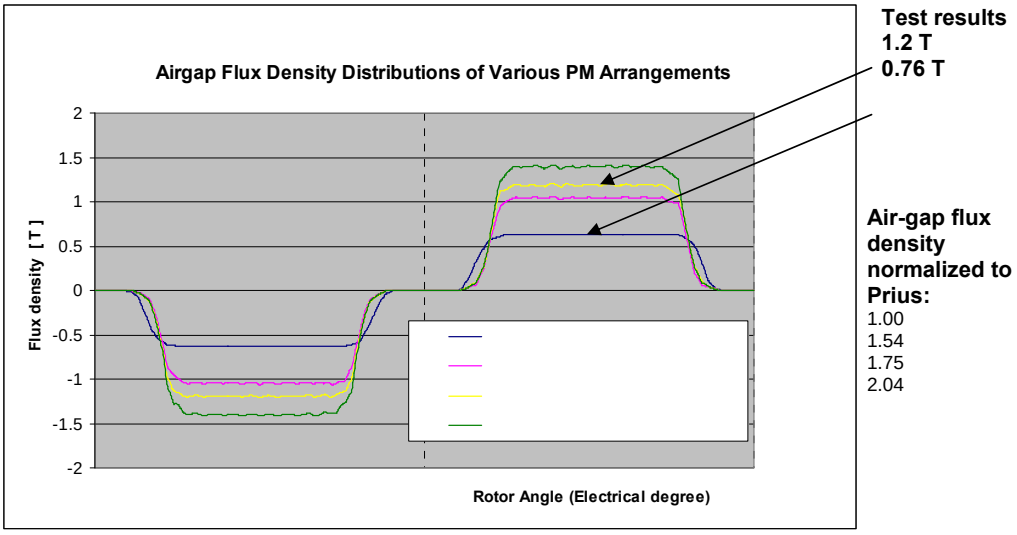


Figure 5. Comparison between simulation and test results of air-gap flux densities produced by PMs for various PM arrangements.

Conclusion

To improve the power density of existing RIPM motors, the rotor of an existing traditional machine was modified to contain additional side magnets. Because the motor being studied in this project does not use any additional external field excitation, it is more in line with conventional motor structures. The new technology resulting from this project can be used for either high- or low-speed motors. A dc/dc boost converter and/or a strong direct-axis current for field weakening might be needed for this motor at high speeds because of the high back-emf produced by the strong PM air-gap flux density.

The new technology derived from this project shows that the air-gap flux density produced by the PMs can be doubled compared with that of the Toyota Prius motor. Because the PM torque component is proportional to the product of the PM fundamental air-gap flux density and the current of the motor, higher PM fundamental air-gap flux density produces higher toque at a given current, yielding a higher-power-density motor.

This project was completed in FY 2006.

Future Direction

Beyond FY 2006, assistance to original equipment manufacturers for commercial prototypes will be provided as needed.

Patents

John Hsu, "Rotor Apparatus for High Strength Undiffused Brushless Electric Machine," U.S. Patent 6,989,619, January 24, 2006.

References

1. Munehiro Kamiya, "Development of Traction Drive Motors for the Toyota Hybrid System," Toyota Motor Corporation, 1, Toyota-cho, Toyota, Aichi, 471-8571, Japan.
2. Masaki Okamura, Eiji Sato, and Shoichi Sasaki, "Development of Hybrid Electric Drive System Using a Boost Converter," Toyota Motor Corporation, 1, Toyota-cho, Toyota, Aichi, 471-8572, Japan.

3.3 Control of Fractional-Slot Surface Mounted Permanent Magnet Motors with Concentrated Windings

Principal Investigator: John W. McKeever
Oak Ridge National Laboratory
National Transportation Research Center
2360 Cherahala Boulevard
Knoxville, TN 37932
Voice: 865-946-1316; Fax: 865-946-1262; E-mail: mckeeverjw@ornl.gov

DOE Technology Development Manager: Susan A. Rogers
Voice: 202-586-8997; Fax: 202-586-1600; E-mail: Susan.Rogers@ee.doe.gov

ORNL Program Manager: Mitch Olszewski
Voice: 865-946-1350; Fax: 865-946-1262; E-mail: olszewskim@ornl.gov

Objectives

The overall objective of this project is to develop techniques to analyze, design, and control fractional-slot concentrated-winding (FSCW) surface permanent magnet (SPM) synchronous machines; to investigate their possible use as a hybrid electric vehicle (HEV) traction motor; and if appropriate, to bring them into competition with internal permanent magnet motors. FSCW motors have potential for fault tolerant, wide constant power speed range (CPSR) operation because of their high inductance. They also have features that can reduce copper costs through improved slot utilization and elimination of copper end turns and reduce fabrication costs through simplified assembly methods.

A second objective, which is a subset of analysis and design, is to improve the model for calculating iron losses in the stator teeth and yoke, in the rotor, and in the magnets. Until more accurate estimates of these losses are available, reliable evaluation of the impact of minimizing them requires laboratory measurements.

Approach

The approach was to use closed-form analytical tools and commercial software to investigate and propose a design for a 55-kW FSCW motor. Originally, the plan was to build the 55-kW traction motor for testing. That approach was changed as it was felt that enough research had been completed on the FSCW motor that original equipment manufacturers could make the transition to market if they thought it had sufficient merit. Consequently, the product at the end of the year was a proposed 55-kW FSCW design whose analysis indicated that it could meet near term FreedomCAR targets.

We also developed a motor/inverter simulator to evaluate control schemes developed to improve efficiency of the FSCW-SPM motor. The approach was to test control schemes using the 6-kW FSCW prototype motor developed and tested at the University of Wisconsin, Madison (UWM), in FY 2005, mounted in a new frame that allowed liquid to cool the stator.

ORNL collaborated with UWM to test the control schemes developed. ORNL has a low cost scheme that controls at rated current or rated power to achieve maximum torque per amp below base speed and maximum power per amp above base speed. It is low cost because it eliminates current sensors. UWM has a modified vector control scheme to maximize motor efficiency at partial load. It determines the machine excitation that will provide the most favorable trade-off between copper losses and iron losses to achieve the highest possible efficiency under light-load conditions.

In FY 2006 the iron loss and magnet loss models were modified to extend the loss calculations to higher frequencies where skin effects alter the results. Plans call for this iron loss model to be

incorporated into the UWM FSCW-SPM machine design program. Point-by-point finite-element analysis (FEA) is being used to verify the iron loss predictions of the closed-form model whenever experimental test results are not available to provide this verification.

Major Accomplishments

1. Incorporated FreedomCAR targets to design and propose two 55-kW SPM motors with FSCWs for study in FY 2006. *SPM2* was selected for an analytical model comparison study. *SPM1* was selected for developing an analytical model to accurately predict the stator tooth and yoke iron losses in FSCW-SPM machines.
2. Modeled the *SPM2* motor with SPEED software and collaborated with UWM to compare design parameters calculated using SPEED's PC-BDC (brushless direct current) module with those calculated by UWM.
3. Created a rapid motor/inverter simulator using MatLab and checked its verity with time domain calculations using PSPICE software to show that the algorithms in the simulator are fast enough to use in a control circuit.
4. Successfully developed a closed-form analytical model that can accurately predict the stator tooth and yoke iron losses in FSCW-SPM machines during open-circuit operation. The status of this work will be included in this report.
5. Completed a detailed point-by-point FEA of FSCW-SPM machines that are proving very helpful in identifying the relative contributions of hysteresis and eddy-current losses in different parts of the machine as a function of rotor speed.
6. Developed three control schemes.
   a. The UWM scheme controls to ensure maximum motor efficiency. It shows how motor losses under load may be sufficiently reduced by field weakening, which increases total current, to offset the additional I^2R losses and thereby improve motor efficiency. This work is described in this report.
   b. The first ORNL scheme is a low-cost scheme because it eliminates current sensors. The ORNL simulator assumes losses that increase with the square of the speed.
   c. The second ORNL scheme uses a set of antiparallel silicon-controlled rectifiers (SCRs) in each phase to ensure that any load is accommodated with minimum current, which ensures that it is a maximum overall efficiency scheme.
7. Performed a successful FEA-based verification of a significant efficiency improvement (>5% at some speeds) that can be achieved in FSCW-SPM machines by using the modified vector control algorithm during partial-load operating conditions.
8. Evaluated the first ORNL control scheme with the simulator for two constraints, first so that rated current is not exceeded and second so that rated power is not exceeded. The limiting current constraint allows considerably more power to be delivered over a large part of the power speed curve.

Technical Discussion

Benefit and Use of Concentrated Windings

Introduction

Until John Hsu began research on motors with flux generated by an external coil and then directed into the rotor to modulate or even replace conventional magnet flux,[1] most of ORNL's PM motor research centered on axial- and radial-gap PM motors with distributed windings with one slot per pole per phase. To operate these motors above base speed, where the back-electromotive force (back-emf) equals the source voltage, making it difficult to deliver power from the source, a technique know as phase advance[2] had to be used. This technique had limitations that could be overcome by adding antiparallel SCRs in each of the three phases thereby increasing the maximum speed but also slightly increasing the cost because of the additional components. This new control technique, called dual mode inverter control,[3] was simulated using a "per-phase" model to show that the SCRs could be represented by a variable

inductance.[4] For PM motors, it has been recognized that one way to increase the maximum speed at which rated power is reached is to increase their inductance. A brute force way to do this was to add an inductor in each line, but a much better way would be to design the inductance into the motor itself. Designing the required inductance into the motor with distributed windings has been difficult as will be discussed later in this report.

In May 2004 an interim report prepared by UWM discussed significant benefits when a distributed winding is replaced by a concentrated winding.[5] The primary benefit is that the inductance necessary to allow high speed operation may be easily designed into the motor. Other benefits included improved fault tolerance, improved slot utilization because stator segments can be bobbin wound to achieve a higher fill factor, easier assembly because the segments can be assembled after winding, and a large reduction in the volume of copper used in end windings.

In FY 2005 ORNL's Power Electronics and Electric Machinery Research Center, in collaboration with UWM's Prof. Tom Jahns and his student, Dr. Ayman M. El-Rafaie, investigated applications of concentrated windings for use in HEV and fuel cell permanent magnet (PM) traction drives. During FY 2005 a 6-kW motor was designed and tested up to 4000 rpm[6] to validate the design procedure developed at UWM.[7] ORNL, a member of the SPEED Consortium at the University of Glasgow in Scotland, modeled the 6-kW design using SPEED software, a detailed motor development tool. The results generally agreed well. In FY 2006 UWM designed a 55-kW traction drive which met the 2010 FreedomCAR targets.[8] ORNL modeled the 55-kW motor, again getting good agreement except for the high speed magnet losses. During e-mail exchanges with the University of Glasgow we found that the algorithm used by SPEED does not consider skin effect, which would lead to increased resistance as the speed increases, and does not consider the effects of circumferential or axial magnet segmentation. The next release will use a 2-D finite-element program linked to a transient solver that produces files read by SPEED to calculate iron and magnet losses to solve the problem.

Distributed windings and concentrated windings

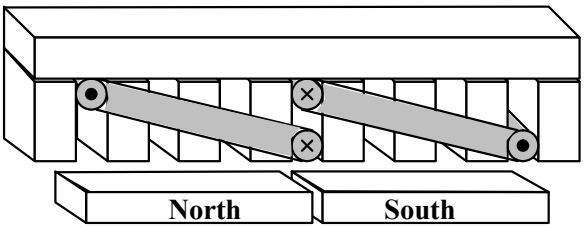
Technology for distributed stator windings has been around for 100 years and is well understood; consequently, it has long been the winding of choice for motor development. The amount of fundamental magnet flux linked by the stator winding coils determines the torque and power produced and is therefore the most important parameter of a PM motor. The reference winding that passes maximum flux is a distributed winding like the one shown in Figure 1(a). For each phase, full pitch coils bypass two slots for the other two phases. Two coils from adjacent poles are overlapped in one slot. This pattern is repeated for each pole and the coils are connected in series to complete the phase. The number of slots per pole per phase is 1. The back-emf is the algebraic rather than vector sum of each coil in a phase. An example of a concentrated winding similar to the one being investigated for use as an HEV traction motor is shown in Figure 1(b). Each coil winding is concentrated in two adjacent slots. After the first coil is wound in one direction, 4 slots are skipped, two for each of the other two phases, before the next concentrated coil is wound in the opposite direction to complete the stator pole pair. The 6-kW FSCW motor built and tested in FY 2005 and the 55-kW FSCW motor designed in FY 2006 have 36 slots and 30 pole pairs.

Winding function

The winding function is a representation of idealized stator coils. It is estimated from a process for counting conductors (personal communication between Professor Tom Jahns, UMW, and John McKeever, ORNL). First, Ampere's law is applied along closed curves to determine $H_g(\theta)$ referenced to $H(0)$. Then Gauss' law is applied to determine $H(0)$. All the wires are assumed to be at the center of the slot for convenience in analysis.

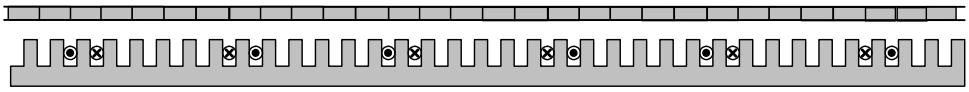
Both laws come from Maxwell's equations:

$$\nabla \times H = J \text{ and } \nabla \bullet B = 0 \quad . \tag{1}$$



(a) Distributed winding (full pitch).

30 alternating N and S poles (15 pole pairs)



One phase consisting of 6 concentrated stator coils each occupying 2 slots.

(b) Concentrated winding for 36-slot, 30-pole configuration with N_{spp}=2/5.

Figure 1. Distributed and concentrated windings.

Stokes' theorem is applied to the surface integral of the left equality in Equation (1), producing a line integral on the left and the product of the number of turns inside the surface times the current in the turns, which is expressed as

$$\oint H(\theta) \bullet dl = n(\theta) i \quad . \tag{2}$$

The divergence theorem is applied to the volume integral on the right equality in Equation (1), which transforms the divergence of *B* over a volume to the integral of *B* over the surface of the volume, which says that the total flux crossing the surface sums to zero. This is expressed as

$$\int_{Surface} B \bullet dA = \int_{Surface} \mu_o H(\theta) L_{stack} r_{gap} d\theta = 0 \quad , \tag{3}$$

where

r_{gap} is the radius of the gap,
L_{stack} is the axial dimension of the rotor.

This technique is applied to a simple example shown in Figure 2.

The line integral of Equation (2) follows the contour abcd in the counterclockwise direction. Evaluation of the line integral in the stator or rotor is negligible because the value of μ, the magnetic permeability, is very large. Evaluation of the line integral in the gap where the value of μ is μ_o provides the primary contribution. Every line integral passes through H_{ref}, which is a constant whose value will be determined so that the total flux through the gap is zero. The direction of H_{ref} is arbitrarily chosen to be radial inward. The actual flux, which is proportional to $H(\theta)$, is radial inward and outward. The number of wires with current, *i*, encircled by the contour is expressed by $n(\theta)$. Wires with current into (minus) and out (plus) of the page are represented by the symbols "x" and "•," respectively. Contour integral evaluation is

$$H_{ref} g + H(\theta)\, g = n(\theta)\, i \quad , \tag{4}$$

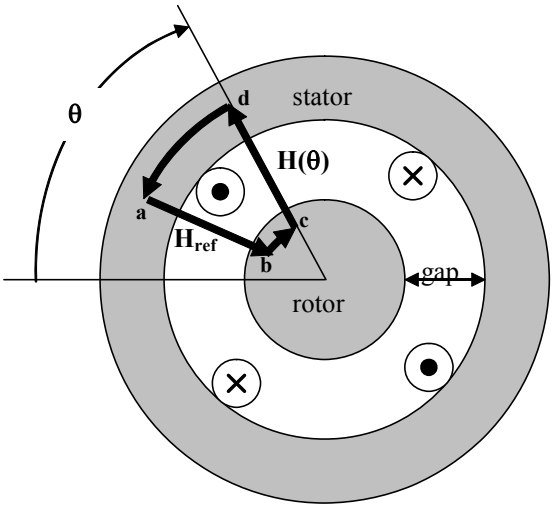


Figure 2. Calculation of the winding function for an idealized motor with a uniform gap.

where g is the gap between the rotor and stator.

This leads to

$$H(\theta) = \frac{n(\theta) i}{g} - H_{ref} \quad . \tag{5}$$

From Equation (3) it follows that

$$\int_{Surface} B \bullet dA = \mu_o r_{gap} L_{stack} \int_0^{2\pi} H(\theta) d\theta = 0 \quad . \tag{6}$$

Substituting the values from Equation (5) into Equation (6) leads to the value:

$$\int_0^{2\pi} \left[\frac{n(\theta) i}{g} - H_{ref} \right] d\theta = 0 \quad , \tag{7}$$

from which we get

$$H_{ref} = \frac{i}{g} \frac{1}{2\pi} \int_0^{2\pi} n(\theta) d\theta = \frac{i}{g} \overline{n(\theta)} \quad . \tag{8}$$

The bar over $n(\theta)$ denotes an average value. If we now substitute Equation (8) into Equation (5), we find that

$$H(\theta) = \frac{i}{g} \left[n(\theta) - \overline{n(\theta)} \right] = \frac{i}{g} N(\theta) \quad . \tag{9}$$

The term in brackets defines the winding function $N(\theta)$. From Equation (4), recall that $n(\theta)$ is the number of wires enclosed by the contour, counting wires into the page as minus and wires out of the page as plus. For the example shown in Figure 2, Figure 3(a) shows a plot of $n(\theta)$, the conductor count versus angle, and Figure 3(b) shows a plot of $N(\theta)$, the winding function.

The winding function indicates the regions in which flux would be produced by current in the conductors and the direction of the flux. None of the preceding discussion has mentioned the magnet pole pairs, which would be attached on the surface of the rotor to interact with the stator conductors. When p pole pairs are introduced, $N(\theta)$ determines the stator regions that link the magnets' flux. The motor's torque is determined by the flux linkages, which will be discussed shortly.

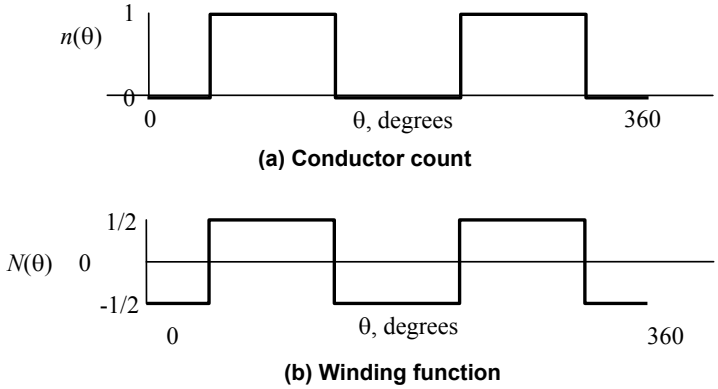


Figure 3. Relation between conductor count and winding function.

Winding factor

The winding function discussed in the previous section is related only to the number of slots and assumes that all of the conductors are placed at the midpoint of each slot to produce a square wave like the one shown in Figure 3(b). The winding factor, which is the subject of this section, is the ratio of actual flux links, ψ_{actual}, to the ideal flux links, ψ_{ideal}, across the gap. The flux links are proportional to the integral from 0 to 2π of the product of the winding function with the magnetic field. In this explanation the magnetic field is approximated by $B = B_{max}\cos(p\theta)$, where p is the number of magnet pole pairs. The actual and ideal winding functions are both expressed as Fourier series.

Recall that the form of the Fourier expansion is

$$N(\theta) = \sum_{n=1}^{\infty} a_n \cos(n\theta) + \sum_{n=1}^{\infty} b_n \sin(n\theta) \quad , \tag{10}$$

where

$$a_n = \frac{\int_0^{2\pi} N(\theta)\cos(n\theta)d\theta}{\pi} \text{ and}$$

$$b_n = \frac{\int_0^{2\pi} N(\theta)\sin(n\theta)d\theta}{\pi} \ .$$

Figure 4 shows the actual winding function, which is a square wave positioned symmetrically so that only the coefficients of the cosine terms survive. The expansion of the actual concentrated winding function is

$$N_{actual}(\theta) = \sum_{n=1,3,5..}^{\infty} a_n \cos(n\theta) \quad . \tag{11}$$

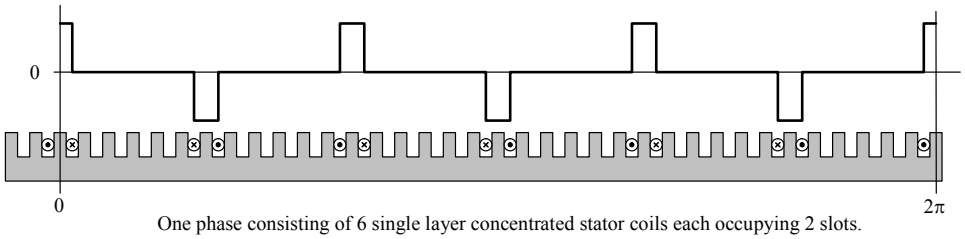


Figure 4. Winding function for the 36-slot, 30-pole concentrated winding being studied for possible use as a hybrid electric vehicle traction motor.

As an illustration, Fourier coefficients of the winding function for the concentrated winding in Figure 4 with $N(\theta) = \pm 1$ inside the coils and 0 elsewhere are shown in Table 1.

Table 1. Fourier coefficients of winding function for a stator with 36 slots

n	a_n	b_n	n	a_n	b_n	n	a_n	b_n
1	0	0	7	0	0	13	0	0
2	0	0	8	0	0	14	0	0
3	0.32954	0	9	0.30011	0	15	0.24597	0
4	0	0	10	0	0	16	0	0
5	0	0	11	0	0	17	0	0
6	0	0	12	0	0	18	0	0

The quantity, N_{spp}, which is the number of slots per pole per phase, is a useful design parameter. It provides the following useful relations for a three-phase winding with p equal to the number of magnet pole pairs and the $N_{slots/coil}$ equal to the number of slots per coil:

$$N_{coils/phase} = \frac{N_{spp}(2p)}{N_{slots/coil}} \quad ,$$

$$N_{slots} = N_{spp}\,3(2p) \quad ,$$

$$N_{slots/phase} = N_{spp}(2p) \quad ,$$

and

$$N_{slots/pole} = N_{spp}\,3 \quad .$$

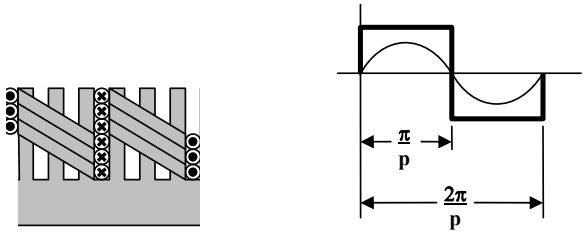
Because an equivalent distributed winding with $N_{spp} = 1$ produces maximum flux links, it is used to estimate the ideal flux links used in the denominator of the winding factor. The six concentrated winding coils, N_{conc}, shown in Figure 4, are reconfigured with no change in coil dimension over one pole pair in the form of a distributed winding ($N_{spp} = 1$) as shown in Figure 5(a). N_{spp} is the number of slots per pole

per phase. When the magnetic field is symmetrically positioned within the coils, this is the configuration that has the maximum flux linkages as shown in Figure 5(b).

Equation (12) gives the ideal number of flux links for one pole pair and Equation (13) the actual number of flux links for the concentrated winding.

$$\psi_{ideal} = L_{stack} \frac{N_{coils/phase}^{conc}}{2} 2 \int_0^{\pi/p} B_{\max} \sin(p\theta) r_{gap} d\theta = \left[r_{gap} L_{stack} B_{\max} \right] \frac{N_{coils/phase}^{conc}}{2} \frac{4}{p} \quad . \tag{12}$$

$$\psi_{actual} = L_{stack} \int_0^{2\pi} \sum_{n=1,3,5..}^{\infty} a_n \cos(n\theta) B_{\max} \cos(p\theta) r_{gap} d\theta = \left[r_{gap} L_{stack} B_{\max} \right] a_p \pi \quad . \tag{13}$$



(a) One pole pair. **(b) Distributed winding function and magnetic field for one pole pair.**

Figure 5. Redistribution of the coils from the concentrated winding shown in Figure 4 into an ideal distributed winding for a rotor with p pole pairs.

Noting that the Fourier coefficient, a_p, is a function of the number of slots, we find that the expression for the winding factor is

$$k_w(N_{slots}, p) = \frac{\psi_{actual}}{\psi_{ideal}} = \frac{a_p \pi}{2 N_{spp}} \quad . \tag{14}$$

The winding factor for the concentrated winding with 36 slots and 15 pole pairs is

$$k_w(36,15) = \frac{0.24597 x \pi}{2\frac{2}{5}} = 0.9659 \ ,$$

which indicates that this configuration, whose N_{spp} = 2/5, yields flux links close to the ideal value.

Concentrated winding (fluxmate) equivalent of a motor with distributed windings

The purpose of this section is to relate a distributed winding for which N_{spp} = 1 to a corresponding single layer concentrated winding and to quantify the amount by which the inductance of the concentrated winding is increased. N_{spp} = 2/5 for the corresponding concentrated winding being examined for use as an HEV traction motor. Another configuration that has the same winding factor has N_{spp} = 2/7. Equations will be used to illustrate how the concentrated winding may be used to design increased inductance into

an SPM motor. As $N_{spp} = 1$ for distributed windings, the quantity N_{spp} in the following equations will refer to the fractional value for the concentrated windings.

For the first step we start with a distributed winding with p magnetic pole pairs and $6p$ slots and determine the number of slots for the concentrated winding specified by its N_{spp}. The corresponding concentrated winding has $N_{slots}^{conc} = N_{spp}(6p)$ slots. For a distributed winding with $6p$ slots and 15 magnetic pole pairs, the corresponding concentrated winding with $N_{spp} = 2/5$ has 36 slots.

Next we ensure that the flux linking the coil for each phase is the same for the two configurations. For the distributed winding, the flux links in one phase are

$$\psi^{dist} = \int_0^{2\pi} \frac{N_{turns}^{dist}}{2} B_{\max} \left|\cos(p\theta)\right| L_{stack} r_{gap} d\theta \quad . \tag{15}$$

The magnet flux is symmetrically positioned in the winding function so that the product of their signs results in the absolute value of the cos term. This may be evaluated with the integral

$$\psi^{dist} = 4p \int_0^{\frac{2\pi}{p}\frac{1}{4}} \frac{N_{turns}^{dist}}{2} B_{\max} L_{stack} r_{gap} \cos(p\theta) \frac{d(p\theta)}{p} = 2N_{turns}^{dist} B_{\max} L_{stack} r_{gap} \quad . \tag{16}$$

For the concentrated winding, the flux links in one phase are

$$\psi^{conc} = \int_0^{2\pi} N_{turns}^{conc} \sum_{n=1,3..}^{\infty} a_n \cos(n\theta) B_{\max} \cos(p\theta) L_{stack} r_{gap} d\theta = N_{turns}^{conc} B_{\max} L_{stack} r_{gap} \pi a_p \quad . \tag{17}$$

When Equation (16) is equal to Equation (17), the ratio of turns for the concentrated winding to the distributed winding is

$$\frac{N_{turns}^{conc}}{N_{turns}^{dist}} = \frac{2}{\pi a_p} \quad . \tag{18}$$

Equation (14) relates the value of a_p to the value of the winding factor. Also in Equation (14) the number of coils/phase for the concentrated winding, which is a single layer winding with $N_{slots/coil}^{conc} = 2$, is $N_{coils/phase}^{conc} = N_{spp} p$. From these relations, Equation (18) may be expressed as

$$\frac{N_{turns}^{conc}}{N_{turns}^{dist}} = \frac{1}{N_{spp} k_w} \quad . \tag{19}$$

For our study example, $N_{spp} = 2/5$ and $k_w = 0.9659$ yielding a ratio of 2.588. This value is also obtained from Equation (18) by using the value of a_{15} from Table 1.

Next we discuss inductance andthe relation between the inductance of distributed windings and that of concentrated windings. Inductance is the proportionality constant between the current flowing in one set of coils and the flux that it produces, which may link the coil producing the flux (self-inductance) or another coil (mutual inductance). The mutual inductance between phases for distributed windings is 1/3 the self-inductance because only 1/3 of any pair of coils from different phases overlap; however, the mutual inductance between phases of concentrated windings is zero because the concentrated winding

coils have no overlap. This may be seen by inspection of Figure 4 and with the addition of the other phase coils. No rectangle in one phase intersects a rectangle in another phase.

We shall consider the two main types of inductance in a PM motor, self-inductance and slot-leakage inductance. Self-inductance is related to flux that crosses the gap and interacts with the magnet. Slot-leakage inductance links wires in each slot but does not contribute to torque production. Both inductances are additive, producing the reactive impedance that must be overcome in the electrical circuit. End turn leakage inductance makes a much smaller contribution to the total inductance and is not included in this discussion. The following equations show the relationship between self-inductance and leakage inductance for the distributed and concentrated windings.

Self-inductance

Self-inductance over one phase is

$$L_{self} = c \int_0^{2\pi} \left(N_{self}(\theta) \right)^2 d\theta^2 \quad , \tag{20}$$

where c = $\mu_o \; r_{gap} \; L_{stack}/g$ and g is the gap between the magnets and the stator teeth. For the distributed winding function the value in parentheses in Equation (20) contributes a constant value, $\left(\frac{N_{turns}^{dist}}{2} \right)^2$, over an angular distance, $2\pi/p$, a total of p times, which by inspection is

$$L_{self}^{dist} = c \left(\frac{N_{turns}^{dist}}{2} \right)^2 \left[\frac{2\pi}{p} \right] \text{rad per pole} \left[p \right] poles = c \left(N_{turns}^{dist} \right)^2 \frac{\pi}{2} \quad . \tag{21}$$

For a concentrated winding, the value in brackets for Equation (20) contributes a constant value, $\left(N_{self}^{conc} \right)^2$, over 1/3 of the stator so that

$$L_{self}^{conc} = c \left(N_{turns}^{conc} \right)^2 \left[\frac{\pi}{3} \right] \quad . \tag{22}$$

The ratio of the inductance of the concentrated winding to that of the distributed winding is

$$\frac{L_{self}^{conc}}{L_{self}^{dist}} = \frac{2}{3} \frac{1}{\left[N_{spp} k_w \right]^2} \quad . \tag{23}$$

For the concentrated winding of interest this ratio is 4.47.

Slot-leakage inductance

Slot-leakage inductance over one phase is

$$L_{slot_leakage} = \mu_o L_{stack} N_{spp} (2p) \left[N_{turns} \right]^2 \left[\frac{h_s^2}{3A_s} + \frac{d_2}{(b_o + w_s)/2} + \frac{d_1}{b_o} \right] \quad , \tag{24}$$

where the dimensions of the slot are shown in Figure 6. A_s is the area of the slot and r_s is the outer radius of the slot.

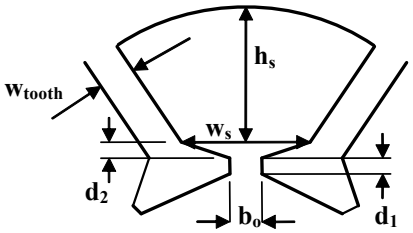


Figure 6. Definition of slot dimensions for inductance calculations.

The area of the slot is

$$A_s = \frac{\pi(r_s^2 - (r_s - h_s)^2)}{N_{spp} 3(2p)} - h_{tooth} w_{tooth} \quad . \tag{25}$$

Flux is carried by all teeth adjacent to a pole and is channeled in both directions in the back iron. The tooth width is chosen to be wide enough to prevent saturation. Its width is given by

$$w_{tooth} = \frac{2 w_{back_iron}}{3 N_{spp}} \quad , \tag{26}$$

where $3N_{spp}$ is the number of slots per magnet pole to carry the flux. The fact that the back iron handles half the flux is described by the equation

$$w_{back_iron} = \frac{\phi_g}{2 B_{\max} L_{stack}} \quad . \tag{27}$$

The final equation for the width of the tooth is

$$w_{tooth} = \frac{\phi_g}{3 N_{spp} B_{\max} L_{stack}} \quad , \tag{28}$$

which leads to the ratio for the width of a tooth in a concentrated winding to the width of a tooth in a distributed winding:

$$\frac{w_{tooth}^{conc}}{w_{tooth}^{dist}} = \frac{1}{N_{spp}} \quad . \tag{29}$$

Using Equation (29) with Equation (25) and a similar procedure for the slot's arc radius, we find that both the ratio of the slot area in a concentrated winding to the slot area in a distributed winding and the ratio of the slot arc width in a concentrated winding to the arc width in a distributed winding are the same:

$$\frac{A_s^{conc}}{A_s^{dist}} = \frac{1}{N_{spp}} = \frac{w_{slot}^{conc}}{w_{slot}^{dist}} \quad . \tag{30}$$

When these relations are substituted into Equation (24) for the slot leakage of the concentrated winding and for the distributed winding, the ratio of the two inductances is

$$\frac{L_{slot_leak}^{conc}}{L_{slot_leak}^{dist}} = \left[\frac{1}{k_w}\right]^2 \frac{\left[\frac{h_s^2}{3A_s^{dist}} + \frac{d_2 2}{(N_{spp}b_o + w_s^{dist})} + \frac{d_1}{N_{spp}b_o}\right]}{\left[\frac{h_s^2}{3A_s^{dist}} + \frac{d_2 2}{(b_o + w_s^{dist})} + \frac{d_1}{b_o}\right]} \quad . \tag{31}$$

The value of $1/(k_w)2$ is 1.07. The ratio of the terms in brackets shows that the $N_{spp}b_o$ term has the effect of reducing the effective slot width. Using the parameters $h_s = 25.4$ cm, $A_s^{dist} = 125$ mm, $w_s^{dist} =$ 4 mm, $d_2 = 3$ mm, $d_1 = 3$ mm, and $b_o = 2$ mm, which represent the slot of the 55-kW motor with concentrated windings being studied, we find that the three terms in the upper right bracket of Equation (31) are 1.72 + 1.25 + 3.75, and the three terms in the lower right bracket are 1.72 + 1.0 + 1.5. The ratio is 1.59, caused by the impact that N_{spp} has on the effective slot opening, b_o. The ratio of the bracketed terms cannot be ignored. The contribution of the slot opening to the slot-leakage inductance is large. For the example under study, the ratio of concentrated to distributed slot-leakage inductances is

$$\frac{L_{slot_leak}^{conc}}{L_{slot_leak}^{dist}} = 1.07 \times 1.59 = 1.70 \quad . \tag{32}$$

The total inductance is the sum of the self-inductance and slot-leakage inductance. From Equations (23) and (31), the total inductance is

$$L_{total} = \frac{2}{3}\left[\frac{1}{N_{spp}k_w}\right]^2 L_{self}^{dist} + \frac{1}{k_w^2} L_{slot_leak}^{dist} \quad , \tag{33}$$

which for the case of interest is $L_{total} = 4.47L_{self}^{dist} + 1.70L_{slot_leak}^{dist}$, clearly showing the increase in inductance from the concentrated windings—mainly in the self-inductance, but also in the slot-leakage inductance.

Finally, we examine the larger slot area of the concentrated winding, which has a fill factor of 0.7 compared to 0.5 for a distributed winding, to see whether it can accommodate the larger number of turns. First recognize that the useable area of the slot for the distributed winding is $A_{useable}^{dist} = 0.5A_s^{dist}$ and that the useable area of the slot for the concentrated winding is $A_{useable}^{conc} = 0.7A_s^{conc} = 0.7\frac{A_s^{dist}}{N_{spp}}$. The ratio of useable areas is

$$\frac{A_{useable}^{conc}}{A_{useable}^{dist}} = \frac{1.4}{N_{spp}} \quad , \tag{34}$$

which for the case of interest is 3.5, meaning that the slot in the concentrated winding can handle 3.5 times the number of turns in the slot of the distributed winding. This will work because the number of distributed turns from Equation (19) must be multiplied by 2.588 to have the same flux links. In fact, only a small improvement in fill factor from 0.5 to 0.5176 will allow the desired 2.588 useable area ratio.

Analysis and Design of Motors with Fractional-Slot Concentrated Windings

Design of an FSCW HEV traction drive motor

A summary of the FreedomCAR targets shown in Table 2 was incorporated by UWM and ORNL to scale the design of a 6-kW FSCW motor built and tested in FY 2005[6] to 55-kW for use as an HEV traction drive motor.[8] The design is a 36 slot-30 pole configuration built from six repeating units, each having six slots and five poles, which can be wound separately and then assembled into the final stator for ease of manufacturing (Figure 7). At the same time, the fractional-slot concentrated winding develops sufficient inductance to allow the required CPSR of 5 from base speed of 2000 rpm to top speed of 10,000 rpm.

Table 2. FreedomCAR traction motor targets

Requirement	Target specification
Minimum top speed [rpm]	10,000
Peak power at 20% of max speed for 18 s and nominal voltage [kW]	55
Continuous power at 20 to 100% of maximum speed and nominal voltage [kW]	30
Battery operating voltage [V_{dc}]	*Nominal:* 325 *Range:* 200 to 450
Maximum current at motor [A_{rms}]	400
Characteristic current [A_{rms}]	< Max current
Efficiency at 10 to 100% of max speed rated power	>93%
Efficiency at 10 to 100% of max speed for 20% of rated torque	>93%
Torque pulsations—not to exceed at any speed [% of peak torque]	<5
Peak power to weight ratio for active materials [kW/Kg]	>2.75
Peak power to volume ratio for active materials [kW/liter]	>12.5

UWM has developed its own software design methodology[7] while ORNL has used the SPEED software from Motorsoft. The design parameters have been developed using the UWM software and verified using SPEED software. The motor as sketched by the SPEED software in Figure 8 consists of six of the segments shown in Figure 7. There are some differences, including the following.

1. SPEED has 30 turns per phase of AWG #19 wire with each turn consisting of 47 conductors and a fill factor of 70%, whereas UWM fills each slot with copper at the same fill factor.
2. SPEED uses ARNON 7 for the laminations, while UWM uses a general lamination model.[9]
3. The present version of SPEED does not consider skin effects nor does it allow segmentation in the circumferential direction, while UWM segments each magnet circumferentially into five pieces.[8]

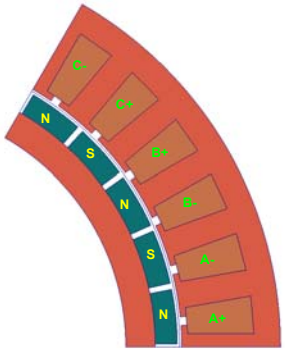


Figure 7. Cross-section of the basic repeating unit of the 55-kW (peak), 36-slot 30-pole (2/5 s/p/ph) *SPM2* machine design.

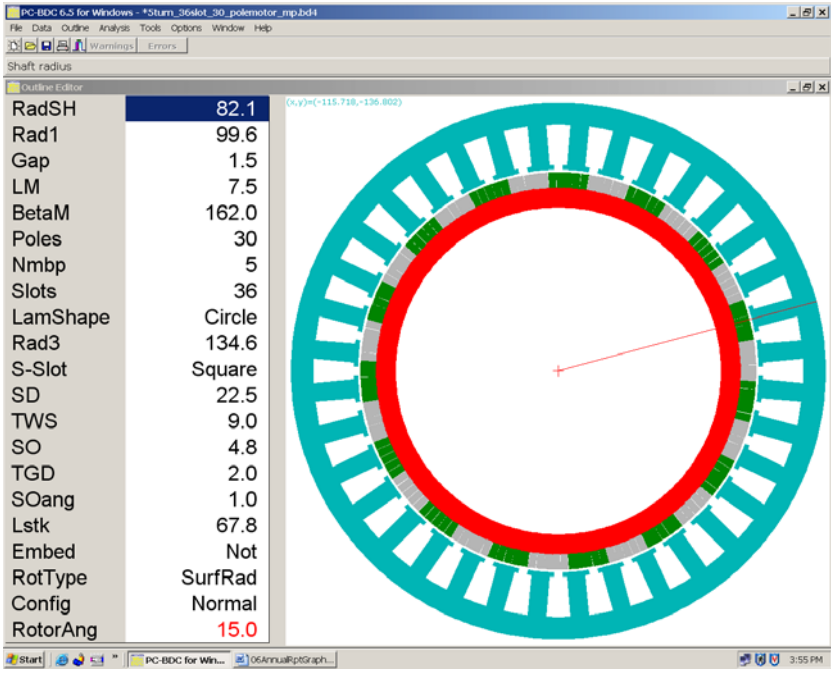


Figure 8. SPEED rendition of the 36-slot, 30-pole *SPM2* with concentrated windings.

A comparison of the results of the two programs is shown in Table. 3.

Table 3. Comparison of UWM and ORNL design parameters for the proposed 55 kW (PEAK) SPM

Design parameter	UWM	ORNL	Remarks
Inductance, [μh]			
Self	**25.5**	**29**	
Slot	41	40	
End	–	4	
Total	66.5	73	
Phase resistance, [mohms]	4.9	4.15	
Fundamental magnet flux linkages [mWebers]	17.5	18.42	
Characteristic current [A_{rms}]	264	252	
Line-to-line back-emf [V_{rms}]	120	124	@ 2000 rpm
Rated current [A_{rms}]	230	181	
Current density [A_{rms}/mm^2]	6.7	5.9	
Base speed efficiency [%]	93	97	@ 2000 rpm
Top speed efficiency [%]	92	87.7	@ 10,000 rpm
Core loss [W]	1676	206	@ 2000 rpm
Armature loss [W]	780	309	@ 2000 rpm
Magnet loss [W]	1288	882	@10000 rpm
Mass [kg]			
Iron	10.3	11.1	
Copper	8.8	4.6	
Magnet	2.2	2.1	
Total	17.3	17.8	

The most significant difference between the two design calculations is the losses. The two methods are explained in the next section.

Core loss calculations

Core loss data from steel suppliers is almost always sinusoidal data and may be characterized by the Steinmetz equation with separate terms for hysteresis and eddy current losses:

$$P = C_h f B_{pk}^n + C_e f^2 B_{pk}^2 \quad , \tag{35}$$

where

P is the power per unit mass, W/kg,
B_{pk} is the peak flux density, T,
f is the frequency, Hz,
C_h is the hysteresis loss coefficient,
C_e is the eddy current loss coefficient.

The exponent, n, is often assumed to be 1.6 to 1.8 but varies some with B_{pk}, and SPEED allows a linear variation in the form $n = a + bB_{pk}$, in which both a and b should be positive.

The flux density in motor laminations may be far from sinusoidal. SPEED uses a modified Steinmetz equation

$$P = C_h f B_{pk}^{a+bB_{pk}} + C_{el} \left| \frac{dB}{dt} \right|^2 \quad . \tag{36}$$

The hysteresis loss component is unchanged, but the eddy-current component is taken to be proportional to the mean squared value of dB/dt over one cycle of the fundamental frequency. SPEED programs apply Equation (36) in the respective sections of the magnetic circuits after calculating the relevant flux-density waveforms.

The eddy current loss coefficient, C_{el}, in the modified form can be derived from the sine wave coefficient, C_e, if we assume that Equation (36) is true when $B = B_{pk} \sin(2\pi f t)$. If so, then $\left| \frac{dB}{dt} \right|^2 = 4(\pi f B_{pk})^2 \cos^2(2\pi f t)$ whose mean value is $\left| \frac{dB}{dt} \right|^2 = 2(\pi f B_{pk})^2$. For the sine wave flux density, Equations (35) and (36) give the same result if $C_{el} = \frac{C_e}{2\pi^2}$. The loss coefficients in the SPEED program have names related to the quantities in Equation (36) as shown in Table 4. The core losses versus speed for ARNON 7 laminated steel are shown in Table 5.

Table 4. Speed software loss equation coefficient definitions

Name in design program	Name in Equation (36)
CfC_h	C_h
Cfa	a
Cfb	b
CfC_e	C_{el}

Table 5. Core losses for ARNON 7 laminations in the 55-kW FSCW-SPM motor

RPM	Loss, W
2000	206
4000	577
6000	1113
8000	1814
10,000	2681

The UWM core loss method follows that of Mi, Slemon, and Bonert.[9] UWM uses a revised approximate model for tooth eddy-current loss. For an m-phase PM motor with *q* slots per pole per phase, there are mq slots per pole. The time, Δt, required for the magnet to pass one tooth is

$$\Delta t = T \frac{1}{m2q} \quad , \tag{37}$$

where

T is the time for a pole pair to pass a slot pitch, which is $2\pi/\omega_{elect}$,
m is the number of phases,
2q is the number of slots per pole pair,
ω_{elect} is the electrical rotational speed of the rotor, rad/s.

Under linear trapezoidal assumptions of the waveforms, the time rate of tooth flux change is

$$\frac{dB}{dt} = \frac{B_{tooth}}{\Delta t} \quad . \tag{38}$$

The change of tooth flux density occurs four times per time period, *T*. The average eddy current loss density in the teeth can now be expressed as

$$p_{eddy_current} = 2k_e \overline{\left(\frac{dB_{tooth}}{dt}\right)^2} = 2k_e \left(\frac{B_{tooth}}{\Delta t}\right)^2 \left(\frac{4\Delta t}{T}\right) = 16k_e mq \left(\frac{B_{tooth}}{T}\right)^2 \quad . \tag{39}$$

Multiplying by the number of phases and expressing *T* in terms of the electrical frequency we obtain the expression,

$$p_{eddy_current} = 12k_e q \left(\frac{\omega_{elect} B_{tooth}}{\pi}\right)^2 \quad . \tag{40}$$

From Equation (39) it can be seen that the eddy current loss is proportional to the number of slots per pole.

The equation for the eddy current losses in the teeth used by UWM[7] is

$$p_{et} = \frac{4m}{\pi^2} q k_q k_l k_e \left(\omega_e B_{tooth}\right)^2 \quad , \tag{41}$$

where

k_q is the motor geometry correction factor,
k_l is a correction factor to account for the contribution of the circumferential component,[9]
k_e is the eddy current constant that depends on the lamination material.

The value of flux density in the tooth is estimated by the equation

$$B_{th} = \frac{w_t + w_s}{w_t} B_{gap}^{pk} \quad , \tag{42}$$

where B_{gap}^{pk} is the peak air gap magnetic flux density. Its value is estimated by

$$B_{gap}^{pk} = \frac{V_{ag}^{rms} p}{\sqrt{2} R_s L_{stack} k_{w1} \omega_e} \quad , \tag{43}$$

where

w_t is the tooth width,
w_s is the slot width,
V_{ag}^{rms} is the rms air gap voltage supply,
k_{w1} is the fundamental winding factor,
ω_e is the electrical frequency in rad/s.

The corresponding equation for the eddy current losses in the yoke is

$$p_{ey} = \frac{1}{\alpha} \frac{8}{\pi^2} k_e k_r \left(\omega_e B_y\right)^2 \quad , \tag{44}$$

where α is the ratio of the magnet span to the pole pitch, B_y is the peak magnetic flux in the stator yoke, and

$$k_r = 1 + \frac{8 k_q d_y^2}{27 \alpha q \lambda_2^2} \quad , \tag{45}$$

where d_y is the stator yoke thickness and λ_2 is the projected slot pitch at the middle of the yoke.

Tooth hysteresis loss and yoke hysteresis loss can be expressed as a function of the maximum flux density in each area. In the teeth the hysteresis loss density is

$$p_{ht} = k_h \omega_{elect} B_{th}^{\beta} \quad . \tag{46}$$

In the yoke the hysteresis loss density is

$$p_y = k_h \omega_{elect} B_{yk}^{\beta} \quad . \tag{47}$$

These are the forms used by UWM.

Magnet loss calculations

The magnet loss algorithm in the SPEED software does not account for the effect of skin depth on magnet loss. A finite-element transient solver has been added to the SPEED software package for its next release. Output from the new package has been provided for ORNL's 55-kW FSCW motor by SPEED's technical support at the University of Glasgow in Scotland. That output is shown in Figures 9 through 13.

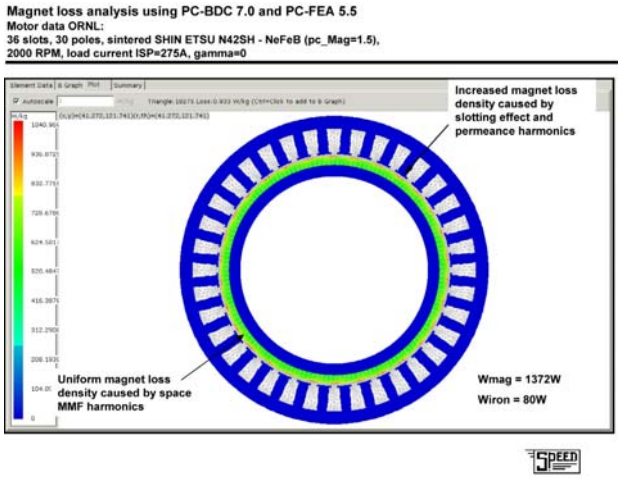


Figure 9. Magnetic loss at 2,000 rpm. (The motor is drawing 275 A ISP under load. Losses are the result of space harmonics, slotting, and permeance. At 2000 rpm the electrical frequency is 500 Hz.)

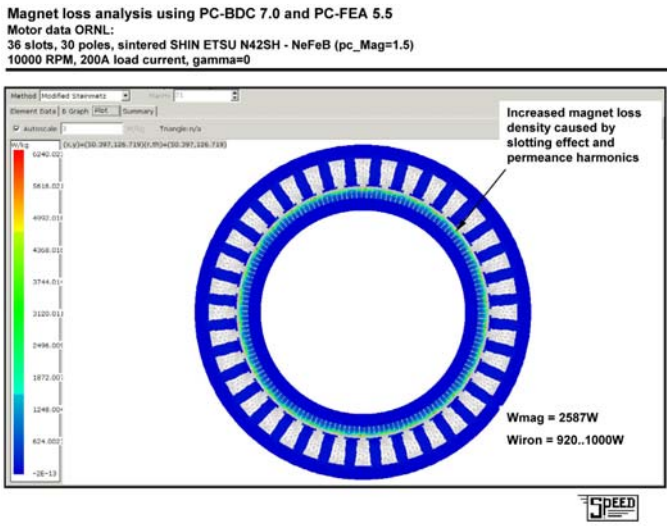


Figure 10. Magnet loss at 10,000 rpm.

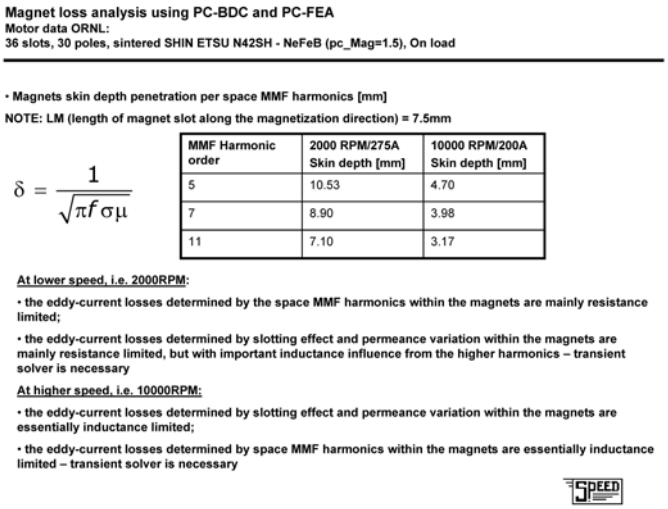


Figure 11. Effect of speed on skin depth penetration.

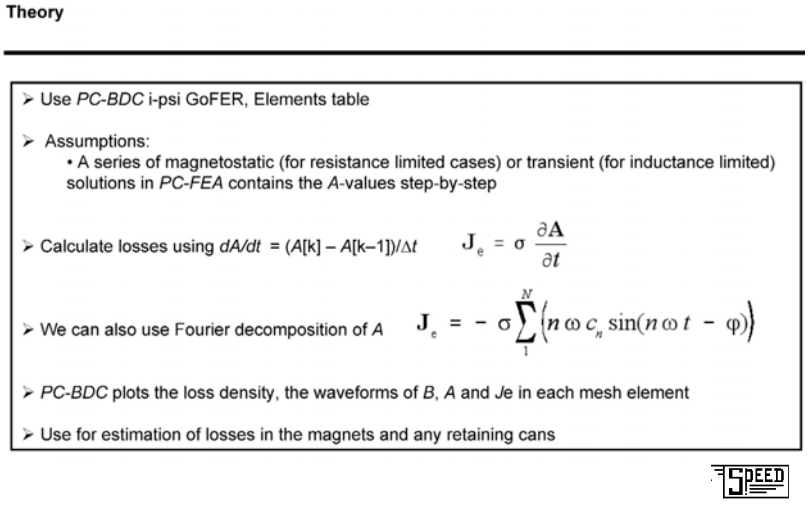


Figure 12. Approach taken by SPEED to determine skin depth penetration.

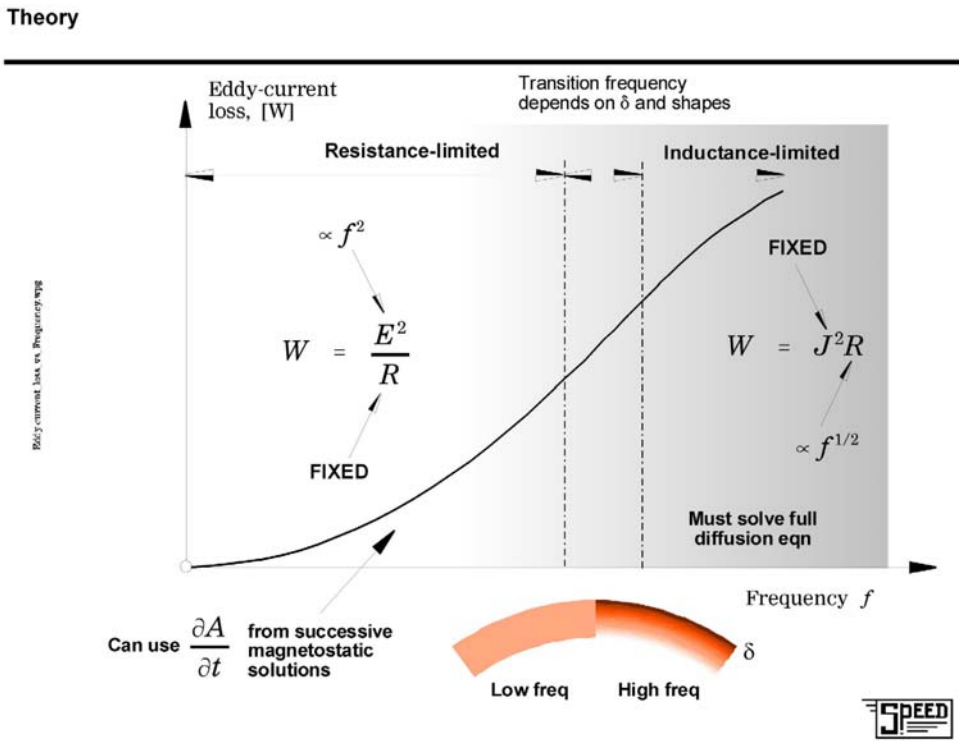


Figure 13. The effect of frequency on magnetic losses.

While the speed has increased fivefold, the loss has increased by a factor of about 2. This is because of the skin effect, shown in Figure 11.

UWM has almost the same procedure as shown in Figures 12 and 13 except for the addition of skin depth penetration. Figure 13 shows that skin effect lowers the magnet loss at high frequencies. This explains why the UWM magnet loss at 10,000 rpm in Table 6 is higher that the value obtained by SPEED.

The procedure used by UWM[10] characterizes the stator winding as a current sheet in the rotor reference. The time dependent expression for current density in the sheet in terms of the angle, θ_r, in the rotor is

$$J_s(\theta_r,t) = \frac{q}{2}\sum_n J_n \cos\left(np_s\theta_r + (np_s - mp_r)\Omega t\right) \text{ for } n = qk+m \ ,$$

$$J_s(\theta_r,t) = \frac{q}{2}\sum_n J_n \cos\left(np_s\theta_r + (np_s + m * p_r)\Omega t\right) \text{ for } n = qk - m \ ,$$

$$J_s(\theta_r,t) = 0 \text{ for n} \neq \text{qk} \pm \text{m} \ , \qquad (48)$$

where

q is the number of phases,
m = -1 when N_{spp}=2/5 and +1 when N_{spp}=2/7,
k = 0, 1, 2, 3, 4, 5…….,
p_s is the number of stator pole pairs,

p_r is the number of rotor pole pairs,
n is the summation index, which is not even for a cosine expansion like the one in Equation (9),
Ω is the rotational speed of the rotor, radians/second.

The value of J_n is

$$J_n = \frac{2N_s I_{pk}}{\pi R_s} k_{wm} \quad , \tag{49}$$

where

N_s is the number of turns in series per phase,
I_{pk} is the peak phase current,
R_s is the radius of the current sheet,
k_{wn} is the n^{th} winding factor.

The expression for the n^{th} winding factor is

$$k_{wn} = \frac{\left| 1 - \exp^{j\frac{2\pi n}{Nsphase}} \right|}{2} \quad , \tag{50}$$

where N_{sphase} is the number of slots per phase.

Table 6 presents the magnet losses calculated by the MatLab program listed in Table 7. Table 8 is a presentation of output from the SPEED calculation for the 36-slot, 30-pole motor delivering 30 kW at 2000 rpm. Table 9 is a presentation of output from the SPEED calculation for the same motor delivering 55 kW at 10,000 rpm.

Summary of Design Analysis

In summary, the 55-kW design has been compared for two design methodologies and all differences have been resolved leading to a viable design for an HEV traction drive motor. The 55-kW motor was designed with 30 poles according to the developed design process. With this knowledge, there is mounting evidence that FSCW motors with low pole and slot count can be feasible in some cases and are worthy of further investigation.

Table 6. Magnet losses for a 36-slot, 30-pole 55-kw FSCW-SPM motor

Angular speed, rpm	Loss from Atallah equations[10] used by UWM, W	Loss calculated by Popescu at SPEED Consortium scaled by current ratio, W
2000	256	898
1018	1018	
2291	2291	
4073	4073	
6364	6364	1693

Table 7. MatLab program to calculate magnet losses

```
%Calculating Magnet Losses in case of SPM machines equipped with concentrated windings
clear all
close all
clc
m=-1; %m=1 in case of 2/7 S/P/Ph  %m=-1 in case of 2/5 S/P/Ph
q=3;  %Number of phases
Ps=3; %Number of stator pole pairs
Pr=15;      %Number of rotor pole pairs
Mu_0=4*pi*10^(-7);
Rho_mg=1.5*10^(-6);    %Resistivity of the magnet material sintered magnets, Ω-m
%Rho_mg=20*10^(-6);    %Resistivity of the magnet material bonded magnets, Ω-m
Alpha_p=0.95; %Ratio of magnet span to pole pitch
N_segments=1; %Number of magnet segments/pole
Alpha=2*pi*Alpha_p/(2*Pr*N_segments);
% Rs=0.1031;  %Stator outer radius
% Rr=0.0993;  %Rotor outer radius
% Rm=0.1025;  %Magnet outer radius
Rs=0.1346;  %Stator outer radius
Rr=0.0921;  %Rotor outer radius
Rm=0.0996;  %Magnet outer radius
n=1;   %Space harmonic order
Ns=30;  %Number of series turns per phase
Irms=180;
Im=Irms*sqrt(2);  %Peak phase current
Kwn=abs(1-1*exp(sqrt(-1)*150*(n/5)*pi/180))/2;
Jn=(2*Ns*Im/(1*pi*Rs))*Kwn;
speed=2*pi*10000/60; %Rotor speeed in rad/sec
leff=0.0678; % Machine active length [m]
if n*Ps==1
    Fn=log(Rm/Rr);
else
    Fn=((Rm/Rr)^(-2*n*Ps+2)-1)/(-2*n*Ps+2);
end
Pcn=((q^2*Mu_0^2*Alpha/(8*Rho_mg))*(Jn^2/(n^2*Ps^2))*(n*Ps-m*Pr)^2*speed^2*...
    ((Rm/Rs)^(2*n*Ps)*((Rs^2*Rm^2)/(2*n*Ps+2))*(1-(Rr/Rm)^(2*n*Ps+2))...
    +((Rr/Rs)^(2*n*Ps))*Rs^2*Rr^2*Fn+((Rr/Rs)^(2*n*Ps))*Rs^2*(Rm^2-Rr^2)))...
    /(1-((Rr/Rs)^(2*n*Ps)))^2;
if n*Ps==2
    Gn=log(Rm/Rr);
else
    Gn=((Rm/Rr)^(-1*n*Ps+2)-1)/(-1*n*Ps+2);
end
Pan=(-q^2*Mu_0^2/(Alpha*Rho_mg))*(Jn^2/(n^4*Ps^4))*(n*Ps+m*Pr)^2*speed^2*...
    (((Rm/Rs)^(n*Ps))*(Rs*Rm^2/(n*Ps+2))*(1-((Rr/Rm)^(n*Ps+2)))...
    +((Rr/Rs)^(n*Ps))*Rs*Rr^2*Gn)^2 ...
    *(sin(n*Ps*Alpha/2))^2/((Rm^2-Rr^2)*(1-(Rr/Rs)^(2*n*Ps))^2);
P=(Pcn+Pan)*leff
P_magnet=P*N_segments*2*Pr
```

Table 8. SPEED design sheets for FSCW-SPM motor delivering 30 kW at 2000 rpm

```
PC-BDC 6.5 for Windows (6.5.2.8) 9/15/2006 3:58:41 PM
c:\program files\speed\magnet dbm\5turn_36slot_30_polemotor_mp.bd4
UT-Battelle LLC
PC-BDC main title
PC-BDC sub-title

1 Dimensions:-------------------------------------------------------------

RotType    SurfRad         Embed          Not         Poles          30
Stator..
StatorOD   269.200 mm      LamShape    Circle         Slots          36
SYoke       11.000 mm      ASD         22.500 mm      SP           1.200
Rad3       134.600 mm      Rad2       123.600 mm      S-Slot      Square
TWS          9.000 mm      SD          22.500 mm      SO           4.800 mm
TGD          2.000 mm      SOang        1.000 mDeg    Stf          0.970
Rotor..
MOH          0.000 mm      Nmbp            5          Skew         0.000
RotorOD    199.200 mm      Rad1        99.600 mm      Gap          1.500 mm
LM           7.500 mm      BetaM      162.000 eDeg    pupa         0.900
RYoke       10.000 mm                                 RadSH       82.100 mm
DHub       184.200 mm      wNeck        0.386 mm
MEdge        7.500 mm      LM_min       7.500 mm
wMag         3.755 mm
Lstk        67.800 mm      Lrotor      67.800 mm      Lstator     76.800 mm

2 Magnet Data:------------------------------------------------------------

Magnet   SHIN-ETSU N42SH-nd-fe-Br Magnet
Br           1.000 T       Hc         955.000 kA/m    MuRec        1.050
CBr         -0.100 %/DegC  CHc         -0.540 %/DegC  DMag      7600.000 kg/m3
BrT          1.004 T       HcT        975.628 kA/m
Nuisance     0.000 mm      BrTnu        1.004 T       MuRecnu      1.050

3 Control Data:-----------------------------------------------------------

RPM       2000.000 rpm     Vs         292.500 V       Drive         Sine
ISP        255.500 A       gamma        0.000 deg     Sw_Ctl      ISP_HB
HBA_act    ISP/300         HB%          0.333         HBtype    Constant
FixfChop        No         fChop        0.000 kHz     fChopAct   598.000 kHz
EMFCalc        BLV         dq0          false
Vq           0.000 V       Rq           0.000 ohm     Vd           0.600 V
t_q          0.000 us                                 Freq1      500.000 Hz
ISP_Act    255.500 A       Tol_Act     ISP/20         ISLA_Act     1/128

4 Winding Data:-----------------------------------------------------------

Connex         Wye
WdgType     Custom
Offset            8        CPP          0.200
Tph          30.000        PPATHS           1         SPP          0.400
Layers        1.000        CSidesPh        12         Z          180.000
MLT         187.393 mm      LgthOEnd    84.286 mm      Ext          0.000 mm
EndFill       0.500         LaxPack     87.399 mm      Liner        0.200 mm
WireSpec  AWGTable          Gauge           19
NSH              47         WireDia      0.912 mm      InsThick     0.000 mm
SFg           0.695         SFn          1.093         MaxSFn       1.093
Aslot       220.890 mm^2    ASlotLL    208.410 mm^2    ACond       30.693 mm^2
```

Table 8. SPEED design sheets for FSCW-SPM motor delivering 30 kW at 2000 rpm (continued)

GPAslot	230.490	mm^2	ATstick	0.253	mm^2	TopStick	false	
TwjWid	2.000	mm	TwjLeg	3.500	mm	TwjThk	0.000	mm
PhsWid	2.000	mm	PhsLeg	3.500	mm	PhsThk	0.000	mm
ATwj	0.000	mm^2	APhs	0.000	mm^2			
XET	1.000		ETCalc	BDC 6.0		Rext	0.000	ohm
Nse	36.896		X_R	1.000		Ax1	15.000	mDeg
T_Wdg	100.000	DegC	Rph0	4.150E-03	ohm	R_LL	8.301E-03	ohm
T_c	20.000	DegC	Rph	3.158E-03	ohm/ph	TFRho	1.000	
Inductances...								
Lph	0.073	mH	Mph	0.000	mH	XL	1.000	
Lg	0.029	mH	LSlot	0.040	mH	Lendt	4.449E-03	mH
Mg	0.000	mH	MSlot	0.000	mH	LDiff	0.024	mH
Lsigma	0.068	mH	Msigma	2.639E-03	mH	XLdiff	1.000	
Lgg	0.133	mH	Mgg	0.000	mH	PCSlot	1.551	
LL_d	0.147	mH	LL_q	0.147	mH	L_LL	0.147	mH
Lg_0	5.279E-03	mH	Lg_2	2.059E-05	mH	Laa_d	0.073	mH
Ld	0.073	mH	Lq	0.073	mH	Laa_q	0.073	mH
Xd	0.230	ohm/ph	Xq	0.230	ohm/ph	Xsigma	0.205	
ohm/ph								
XCd	1.000		XCq	1.000		Lext	0.000	mH
Gd	0.177		Gq	0.176		XLendt	1.000	
kw1	0.966		Xm0	0.141	ohm/ph			
ks1	1.000		kp1	1.000		kd1	1.000	
ksg	0.182		fz	1.133		PSSlot	S-Closed	
Saliency	Auto		CalcLdLq	Auto		muPlug	1.000	
i1_Ang	2.023	A	i2_Ang	-222.394	A	i3_Ang	220.371	A

5 Magnetic Circuit Design:----------

T_Mag	100.000	DegC	T_r	16.000	DegC	XBrT	1.000	
BrT	1.004	T	BgOC	0.898	T	Hca	760.912	kA/m
BgAvOC	0.676	T	PhiG	0.964	mWb	BgA/BgOC	0.753	
Bg1OC	0.964	T	PhiM1	0.874	mWb	Bg1/BgOC	1.073	
BmOC	0.828	T	Bm/BrT	0.825		XBtpk	1.000	
HmOC	-133.421	kA/m	Hm/HcT	-0.137		PC	4.938	
Bst	1.474	T	Bsy	0.666	T	Bry	0.711	T
XTw	0.000		XSYoke	0.000		XRYoke	0.000	
kT	0.570	Nm/A	kE	0.641	Vs/Rad	krpmNL	4.679	krpm
kSat	1.000		XSatn	1.000		CalcSatn	Fixed	
SatnTol	0.000							
Xks	0.000		ks	0.000		XTTarc	1.000	
EffWst	9.000	mm	EffLst	20.410	mm	ukCL	0.000	
XBgap	1.000		X_EMF	1.000		k_rpf	1.000	
Btpk_OC	1.508	T	Btpk_Ld	1.541	T	Btpk_LdS	1.541	T
Bypk_OC	0.661	T	Bypk_Ld	0.961	T	Bypk_LdS	0.961	T
eLLpk	134.285	V	eTmax	2.277	V	Bslot	4.879E-03	T
IBk	2853.421	A	Bk	0.000	T	Hk	-760.912	kA/m
ILR	46315.717	A	BmLR	-15.255	T	HmLR	-1.23E+04	kA/m
IC180	67578.987	A	BmC180	-22.718	T	HmC180	-1.80E+04	kA/m
BHmag	110.467	kJ/m3	Carter	1.027		Xrm	0.500	
Amhp	612.481	mm^2	Aghp	641.236	mm^2	Rghp	1.912E+06	At/Wb
Pm0	0.108	uWb/At	Xrl	1.000		prl	0.256	
apEnd	1.000		Pend	0.000		Lme	7.500	mm
u_LKG	0.000		f_Lkg	0.950		if_Lkg	1.053	
Fringing	ON		XFringe	1.000		XBetaM	1.000	
SlotMod	No		XSlotMod	1.000				

Table 8. SPEED design sheets for FSCW-SPM motor delivering 30 kW at 2000 rpm (continued)

```
7 Dynamic design (time-stepping simulation):---------------------------------

OpMode     Motoring          Vs          292.500 V        RPM        2000.000 rpm
Tshaft      143.249 Nm       Pshaft    30001.993 W        Eff          97.384 %
WCu         309.103 W        WFe         256.306 W        WWF           0.000 W
WCan          0.000 W        WMagnet     240.576 W        WShaft        0.000 W
WTotal      805.984 W        TempRise      0.000 DegC     Jrms          5.885
A/mm^2
IWpk        255.948 A        IWav        162.624 A        IWrms       180.637 A
ILpk        255.948 A        ILav        162.623 A        ILrms       180.637 A
IQchpk      255.951 A        IQchav       58.267 A        IQchrm      108.823 A
IQcmpk      255.951 A        IQcmav       58.267 A        IQcmrm      108.823 A
IDchpk      255.927 A        IDchav       23.050 A        IDchrm       66.884 A
IDcmpk      255.927 A        IDcmav       23.050 A        IDcmrm       66.884 A
IDC_W       105.652 A        WConv        82.979 W        EffDCSh      97.122 %
IDC_P       105.610 A        WSwitch       0.000 W        Pelec     30807.978 W
Tgap        145.621 Nm       Tei         145.622 Nm       Trel          -0.001 Nm
Tloop       145.617 Nm       WFeCalc          OC          CalcVwfm       None
V1rms         0.000 V        I1rms       180.635 A        phi_1        -0.739 deg
phV1         90.000 deg      phI1         90.739 deg      phEq1        90.247 deg
V1d           0.000 V        I1d          -2.329 A
V1q           0.000 V        I1q         180.651 A

8 Steady-State Thermal Model:-----------------------------------------------

TempCalc      DegCW          FixTMag       IterX          Ambient      20.000 DegC
DegCW         0.000 degC/W   HTCcyl        0.000 W/m2/C   HTCend        0.000
W/m2/C
TempRise      0.000 DegC     T_c          20.000 DegC     T_r          16.000 DegC
T_f          20.000 DegC     T_y          20.000 DegC     HeatFlux      3.980
kW/m^2
SlotPeri     57.597 mm       Liner         0.200 mm       ct_Liner      0.200 W/mC
SSArea     3905.110 mm^2     C_motor      17.751 kJ/C     ThRSlot   7.113E-03 C/W
FSArea    2.025E+05 mm^2     ThermTC       0.000 min      R_fa          0.000 C/W

9 Miscellaneous:------------------------------------------------------------

Weights...
wt_Cu         4.602 kg       wt_Fe        11.154 kg       wt_Mag        2.095 kg
wt_Tot       17.851 kg       wt_Shaft     13.310 kg       wt_Frame      2.880 kg
wt_FeS        8.313 kg       wt_FeR        2.841 kg       wt_RSS       18.496 kg
Inertia components...
RotJ          0.086 kg-m2    RotJSS        0.088 kg-m2    RotJSh        0.045 kg-m2
RotJFe        0.022 kg-m2    RotJMag       0.019 kg-m2    LShaft       80.000 mm
sigma         4.997 psi
Wf0           0.000 W        RPM0       1000.000 rpm      NWFT          1.000
Fringing         ON          XFringe       1.000          NHx             21
CanStyle       None
Ecc           0.000          UMPavg    -6.11E-15 kg       UMPmax    -4.31E-15 kg
TRFrms       21.667 kg       TRFavg       17.038 kg       TRFmax       37.738 kg
CForce       29.935 kg                                    LamThk        0.500 mm
NLams          132           pcLam         3.000 %        RFei      1.000E+06

10 Core loss analysis:------------------------------------------------------
-

WFeCalc          OC          LossFE         Mech          XFe           1.000
```

Table 8. SPEED design sheets for FSCW-SPM motor delivering 30 kW at 2000 rpm (continued)

```
DFekgS    7656.829 kg/m^3  St.Steel Arnon 7  3.25% Si
DFekgR    7656.829 kg/m^3  Ro.Steel Arnon 7  3.25% Si
DFekgSh   7857.007 kg/m^3  Sh.Steel Low Carbon Steel 26g
wt_Teeth     3.820 kg      wt_Yoke      4.493 kg      wt_Troot     0.897 kg
Specific core losses...
cFe_E50      0.192 W/kg    cFe_H50      3.176 W/kg    cFe_50       3.368 W/kg
cFe_E_F     19.182 W/kg    cFe_H_F     31.758 W/kg    cFe_F       50.941 W/kg
cFe_T_E     17.299 W/kg    cFe_T_H     29.856 W/kg    cFe_T       47.155 W/kg
cFe_Y_E      3.405 W/kg    cFe_Y_H      4.134 W/kg    cFe_Y        7.539 W/kg
Core loss analysis...
WFe_T_E     81.600 W       WFe_T_H    140.832 W       WFe_T      222.432 W
WFe_Y_E     15.299 W       WFe_Y_H     18.574 W       WFe_Y       33.873 W


End of Design sheet-------------------------------------------------------
-
```

Table 9. SPEED design sheets for FSCW-SPM motor delivering 55 kW at 10,000 rpm

```
PC-BDC 6.5 for Windows (6.5.2.8) 9/29/2006 10:41:46 AM
c:\program files\speed\magnet dbm\5turn_36slot_30_polemotor_mp.bd4
UT-Battelle LLC
PC-BDC main title
PC-BDC sub-title

1 Dimensions:-------------------------------------------------------------
RotType    SurfRad         Embed          Not         Poles          30
Stator..
StatorOD   269.200 mm      LamShape    Circle         Slots          36
SYoke       11.000 mm      ASD         22.500 mm      SP           1.200
Rad3       134.600 mm      Rad2       123.600 mm      S-Slot      Square
TWS          9.000 mm      SD          22.500 mm      SO           4.800 mm
TGD          2.000 mm      SOang        1.000 mDeg    Stf          0.970
Rotor..
MOH          0.000 mm      Nmbp            5          Skew         0.000
RotorOD    199.200 mm      Rad1        99.600 mm      Gap          1.500 mm
LM           7.500 mm      BetaM      162.000 eDeg    pupa         0.900
RYoke       10.000 mm                                 RadSH       82.100 mm
DHub       184.200 mm      wNeck        0.386 mm
MEdge        7.500 mm      LM_min       7.500 mm
wMag         3.755 mm
Lstk        67.800 mm      Lrotor      67.800 mm      Lstator     76.800 mm

2 Magnet Data:------------------------------------------------------------
Magnet   SHIN-ETSU N42SH-nd-fe-Br Magnet
Br           1.000 T       Hc         955.000 kA/m    MuRec        1.050
CBr         -0.100 %/DegC  CHc         -0.540 %/DegC  DMag      7600.000 kg/m3
BrT          0.920 T       HcT        542.440 kA/m
Nuisance     0.000 mm      BrTnu        0.920 T       MuRecnu      1.050

3 Control Data:-----------------------------------------------------------

RPM      10000.000 rpm     Vs         292.500 V       Drive         Sine
ISP        325.000 A       gamma       77.500 deg     Sw_Ctl      ISP_HB
HBA_act    ISP/300         HB%          0.333         HBtype    Constant
FixfChop        No         fChop        0.000 kHz     fChopAct     0.000 kHz
EMFCalc        BLV         dq0          false
```

Table 9. SPEED design sheets for FSCW-SPM motor delivering 55 kW at 10,000 rpm (continued)

Vq	0.000	V	Rq	0.000	ohm	Vd	0.600	V	
t_q	0.000	us				Freq1	2500.000	Hz	
ISP_Act	325.000	A	Tol_Act	ISP/20		ISLA_Act	1/128		
4 Winding Data:----------									
Connex	Wye								
WdgType	Custom								
Offset	8		CPP	0.200					
Tph	30.000		PPATHS	1		SPP	0.400		
Layers	1.000		CSidesPh	12		Z	180.000		
MLT	187.393	mm	LgthOEnd	84.286	mm	Ext	0.000	mm	
EndFill	0.500		LaxPack	87.399	mm	Liner	0.200	mm	
WireSpec	AWGTable		Gauge	19					
NSH	47		WireDia	0.912	mm	InsThick	0.000	mm	
SFg	0.695		SFn	1.093		MaxSFn	1.093		
Aslot	220.890	mm^2	ASlotLL	208.410	mm^2	ACond	30.693	mm^2	
GPAslot	230.490	mm^2	ATstick	0.253	mm^2	TopStick	false		
TwjWid	2.000	mm	TwjLeg	3.500	mm	TwjThk	0.000	mm	
PhsWid	2.000	mm	PhsLeg	3.500	mm	PhsThk	0.000	mm	
ATwj	0.000	mm^2	APhs	0.000	mm^2				
XET	1.000		ETCalc	BDC 6.0		Rext	0.000	ohm	
Nse	36.896		X_R	1.000		Ax1	15.000	mDeg	
T_Wdg	100.000	DegC	Rph0	4.150E-03	ohm	R_LL	8.301E-03	ohm	
T_c	100.000	DegC	Rph	4.150E-03	ohm/ph	TFRho	1.314		
Inductances...									
Lph	0.073	mH	Mph	0.000	mH	XL	1.000		
Lg	0.029	mH	LSlot	0.040	mH	Lendt	4.449E-03	mH	
Mg	0.000	mH	MSlot	0.000	mH	LDiff	0.024	mH	
Lsigma	0.068	mH	Msigma	2.639E-03	mH	XLdiff	1.000		
Lgg	0.133	mH	Mgg	0.000	mH	PCSlot	1.551		
LL_d	0.147	mH	LL_q	0.147	mH	L_LL	0.147	mH	
Lg_0	5.279E-03	mH	Lg_2	2.059E-05	mH	Laa_d	0.073	mH	
Ld	0.073	mH	Lq	0.073	mH	Laa_q	0.073	mH	
Xd	1.152	ohm/ph	Xq	1.151	ohm/ph	Xsigma	1.027	ohm/ph	
XCd	1.000		XCq	1.000		Lext	0.000	mH	
Gd	0.177		Gq	0.176		XLendt	1.000		
kw1	0.966		Xm0	0.704	ohm/ph				
ks1	1.000		kp1	1.000		kd1	1.000		
ksg	0.182		fz	1.133		PSSlot	S-Closed		
Saliency	Auto		CalcLdLq	Auto		muPlug	1.000		
i1_Ang	-174.622	A	i2_Ang	324.691	A	i3_Ang	-150.068	A	
5 Magnetic Circuit Design:----------									
T_Mag	100.000	DegC	T_r	100.000	DegC	XBrT	1.000		
BrT	0.920	T	BgOC	0.829	T	Hca	697.250	kA/m	
BgAvOC	0.624	T	PhiG	0.889	mWb	BgA/BgOC	0.753		
Bg1OC	0.890	T	PhiM1	0.807	mWb	Bg1/BgOC	1.073		
BmOC	0.764	T	Bm/BrT	0.831		XBtpk	1.000		
HmOC	-117.999	kA/m	Hm/HcT	-0.218		PC	5.154		
Bst	1.361	T	Bsy	0.615	T	Bry	0.656	T	
XTw	0.000		XSYoke	0.000		XRYoke	0.000		
kT	0.526	Nm/A	kE	0.592	Vs/Rad	krpmNL	5.069	krpm	
kSat	1.000		XSatn	1.000		CalcSatn	Fixed		
Xks	0.000		ks	0.000		XTTarc	1.000		
EffWst	9.000	mm	EffLst	20.410	mm	ukCL	0.000		
XBgap	1.000		X_EMF	1.000		k_rpf	1.000		
eLLpk	619.807	V	eTmax	10.508	V	Bslot	2.052E-03	T	

Table 9. SPEED design sheets for FSCW-SPM motor delivering 55 kW at 10,000 rpm (continued)

IBk	2614.688	A	Bk	0.000	T	Hk	-697.250	kA/m
ILR	35237.155	A	BmLR	-11.450	T	HmLR	-9375.134	kA/m
IC180	1.099E+05	A	BmC180	-37.658	T	HmC180	-2.92E+04	kA/m
BHmag	90.187	kJ/m3	Carter	1.027		Xrm	0.500	
Amhp	612.481	mm^2	Aghp	641.236	mm^2	Rghp	1.912E+06	At/Wb
Pm0	0.108	uWb/At	Xrl	1.000		prl	0.256	
apEnd	1.000		Pend	0.000		Lme	7.500	mm
u_LKG	0.000		f_Lkg	0.950		if_Lkg	1.053	
Fringing	ON		XFringe	1.000		XBetaM	1.000	

6 Sine-wave static design [phasor diagram]:----------

OpMode	Motoring		Vs	292.500	V	RPM	10000.000	rpm
Tshaft	28.683	Nm	Pshaft	30036.330	W	Eff	76.255	%
WCu	657.587	W	WFe	2681.160	W	WWF	0.000	W
WCan	0.000	W	WMagnet	6014.394	W			
WTotal	9353.141	W	TempRise	80.000	DegC	Jrms	7.487	A/mm^2
IWpk	325.000	A	IWav	206.900	A	IWrms	229.810	A
ILpk	325.000	A	ILav	206.900	A	ILrms	229.810	A
IDC_P	134.665	A	WFeCalc	OC		Pelec	39389.470	W
Eq1	259.780	V	Vph1	58.190	V	VLL1	100.788	V
Iq1	49.740	A	Id1	-224.362	A	gamma	77.500	deg
Vq1	1.589	V	Vd1	-58.168	V	delta	88.435	eDeg
Bg1Load	0.794	T	phi	10.935	eDeg	PF	0.982	
Bqad	0.000	T	Phida1	-0.087	mWb	Phiqa1	0.019	mWb
BmLoad	0.679	T	Bma	-0.085	T	Fda1	-585.342	At/gap
Tgap_PS	36.986	Nm	TEI_PS	37.017		Trel_PS	-0.031	Nm
Tgap	36.986	Nm	Tei	37.017	Nm	Trel	-0.031	Nm
Tloop	36.986	Nm						
Available voltage...								
Vs120	197.507	Vrms	Vs1	228.061	Vrms	Vs1Lin	179.119	Vrms

8 Steady-State Thermal Model:----------

TempCalc	DegCW		FixTMag	IterX		Ambient	20.000	DegC
DegCW	0.000	degC/W	HTCcyl	0.000	W/m2/C	HTCend	0.000	W/m2/C
TempRise	80.000	DegC	T_c	100.000	DegC	T_r	100.000	DegC
T_f	100.000	DegC	T_y	100.000	DegC	HeatFlux	0.000	kW/m^2
SlotPeri	57.597	mm	Liner	0.200	mm	ct_Liner	0.200	W/mC
SSArea	3905.110	mm^2	C_motor	17.751	kJ/C	ThRSlot	7.113E-03	C/W
FSArea	2.025E+05	mm^2						

9 Miscellaneous:----------

Weights...								
wt_Cu	4.602	kg	wt_Fe	11.154	kg	wt_Mag	2.095	kg
wt_Tot	17.851	kg	wt_Shaft	13.310	kg	wt_Frame	2.880	kg
wt_FeS	8.313	kg	wt_FeR	2.841	kg	wt_RSS	18.496	kg
Inertia components...								
RotJ	0.086	kg-m2	RotJSS	0.088	kg-m2	RotJSh	0.045	kg-m2
RotJFe	0.022	kg-m2	RotJMag	0.019	kg-m2	LShaft	80.000	mm
sigma	1.269	psi						
Wf0	0.000	W	RPM0	1000.000	rpm	NWFT	1.000	
Fringing	ON		XFringe	1.000		NHx	21	
CanStyle	None							
Ecc	0.000		UMPavg	-9.64E-16	kg	UMPmax	1.166E-14	kg
TRFrms	18.464	kg	TRFavg	14.519	kg	TRFmax	32.158	kg
CForce	748.387	kg				LamThk	0.500	mm
NLams	132		pcLam	3.000	%	RFei	1.000E+06	

Table 9. SPEED design sheets for FSCW-SPM motor delivering 55 kW at 10,000 rpm (continued)

```
10 Core loss analysis:-----------------------------------------------------------
WFeCalc         OC          LossFE         Mech          XFe          1.000
DFekgS    7656.829 kg/m^3  St.Steel Arnon 7  3.25% Si
DFekgR    7656.829 kg/m^3  Ro.Steel Arnon 7  3.25% Si
DFekgSh   7857.007 kg/m^3  Sh.Steel Low Carbon Steel 26g
wt_Teeth     3.820 kg      wt_Yoke      4.493 kg      wt_Troot     0.897 kg
Specific core losses...
cFe_E50      0.192 W/kg    cFe_H50      3.176 W/kg    cFe_50       3.368 W/kg
cFe_E_F    479.560 W/kg    cFe_H_F    158.791 W/kg    cFe_F      638.350 W/kg
cFe_T_E    368.532 W/kg    cFe_T_H    113.605 W/kg    cFe_T      482.137 W/kg
cFe_Y_E     72.541 W/kg    cFe_Y_H     18.015 W/kg    cFe_Y       90.556 W/kg
Core loss analysis...
WFe_T_E   1738.393 W       WFe_T_H    535.885 W       WFe_T     2274.278 W
WFe_Y_E    325.937 W       WFe_Y_H     80.945 W       WFe_Y      406.882 W

End of Design sheet--------------------------------------------------------------
```

Differences between the results of UWM and SPEED have been resolved. Such differences, which concern magnet losses, are because of the skin effect at higher speeds and are essentially inductance limited at higher speeds. These results emphasize the necessity of circumferentially segmenting the magnets and do not detract from the results of El Refaie, Jahns, and McKeever.[8]

Speed Control of Fractional-Slot Concentrated Winding PM Motors

A wide and theoretically infinite CPSR can be achieved with a PM synchronous motor if the winding inductance is sufficiently large.[11–13] Recent work at UWM[6] has shown that winding inductance of FSCW-SPM machines can easily be made sufficiently large to achieve satisfactory CPSR performance. Electric/hybrid electric vehicles require not only wide CPSR operation but also high efficiency. While CPSR performance can be resolved through proper machine design using FSCW technology, the efficiency of traction drives can depend on how they are controlled. Of particular concern is the efficiency of the traction drive when operating at fractional load conditions. In the present work the effect of control on the efficiency of the overall drive system and on the efficiency of the motor alone is considered.

Introduction

At ORNL investigators have analyzed the requirements of a speed control scheme whose objective is to minimize the motor current magnitude at all operating conditions.[13] Below base speed, in the constant torque operating mode, a traction drive with this type of control maximizes the motor shaft torque (Nm) produced per amp of motor current. Above base speed in the constant power operating mode, this type of control maximizes the power (watts) per amp of motor current. During FY 2006 the ORNL team developed a closed-loop speed control for an FSCW machine which implements motor current magnitude minimization. A 6-kW, 30-pole, FSCW motor developed by UWM, FSCW-1, is to be tested using the closed-loop speed control system developed by ORNL and drive/motor efficiency will be determined experimentally. Details of the speed control and test setup and procedures are described below.

In companion work, investigators at UWM have shown that minimum motor current control does not necessarily ensure maximum motor efficiency.[14] Their work showed that, for a specific FSCW design, a blend of maximum torque per amp and maximum torque per volt control may improve overall motor efficiency by reducing motor core losses.[14] In the light load condition cited in the reference, the motor current magnitude for maximum motor efficiency was approximately three times larger than for the maximum torque per amp control at the same condition. The overall reduction in core losses was sufficient to overcome a ninefold increase in motor copper losses. Because loss mechanisms in the inverter are approximately linear in motor current magnitude, it is not clear whether the maximum motor

efficiency condition will also result in maximum overall system efficiency. The testing of the 6-kW FSCW prototype may be extended to study whether the minimum motor current control or minimum motor loss control has the best overall system efficiency. Further details of the UW maximum motor efficiency control concept are contained in the section entitled "Enhanced Partial Load Efficiency Control Algorithm."

Parameters of the 6-kW prototype FSCW motor

The 6-kW FSCW prototype was laboratory tested by ORNL to determine the values of key machine parameters and to characterize speed dependent zero current losses. The winding resistance, inductance, and fundamental back-emf constant are

$$\begin{aligned} R &= 0.075\,\Omega \text{ per phase} \\ \mathrm{L} &= 1.2 \text{ mH per phase} \\ \mathrm{K_v} &= 0.05494 \text{ volts per rpm} \\ &\quad (49.45 \text{ V rms at } 900 \text{ rpm}) \end{aligned} \tag{51}$$

The zero current speed sensitive losses are shown in Figure 14. The figure shows data points taken from dynamometer measurements and a least squares fit to the experimental data. Dynamometer measurements were taken only up to 4000 rpm, which is the highest speed at which the 6-kW prototype has been driven, but the least squares fit predicts losses of 1867 W at 6000 rpm. The ORNL model of motor losses includes only speed sensitive effects.

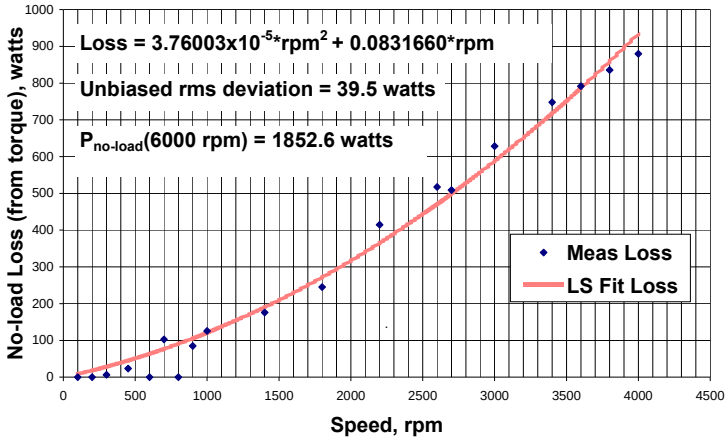


Figure 14. Zero current losses of the FSCW-1 prototype.

The prototype machine has 30 poles, a base speed of 900 rpm, and a rated output power of 6 kW. Let "subscript b," $_b$, denote "at base speed" and let n denote speed relative to base speed. Then the reactance of the winding inductance and magnitude of the back-emf at base speed and at any relative speed, n, are given by the following:

p = 30 poles,
N_b = 900 rpm,

N = speed in rpm,

$n = \dfrac{N}{N_b} =$ normalized speed,

Ω_b = 1413.7 electrical radians/second,

Xb = $\Omega_b L$ = 1.6965 Ohms reactance at base speed,

$X = nX_b$ reactance at relative speed, n, and

$E = nE_b$back—emf magnitude at relative speed, n.

Let "subscript capital R," $_R$, denote "rated" values so that rated useful average output power and rated rms motor current are

$$P_R = 6{,}000 \text{ W}$$

and

$$I_R = \frac{P_R}{3E_b} = 40.44 \text{ A rms} \tag{52}$$

The minimum dc supply voltage necessary to support rated power at base speed for this motor is given by

$$V_{dc-\min} = \pi\sqrt{\frac{\left(E_b + RI_R\right)^2 + \left(X_b I_R\right)^2}{2}} = 192 \text{ V} \quad . \tag{53}$$

Simplified Per-Phase Model

ORNL has used simplified per phase models with considerable success to study the performance of PM machine drives with either trapezoidal or sinusoidal back-emf wave shapes. The per-phase model represents only the fundamental frequency component response of the machine; consequently, some factors such as torque ripple cannot be studied while using this simplification. In general the fundamental frequency component dominates the motor current response and accurately preserves power. The main advantage of the simplified fundamental frequency model is that it eliminates the need for simulating the pulse-width modulation (PWM) switching actions. Although the effects of switching are not explicit in this model, it was recently extended to predict all of the inverter loss mechanisms.[13] The model is shown in Figure 15. This model was used extensively in the development of the closed-loop control schemes described below.

Closed-loop speed control system for FSCW PM traction motors

An objective in the development of the closed-loop speed control was to have low complexity and minimum use of sensors. The control structure selected is a proportional speed control (Figure 16). The speed command, labeled as "spdcom" in the figure, is processed through a simple gain, Ks in the figure, and the actual speed is subtracted to form a speed error. The speed error is multiplied by a gain, Ke in the figure, and the output is a desired rms motor current, Id. The desired current is processed through a saturation function whose upper limit is the specified rms current rating of the motor, I_R, and whose lower limit is zero because a negative rms value makes no physical sense. The output of the saturation function is the commanded rms current, I_{com}. This commanded current and the measured instantaneous shaft speed and position are all that are required in this controller to generate inverter commands. It is presumed that sinusoidal PWM control will be used to generate inverter switching commands;

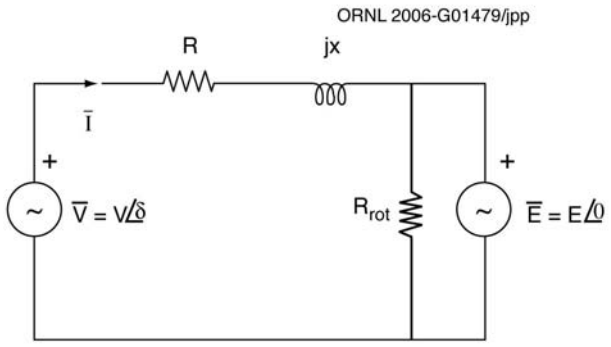


Figure 15. Fundamental frequency model of a permanent magnet motor driven by a pulse-width modulation controlled voltage source inverter.

consequently, the required control variables are the amplitude modulation index, denoted as M_a, and the inverter lead angle, δ . Values of M_a between 0 and 1 are referred to as the linear modulation region. In this region the rms value of the fundamental frequency component of the line-to-neutral voltage applied to the motor is given by

$$V_1 = \frac{M_a V_{dc}}{2\sqrt{2}} \text{ for } 0 \le M_a \le 1 \quad . \tag{54}$$

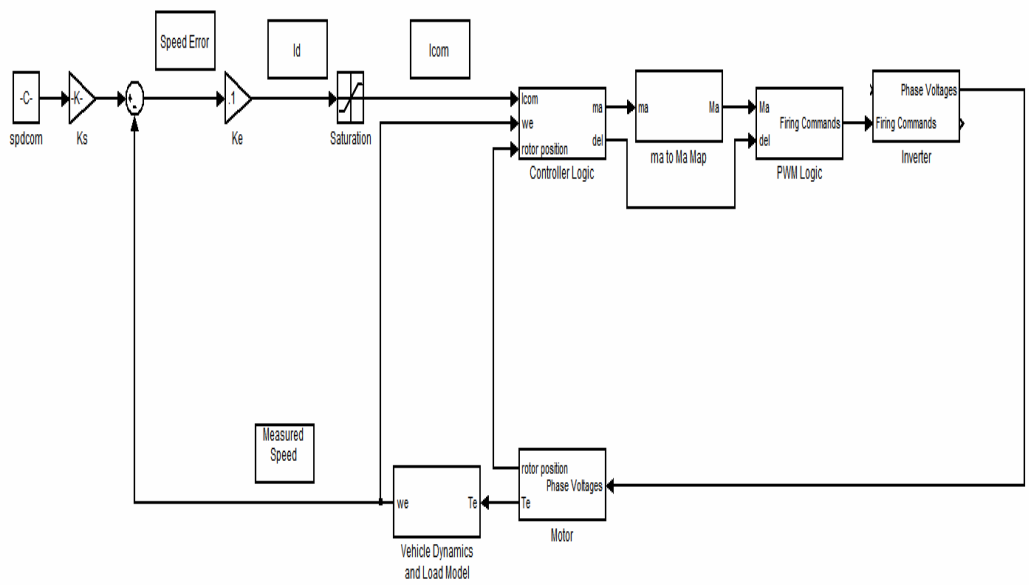


Figure 16. Closed-loop speed control block diagram.

Values of M_a greater than 1 are called the nonlinear modulation region, and in this region the high frequency switching of PWM degenerates towards six-step operation. The value of the rms fundamental

component increases with values of M_a greater than 1 but less than linearly, and in fact, once the PWM has degenerated to six-step switching, no further increase is observed in fundamental voltage. The fundamental voltage for a six-step waveform is the maximum possible value and is given by

$$V_{1-max} = \frac{\sqrt{2}V_{dc}}{\pi} \quad . \tag{55}$$

The controller logic block calculates a "pseudo amplitude modulation index," ma, which is the ratio of the rms fundamental voltage to the rms fundamental voltage at the end of linear modulation; that is

$$ma = \frac{V_1}{\frac{V_{dc}}{2\sqrt{2}}} = \frac{2\sqrt{2}V_1}{V_{dc}} \quad . \tag{56}$$

Values of ma lie between 0 and $\frac{4}{\pi}$. For a given ma, the value of the corresponding M_a is dependent on the frequency modulation index. The frequency modulation index is the ratio of the frequency of the triangular carrier wave of the PWM logic to fundamental frequency. Because the fundamental frequency of the motor increases with motor speed, the frequency modulation index is not constant unless the carrier frequency is varied in proportion to any change in motor speed. Generally the carrier frequency is not fixed but held constant at the highest switching frequency that can be tolerated by the inverter switches. A map of ma into M_a is shown in Figure 17 for a frequency modulation index of 39. The ma to M_a map in the control block diagram is implemented as a table lookup. If necessary, several maps can be stored for various values of frequency modulation index and interpolation can be used to account for changes in frequency modulation arising from changes in motor speed. Once amplitude modulation index, M_a, and lead angle, δ, are determined, the control function is complete, and the remaining components in the diagram would be the same as for any other PWM controlled drive and include the PWM switching logic to firing commands block, the inverter, the motor, and the vehicle and load dynamics blocks.

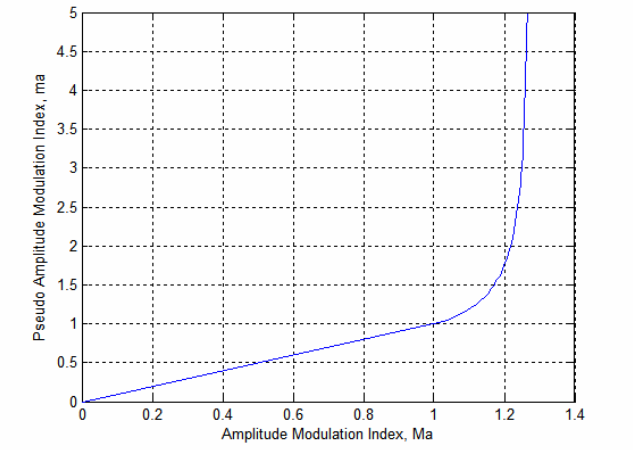


Figure 17. Amplitude modulation index versus pseudo amplitude modulation index for a frequency modulation index of 39.

Notice that current sensing is not used in this control. This does leave the performance of the controller vulnerable to variations in machine and drive parameters, especially the direct current supply voltage, the winding inductance, and the back-emf voltage constant. The direct current supply voltage is easily measured and consequently variation in V_{dc} is readily accounted for. Handling variations in the back-emf constant and winding inductance will be studied in the future. For the experiments at hand, the laboratory measurements of inductance and back-emf constant will suffice.

The core of the control strategy is contained in the Figure 16 block labeled "Controller Logic," which processes the current command, I_{com}; measured speed, we; and measured rotor position into the pseudo amplitude modulation index, ma, and the inverter lead angle, del, which appears as δ in the equations. Two variations of the controller logic block are discussed below.

Rated Current Limiting Controller Logic

The specified rms current rating of the motor, , is not to be exceeded at any operating condition. PM machines with low speed and core losses may be able to develop more power in the constant power zone than at base speed without exceeding the rms current rating. For such machines, the onboard direct current supply may have to provide power in excess of its rating if the motor is allowed to approach rated current during operation above base speed. The controller logic can be adapted to preclude exceeding rated power as discussed in the section entitled "Rated Current and Rated Power Limiting Controller Logic." In this section the constraint is to limit motor current to be no greater than the rated value.

Consider operating at relative speed, n, at pseudo amplitude modulation index, ma, and inverter lead angle,. The linear model of Figure 15 has rms current

$$I = \frac{\sqrt{V^2 - 2nVE_b \cos\delta + n^2 E_b^2}}{Z} \quad . \tag{57}$$

where

$$V = \frac{maV_{dc}}{2\sqrt{2}}$$

and

$$\mathrm{Z} = \sqrt{\mathrm{R}^2 + \left(nE_b\right)^2}$$

If the rms current is to be no greater than the rated value, I_R, then the inverter lead angle must be limited to a value no larger than

$$\delta_{\max} = \cos^{-1}\left[\frac{V^2 + n^2E_b^2 - Z^2I_R^2}{2nVE_b}\right] \quad . \tag{58}$$

Maximum power transfer between the inverter and the motor occurs when the inverter lead angle is equal to β where

$$\beta = \tan^{-1}\left(\frac{nX_b}{R}\right) \quad . \tag{59}$$

If the value of δ_{max} exceeds the value of β, then more power can be produced at a lower current than the rated current. It isn't reasonable to maintain rated current if more power can be developed at a lower current level. As the objective of the control is to meet the load condition at the minimum current, the best value of δ_{max} is

$$\delta_{\max} = \min\left(\beta, \cos^{-1}\left[\frac{V^2 + n^2E_b^2 - Z^2I_R^2}{2nVE_b}\right]\right) \quad . \tag{60}$$

Rated current and rated power limiting controller logic

Above base speed a PM motor may be capable of developing more power than the rated value while operating below rated current. If it is desired to restrict developed power to a value no greater than rated, then the inverter lead angle must be restricted to a lower value than required for current limitation. At relative speed *n* (greater than one), such that the pseudo amplitude modulation index is at the maximum value of $\frac{4}{\pi}$ and the applied rms motor voltage at fundamental frequency is likewise at its maximum,

$$V_1 = V_{1-\max} = \frac{\sqrt{2}V_{dc}}{\pi} \quad . \tag{61}$$

Then the total developed power per phase, including useful load power and speed sensitive losses, is given by

$$\frac{P}{3} = \frac{nE_bV_1}{Z}\cos(\beta - \delta) - \frac{n^2E_b^2}{Z}\cos\beta \quad , \tag{62}$$

where

$$\beta = \tan^{-1}\left(\frac{nX_b}{R}\right).$$

To limit this power to be no greater than rated power, P_R, requires that the inverter lead angle be limited to

$$\delta_{\max} = \beta - \cos^{-1}\left(\frac{ZP_R/3 + n^2E_b^2\cos\beta}{nV_1E_b}\right) \quad . \tag{63}$$

Under some conditions, particularly low supply voltage, it may be necessary to restrict δ to be no larger than the value of β. In such cases, the rated power cannot be developed and having δ = β allows maximum possible power.

To avoid having the motor enter regeneration mode during coasting operation, such as when the vehicle is in motion but the speed command is temporarily reduced to zero, the value of lead angle, δ, must be larger than

$$\delta_{\min} = \beta - \cos^{-1}\left(\frac{ZP_{rot}(n) + n^2E_b^2}{nV_1E_b}\right) \quad . \tag{64}$$

This limit should also be applied in the rated current magnitude limiting logic described in the previous section.

Simulation of the closed-loop speed control

The speed control system described in the preceding section was simulated using the fundamental frequency model developed in previous work.[13] This eliminates the need to include the PWM switching logic and greatly decreases the simulation time required to investigate vehicle response to speed commands. Even though the details of PWM switching are suppressed, the model is still able to capture the inverter losses described in Lawler.[13]

Only the step response to large speed commands is considered here. One simulation is shown for the current limiting control logic and the same simulation is shown for the power limiting control logic. The simulations are done for standing start conditions, zero initial vehicle speed, and a step command to one-half full speed (or 3000 rpm). It is assumed that the vehicle load is quadratic in speed with the full 6-kW rated power required for 6000 rpm. The equivalent rotational inertia was selected so that the vehicle driven by the 6-kW prototype weighed approximately 500 kg. Although this is a very heavy vehicle for the size of the motor, the use of a large rotational moment of inertia will decrease the speed of response to speed commands and make the comparison of the rated current limiting control and the rated power limiting control clearer.

Figure 18 displays the response of motor revolutions per minute, commanded and root-mean-square motor current, and developed power to the step command from 0 rpm to 3000 rpm for both the rated current limiting logicl [Figure 18(a), (c), and (e)] and the rated current and rated power limiting logic [Figure 18(b), (d), and (f)]. Notice that in steady state both cases have a steady state error because of the

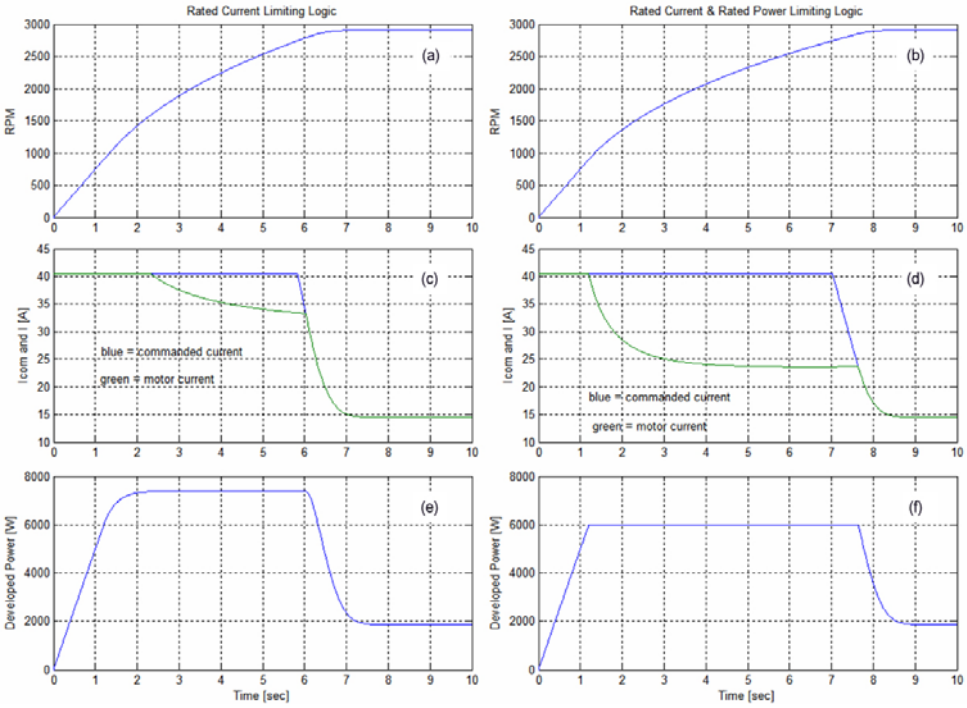


Figure 18. Rated current limiting control (left) and rated current plus rated power limiting control (right).

use of a simple proportional control. This error could be suppressed by increasing the proportional gain, Ks, of Figure 16 by adding an integrator to the controller or by the vehicle operator simply increasing the speed command slightly.

Notice that for the rated current limiting logic [Figure 18(a), (c), and (e)] the actual motor current begins decreasing at about 2.4 s despite the fact that the commanded current remains at the rated value. This is an instance where forcing the motor current to remain at rated power would result in less developed power. Figure 18(e) demonstrates that despite the reduction in current between 2.4 and 5.8 s, the developed power remains constant at 7400 W.

For the rated current and rated power limiting logic, the acceleration of the motor is slower than for the rated current limiting logic. This is because the developed power is limited to 6000 W, whereas, with only current limiting control, the developed power peaked at 7400 W. The current and power limited control took more than 8 s to reach steady state, whereas the current limiting control took less than 7 s. In the rated current and rated power limiting control, the motor current begins decreasing at 1.3 s and this decrease is associated with limiting the developed power to 6000 W.

The final steady state condition of the two cases is identical. The two methods will differ in response during transient conditions, but the steady states will be the same for any load condition that does not exceed rated power.

Conclusion

A simple proportional speed control has been developed for FSCW-SPM motors. Detailed simulation of the control shows that it can be effective in controlling motor speed while minimizing the motor current magnitude during operation above and below base speed. Laboratory testing of this method and the maximum motor efficiency control described below will allow comparisons to be made as to which method results in the greatest overall drive efficiency.

Iron Loss Model Development

As noted in the objectives, significant effort is being devoted to the development of closed-form analytical models of the iron losses in the FSCW-SPM machine. This section will summarize the nature of the analytical models and the progress that has been achieved towards verifying their accuracy.

Two FSCW-SPM machines designed to meet the FreedomCar advanced traction motor performance targets were proposed for use in analytical studies during FY 2006.[8] The first, named *SPM1*, exhibited a 900-V back-emf at top speed (10,000 rpm), which was above the 600-V target. *SPM1* has been used as the basis for comparisons between iron loss predictions of the closed-form analytical model and more detailed predictions from FEA. The second, named *SPM2*, exhibited a 600-V back-emf at top speed and had the best match between target values and performance estimates; consequently, it was chosen for the "Analysis and Design of Motors with Fractional-Slot Concentrated Windings" part of this study.

This 55-kW (peak) machine, *SPM1*, is used as an example for exploring the proposed analytical approach for calculating the iron losses. A cross-section of the basic repeating unit of this machine was shown in Figure 7, and some key machine dimensions and parameters are summarized in Table 10. More details about this machine can be found in El-Refaie, Jahns, and McKeever.[8]

The electromagnetic FEA programs MagNet2D (Infolytica) and JMag (JRI, Inc.) have been used to provide more accurate predictions of the magnetic fields and iron losses in the FSCW-SPM machine. In particular, the JMag program is capable of providing a point-by-point frequency spectrum calculation of the iron losses over the complete cross-section of the machine. Both hysteresis and eddy-current losses are calculated for *SPM1*, using iron loss characteristics provided by the lamination steel manufacturer. This approach provides the highest possible accuracy for predicting the iron losses in such a machine, but the calculations are very time-consuming.

Table 10. *SPM1* machine dimensions and parameters

Slots/pole/phase	2/5	Slots	36
Poles	30	Rotor outer radius [mm]	92.1
Stator OD [mm]	269	Active length [mm]	63.5
Total length [mm]	75.4	Magnet thickness [mm]	7.5
Air-gap thickness [mm]	1.5	Magnet remanent flux density [T]	1.0 @ 140°C
Copper mass [kg]	4.6	Magnet mass [kg]	2.0
Iron mass [kg]	9.7	Total mass [kg]	16.3

Open-Circuit Machine Model and Loss Predictions

SPM1, summarized in the preceding section, was analyzed to determine its magnetic flux density distribution and losses under open-circuit conditions. The major parts of the machine that contribute to the iron losses include

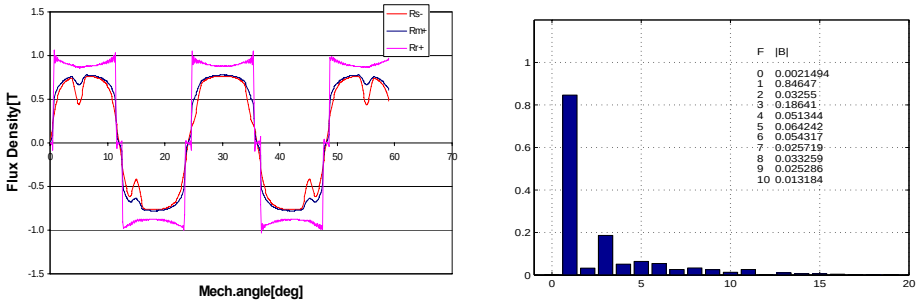
1. stator iron teeth and yoke,
2. rotor iron inner yoke, and
3. rotor magnets.

Under open-circuit conditions for which there is no stator excitation, the rotor losses are minimal[15] because the rotor back-iron that carries the magnet flux does not see much temporal change in flux density as the rotor moves.

Closed-form expressions for the magnetic flux density distribution under open-circuit conditions have been derived as a function of radius inside the air gap by solving the associated Laplace equations.[16,17] The accuracy of this technique depends on the assumption that magnetic saturation is not significant in the machine iron, an assumption that is typically quite reasonable for this type of machine. These equations determine the spatial harmonic components of the flux density distribution for a specified machine configuration. In particular, attention is paid to three different radii—the rotor iron outer radius (R_r+), the rotor magnet outer radius (R_m+), and stator inner radius ($R_s–$).

Figure 19(a) shows the predicted spatial distribution of the air-gap flux density at these three different radii inside the air gap for a slotted version of the *SPM1* machine. The harmonic spectrum for the flux density distribution at radius, $R_s–$, is shown in Figure 19(b). The effect of the slots is to introduce even harmonics into the distribution as well as lowering the amplitude of the fundamental component. More details about the analytical model including mathematical expressions have been included in a separate report.

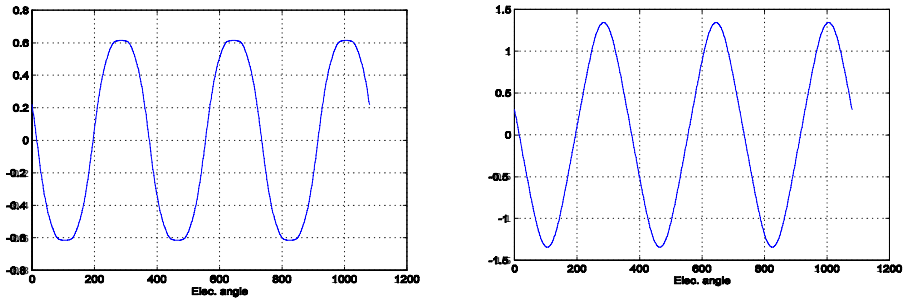
The tooth flux density can be approximately calculated by assuming that the flux density[18] is uniform across the width of each tooth, *TW*, for all of its length, h_g, excluding the tooth tip. The resulting flux density in the tooth can then be approximately determined by integrating the flux density waveform over the tooth pitch and dividing by the tooth width, *TW*. Figure 20(a) shows the resulting tooth flux density distribution predicted using the approach described above as the rotor is rotated. Higher-order harmonic components are attenuated in the spatial flux density distribution so that the resulting waveform in Figure 20(a) is dominated by its fundamental component. The peak value of the tooth flux density, B_{th}, as the rotor rotates through a complete pole pitch is approximately 0.62 T for the *SPM1* machine.



(a) Three different radii **(b) Harmonic spectrum at stator inner radius, R_s–**

Figure 19. Analytical predictions of the spatial air-gap flux density distribution for a slotted version of the *SPM1* machine for a rotor angular position of 5 mechanical degrees.

The same type of simplifying assumption made about the uniformity of the flux density across the tooth width can be extended to the stator yoke, for which it will be assumed that the flux density is the same everywhere in the cross-sectional area of the stator yoke behind each stator slot. Figure 20(b) shows the predicted yoke flux density distribution waveform as the rotor is rotated. As in the case of the tooth flux density waveform, the amplitudes of the harmonic components are significantly attenuated. The peak amplitude of the *SPM1* yoke flux density B_{ykn} as the rotor rotates through a complete pole pitch is determined to be approximately 1.32 T.



(a) Stator tooth **(b) Stator yoke**

Figure 20. Predicted flux density waveform in different parts of the stator based on the assumption of uniform tooth flux density.

Figure 21 provides a direct comparison of the predicted spatial flux density distributions at radius, R_s–, for the closed-form analytical model and FEA. The high-quality agreement between the two waveforms and their dominant frequency components indicates that the closed-form analytical approach can do an excellent job of predicting the air-gap flux density distributions for this type of SPM machine.

The stator iron core loss can be predicted using the stator tooth and yoke flux density waveforms that have been calculated using closed-form analysis based on the uniform flux density principle as described above. The analytical model for determining the stator core losses is based on summing the loss contributions of each of the dominant harmonic components in the frequency spectra for the tooth and yoke flux densities.

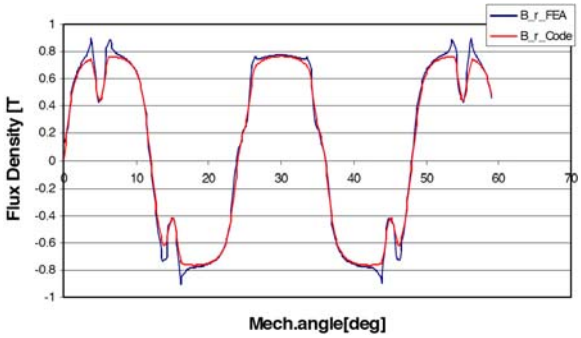


Figure 21. Comparison of predicted air gap magnetic flux density distribution at radius R_s– using closed-form (B_r_Code) and finite-element (B_r_FEA) analysis.

The familiar Steinmetz equation[9] for calculating the hysteresis loss associated with each of the frequency components in the flux density waveform is given by

$$P_{ht} = k_h B_{th}^{\beta} \omega_S \ [\mathrm{W/m^3}] \ . \tag{65}$$

The corresponding eddy current loss equation is given by

$$P_{et} = k_e B_{th}^{2} \omega_S^{2} \ [\mathrm{W/m^3}] \ . \tag{66}$$

Typical values have been adopted for the coefficients and exponents that appear in the above loss equations for grades of silicon iron laminations commonly used in small and medium induction motors. They are $k_h = 48$, $\beta = 2$, and $k_e = 0.055$.

Figure 22 provides a comparison of the predicted total iron losses in different parts of the machine using the closed-form analytical model and the more accurate point-by-point FEA technique described previously. There are several observations that can be made from this figure.

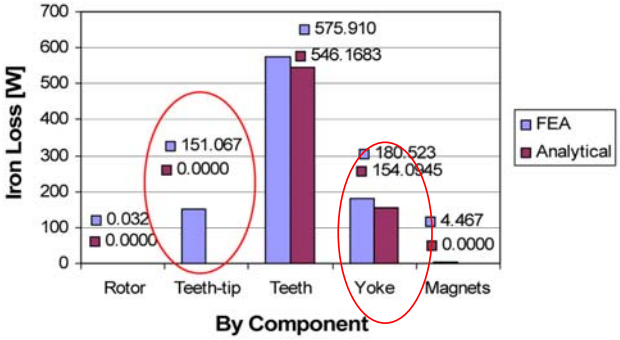


Figure 22. Comparison of predicted iron losses in different parts of the *SPM1* machine at 2000 rpm in an open-circuit condition using closed-form analysis and point-by-point finite-element analysis technique.

On the positive side, the agreement between the iron loss predictions, including both hysteresis and eddy current losses, for the closed-form analysis and point-by-point FEA is quite good, with the closed-form predictions approximately 5% and 14% below the FEA predictions for the teeth and yoke portions of the machine, respectively.

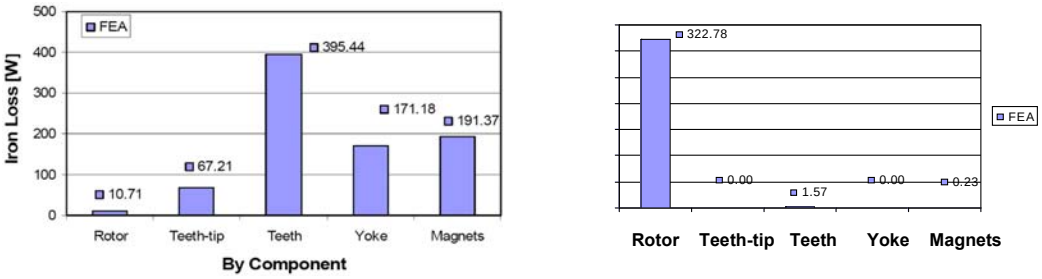
Figure 22 also highlights the fact that a technique for predicting the iron losses in the stator tooth tips along the inner stator bore has not yet been developed for the closed-form analysis, explaining why this bar is absent from the figure. The tooth tips are exposed to a richer harmonic mix of spatial flux density components than the rest of the teeth or yoke. These harmonics explain why the FEA predictions for the tooth-tip iron losses are nearly as high as for the yoke in the *SPM1* machine. As a result of these additional losses, which are not accounted for using the closed-form analysis, the total error between the predicted iron losses using the two techniques is approximately 23%. **This clearly identifies an area where further work is needed to improve the closed-form analytical model.**

Finally, the FEA-predicted iron loss results in Figure 22 confirm that the rotor magnet and iron yoke losses are very low in the *SPM1* machine for open-circuit conditions.

Armature Reaction Loss Predictions

The next major step in developing the iron loss model for the FSCW machine is to predict the iron losses associated with magnetic flux density components induced by the presence of current in the stator coils. This type of loss is called armature reaction loss. Progress has been made towards predicting these armature reaction iron losses using the point-by-point FEA technique.

Figure 23(a) shows the FEA-predicted iron losses in the *SPM1* machine, broken down by the major sections of the machine, when it is rotating at 2000 rpm with alternating current stator currents of 200 A.



(a) Machine section breakdown **(b) Harmonic content in teeth**

Figure 23. Finite-element-analysis-predicted iron eddy current losses at 2000 rpm with a peak armature current of 200 A.

The magnets were physically present for this analysis, but they were assumed to be completely demagnetized for this analytical exercise to focus attention exclusively on the armature reaction effects. For this analysis, it has been assumed that each magnet pole piece is broken into five identical pieces along the circumferential direction. This was done on the basis of previous work,[19] which showed that the magnet losses can be reduced by more than 80% when this kind of segmented magnet structure is adopted.

Among all of the laminated steel components except for the magnets the predicted iron losses are highest in the stator teeth and lowest in the rotor yoke [Figure 23(a)], following trends similar to those observed in the preceding section for the open-circuit conditions. The major difference between the previous open-circuit and the armature reaction case studied here is that the eddy current losses in the magnets become a significant loss component in the machine when substantial stator currents are flowing.

These magnet losses would have been considerably higher if the magnet poles had not been broken into multiple pieces.

Figure 23(b) presents a different perspective on the FEA-predicted eddy current losses in the teeth caused by the stator currents, broken down in this part of the figure by harmonic component. It is clear from this breakdown that iron losses for the armature reaction operating condition are attributable almost completely to the fundamental component. Additional results not included here show that this is true for the stator yoke and tooth-tips as well. This is good news because it is likely to simplify the task of developing a closed-form analytical model that can predict these iron losses contributed by the stator currents with reasonable accuracy. Efforts to develop this feature of the iron loss prediction method using closed-form analysis are presently under way.

Enhanced Partial Load Efficiency Control Algorithm

High-performance torque control in SPM machines can be achieved using current-regulated vector control. According to this technique, the amplitudes of the instantaneous currents in the three stator phases are controlled so that their combined effect can be represented on a cross-section of the machine as a vector that has an amplitude and angle. A simple representation of this concept that illustrates a current vector, $\vec{i}_s$, for a two-phase alternating current machine is provided in Figure 24. Newcomers to this concept are referred elsewhere for more details.[20]

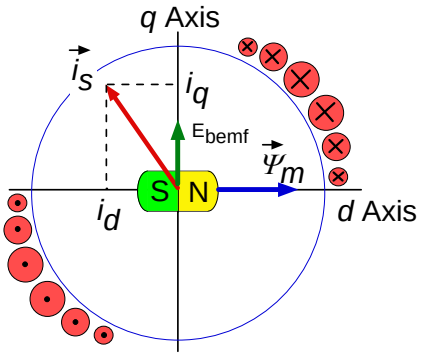


Figure 24. Cross section of two-pole machine illustrating a stator current vector and its decomposition into *d*- and *q*-axis components to achieve vector control of a surface permanent magnet machine.

According to the basic concept of vector control, the amount of torque that is produced by an SPM machine is determined by both the amplitude of the current vector and, very importantly, by its angle with respect to the orientation of the rotor magnets. In Figure 24 the rotor magnet orientation is represented by the magnet flux linkage vector, , aligned with the north pole of the rotor magnets. A two-axis plane can be uniquely defined that is locked to the rotor's instantaneous angular position at every time instant so that the orientation of is defined to be the direct or *d*-axis, and an orthogonal axis is defined as the quadrature or *q*-axis. As a result, any current vector such as in Figure 24 can be uniquely decomposed into an i_d component along with the *d*-axis and an i_q component aligned with the *q*-axis. The torque and the terminal voltage developed by the SPM machine are determined by the values of i_d and i_q, so controlling these two orthogonal current components provides the basis for controlling the torque production of the machine.

Conventional vector control algorithms for SPM machines are based on minimizing the stator copper losses by adjusting the stator current in the rotor-based *dq* frame to achieve maximum torque-per-amp

(*max T/A*) operation.[12, 21] Figure 25 shows the calculated current vector trajectory line for maximum torque/amp operation of the *SPM1* machine over a wide range of rotor speeds in the i_q-i_d plane when delivering 20% of rated torque. According to this algorithm, the value of i_q is essentially constant while i_d is gradually increased (with negative polarity) as the speed is increased beyond the corner point value to accomplish the necessary flux weakening. Flux weakening is required at elevated speeds to counteract the effect of the magnet flux linkage, , sufficiently so that the terminal voltage of the machine at each speed will remain within the maximum limit set by the available source voltage.

It is useful to identify an alternative version of this vector control algorithm to minimize the machine's terminal voltage under all operating conditions by using as much negative *d*-axis current as available to accomplish this objective. The current vector trajectory for this maximum-torque-per-volt strategy is shown in Figure 26 for the *SPM1* machine at 20% of rated torque, exhibiting very little motion over the full speed range. That is, the same current vector amplitude is applied at all speeds, adjusted so that its amplitude equals the rated continuous current value. This algorithm is referred to as maximum torque-per-volt (*max T/V*).

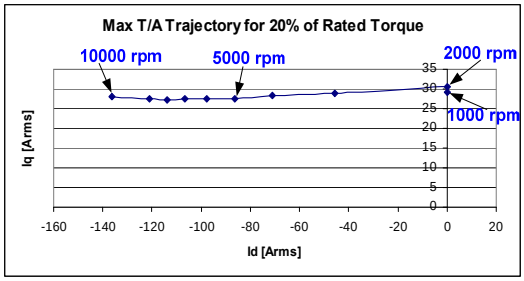


Figure 25. Maximum torque/amp current vector trajectory for *SPM1* machine at 20% of rated torque.

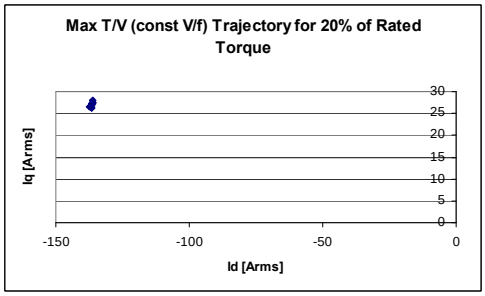


Figure 26. Maximum torque/volt current vector trajectory for *SPM1* machine at 20% of rated torque.

This *max T/V* algorithm is useful for illustration purposes in this discussion because it has the special feature of minimizing the stator core loss by minimizing the stator flux density at all speeds. However, its practical usefulness is very limited because this iron loss minimization is accomplished at the price of maximizing the copper loss.

Some valuable insights are also available by comparing the calculated loss components with each of these two vector control algorithms. Figure 27 confirms that the maximum torque-per-amp algorithm (*max T/A*) delivers lower copper losses at all speeds below maximum speed (10,000 rpm) compared to the *max T/V* algorithm. On the other hand Figure 28 shows that the roles reverse for iron core losses,[9] with the *max T/V* algorithm achieving significantly lower core losses than the *max T/A* algorithm at all speeds below 10K rpm.

An important observation from this exercise is that the *max T/V* algorithm tends to yield higher efficiency at speeds where the iron losses are dominant, while the *max T/A* algorithm tends to achieve higher efficiency at speeds where copper losses are dominant. Figure 29 confirms this observation by comparing the predicted efficiency of the *SPM1* machine at 20% of rated torque for the two algorithms over a wide speed range. More specifically, Figure 29 shows that the *max T/A* algorithm is significantly better for minimizing the total machine losses at low speeds where the iron losses tend to be the lowest, but the *max T/V* algorithm demonstrates its superiority at higher speeds above approx. 2000 rpm, where iron losses are much higher. Unfortunately, Figure 29 also shows that neither algorithm is capable of achieving the 93% efficiency target for the FreedomCAR traction motor, with the largest deficiencies appearing at low speeds.

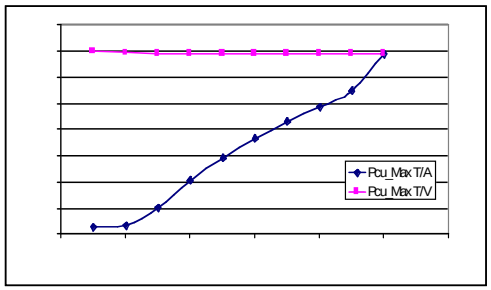


Figure 27. Comparison of predicted copper losses for 20% of rated torque with *max T/A* and *max T/V* algorithms.

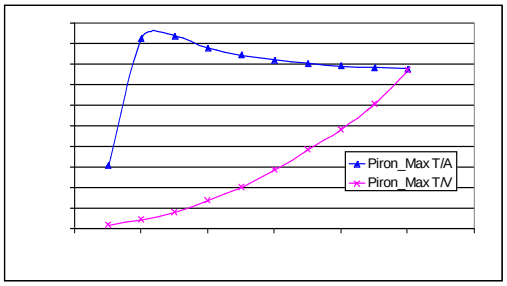


Figure 28. Comparison of predicted iron losses for 20% of rated torque with *max T/A* and *max T/V* algorithms.

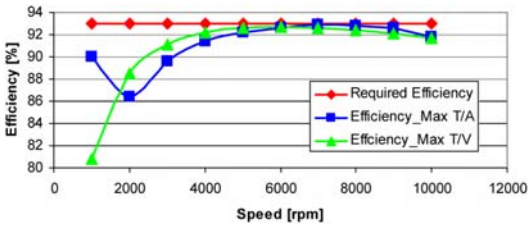


Figure 29. Predicted efficiency of *SPM1* machine at 20% of rated torque for *max T/A* and *max T/V* algorithms, plus specified minimum efficiency line.

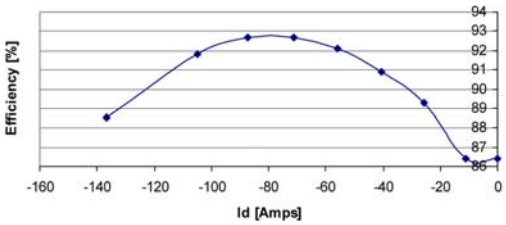


Figure 30. Variation of *SPM1* efficiency at 2000 rpm as a function of i_d with i_q adjusted to hold the torque constant at 20% of rated torque.

A critical observation at this stage is that the *max T/A* and *max T/V* algorithms represent two distinct extremes in the vector control spectrum. In between these two extremes are an infinite number of alternative formulations. Each candidate algorithm represents a different weighted blending of the two extreme algorithms, raising the possibility that a blended algorithm might perform better than either *max T/A* or *max T/V* alone.

An investigation was launched to determine whether there might be another combination of I_q, which determines the resulting torque, and I_d, which is used to adjust the flux level in the machine, that will lead to higher machine efficiency values than either the pure *max T/A* or *max T/V* algorithms.

The results of this investigation have been very promising, indicating that the appropriate blend of the two algorithms can yield significant improvements in the machine efficiency, particularly at those speeds that exhibit the largest deficiencies in Figure 29. As an example, Figure 30 shows the variation of predicted *SPM1* efficiency at 2000 rpm and 20% of rated torque as a function of I_d. The predicted efficiency is approx. 86.5% for the *max T/A* algorithm (when I_d is zero), while the efficiency is approx. 88.5% for the *max T/V* algorithm (I_d = -140 A_{rms}). In between these extremes, the partial-load machine efficiency peaks when I_d = -80 A_{rms} at a value very close to the specified value of 93%. This is a clear indication that choosing the optimum combination of I_d and I_q can have a very significant effect on maximizing the partial-load efficiency of the machine. These results will be discussed further based on the FEA results presented in the following section.

Figure 31 presents the calculated current vector trajectory for achieving the highest partial-load efficiency as the rotor speed is increased from 1000 to 10,000 rpm. By comparing this trajectory to the *max T/A* and *max T/V* current vector trajectories in Figures 25 and 26, it can be observed that the new trajectory adds a higher-level of negative *d*-axis current as a function of rotor speed compared to the *max T/A* trajectory in order to reduce the iron losses, but not as much I_d as the *max T/V* algorithm would require.

Figure 32 shows the new predicted efficiency curve for the *SPM1* machine at 20% of rated torque when the current vector trajectory in Figure 31 is applied as a function of rotor speed. The partial-load efficiency values are boosted at every speed compared to the values plotted in Figure 29 for the *max T/A* and *max T/V* trajectories. In fact, the results in Figure 32 predict that the *SPM1* machine will be able to meet the minimum efficiency requirements (93%) for 20% rated torque over the complete speed range.

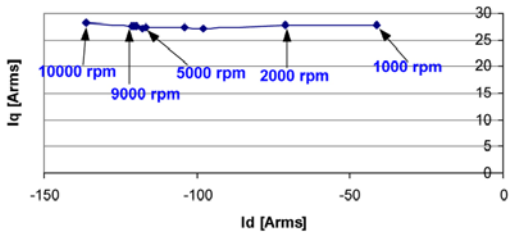


Figure 31. Current vector trajectory for *SPM1* machine to deliver maximum partial-load efficiency at 20% of rated torque.

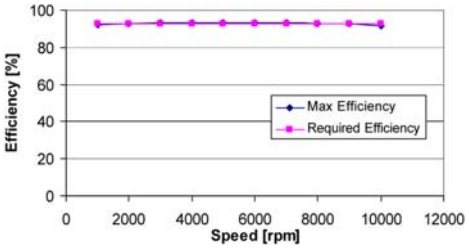


Figure 32. Predicted efficiency of *SPM1* machine at 20% of rated torque for maximum partial-load efficiency, plus specified minimum efficiency line.

Finite-Element Analysis Results

To verify the assumptions used in the analytical calculations of core losses and to gain more insights into the tradeoffs between the copper and core losses for maximizing the partial-load efficiency, FEA simulations using *MagNet 2D* (Infolytica) were carried out. Three operating points at 2000 rpm and 20% rated torque are considered. These points correspond to three distinct points on the partial-load efficiency curve shown in Figure 30, representing *max T/A* (far right), *max T/V* (far left), and *max efficiency* operation at the peak of the curve.

The FEA-predicted magnetic flux density time-domain waveforms in the stator teeth are shown in Figures 33 to 35 for the three highlighted operating points. The harmonic spectrum of the stator-tooth flux density waveform is presented in Figure 36.

The first key observation drawn from these figures is that the magnetic flux density waveforms in the stator teeth are almost purely sinusoidal, as confirmed by the harmonic spectrum in Figure 36. This result is striking because the fractional-slot concentrated windings produce many spatial harmonics in the air-gap flux density waveform.[22] The sinusoidal wave shapes in Figures 33 to 35 justify the sinusoidal approximation adopted for calculating the peak air gap magnetic flux density and, subsequently, for calculating the peak magnetic flux density in the stator teeth and yoke.

The second key observation, drawn from comparing Figures 33 and 34, is that there is an 80% reduction of the peak magnetic flux density in the stator tooth for the *max T/V* algorithm compared to the *max T/A* algorithm. This flux density reduction leads to a significant reduction of the predicted core losses in the stator teeth. This reduction in the stator core loss comes at the expense of an increase in the rms phase current from 30.6 to 139.3 A_{rms} and a corresponding increase in the copper losses, as discussed in the previous section. This result is consistent with the results shown earlier in Figures 27 and 28.

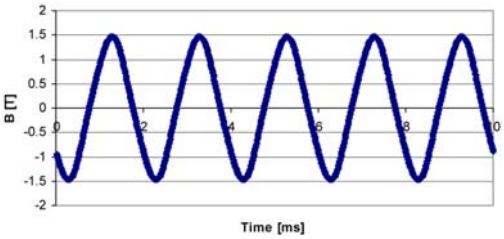


Figure 33. Predicted stator tooth magnetic flux density waveform at 2000 rpm and 20% rated output torque under *max T/A* operating conditions.

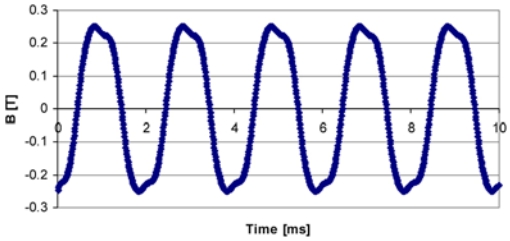


Figure 34. Predicted stator tooth magnetic flux density waveform at 2000 rpm and 20% rated output torque under *max T/V* operating conditions.

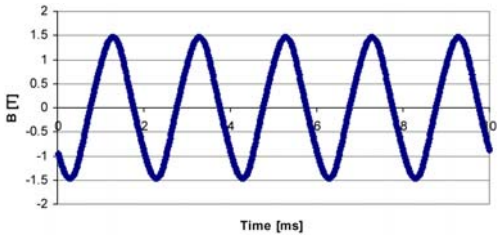


Figure 35. Predicted stator tooth magnetic flux density waveform at 2000 rpm and 20% rated output torque under *max efficiency* operating conditions.

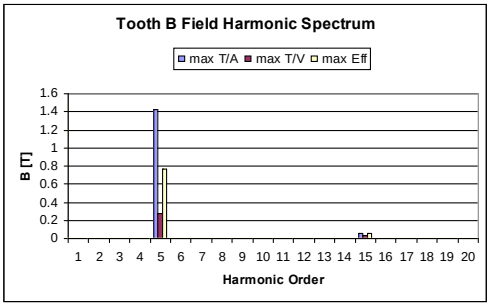


Figure 36. Predicted harmonic spectra for stator tooth magnetic flux density at 2000 rpm, 20% rated torque for the three operating conditions.

Figure 35 shows the predicted stator tooth magnetic flux density waveforms under the *max efficiency* operating conditions. It can be observed that there is almost a 50% reduction in the stator tooth peak magnetic flux density compared to the *max T/A* case. At the same time, there is an increase in the phase current from 30.6 to 76.4 A_{rms}. This blend of the *max T/A* and the *max T/V* algorithms yields the maximum partial-load efficiency for operation at 20% rated torque with a rotor speed of 2000 rpm.

Preparations to Test Control Schemes for the FSCW-SPM Motor

Upgraded hardware and software for use with OPAL-RT have been acquired during FY 2006 to conduct efficiency tests on the 6-kW FSCW-SPM motor for evaluating several control schemes developed by UWM and ORNL. An inverter and an interface card with dead time insertion capability, which communicates with the inverter's control unit while maintaining internal fault protection, allow a rapid prototype system such as OPAL-RT to control the semiconductor device gates while the motor is under actual load. Results of these tests will be used to compare and evaluate the control schemes. The new inverter is a Danfoss VLT 5252, which was purchased to deliver a range of powers up to the 55-kW target of an HEV traction drive system. The VLT 5252 has a typical shaft output power of 200 to 250 kW with normal 110% overload torque and 160 to 200 kW for high 160% overload torque. Figures 37 and 38 show the portable inverter and the internal arrangement of its control unit and power switching section.



Figure 37. Danfoss VLT 5252 inverter on mobile base.



Figure 38. Open door shows Danfoss control unit at top and power switching section at bottom.

Figure 39 shows the special interface card provided by Aalborg University in Denmark. It replaces a card in the Danfoss, which allows gate signals generated by the OPAL-RT system to control inverter switching. This is an effective way of bypassing an inverter's control unit to impress a new control scheme on a motor so that its effect on the motor/inverter system may be evaluated during actual operation.



Figure 39. Interface card with fiber optics and dead time insertion prepared at Aalborg University to allow control of a commercial inverter while maintaining its fault protection features.

ORNL's old OPAL-RT system encountered a problem generating stable PWM signals. It was necessary to upgrade the ORNL target computer and the OPAL-RT software to remedy this problem. The new target PC uses a QNX Version 6.2 operating system with a significantly faster bus speed. Field-programmable-gate-array-based I/O cards, which are expected to solve the unstable PWM problem, are part of the acquisition. Figure 40 shows the new target computer with its two white terminal buses mounted on the front, and Figure 41 shows one terminal bus replaced by a card used during the OPAL-RT pre-test check-out procedure to verify that all cards and software are working properly. Voltage, current, and speed sensor signals will enter the white terminal bus, and gate drive signals for the Aalborg

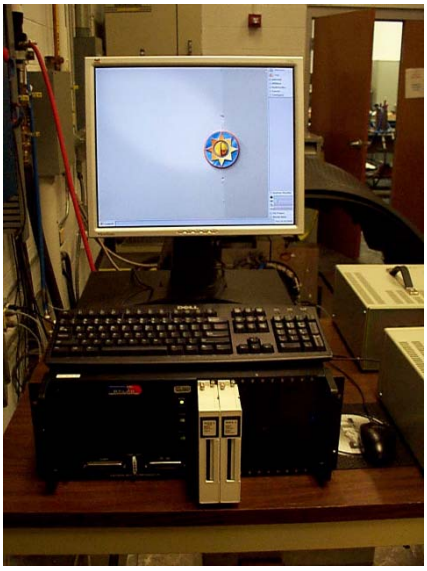


Figure 40. New OPAL RT target PC and connection box.

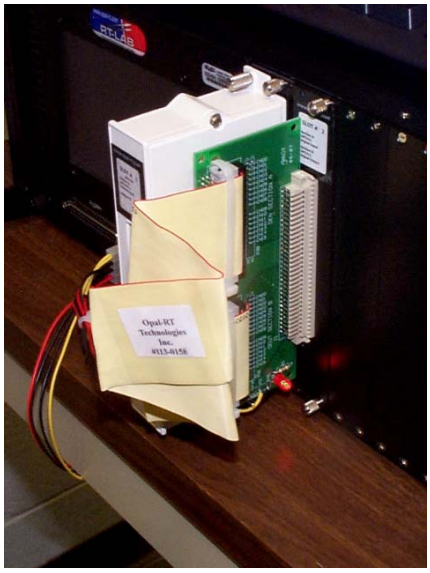


Figure 41. Pre-test diagnostic verification signal bypass card.

card will leave the bus. Current and voltage sensors are shown in Figure 42. The 6-kW motor in its new frame that allows water cooling of the stator is shown in Figure 43.

The checkout procedure for the inverter is in the approval cycle and the pre-test check-outs of the OPAL-RT target computer are in progress. Preparation of the final test plan for efficiency measurements as a function of speed for several partial loads will begin in FY 2007. This plan will be prepared in collaboration with UWM because it must be compatible with their control scheme so that a meaningful comparison of the two schemes may be made.

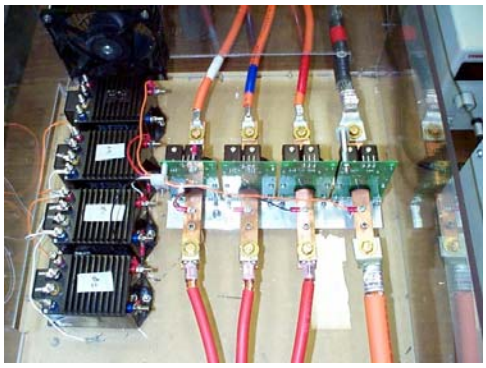


Figure 42. Voltage (black-left), motor current (red-middle) and direct current supply current (orange-right) sensors.

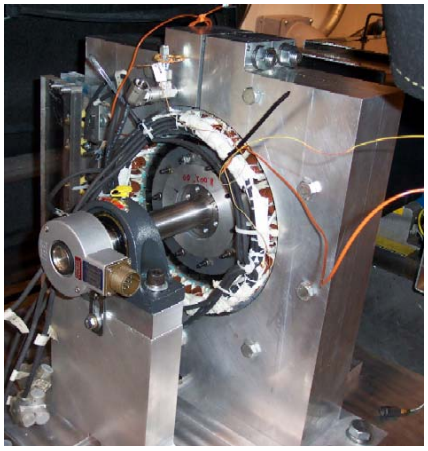


Figure 43. 6-kW fractional-slot SPM motor with concentrated windings.

Conclusions

Equations have been presented showing how a concentrated winding may be used to design increased inductance into an SPM motor with distributed windings. A distributed winding with $N_{spp} = 1$ has the maximum flux linkage with the stator; consequently, to produce comparable torque, a stator with concentrated windings must be able to produce a comparable number of flux links. A relation between the SPM motor with concentrated windings and its fluxmate with distributed windings emerges from the equations. Further, these equations show that there is always sufficient room in the slots of the concentrated windings to add the wire turns necessary to ensure that the flux across the gap for the concentrated windings is the same as that of its corresponding distributed winding, thus the name fluxmate.

The 55-kW design, *SPM2,* proposed by UWM has been evaluated using two design methodologies. The result is a viable design for an HEV traction drive motor. Two such motors, the other being *SPM1,* were designed according to the UWM methodology with a similar pole and slot count to UWM's 6-kW FSCW-SPM prototype now being used to evaluate control schemes at ORNL. With this knowledge, there is mounting evidence that FSCW motors with low pole and slot count are worthy of further investigation for traction applications.

Slight differences between the design results from UWM's application of its design methodology and ORNL's application of commercially available SPEED software have been identified and resolved. These differences relate to methods used to calculate magnet losses. At higher speeds these losses are reduced because more of the current flows at the surface of the conductor, thereby increasing its resistance. This effect is described by saying that the losses at high speeds are inductance limited. These results emphasize the importance of circumferentially stacking the magnets. The differences do not alter the conclusions or the designs proposed by UWM.

A simple proportional speed control has been developed at ORNL for FSCW-SPM motors. Detailed simulation of the control shows that it can effectively control motor speed while minimizing the motor current magnitude during operation above and below base speed. Laboratory testing of this control method and UWM's maximum motor efficiency control will allow comparison and determination of which method exhibits the greatest overall drive efficiency

Significant progress has been achieved during the past year in the development of advanced machine analysis/design and control techniques that will improve the operating efficiency of future FSCW-SPM machines. In particular, the work is contributing to a much-improved understanding of the sources and distribution of FSCW-SPM machine iron losses that play a major role in determining machine efficiency. This new knowledge is being put to use immediately in other programs to design more powerful FSCW-SPM machines for electric traction applications with improved efficiency characteristics.

Future Directions

Setup of the prototype 6-kW FSCW-SPM machine for dynamometer testing at ORNL is in progress. We will prepare a detailed plan to present the specifics for measuring the inverter and motor efficiencies so that the different control schemes may be compared. Each of the control schemes will be programmed in MatLab, compiled for use with OPAL RT, and used to drive the motor.

The detailed test plan will precede efficiency measurements of ORNL's low-cost control scheme to achieve maximum torque per amp below base speed and maximum power per amp above base speed at various speeds and partial loads. Similar test regimens will be used to test UWM's modified vector control algorithm under partial-load operating conditions so that the results may be used to compare control schemes.

During the first quarter of FY 2007 the prototype machine will be exercised under OPAL RT control to obtain the necessary comparative tests. Work is continuing at UWM to enhance the capabilities of the closed-form analytical model for accurately predicting iron losses in FSCW-SPM machines during operation over wide ranges of speed and load conditions. This improved iron loss model will be used to

develop an optimized design of a 55-kW (peak) FSCW-SPM machine to meet the demanding performance requirements for the FreedomCar.

Publications

A. M. EL-Refaie, T. M. Jahns, P. J. McCleer, and J. W. McKeever, "Experimental Verification of Optimal Flux Weakening in Surface PM Machines Using Concentrated Windings," in *Rec. of 2005 IEEE Ind. Appl. Soc. Ann. Mtg.*, Hong Kong, October 2005. *Accepted for publication in IEEE Trans. on Ind. Applications*.

A. M. EL-Refaie, T. M. Jahns, and J. W. McKeever, "Effect of Back-EMF Constraints on Fractional-Slot Surface PM Machines Designed for Wide Constant-Power Speed Range Operation," in *Proc. of 2006 Intl. Conf. on Electrical Machines*, Chania, Greece, September 2006.

A. M. EL-Refaie, T. M. Jahns, and J. W. McKeever, "Modified Vector Control Algorithm for Increasing Partial-Load Efficiency of Fractional-Slot Concentrated Winding Surface PM Machines," in *Rec. of 2006 IEEE Ind. Appl. Soc. Ann. Mtg.*, Tampa, October 2006.

References

1. J. S. Hsu, *Permanent Magnet Energy Conversion Machine,* U. S. Patent No. 5,952,756, September 14, 1999.
2. Cambier et al., *Brushless DC motor Using Phase Advance Timing Advancement*, U.S. Patent 5,677,605, October 14, 1997.
3. J. S. Lawler, J. M. Bailey, and J. W. McKeever, "Extended Constant Power Speed Range of the Brushless DC Motor Through Dual Mode Inverter Control," ORNL/TM-20000/130, July 2000.
4. J. S. Lawler, J. M. Bailey, and J. W. McKeever, "Minimum Current Magnitude Control of Surface PM Synchronous Machines during Constant Power Operation," *IEEE Power Electronics Letters* **3**(2) (June 2005).
5. T. M. Jahns, *Cost Reduction Opportunities for Permanent Magnet Synchronous Machines*, Interim Report prepared for ORNL Technical Project Manager, May 24, 2005.
6. A. M. EL-Refaie, T. M. Jahns, P. J. McCleer, and J. W. McKeever, "Experimental Verification of Optimal Flux Weakening in Surface PM Machines Using Concentrated Windings," *IEEE Ind. Appl. Soc. Annual Meeting*, Oct. 2–6, 2005, Hong Kong.
7. Ayman M. EL-Refaie, *High Speed Operation of Permanent Magnet Machines*, Electrical and Computer Engineering Ph.D. Thesis at the University of Wisconsin–Madison, 2005.
8. A. M. EL-Refaie, T. M. Jahns, and J. W. McKeever, "Effect of Back-EMF Constraints on Fractional-Slot Surface PM Machines Designed for Wide Constant-Power Speed Range Operation," *Int. Conf. on Electric Machines*, September 2006, Greece.
9. C. Mi, G. R. Slemon, and R. Bonert , "Modeling of Iron Losses of Permanent-Magnet Synchronous Motors," *IEEE Transactions on Industry Appl.* **39(**2) (May/June 2003).
10. K. Atallah, D. Howe, P. H. Mellor and D. A. Stone, *Rotor Loss in Permanent-Magnet Brushless AC Machines*, *IEEE Tran. on Ind. Appl*. **36**(6) (November/December 2000).
11. T. Sebastian and G. R. Slemon, "Operating Limit of Inverter Driven Permanent Magnet Motor Drives," *IEEE Trans. Ind. Appl*. **IA-23**(2) 327–333 (March 1987).
12. W. Soong and T. J. E. Miller, "Field Weakening Performance of Brushless Synchronous AC Motor Drives," *IEE Proc. Of the Electronics Power Applications* **141**(6), 331–340 (November 1994).
13. J. S. Lawler, "Control of Surface Mounted Permanent Magnet Motors with Special Application to Fractional-slot Motors with Concentrated Windings," ORNL/TM-2005-184, September 2005.
14. A. M. EL-Refaie, T. M. Jahns, J. W. McKeever, "Modified Vector Control Algorithm for Increasing Partial-Load Efficiency of Fractional-slot Concentrated Winding Surface PM Machines," *IEEE Ind. Appl. Soc, 41st Annual Mtg*., Marriott Waterside Hotel, Tampa, Fl, October 8–12, 2006.
15. V. Zivotic-Kukolj, W. L. Soong, N. Ertugrul, "Iron Loss Reduction in an Interior PM Automotive Alternator," pp. 1736–43 in *Rec. of 2005 IEEE Ind. Appl. Soc. Ann. Mtg*., Hong Kong, October 2005.

16. Z. Q. Zhu, D. Howe, C. C. Chan, "Improved Analytical Model for Predicting the Magnetic Field Distribution in Brushless Permanent-Magnet Machines," *IEEE Trans. Magnetics* **38**(1) (January 2002).
17. Z. Q. Zhu, and D. Howe, "Instantaneous Magnetic Field Distribution in Brushless Permanent Magnet dc Motors, Part I: Open-Circuit Field," *IEEE Trans. Magnetics* **29**(1) (January 1993).
18. D. Zarco, *A Systematic Approach to Optimized Design of Permanent Magnet Motors with Reduced Torque Pulsations*, Ph.D. Thesis, Department of Electrical and Computer Engineering, University of Wisconsin–Madison, 2004.
19. A. M. EL-Refaie and T. M. Jahns, "Comparison of Synchronous PM Machine Types for Wide Constant Power Speed Range Operation," in *Rec. of 2005 IEEE Ind. Appl. Soc, Annual Meeting*, Hong Kong, Oct. 2005.
20. D. W. Novotny and T. A. Lippo, *Vector Control and Dynamics of AC Drives*, New York, Oxford University Press, 1996.
21. Z. Q. Zhu, U. S. Chen, and D. Howe, "Iron Loss in Permanent-Magnet Brushless AC Machines Under Maximum Torque per Ampere and Flux Weakening Control," *IEEE Trans. Magnetics*, **38**, 3285–3287, September (2002).
22. A. M. EL-Refaie, T. E. Jahns, and D. W. Novotny, "Analysis of Surface Permanent Magnet Machines Equipped with Concentrated Windings," *IEEE Trans. Energy Conversion*, **21**, 34–43, March 2005.

3.4 Extending the CPSR of Synchronous Reluctance Motors

Principal Investigator: John W. McKeever
Oak Ridge National Laboratory
National Transportation Research Center
2360 Cherahala Boulevard
Knoxville, TN 37932
Voice: 865-946-1316; Fax: 865-946-1262; E-mail: mckeeverjw@ornl.gov

DOE Technology Development Manager: Susan A. Rogers
Voice: 202-586-8997; Fax: 202-586-1600; E-mail: Susan.Rogers@ee.doe.gov

ORNL Program Manager: Mitch Olszewski
Voice: 865-946-1350; Fax: 865-946-1262; E-mail: olszewskim@ornl.gov

---

Objectives

The objective of this project was to determine if a reliable per-phase analytical model could be developed for a synchronous reluctance motor. A per-phase model, which has been developed for brushless dc permanent magnet (PM) motors and for switched reluctance motors, has been used to show that both of these motor types have unbounded constant power speed ratios (CPSRs) if resistance and speed sensitive losses are neglected. If a reliable per-phase model could be developed, it could be used to determine if a synchronous reluctance motor also has an unbounded CPSR. During the development of a per-phase model of the switched reluctance motor, detailed computer modeling revealed that, as the speed of the model increased, saturation did not impact its performance. The question is whether saturation-independent behavior is true for a synchronous reluctance motor, considering the different drive mechanisms.

Another objective was to model a synchronous reluctance motor using available commercial motor design software to determine performance targets that may be compared with the FreedomCAR targets. This would provide an idea of the extent to which performance targets had to be improved to make this motor an a hybrid electric vehicle (HEV) traction drive candidate.

Approach

Commercial software was used extensively during this part of the project. ORNL is a member of the SPEED Consortium, based at the University of Glasgow, Scotland. Consequently, SPEED software was used to model two synchronous reluctance motor inverter designs and to check their performance characteristics. Two other software packages employed were FLUX2D and COMSOL. Although FLUX2D has a good magnetic solution capability, construction of models was difficult, requiring extensive technical support from Magsoft. COMSOL proved to be far more versatile and, because of its ability to represent saturation, was helpful in determining how important it is that saturation be a part of any model we develop.

An attempt was made to define a per-phase model like the one used for brushless dc motors and switched reluctance motors. The winding function, which assumes an idealized machine with uniform air gap, was applied to a reluctance motor with salient rotor and salient stator poles. The double salient poles have a very nonuniform gap. This nonuniformity caused flux fringing at all positions of the rotor pole from its aligned to unaligned positions, making use of the winding function an approximation. A model of a synchronous reluctance motor using COMSOL showed that flux fringing effects are significant. Use of the winding function as an approximation gave equations for direct and quadrature inductances

corresponding to the aligned and unaligned positions of the rotor. A detailed finite-element analysis will be necessary to quantify the reliability of the per-phase model.

Meaningful analyses were provided by using COMSOL to examine the flux patterns between the rotor and stator during operation of a synchronous reluctance motor. The results and conclusions of this analysis are included in this report.

Major Accomplishments

1. We applied FLUX2D software to determine the phase advance, which is the angle between the center of a rotor pole and the stator current orientation, that will produce maximum torque. ORNL created a model of a PM motor with inset magnets and turned off the magnets to simulate a synchronous reluctance motor with doubly salient poles. The torque produced was then calculated for a fixed rotor as the current in the stator was varied over one pole and for current fixed in the stator with the rotor turned through one pole angle. Definite maxima were found with only rough agreement between the two approaches. A similar exercise with COMSOL demonstrated good agreement between the two approaches for estimating the phase advance for maximum torque.
2. Using SPEED as a design tool, two synchronous reluctance motors were modeled to try to meet FreedomCAR targets. The first model with four turns per pole could not deliver maximum power at 2000 rpm. Adequate power at 2000 rpm required eight turns per pole, which doubled the amount of copper to increase both cost and weight. The motor was too heavy and too expensive to meet FreedomCAR goals.
3. We defined a per-phase model by applying a winding function to a synchronous reluctance motor with salient rotor and stator poles to determine the inductance that should be used. This approach yielded direct and quadrature inductances, which had to be added for use in the model. Unfortunately, flux fringing, verified by a COMSOL analysis, indicated that use of the winding function was clearly an approximation. Later work showed that a reliable model should include not only flux fringing but also saturation.
4. We constructed detailed models of switched reluctance motors to study flux behavior in a synchronous reluctance motor. Variations in the study included (1) a solid rotor to study the effect of eddy currents on the rotor; (2) regular reluctance rotors turning inside stators with and without shoes in their teeth; and (3) a comparison of synchronous reluctance motor performance, assuming no saturation with performance, that included saturation as part of the model. Overall results strongly suggested that any reliable model of a synchronous reluctance motor must incorporate flux fringing as well as saturation.

Technical Discussion

Modeling a Synchronous Reluctance Motor using SPEED Software

Two SPEED models of a synchronous reluctance motor

Two similar synchronous reluctance motor designs were studied to assess their potential to meet the targets of the FreedomCAR program. The two designs differ in the number of turns used in the stator. Their rotors are identical and consist of four poles made of six U-shaped plates of magnetic steel separated by five air gaps. Figure 1 shows a schematic drawing of the synchronous reluctance motor design considered.

Table 1 contains the performance data for a synchronous reluctance motor with four stator turns per pole. Top speed is 10,000 rpm, and performance values are at 20% of top speed.

Table 2 contains the performance data for a synchronous reluctance motor with eight stator turns per pole. Again top speed is 10,000 rpm, and performance values are calculated at 20% of top speed.

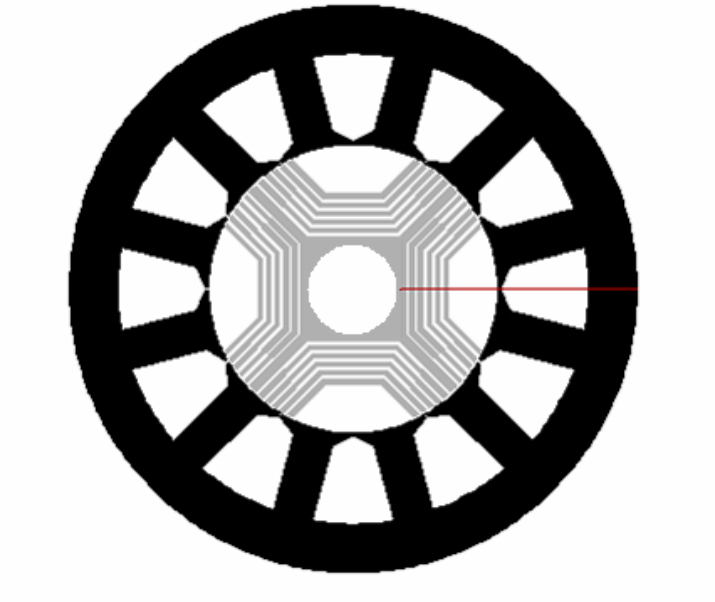


Figure 1. Schematic of a synchronous reluctance motor (4 poles, 12 slots, 40-cm diameter, 100 cm long, no permanent magnets).

Table 1. SPEED performance data for a synchronous reluctance motor whose stator has four turns per pole

25 kW at 2,000 rpm with 93% efficiency using γ = 65 eDeg 565-A peak current, 400-A_{rms} current, 92 V_{LL} => 118 V_{dc} Current density = 5.1 A/mm^2
55 kW at **10,000** rpm with 96% efficiency using γ = 49.5 eDeg 322-A peak current, 228-A_{rms} current, 342 V_{LL} => 438 V_{dc} Current density = 2.9 A/mm^2
30 kW at **10,000** rpm with 96% efficiency using γ = 46 eDeg 233-A peak current, 165-A_{rms} current, 262 V_{LL} => 336 V_{dc} Current density = 2.1 A/mm^2
Total weight 65.6 kg (30 kg of Cu and 45 kg of Fe) Total volume = 12.6 L Peak power/weight = 0.73 kW/kg [<**2.75**] Peak power/volume = 4.4 kW/L [<**12.5**] (i.e., about factor of 3 below target for power density)

Table 2. SPEED performance data for synchronous reluctance motor whose stator has eight turns

55 kW at **2,000** rpm with 94% efficiency using γ = 75 eDeg 565-A peak current, 400-A_{rms} current, 297 V_{LL} => 381 V_{dc} Current density = 5.1 A/mm^2 30 kW at **2,00**0 rpm with 96% efficiency using γ = 65 eDeg 330-A peak current, 233-A_{rms} current, 203 V_{LL} => 260 V_{dc} Current density = 2.9 A/mm^2
7.5 kW at **10,000** rpm with 96% efficiency using γ = 45 eDeg 58-A peak current, 41-A_{rms} current, 262 V_{LL} => 336 V_{dc} Current density = 0.5 A/mm^2
Total weight 106 kg (**61** kg of Cu and 45 kg of Fe) Total volume = 12.6 L Peak power/weight = **0.52** kW/kg [<**2.75**] Peak power/volume = 4.4 kW/L [<**12.5**] (i.e., about 5 and 3 times below targets for power density)

A sample SPEED design sheet for the Table 2 case is contained in Table 3.

Table 3. Design sheet for the reluctance motor shown in Figure 1

PC-SREL 1.5 for Windows (1.5.2.1) 2/8/2006 11:50:00 AM
F:\My Documents\pjo_srel_motor55kwFC2krp.sy1
UT-Battelle, LLC
PC-SREL main title
PC-SREL sub-title

1 Dimensions:----------

RotorRad	100.000 mm	BoreRad	102.000 mm	Gap	2.000 mm
FrameRad	200.000 mm	ShaftRad	34.000 mm	POLES	4
SLOTS	12	TWS	28.000 mm	SD	64.000 mm
SO	2.000 mm	TGD	2.000 mm	TGANG 4	0.000 mDeg
RNSQ	Square	Stf	0.970	RotType	Ax. Lam
LStator	100.000 mm	LRotor	100.000 mm	LShaft	150.000 mm
LMotor	175.000 mm	1stLayer	Guide	PoleMat	Insulation
NLayers	12	B_Thick	2.000 mm	G_Thick	4.000 mm
NumGuide	6	NumBarrs	6	PoleArc	42.200 mDeg

2 Control Data:----------

RPM	2000.000 rpm	I(rms)	233.000 A	Gamma	65.000 eDeg
Vs(dc)	450.000 V				
Vtrans	0.000 V	Rtrans	0.000 Ohms	Vdiode	0.600 V

3 Winding Data:----------

WdgType	Lap	Connex	Wye	Throw	3
TC	8	CoilsPer	1.000	NSH	1
Tph	32.000	PPATHS	1	SPP	1.000
Layers	2.000	CSidesPh	8	Z	0.000
MLT	917.191 mm	Ext	0.000 mm	LgthOEnd	328.289 mm
MaxSFill	0.492	EndFill	0.500	LaxPack	314.087 mm
SFill	0.492	WDia	10.000	WireSpec	BareDia
WireDia	10.000 mm	Liner	0.400 mm		
SlotArea	2554.242 mm^2	CondArea	78.540 mm^2	ASlotLL	2473.684 mm^2
WdgTemp	25.000 DegC	Rph	6.478E-03 Ohm/Ph	Rterm	0.013 Ohms
PCSlot	3.455	XET	1.000	Ax1	75.000 mDeg
ks1	1.000				
kw1	1.000	Nse	40.744		

Table 3. (continued)

4 Magnetic Circuit Design:----------					
Bg1OC	0.821 T	PhiM1	8.374 mWb	Bt_pk	1.614 T
Bg_pk	0.821 T	Bf_pk	1.270 T	Bg_pk	1.370 T
				BgBH_pk	3.426 T
5 Inductance Values:----------					
Kc_Rotor	1.054	Kc_Stat	1.007	Kc_Total	1.061
XLq_m	1.000	XLd_m	1.000	XLslot	1.000
XLendt	1.000	LSlot	0.445 mH/Ph	Lendt	0.088 mH/Ph
XLTthTip	1.000	LTthTipD	0.246 mH/Ph		
MSlot	0.000 mH/Ph	fz	1.020	Xq	0.860 Ohm/Ph
Xm0	1.249 Ohm/Ph	Xsigma	0.223	Xq	0.860 Ohm/Ph
Lq/Ld_i	25.500	L_m	2.982 mH	Ld_i	0.125 mH
Lq/Ld_mU	6.231	Lq_m(U)	2.343 mH	Ld_m	0.376 mH
Lq/Ld_mS	5.150	Lq_m(S)	1.936 mH	Ksat_Lmq	1.210
Lq/Ld(U)	2.491	Lq(Usat)	2.876 mH	Ld	1.154 mH
Lq/Ld(S)	2.139	Lq(Sat)	2.469 mH		
6 Sine-wave static performance [phasor diagram]:----------					
Torque	142.904 Nm	PowerM	29929.669 W	Eff	96.015 %
LossCu_S	1055.105 W	LossFe_R	0.000 W	LossFe_S	187.249 W
LossWF	0.000 W	LossTot	1242.354 W	Jrms	2.967 A/mm^2
IWpk	329.512 A	IWav	209.774 A	IWrms	233.000 A
ILpk	329.512 A	ILav	209.774 A	ILrms	233.000 A
IDchpk	0.000 A	IDchav	0.000 A	IDchrm	0.000 A
IDClinkS	69.271 A	LossConv	0.000 W	kVA	82027.629 kVA
Iq1	98.470 A	Id1	–211.170 A	Gamma	65.000 eDeg
Vq1	–79.742 V	Vd1	–86.094 V	Delta	132.806 eDeg
Vs1	350.864 V	Vs1Lin	275.568 V	Phi	67.806 eDeg
Vph1	117.350 V	VLL1	203.256 V	TempRise	37.271 DegC
PF_fund	0.378	PF	0.380	Appt_PF	0.365
7 Mechanical Data:----------					
NumBolts	6	BoltDia	10.000 mm	BoltLgth	66.000 mm
BoltTdDp	0.167 mm	BoltSpac	13.333 mm	BoltHdCl	1.650 mm
BoltInSh	1.650 mm	BtClInSh	64.700 mm	BHdClMin	1.149 mm
BltLoss%	0.600	BoltYStr	230.000 MPa	ShftYStr	300.000 MPa
TensBlt	16879.952 N	ShearThB	2881.233 N	ShearThS	3887.721 N
SpeedMax	2157.190 rpm				
8 Miscellaneous:----------					
WtCu	60.856 kg	WtFe	45.189 kg	WtMag	0.000 kg
WtTot	106.045 kg	RotJ	0.000 kg-m^2	LosFe/Wt	4.144 W/kg
Sigma	3.298 psi	XFe	1.000	Freq1	66.667 Hz
TempCalc	DegCW	DegCW	0.030 degC/W	HTransCo	265.258 W/m^2/C
Ambient	25.000 DegC	HTransCo	0.000 W/m^2/C		
Wf0	0.000 W	RPM0	1000.000 rpm	NWFT	1.000
9 Core loss analysis:----------					
SSteelNa Transil Bs=1.3T 35					
RSteelNa Transil Bs=1.3T 35					
WtTeeth	16.823 kg	WtYoke	28.366 kg	WtTroot	4.145 kg
LossTthE	25.082 W	LossTthH	82.736 W	LossTth	107.818 W
LTthE/Wt	1.196 W/kg	LTthH/Wt	3.946 W/kg	LTth/Wt	5.142 W/kg
LossYkE	20.985 W	LossYkH	58.446 W	LossYk	79.431 W
LYkE/Wt	0.740 W/kg	LYkH/Wt	2.060 W/kg	LYk/Wt	2.800 W/kg
LossE50	0.581 W	LossH50	2.376 W	LossFe50	2.957 W
End of Design sheet----------					

Both designs have the same overall volume and the same mass of steel. The motor with four stator turns has one-half the mass of copper of the motor with eight turns.

Because of its lower number of turns, the four-turn motor excels at high speeds, while the eight-turn motor is best for low speeds. Specifically, at 2,000 rpm, with the same 400-A_{rms} current limit, the four-turn motor produces 25 kW, while the eight-turn motor produces 55 kW. At 10,000 rpm, with the same voltage limit of 336 V_{dc}, the four-turn motor produces 30 kW, while the eight-turn motor produces only 7.5 kW.

The purely synchronous reluctance motor (no PM) will be large and must be capable of changing the number of active turns to cover the whole range of operation as required by the FreedomCAR specifications. The power density of both motors is one-third of the FreedomCAR goal.

Conclusions from the SPEED Modeling

The power density of synchronous reluctance motors will always benefit from the addition of PM in the rotor; however, adding magnets makes this motor configuration an internal permanent magnet motor, which should be researched with other IPMs. A major reason for studying reluctance motors is to learn how to harvest additional magnet-free torque from them at all speeds. Eliminating magnets could become strategic if their cost rises. Heavy vehicle manufacturers such as LeTorneau have incorporated this type of motor in their loaders and bulldozers because of their sturdy construction, high performance, efficiency, productivity, and simplicity. It is very likely that the synchronous reluctance motor can overcome the torque ripple problems encountered by switched reluctance motors because of its synchronous operation. Some fruitful areas for further research are (1) employing non-sinusoidal waveforms; (2) placing PM materials at symmetrical as well as asymmetrical places on the rotor; and (3) determining how to match the effective number of stator turns to the speed and power requirements of the motor and exploring how to switch the stator turns in and out of the circuit during operation of the motor.

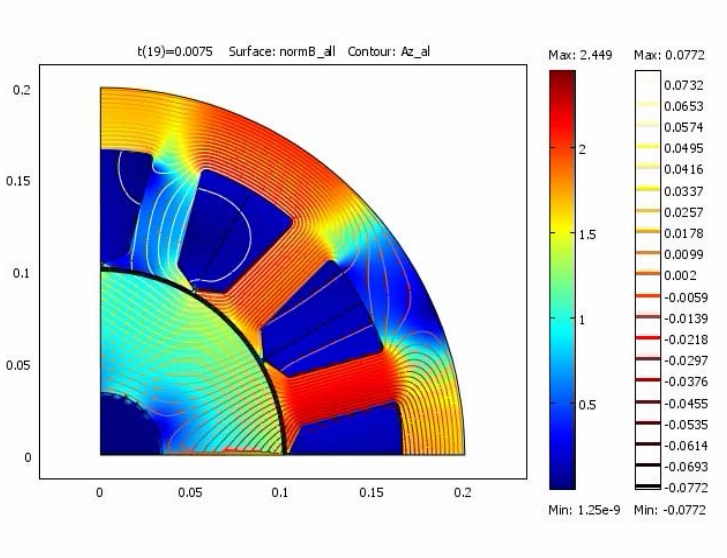
Finite-Element Analysis of Reluctance Motors using COMSOL

Finite-element models of the synchronous reluctance motor were run using stators with and without shoes in their teeth and using several different rotors. To assess the effect of saturation and discreteness of the stator teeth, slot openings, and nonsinusoidal winding distribution on the shape of the rotating magnetic flux produced in the stator and motor, a solid cylindrical rotor was simulated. It was also used to compute the eddy currents induced when the cylinder is a good electrical conductor. The other rotors sported a conventional layered structure with different additions of PM material.

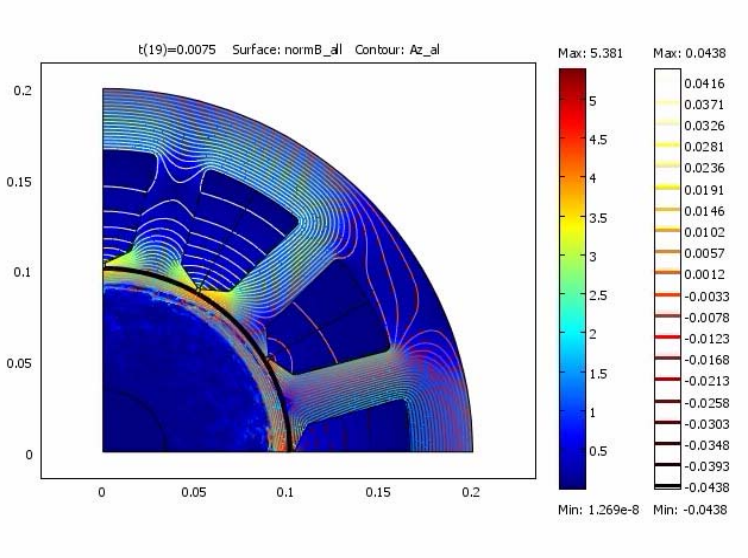
Solid Rotor Study

The colors in Figure 2 show the flux in Tesla, and the contours are lines of constant magnetic potential. Comparing Figures 2(a) and 2(b) illustrates the impact of eddy currents in the rotor. In Figure 2(b) the eddy currents induced in the rotor's surface prevent the stator magnetic flux from crossing the air gap into the rotor, as evidenced by the fact that the contours do not cross the gap.

The effect of magnetic saturation and the stator's heterogeneity on the magnetic flux crossing the air gap is shown in Figure 3. Figure 3(a) shows that the rotor's surface-averaged flux has a trapezoidal ripple of about 6% with a frequency equal to that of the slot-opening crossing. Colored dots correspond to the colored curves in Figure 3(b). The distribution of the flux around the rotor surface is shown in Figures 3(b) and 3(c) to be far from sinusoidal. The generation of torque around the periphery of the solid rotor is shown in Figure 4 to be very small but not uniform.

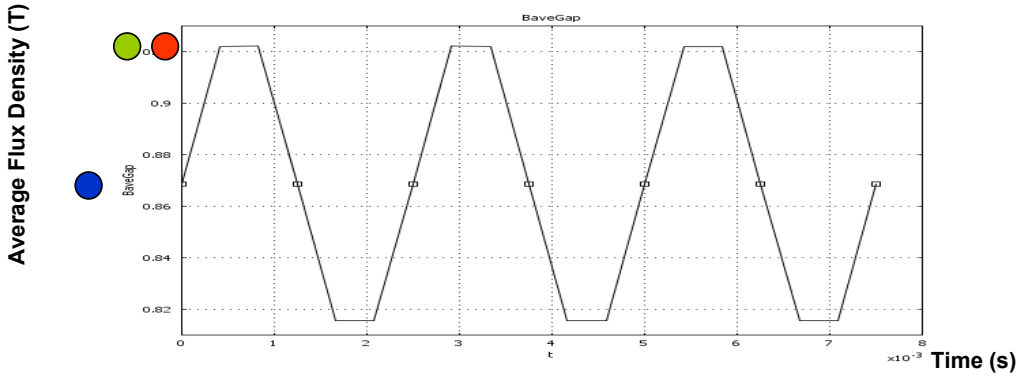


(a) Electrically nonconductive steel rotor.

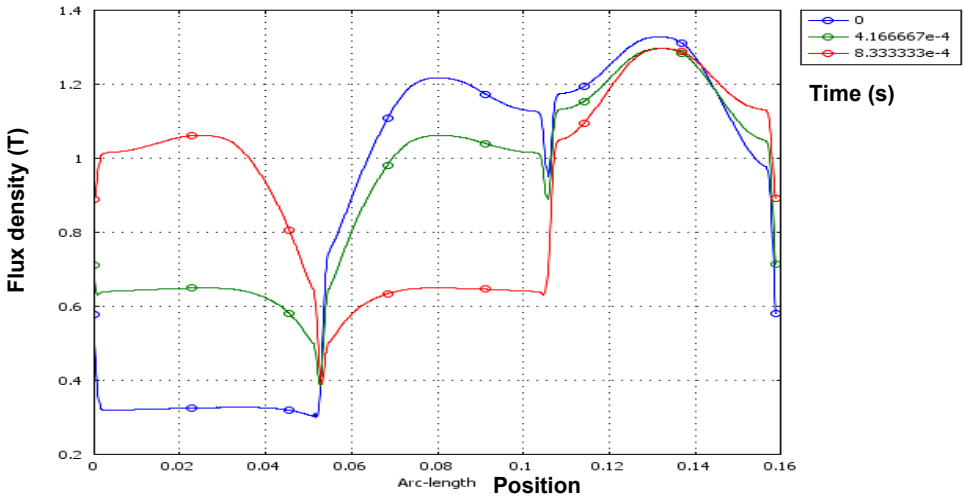


(b) Electrically conductive iron rotor.

Figure 2. Magnetic flux lines generated by the stator's rotating field in a reluctance motor with a solid rotor.

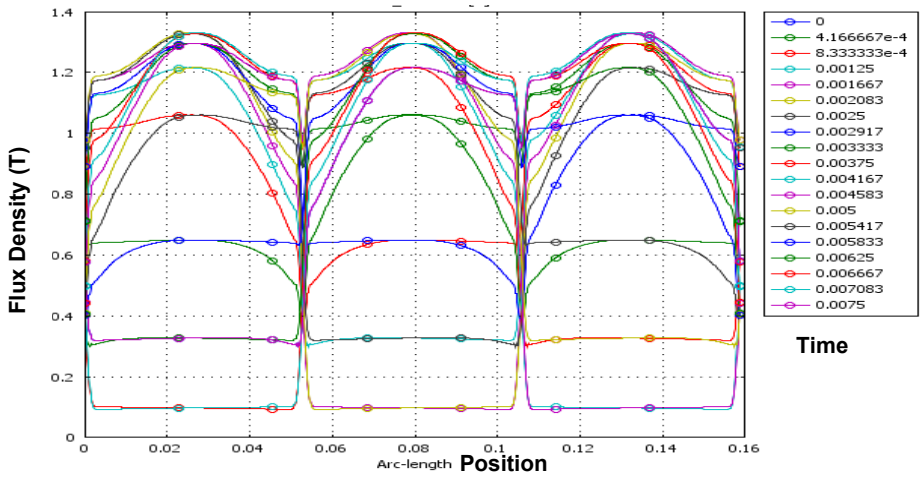


(a) Average air gap flux density for a solid nonconductive steel rotor as a function of time.



(b) Flux density distribution for a nonconductive steel rotor at the three times marked in (a).

Figure 3. Distribution of magnetic flux crossing the air gap generated by the stator's rotating field in a motor with a solid rotor.



(c) Flux distribution for a nonconductive steel rotor at times spanning a quarter turn.

Figure 3. (continued).

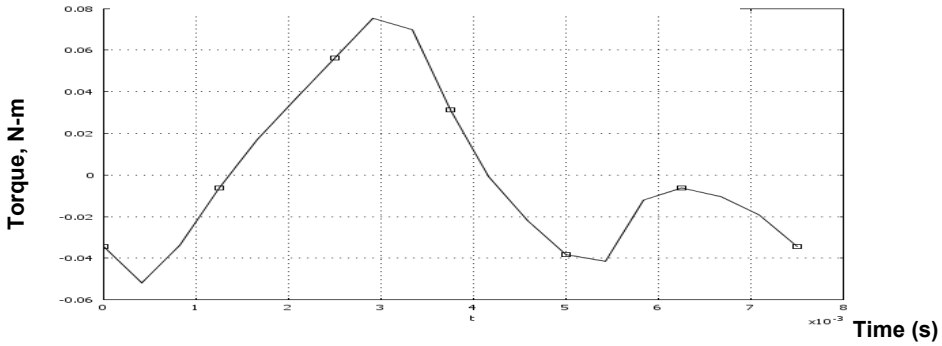


Figure 4. Total torque in the motor with a solid rotor made of nonconductive steel as a function of time for a quarter turn.

Layered Reluctance Rotors

In addition to the stators with and without shoes and the classic rotor shown in Figure 1, several configurations with varying amounts and locations of PM material inserted between the steel layers were simulated. The definitions of these configurations appear in Figure 5.

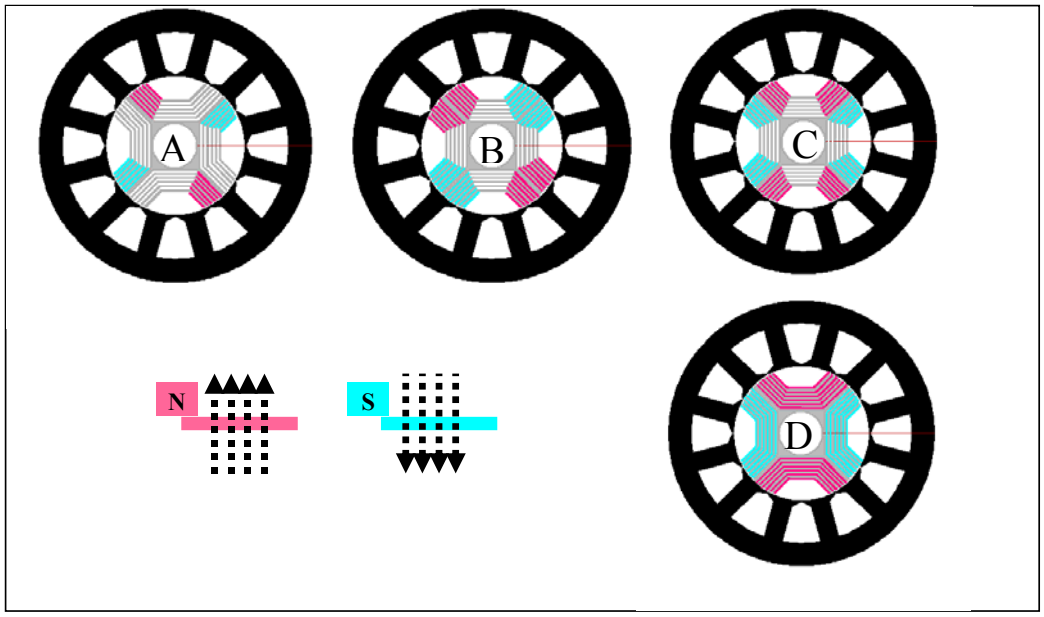


Figure 5. Modified synchronous reluctance motor types with PMs added between the rotor's steel layers. (a) alternating single magnets, (b) back-to-back magnets, (c) alternating dual magnets, and (d) full pole magnets.

Comparison of Torque Generation

In the following figures, the suffix to the rotor type _s indicates that the stator teeth had shoes attached, and _ns indicates that the teeth had no shoes attached. Figure 6 compares designs B_s and C_s and shows that C, the rotor with consecutive poles partially loaded with PMs of the **same** polarity has the highest peak torque value. For about one-half of the angle range, though, the type B design exhibits higher torque values.

Figure 7 compares the torque as a function of control angle for motors with different rotors for each of the two stator types. The designs fully loaded with PMs, D_ns and D_s, have the highest peak torque values. The design without shoes has a slightly higher maximum torque. Although torque is zero for γ = 120 eDeg, which is the angle where the radial flux is maximum corresponding to the green line in Figure 8, the maximum torque occurs for γ = 265 eDeg rotating in one direction and 335 eDeg in the other. The notation, eDeg, means electrical degrees. The average flux at 335 eDeg also happens to be a minimum. Comparison of the peaks and valleys in Figures 7 and 8 shows that higher average fluxes do not necessarily produce higher torques at the corresponding control angles.

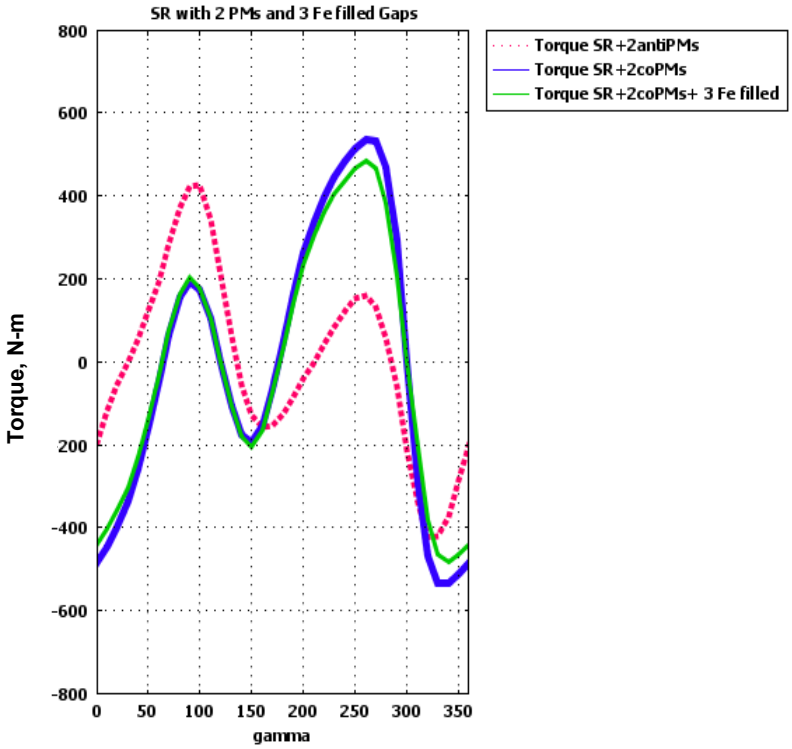


Figure 6. Torque as a function of stator current angle, γ.

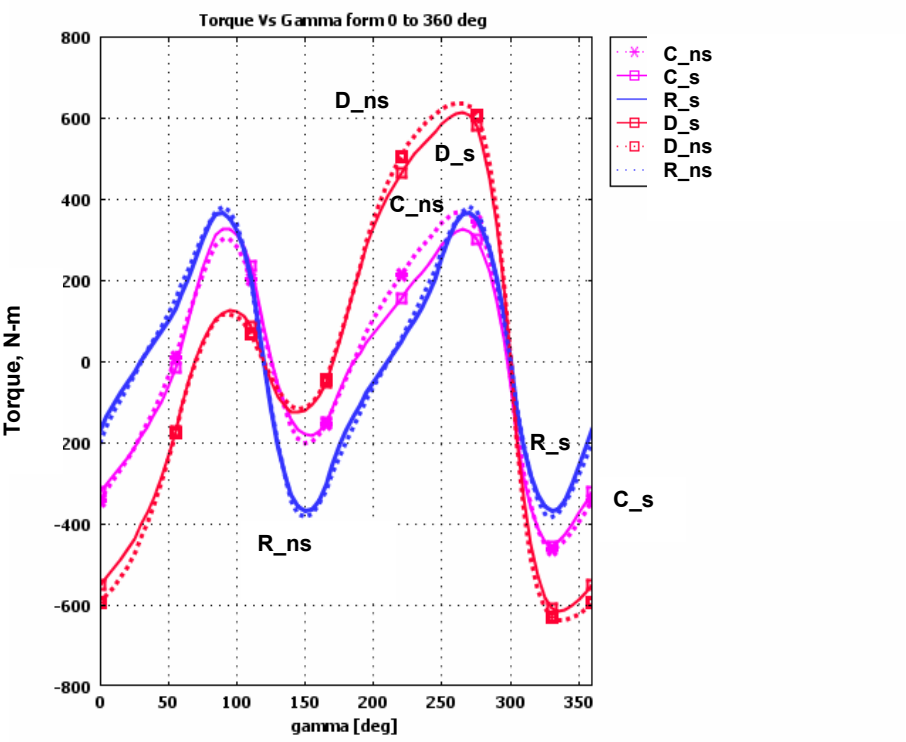


Figure 7. Torque as a function of stator current angles from 0 to 360 eDeg.

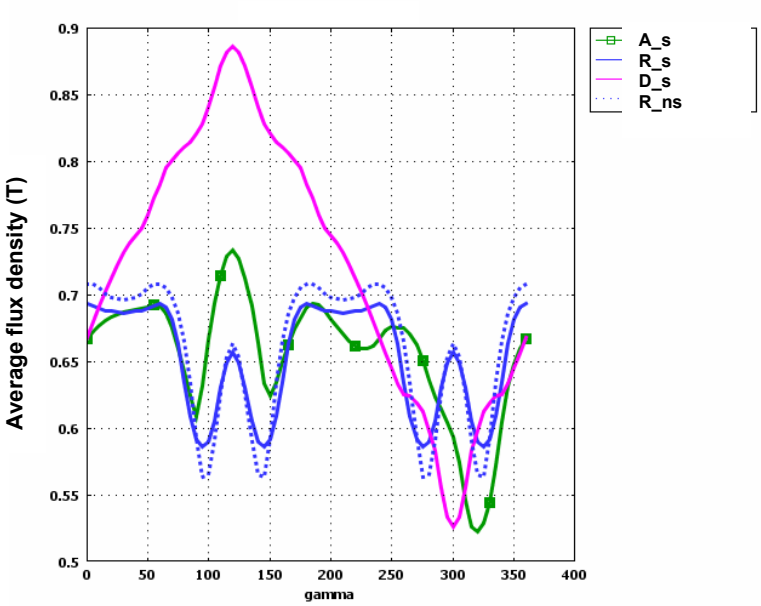


Figure 8. Average flux at the rotor surface for stator current angles from 0 to 360 eDeg.

Flux Shapes along the Rotor Periphery

In this section we illustrate the impact of saturation and stator/rotor nonuniformity on the magnitude and shape of the stator and rotor. Figure 9 shows the permeability dependence on local magnetic flux for the two cases considered: saturating and nonsaturating. The figures below correspond to a motor of type A with no shoes in the stator teeth. The stator current is 400 Arms. Figures 10 and 11 show the dramatic reduction in torque and flux levels and shape distortion when saturation is considered. The peak torque is three times smaller when saturation is considered.

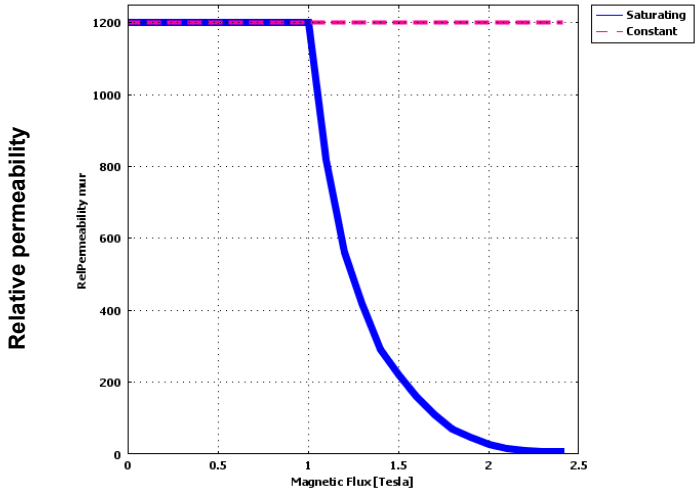


Figure 9. Permeability dependence on flux for study on the effect of saturation.

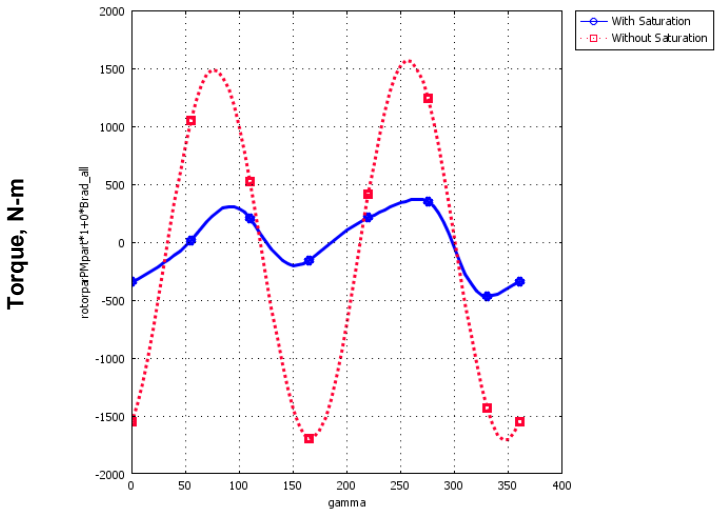


Figure 10. Torque vs control angle, γ, with and without saturation.

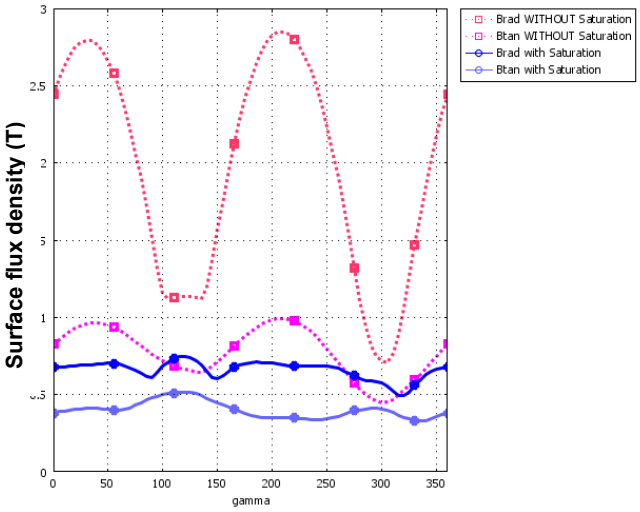
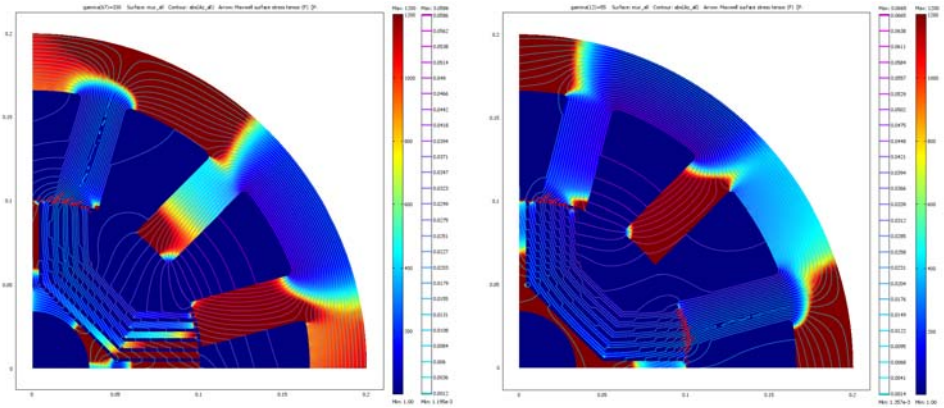


Figure 11. Average radial and tangential rotor surface flux components vs control angle, γ, with and without saturation.

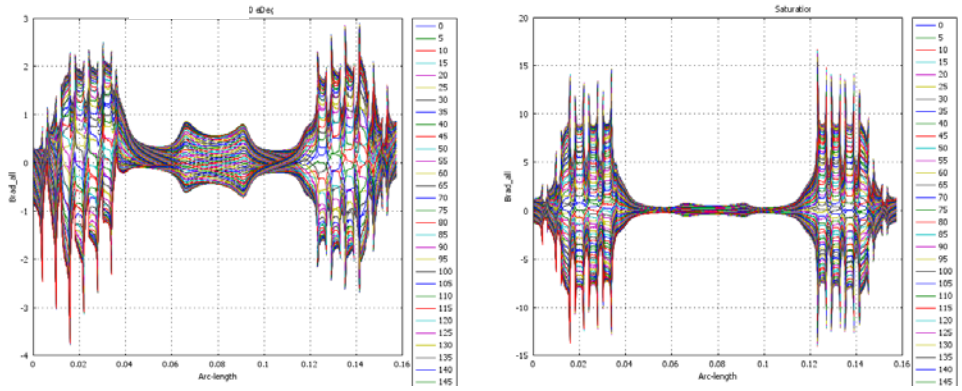
Note that maximum torque corresponds to the situation in which the control angle is such that the two stator teeth close to the rotor iron pieces are unevenly loaded with magnetic energy. In Figure 12(b) the two are heavily loaded, saturated, and because they attract the rotor's iron in opposite directions, they cancel each other and produce no net torque.



(a) for γ= 330 eDeg where torque is maximum **(b) for γ = 55 eDeg where torque is zero**

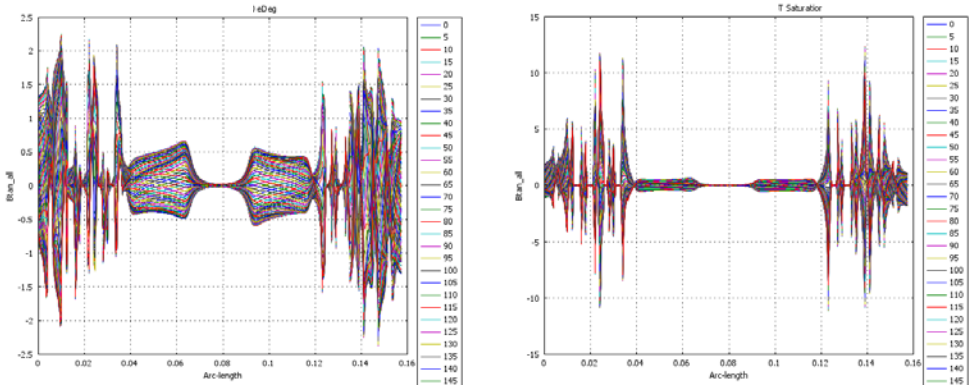
Figure 12. Permeability and flux lines in a type A motor with no shoes on the stator teeth. The bottom of the scale (dark blue) corresponds to $\mu_r = 1$ (saturated iron), and the top of the scale (dark red) corresponds to $\mu_r = 1200$ (unsaturated iron).

In Figures 13 and 14, the envelope created by the shapes of the radial and tangential components of the flux distribution around the rotor surface are shown for all angle control positions from 0 to 360 eDeg. For clarity, the same is shown only for control angles from 0 to 45 eDeg in Figures 15 and 16. Better yet, Figure 17 shows the flux shapes only for the control angle that produces optimal torque in the motor. As can be seen in Figure 10, these angles are 330 eDeg with saturation and 350 eDeg without saturation.



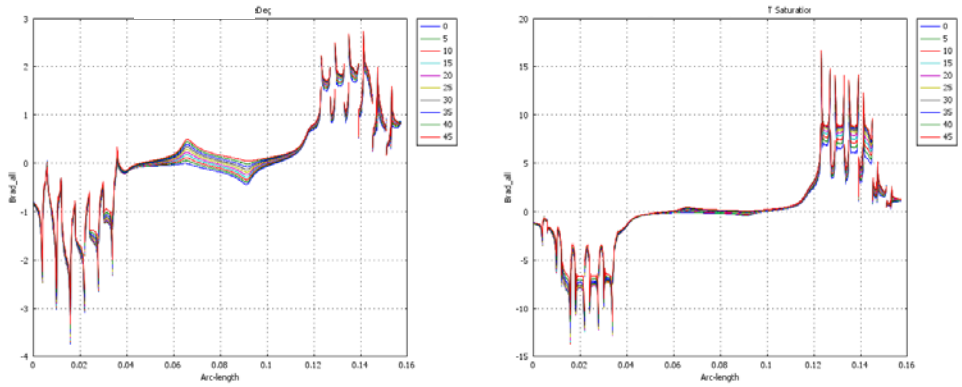
(a) Saturation **(b) No saturation**

Figure 13. Radial flux distribution along the rotor periphery for γ = 0 to 360 eDeg. [The Y-axis scale in (b) is much larger for the nonsaturating case.]



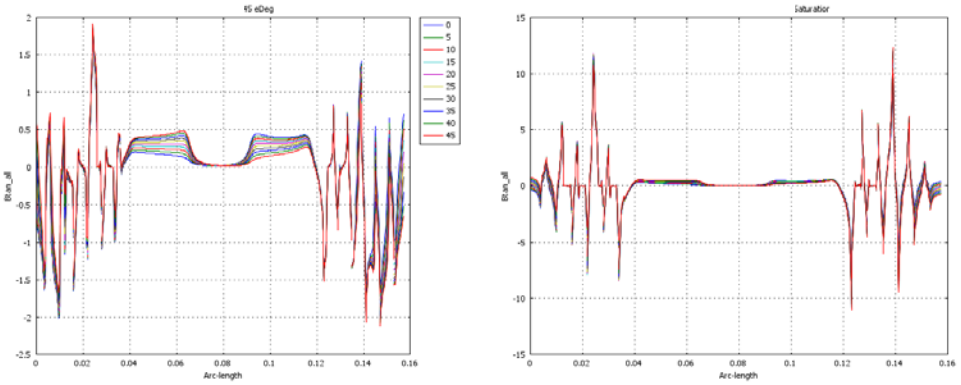
(a) Saturation **(b) No saturation**

Figure 14. Tangential flux distribution along the rotor periphery for γ = 0 to 360 eDeg. [The Y-axis scale in (b) is much larger for the nonsaturating case.]



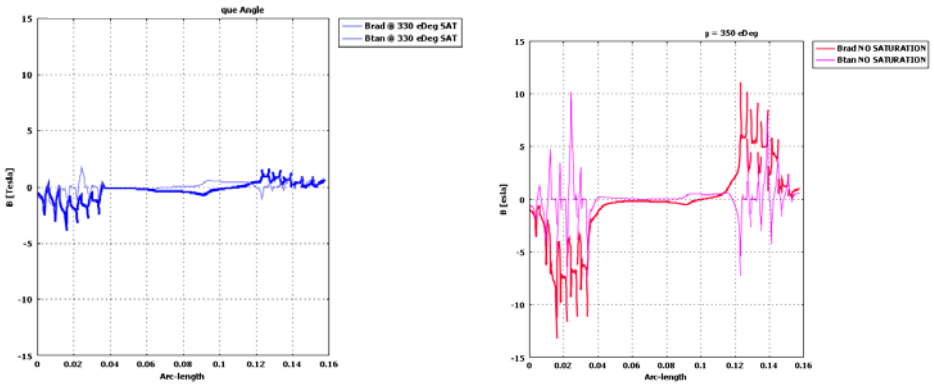
(a) Saturation (b) No saturation

Figure 15. Radial flux distribution along the rotor periphery for γ = 0 to 45 eDeg. [The Y-axis scale in (b) is much larger for the nonsaturating case.]



(a) Saturation (b) No saturation

Figure 16. Tangential flux distribution along the rotor periphery for γ = 0 to 45 eDeg. [The Y-axis scale in (b) is much larger for the nonsaturating case.]



(a) Saturation for γ = 330 **(b) No saturation for γ = 350**

Figure 17. Radial and tangential flux distributions along the rotor periphery for optimal control angle.

Conclusions

Because today's performance of synchronous reluctance motors is below the FreedomCAR targets the potential of the synchronous reluctance motor is often overlooked. These motors exhibit sturdy construction, high performance, efficiency, productivity, and simplicity. It is very likely that the synchronous reluctance motor can overcome the torque ripple problems encountered by switched reluctance motors because of its synchronous operation. For these reasons it is plausible that synchronous reluctance motors may one day be utilized as traction motors if the cost of PMs escalates.

Motor modeling must use actual geometries and solve fundamental equations with as few approximations as possible. At this time finite element analysis seems the best way to directly solve the mathematical equations and account for specific geometric and material properties as well as nonlinear effects such as those introduced by magnetic saturation. Saturation needs to be accounted for as accurately as possible because it affects very significantly the magnitude and shape of the torque and flux distributions.

Because of geometry of stator slots, discreteness of windings, rotor asymmetries, and saturation, actual flux distribution shapes are far from sinusoidal; thus, lumped parameter simulations are always suspect until measured data are available and adjustments are made to the models. This suggests that it will be a challenge to develop a reliable per-phase model of a synchronous reluctance motor.

Our finite-element studies described above have shown that the power density of synchronous reluctance motors will always benefit from the addition of PM in the rotor; however, adding magnets makes this motor configuration an internal permanent magnet motor, which is a different research area. A major reason for studying reluctance motors is to learn how to harvest maximum magnet-free torque from them at all speeds; furthermore, eliminating magnets could become strategic in the future because of market trends.

Although these conclusions come from computations of a reluctance motor, they can be extended generically to modeling electric motors in general because most stators are similar and because saturation is unavoidable for high power densities.

Future Direction

Fruitful areas for further research on synchronous reluctance motors include developing ways to harvest additional torque. Approaches are to drive the motor with a nonsinusoidal waveform, to optimize the control for high-speed operation, and to match the effective number of stator turns to the speed and power requirements of the motor and explore how to switch the stator turns in and out of the circuit

during operation of the motor. It is expected that combining these approaches in a single design can meet the FreedomCAR performance targets as well as the cost targets.

Integrated design and modeling tools are needed to accurately compute the performance of a motor. Traditionally the interfacing between computer-aided drafting (CAD) and finite-element (FE) programs is limited to being able to import the CAD-created geometry to the FE software for analysis. Changes in the geometry require not only reimporting the drawing but also redefining properties, sources, and boundary conditions on the FE side. As a result progress has been slow and tedious. To overcome these interface problems, there is a new approach in which CAD and FE programs interact seamlessly so that changes in the CAD side are automatically incorporated into the FE side, and motor performance can be assessed quickly and effortlessly. Our experience has pointed toward the 64-bit operating system with SolidWorks CAD and COMSOL Multiphysics finite element packages as very promising for the simultaneous solution of electromagnetic, mechanical, and thermal equations of interest in motor design and evaluation computing.

Publications

P. J. Otaduy and J. W. McKeever, *Modeling Reluctance Assisted PM Motors*, ORNL/TM-2005/185, Oak Ridge National Laboratory, Jan. 2006.

References

1. T. J. E. Miller, *SPEED's Electric Motors*, University of Glasgow, 2002.
2. T. J. E. Miller, *SPEED CONSORTIUM PC-BDC Ver. 6 User's Manual,* University of Glasgow, May 1, 2002.
3. *COMSOL Multiphysics User's Manual*, Version 3.2, COMSOL, Inc., 2006.

3.5 Advanced Traction Motor Development

Principal Investigator: Sam Nelson
Oak Ridge National Laboratory
National Transportation Research Center
2360 Cherahala Boulevard
Knoxville, TN 37932
Voice: 865-946-1327; Fax: 865-946-1262; E-mail: nelsonscjr@ornl.gov

DOE Technology Development Manager: Susan A. Rogers
Voice: 202-586-8997; Fax: 202-586-1600; E-mail: Susan.Rogers@ee.doe.gov

ORNL Program Manager: Mitch Olszewski
Voice: 865-946-1350; Fax: 865-946-1262; E-mail: olszewskim@ornl.gov

---

Objectives

The objective of this task is the development of advanced traction drive motors that would not be pursued by industry alone because of the high risks and uncertainty of long-term earnings. The goal of this task is to develop an advanced traction drive motor with improvements in motor torque capability, efficiency, power density, and cost reductions that will meet the 2010 FreedomCAR goals.

Approach

As a result of a request for proposals, Unique Mobility, Inc. (UQM) was awarded a subcontract to design a state of the art motor to meet FreedomCAR targets. The approach by UQM was to consider the many motor topologies that have been used for traction drive applications, including brushed direct current (dc), permanent magnet (PM) brushless dc (BLDC), alternating current (ac) induction, switched reluctance, and synchronous reluctance machines. Each motor topology was assessed to determine the design that could best meet the 2010 FreedomCAR goals and traction motor technical targets. The advantages and disadvantages of each motor topology were considered, and it was determined that the PM BLDC has consistently demonstrated an advantage in terms of power density and efficiency. After the determination of the motor topology, a design trade study was performed to direct the design approach within that motor topology. A combination of finite-element analysis (FEA) and motor design equations was used to evaluate the design choices. A final design was solidified, and the expected performance of the design was determined.

Major Accomplishments

The technical report, *FreedomCAR Advanced Traction Drive Motor Development Phase 1*, was issued September 2006. This report documents the design effort and conclusions reached by UQM during the Phase 1 task. A 6 pole-pair machine with 36 slots in a 3-slot per pole configuration was determined to be the final design choice. The final design met or exceeded the majority of the 2010 FreedomCAR goals and traction motor technical targets.

Technical Discussion

Of the machine technologies, the PM brushless dc (PMDC) motor has consistently demonstrated an advantage in terms of power density and efficiency. A design trade study was performed for the PMDC motor to determine the motor configuration best suited to meet the motor requirements for the FreedomCAR specification. The three motor configurations that were evaluated in the trade study were the magnet-dominant internal PM machine (IPM), a reluctance-dominant IPM, and a surface-mounted PM machine (see Figure 1). Parametric finite-element models that define the geometry

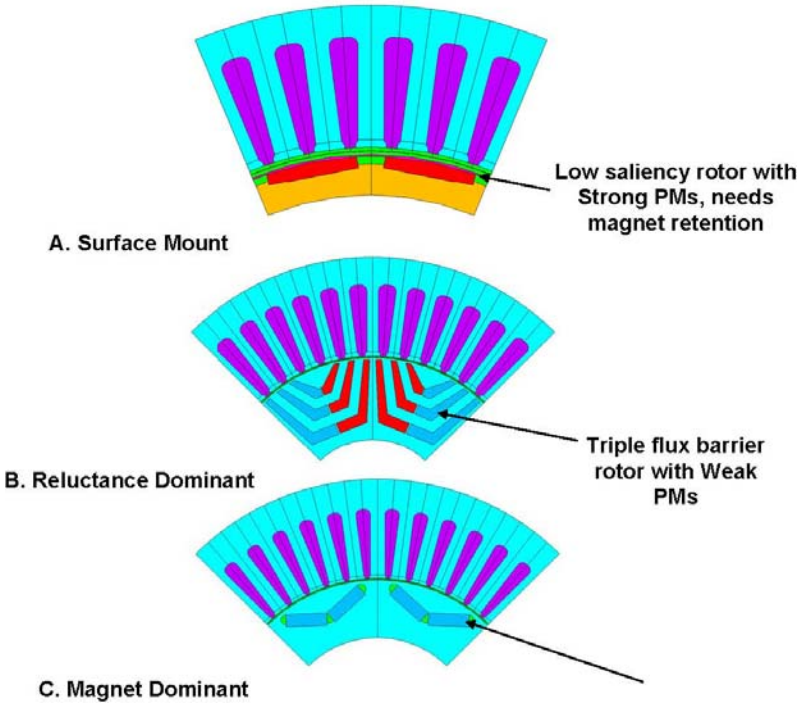


Figure 1. Physical topology, three designs.

of each configuration were created such that the geometry for each design could be quickly manipulated and reevaluated. FEA was used to evaluate motor parameters such as the back-emf constant (Ke) as well as the quadrature axis (q-axis) and direct axis (d-axis) inductance at a variety of currents. The flux density in the stator teeth and return path was also evaluated for use in calculating the iron losses. After the machine parameters were evaluated with FEA, a Mathcad model was used to simulate performance. The Mathcad model is based on the motor design equations and the equations for electric machine vector analysis. This model was used to predict motor performance by utilizing the motor parameters that were determined by FEA. This sequence of design iteration was chosen to provide a quick yet accurate method of design evaluation, given the geometry dependence on the motor parameters. The designs were iterated until each could meet as many of the FreedomCAR motor requirements as possible.

Trade Study

The purpose of the trade study was to identify a design direction for the FreedomCAR advanced traction motor and to identify aspects of each design that should be integrated into the advanced traction motor design. The results of the trade study indicated that the magnet-dominant design configuration would best fit the FreedomCAR specifications. Table 1 compares the performance predictions for each design with the FreedomCAR specifications. In Table 1, the values marked in red type indicate the performance predictions that did not meet the specification. The magnet-dominant design met all specifications except the peak power-to-volume specification (power density).

Table 1. Comparison of three design performances with specification

	Freedom Car Specification	Magnet Dominant Design MGDOM11	Reluctance Dominant Design REDOM	Surface Mount Design SURMO5
Top Speed (rpm)	10,000	10,000	10,000	10,000
325 Vdc (kW)	55	55	55	55
Battery Operating Range (V)	200-450	same	same	same
Nominal Battery Voltage (V)	325	same	same	same
Maximum Current at motor (Arms)	400	345	480	428
Characteristic Current (Arms)	<400	240.38	272.5	319.4
Efficiency at 10% of maximum Speed and 20% of Rated Torque (1000 rpm, 52.4 Nm)	>93	93.9	93.0	95.0
Efficiency at 20% of maximum Speed and 20% of Rated Torque (2000 rpm, 52.4 Nm)	>93	96.2	95.8	95.9
Efficiency at 100% of maximum Speed and 20% of Rated Torque (10,000 rpm, 52.4 Nm)	>93	95.4	97.2	92.7
Back-EMF at 100% of Maximum Speed (Vpeak, Line to Line)	<600	600	310	670
Peak Power to Volume Ratio (kW/Liter)	>12.5	10.4	8.8	10.0
Torque Pulsations % of peak Torque	<5	??	??	??
Peak Power to weight Ratio (kW/Kg)	>2.75	2.774	2.228	2.795

Magnet Cost Study

A magnet cost study was conducted to get an accurate picture of current magnet prices for NdFeB magnet materials from a variety of magnet sources, domestic and offshore. Because magnets are a relatively significant part of the total cost of a PM machine, it is beneficial to have good cost data for estimating manufacturing costs. UQM decided that the most accurate way to get cost data in volume is to have actual magnet suppliers quote a simple arbitrary shape in various volume quantities. After receiving the quotes, UQM calculated the magnet cost per pound from the official quotations. UQM requested quotes from magnet sources from the United States, Europe, Japan, and China. Also quoted were Chinese magnets distributed through a U.S. company and a U.S. company that processes finished magnets from Japanese magnet materials.

Each magnet manufacturer or distributor was given the same package of material and part specifications to quote pricing. The package included the drawing and magnetic material specifications. Each manufacturer or distributor was asked to quote each magnet specification in quantities of 10K/year to 100M/year. Each magnet manufacturer was asked to quote four different sets of material properties.

The magnet properties were chosen to a represent high-energy and a high-coercivity magnet in both a sintered and a bonded NdFeB magnet type.

The conclusion from the magnet cost study supports the conclusion from the trade study that the motor development effort should utilize sintered NdFeB magnets. The reason is that the cost per pound of high-coercivity sintered magnets is the same as that of bonded magnets (i.e., about $17 to $20 per pound). The trade study demonstrated that a motor with bonded magnets will utilize significantly more weight in magnets as well as total motor weight for the same performance level. This will significantly increase the cost for the motor.

Rotor Configuration Study

A rotor configuration study was performed with seven different rotor configurations. Characteristics that varied in the study were arranged for magnets (i.e., V-shape and U-shape), number of barriers (single or double), number of bridges (i.e., two, three, and four), and number of magnets per pole (two, three, and four). The stator arrangement, length of rotor, air gap, and current were constant for each configuration. The rotor configuration with U-shape barrier, two bridges, and three magnets per pole was determined to be the best configuration based on significantly more torque for the same size motor and same magnet mass. This rotor configuration will be slated for use in the final design (see Figure 2).

Many design iterations were generated in the development of the final design. The design iterations in this section illustrate the pros and cons of the possible pole count selections. Other design iterations that were not published were generated with a varying amount of analysis. For example, if the torque profile for a given design iteration was not acceptable, the design iteration would be dropped without further analysis. Analysis was performed on a given design iteration until it was found to be unacceptable or it was apparent that improvements could be made to meet the FreedomCAR specification.

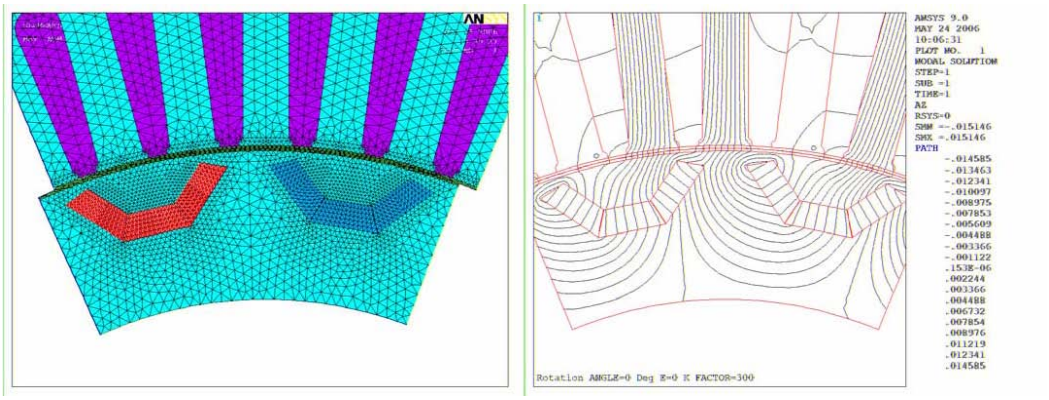


Figure 2. U-barrier, two bridges, three magnets per pole.

Iterative Design Method

All simulations in this section and following sections were conducted assuming an operating temperature of 150°C. This temperature was chosen as a target steady state design point, considering that 105°C is the required maximum inlet temperature and 150°C will allow for a reasonable temperature rise. All design iterations presented here were adjusted so that the maximum required torque, 262 Nm, was reached with 400 Arms leg current. The maximum allowable current according to the specification is 400 Arms. Designs were adjusted in length or turns to make 262 Nm at the maximum current to minimize the inductance and allow peak performance down to 200-V supply voltage. Higher turn counts and inductance will bring down the current but will not allow low-voltage operation.

Motor performance was predicted through means of evaluating the motor parameters, inductance profile (q- and d-axis inductance vs. current), and torque mapping in FEA. These values were then used in conjunction with vector analysis to predict motor performance. The performance models calculated the necessary current at a given operating point from the torque maps. The vector diagram was also evaluated for each point using the inductance values that corresponded to the current demand. The vector analysis determines what phase angle is necessary for operation at a given operating point and if the system will be voltage limited at that point.

The requirement for full-power operation down to 200 V of supply voltage drove the selection of many design features and contributed in determining the pole-pair selection as well. UQM took the approach that the highest pole count that would still allow the efficiency and power requirements to be met would lead to the most compact and power dense design, saving materials and cost. A higher pole count will nearly always give a net benefit in terms of power density so long as the other requirements can be accomplished, such as efficiency and the operating range for voltage, speed, and power.

Six-Pole Pair Design

Meeting the requirements of the specification at a higher power density, but a lower efficiency with the eight pole-pair design as compared with the four pole-pair design, prompted the study of pole-pair combinations between the two. The 6 pole-pair selection was a logical choice, having 36 slots in a 3-slot per pole configuration that allows a simple winding and relatively short end-turns. Iterations of the six pole-pair design led to the final design proving to have a better efficiency and power density than the designs with the other pole combinations.

Table 2 lists the important parameters of the six pole-pair design iteration that became the final design (see Figure 3). This combination yielded short end-turns (0.88 in.) and allowed a relatively short (3.4-in.)

Table 2. Motor parameters, six-pole pair, 3.4 in. (final design)

Overall stator diameter (in.)	8.7
Inner stator diameter (in.)	6.10
Rotor outside diameter (in.)	6.04
Stator stack length (in.)	3.4
End-turn length	0.88
Total axial length (over the end-turns) (in.)	5.165
Tooth thickness (in.)	0.380
Back-iron thickness (magnet return path) (in.)	0.39
Magnet strength (residual induction Br) (T)	1.10
Magnet thickness (in.)	0.165
Magnet weight (lb)	2.21
Minimum bridge thickness (in.)	0.04 (2 bridges)
Torque density (Nm/L)[a]	52.2
Power density (kW/L)[a]	11.0
Winding turns	3
Slots per pole	3
Back-EMF constant (Vpeak/krpm L-L)	47
Winding fill factor (%)[b]	74
Winding resistance (Ω L-L)	0.011
q-axis inductance (μH L-L)[c]	111
d-axis inductance (μH L-L)[c]	75

[a]Calculated using FEA at a 1200 ampere-turn load.
[b]Calculated using the conservative volume calculation.
[c]Includes insulation and copper in magnet wire based sum of square areas.

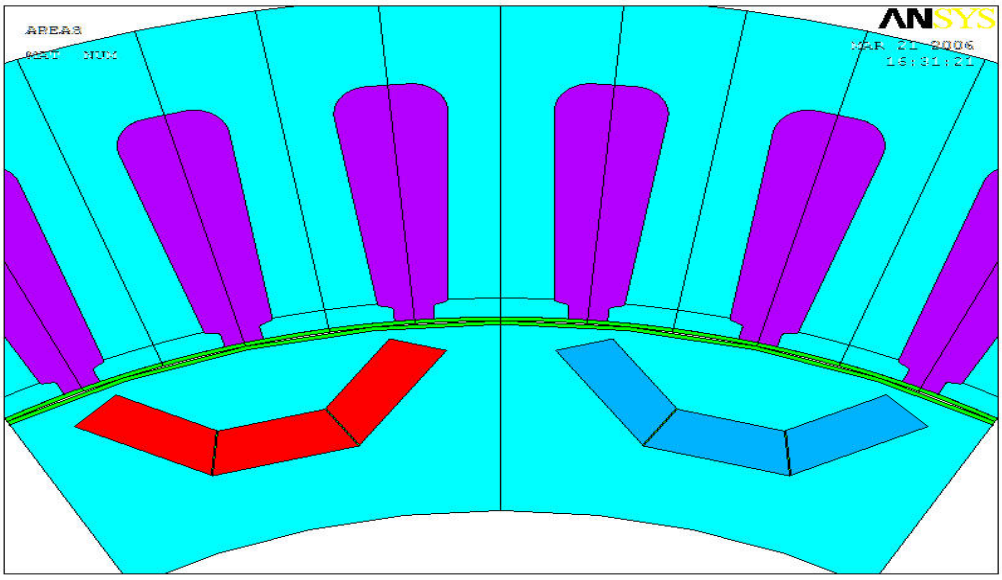


Figure 3. Six-pole pair machine configuration.

stack length as well. At 8.7-in. overall diameter and a total volume of 5 L, the power density is 11 kW/L, better than the design iterations in either of the other pole configurations.

Relatively wide stator teeth (0.380 in.) and back-iron (0.390 in.) reduced flux density and helped to control iron losses, giving good efficiency at high speeds. The motor will be 94.8% efficient at 1000 rpm and 95.6% at 10 krpm, well above the efficiency target of 93%. The peak efficiency, 96.5% is reached at about 4000 rpm and 52 Nm. Also, vector analysis indicated that operation at full power with a 200-V supply would be easily accomplished with this design. The minimum voltage for operation can be maintained below the buss voltage (Vdc) by phase advancing the current to a reasonable angle, and the current never exceeds the maximum allowable current of 400 Arms (see Figure 4).

The eight pole-pair version was able to meet most of the performance specs, but the girth of the iron in the magnetic circuit and the length had to be increased until the weight and volume were higher than expected. The tooth width and return path thickness had to be increased to lower flux density and therefore iron losses. Even so, this design barely met the 93% specification at 10 krpm. In addition, the turn count was dropped from three down to two to lower the inductance and allow performance down to 200 V. The length was increased to compensate for the loss of a turn. Although the end-turns are the shortest of all the designs (0.68 in.), the stack length was the longest (4.2 in.). Unfortunately, with the increased length, the power density of the machine was decreased, and the efficiency was reduced at high speeds. The eight-pole pair machines could not meet the required specification and were eliminated from consideration for the final machine design.

The four-pole pair configuration was evaluated; this configuration has been used in the Prius and other similar applications. The four-pole pair design was able to meet the performance specifications in terms of efficiency, peak power, and voltage range of operation. However, the resulting volume and weight were too high, making the power and torque densities low. Larger volume and weight are partially due to inherently longer end-turns and the requirement for thick stator features. More copper, iron, and magnet are necessary to compensate for less emf because of the lower-frequency operation in comparison to the higher pole counts. Additionally, because there is more magnet weight per pole, more structural support is needed to retain the magnets at high speeds. Consequently, the bridge thickness needed to be greater. With more bridges and/or thicker bridges, more magnet flux is shunted away from

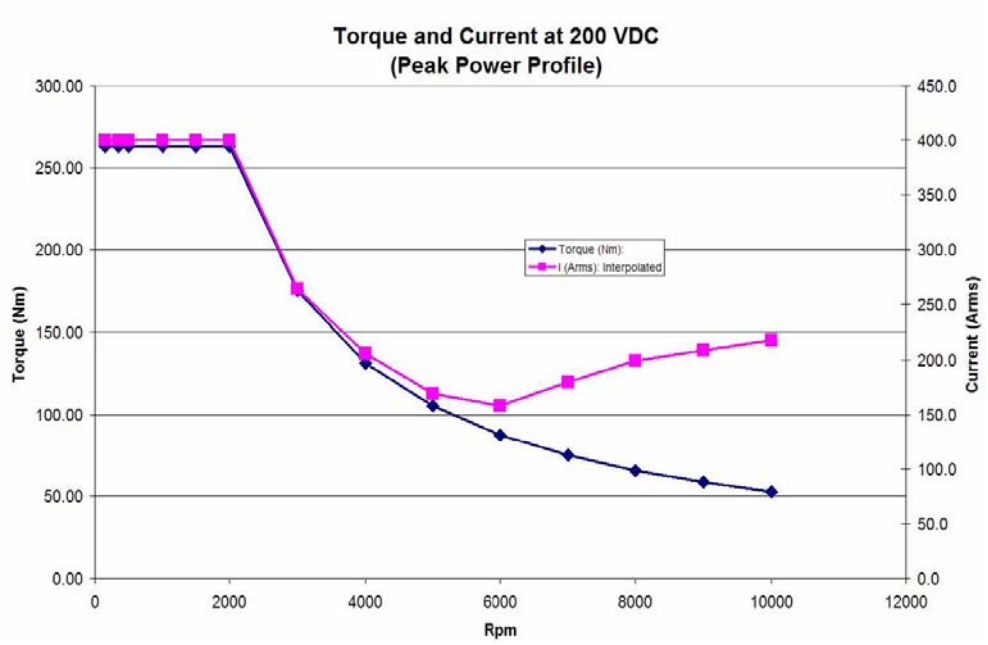


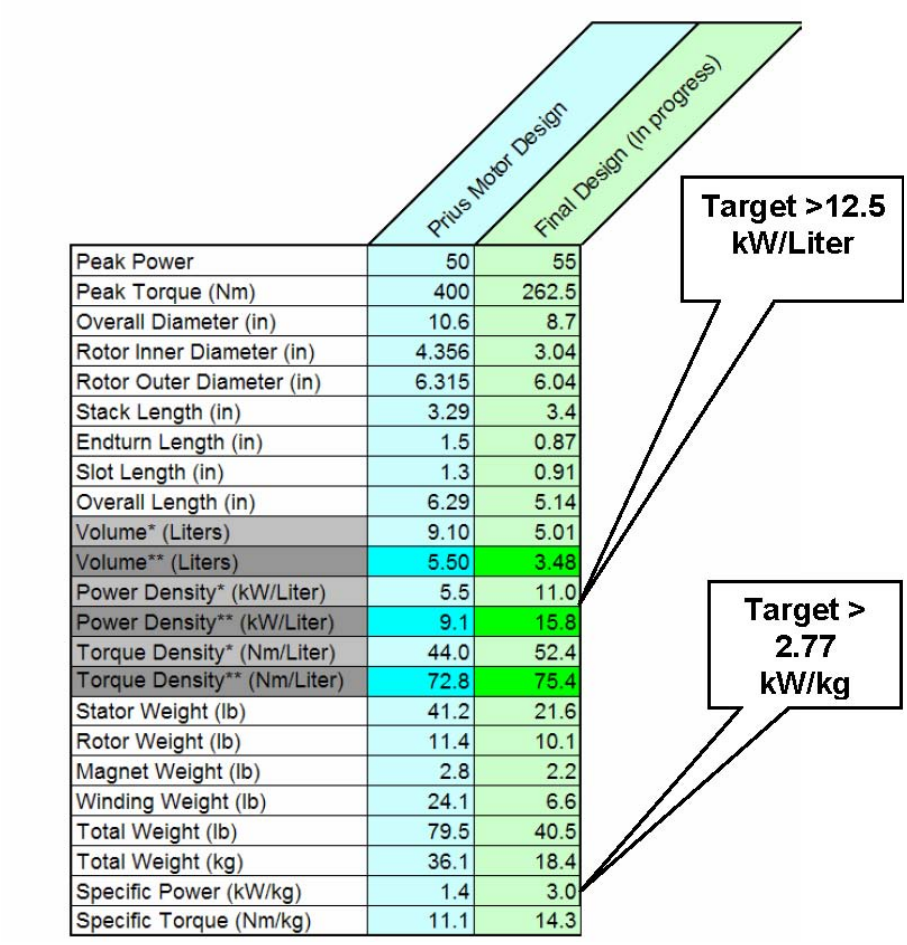
Figure 4. Current and torque profile at 200-Vdc, peak power.

the stator, reducing performance. The four-pole pair design met the efficiency requirements at 52 Nm across the speed range. The efficiency at 1000 rpm was slightly above 95% and slightly below 95% at 10,000 rpm. This four-pole pair design does meet the requirement for full power (i.e., 55 kW) at 200 V across the speed range and was eliminated from consideration for the final design.

During the Phase 1 design effort, pole-pair combinations between four- and eight-pole pairs were investigated. The six-pole pair configuration proved to be the best choice. Magnet weight was the lowest, and the power density was the best of the three: 11.0 kW/L for six-pole pairs, 10.4 kW/L for eight-pole pairs, and 8.6 kW/L for four-pole pairs. These power densities are based on conservative volume calculations.

Comparison with Prius Motor

The Prius motor is held in high regard in the industry and probably considered state-of-the-art in terms of electric propulsion motors for hybrid electric cars. For this reason, it makes sense to compare the motor design developed in this program with the Prius benchmark, in order to determine the value in continued development of this motor design. Because materials represent the most significant part of the cost in automotive volume production, size reduction is paramount. Figure 5 compares some of the major dimension and figures of merit of the two motors. In this section, all comparisons are made at the active materials level. Note that overall diameter and length are greatly reduced in the FreedomCAR design over the Prius motor design. Overall diameter of the Prius motor is 10.6 in., but the FreedomCAR design is only 8.7 in. The FreedomCAR design is nearly 2 in. smaller in diameter and down from 6.29 to 5.14 in. in overall length. Also, the reduction in the volume of the FreedomCAR design is approximately 40%, and weight is reduced by nearly 50% from the Prius motor. Some of this size reduction is due in part to the difference in operating profiles of the two motors. The FreedomCAR design makes more power, 55 kW as opposed to 50 kW for the Prius motor; however, the Prius motor operates in a lower speed range and



	Prius Motor Design	Final Design (In progress)
Peak Power	50	55
Peak Torque (Nm)	400	262.5
Overall Diameter (in)	10.6	8.7
Rotor Inner Diameter (in)	4.356	3.04
Rotor Outer Diameter (in)	6.315	6.04
Stack Length (in)	3.29	3.4
Endturn Length (in)	1.5	0.87
Slot Length (in)	1.3	0.91
Overall Length (in)	6.29	5.14
Volume* (Liters)	9.10	5.01
Volume** (Liters)	5.50	3.48
Power Density* (kW/Liter)	5.5	11.0
Power Density** (kW/Liter)	9.1	15.8
Torque Density* (Nm/Liter)	44.0	52.4
Torque Density** (Nm/Liter)	72.8	75.4
Stator Weight (lb)	41.2	21.6
Rotor Weight (lb)	11.4	10.1
Magnet Weight (lb)	2.8	2.2
Winding Weight (lb)	24.1	6.6
Total Weight (lb)	79.5	40.5
Total Weight (kg)	36.1	18.4
Specific Power (kW/kg)	1.4	3.0
Specific Torque (Nm/kg)	11.1	14.3

*Utilizes the most conservative method of calculating volume.
**Utilizes the least conservative method of calculating volume.

Figure 5. Power density comparison—FreedomCAR design vs Prius motor.

produces more torque, 400 Nm at 1200 rpm as opposed to 262 Nm at 2000 rpm for the FreedomCAR motor. Because electric motors scale with torque more closely than with power, note that the torque density of the FreedomCAR motor design is still 18% higher than that of the Prius Motor and its power density is 100% higher than that of the Prius.

The difference in motor parameters between the two machines includes a much higher back-emf voltage for the Prius motor, 141 as opposed to 48 Vpeak/Krpm (see Figure 6). This gives a maximum voltage of 480 V for the FreedomCAR design and 846 V for the Prius, necessitating a higher inverter voltage rating for the Prius system. Conversely, the Prius motor would require a lower current rating for the inverter, having a maximum motor current of 250 A, as opposed to 400 A for the FCVT motor.

	Prius Motor Design	Final Design (In progress)
Pole Pairs	4	6
Slots Per Pole	6	3
Back-EMF Constant @ 20 C	141.7	48
Resistance (Ohms L-L) at 20 C	--	0.011
Phase Inductance Lq (uH)*	--	111
Phase Inductance Ld (uH)*	--	75
Saliency Ratio	--	1.48
Slot Fill Factor	0.84	0.77
Residual Induction (T)	1.12	1.15
Maximum Current (Arms)	250	400
Maximum Speed (rpm)	6000	10000
Minimum Voltage	**200	200
Maximum Voltage	500	450
Max Operating Temp (Celcius)	170	>180
Magnet Retention Sleeve Required	No	No
Flux Barriers	V-Shape	U-Shape
Magnet Shapes	Rectangle	Rectangle

*Boost converter required to achieve this voltage range.

Figure 6. Motor parameter comparison—FreedomCAR design vs Prius motor.

Manufacturing Cost Estimate

UQM chose to estimate the cost of this machine in the most likely automotive production scenario, as a Tier 3 motor manufacturer supplying to a Tier 2 transmission manufacturer. As a result, the gearing cost is not included in the estimate, and the housing is at least partially integrated with the transmission as electric machines are presently being integrated in hybrid vehicles. UQM anticipates this transmission—electric machine integration trend to continue and therefore has chosen to estimate cost as a motor manufacturer would supply to the transmission manufacturer. The water jacket or heat sink is considered part of the motor, which will be included in the cost estimate. The water jacket will encompass the outer diameter of the stator laminations, and the assembly will be pressed into the transmission housing or bolted to the transmission housing as an attachment. The rotor is expected to be coupled and installed on one of the primary shafts of the transmission. Therefore, a hub that supports the rotor ring will be needed to adapt to the shafting of the transmission. Obviously, exact hardware would be application-specific; however, for the purpose of this cost study, a conceptual rendition of the applicable motor parts is depicted in Figure 7. This figure represents a good estimation of the necessary motor parts as supplied to a transmission manufacturer for electric machine integration within a transmission.

The parts and their estimated weights that were considered in this manufacturing cost analysis are listed in Table 3.

Material prices for copper, NdFeB, aluminum, and other materials were based on current market prices.

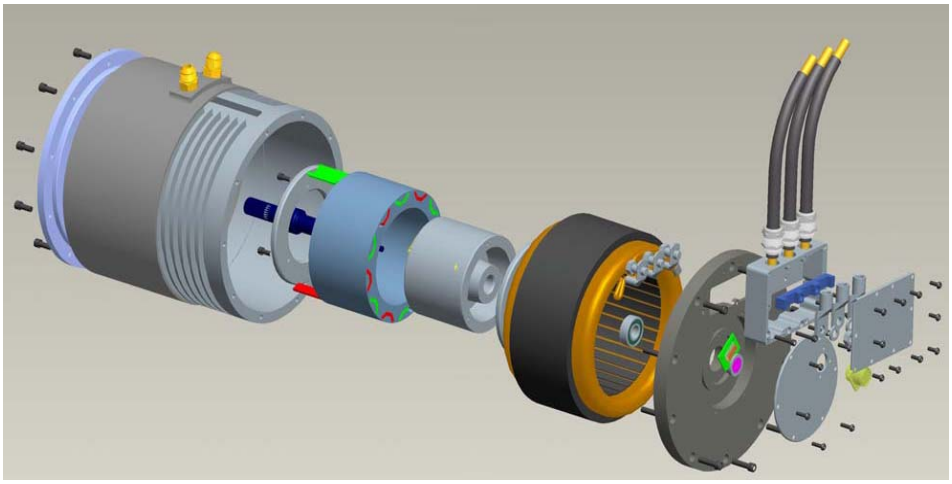


Figure 7. Motor assembly—exploded view.

Table 3. Parts included in manufacturing cost estimate

Part description	Weight of parts/unit (lb)
Stator lamination stack (243 laminations)	21.6
Rotor lamination stack (243 laminations)	10.0
Magnets NdFeB	2.215
Winding magnet wire (copper)	7.0
Bearings	2[a]
2 piece housing/water jacket (as cast)	5[a]
Stator finished (wound and insulated)	N/A
Rotor hub (as cast)	4[a]
Hub machining	N/A
Housing machining	N/A
Circuit board with position sensors (hall effects)	N/A

[a]Weights that are estimated, not actual values.

Figure 8, illustrates the results of the cost study generated by the UQM manufacturing group. The cost data presented here represent the cost of the motor and do not include tooling amortization or margin. The estimated unit prices are $399.60, $299.73, $239.78, and $203.85 at volumes of 100K, 250K, 500K, and 1M per year, respectively. The cost target for the 2010 specification was specified in at $7/kW. The chart also graphs the cost data in terms of cost/kW. The red horizontal line represents the cost target. At 55-kW peak power, the cost target is met for all quantities slightly over 100K units per year and above. As explained in the report, *FreedomCAR Advanced Traction Drive Motor Development-Phase 1*, the final design will actually be capable of up to 110 kW peak at nominal voltage and 4000 rpm. At 110 kW above 4000 rpm, the cost/kW is reduced well below the target.

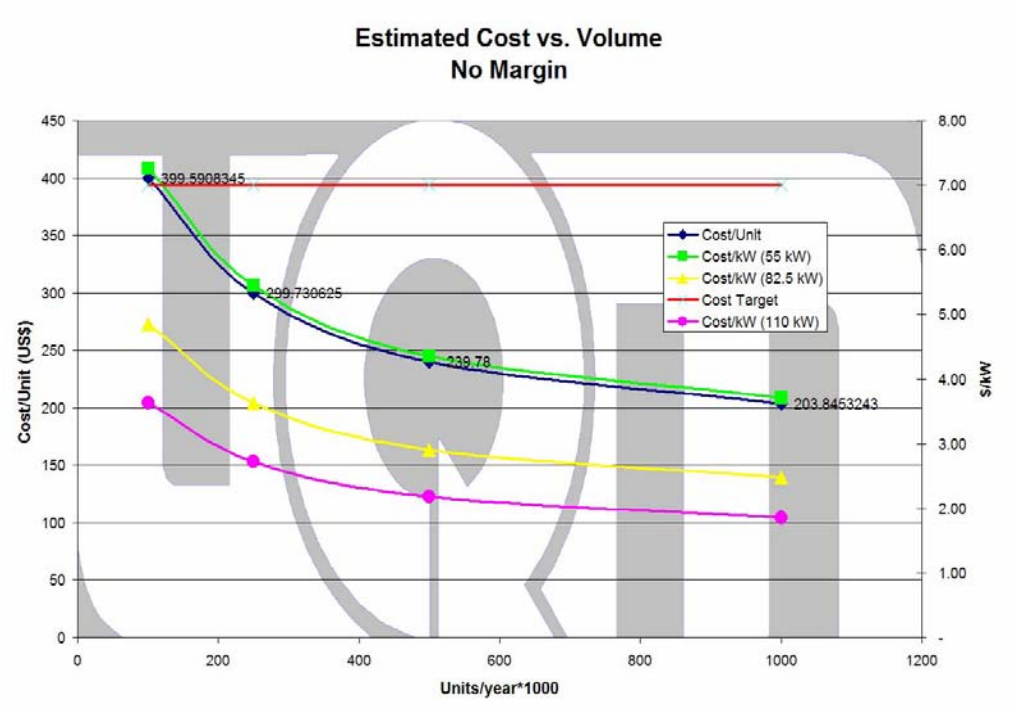


Figure 8. Cost vs volume for the FreedomCAR motor.

Conclusion

A six-pole pair configuration PM motor was determined to be the best choice for the FreedomCAR design. The rotor configuration has U-shaped barriers with two bridges per pole. The stator has 36 slots in a 3-slot per pole configuration that allows a simple winding and relatively short end-turns. Iterations of the six-pole pair design led to a final design with a better efficiency and power density than the designs with other pole combinations.

Table 4 compares the FreedomCAR target with the predicted performance for the FreedomCAR motor design. The motor meets or exceeds the target for power (i.e., continuous and peak) and efficiency. Because the peak power capability of the motor ranges from 55 kW at 2000 rpm to 110 kW at 4000 rpm, power density, specific power, and cost per kilowatt were calculated at both 55 and 100 kW.

Table 4. Comparison of FreedomCAR motor with target

Description	Predicted for FreedomCAR design	FreedomCAR target
Peak power (kW)	55–110[a]	55 kW
Duration at 55 kW (s)	40	18
Continuous power (kW)	30	30
Quantities based on active materials		
Power density (kW/L)—based on 55 kW	11–15.8[b]	>12.5
Power density (kW/L)—based on 110 kW	22–31.6[b]	>12.5
Specific power (kW/kg)—based on 55 kW	3	>2.75
Specific power (kW/kg)—based on 110 kW	6	>2.75
Cost per kW ($/k/W)—based on 55 kW	3.4–6.8[c]	<3.2
Cost per kW ($/k/W)—based on 110 kW	1.7–3.4[c]	<3.2
Quantities based on full motor package		
Power density (kW/L)—based on 55 kW	6.6	>5
Power density (kW/L)—based on 110 kW	13.3	>5
Specific power (kW/kg)—based on 55 kW	1.74	>1.3
Specific power (kW/kg)—based on 110 kW	3.47	>1.3
Cost per kW ($/k/W)—based on 55 kW	5–9.5[c]	<7
Cost per kW ($/k/W)—based on 110 kW	2.5–4.8[c]	<7
Other motor requirements		
Maximum current (Arms)	400	400
Back-EMF (V)	480	<600
Efficiency (%)	94.8–96.5	>93
Characteristic current (Arms)	344.6	<400
Maximum coolant temperature (ºC)	105	105

[a]Peak power is 55 kW at 2000 rpm, 82.5 kW at 3000 rpm, and 110 kW at 4000 rpm.
[b]The low end of the range is based on the most conservative volume calculation, and the high end of the range is based on the least conservative volume calculation.
[c]The range refers to the cost at 100k volume per year to the cost at 1M per year quantities.

Future Direction

This task completes the Phase 1 traction drive development task. Development of an advanced traction drive motor will continue with other tasks.

Publications

FreedomCAR Advanced Traction Drive Motor Development—Phase 1—September 2006, ORNL/TM-2006/UQM, Oak Ridge National Laboratory, September 2006.

3.6 Development of Improved Powder for Bonded Permanent Magnets

Principal Investigator: Iver E. Anderson
Metallurgy and Ceramics Program
Ames Laboratory, Iowa State University
Ames, IA 50011
Voice: 515- 294-9791; Fax: (515) 294-8727; E-mail: andersoni@ameslab.gov

DOE Technology Development Manager: Susan A. Rogers
Voice: 202-586-8997; Fax: 202-586-1600; E-mail: Susan.Rogers@ee.doe.gov

Program Manager: Mitch Olszewski
Voice: 865-946-1350; Fax: 865-946-1262; E-mail: olszewskim@ornl.gov

---

Objectives

- Increase the maximum operating temperature from 120 to 200˚C while maintaining desirable magnetic properties of permanent magnet (PM) materials to enable electric drive motors with improved operating characteristics.
- With goal of cost reduction for the new high temperature PM materials in electric drive motors, develop improved processing for bonded isotropic magnets produced by net-shape molding technologies for high-volume manufacturing.

Approach

- Develop innovative permanent magnet alloy design and processing technology for production of improved PM alloy powders for bonded isotropic magnets with a tolerance for high temperatures.
- Investigate PM alloy design improvements through melt-spinning methods, with the specific goal of developing an improved spherical magnet alloy powder through gas atomization processing.
- Develop an enhanced gas atomization process and a gas-phase powder surface reaction capability for simplified production and environmental protection of fine spherical powder for isotropic bonded magnets.
- Conduct experimental isotropic permanent magnet molding trials on as-atomized and annealed magnet powders to characterize isotropic bonded magnet properties and microstructures in collaboration with industrial partners, e.g., Arnold Magnetic Technologies (AMT) and Unique Mobility (UQM) and research partners, e.g., ORNL.

Major Accomplishments

- Achieved a further improvement of the room temperature maximum magnetic energy product, BH_{max}, with a reduced Co content (33% less) of our MRE-(Fe,Co)-B-TiC magnet alloy, demonstrating significant alloy cost benefits without any detectable decrease in magnetic performance up to 200C.
- Compression molded a large set of bonded magnet samples from a portion of the 100 kg commercial (Magnequench International) batch of magnet flake particulate (MQP-11HTP), formulated from an enhanced Ames magnet alloy design (WT-096), for the first stage of external testing of uncoated flake particulate.

- Successfully gas atomized the Zr + TiC modified MRE-Fe,Co-B magnet alloy with effective control of the composition and with the first demonstration of in-situ fluoride passivation (with NF_3), resulting in an energy product of 9.1 MGOe for a significant fraction (greater than 80% yield) of the spherical powder.
- Developed (and started atomization experiments on) a combined Zr and ZrC addition for the MRE-Fe,Co-B magnet alloy with phase nucleation and temperature stability properties more suitable than the previous Zr and TiC addition for direct translation to gas atomization of fine spherical powders for advantageous injection molding of bonded magnets.
- Confirmed the improved environmental stability with standard long term irreversible loss tests (LTILT) of bonded magnets that were compression molded with PPS at Ames Lab from as-received MQP-11HTP particulate and commercial MQP-14-12 particulate, where the LTILT testing was performed at Arnold Magnetic Technologies (AMT) and verified that our prototype (uncoated) powder matches the stability of the best commercial powders at 150C and provides enhanced magnetic performance at that temperature.
- Provided the second of two sets of net-shape isotropic bonded magnet samples to ORNL for testing in their experimental electric motor and in other devices to enable head-to-head comparisons, including high operating temperatures, of industrially bonded magnets (produced by AMT) made from commercial (MQP-type O) and experimental (MQP-11HTP) particulate, but testing problems have forced another partner to be sought.

Technical Discussion

Executive Summary

To meet performance and cost goals for advanced electric drive motors, it is essential to improve the alloy design and processing of permanent magnet (PM) powders. This project is expected to develop the materials and processes needed to fabricate high performance, isotropic bonded permanent magnets (PM) that can be used for traction motors with an internal PM rotor design. The fully developed PM material must be suitable for elevated temperature (180-200˚C) operation to minimize cooling needs, where the increased high temperature magnetic performance is more critical than room temperature magnetic properties. In addition to the importance of the magnetic alloy design for high temperature operation, a novel spherical powder production process, ideally with in situ powder coating capability, is a final project outcome. It should be noted that the starting alloy cost will be about the same as current alloys, but the powder production costs could be reduced and the total magnet material used per motor could be less, if motor design is optimized for bonded magnet use. Moreover, the spherical coated powder can promote manufacturing simplicity by reducing molding pressures and can enhance performance and reliability for the bonded magnets, through increased volumetric loading and reduced irreversible magnetic losses from oxidation and corrosion. The final project outcome is likely to be a significant reduction in the total manufacturing cost of PM traction motors, since isotropic bonded PM processing can utilize injection or compression molding technology in a net shape/assembly forming approach for mass production of internal PM rotors. These advantages should accelerate the widespread introduction of fuel-saving hybrids and could be claimed by the AEEPM program as a clear beneficial outcome.

Introduction

Permanent magnets based on RE2Fe14B intermetallic compounds, mostly Nd2Fe14B have had a large technological impact. Over the past 20 years, extensive research has been performed to develop and improve its magnetic properties. Commercially, two classes, aligned-sintered and isotropic nanocrystalline, Nd2Fe14B magnets have been successfully developed. It should be noted that aligned-sintered Nd2Fe14B magnets are used in current hybrid vehicle systems with motor designs that require high magnetic torque, but this magnet class and motor design have been judged to be impractical for very

large scale mass production at reduced cost. Alternatively, the opportunity exists to use a new motor design that utilizes reluctance torque, and, as such, is well suited to the reduced magnetic flux available (even at optimum) from bonded magnets.

To fully exploit this opportunity to switch to bonded magnets with great inherent advantage for mass production, one primary focus of this project is to develop an improvement of the existing magnet alloy that will enhance the performance of advanced motors that need high temperature tolerance. Current Nd2Fe14B magnet alloys exhibit excellent room temperature magnetic properties and they are well suited for applications with operating temperature at or below 120°C. However, the poor temperature stability of these magnets above 120°C limits their application for advanced drive motor designs. Although many approaches have been tried to improve high temperature properties of Nd2Fe14B magnets, the intrinsic properties of the Nd2Fe14B phase dictate large negative values of the temperature coefficients for coercivity and remanence. Consequently, it is necessary to find other compositions to improve the thermal stability of RE2Fe14B magnets. Recently, we have conducted a systematic study by melt spinning on magnetic properties of a series of isotropic nanocrystalline magnet alloys where a YDy-mixture replaces Nd or Pr as the primary RE constituent in MRE2Fe14B (MRE=Y+Dy+Nd). Our results show that the YDy-based MRE2Fe14B alloy can develop into isotropic magnets with superior magnetic properties above 125°C by a judicious mixture of Y, Dy, and Nd.

It should be noted that current Nd2Fe14B bonded magnets are produced from fragmented melt spun ribbon particulate with a flake morphology, and that the improved MRE2Fe14B alloy could be used as an immediate outcome to generate bonded magnets for experimental motor trials. In fact, this has been done recently within this project to help generate useful motor performance data to assess the benefits of the new alloy design. However, this flake particulate morphology has been judged unsuitable for optimum injection molding characteristics (critical for mass production of motor components) due to its excessive viscosity when heavily loaded into a polymer matrix. This results in molding pressures that are too high for practical use, requiring the magnet particulate loading to be reduced, which places an unacceptable upper limit on magnetic strength of the finished magnet. To overcome this limitation, the second primary focus of this project is to translate the enhanced alloy design that is being optimized for melt spinning to work with an alternative rapid solidification process, high pressure gas atomization (HPGA). The beneficial result of HPGA is a fine spherical powder which is known to have ideal (lowest viscosity) behavior in an injection molding process and, therefore, simplified molding of bonded magnets with increased magnetic strength. The challenge of translating the alloy design from melt spinning to HGPA lies in the differences in the heat transfer and the resulting solidification microstructure patterns between the two processes, although their average quenching rates are similar. Our latest results show the promise of using an alloy addition to promote direct nucleation of the most desirable phase in the HPGA powder, as will be discussed.

The challenge is to develop improved permanent magnet material for high-volume, low-cost production of advanced electric drive motors while meeting the system performance targets. As clearly stated in the APEEM Activity Plan of 2004, in the section on Electronics and Electric Machines and the subsection on Electric Motors and Generators (Task 2), we must perform this project to enable development of advanced motor materials and manufacturing processes to reduce costs. These lower-cost magnetic materials must be able to be implemented without sacrificing the performance of the drive motors.

Approach

Efficient screening of magnet alloy design modifications is accomplished by melt spinning methods, primarily using parameters (e.g., wheel speed of 10-16 m/s) that simulate the quenching rates accessible during gas atomization, the desired spherical powder processing method. A major aspect of

the project is the refinement of our design strategy for a family of novel MRE-Fe-B magnetic alloys (MRE = mixed rare earth, e.g., Y, Dy, Nd) to increase the remanence and energy product at ambient temperatures for isotropic PM material while maintaining superior temperature coefficient values to 200˚C, with commercial isotropic flake particulate and spherical atomized powder properties as benchmarks. The coupling of this melt spinning work with an increased number of gas atomization trials has accelerated the pace of alloy design specifically for the rapid solidification of fine spherical powders. During the last two years, the alloy design model for melt spinning (overquench to glass/anneal to nanocrystalline 2-14-1 phase) produced the MRE-Fe-Co-B-TiC (WT-096) that was selected for an industrial melt spinning batch. This particulate, called MQP-11HTP, was delivered by Magnequench International at the end of FY2005 and proved superior to the best commercial flake particulate (MQP-14-12) above 125C. Thus, for the last 18 months we could turn our attention to a specific alloy design model for gas atomized spherical powders (direct solidification to a nanocrystalline 2-14-1 phase, without annealing) and developed first an improved alloy, MRE-Fe-Co-B-TiC-Zr (WT-102) composition that was successfully gas atomized (GA-1-66) at the end of FY2005 and fully characterized during this year. Further alloy development for gas atomization produced MRE-Fe-Co-B-ZrC-Zr (WT-127) that replaced the TiC content with ZrC to enhance the crystallization potency for 2-14-1 phase. Gas atomization trials were partially successful at the high Zr level, truncated by apparent premature precipitation of ZrC in the atomizer nozzle. This result defined a direction, i.e., reduced Zr content, for continued work on this alloy type. It should be mentioned that a reduction in the Co level (reducing alloy cost) and an increase in the remanence and energy product while maintaining high temperature performance are all part of the current alloy design equation for the PM drive motor applications that can see operating temperatures up to 200C.

Comprehensive characterization of closely-related gas atomized and melt spun samples of a variety of promising MRE-Fe-B compositions continues as a strong emphasis in both as-solidified and annealed states. The initial magnetic characterization at both ambient and elevated temperatures is followed by x-ray diffraction and calorimetric characterization on all new samples. In addition, the bulk property measurements are clarified by microstructural observation with SEM, TEM, and 3-D atom probe (at HTML) to gain critical understanding about the product phase morphologies and spatial distributions that give rise to differences in as-solidified properties and in annealing response. After observing the similar microstructural basis for improved temperature stability (during annealing) of the magnetic properties of MRE-Fe-Co-B-TiC and MRE-Fe-Co-B-TiC-Zr and MRE-Fe-Co-B-ZrC-Zr alloys, we have continued searching for the mechanism that enhances nucleation of the 2-14-1 phase in melt spun ribbons and in the interior of atomized particles. Our overall goal is to explore the generality of MRE-Fe-B alloy rapid solidification behavior during gas atomization that minimizes glass formation and allows annealing to be avoided, because of the potential processing simplification advantage that can lead to reduced costs for bonded magnet production.

Some beneficial use has been made this year of the large (100kg) batch of annealed, flake particulate (MQP-11HTP) made from our improved MRE-Fe-Co-B-TiC alloy (WT-096) that was delivered at the end of FY2005. As reported in the results section a considerable quantity was blended with PPS polymer and compression molded in-house to provide a large set of samples for industrial bonded magnet testing at Arnold Magnetic Technologies (AMT) and for more detailed magnet characterization at ORNL. Since the flake particulate is already in a fully annealed state from the vendor, the immediate upscaling of the powder annealing capability is not needed. However, to enable this extensive work, the compression molding process was streamlined for fabrication of bonded magnet samples with conventional (about 60%) loading from a PPS binder blended with the new MQP-11HTP flake and with commercial PM particulate. This involved production of multiple heated die sets and other modifications. The industrial testing focused on short and long term exposure to high temperature environments and monitored the decay of magnetization. The ORNL testing utilized a hysteresis-graph and verified some in-house magnetic property characterization with a larger sample configuration. Extensive in-house development and testing at our partners of a protective coating for flake particulate

was delayed due to the need for significant up-scaling of our experimental coating capabilities. This up-scaling work expanded greatly (5-10X) the batch size of the current fluidized bed (fluorination) coating process, specifically intended to coat the flake particulate that is now available, as well as the spherical powder that will be produced from the improved alloys. Two experimental configurations, a gas-levitated or magnetically-stirred fluidized bed system and a horizontal rotating kiln system were designed and are in the fabrication stage. When completed early in FY2007, bonded isotropic magnet samples from fluoride coated commercial and experimental atomized powders will be provided to our industrial partner to compare the effect on reversible and irreversible magnetic loses. Also, at the request of ORNL, 20 kg of the as-received flake particulate (MQP-11HTP) was provided to AMT for industrial quality fabrication of bonded magnets that were precision machined for testing in a specific experimental PM motor system at ORNL. Unfortunately, funding limitations at ORNL prevented motor testing of these bonded magnets of this new high temperature alloy, in a direct comparison with an identical set of bonded magnets that were made from commercial MQP-14-12 particulate and delivered to ORNL in FY2005. Due to the extremely high value of such head-to-head testing of these two bonded magnet types that was recognized clearly by our peer reviewers, we will continue to seek this type of collaboration from other potential partners within the FreedomCAR program.

When an alloy is developed for gas atomization that has the same promise as the WT-096 alloy did for melt spinning, an up-scaling of gas atomization also will be needed to enable extensive injection molding process development with our recently installed compounding and injection molding equipment and in collaboration with AMT. As described above, a reasonably optimized alloy soon may be available, but another factor needed to be developed and verified to enable production of these modified MRE-Fe-B alloys as fine powder in our 5X scale gas atomization system and, eventually, in any commercial atomization system. This factor is adaptation of the fluorination process or another type of surface reaction/passivation approach for in situ treatment during the high-pressure gas atomization process to reduce the hazard and oxidation losses that are typical for powders with high surface area of this type of RE alloy. Our passivation process development built on the results of our post-atomization fluidized bed coating experiments and was extended to provide in-situ coating capability during the gas atomization process, using the atomization spray chamber of our research gas atomizer as a reaction vessel and the dispersed, high temperature state of the as-atomized powder spray as a natural fluidized (turbulent) state. This was explored by using the downstream addition of an NF^3-Ar gas mixture during the atomization process on two different experiments. The proper downstream location was determined by analysis of multiple process temperatures within the research atomizer chamber and by consideration of the spray chamber flow patterns and dynamic thermal conditions. The powder surface film effects were investigated by bulk oxygen content measurements, by air oxidation tests in a thermo-gravinometric analyzer (TGA), and by explosivity testing at an independent laboratory. If the current hazard reduction measurement (to a “moderate” explosivity level) can confirmed, both the larger scale and research scale atomization systems can be employed to produce prototype spherical powder batches that can be used for experimental injection molding trials. The resulting surface film structure and composition also was characterized by x-ray photoelectron spectroscopy (XPS), by Auger electron spectroscopy, and by microstructural analysis.

Results

The hard magnetic properties of any material are controlled by two sets of factors. The intrinsic properties of the hard magnetic phase, in our case $MRE_2TM_{14}B$, determine the saturation magnetization and magnetic anisotropy which are both temperature dependent, where MRE is a combination of Y, Dy and Nd, and TM is a combination of transition metals, primarily Fe and Co. Extrinsic properties, remnant magnetization and coercivity, are determined by the microstructure of the material which is in turn determined by the solidification process and thermal history of the material. These factors are significantly different for melt spinning and gas atomization. As demonstrated by the prototype

production of MQP-11HTP, based on $MRE_2TM_{14}B$ with TiC (WT-096), a magnet alloy microstructure can be very precisely controlled during melt spinning at normal (high wheel speed) ribbon production rates. Discussions with Magnequench about licensing of the new magnet alloy raised a question about the high cost of the Co in the TM portion and lead to a brief study of Co levels in the WT-096 alloy. Thankfully, it was found that a reduction of the Co level from TM = $(Fe_{12.5},Co_{1.5})$ to TM = $(Fe_{13},Co_{1.0})$, a reduction of 33% of the Co, actually improved the maximum magnetic energy product from 11.6 MGOe to 12.7 MGOe. Because of the Co reduction, the temperature coefficients for coercivity, $H_c(T)$, did not change, but the $B_r(T)$ did increase slightly to –0.078%/C, but this is still almost half of the benchmark commercial flake particulate, MQP-14-12. The effect of these differences in the optimized melt spun ribbon properties can be seen in Fig. 1, which shows the curves for the WT-096 (MS-FY2005) and the new low Co version (MS-FY2006).

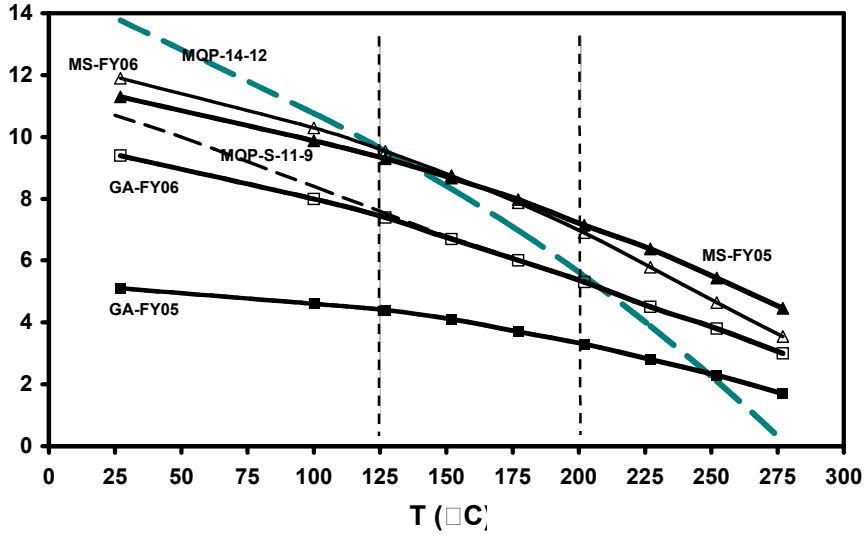


Figure 1. Comparison of the temperature dependence of maximum energy product for the experimental magnet alloys of this study as a function of the project year and of the type of processing, where MS is melt spun and GA is gas atomized, and the commercial benchmarks are listed by catalogue number, where MQP-S-11-9 is spherical (centrifugally atomized) powder and MQP-14-12 is melt spun.

This year, our magnet alloy development is focused primarily on microstructural control for the solidification conditions that exist during gas atomization, which is simulated by low speed melt spinning for this purpose, e.g., wheel speeds of 10, 13 and 16 m/sec. The microstructure of the as solidified ribbon is controlled by adjusting the chemistry of the alloy to influence the relative ease of nucleation of the competing phases during solidification. Alloy additions that control grain growth (once a phase has nucleated) also are employed to tailor the competition between nucleation and growth of the various phases. We have investigated these aspects by studying the effect of Zr substitution for MRE to enhance nucleation and by investigating additions of TiC and ZrC to control grain growth. The results for an improved gas atomized magnet alloy with Zr and TiC are shown in Fig. 1, as well, and more will be discussed about this alloy in the section below. Due to the similar structures and precipitation behavior of ZrC and TiC, it was expected that ZrC also could improve the as-solidified and annealed microstructure of both ribbons and powder. In addition, previous studies of Zr substitution for MRE show that Zr can change the crystallization behavior of ribbons or powder, apparently as an active solidification catalyst for 2-14-1 phase. Initial results on the effect of ZrC on magnetic properties in a base alloy with a fixed Zr substitution level, $[Nd_{0.45}(Y_2Dy_1)_{1/3*0.55}]_{2.2/17.3}Zr_{0.1}Co_{1.5}Fe_{12.5/17.3}B_{1/17.3}\}_{1-0.04}+Zr_xC_x$ resulted in very good magnetic properties for material melt spun at 16 m/sec. TEM images clearly showed that ZrC grains

(confirmed by convergent-beam electron diffraction) were formed along grain boundary regions (including triple-junction locations) with a grain size about 10 nm in diameter, or even less. The 2-14-1 phase microstructure has about 100 nm grain size. Hysteresis loops were generated of as-spun samples with x=0.01, 0.02 and 0.04. The addition of ZrC does not result in any serious decrease of saturation magnetization for these samples. The coercivity of these ribbon samples is in a very respectable range of 12.3 to 13.7 kOe. The remanence ranged from 6.6 to 6.8kG and the resulting energy product was 9.0 to 9.3MGOe, both very good for the as-solidified condition. Work to optimize the Zr and ZrC additions is on going.

Using the upgraded laboratory compression molding apparatus that was completed during this year, the initial set of 22 bonded isotropic magnets were compression molded with PPS polymer binder for extended environmental testing at AMT and ORNL. The particulate for this initial set was drawn from the large quantity of prototype commercial particulate, given the designation of MQP-11HTP by Magnequench International, as illustrated in Fig. 2.



Figure 2. Photograph of one of the packages that contained a total of 100 kg of industrially prepared flake particulate, formulated with the WT-096 magnet alloy composition.

The polymer processing temperature (slightly above melting) for the high temperature PPS (polyphenylene sulfide) polymer binder is approximately 300 C. Even with an inert processing atmosphere, the magnet material still must resist this aggressive environment during the molding process, in addition to possible long-term degradation during extended operation. We are currently developing a suitable surface fluorination process to provide protection (passivation) for flake particulate during compounding and molding at high temperature and to provide long term stability during high temperature bonded magnet use. This fluorination process is performed currently in a small (10 g capacity) gas flow reactor and incorporates magnetic stirring, gas mass flow control, and residual gas analysis for complete control of the process. The promise of this process was indicated last year when non-optimized fluorination parameters were used to produce 25 g of passivated WT-076 flake particulate that was bonded in PPS. The resulting bonded magnet was STILT tested at AMT and demonstrated about half of the Helmholtz field loss of a PPS bonded magnet made with commercial (uncoated) Magnequench

particulate at 200C. An investigation of controlled fluorination was initiated to determine the relationship between process parameters and coating thickness, using the highly controlled coating system and Auger electron spectroscopy (AES), but upgrades in the Auger signal analysis software must be completed before further progress can be made. Fortunately, x-ray photoelectron spectroscopy (XPS) was still useful for providing qualitative surface coating architecture information to help with our analysis of passivation in gas atomized powders (discussed below). Also, it was recognized that to provide a companion set of 22 compression molded bonded magnets to AMT for verification of the passivation effect; the small reaction vessel required a significant capacity upgrade. Thus, two alternative designs for scaled up batch processing of the fluoride coating layer were developed to compare the operating characteristics. Material to construct a larger fluidized bed reactor has been ordered. This reactor will allow 25-50 g of powder/flake to be fluorinated instead of only 10g in the current reactor and can use either a vertical-axis magnetic stirrer for flake or a gas distribution frit for spherical powder. The reaction vessel and drive train for a horizontal-axis rotary kiln reactor also have been completed. This reactor will process ~100g per batch of either flake or spherical powder without any modifications to the chamber. Both types of enhanced capacity will allow us to produce fluorinated bonded magnet samples to enable our industry partner, Arnold Magnetic Technologies, to perform STILT and LTILT measurements, which will be described below.

As reported last year, the first successful (operational) attempt at high pressure gas atomization of the MRE-Fe,Co-B magnet alloy with Zr and TiC additions did not exhibit improved magnetic properties, due to insufficient retention of Zr and B in the resulting fine spherical powder (GA-1-52). Thus, a repeat trial was performed with same starting parameters, but with boosted levels of Zr and B to compensate for anticipated losses. The resulting powder (GA-1-66) did exhibit an acceptable final composition and did produce improved magnet properties, especially in the powder with dia. < 20µm. It should be noted that particle size distribution analysis of the GA-1-66 powder batch showed that the average particle diameter is 8 µm and that about 80% of the total yield has dia. < 20 µm. A SQUID magnetometer trace of the hysteresis loop is given in Fig. 3, showing that annealing (700C, 15 min.) was required to transform the as-atomized powder microstructure into 2-14-1 phase with impressive magnetic properties, including a maximum energy product of 9.1 MGOe.

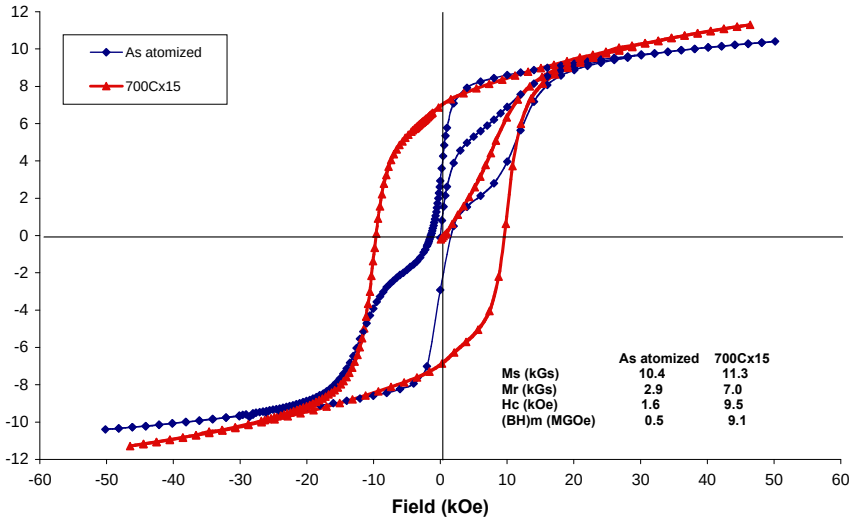


Figure 3. SQUID magnetization/demagnetization loop for the GA-1-66 powder with dia. < 20 µm.

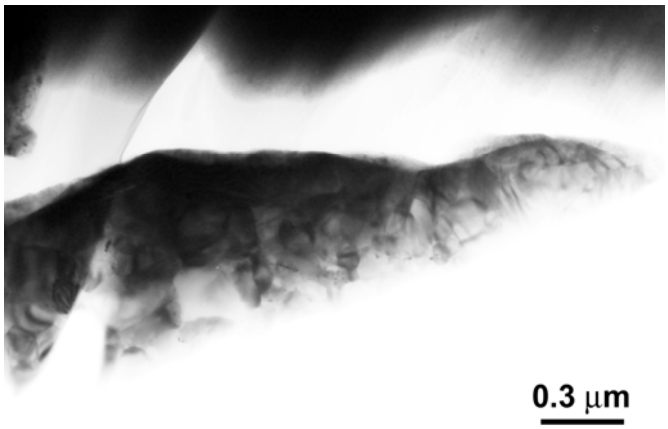
One other significant accomplishment for the atomization experiment that produced the GA-1-66 powder batch was the successful downstream injection of Ar + 5%NF_3 gas to promote a fluoride reaction on the surface of newly-solidified particulate that were still at least 200C while freely falling in the spray chamber. Analysis of this first in situ passivation attempt was conducted initially by comparing the fluorinated powders from GA-1-66 to powders from GA-1-52, with our standard nitride and carbonaceous surface film reaction products. First, bulk tests of the average oxygen content were performed on the dia. < 45µm samples from each run. This test gives a metric for the total amount of oxide that forms on the particles following atomization. The average oxygen level for GA-1-52 was 1800ppm, a typical value for our magnet alloys under these conditions. For the in situ passivated material, GA-1-66, the average oxygen level was 585ppm. This significant decrease in oxygen indicates that we were successful at coating the resulting powder with a passivating (protective) layer of rare-earth fluoride or oxy-fluoride during atomization. For more detailed analysis of the coating, XPS was used to give highly surface specific chemical composition information that can detect F, Fe, O, and RE metals as discrete signals, unlike the more limited capabilities of AES. XPS measurements were made on samples of powder that had minimal exposure to air as well as those that had 24 h exposure to dry air. The results of these measurements indicated that an initial fluorine-containing layer is formed, probably not a pure $(RE)F_3$ compound, but likely to be a RE oxy-fluoride compound. When this layer was exposed to air, it remained a RE oxy-fluoride, but the oxygen content was increased. While the XPS measurements cannot quantify the thickness of the oxy-fluoride layer, the bulk oxygen analysis suggests that it is significantly thinner than the layer that forms without the passivating treatment. As an additional test of the passivation effectiveness, powders (dia. < 45 µm) of both the GA-1-52 and the fluorinated GA-1-66 powder were sent to a commercial laboratory to determine the minimum explosible concentration (MEC) of powder particles. In the MEC test, a higher concentration refers to a reduced explosibility hazard, an important property for powder handling and critical for successful technology transfer. The results given in Table 1 suggest that the passivated powder has a significantly reduced hazard and a consistent onset value, an improvement over the uncoated powder, but more such characterization will be needed on future powder batches to further quantify these results.

Table 1. A summary of the MEC test results for GA-1-66 powder with dia. < 45 µm.

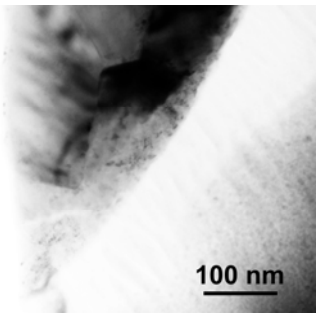
MINIMUM EXPLOSIBLE CONCENTRATION (MEC):			**120-130g/m^3**	
Test No.	**Concentration (g/m^3)**	**Pressure (bar)**	**Rate of Pressure Rise (bar/s)**	**Ignition**
1	150	0.8	180	Yes
2	130	0.5	146	Yes
3	120	0.0	0	No
4	120	0.0	0	No
5	120	0.0	0	No

The translation of an alloy composition from melt spinning to gas atomization is complicated by not only the change in particle geometry, heat flow, undercooling potential, and cooling rate; but also by an increase in batch size of more than two orders of magnitude, a change in the crucible material, the complications of charge pre-alloying prior to atomization, and an increase in the superheat temperature required to reduce the melt viscosity when it passes through the pour tube. Increased superheat

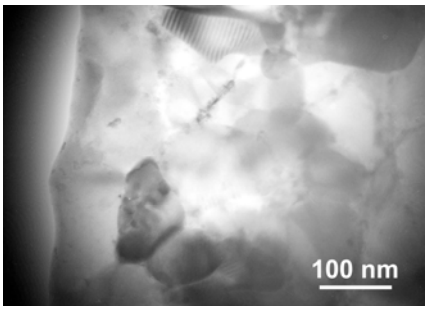
temperature and possible crucible reaction can result in changes in the melt chemistry and produce unwanted secondary phases that are detrimental to the magnetic properties. Last year, the addition of TiC to the alloy resulted in attack on the typical crucible material (alumina) and a number of failed runs, before a crucible coating and a reduced superheat temperature permitted successful production of the GA-1-52 powder. These modifications and other alloy adjustments (see above) permitted atomization of the GA-1-66 powder and further trials with Zr and ZrC additions to the MRE-Fe,Co-B magnet alloy, which all included the new in situ passivation treatment. The resulting spherical powders were size classified, providing a complete range of particle size fractions for characterization by SEM, TEM, XRD, DTA, SQUID (magnetometer), and VSM. In our TEM studies of the gas atomized GA-1-66 powder microstructures, the as-atomized 20-25μm powder was predominantly nanocrystalline with a extremely fine grained (<3 nm) rim region and occasional 50nm interior grains, and a sub-optimum (20 nm) average grain size, very consistent with the reduced coercivity in the SQUID measurements for the as-atomized dia. < 20 μm powder in Fig. 3. After annealing at 700C for 15 min., the TEM results show (in Fig. 4) that the average interior grain size has increased to about 100nm and each particle retains an outer rim of about 50nm thickness with a 10nm grain size. Line scan analysis by EDS has demonstrated that there is no significant difference in composition between the rim and the interior region of these particles, i.e., the apparent sharp boundary seems to be only a remnant of the as-atomized quench history.



a)



b)



c)

Figure 4. TEM bright-field images of GA-1-66, 20–25 μm powder size, after annealing at 700˚C for 15 min, showing: a) a fragment of a spherical particle that contains both rim and interior

microstructures, b) a nanocrystalline rim layer of about 50 nm thickness formed at the exterior of the particle, and c) an increased grain size (~100 nm) inside the particle.

As result of the most recent alloy studies, a new (nominal) composition, WT-127, with Zr substitution and ZrC addition was developed: $\{[Nd_{0.45}(Y_2Dy_1)_{1/3*0.55}]_{1.9/17.3}Zr_{0.4/17.3}Co_{1.5/17.3}Fe_{12.5/17.3}B_{1/17.3}\}_{0.96}+Zr_{0.02}C_{0.02}$. The initial atomization experiment with this alloy was not a full operational success, since about half of the molten charge remained in the crucible due to an apparent blockage of the pour tube. Metallographic analysis, including optical microscopy and SEM (with EDS) allowed identification of premature precipitation of massive primary ZrC particles as the cause of the run termination. While future work will be focused on reduction of the apparent supersaturation condition without losing the beneficial nucleation effect, sufficient powder was produced to permit additional analysis as a function of powder size. The as-atomized dia. ≤ 5μm powder was mostly amorphous and highly spherical with a few irregular shapes. As-atomized spherical particles in the 10-15μm range exhibited a noticeable increase in (2-14-1 phase) crystallinity based on the amount of etching taking place, correlated with XRD and SQUID results. This size fraction was also investigated after annealing at 700°C for 15 minutes. The annealed samples contained multiple particles with large and highly faceted primary ZrC precipitates, consistent with the observation of pour tube blockage by the same particles. The best magnetic properties for GA-1-74 occur in the 5-15 μm powder, where an energy product of 5.9 MGOe was obtained for as-atomized powder. While not as high as GA-1-66 (see Fig. 3), no annealing was required to reach this level. In 20-45μm particles, a highly dendritic microstructure is seen throughout the matrix. This finding is consistent with some previous as-atomized powder, where particles typically above 20μm posses a dendritic and or cellular structure due to reduced solidification rates. XRD analysis of as-atomized and annealed GA-1-74 with a particle size of 10-15 μm show that the as-atomized sample is mainly composed of 2:14:1 and amorphous phases. After annealing at 700°C for 15 min., the sample exhibits a typical 2:14:1 structure. No other phases were detected. The new GA-1-74 powder, with a combination of Zr and ZrC obtained as-atomized magnetic properties enhanced over those of previous runs, but still below the as-solidified melt spun samples with the similar compositions, providing motivation for further study of this type of MRE-Fe,Co-B magnet alloy with Zr and ZrC additions.

A major goal of this project is the industrial validation of the alloys and coating processes that are being developed. This includes contracting for production scale melt spinning runs, making compression molded bonded magnets, and subjecting those magnets to industry standard tests. As reported above, a major step in this validation was the preparation of 100 kg of melt spun ribbon material by Magnequench International (MQI). Short term irreversible loss tests (STILT), performed by AMT were also reported previously and mentioned above. At this time it can be reported that long term irreversible loss tests (LTILT) on 22 compression molded bonded magnet samples made from unfluorinated MQP-11HTP and MQP-14-12 magnet alloy flake particulate have now been completed at AMT. As Fig. 5 illustrates, the long term stability of our materials matches that of currently available commercial material at 150 C. Thus the superior behavior of our alloy at this temperature is maintained after prolonged exposure to high temperature. Since the particulate material used in these test samples was in the uncoated condition, it is expected that the surface passivation process currently being developed will significantly enhance both the STILT and LTILT behavior.

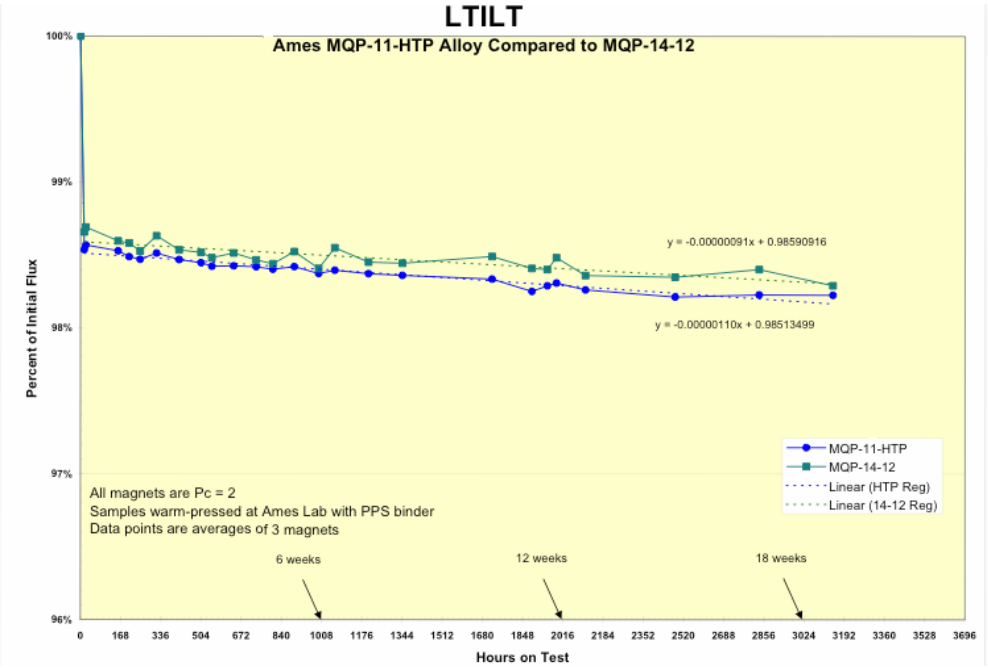


Figure 4. Summary of LTILT measurements performed by AMT that compare PPS bonded magnets made from uncoated MQP-11HTP and commercial MQP-14-12 flake particulate, showing essentially identical results out to 18 weeks.

Additional plans have proceeded for utilizing portions of our 100kg batch of melt-spun, annealed, and milled flake particulate, produced by Magnequench International (MQI) from our WT-096 alloy. These plans include collaborations with ORNL, Ford, and GM. In the plans with Ford, a new exploratory project has been developed that involves cold spray deposition of soft phase coated magnet alloy particulate.. Since Ford anticipates performance of a significant share of the experimental work and these processing experiments may develop new methods, a CRADA project is anticipated. The plans also include collaborations with GM for prototype motor testing, where Daimler-Chrysler may collaborate with GM in their efforts. In support of the motor design activity at ORNL, we reported last year on the production of PPS bonded magnets (produced by AMT from MQP-O type powder) designed for incorporation in the ORNL prototype motor. During the current year, a second identical set of magnets made from MQP-11HTP powder was produced also for the ORNL motor specifications to allow head-to-head bonded magnet tests. Unfortunately, we were informed by ORNL toward the end of the year that it was not possible to perform the motor tests at ORNL because of a shortage of funding. This circumstance has motivated a search for an alternative motor testing partner, with the possibility of re-machining the existing bonded magnets to fit a new rotor cavity design or starting the bonding and molding process over again with the available particulate to fit a new partner's requirements.

It is also worth noting that Ames Lab was instrumental in organization of a Motor/Magnet workshop at Ames during the current year, gathering many industrial and laboratory investigators for a 2-day set of discussions on strategies to move forward with collaborative efforts, where the presentations were collected on a C-D as a record (available on request). Another beneficial outcome was the shared recognition that the participants at this workshop should become more closely linked in future magnet development efforts. Moreover, during the year our ability to perform TEM studies on the spherical

powder was significantly enhanced at Ames Lab by the acquisition of two new pieces of equipment funded by the Office of Basic Energy Sciences, Department of Energy. Early in the year a new specimen thinning device termed a PIPS was purchased from Gatan Instruments The PIPS can operate its ion beam etching device at an extremely low angle, permitting much wider regions of thin area to be revealed in the powder particle cross-sections. Just prior to the end of the year, the installation of the state-of-the-art FEI Tecnai G^2 F20 scanning transmission electron microscope (STEM) also was completed.

Conclusions

During this year this project has achieved a further improvement of the room temperature maximum magnetic energy product, BH_{max}, with a reduced Co content (33% less) of our MRE-(Fe,Co)-B-TiC magnet alloy, demonstrating significant alloy cost benefits without any detectable decrease in magnetic performance up to 200C. A large set of bonded magnets were also compression molded from a portion of the 100 kg commercial (Magnequench International) batch of magnet flake particulate (MQP-11HTP) that was formulated from an enhanced Ames magnet alloy design (WT-096), for the first stage of external testing of uncoated flake particulate. The previous Zr + TiC modified MRE-Fe,Co-B magnet alloy also was gas atomized with effective control of the composition. This run was also the first demonstration of in-situ fluoride passivation (with NF_3), resulting in an energy product of 9.1 MGOe for a significant fraction (greater than 80% yield) of the spherical powder. A new magnet alloy design direction also lead to development of combined Zr and ZrC addition for the MRE-Fe,Co-B magnet alloy with phase nucleation and temperature stability properties more suitable than the previous Zr and TiC addition for direct translation to gas atomization of fine spherical powders for advantageous injection molding of bonded magnets. Confirmation also was obtained of improved environmental stability with standard long term irreversible loss tests (LTILT) of bonded magnets that were compression molded with PPS at Ames Lab from as-received MQP-11HTP particulate and commercial MQP-14-12 particulate. This LTILT testing was performed at Arnold Magnetic Technologies (AMT) and verified that our prototype (uncoated) powder matches the stability of the best commercial powders at 150C and provides enhanced magnetic performance at that temperature. The project also provided the second of two sets of net-shape isotropic bonded magnet samples to ORNL for testing in their experimental electric motor and in other devices to enable head-to-head comparisons, including high operating temperatures, of industrially bonded magnets (produced by AMT) made from commercial (MQP-type O) and experimental (MQP-11HTP) particulate. Unfortunately, testing problems have forced another partner to be sought.

Future Directions

Pursue the specific alloy design strategy for gas atomized spherical powders based on the novel MRE-Fe-B magnetic alloys (MRE = mixed rare earth, e.g., Y, Dy, Nd) that attempts to generate direct crystallization of the hard magnetic (2-14-1) phase with a desirable grain size in a dominant portion of the powder yield. Achieving this goal should lead to simplified (low-cost) processing and high yields of spherical isotropic magnet alloy powders with increased remanence and energy product at room temperature while maintaining superior magnetic performance to 200˚C, compared to commercial isotropic magnet alloy powder.

Continue comprehensive characterization of closely-related spherical powder and flake particulate samples of promising MRE-Fe-B compositions in both as-solidified and annealed states using magnetic, calorimetric, and microstructural methods to gain critical understanding of the linkage between rapid solidification structures and magnetic properties in gas atomization and melt spinning processes. This will enable successful translation of improved alloy designs from flake to spherical powders, which could be superior for injection molding of bonded magnets to net shape.

Perform comparison of flake and spherical powder in injection molding with initial series of lab injection molding trials on fine spherical powders and as-received flake particulate to determine practical upper range of magnet loading for both forms of magnet particulate without significant modification of the size distributions. Measure magnetic properties of bonded magnets with maximum loading.

Complete fabrication and testing of the up-scaled fluidized bed and rotating kiln processing options for batch fluorination of MRE-Fe-B alloy powder to enable selection of the best device for critical coating experiments that will lead to optimized protection of PM powders during magnet molding and bonded magnet use. The coating improvement experiments will include surface characterization and oxidation resistance testing of melt spun flake particulate and gas atomized spherical powders and should permit the full potential for high temperature use to be achieved with the new bonded magnets.

Collaborate with industrial partners, e.g., AMT, and research partners, e.g., ORNL, on an expanded range of environmental and magnetic testing for further study of bonded isotropic magnet samples produced by laboratory molding processes using fluoride-coated experimental flake particulate and spherical powders to facilitate direct comparisons with commercial flake particulate and spherical powders in coated and uncoated (as-received) forms, measuring progress against APEEM goals.

Seek appropriate partnerships to test bonded isotropic net shape magnets produced by industrial molding and fabrication processes using the prototype batch (MQP-11HTP) of flake particulate and commercial (e.g., MQP-14-12) flake particulate (coated and uncoated) in experimental motor designs in collaboration with industrial partners, e.g., Unique Mobility, or research partners, e.g., University of Wisconsin-Madison, to characterize motor performance and temperature tolerance, measuring progress against APEEM goals.

Continue development of the dynamic surface reaction (fluorination) approach to in situ passivation of the fine spherical MRE-Fe-B powders during the gas atomization process experiments that test improved magnet alloy designs. Successful development will result in minimal flammability and explosivity during the gas atomization process and will enable successful formation of an industrial partnership with a commercial powder producer.

Perform initial evaluation by a melt spinning approach of the compatibility of the MRE-Fe-B magnet alloy design to composition modification that produces a dual (soft/hard) phase "nanocomposite" magnetic microstructure with a suitable interphase spacing. If successful, the enhanced exchange coupling of bonded magnets produced from this nanocomposite flake particulate could generate a superior room temperature energy product that is maintained to 200C, completely surpassing commercial isotropic magnet alloy flake particulate.

Eventual plans are to explore methods to generate anisotropic MRE-Fe-B magnet alloy particulate using modified melt spinning processes and/or gas atomization approaches to facilitate a major boost in the magnetic energy product of bonded magnets.

Publications

P.K. Sokolowski, I.E. Anderson, W. Tang, Y.Q. Wu, K.W. Dennis, M.J. Kramer, and R.W. McCallum, "Microstructural and Magnetic Studies of Gas Atomized Powder and Melt Spun Ribbon for Improved $MRE_2Fe_{14}B$," in *Advances in Powder Metallurgy and Particulate Materials-2006* , compiled by W.R. Gasbarre and J.W. von Arx (Metal Powder Industries Federation, Princeton, NJ, 2006), Part 9, pp. 152-167.

Wu, Y. Q.; Tang, W.; Miller, M. K.; Anderson, I. E.; McCallum, R. W.; Dennis, K. W.; Kramer, M. J. Microanalytical characterization of multi-rare-earth nanocrystalline magnets by transmission

electron microscopy and atom probe tomography. Journal of Applied Physics (2006), 99(8, Pt. 2), 08B515/1-08B515/3.

Xu, Youwen; Kramer, M. J.; Wu, Y. Q.; Dennis, K. W.; McCallum, R. W.. The mechanism of magnetic properties improvement and microstructure refinement of Zr in Nd2Fe14B. Journal of Applied Physics (2006), 99(8, Pt. 2), 08B511/1-08B511/3.

Tang, W.; Wu, Y. Q.; Dennis, K. W.; Kramer, M. J.; Anderson, I. E.; McCallum, R. W.. Effect of TiC addition on microstructure and magnetic properties for MRE2(Fe,Co)14B melt-spun ribbons (MRE=Nd+Y+Dy). Journal of Applied Physics (2006), 99(8, Pt. 2), 08B510/1-08B510/3.

Patents

None

References

R. W. McCallum, K. W. Dennis, B. K. Lograsso, and I. E. Anderson, "Method of Making Bonded or Sintered Permanent Magnets," U.S. Patent 5,240,513, August 31, 1993.

I. E. Anderson, B. K. Lograsso, and R. L. Terpstra, "Environmentally Stable Reactive Alloy Powders and Method of Making Same," U.S. Patent 5,372,629, December 13, 1994.

R. W. McCallum, K. W. Dennis, B. K. Lograsso, and I. E. Anderson, "Method of Making Bonded or Sintered Permanent Magnets (continuation)," U.S. Patent 5,470,401, November 28, 1995.

I. E. Anderson and R. L. Terpstra, "Apparatus for Making Environmentally Stable Reactive Alloy Powders," U.S. Patent 5,589,199, December 31, 1996.

I. E. Anderson, B. K. Lograsso, and R. L. Terpstra, "Environmentally Stable Reactive Alloy Powders and Method of Making Same," U.S. Patent 5,811,187, September 22, 1998.

R. W. McCallum and D. J. Branagan, "Carbide/Nitride Grain Refined Rare Earth-Iron-Boron Permanent Magnet and Method of Making," U.S. Patent 5,803,992, September 8, 1998.

R. W. McCallum and D. J. Branagan, "Carbide/Nitride Grain Refined Rare Earth-Iron-Boron Permanent Magnet and Method of Making," U.S. Patent 5,486,240, January 23, 1996.

D. J. Branagan and R. W. McCallum, "The Effects of Ti, C, and TiC on the Crystallization of Amorphous $Nd_2Fe_{14}B$," *J. Alloys and Compds.*, **245** (1996).

D. J. Branagan, T. A. Hyde, C. H. Sellers, and R. W. McCallum, "Developing Rare Earth Permanent Magnet Alloys for Gas Atomization," *J. Phys. D: Appl. Phys.*, **29**, p. 2376 (1996).

M. J. Kramer, C. P. Li, K. W. Dennis, R. W. McCallum, C. H. Sellers, D. J. Branagan, L. H. Lewis, and J. Y. Wang, "Effect of TiC Additions to the Microstructure and Magnetic Properties of $Nd_{9.5}Fe_{84.5}B_6$ Melt-spun Ribbons," *J. Appl. Phys.*, **83**(11), pt. 2, p. 6631 (1998).

D. J. Branagan and R. W. McCallum, "Changes in Glass Formation and Glass Forming Ability of $Nd_2Fe_{14}B$ by the Addition of TiC," *J. Alloys and Compds.*, **244** (1–2), p. 40 (1996).

4. Power Electronics Research and Technology Development

4.1 Wide Bandgap Materials

Principal Investigator: Burak Ozpineci
Oak Ridge National Laboratory
National Transportation Research Center
2360 Cherahala Boulevard
Knoxville, TN 37932
Voice: 865-946-1329; Fax: 865-946-1262; E-mail: ozpinecib@ornl.gov

DOE Technology Development Manager: Susan A. Rogers
Voice: 202-586-8997; Fax: 202-586-1600; E-mail: Susan.Rogers@ee.doe.gov

ORNL Program Manager: Mitch Olszewski
Voice: 865-946-1350; Fax: 865-946-1262; E-mail: olszewskim@ornl.gov

---

Objectives

- Assess the impact of replacing silicon (Si) power devices in transportation applications with devices based on wide-bandgap (WBG) semiconductors.
- Develop device models for system level simulation studies and analyze the impact of silicon carbide (SiC) devices on the system performance.
- Build high-temperature packages for SiC power devices to operate at 200°C.
- Study the feasibility of building a 55-kW all-SiC inverter.

Approach

- Develop models of WBG semiconductor devices, especially SiC diodes, junction field-effect transistors (JFETs), and metal oxide semiconductor field-effect transistors (MOSFETs).
- Model a 55-kW all-SiC inverter and compare it with similarly rated all-Si and Si-SiC hybrid inverters.
- Build high-temperature packages for SiC power devices to operate at 200°C.
- Survey possible device packaging techniques.

Major Accomplishments

- Acquired several SiC Schottky diodes, JFETs, and GaN Schottky diodes.
- Tested, characterized, and modeled SiC Schottky diodes, JFETs, and GaN Schottky diodes.
- Modeled a 55-kW all-SiC inverter and compared its performance with that of similarly rated all-Si and Si-SiC hybrid inverters.
- Built high-temperature packages for SiC power devices to operate at 200°C.
- Built and tested all-Si and Si-SiC hybrid inverters [Si insulated gate bipolar transistors (IGBTs) and SiC Schottky diodes] and compared the results.

Technical Discussion

A. Device Modeling

Several new WBG devices were acquired this year and were tested, characterized, and modeled. The list of devices includes SiC JFETs, Schottky diodes, and GaN Schottky diodes. All the devices obtained

were experimental samples. A data record of devices tested to date is located in the appendix to this section.

A.1 SiC Schottky Diode

SiC Schottky diodes are majority carrier devices and are attractive for high-frequency switching because they have lower switching losses than pn diodes. However, they have higher leakage currents, which affect the breakdown voltage rating of the devices. Tests were conducted of 600-V/75-A SiC Schottky diodes, and the results are presented in the following subsections.

Static characteristics

I-V characteristics of the 600-V/75-A SiC Schottky diode were obtained at different temperatures in the –50°C to 175°C temperature range (Figure 1). Considering the piece-wise linear (PWL) model of a diode—which includes a dc voltage drop, V_D, and a series resistor, R_D— the diode I-V curves can be approximated with the following equation:

$$V_d = V_D + R_D \cdot I_d \tag{1}$$

where V_d and I_d are the diode forward voltage and current, and V_D and R_D are the diode PWL model parameters.

Figure 2 shows R_D and V_D values of the 600-V /75-A SiC Schottky diodes with respect to temperature. As seen in the figure, V_D decreases with temperature and R_D increases with temperature. The increase in R_D is an effect of the positive temperature coefficient of the SiC Schottky diodes, which enables these devices to be paralleled easily. Equations (2) and (3) show the temperature dependence of the SiC Schottky diode PWL model parameters.

$$V_D = -0.001 \cdot T + 0.94 \text{ (Volts)} \tag{2}$$

$$R_D = 8.9 \times 10^{-5} \cdot T + 0.013 \text{ (Ohms)} \tag{3}$$

where T is the temperature in degrees C.

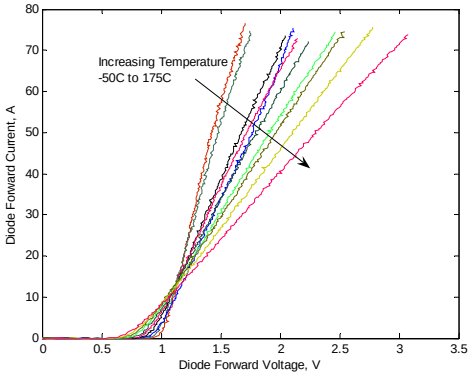


Figure 1. Experimental I-V curves of the 75-A SiC Schottky diode.

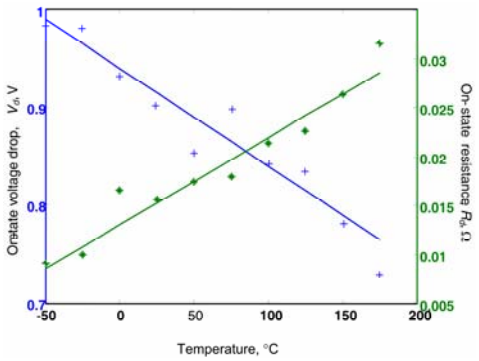


Figure 2. R_D and V_D obtained from the experimental data in Figure 1.

Dynamic characteristics

The SiC Schottky diode was also tested in a chopper circuit (Figure 3) to observe its dynamic characteristics. The IGBT in the circuit was switched at a low switching frequency of 1 Hz to prevent self-heating effects on the diode. The double pulse circuit enables the use of an inductive load instead of the resistive and inductive load together. The current through the inductor builds up during the first pulse and peak forward current is adjusted by changing the width of the first pulse. The switch is turned off and turned on for short periods after the first pulse. The turn-on and turn-off energy losses can be obtained during the short pulse intervals. The double pulse waveforms are shown in Figure 4.

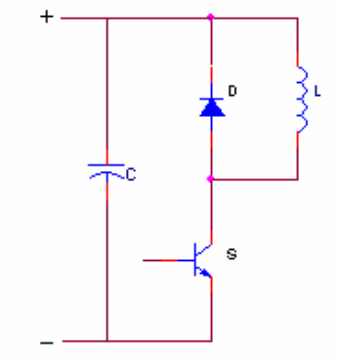


Figure 3. Test circuit for dynamic characterization.

To obtain the switching characteristics at high temperatures, a test set-up was built as shown in Figure 5. The device under test was placed inside the box on a heat sink, and the temperature was controlled using a resistive load paced in the box on the heat sink. The temperature of the heat sink was monitored using a thermistor.

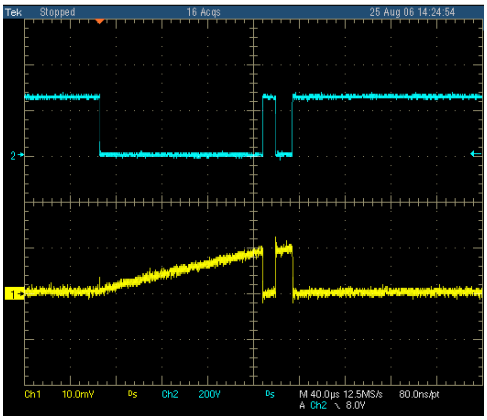


Figure 4. Current and voltage waveforms of SiC JFET S3—double pulse test.

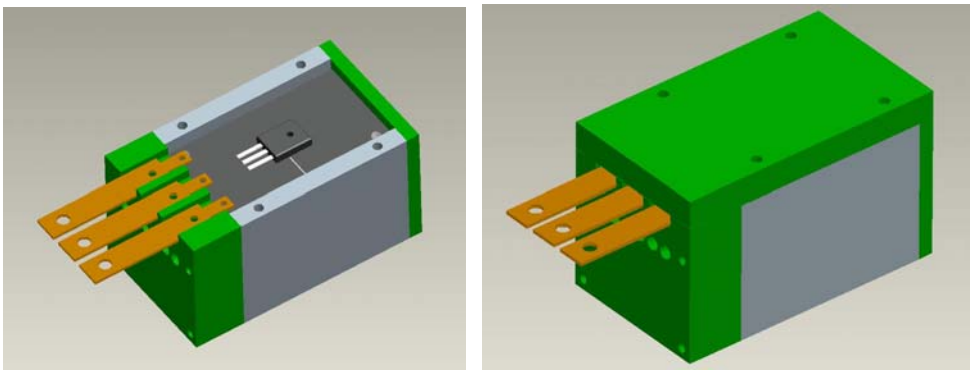


Figure 5. Temperature-controlled box used for high-temperature testing.

The reverse recovery current waveforms obtained for different forward currents at room temperature are shown in Figure 6. The reverse recovery current did not change with forward current. Note that, theoretically, Schottky diodes do not display reverse recovery phenomenon because they are majority carrier devices and do not have a stored charge. The switching losses obtained at different temperatures are shown in Figure 7. The switching loss equation is given below in Equation (4).

$$E_{sw} = -6.5\times10^{-9}\cdot I + 3.2\times10^{-7} \quad \text{(Joules)} \tag{4}$$

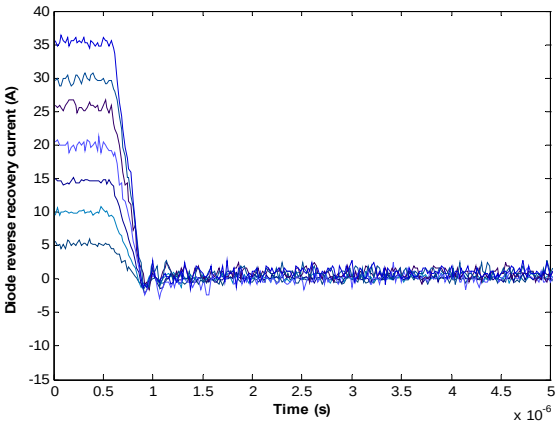


Figure 6. Reverse recovery current waveforms of the SiC Schottky diode for different forward current values.

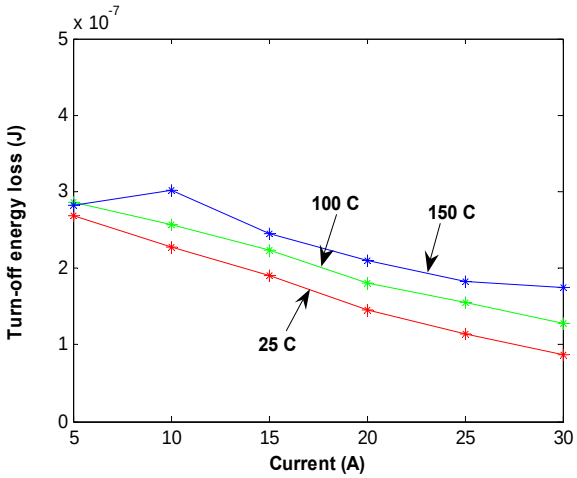


Figure 7. Switching energy losses of SiC diode at different temperatures.

A.2 GaN Schottky Diodes

Static characteristics

The static characteristics of a 600-V/4-A GaN diode in a temperature range of 25 to 175°C are shown in Figure 8. The PWL model parameters were extracted from the static curves (as discussed in the previous section) and plotted in Figures 9 and 10. V_d decreases and R_d increased with an increase in temperature, as expected. The static characteristics of a similarly rated SiC diode are better compared with the GaN diode, as shown in Figure 11. It should be noted that the GaN device is still an experimental sample and SiC Schottky diode technology is more mature.

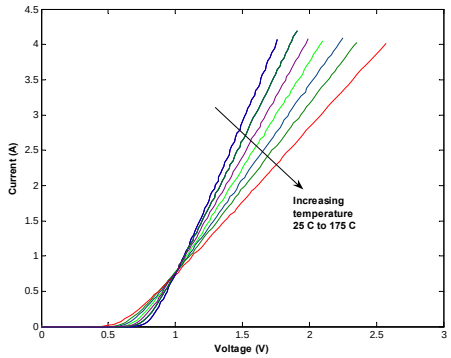


Figure 8. Static characteristics of GaN Schottky diode.

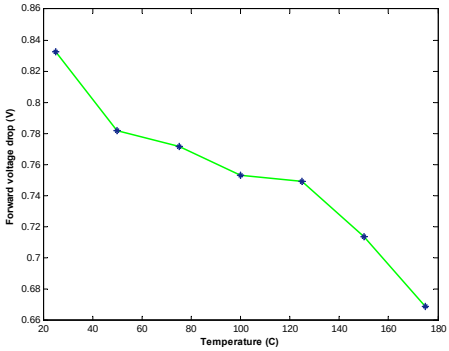


Figure 9. V_d forward voltage drop of GaN Schottky diode.

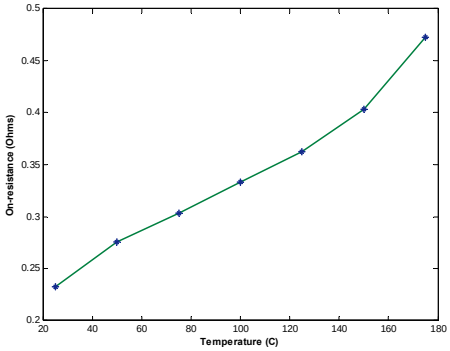


Figure 10. R_d on-state resistance of GaN Schottky diode.

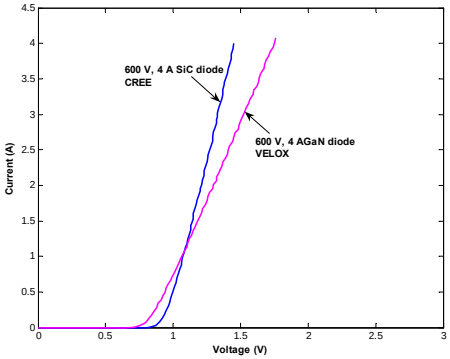


Figure 11. Comparison of i-v curves of SiC and GaN Schottky diodes.

Dynamic characteristics

The dynamic characteristics of the GaN Schottky diode were obtained using the same chopper circuit and high-temperature test set-up as the SiC Schottky diode. Results show that the GaN Schottky diode also has almost zero recovery losses, as expected, similar to the SiC diode (Figure 12). The corresponding turn-off energy losses are shown in Figure 13 for three different temperature conditions. The switching

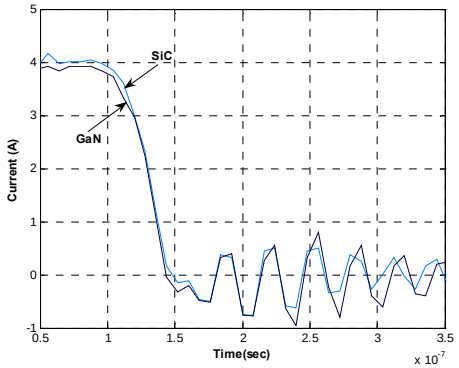


Figure 12. Comparison of reverse recovery currents between SiC and GaN at 25°C.

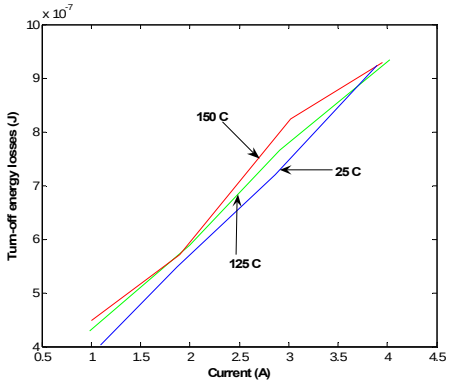


Figure 13. Turn-off energy losses of GaN diode at different temperatures.

losses of the GaN diode were compared with those of a similarly rated 600-V, 4-A SiC Schottky diode, shown in Figure 14, for 125°C operation. The losses of the SiC Schottky diode are slightly less than those of the GaN Schottky diode for this operational condition.

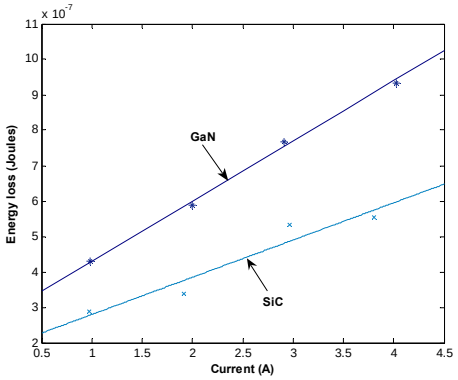


Figure 14. Energy losses comparison between Si and GaN diodes at 125°C.

A.3 JFETs

Static characteristics

Several experimental JFET samples were obtained from different manufacturers. Static characteristics of three different JFETs—S1 (600-V, 5-A), S2 (1200-V, 15-A), and S3 (1200-V, 10-A)—at different temperatures are shown in Figures 15–17, respectively. SiC JFETs have a positive temperature coefficient, which means that like SiC Schottky diodes, their conduction losses will be higher at higher temperatures. However, positive temperature coefficient makes it easier to parallel these devices and reduce the overall on-resistance.

The on-resistance of the switch S3 increases from 0.25 Ω at −50°C to 0.58 Ω at 175°C, as shown in Figure 18. The on-state resistance can be expressed as a function of temperature as shown in Equation (5).

$$R_D = 7.6\times10^{-5}\cdot T^2 + 0.00068\cdot T + 0.26 \ \text{(Ohms)} \qquad (5)$$

The transfer characteristics of an SiC JFET are shown in Figure 19. The negative gate pinch-off voltage required to turn off the device is higher than that required for Si devices. The earlier-generation devices had pinch-off voltages that varied between samples, as shown in Figure 20. The pinch-off voltages of the newer-generation devices obtained this year do not vary as much. The transfer characteristics obtained for ten different samples are shown in Figure 20. This is a significant improvement that indicates that SiC JFET technology is maturing.

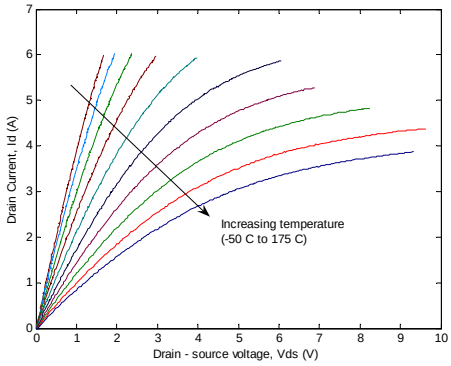


Figure 15. i-v curves of JFET S1.

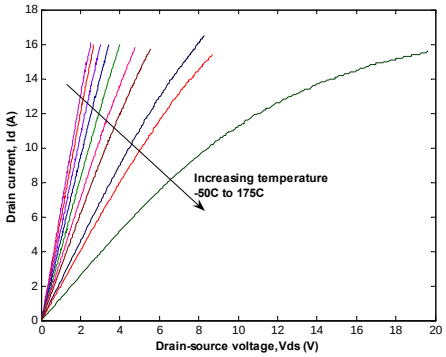


Figure 16. i-v curves of JFET S2.

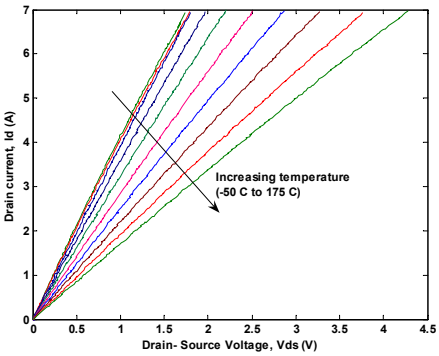


Figure 17. i-v curves of JFET S3.

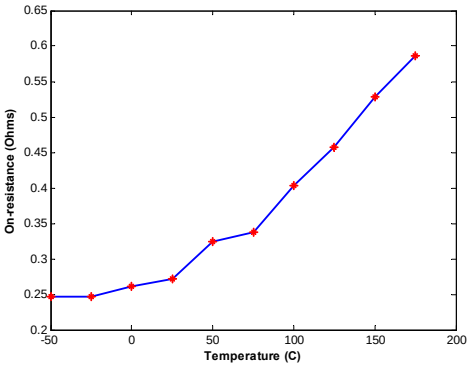


Figure 18. On-resistance of S3.

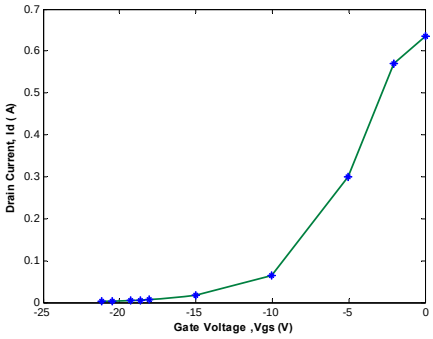


Figure 19. Transfer characteristics of JFET S3.

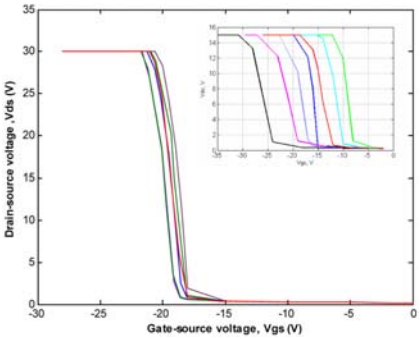


Figure 20. Transfer characteristics of several SiC JFET samples.

Dynamic characteristics

SiC JFETs are normally-on devices, and they can be turned off only by applying a negative voltage. Based on the transfer characteristics (Figure 20), a gate voltage of –22 V has been selected, as that would be enough to turn off most of the samples tested. The dynamic characteristics of the JFET S3 at several temperatures and currents were obtained using the high-temperature set-up and the double pulse circuit test. The total energy losses of the JFET during switching are shown in Figure 21. The losses do not change much with temperature The switching loss equation is given below in Equation (6).

$$E_{swtotal} = 12.2 \times 10^{-5} \cdot I + 1.7 \times 10^{-5} \text{ (Joules)} \quad (6)$$

B. 55-kW Inverter Modeling

Three different inverters were modeled in Simulink to compare and study the system-level benefits of replacing SiC devices with Si devices. The total system-level model with a control system block, device loss model blocks, and a heat sink model block is shown in Figure 22. The power losses of the switches are calculated and fed to the heat sink model, which calculates the junction temperatures of the devices. These temperatures are fed back to the device loss models so that the temperature-dependent device parameters are updated. The blocks in the model will be explained in detail in the next few subsections.

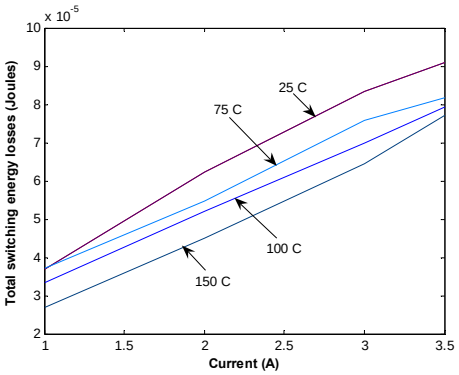


Figure 21. Total switching energy losses of JFET S3 at different currents and temperatures.

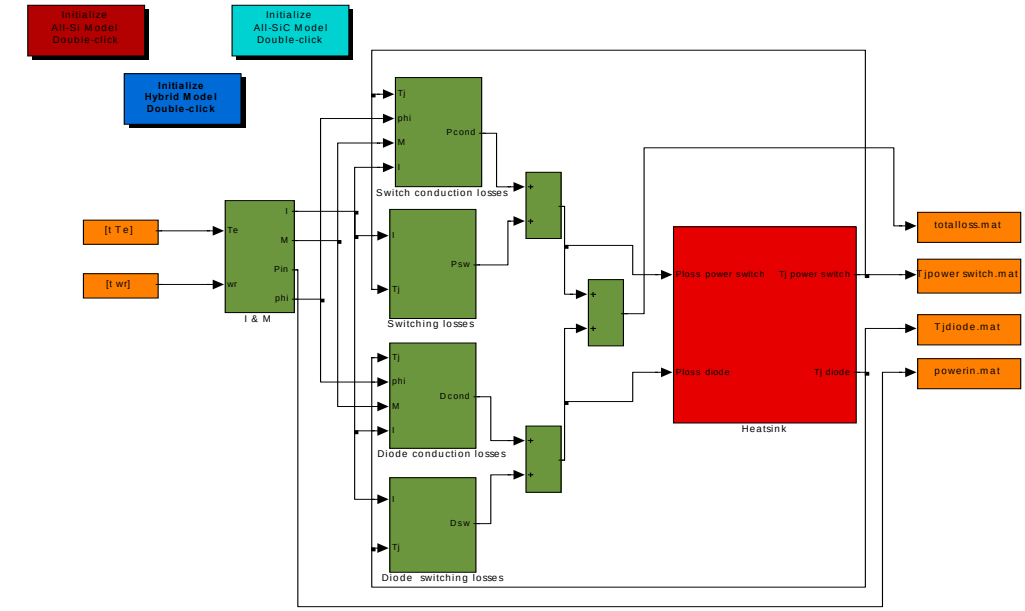


Figure 22. Block diagram of the system level model.

B.1 Control Block Model

The speed and torque profiles for a Federal Urban Driving Schedule (FUDS) cycle were obtained from the power train system analysis toolkit (PSAT), a drive train simulation software developed by Argonne National Laboratory. The speed and torque profiles were fed to the control block, which calculates the peak current, modulation index, input power, and power factor for the average loss model. The control block is explained in detail by Ozpineci.[1]

B.2 Device Models

The devices used in three different inverters are listed in Table 1.

Table 1. Ratings of the devices used in the inverters

	Switch	Diode
All-SiC inverter	1200-V/10-A SiC JFET	600-V/75-A SiC Schottky diode
Hybrid inverter	600-V/50-A Si IGBT	600-V/75-A SiC Schottky diode
All-Si inverter	600-V/50-A Si IGBT	600-V/80-A Si pn diode

The devices listed in Table 1 were scaled to a rating of 600 V and 600 A for the power switches and 600 V and 450 A for the diodes to be able to simulate a 55-kW inverter. The device loss models were developed from the static and dynamic characteristics of the devices. The conduction losses were calculated using an average modeling technique that is explained in detail in Ozpineci.[1] The conduction loss parameters derived from the test data were used in the modeling equations. The switching loss models were calculated from total energy losses during switching. The SiC JFET and SiC diode modeling was discussed in earlier sections of this report. Si IGBT and Si pn diode modeling will be presented in the following sections.

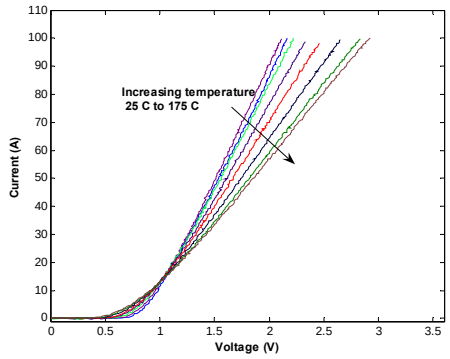


Figure 23. i-v characteristics of IGBT at different temperatures.

Si IGBT model

A 600-V, 50-A trench-stop technology–based IGBT with a maximum junction temperature specification of 175°C was chosen for the all-Si and hybrid inverter simulations. This IGBT is a commercial device from Infineon, part number IGP60N50T.

Static characteristics

The static characteristics of the IGBT at different temperatures are shown in Figure 23. The IGBT has a positive temperature coefficient similar to that of an SiC diode. The static characteristics of the IGBT are very similar to those of the diode and can be modeled using the PWL model. The PWL model parameters were extracted from the static curves and are derived as a function of temperature as shown in Equations (7) and (8).

$$V_D = 1.7\times10^{-7}\cdot T^3 + 4.3\times10^{-5}\cdot T^2 - 0.0032\cdot T + 0.91 \text{ (Volts)} \quad (7)$$

$$R_D = 1.9\times10^{-7}\cdot T^2 + 2.5\times10^{-5}\cdot T + 0.012 \text{ (Ohms)} \quad (8)$$

Dynamic characteristics

The dynamic characteristics of the IGBT were obtained using the double pulse circuit and the high-temperature setup described earlier with both an SiC Schottky diode and a Si pn diode to model the effects of the reverse recovery on the turn-on current of the IGBT. Figure 24 shows the difference in turn-on losses of the IGBT. The better reverse-recovery characteristics of the SiC diode help in reducing the losses of the IGBT. This is because when a diode in an inverter is turning off, the diode-reverse-recovery current passes through the other IGBT in the same phase leg, causing additional losses. The IGBT turn-off losses do not change much with Si or SiC diodes because the diode affects only the turn-on losses of the IGBT, as shown in Figure 25.

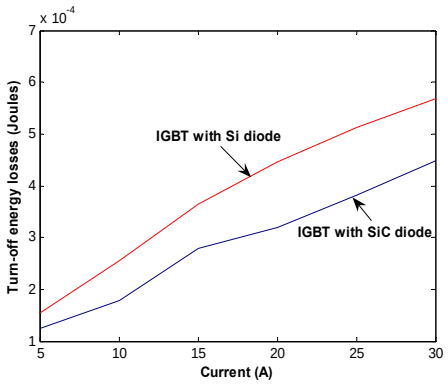


Figure 24. Turn-on switching energy losses of IGBT with Si and SiC diodes at 25°C.

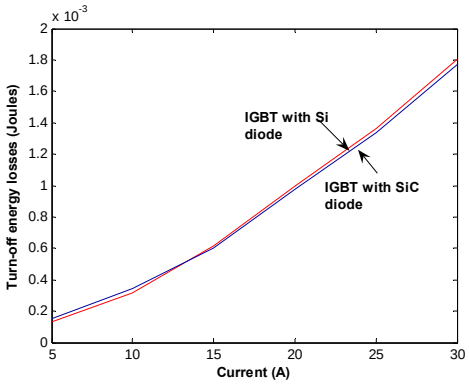


Figure 25. Turn-off switching energy losses of IGBT with Si and SiC diodes at 25°C.

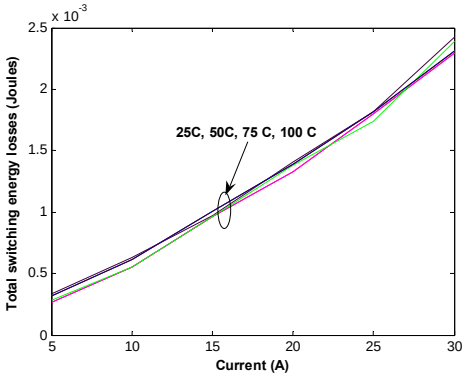


Figure 26. Total switching energy losses of IGBT at different currents and temperatures

The diodes in the test were kept outside the temperature-controlled box and hence did not affect the IGBT losses at different temperatures. The turn-off losses of the IGBT dominated the turn-on losses. Since the turn-off losses did not change much with temperature, the total switching losses of the IGBT did not change much with temperature (Figure 26). The variation in switching losses of the IGBT at different temperatures obtained from tests matched the data presented in the data sheet. The switching loss equation is given below in Equation (9).

$$E_{swtotal} = 1.2\times10^{-6}\cdot I^2 + 3.8\times10^{-5} \cdot I + 3.2\times10^{-5} \text{ (Joules)} \quad (9)$$

Si diode model

A 600-V/ 80-A Si pn diode with a maximum junction temperature specification of 175°C was chosen for the all-Si and hybrid inverter simulations. The diode is a commercial device from Infineon and the part number is RURG8060.

Static characteristics

The static characteristics of the diode at different temperatures are shown in Figure 27. The Si diode has a negative temperature coefficient, as expected, unlike the SiC Schottky diode. The static characteristics of the diode can be modeled using the PWL model. The PWL model parameters were extracted from the static curves and are derived as a function of temperature as shown in Equations (10) and (11).

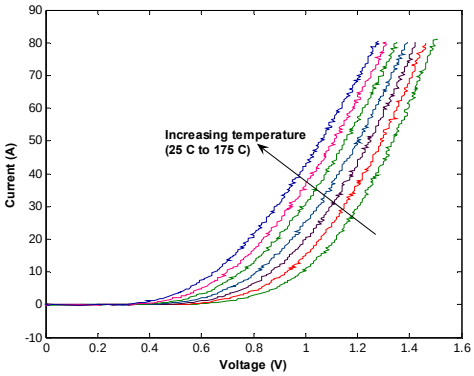


Figure 27. i-v characteristics of Si pn diode at different temperatures.

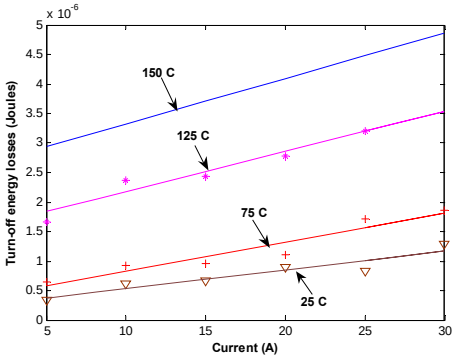


Figure 28. Turn-off energy losses of Si pn diode at different currents and temperatures.

$$V_D = -0.0012 \cdot T + 0.59 \,(\text{Volts}) \qquad (10)$$

$$R_D = 1.5\times10^{-7} \cdot T^2 + 1.5\times10^{-5} \cdot T + 0.0078 \,(\text{Ohms}) \qquad (11)$$

Dynamic characteristics

The dynamic characteristics of the Si pn diode were obtained using the same chopper circuit and high-temperature set-up as used for the SiC Schottky diode. The switching energy losses due to the reverse recovery current are shown in Figure 28. The reverse recovery losses of the Si pn diode increase with an increase in current and temperature, as seen in Equations (12) and (13)

$$E_{swoff} = \mathrm{a} \cdot I + b \ \text{(Joules)} \qquad (12)$$

$$a = 3.6\times10^{-10} \cdot T + 2.3\times10^{-8} \qquad (13)$$

$$b = 2.1\times10^{-10} \cdot T^2 - 1.8\times10^{-8} \cdot T + 5.3\times10^{-7} \qquad (14)$$

where T is in °C.

B.3 Thermal Model

The thermal model developed is a 1-dimensional thermal resistance model with 2-dimensional heat spreading effects modeled using finite element analysis. The thermal resistance calculated is a sum of 1-dimensional cross section resistance and the resistance due to heat spreading through the cross section area. A side view of the cross section is shown in Figure 29. The structure, thicknesses, and materials of the layers used in the model were taken from Semikron's SKAI module. The heat sink model was based on the commercially available air-cooled inverter. Note, however, that the heat sink used in the calculation is a model with adjustable fin length and thickness and is designed for natural convection. The equivalent circuit is shown in Figure 30. The model assumes that the temperature along the top of the base plate is uniform. This is a valid assumption because the thermal resistance in the entire cross section is high, from the base plate to the tip of the fins

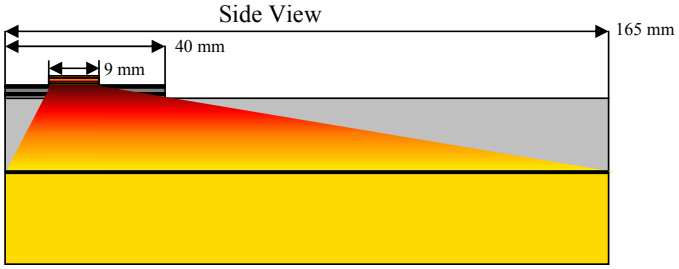


Figure 29. Side view of the cross section of the inverter.

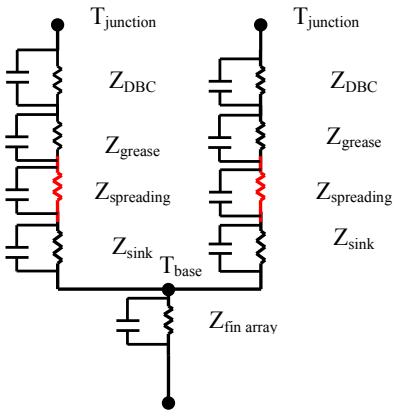


Figure 30. The equivalent circuit of the thermal model.

on the heat sink. The spacing between devices on top of the direct bonded copper is based on the number of devices and the length of the DBC sled and is the same as in the Semikron SKAI unit. The dimensions of each device on top of the DBC can be changed. However, the diodes and the main power switches are assumed to be the same dimensions so that there is a line of symmetry along the cross section.

B.4 Simulation Results

The three different inverter models were simulated for several operating conditions, and some of the results are discussed below. Efficiency vs output power plots for several operating conditions comparing the inverters are shown in Figures 31 and 32. The hybrid inverter and all-SiC efficiencies are higher than those of the all-Si inverter for all operating conditions. The percentage loss reduction was calculated comparing the power loss differences between the hybrid inverter and the all-SiC inverter with respect to the all-Si inverter, as shown in Equation (15).

$$\%\,loss\ reduction = \frac{P_{loss}^{All-Si} - P_{loss}^{All-SiC}}{P_{loss}^{All-Si}} \times 100 \qquad (15)$$

The temperature profiles of the JFETs and Schottky diodes in the all-SiC inverter over a FUDS cycle are shown in Figure 33.

The heat sink used in the simulations was designed for 30-kW continuous power. Using the inverter loss model and the thermal model, the junction temperatures calculated for 30-kW operation of the all-Si and all-SiC inverters at different ambient temperatures are shown in Figure 34. The figure also shows the volume of the heat sink required, corresponding to the junction temperature of the device. Figure 34 shows that with natural convection, the all-Si inverter can operate only at 25°C ambient conditions because of the junction temperature limitations. At 105°C ambient, the junction temperatures are beyond the theoretical limits of the Si devices, and even increasing the heat sink volume does not reduce the junction temperatures because the heat sink is saturated. The temperatures of the SiC devices are much lower because of the reduced losses compared with the Si devices. Hence, for the same junction temperature of 150°C, the heat sink volume needed is two-thirds less for an all-SiC inverter than for an all-Si inverter.

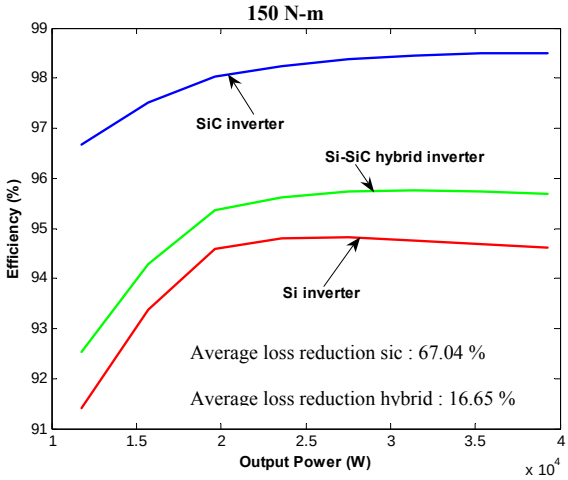


Figure 31. Efficiency vs output power of three different inverters at 150 N-m load.

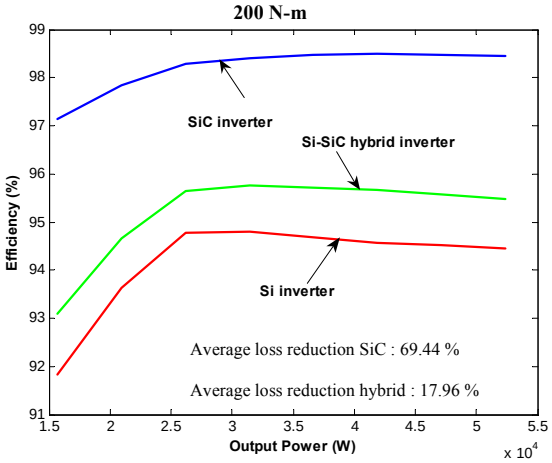


Figure 32. Efficiency versus output power of three different inverters at 200 N-m load.

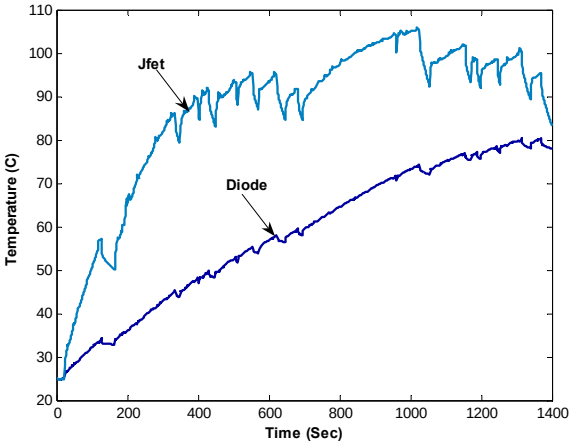


Figure 33. Temperature profile of devices over FUDS cycle.

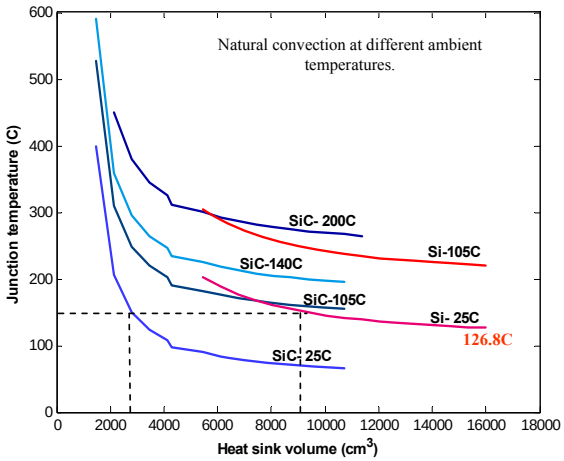


Figure 34. Heat sink volume vs device junction temperatures for all-Si and all-SiC inverters.

C. High-Temperature Packaging Tests

One of the most important characteristics of SiC power devices is that they can operate at much higher temperatures (>300°C) than do Si power devices. Presently, SiC devices use Si device packages that limit the operation temperature (~125°C). Tests at Oak Ridge National Laboratory (ORNL) have shown that at high temperatures, these packages break open and leave the devices inoperable. This year, ORNL collaborated with the University of Arkansas to build several high-temperature packages to demonstrate packages that can operate at 200°C ambient. Two different packages with SiC Schottky diodes were delivered and tested at ORNL.

- TO-220 package

A single-die 600-V/75-A SiC Schottky diode was packaged in a TO-220 through-hole style package (Figure 35). The package was tested at different current levels at 200°C ambient temperature without a heat sink. The case temperature of the diode was measured using a thermocouple. The diode forward voltage drop was measured at different current levels using a Keithley data acquisition system. The voltage drop of the diode and case temperature as measured are shown in Figures 36 and 37. The diode operated at 361°C at 20 A for over an hour without a failure. However, at 25 A, the diode operated for a short time and then failed by shorting across the junction. This is a significant milestone in terms of operating temperature of the device; it clearly demonstrates the high-temperature operation capability of SiC devices.

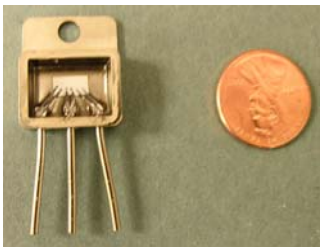


Figure 35. TO-220 through-hole high-temperature package of 75-A SiC Schottky diode.

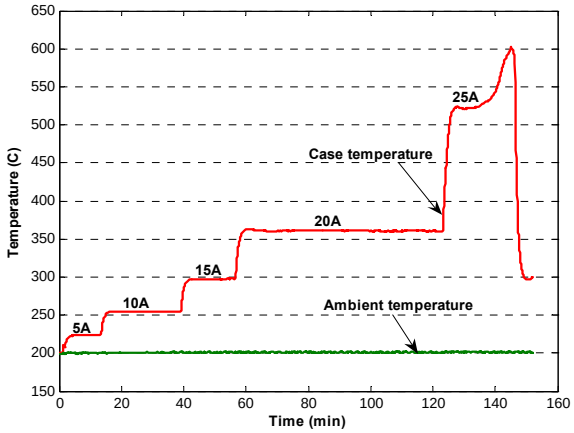


Figure 36. Case temperature of 75-A diode at different current level measured at 200°C ambient.

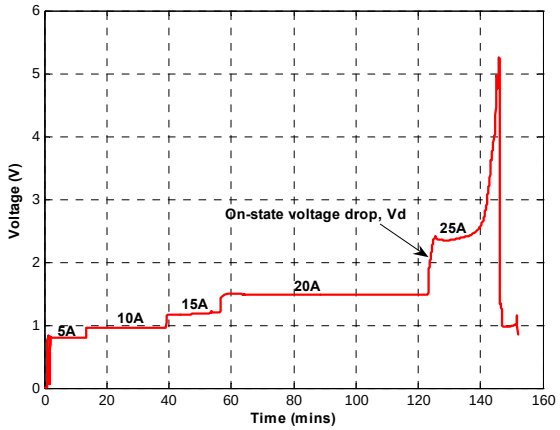


Figure 37. Voltage drop across the diode at different currents.

- 450-A package

Six 600-V/75-A SiC Schottky diodes were packaged in a module yielding a combined rating of 600 V and 450 A, as shown in Figure 38. The static characteristics of the module obtained at different temperatures are shown in Figure 39. The module was also tested at 200°C ambient at different current levels, similar to the testing of the single-die package. The case and ambient temperatures of the diode module were measured using a thermocouple. The forward voltage drop and temperatures are shown in Figures 40 and 41. The module was limited by the contact solder to a maximum operating temperature of 308°C. The upper test temperature limit was set to 282°C so that it would remain below the solder limitation. The operating current corresponding to 282°C was 50 A. The diode operated without any failure for a long duration at this operating point. The effect of the temperature coefficient of the device is evident in the voltage drop plot. The change in current increases the voltage drop, and then the effect of the temperature increase decreases the voltage. Note from Figure 39 that the diode module has a negative temperature coefficient below 120 A and a positive temperature coefficient above that temperature. The maximum current to which the diode module was tested was limited to 50 A.

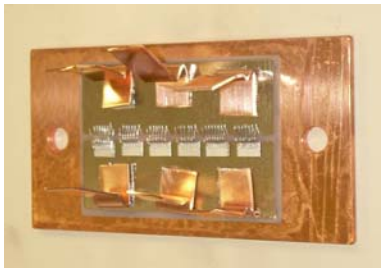


Figure 38. A 450-A high-temperature SiC diode module with six 75-A Schottky diodes in parallel.

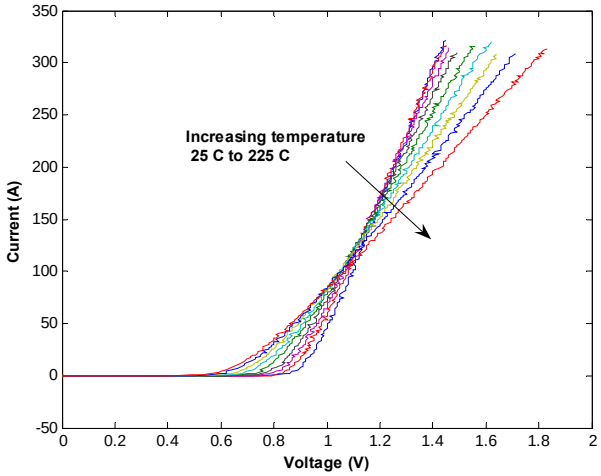


Figure 39. i-v curves of the 450-A diode module.

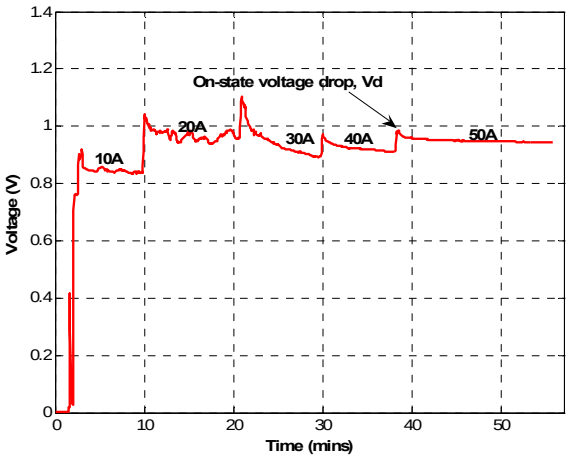


Figure 40. Voltage drop across the diode module at different currents.

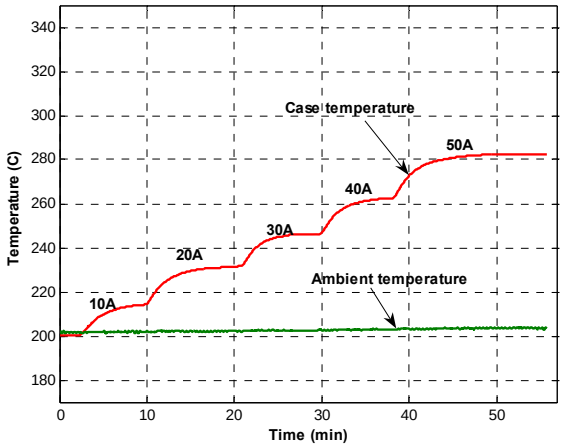


Figure 41. Case temperature of 75-A diode at different current levels measured at 200°C ambient.

D. Hybrid Inverter Tests

The inverter shown in Figure 42 was built at ORNL using power modules delivered by CREE. Two different inverters were built: an all-Si inverter using Si-IGBTs and Si pn diodes, and a hybrid inverter using the same Si IGBTs but SiC Schottky diodes instead of Si pn diodes. The performances of the inverters was compared after an inductive load test. The hybrid inverter and the all-Si inverter were tested with the same test procedure and using the same controller on the same benchtop system.

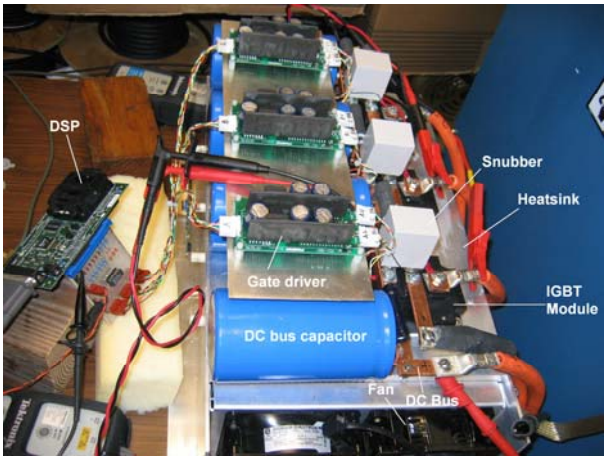


Figure 42. Three-phase inverter built at ORNL.

Test Setup

The output leads of the inverter were connected to a 3-phase star-connected variable resistor bank with a 3-phase inductor in series. The dc inputs were connected to a voltage source capable of supplying

the maximum rated operating voltage and current levels for the inverter. The test setup is shown in Figure 43.

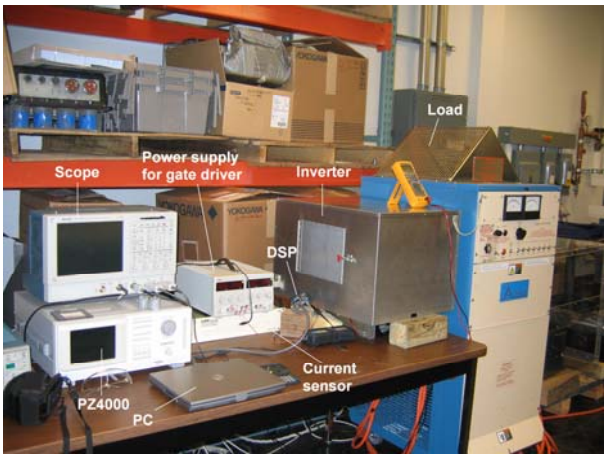


Figure 43. R-L load test setup.

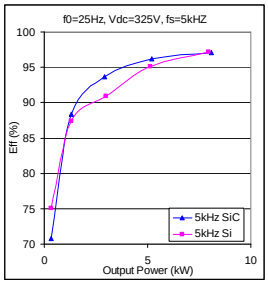
The device modules used in the hybrid inverter were Si IGBT/SiC Schottky diode modules (QID1230009-ES), and the modules used in the all-Si inverter were Si IGBT/Si pn diode modules (CM300DY-24NF). The controls for the inverter were generated using a DSP TMS320F2812. A space vector pulse width modulation technique was used as the control scheme. IGBT modules were driven by a BG2A board (from POWEREX), which used two VLA502-01 gate drivers. The inverter was mounted on a heat sink with fans.

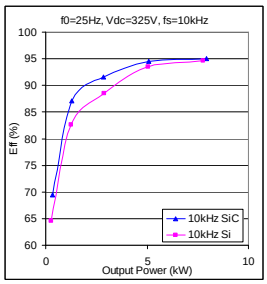
Results

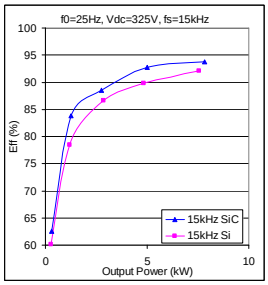
Voltage, current, switching frequency, and the frequency of the output current are important parameters that have significant influences on power losses and efficiency. Thus the tests were conducted under different combinations of these parameters.

dc voltage: 200 V and 325 V
ac side current (rms): 10 A to 50 A
Frequency of output ac current: 25, 50, 75, and 100 Hz
Switching frequency of inverter: 5, 10, and 15 kHz

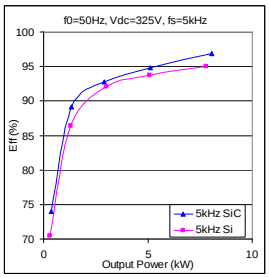
The data obtained for both of the inverters were analyzed and the corresponding efficiencies were calculated. The efficiency versus output power plots for several operating conditions comparing the inverters are shown in Figure 44. The Si-SiC inverter had a higher efficiency than the all-Si inverter. The difference in efficiencies between these two inverters is smaller at low output power and larger at high output power. This is because power losses of both inverters are lower at low output power, and the power losses of the Si inverter increase more quickly as the output power (or current) increases. In some cases, the efficiency of the SiC inverter is even lower than that of the Si inverter at low current levels because the Si pn diode voltage drop is much lower than the SiC Schottky diode voltage drop at low currents; however, most applications will be operating in the higher current regions. The efficiencies of both inverters increase as output power increases (see Figure 44) and decrease as switching frequency increases (see Figure 45), as expected.

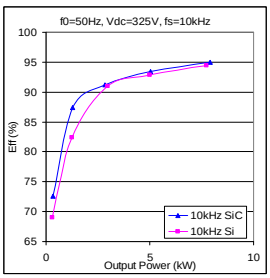


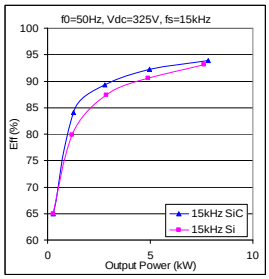




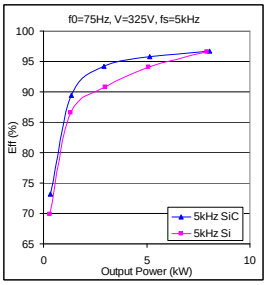
(a) dc voltage 325 V and output frequency 25 Hz

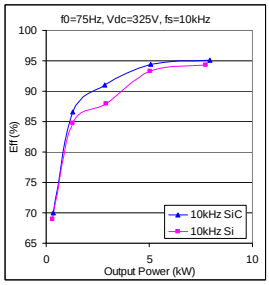


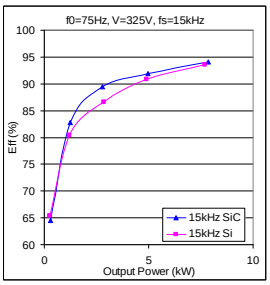




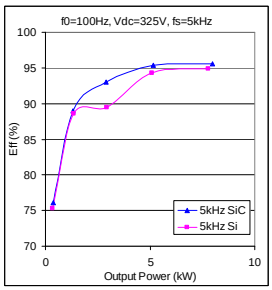
(b) dc voltage 325 V and output frequency 50 Hz

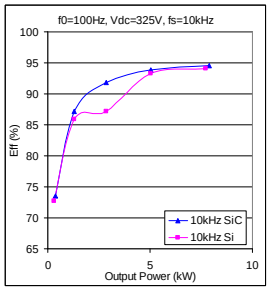


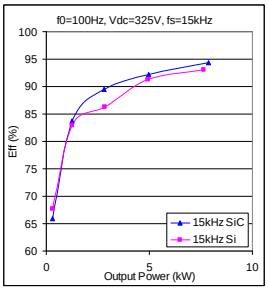




(c) dc voltage 325 V and output frequency 75 Hz

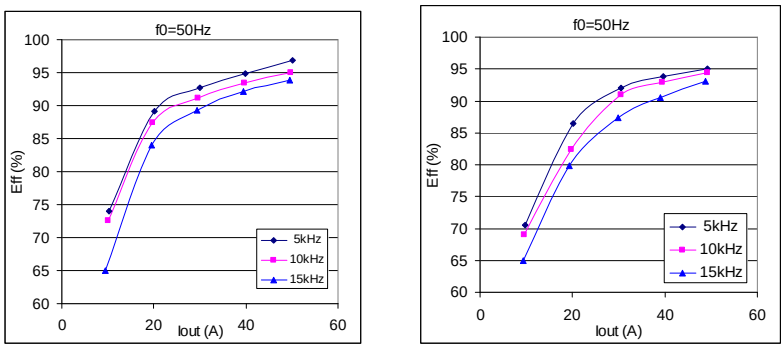






(d) dc voltage 325 V and output frequency 100 Hz

Figure 44. Efficiency vs output power at 325-V dc voltage.



(a) Si-SiC hybrid inverter **(b) All-Si inverter**

Figure 45. Efficiency of inverters at 325 V dc voltage and 50 Hz output.

Conclusion

Several new devices (SiC Schottky diodes, JFETs and GaN Schottky diodes) were acquired, tested, and modeled. There is a significant improvement in performance of the new-generation JFETs, which indicates that SiC switch technology is maturing. The 55-kW inverter simulations showed reduced losses of up to 69% for the all-SiC inverter and up to 28% for the hybrid inverter compared with the all-Si inverter. The inverters were simulated over a FUDS cycle, and the results showed that with natural convection, a two-thirds reduction in heat sink volume can be realized using an all-SiC inverter rather than an all-Si inverter. Two high-temperature packages delivered by the University of Arkansas were tested to demonstrate a high-temperature packaging technology that can operate at 200°C. The diode operated at a temperature of as high as 361°C at 200°C ambient without any failure.

Future Direction

FY 2007 and Beyond

- Acquire, test, and characterize newer-technology WBG power devices.
- Study the impact of SiC devices on plug-in hybrid vehicles.
- Study the fault current limiting capability of SiC devices for safety and protection.
- Study the possibility of using a thermal boundary in SiC power modules where Si gate drivers can be used.

Publications

M. Chinthavali, L. M. Tolbert, B. Ozpineci, and H. Zhang, "High Temperature Power Electronics—Application Issues of SiC Devices," in *International Conference on High Temperature Electronics (HiTEC 2006)*, International Microelectronics and Packaging Society, Santa Fe, New Mexico, May 15–18, 2006.

B. Ozpineci, M. S. Chinthavali, and L. M. Tolbert, "Enhancing Power Electronic Devices with Wide-Bandgap Semiconductors," *Journal of High Speed Electronics*, in press.

B. Ozpineci, M. S. Chinthavali, L. M. Tolbert, A. Kashyap, and A. H. Mantooth, "A 55-kW Three Phase Inverter with Si IGBTs and SiC Schottky Diodes," *IEEE Annual Applied Power Electronics Conference and Exposition*, March 19–23, 2006, Dallas.

H. Zhang, M. Chinthavali, B. Ozpineci, L. M. Tolbert, "Power Losses and Thermal Modeling of 4H-SiC VJFET Inverter," pp. 2630–2634 in *IEEE Industry Applications Society Annual Meeting*, October 2–6, 2005, Hong Kong, China,.

B. Ozpineci, M. S. Chinthavali, and L. M. Tolbert, ”A 55-kW Three Phase Automotive Traction Inverter with SiC Schottky Diodes,” pp. 541–546 in *IEEE Vehicle Power and Propulsion Conference*, Chicago, September 7–9, 2005.

References

1. B. Ozpineci, “System Impact of Silicon Carbide Power Electronics on Hybrid Electric Vehicle Applications,” Ph.D. Dissertation, Department of Electrical Engineering, The University of Tennessee, Knoxville, Tennessee, 2005.

Appendix. List of Devices Tested and Their Parameters

Power Diodes

Device type	Ratings	On-resistance (Ω)	Forward voltage drop (Volts)	Manufacturer	Year tested
SiC Schottky Diode	1200 V, 7.5 A	0.15 **Ω** at –50°C to 0.32 **Ω** at 175°C	1.42 **V** at –50°C to 1.21 **V** at 175°C	Rockwell	2004
SiC Schottky Diode	300 V, 10 A	0.15 **Ω** at –50°C to 0.16 **Ω** at 175°C	1.11 **V** at –50°C to 0.83 **V** at 175°C	Infineon	2004
SiC Schottky Diode	600 V, 4 A	0.19 **Ω** at –50°C to 0.39 **Ω** at 175°C	1.09 **V** at –50°C to 0.87 **V** at 175°C	Cree	2004
SiC Schottky Diode	600 V, 10 A	0.14 **Ω** at –50°C to 0.25 **Ω** at 175°C	1.09 **V** at –50°C to 0.82 **V** at 175°C	Cree	2004
SiC Schottky Diode	600 V, 75 A	0.01 **Ω** at –50°C to 0.03 **Ω** at 175°C	0.91 **V** at –50°C to 0.61 **V** at 175°C	Cree	2005
GaN Schottky Diode	600 V, 4 A	0.23 **Ω** at 25°C to 0.47 **Ω** at 175°C	0.83 **V** at 25°C to 0.67 **V** at 175°C	Velox	2006

Power Switches

Device type	Ratings	On-resistance (Ω)	Voltage drop at rated current @ room temperature (Volts)	Manufacturer	Year tested
SiC JFET	1200 V, 2 A	0.36 **Ω** at -50 °C to 1.4 **Ω** at 175 °C	1.3 V @ Vgs = 0V	SiCED	2004
SiC JFET	1200 V, 10 A	0.25 **Ω** at -50 °C to 0.58 **Ω** at 175 °C	2.71 V @ Vgs = 0V	SiCED	2006
SiC JFET	1200 V, 15 A	0.15 **Ω** at -50 °C to 2.2 **Ω** at 175 °C	3.2 V @ V_{gs} = 3V	Rockwell	2006
SiC JFET	600 V, 5 A	0.26 **Ω** at -50 °C to 1.87 **Ω** at 175 °C	2.25 V @ V_{gs} = 3 V	Semisouth	2006
SiC MOSFET	1200 V, 5 A	(0.48 **Ω** at -50 °C to 0.23 **Ω** at 50 °C) (0.24 **Ω** at 75 °C to 0.29 **Ω** at 175 °C)	1.5 V@ V_{gs}= 20 V	Cree	2005

4.2 Integrated dc-dc Converter for Multi-Voltage Bus Systems

Principal Investigator: Gui-Jia Su
Oak Ridge National Laboratory
National Transportation Research Center
2360 Cherahala Boulevard
Knoxville, TN 37932
Voice: 865-946-1330; Fax: 865-946-1262; E-mail: sugj@ornl.gov

DOE Technology Development Manager: Susan A. Rogers
Voice: 202-586-8997; Fax: 202-586-1600; E-mail: Susan.Rogers@ee.doe.gov

ORNL Program Manager: Mitch Olszewski
Voice: 865-946-1350; Fax: 865-946-1262; E-mail: olszewskim@ornl.gov

---

Objectives

- Develop a dc-dc converter topology that
  - — can significantly reduce the component count,
  - — is applicable to both triple-voltage and dual-voltage systems with essentially no hardware modifications,
  - — provides easy power scaling capability to meet power requirements for varying vehicle sizes, and
  - — can incorporate all future advanced components such as silicon carbide (SiC) devices and thermal management technologies as they become available.

- Produce a 4-kW prototype using 2-kW modules as building blocks and testing data to evaluate the prototype's capability to meet the FreedomCAR targets and power scaling capability.
- Establish requirements for dc-dc converters for various power system configurations in fuel cell–powered vehicles (FCVs).

Approach

The following approaches are taken to reduce the cost and size and increase the efficiency and power density of dc-dc converters for multi-bus systems in hybrid electric vehicles (HEVs) and FCVs.

- Increase the level of integration to minimize the number of switches and thus the associated gate drivers in order to reduce component count and still maintain a flexible topology: same circuit applicable to both dual- and triple-voltage systems.
- Increase switching frequency to reduce the weight, size, and volume of passive components.
- Employ soft switching and synchronous rectification to increase efficiency and power density.
- Employ soft switching to lower electromagnetic interference (EMI) noise.
- Use an interleaved modular approach for scaling power up.
- Optimize packaging.
- Conduct a literature search on dc-dc converters for FCV power systems.

Major Accomplishments

- Topology development
  - – A half-bridge–based dc-dc converter has been developed that can interconnect the 14-V, 42-V, and high–voltage (HV) buses and can reduce the component count by 50% over conventional full-bridge–based technologies. Further refinements have eliminated the LC filter for the 14-V bus.

- Interleaved modular configurations using the half-bridge as a building block share the capacitor legs and provide a greater degree of component count reduction as the number of modules increases when the power level is scaled up.
- The capacitor leg current in the interleaved configurations can be significantly reduced, thus decreasing the capacitance.
- A novel control scheme has also been devised that can control the power flow among the three buses and reduce the flux density of the transformers.

- Prototype demonstration
  - A 4-kW prototype has been designed and built using two 2-kW modules.
  - The prototype has been successfully tested at load power levels of up to 4.6 kW.
  - Measured efficiencies are between 93.0 and 95.8 % over a wide power range of 0.5 to 4.6 kW.
  - Evaluation of the prototype indicates that it exceeds the 2015 FreedomCAR targets for specific power and power density, and the 2010 cost target.
- dc-dc converter requirements study for FCV applications
  - Several possible power system configurations and the requirements for dc-dc converters have been identified.

Technical Discussion

Background

As the automotive industry moves to drive-by-wire through the electrification of power steering, braking, and suspension, a 42-V net will probably be needed, as the existing 14-V system cannot efficiently power these loads. The HV bus (200~500V) for traction drives will add to the difficulty in meeting the safety requirements and in coping with EMI issues caused by running HV wires throughout the vehicle. While this move is especially needed for FCVs, which have no internal combustion engines to assist with electrification mechanisms, drive-by-wire technology has already been employed in luxury vehicles. For instance, the Toyota RX400h hybrid sport utility vehicle (SUV) uses dc-dc converters to transform the traction battery voltage to 14 V for onboard electronics and to 42 V for electric power steering. In an SUV, the steering load alone demands a 42-V supply. In summary, a triple voltage bus (14-V/42-V/HV) system is likely to be employed in future HEVs and fuel cell–powered vehicles (FCVs).

Figure 1 illustrates a simplified diagram for power management in future FCVs that employs a triple voltage bus (14-V/42-V/HV) system. With presently available technologies, two separate dc-dc converters are needed to fulfill power management demands among the three buses: one for converting high voltage to 42 V and the other for transforming 42 V to 14 V. The cost and volume of this two-converter solution make it difficult to meet the FreedomCAR power density and cost targets. In addition, the dc-dc converters must provide bidirectional power flow control to enable the use of the 14-V or 42-V battery for fuel cell startup and for storing the energy captured by regenerative braking. During vehicle starting, the HV bus is boosted up to around 300 V by the dc-dc converter drawing power from the 14-V

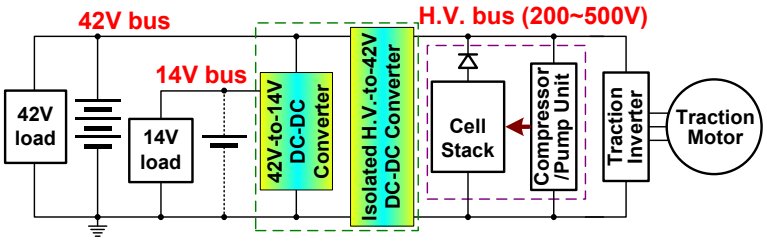


Figure 1. Power management in future fuel cell vehicles.

or 42-V battery. This HV bus then supplies power for the fuel cell compressor motor expanding unit controller and brings up the fuel cell voltage, which in turn feeds back to the HV bus to release the loading from the battery. During normal vehicle operation, power is transferred from the fuel cell stack to the low-voltage nets through the dc-dc converters to supply the vehicle accessory loads. The power management situation is similar in HEVs and plug-in HEVs, where the fuel cell power unit is replaced by an HV battery pack.

Although dc-dc converters are available to interconnect any two of the buses, to reduce component count, size, cost, and volume, it is desirable to employ an integrated dc-dc converter to interconnect the three voltage buses instead of using two separate ones. Aside from the bi-directional power control capability, the converter needs to provide galvanic isolation between the low-voltage and HV buses to meet safety requirements, which dictate the use of a transformer. Further, soft switching is preferred over hard switching because it reduces the level of EMI and switching losses.

In this project, a low-cost, soft-switched, isolated bi-directional dc-dc converter is being developed for interconnecting the three bus nets. The converter is based on a dual half-bridge topology to eliminate half of the switches required in a full-bridge counterpart. Further developments in the topology have led to the elimination of additional components. Figure 2 shows a diagram of the original converter, in which the 14-V bus is connected to the midpoint of the 42-V switch leg through an LC filter. This LC filter is eliminated in the modified topology shown in Figure 3, in which the 14-V bus is derived from the

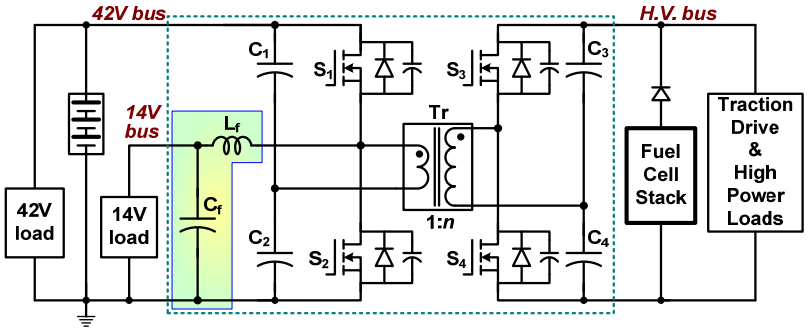


Figure 2. Original topology with LC filter.

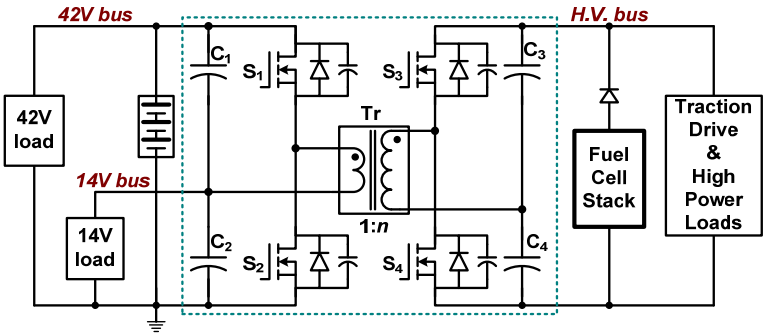


Figure 3. Modified topology that eliminates the LC filter.

capacitor leg. The converter uses the parasitic capacitance of the switches and the transformer leakage inductance to achieve zero-voltage-switching (ZVS). Therefore, no extra resonant components are required for ZVS, further reducing the component count. The inherent soft-switching capability and the low component count of the converter allow high power density, efficient power conversion, and compact packaging. A novel power flow control scheme based on a combined duty ratio and phase shift angle control has also been devised. The operation of the converter at a duty ratio other than the usual 50% reduces the peak flux density of the transformer, and thus a smaller core can be used.

To provide power scaling capability to meet the power requirements of vehicles of various sizes, without incurring the recurring engineering costs, a modular approach employing an interleaved multiphase configuration is the focus of the FY 2006 efforts. To this end, a 4-kW prototype using two 2-kW modules has been designed, built, and tested to evaluate its performance against the FreedomCAR targets.

In FCVs, in addition to the dc-dc converter for power management, higher-power dc-dc converters may be required to interface the fuel cell stack and/or high-power energy storage devices such as batteries and ultracapacitors. A study of dc-dc converter requirements for FCV applications was also performed in FY 2006.

Description of the dc-dc Converter for Triple Voltage Buses

Figure 4 shows a schematic of the 4-kW dc-dc converter, which consists of two half-bridge converter modules with shared capacitor legs. The high-frequency transformers, Tr_a and Tr_b, provide the required galvanic isolation and voltage level matching between the 42-V and the HV buses, while the 14-V and 42-V buses share a common ground. The leakage inductances of the transformers are used as the intermediate energy storage and transferring element between the two low-voltage buses and the HV net. The parasitic capacitors in parallel with the switches in each module resonate with the transformer leakage inductance to provide ZVS for the switches.

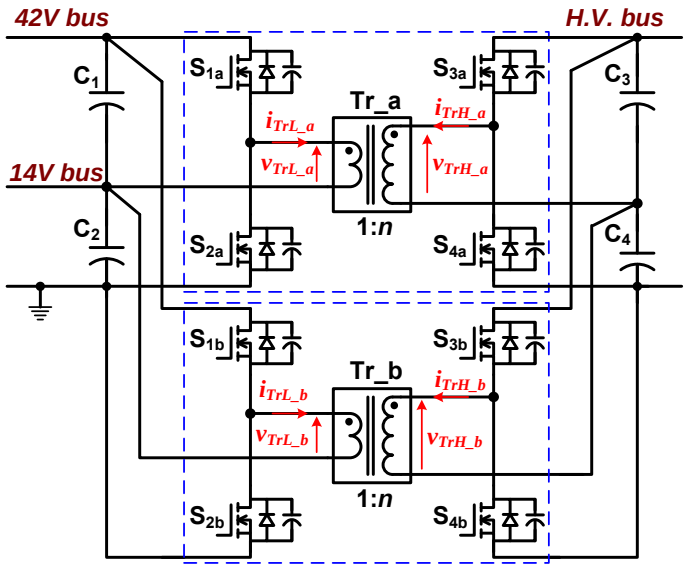


Figure 4. Schematic of the 4 kW dc-dc converter.

Figure 5 shows the transformer terminal voltages and currents waveforms to illustrate the operating principle of the converter. Duty ratio control is used for power flow control between the 14-V and 42-V buses, making the two bus voltages, V_{14V} and V_{42V}, track to each other by $V_{14V} = d \cdot V_{42V}$, where d is the duty ratio of the switches S_{1a} and S_{3a}, and S_{1b} and S_{3b}. It is defined by

$$d = \varphi/2\pi \quad , \tag{1}$$

where φ is the conduction angle of the switches S_{1a} and S_{3a}, and S_{1b} and S_{3b}. For 14-V/42-V systems, the duty ratio is fixed at $d = 1/3$, $\varphi = 2\pi/3$ at steady state for normal operation and can be changed to adjust the state of charge of the low-voltage batteries if necessary. In addition, a phase shift angle, ϕ, between the primary and secondary voltages of each transformer, v_{TrL_a} and v_{TrH_a} and v_{TrL_b} and v_{TrH_b}, is employed for power flow control between the 42-V and HV buses; $\phi > 0$ for low to high, $\phi < 0$ for high to low power transfer. Moreover, the transformer currents, i_{TrL_a} and i_{TrL_b} and i_{TrH_a} and i_{TrH_b}, are interleaved to reduce the capacitor leg currents, $i_{TrL_a} + i_{TrL_b}$ and $i_{TrH_a} + i_{TrH_b}$, and the capacitance by displacing the voltages of the two transformers by 180°, as shown in Figure 5.

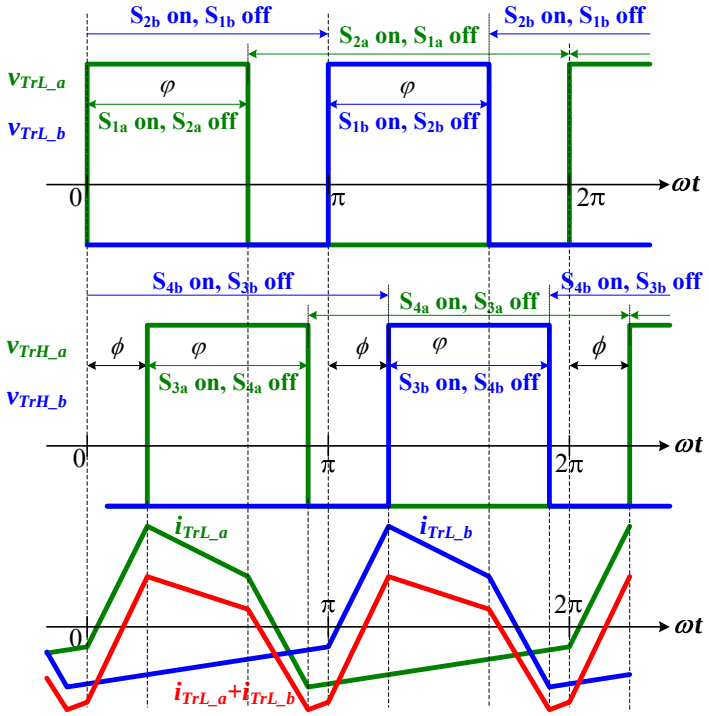


Figure 5. Transformer terminal voltages and currents waveforms illustating the operating principle.

The power transferred through the transformers at steady state with d = 1/3 can be expressed by

$$P = \frac{V_{42v} V_{HV}}{n} \cdot \frac{\phi}{2\pi f_{sw} L_s} \cdot [\frac{4}{9} - \frac{\phi}{2\pi}] \quad , \tag{2}$$

where n—transformer turns ratio, Ls—transformer leakage inductance, and fsw—switching frequency. For a given design, the maximum power is determined by

$$P_{\max} = \frac{V_{42v} V_{HV}}{n} \cdot \frac{4}{81 f_{sw} L_s} \text{ at } \phi_{P_{\max}} = \frac{4\pi}{9} \quad . \tag{3}$$

For a given bus voltage, V_{42V}, and switching frequency, f_{sw}, varying the duty ratio, d, will change the peak flux linkage, ψ_{peak}, of the transformer but will not introduce a dc bias. This is because the positive transformer terminal voltage, V_P, is $(1–d) \times V_{42V}$ at an interval of $t_P = d/f_{sw}$; and the negative transformer terminal voltage, V_N, is dV_{42V} but at an interval of $t_N = (1\text{-}d)/f_{sw}$, leading to the same product of volt × second of $d(1–d)V_{42V}/f_{sw}$ over the positive cycle and negative cycle. Further, operating at a duty ratio other than the usually employed 50% will decrease the peak flux linkage and thereby the transformer stress. The peak flux linkage is determined by $\psi_{peak} = \pm d(1\text{-}d)V_{42V}/(2f_{sw})$. At $d = 50$ %, $\psi_{peak} = \pm V_{42V}/(8f_{sw})$ while at $d = 1/3$ for our converter, the peak flux linkage is reduced to $\psi_{peak} = \pm V_{42V}/(9f_{sw})$ and thus a smaller transformer core can be used at the same switching frequency and number of turns.

Prototype Design and Experimental Results

Simulation study

A detailed circuit simulation was first performed for the 4-kW prototype design. Figure 6 shows simulation results where power is transferred from the 42-V bus to the 14-V and HV net at the level of 4.1 kW. Figure 7 shows simulated waveforms when the power flow is reversed. The simulation results confirm the design goal, that the power rating and the capacitor leg currents can be reduced to half of those in a single channel converter.

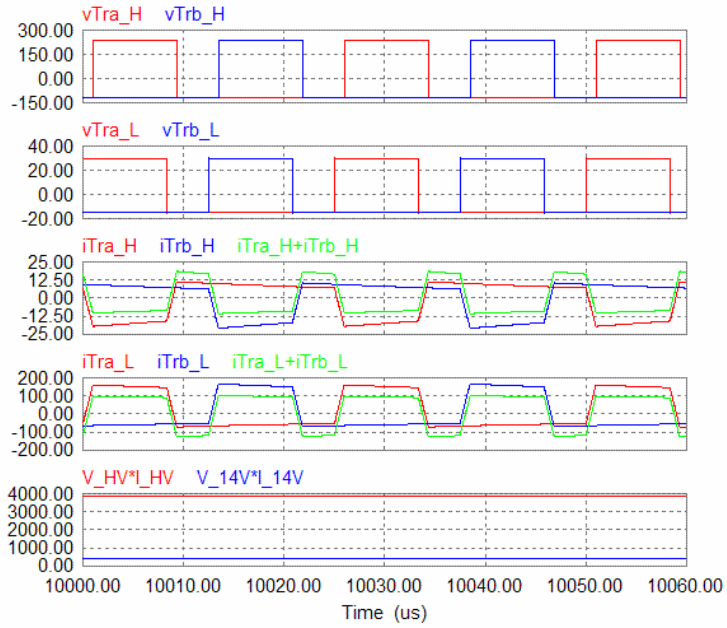


Figure 6. Simulation results showing power transfer from 42 V to 14 V and HV.

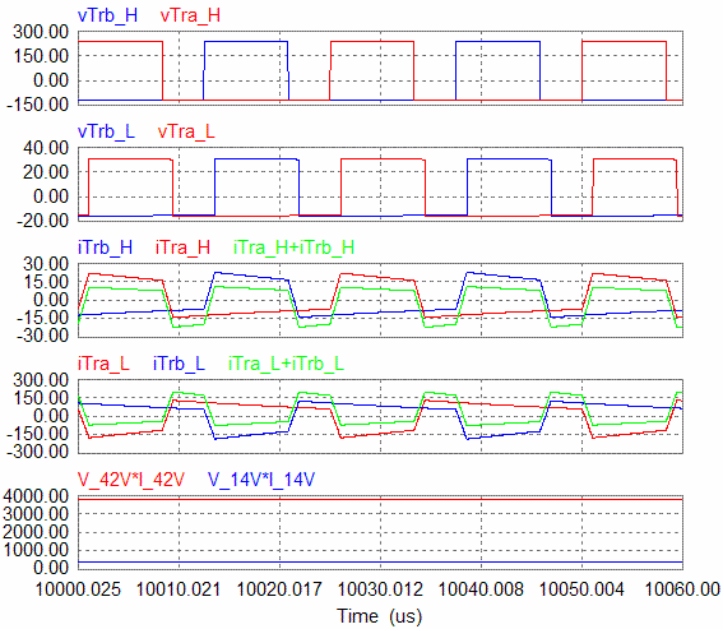


Figure 7. Simulation results showing power transfer from HV to 42 V and 14 V.

Converter design

A 4-kW prototype was then designed and built based on the analytical, simulation, and test results for a single-phase module. The design uses planar transformers, printed circuit power planes, and metal oxide semiconductor field effect transistors (MOSFETs) for both low and high voltages.

- Planar transformer design
  - Core, Ferroxcube E64/10/50
  - 4-layer PCB, 6 oz copper
  - Turns ratio, 1:8

- Power plane, 2-layer PCB
  - Low voltage: 6 oz copper
  - High voltage: 3 oz copper

- Benefits
  - Tight control of the leakage inductance—*important for soft-switching*
  - Easy assembly

- MOSFETS
  - Low-voltage side: SEMIKRON SK 300MB075, 75V/210A
  - High-voltage side: IXYS CoolMOS Power MOSFETVKM40-06P1, 600V/38A

Figure 8 shows a photo of the planar transformer.



Figure 8. Photo of the planar transformer.
Footprint: 4.875 × 2.125 in.

A new digital signal processor (DSP) control board based on a Texas Instruments chip, TMS320F2812, has been designed and fabricated for controlling the MOSFETs. The DSP chip has two sets of pulse width modulation hardware that can control up to three modules simultaneously. Figure 9 shows a photo of the DSP control board.



Figure 9. Photo of the DSP control board. Size: 7.0 × 3.5 in.

Figure 10 shows a 3-dimensional assembly layout of the prototype. As clearly indicated in the side view, there are quite large unoccupied spaces. The total converter volume is 203 in.^{3} with 93 in.^{3} accounted for by the individual components. This is partly because it was intentionally designed to provide space for easy probing access and partly because commercial-off-the-shelf components were used. It is estimated that 65% of the unoccupied space can be eliminated by optimizing the layout and by using customized packages for the major components.

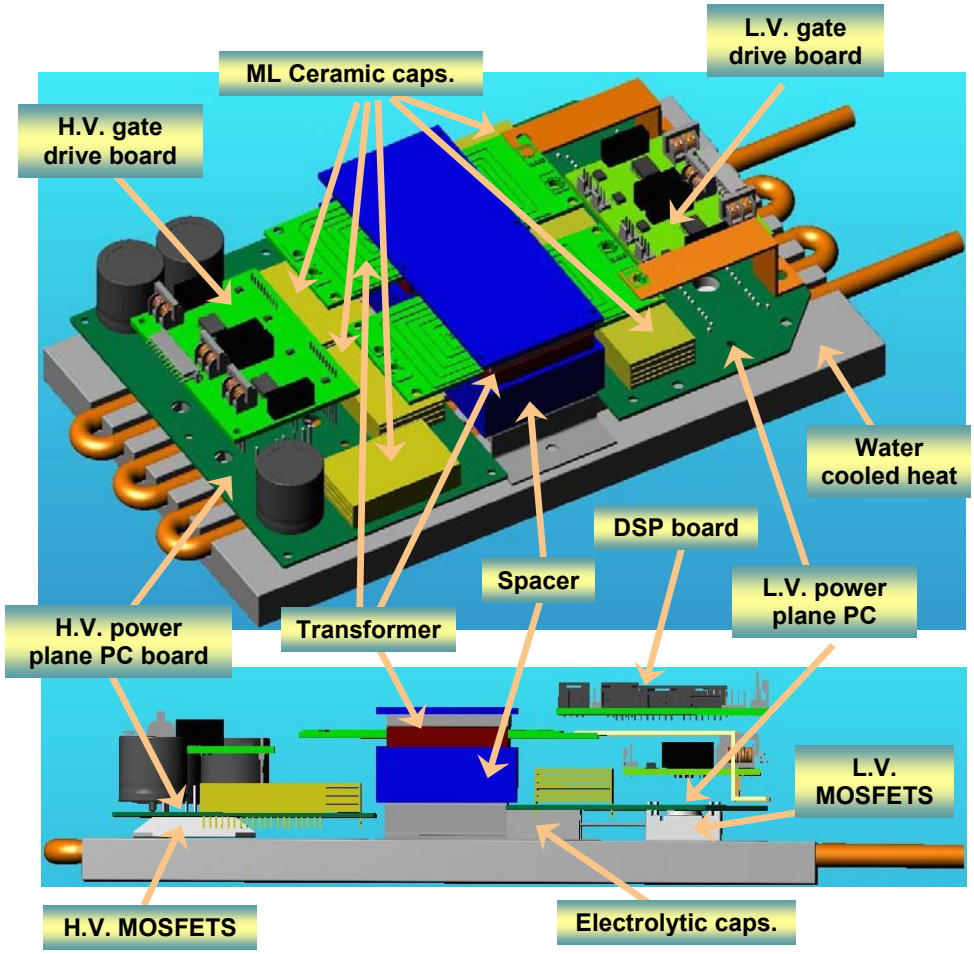


Figure 10. Three-dimensional assembly layout.

Figure 11 shows a photo of the 4-kW prototype. All components are mounted on a water-cooled heat sink 12 in. wide × 7.0 in. deep. The actual occupied footprint is 10.7 in. wide × 7.0 in. deep with a maximum height of 2.7 in. Evaluation of the prototype, assuming 65% of the unoccupied space can be removed, yielded performance numbers of 1.1 kW/kg, 2.1 kW/L, and $60/kW, which exceeds the 2015 FreedomCAR targets for specific power and power density and the 2010 cost target.

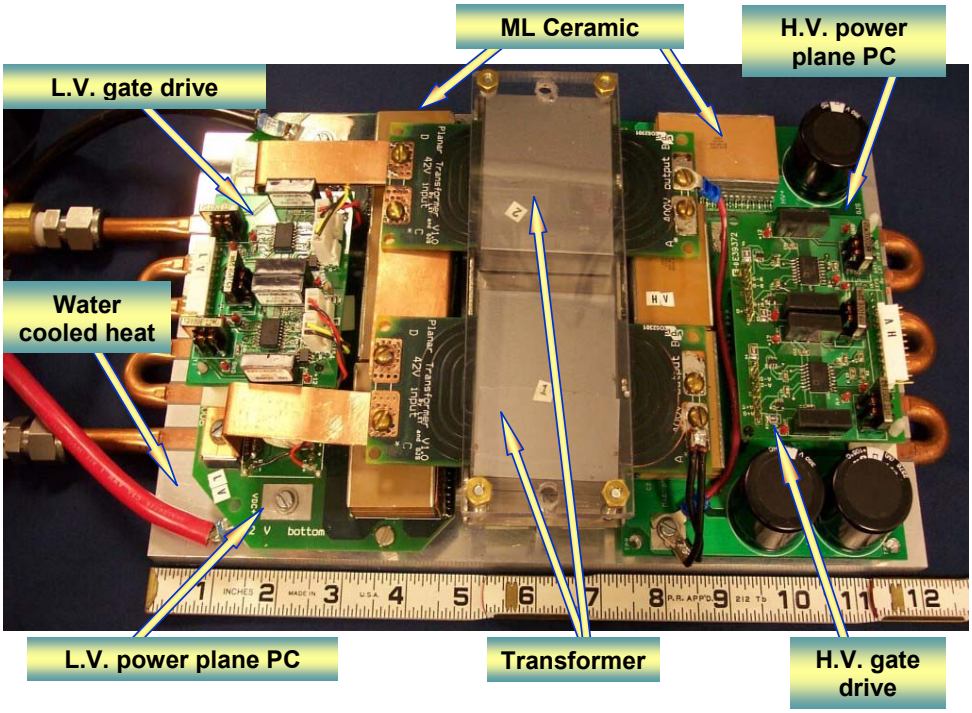
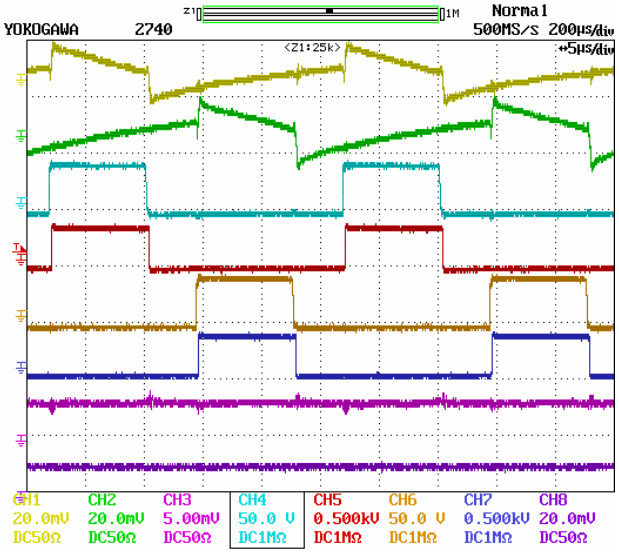


Figure. 11. The 4-kW prototype. Footprint: 10.7 in. wide × 11.0 in. deep × 2.7 in. maximum height.

Experimental results

The prototype was fully tested at power levels of up to 4.6 kW. Figures 12 and 13 show typical testing waveforms at different load power levels when power was transferred from the 42-V bus to the 14-V and HV buses, and from the HV bus to the 14-V and 42-V buses, respectively. The smooth rising and falling edges of the transformer voltages indicate soft-switching operation.

Figure 14 plots power conversion efficiency against the load power for both low-to-high and high-to-low conversion. Measured efficiencies are between 93.0 and 95.8 % over a wide power range of 0.5 to 4.6 kW for low-to-high conversion, against 93.0 to 95.7 % over a power range of 0.7 to 4.2 kW for high-to-low conversion.



i_{TrH_a}: 20A/div

i_{TrH_b}: 20A/div

v_{TrL_a}: 50V/div

v_{TrH_a}: 500V/div

v_{TrL_b}: 50V/div

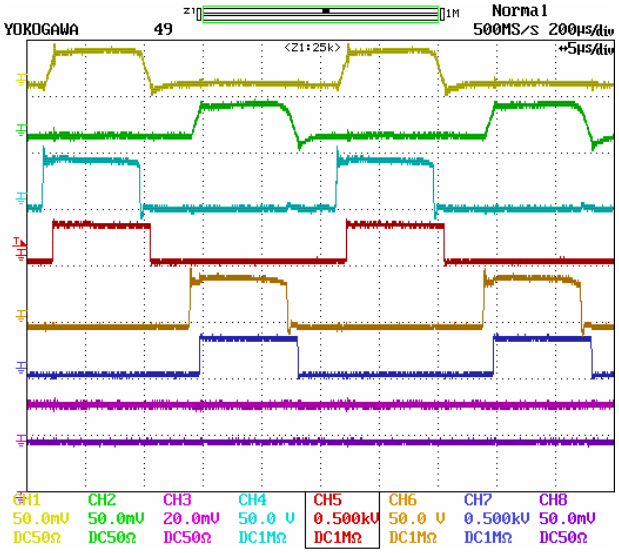
v_{TrH_b}: 500V/div

I_{HV_Load}: 5A/div

I_{14V_Load}: 20A/div

Time: 5µs/div

(a) Load power: 1.18 kW



i_{TrH_a}: 50A/div

i_{TrH_b}: 50A/div

v_{TrL_a}: 50V/div

v_{TrH_a}: 500V/div

v_{TrL_b}: 50V/div

v_{TrH_b}: 500V/div

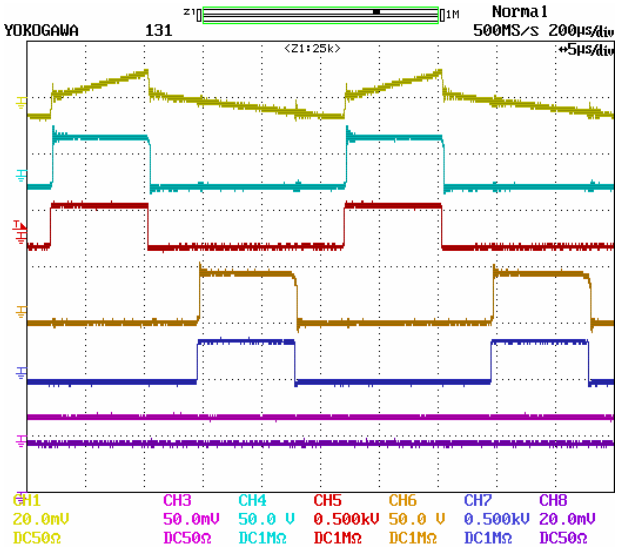
I_{HV_Load}: 20A/div

I_{14V_Load}: 50A/div

Time: 5µs/div

(b) Load power: 4.2 kW

Figure 12. Typical testing waveforms for power transfer from 42 V to 14 V and HV.



i_{TrH_a}: 20A/div

v_{TrL_a}: 50V/div

v_{TrH_a}: 500V/div

v_{TrL_b}: 50V/div

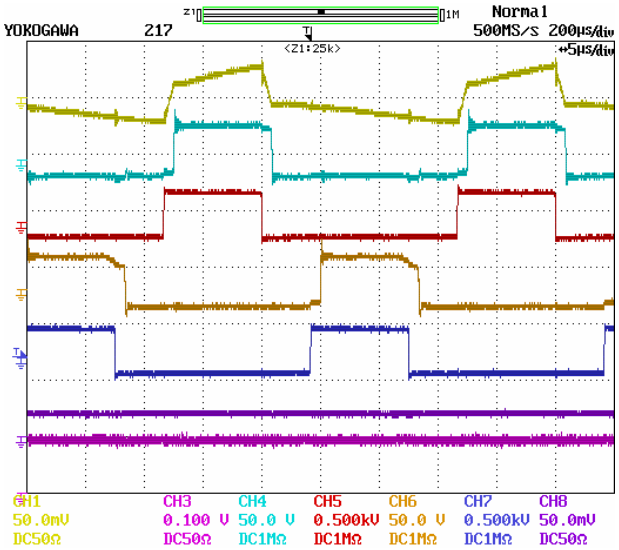
v_{TrH_b}: 500V/div

I_{42V_Load}: 50A/div

I_{14V_Load}: 20A/div

Time: 5µs/div

(a) Load power: 0.991 kW



i_{TrH_a}: 50A/div

v_{TrL_a}: 50V/div

v_{TrH_a}: 500V/div

v_{TrL_b}: 50V/div

v_{TrH_b}: 500V/div

I_{14V_Load}: 50A/div

I_{42V_Load}: 100A/div

Time: 5µs/div

(b) Load power: 4.23 kW

Figure 13. Typical testing waveforms for power transfer from HV to 42 V and 14 V.

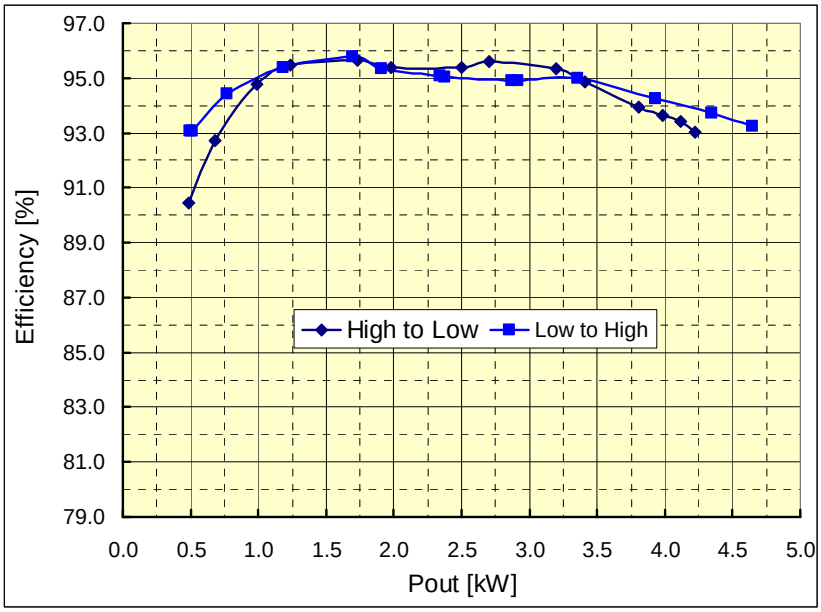
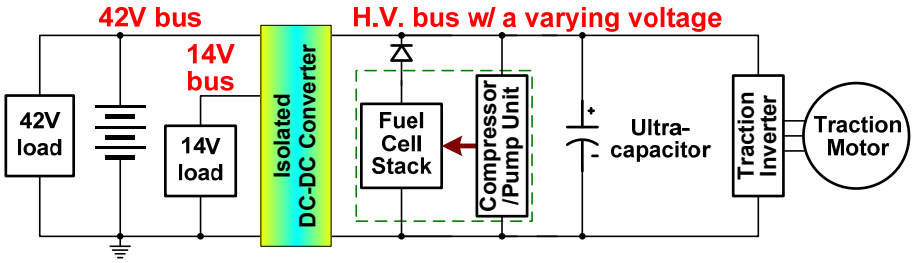


Figure 14. Efficiency chart.

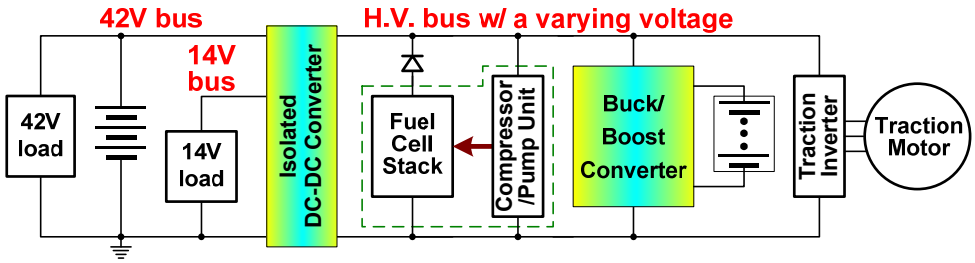
dc-dc Converter Requirements Study for Fuel Cell Vehicle Applications

A literature search was conducted to determine what power system architectures are being considered by original equipment manufacturers. While a few publications did turn up data on the Hyundai Tucson fuel cell electric vehicle, Honda FCX, and Toyota fuel cell hybrid vehicle, published information is presently quite scarce. Based on the limited findings, several possible power system configurations are identified in Figure 15, along with the requirements for the dc-dc converter needed in each architecture.

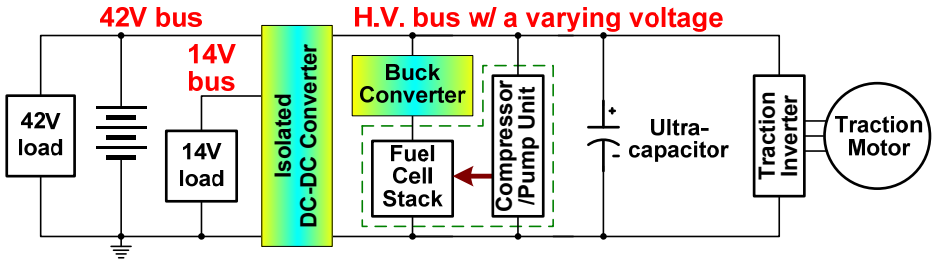


(a) This topology uses the capability of ultracapacitors to operate over a widely fluctuating bus voltage produced by the fuel stack as load power changes. The ultracapacitors compensate for the slow response of the fuel cell stack and store regenerative power during braking. The isolated dc-dc converter must be bi-directional to power the compressor/pump unit for startup of the fuel cell stack and needs to provide a peak power of several kilowatts, typically around 5 kW.

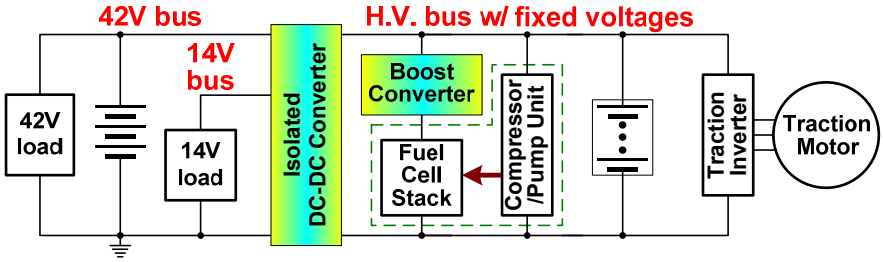
Figure 15. Possible electrical power system architectures for fuel cell vehicles.



(b) In this topology, a buck/boost converter is required to employ batteries at the high-voltage bus because batteries cannot operate at the widely fluctuating bus voltage produced by the fuel stack as load power changes. The peak power rating of the buck/boost is in the range of several tens of kilowatts, typically around 30 kW.



(c) A buck converter is employed in this scenario to control the power of the fuel stack. The benefits of doing so are twofold: it enables the ultracapacitors to capture more regenerative power during braking while keeping the bus voltage below a safe level, and it keeps the bus voltage below a safe level at light load conditions under which the fuel cell stack output voltage rises significantly. The buck converter needs to handle the peak power of the fuel cell stack, typically in the range of 80–100 kW. The isolated dc-dc converter must be bi-directional to power the compressor/pump unit for startup of the fuel cell stack and needs to provide a peak power of several kilowatts, typically around 5 kW.



(d) A boost converter is employed in this topology to regulate the output voltage of the fuel cell stack to provide a stable bus voltage so the batteries can be directly connected to the dc bus. The peak power rating of the boost converter is the same as that of the fuel cell stack, typically 80–100 kW. If desired, a buck/boost converter can be used to interface a lower-voltage battery as in configuration (b), possibly reducing the battery cost and facilitating the use of a higher bus voltage optimized for a more efficient traction drive system.

Figure 15. (continued).

Conclusion

The integrated dc-dc converter for triple-voltage-bus systems (14-V/42-V/HV) for HEVs and FCVs applications has the following features:

- Employs interleaved half-bridge modules with each one using only four switching devices and all modules sharing the capacitor legs, leading to significant cost savings and higher power density.
- Requires no LC filter for the 14-V bus.
- Employs soft switching and synchronous rectification for high efficiency and low EMI.
- Requires no auxiliary circuit or complex control dedicated for soft switching.
- Provides flexible power flow management owing to the capability to transfer power among all three voltage buses by employing the combined duty ratio and phase shift angle control scheme, which also reduces the flux density of the transformers.

A 4-kW prototype has been designed and built using two 2-kW modules and has been successfully tested at load power levels all the way up to 4.6 kW. Measured efficiencies are between 93.0 and 95.8% over a wide power range of 0.5 to 4.6 kW. Evaluation of the prototype indicates that it exceeds the 2015 FreedomCAR targets for specific power and power density and the 2010 cost target.

The information on the possible power system configurations and the requirements of dc-dc converters identified in this report is useful to guide future dc-dc converter development for FCV applications.

Future Direction

- Develop control algorithms to reduce the capacity of the 42-V battery or eliminate it and test with the 4-kW prototype
- Further improve the efficiency through optimization of the topology and packaging

Publications and Presentations

G. J. Su, L. Tang, and X. Huang, "Control of Two Permanent Magnet Machines Using a Five-Leg Inverter for Automotive Applications," presented at IEEE IAS 2006, October 8–12, 2006.

L. Tang, G. J. Su, and X. Huang, "Experimental High Performance Control of Two Permanent Magnet Synchronous Machines in an Integrated Drive for Automotive Applications," presented at IEEE COMPEL 2006 Workshop, July 16–19, 2006.

G. J. Su and J. S. Hsu, "A Five-Leg Inverter for Driving a Traction Motor and a Compressor Motor," *IEEE Trans. on Power Electronics* **21**(3), 687–692 (May 2006).

G. J. Su, "Pulse-Width-Modulation Schemes for an Integrated Traction and Compressor Drive System," pp. 640–645 in *IEEE APEC 2006*, vol. 2, March 19–23, 2006.

Patents

G. J. Su, "Multi-Level DC Bus Inverter for Providing Sinusoidal and PWM Electrical Machine," U.S. No. 6,969,967, November 29, 2005.

G. J. Su, "Integrated Inverter for Driving Multiple Electrical Machines," U.S. Patent No. 7,023,171, April 4, 2006.

G. J. Su, "Triple Voltage dc-to-dc Converter and Method," U.S. Patent Office Disclosure No. 1300001646, October 28, 2005.

References

1. G. J. Su and F. Z. Peng, "A Low Cost, Triple-Voltage Bus DC/DC Converter for Automotive Applications," pp. 1015–1021 in *IEEE Applied Power Electronics Conference and Exposition* (APEC), vol. 2, Austin, Texas, March 6–10, 2005.
2. G. J. Su, D. J. Adams, F. Z. Peng, and H. Li, "A Soft-Switched DC/DC Converter for Fuel Cell Applications," *SAE 2002 Transactions—Journal of Passenger Cars: Electronic and Electrical Systems*, ISBN 0-7680-1291-0, pp. 757–764, September 2003.

3. G. J. Su, F. Z. Peng, and D. J. Adams, "Experimental Evaluation of a Soft-Switching DC/DC Converter for Fuel Cell Vehicle Applications," pp. 39–44 in *Seventh IEEE Workshop on Power Electronics in Transportation* (WPET2002), DaimlerChrysler Technical Center, Auburn Hills, Michigan, October 24–25, 2002.
4. D. M. Divan and O. Patterson, "A Pseudo-resonant Full Bridge dc/dc Converter," pp. 424–430 in *Conf. Rec. 1987 IEEE Power Electronics Specialist Conf.*, 1987.
5. M. H. K. Wang et al., "Bi-directional dc to dc Converters for Fuel Cell Systems," pp. 47–51 in *Conf. Rec. 1998 IEEE Power Electronics In Transportation*, 1998.
6. T. Ishikawa, S. Hamaguchi, and T. Shimizu, "Development of Next Generation Fuel Cell Hybrid System—Consideration of High Voltage Systems," SAE technical paper 2004-01-1304, Society of Automotive Engineers 2004 World Congress and Exhibition, Detroit, March 2004.
7. S-H. Choi and S-K. Kim, "Development of Fuel Cell Hybrid Vehicle by Using Ultra-Capacitors as a Secondary Power Source," SAE technical paper 2005-01-0015, Society of Automotive Engineers 2005 World Congress and Exhibition, Detroit, April 2005.
8. S. H. Kim and J. A. Ferro, "Development of Hyundai's Tucson FCEV," SAE technical paper 2005-01-0005, Society of Automotive Engineers 2005 World Congress and Exhibition, Detroit, April 2005.
9. A. Ohkawa, "Electric Power Control System for a Fuel Cell Vehicle Employing Electric Double-Layer Capacitor," SAE technical paper 2004-01-1006, Society of Automotive Engineers 2004 World Congress and Exhibition, Detroit, March 2004.

4.3 Cascaded Multilevel Inverter

Principal Investigator: Burak Ozpineci
Oak Ridge National Laboratory
National Transportation Research Center
2360 Cherahala Boulevard
Knoxville, TN 37932
Voice: 865-946-1329; Fax: 865-946-1262; E-mail: ozpinecib@ornl.gov

DOE Technology Development Manager: Susan A. Rogers
Voice: 202-586-8997; Fax: 202-586-1600; E-mail: Susan.Rogers@ee.doe.gov

ORNL Program Manager: Mitch Olszewski
Voice: 865-946-1350; Fax: 865-946-1262; E-mail: olszewskim@ornl.gov

Objectives

- To produce a cascade multilevel inverter that combines inverter and converter functions.
- To eliminate the magnetics required for the dc-dc boost converter, therefore reducing the weight, volume, and cost of the system while increasing its efficiency.

Approach

- Assess the performance and cost trade-offs to come up with a viable design.
- Simulate the inverter/converter in PSpice for circuit operation.
- Design simulation of the electric traction drive system (inverter/converter/motor) in Simulink.
- Design a 1.2-kW unit.

Major Accomplishments

- Developed a control algorithm to keep the capacitors charged.
- Simulated the inverter/converter in PSpice and Simulink.
- Developed a design simulation of an electrical drive system with the inverter/converter.
- Designed a 1.2-kW prototype.

Technical Discussion

A cascade multilevel inverter is a power electronic device built to synthesize a desired ac voltage from several levels of dc voltages. Such inverters have been the subject of research in the last several years,[1–4] where the dc levels were considered to be identical because all of them were batteries, solar cells, etc. In Reference 5, a multilevel converter was presented in which the two separate dc sources were the secondaries of two transformers coupled to the utility ac power. Corzine et al.[6] have proposed using a single dc power source and capacitors for the other dc sources. A method was given to transfer power from the dc power source to the capacitor in order to regulate the capacitor voltage. A similar approach was later (but independently) proposed by Du et al.[7] These approaches required a dc power source for each phase. Similar methods have also been proposed by Veenstar and Rufer.[8,9] The approach here is very similar to that of Corzine et al.[6] and Du et al.[7] with the important exception that only a single standard three-leg inverter is required as the power source (one leg for each phase) for the three-phase multilevel inverter.

Specifically, the interest here is in using a single dc power source connected to a standard three-leg inverter, which in turn is connected to capacitors to form a three-phase five-level cascade multilevel inverter to be used as a drive for a permanent magnet (PM) traction motor. The five-level inverter consists of a standard three-leg inverter (one leg for each phase) and an H-bridge in series with each inverter leg

and using a capacitor as a dc source. It is shown that one can simultaneously maintain the regulation of the capacitor voltage while achieving an output voltage waveform that is 25% higher than that obtained using a standard three-leg inverter by itself.

Multilevel Inverter Architecture

Figure 1 shows a dc source connected to a single leg of a standard three-leg inverter.

The output voltage v_1 of this leg (with respect to the ground) is either $+V_{dc}/2$ (S_5 closed) or $-V_{dc}/2$ (S_6 closed). This leg is connected in series with a full H-bridge, which in turn is supplied by a capacitor voltage. If the capacitor is kept charged to $V_{dc}/2$, then the output voltage of the H-bridge can take on the values $+V_{dc}/2$ (S_1 and S_4 closed), 0 (S_1 and S_2 closed or S_3 and S_4 closed), or $-V_{dc}/2$ (S_2 and S_3 closed). An example output waveform that this topology can achieve is shown in Figure 2.

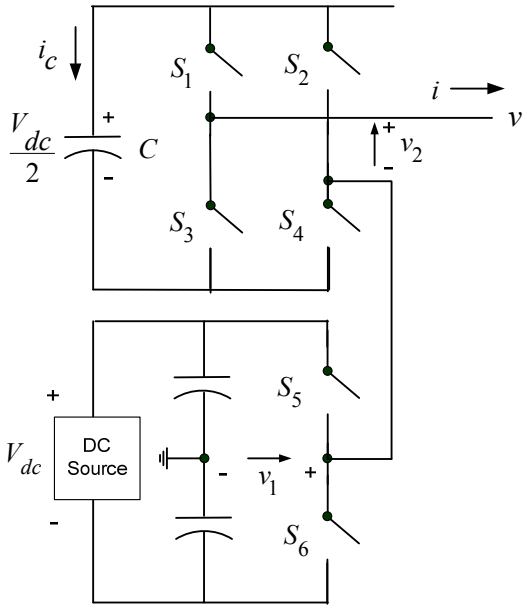


Figure 1. One leg of a three-leg inverter connected to a full H-bridge with a capacitor dc source.

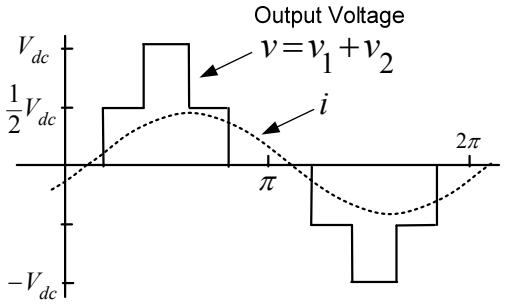


Figure 2. Five-level output waveform of the multilevel inverter.

When the output voltage $v = v_1 + v_2$ is required to be zero, one can either set $v_1 = +V_{dc}/2$ and $v_2 = -V_{dc}/2$ or $v_1 = -V_{dc}/2$ and $v_2 = +V_{dc}/2$. It is this flexibility in choosing how to make that output voltage zero that is exploited to regulate the capacitor voltage. In more detail, consider Figure 3.

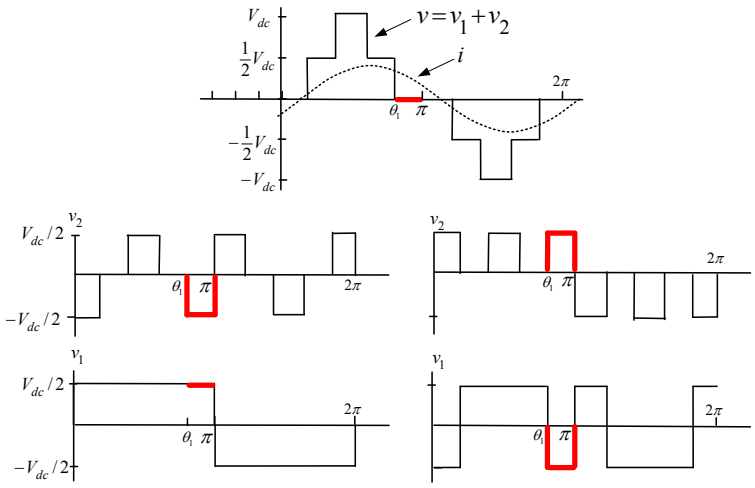


Figure 3. To make the output voltage zero for $\theta_1 \le \theta \le \pi$, one can either set $v_1 = +V_{dc}/2$ and $v_2 = -V_{dc}/2$ (bottom left) or $v_1 = +V_{dc}/2$ and $v_2 = +V_{dc}/2$ (bottom right).

In the interval $\theta_1 \le \theta \le \pi$, the output voltage in Figure 3 is zero, and the current $i > 0$. If S_1 and S_4 are closed (so that $v_2 = +V_{dc}/2$) along with S_6 closed (so that $v_1 = +V_{dc}$), then the capacitor is discharging ($i_c = -i < 0$; see Figure 1) and $v = v_1 + v_2 = 0$. On the other hand, if S_2 and S_3 are closed (so that $v_2 = -V_{dc}/2$) and S_5 is also closed (so that $v_1 = -V_{dc}/2$), then the capacitor is charging ($i_c = i > 0$; see Figure 1) and $v = v_1 + v_2 = 0$.

The case $i < 0$ is accomplished by simply reversing the switch positions of the $i > 0$ case for charge and discharge of the capacitor. Consequently, the method consists of monitoring the output current and the capacitor voltage so that during periods of zero voltage output, either the switches S_1, S_4, and S_6 are closed or the switches S_2, S_3, and S_5 are closed depending on whether it is necessary to charge or discharge the capacitor.

Remark

As Figure 3 illustrates, this method of regulating the capacitor voltage depends on the voltage and current not being in phase. That is, one needs positive (or negative) current when the voltage is passing through zero to charge or discharge the capacitor. Consequently, the ability to regulate the capacitor voltage depends on the power factor.

Simulation Results Using Multilevel PWM

A simulation of the multilevel converter driving a PM synchronous machine was carried out. The basic block diagram for the simulation is shown in Figure 4.

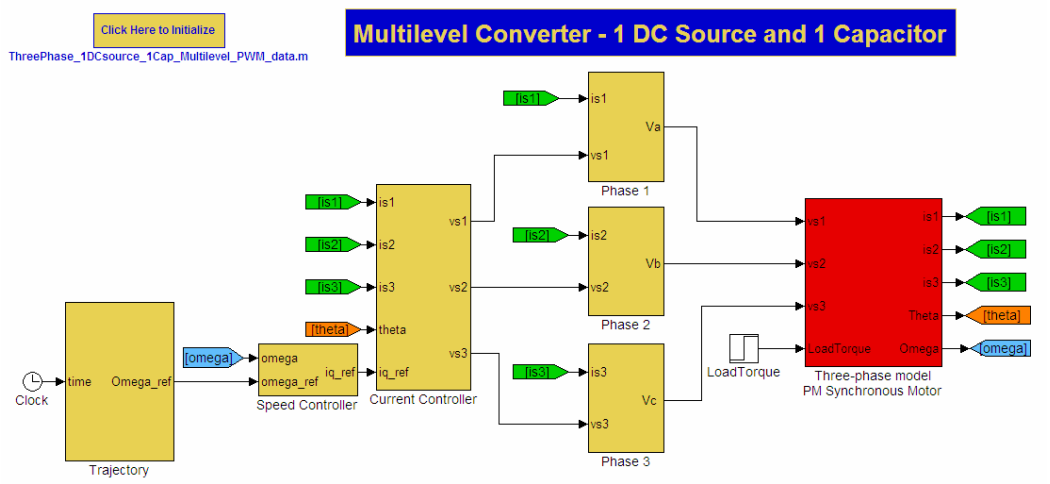


Figure 4. Top level Simulink block diagram.

The motor is controlled using a standard field-oriented controller.[10] The blocks marked phase 1, phase 2, and phase 3 contain the modeling of the multilevel converter. The switching scheme is based on the standard multilevel pulse width modulation (PWM) scheme.[11] The scheme is modified so that during those time periods when the multilevel inverter has an output of zero volts, either the switches S_1, S_4, and S_6 are closed or the switches S_2, S_3, and S_5 are closed, depending on whether the current is positive or negative and whether it is necessary to charge or discharge the capacitor.

The dc link voltage V_{dc} was set to 200 V so that the three-leg inverter supplies ±100 V. The capacitors were regulated to 100 V. The motor's inertia is $J = 0.1$ kg-m^2, the motor has $n_p = 4$ pole-pairs, the stator resistance is $R_S = 0.065\ \Omega$, the stator inductance is $L_S = 3$ mH, the torque/back-emf constant $K_T = K_b = 0.37$ Nm/A (V/rad/s) and the load torque $\tau_L = 19$ Nm. The capacitor value is $C = 0.01$ F.

For comparison purposes, simulations were performed using both the multilevel inverter of Figure 1 capable of supplying up to ±200 V and a standard three-leg inverter (i.e., only the bottom half of Figure 1) capable supplying ±100 V. Though the multilevel inverter can supply up to ±200 V, it cannot do this and maintain regulation of the capacitor voltages. As pointed out earlier, the ability to regulate the capacitor voltage depends on the power factor of the load. The PM motor was run to achieve the highest possible speed under the given load and available voltage. This is shown in Figure 5. The standard three-leg inverter could only achieve a maximum speed of 212 rad/s, while the proposed multilevel inverter could get the motor up to 275 rad/s using the same dc source voltage.

The corresponding voltages for the speed trajectories of Figure 5 are shown in Figure 6. The standard three-leg inverter is supplying a nearly six-step wave form of $V_{dc}/2 = 100$ V maximum corresponding to a fundamental voltage of $(4/\pi)V_{dc}/2 = 127$ V peak, while the multilevel inverter output is 170 V peak in steady state and up to 180 V before steady state.

The corresponding torques for the above trajectories are shown in Figure 7. The chattering shown in the torque response of the standard three-leg inverter results from the voltage undergoing saturation (see the left side of Figure 6).

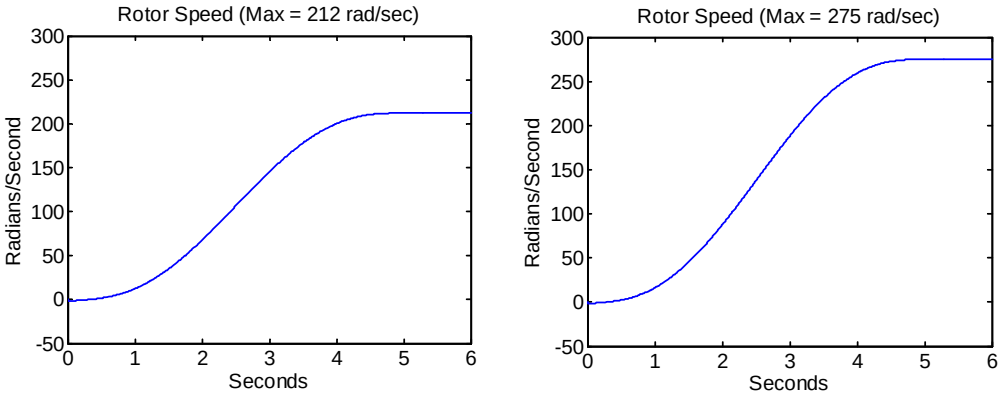


Figure 5. Rotor speeds achievable using a standard three-leg inverter (left) and the proposed multilevel inverter (right).

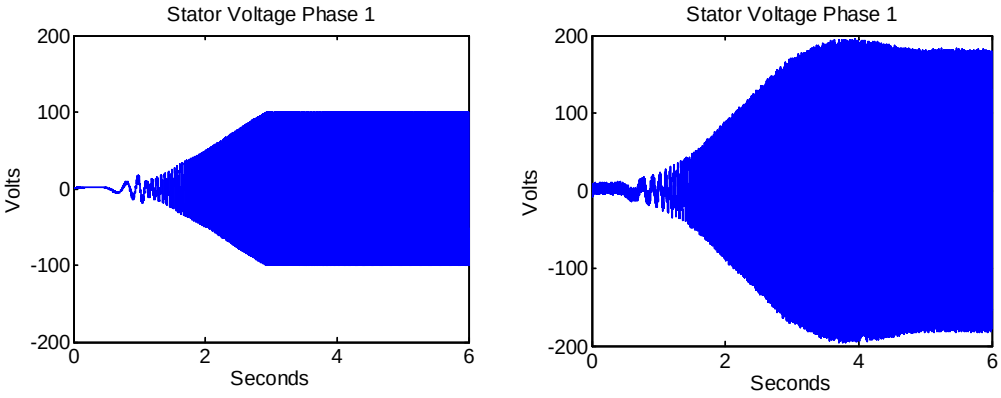


Figure 6. Left: Voltage using a standard three-leg inverter. Right: Voltage obtained using the proposed multilevel inverter.

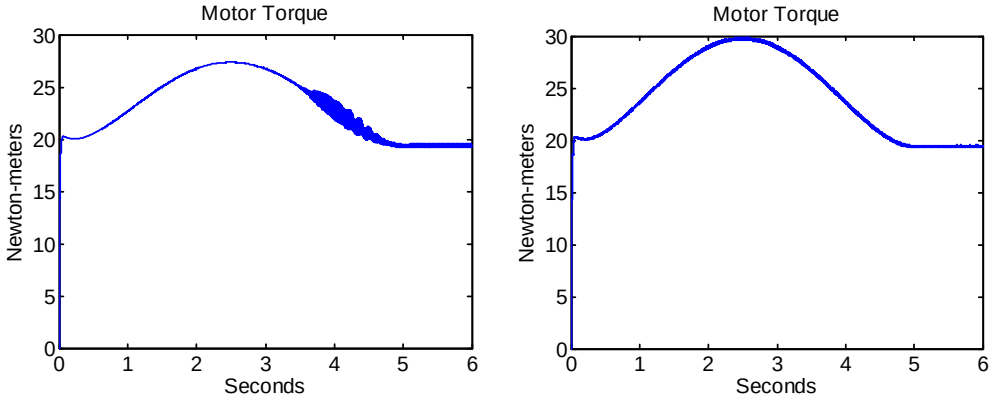


Figure 7. Left: Motor torque using standard three-leg inverter. Right: Motor torque using proposed multilevel inverter.

The stator currents are shown in Figure 8. The current used in the multilevel inverter is higher because it requires more torque to accelerate the motor to its higher speed (see Figure 5).

The capacitor voltage as a function of time is plotted in Figure 9, showing that it is kept within about 2 V of the desired value.

An enlarged view of the capacitor voltage is shown in Figure 10, showing the regulation of the voltage in more detail. The variation in the voltage will be less if a larger value of capacitance is used ($C = 0.01$ F in the simulation).

Note that the capacitor voltage decreases during those times when the inverter is supplying ±100 V, is constant during those times the inverter is supplying ±50 V, and is increasing (recharging) during those times the inverter is supplying 0 V. For example, a little after $t = 5.577$ s, the current becomes positive, and the inverter is required to put out (up to) 200 V (only 100 in the figure due to the scaling) by the PWM scheme. The capacitor voltage (red) then decreases. Then shortly before $t = 5.579$ s, the inverter is only required to supply up to 100 V (only 50 in the figure due to the scaling), and the capacitor voltage is constant. At about $t = 5.579$ s, the multilevel PWM scheme is having the inverter supply 0 V for significant time intervals, so the capacitor voltage increases.

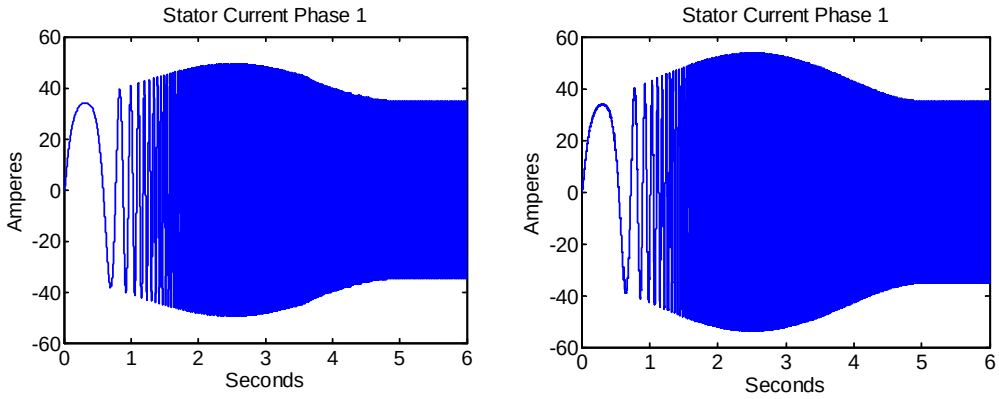


Figure 8. Left: Stator current for the standard three-leg inverter. Right: Stator current for the proposed multilevel inverter.

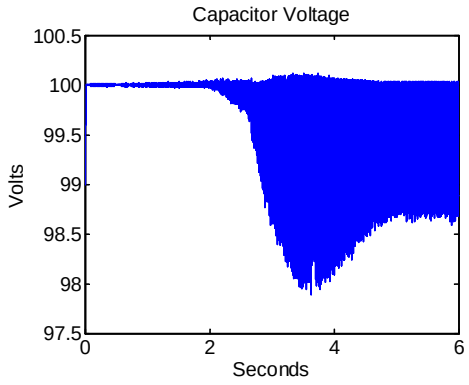


Figure 9. Capacitor voltage vs time.

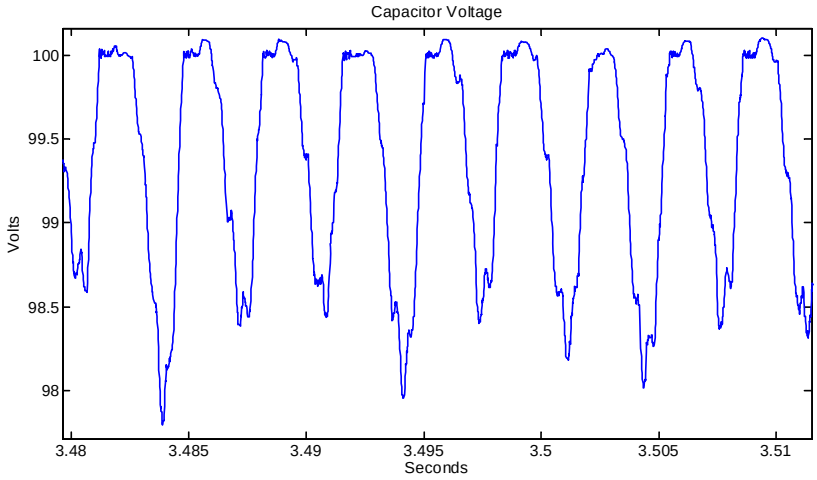


Figure 10. Expanded view of the capacitor voltage as a function of time.

Simulation Results—Fundamental Frequency Switching

In this section a fundamental frequency switching scheme is used. By fundamental frequency switching, it is meant that each device switches once per cycle in contrast to a PWM scheme for which each device turns on and off several times a cycle. Typically a fundamental switching scheme results in a higher harmonic content in the lower frequency spectrum (closer to the fundamental) than a PWM method, but has lower switching losses. In the five-level multilevel inverter under consideration here, a fundamental switching scheme is implemented by choosing two angles θ_1 and θ_2 for when the devices are to be switched on as indicated in Figure 11. By symmetry of the waveform, the rest of the switching occurs at $\pi-\theta_1, \pi-\theta_2, \pi+\theta_1, \pi+\theta_2, 2\pi-\theta_1$, and $2\pi-\theta_2$.

With the nominal capacitor voltage chosen as $V_{dc}/2$, one computes the switching angles θ_1 and θ_2 as in References 12 and 13. Briefly, the Fourier series expansion of the (staircase) output voltage waveform of the multilevel inverter as shown in Figure 11 is

$$V(\omega t)=\frac{4}{\pi}\frac{V_{dc}}{2}\times\sum_{n=1,3,5,\ldots}^{\infty}\frac{1}{n}\left(\cos(n\theta_1)+\cos(n\theta_2)\right)\sin(n\omega t) \quad . \tag{1}$$

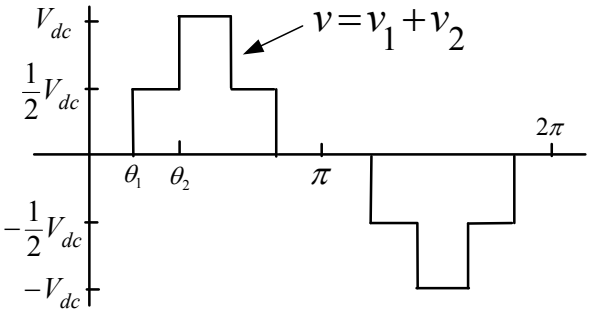


Figure 11. Fundamental frequency waveform.

Ideally, given a desired fundamental voltage V_1, one wants to determine the switching angles θ_1 and θ_2 so that (FS) becomes $V(\omega t) = V_1 \sin(\omega t)$. In practice, one is left with trying to do this approximately. For three-phase systems, the triplet harmonics in each phase need not be canceled as they automatically cancel in the line-to-line voltages. In this case, where there are two dc sources, the desire is to cancel the fifth order harmonic as it tends to dominate the total harmonic distortion. The mathematical statement of these conditions is then

$$\cos(\theta_1) + \cos(\theta_2) = m = \frac{V_1}{\frac{4}{\pi}\frac{V_{dc}}{2}} \quad . \qquad (2)$$

$$\cos(5\theta_1) + \cos(5\theta_2) = 0 \quad .$$

This is a system of two transcendental equations in the two unknowns θ_1 and θ_2. There are many ways one can solve for the angles (see, for example, References 14–16). Here the approach in Reference 12 and Reference 17 is used. It is found that a solution to (conditions1) exists for $0.6 \le m \le 1.909$, and these solution angles are plotted in Figure 12. Note that the fundamental is given by

$$V_1 = m\frac{4}{\pi}\frac{V_{dc}}{2} \quad . \qquad (3)$$

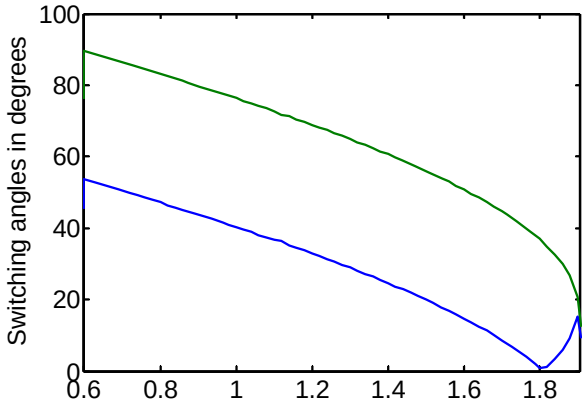


Figure 12. θ_1 and θ_2 vs m.

In the simulations presented here, the same PM motor as chosen for the multilevel PWM scheme was used, but the motor was driven open-loop rather than closed-loop. The voltage magnitude was ramped from 90 V to 180 V during the time interval from 0 to 3 s. The stator electrical frequency f_S was brought up smoothly from 0 to 175 Hz in 5 s resulting in a peak speed of $2\pi f_S / n_p = 275$ rad/s. This is the same speed trajectory as used in the closed-loop multilevel PWM implementation above. The resulting speed response is shown in Figure 13, which is somewhat oscillatory due to the open-loop control. Because it is driven open loop, it is much more difficult to have the machine go up in speed with a significant load torque at the start. As a result, only a viscous friction load torque was used with the viscous friction coefficient chosen as $f = 0.07$ so that at maximum speed the load torque is $f\omega_{\max} = f(2\pi f_S / n_p) = 0.07 * 275 = 19$ Nm, giving the same steady-state load-torque as in the multilevel PWM case.

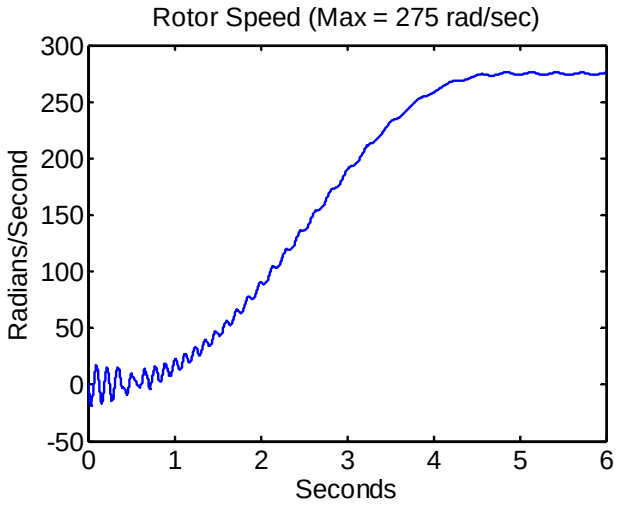


Figure 13. Rotor speed in rad/s vs time in seconds.

The commanded voltage magnitude [see (fund)] and the computed fundamental of the inverter output are given in Figure 14.

The computed fifth harmonic of the voltage is plotted vs time in Figure 15. During the end of the run when the speed is close to being constant, the fifth-harmonic is about 0.7 V compared with the 180 V of the fundamental.

The motor torque is shown in Figure 16, which is oscillatory as a result of the open-loop control. Note that at the end of the run, the torque is oscillating about 19 Nm to counteract the (viscous-friction) load torque.

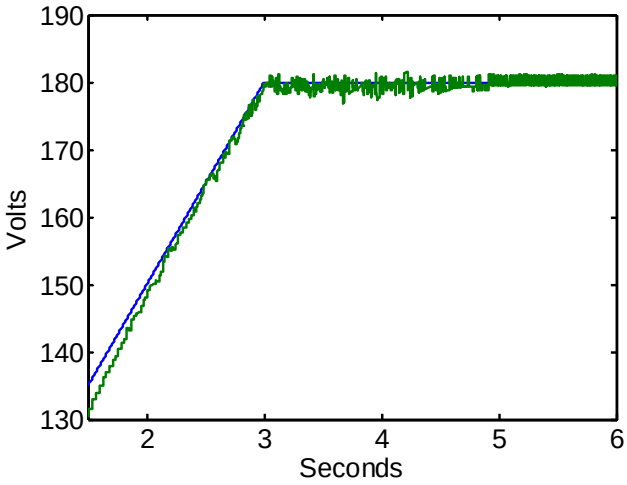


Figure 14. Commanded and computed fundamental voltage in volts vs time in seconds.

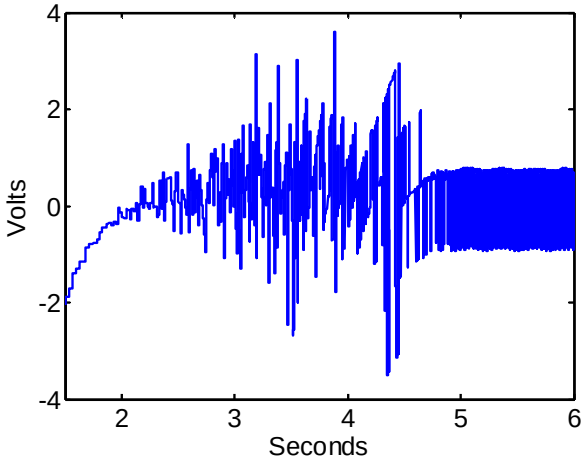


Figure 15. Computed fifth-harmonic of the voltage in volts vs time in seconds.

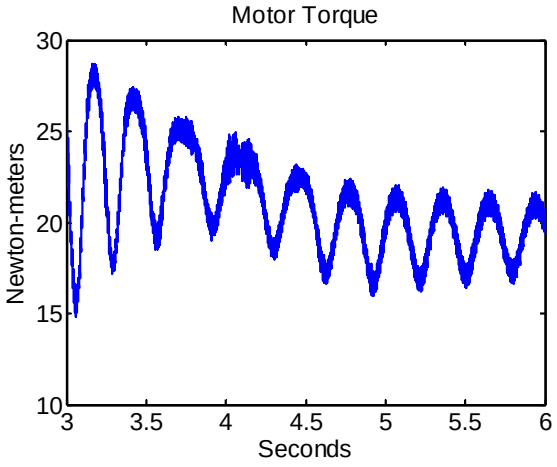


Figure 16. Torque in N-m vs time in seconds.

An enlarged section of the inverter output voltage of phase 1 is given in Figure 17 and shows the fundamental switching scheme for a stator frequency of $f_S = 175$ Hz.

The stator current response of phase 1 is plotted in Figure 18 and uses somewhat more current than the closed-loop PWM scheme (see Figure 8).

The capacitor voltage is shown in Figure 19, showing that the scheme regulates the voltage within 3 V of the nominal value. The value of the capacitance is $C = 0.01$ F as in the multilevel PWM case. An enlarged view of the capacitor voltage for $5.5 \le t \le 5.525$ is shown in Figure 20.

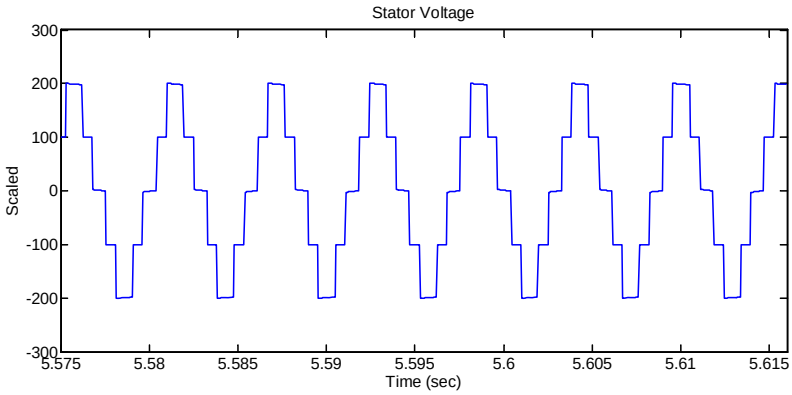


Figure 17. Enlarged view of the phase 1 voltage in volts vs time in seconds.

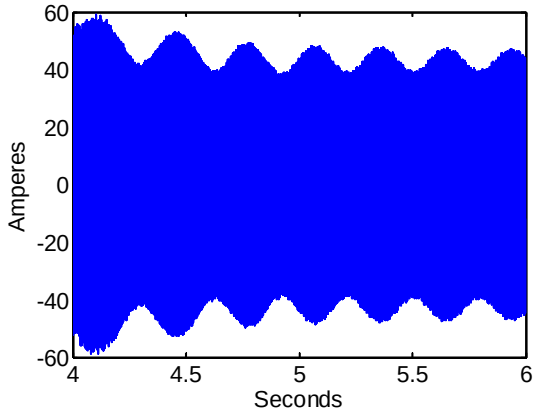


Figure 18. Phase 1 stator current vs time.

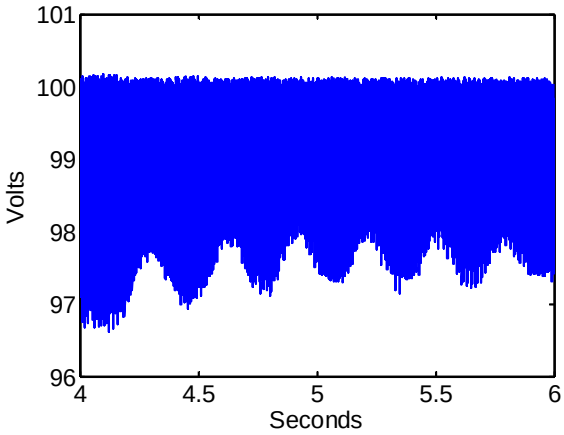


Figure 19. Capacitor voltage in volts vs time in seconds.

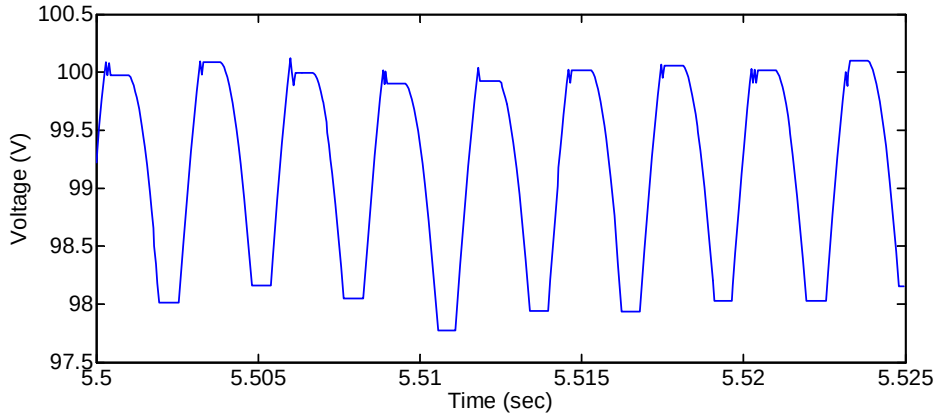


Figure 20. An enlarged view the capacitor voltage in volts vs time in seconds.

Scaled versions of the capacitor voltage, stator current, and stator voltage vs time are shown in Figure 21. Note that the capacitor discharges when the inverter is supplying ±200 V, stays constant when the inverter is supplying ±100 V, and recharges when the inverter is supplying 0 V.

For example, a little after $t = 5.575$ s, the stator current becomes positive, and the inverter is required to supply 200 V. The capacitor voltage then decreases. Following this, when the inverter is only required to supply 100 V, the capacitor voltage is constant. Next, the inverter is putting out 0 V so that the capacitor is charging and its voltage increases.

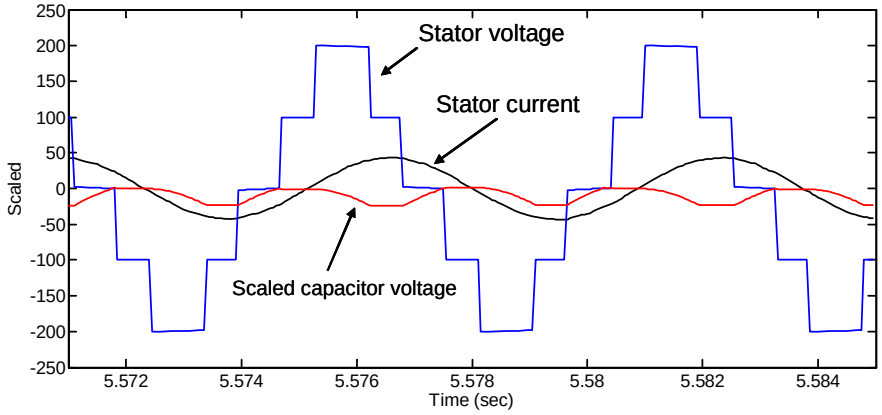


Figure 21. Scaled capacitor voltage, stator current, and stator voltage vs time in seconds.

Conditions for Capacitor Voltage Regulation

Let

$$v_f(\theta) = V\sin(\theta)\ ,$$
$$i(\theta) = I\sin(\theta - \varphi)\ , \tag{4}$$

where $v_f(\theta)$ is the fundamental component of the voltage, $i(\theta)$ is the current, and φ is the power factor angle. The objective here is to compute the conditions on θ_1, θ_2, and φ to ensure the capacitor can be regulated to a desired value.

Interval 1: $0 < \varphi < \theta_1$

Consider the case where $0 < \varphi < \theta_1$ as illustrated in Figure 22. During the interval $\theta_2 < \theta < \pi - \theta_2$, the capacitor loses the amount of charge $\int_{\theta_2}^{\pi-\theta_2} I\sin(\theta-\varphi)d\theta$, while during the intervals $0 < \theta < \theta_1$ and $\pi - \theta_1 < \theta < \pi$ the capacitor can be recharged (by choosing the switch positions appropriately) by the amounts $\int_0^{\varphi} I\left|\sin(\theta-\varphi)\right|d\theta + \int_{\varphi}^{\theta_1} I\sin(\theta-\varphi)d\theta$ and $\int_{\pi-\theta_1}^{\pi} I\sin(\theta-\varphi)d\theta$, respectively.

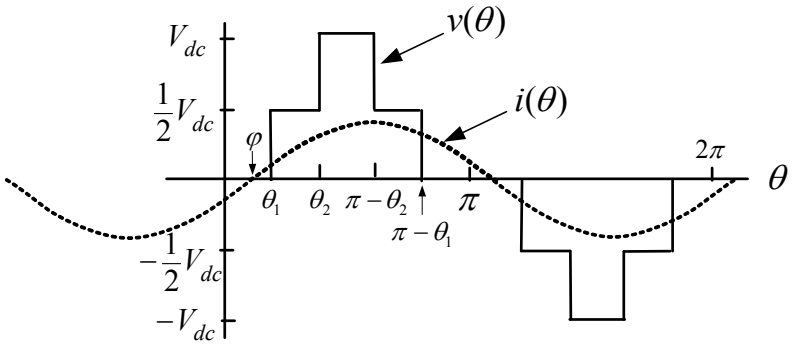


Figure 22. $0 < \varphi < \theta_1$.

In this case, keeping the capacitor charged requires

$$\begin{aligned} \int_{\theta_2}^{\pi-\theta_2} I\sin(\theta-\varphi)d\theta &< \int_0^{\varphi} I\left|\sin(\theta-\varphi)\right|d\theta + \int_{\varphi}^{\theta_1} I\sin(\theta-\varphi)d\theta + \int_{\pi-\theta_1}^{\pi} I\sin(\theta-\varphi)d\theta \\ I\cos(\theta_2+\varphi) + I\cos(\theta_2-\varphi) &< \left(I\cos(0) - I\cos(\varphi)\right) + \left(-I\cos(\theta_1-\varphi) + I\cos(0)\right) + \\ &\quad \left(I\cos(\varphi) - I\cos(\theta_1+\varphi)\right) \\ \cos(\theta_2)\cos(\varphi) &< \cos(0) - \cos(\theta_1)\cos(\varphi)\ , \end{aligned} \tag{5}$$

or finally, the condition in this case is

$$\cos(\varphi) < \frac{1}{\cos(\theta_1)+\cos(\theta_2)}\ . \tag{6}$$

Interval 2: $\theta_1 < \varphi < \theta_2$

Consider the case $\theta_1 < \varphi < \theta_2$ as in Figure 23. During the interval $\theta_2 < \theta < \pi - \theta_2$, the capacitor loses the amount of charge $\int_{\theta_2}^{\pi-\theta_2} I\sin(\theta-\varphi)d\theta$, while during the intervals $0 < \theta < \theta_1$ and $\pi - \theta_1 < \theta < \pi$ the capacitor can be recharged (by choosing the switch positions appropriately) by the amount $\int_0^{\theta_1} I\left|\sin(\theta-\varphi)\right|d\theta + \int_{\pi-\theta_1}^{\pi} I\sin(\theta-\varphi)d\theta$.

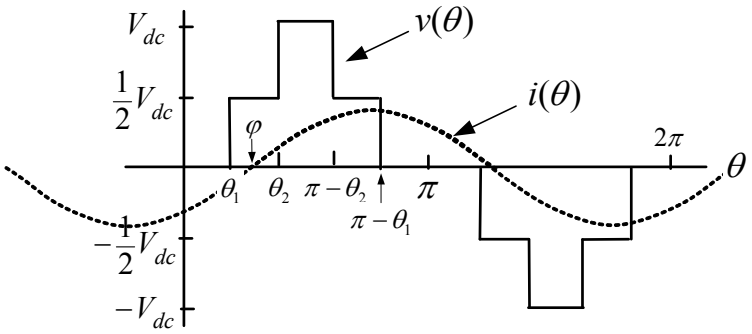


Figure 23. $\theta_1 < \varphi < \theta_2$.

Thus, keeping the capacitor voltage regulated requires

$$\int_{\theta_2}^{\pi-\theta_2} I\sin(\theta-\varphi)d\theta < \int_0^{\theta_1} I\left|\sin(\theta-\varphi)\right|d\theta + \int_{\pi-\theta_1}^{\pi} I\sin(\theta-\varphi)d\theta \quad . \tag{7}$$

Expanding

$$\begin{aligned} I\cos(\theta_2+\varphi)+I\cos(\theta_2-\varphi) &< \left(I\cos(\theta_1-\varphi)-I\cos(\varphi)\right)+\left(I\cos(\varphi)-I\cos(\theta_1-\varphi)\right) \\ 2I\cos(\theta_2)\cos(\varphi) &< 2I\sin(\theta_1)\sin(\varphi)\,, \end{aligned} \tag{8}$$

or finally, the condition is

$$\frac{\cos(\theta_2)}{\sin(\theta_1)} < \tan(\varphi) \quad . \tag{9}$$

Interval 3: $\theta_2 < \varphi < \pi/2$

Finally, consider the case where $\theta_2 < \varphi < \pi/2$ as shown in Figure 24. During the subinterval $\theta_2 < \theta < \varphi$, the capacitor is being charged as the current is negative while it is discharging in subinterval $\varphi < \theta < \pi - \theta_2$. Thus the total discharge in the interval $\theta_2 < \theta < \pi - \theta_2$ is $\int_{\theta_2}^{\pi-\theta_2} I\sin(\theta-\varphi)d\theta$.

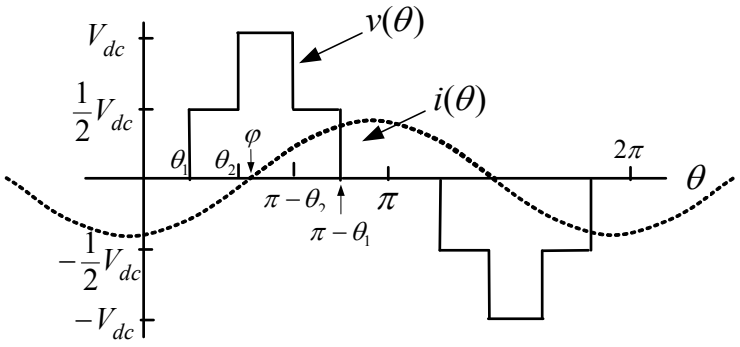


Figure 24. $\theta_2 < \varphi < \pi/2$.

Thus, keeping the capacitor voltage regulated requires

$$\int_{\theta_2}^{\pi-\theta_2} I\sin(\theta-\varphi)d\theta < \int_0^{\theta_1} I\left|\sin(\theta-\varphi)\right|d\theta + \int_{\pi-\theta_1}^{\pi} I\sin(\theta-\varphi)d\theta \quad . \tag{10}$$

Expanding

$$\begin{aligned} I\cos(\theta_2+\varphi)+I\cos(\theta_2-\varphi) &< \left(I\cos(\theta_1-\varphi)-I\cos(\varphi)\right)+\left(I\cos(\varphi)-I\cos(\theta_1+\varphi)\right) \\ 2I\cos(\theta_2)\cos(\varphi) &< 2I\sin(\theta_1)\sin(\varphi)\,, \end{aligned} \tag{11}$$

or finally, the condition is

$$\frac{\cos(\theta_2)}{\sin(\theta_1)} < \tan(\varphi) \quad , \tag{12}$$

which has the same form as the previous case.

Capacitor voltage regulation as a function of *m* and φ

In summary, the conditions for capacitor voltage regulation in terms of θ_1, θ_2, and φ are

$$\begin{aligned} &0<\varphi<\theta_1 && \cos(\varphi) < \frac{1}{\cos(\theta_1)+\cos(\theta_2)} = \frac{1}{m}\,. \\ &\theta_1<\varphi<\pi/2 && \frac{\cos(\theta_2)}{\sin(\theta_1)} < \tan(\varphi)\,. \end{aligned} \tag{13}$$

Notice at the boundary of the two conditions where $\varphi=\theta_1$, the two conditions are identical. These conditions can be rewritten as

$$\begin{aligned} &0<\varphi<\theta_1 && \varphi > \cos^{-1}(1/m)\,. \\ &\theta_1<\varphi<\pi/2 && \varphi > \tan^{-1}\left(\frac{\cos(\theta_2)}{\sin(\theta_1)}\right). \end{aligned} \tag{14}$$

Figure 12 is a plot of θ_1 and θ_2 in degrees vs *m* (the modulation index is *m*/2). For any given value of *m* and φ, the values of θ_1 and θ_2 are found via Figure 12, and thus whether or not the capacitor voltage can be regulated is straightforwardly checked using the conditions (conditions2). What these conditions say is, for any given value of *m* in the interval $0.6 \le m \le 1.909$ [i.e., where conditions (conditions1) have a solution], the capacitor voltage can be regulated provided the power factor angle is large enough.

Conclusions

A cascade multilevel inverter topology has been proposed that requires only a single standard three-leg inverter and capacitors as the power sources. The capacitors obtain their power from the three-leg inverter, allowing the cascade multilevel inverter to put out significantly more voltage from a given dc power source than just a three-leg inverter alone. Both multilevel PWM and fundamental frequency

switching schemes were considered. Finally, subject to conditions in terms of the power factor and modulation index (= $m/2$), it was shown that the capacitor voltages could be regulated.

Future Direction

- A 1.2-kW prototype will be built to demonstrate the operation of the converter with a fuel cell (FY 2007).
- More simulation studies will be done to add plug-in hybrid capabilities to the cascaded multilevel inverter (FY 2007).
- If the 1.2-kW prototype is successful, a full-power 105-kW unit will be built (FY 2008–2009).

Publications

Z. Du, L. M. Tolbert, J. Chiasson, and B. Ozpineci, "A Cascade Multilevel Inverter Using a Single DC Source," Applied Power Electronics Conference, APEC 2006, Dallas, Texas.

Z. Du, L. M. Tolbert, J. Chiasson, B. Ozpineci, H. Li, and A.Q. Huang, "Hybrid Cascaded H-bridges Multilevel Motor Drive Control for Electric Vehicles," Power Electronics Specialists Conference, PESC 2006, Jeju Korea.

References

1. M. Klabunde, Y. Zhao, and T. A. Lipo, "Current control of a 3-level Rectifier/Inverter Drive System," pp. 2348–2356 in *Conference Record 1994 IEEE IAS Annual Meeting*, 1994.
2. W. Menzies, P. Steimer, and J. K. Steinke, "Five-level GTO Inverters for Large Induction Motor Drives," *IEEE Transactions on Industry Applications*, **30**(4), 938–944 (July 1994).
3. J. K. Steinke, "Control Strategy for a Three Phase AC Traction Drive with Three Level GTO PWM Inverter," pp. 431–438 in IEEE *Power Electronic Specialist Conference*, 1988.
4. J. Zhang, "High Performance Control of a Three Level IGBT Inverter Fed AC Drive," pp. 22–28 in *Conf. Rec. IEEE IAS Annual Meeting,* 1995.
5. M. Manjrekar, P. K. Steimer, and T. Lipo, "Hybrid Multilevel Power Conversion System: A Competitive Solution for High-Power Applications," *IEEE Transactions on Industry Applications*, **36**(3), 834–841 (May/June 2000).
6. K. A. Corzine, F. A. Hardrick, and Y. L. Familiant, "A Cascaded Multi-level H-bridge inzverter Utilizing Capacitor Voltage Sources," pp. 290–295 in *Proceedings of the IASTED International Conference*, Palm Springs, California, 2003.
7. Z. Du, L. M. Tolbert, J. N. Chiasson, and B. Ozpineci, "Cascade Multilevel Inverter Using a Single dc Source," pp. 426–430 in *Proceedings of the Applied Power Electronics Conference*, Dallas, Texas, 2006.
8. M. Veenstra and A. Rufer, "Non-equilibrium State Capacitor Voltage Stabilization in a Hybrid Asymmetric Nine-level Inverter: Non-linear Model-predictive Control," in *Proceedings of the European Control Conference, Toulouse, France,* 2003.
9. M. Veenstra and A. Rufer, "Control of a Hybrid Asymmetric Multilevel Inverter for a Competitive Medium-voltage Industrial Drive," *IEEE Transactions on Industry Applications*, **IAS-41**(2), 655–664 (March/April 2005).
10. J. Chiasson, *Modeling and High-Performance Control of Electric Machines*, John Wiley & Sons, New York, 2005.
11. D. G. Holmes and T. Lipo, *Pulse Width Modulation for Power Electronic Converters*, Wiley Interscience, 2003.
12. J. Chiasson, L. M. Tolbert, K. McKenzie, and Z. Du, "Control of a Multilevel Converter Using Resultant Theory," *IEEE Transactions on Control System Technology*, **11**(3), 345–354 (May 2003).
13. L. M. Tolbert, F. Z. Peng, and T. G. Habetler, "Multilevel Converters for Large Electric Drives," *IEEE Transactions on Industry Applications*, **35**(1), 36–44 (Jan./Feb. 1999).

14. P. N. Enjeti, P. D. Ziogas, and J. F. Lindsay, "Programmed PWM Techniques to Eliminate Harmonics: A Critical Evaluation," *IEEE Transactions Industry Applications*, **26**(2), 302–316 (March/April 1990).
15. J. Vassallo, P. W.Wheeler, and J. C. Clare, "Optimal Waveform Generation for Utility-connected Multilevel Converters," in *European Power Electronics Conference,* September 2003.
16. T. Kato, "Sequential Homotopy-based Computation of Multiple Solutions for Selected Harmonic Elimination in PWM Inverters," *IEEE Transactions on Circuits and Systems—1: Fundamental Theory and Applications*, **46**(5), 586–593 (May 1999).
17. J. Chiasson, L. Tolbert, K. McKenzie, and Z. Du, "Elimination of Harmonics in a Multilevel Converter Using the Theory of Symmetric Polynomials," *IEEE Transactions on Control Systems Technology*, **13**(2), 216–223 (March 2005).

4.4 Advanced Converter Systems for High-Temperature HEV Environments

Principal Investigator: Leon M. Tolbert
Oak Ridge National Laboratory
National Transportation Research Center
2360 Cherahala Boulevard
Knoxville, TN 37932
Voice: 865-946-1332; Fax: 865-946-1262; E-mail: tolbertlm@ornl.gov

DOE Technology Development Manager: Susan A. Rogers
Voice: 202-586-8997; Fax: 202-586-1600; E-mail: Susan.Rogers@ee.doe.gov

ORNL Program Manager: Mitch Olszewski
Voice: 865-946-1350; Fax: 865-946-1262; E-mail: olszewskim@ornl.gov

---

Objectives

The goal of this project is to develop a new and unique bidirectional dc-dc power converter that incorporates high-temperature power devices and capacitors with a high-temperature packaging technology and gate drives that will enable the converter to operate in high ambient temperature conditions. This project will develop a converter that has greatly reduced weight/mass, volume, and maintenance/service with high system efficiency, performance, and reliability compared with existing dc-dc converters for hybrid electric vehicles (HEVs).

Air-cooled high-temperature capacitors and SiC power electronics will lead to smaller thermal management systems, which will increase the peak power-to-weight ratio. Reduction of thermal management systems and lack of magnetic devices should offset the higher cost for SiC devices and high-temperature capacitors. Lower switching losses in a multilevel dc-dc converter will increase the efficiency to >97%. The converter topology will allow the battery pack to be subdivided into smaller modules in which the failure of a single cell does not disable the entire battery pack and only a single battery module need be replaced instead of the entire pack.

Approach

Several design tasks are being conducted in parallel by different organizations. These products will be integrated during the final year of this project to achieve a dc-dc converter that can operate at high temperatures. The other reason for the parallel design approach is that some technologies, such as the multilevel converter topologies, can be fabricated and tested now with conventional cooling techniques while other technologies, such as high-temperature packaging, SiC switches, and high-temperature capacitors, mature.

Multiple institutions are involved in this project to draw on the strengths of the particular institutions. Michigan State University, The University of Tennessee (UT), and Oak Ridge National Laboratory (ORNL) have devised two different magnetic-less dc-dc converter topologies. The Pennsylvania State University (Penn State) has used its experience in high-temperature capacitors to determine a figure of merit for new capacitor materials. UT and ORNL have designed a high-temperature gate drive.

Major Accomplishments

During FY 2006, there were major several accomplishments.

1. Michigan State University designed and fabricated a 10-kW dc-dc converter module based on some of its earlier topologies.

2. UT and ORNL devised an alternative dc-dc converter topology and fabricated a low-power proof-of-concept circuit to demonstrate its feasibility. More details on these accomplishments are given in the next section.
3. UT and ORNL designed a high-temperature gate drive using a new silicon-on-insulator (SOI) process by Atmel.
4. Penn State evaluated capacitors for high-temperature applications.

Each of these tasks is further elucidated in the next section.

Technical Discussion

Bidirectional dc-dc Converter Module

The design and fabrication of a 10-kW bidirectional dc-dc converter module was initiated during FY 2006. The converter module is able to output either the battery voltage or twice the battery voltage. Thus a power conversion system with *n* modules is able to output 1 to 2*n* different voltages with an increment of 42 V, as shown in Figure 1.

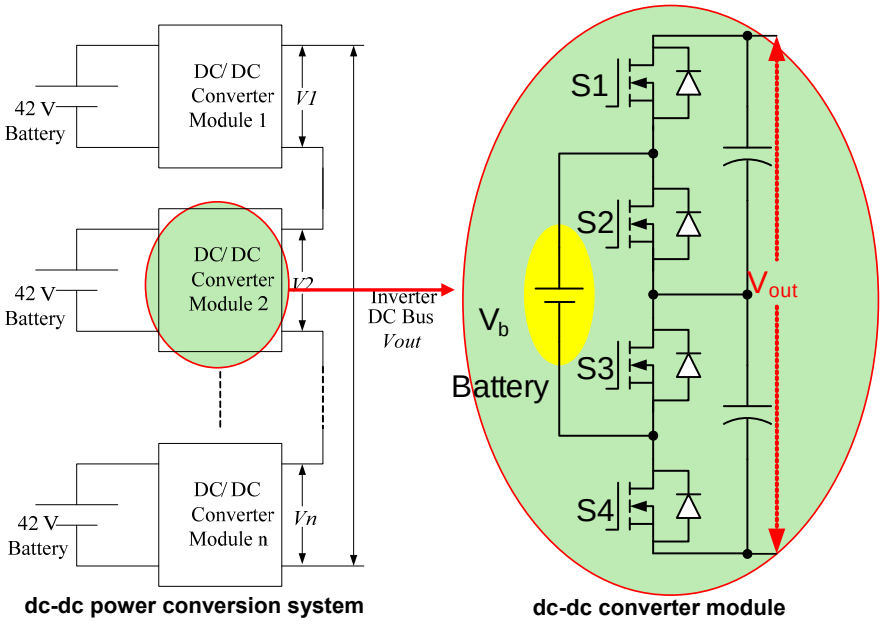


Figure 1. The dc-dc power conversion system and dc-dc converter module.

An individual module has been fabricated and is pictured in Figure 2. Specifications are as follows:

- nominal input voltage—42 V
- minimum input voltage—25 V
- maximum input voltage—45 V
- output voltage—42V/80V for nominal input voltage,
- nominal input current—240 A
- maximum input current—350 A,
- nominal output current—120 A

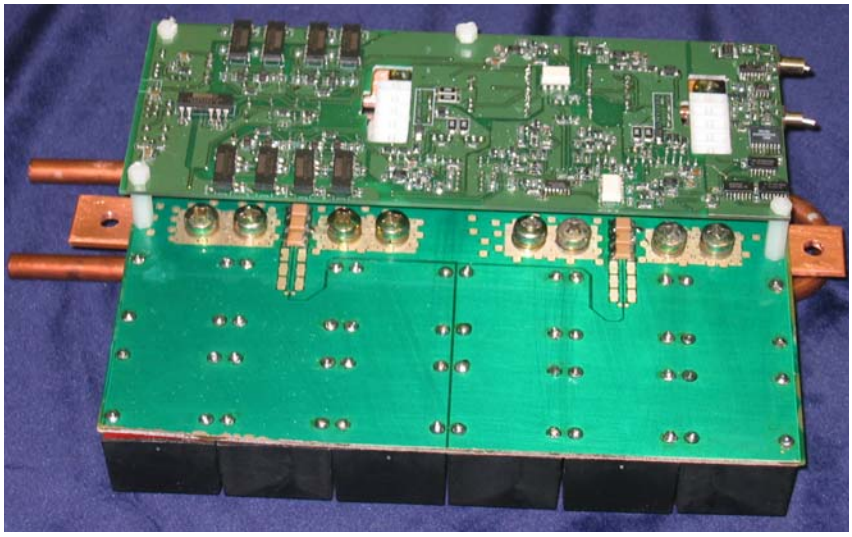


Figure 2. 10-kW dc-dc converter module.

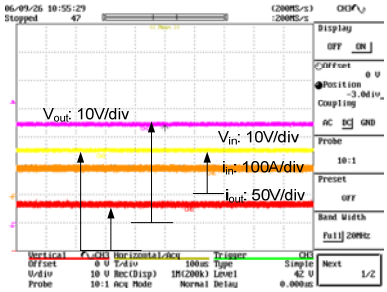
- maximum output current—180 A
- heat-sink—liquid cooled
- devices—2 metal oxide semiconductor field effect transistors (MOSFET) Modules: FM600TU-07A

A custom bus bar was fabricated to reduce the output voltage noise. Some initial tests of the converter were done with conventional car batteries, and converter efficiency was measured. Some experimental results are shown in Figure 3. The efficiency test was conducted using a YOKOGAWA power meter WT1600. The measured efficiency when output voltage equals input voltage was 99.4%, including the losses in the gate drive power supplies; the efficiency when output voltage equaled twice the input voltage was 98.1%, including the gate drive power losses. During the test, the battery voltage was around 30 V. When the input voltage increases to 42 V, the efficiency should be higher because the conduction loss will be less at this higher voltage level and it is the major loss.

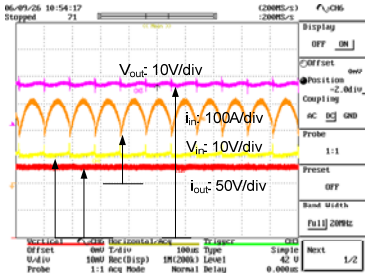
Additional testing of the converter will be conducted during FY 2007 to characterize its efficiency over a wide load and temperature range. The use of high-temperature devices in place of the conventional silicon switches will be made and a high-temperature module will be designed.

Multilevel Modular Capacitor Clamped dc-dc Converter (MMCCC)

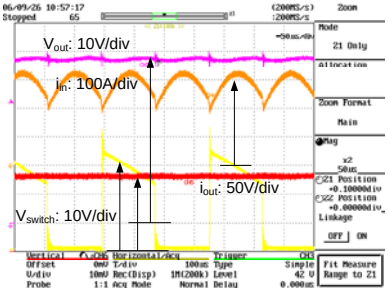
A second magnetic-less dc-dc converter topology explored as part of this project is the multilevel modular capacitor clamped dc-dc converter. The proposed 5-level MMCCC shown in Figure 4 has an inherent modular structure and can be designed to achieve any conversion ratio. For the schematic shown in Figure 4 with four modular blocks, the high-voltage side of the converter will be a factor of 5 greater than the low voltage side. Each modular block has one capacitor and three transistors leading to three terminal points. A modular block is shown in Figure 5. The terminal Vin is connected to either the high-voltage battery or to the output of the previous stage. One of the output terminals Vnext is connected to the input of the next stage. The other output terminal VLB is connected to the low-voltage side + battery terminal. Figure 6 shows the proof-of-concept 6-level MMCCC.



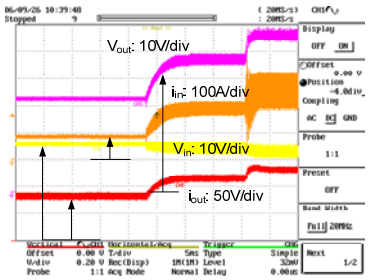
(a) Steady state waveform when outputting 1X



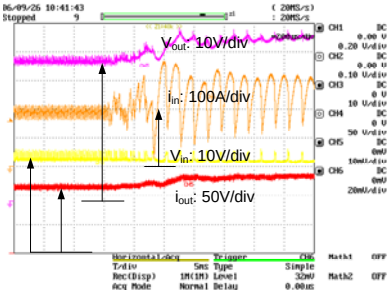
(b) Steady state waveform when outputting 2X



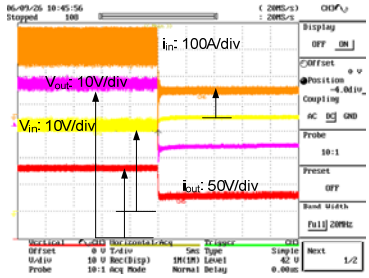
(c) Switch voltage when outputting 2X



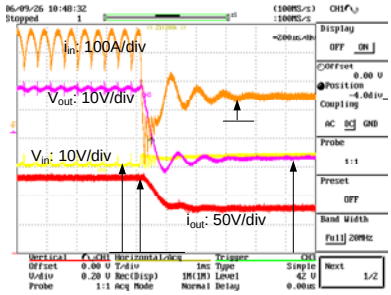
(d) Transition from 1X to 2X



(e) Details of transition from 1Xto 2X



(f) Transition from 2X to 1X



(g) Details of transition from 2X to 1X

Figure 3. Experimental results of the converter. 1X means the output voltage equals to input voltage; 2X means the output voltage is twice the input voltage.

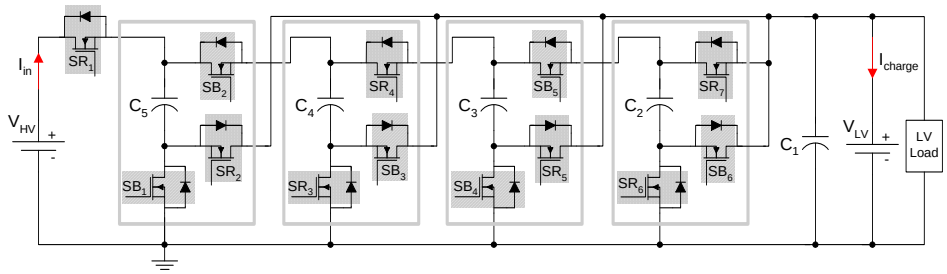


Figure 4. The proposed 5-level MMCCC with four modular blocks.

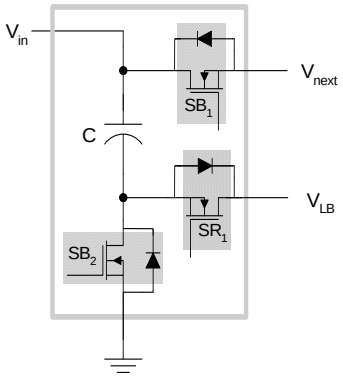


Figure 5. The modular block.

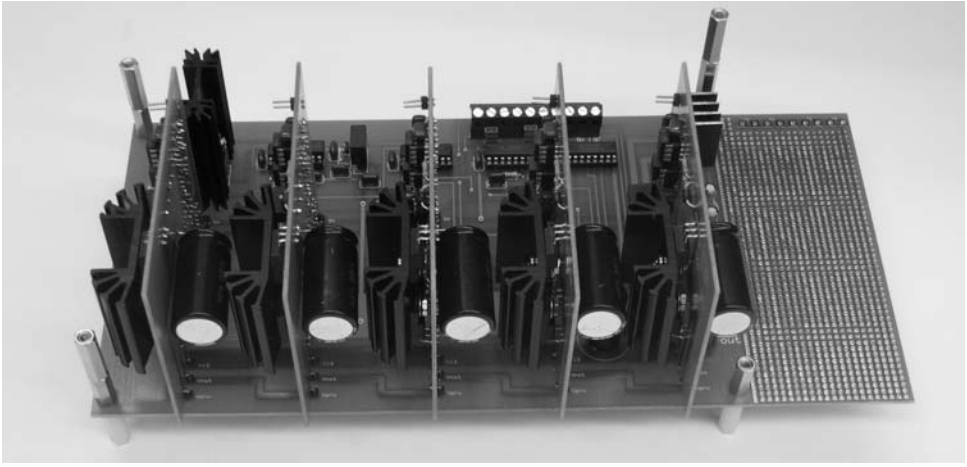


Figure 6. The proof-of-concept six-level MMCCC.

The new converter has much better voltage regulation compared with the conventional converter. In up conversion mode, the conventional converter's input current flows though (N-1) series connected transistors and one diode. The situation will be worse when the conventional converter attempts to deliver current from the high-voltage side to the low-voltage side. During this time the current flows through (N-1) diodes and only one transistor. Usually the voltage drop across the diode is higher than the voltage drop across any transistor, and thereby the regulation is very poor during this time. In contrast, the current flows through at most three transistors or diodes in the new converter irrespective of the conversion ratio. The reduced number of series connected devices in the new converter is responsible for less voltage drop and better regulation.

The new circuit suffers from one limitation. The MMCCC uses more transistors than are required for the conventional flying capacitor multilevel dc/dc converter with the same conversion ratio. For an N-level design, the conventional converter requires 2N transistors, whereas the new converter needs (3N-2) transistors. Thus, for a five- level design, the conventional converter needs 10 transistors; 13 transistors are needed for the new converter. However, the use of more transistors is truly compensated by obtaining all the desirable features from the new converter.

A new topology of the modular multilevel dc-dc converter has been proposed and validated by both simulation and experimental results. The new converter outperforms the conventional converters by having complete modular construction, high power transfer capability, simpler gate drive circuit requirements, high-frequency operation capability, onboard fault bypassing, and bi-directional power management capability. By virtue of the modular topology, the circuit obtains redundancy and the reliability can be increased significantly. The modular nature also introduces the use of one additional level to establish the fault bypassing and bidirectional power flow management. Thus this converter could be a suitable choice in various applications to establish a bidirectional power management between buses having different voltages.

High-Temperature Gate Driver

Layout of a gate driver chip capable of operating from –50 to 200ºC was completed and submitted to Atmel for fabrication in September 2006. Figure 7 is the schematic of the circuit, and Figure 8 shows the complete layout. The process used by Atmel is referred to as a BCD (bipolar-CMOS-DMOS) on SOI commonly known as SMARTIS. The total size of the chip is 5 mm^2 (2240 µm × 2240 µm).

Figure 9 shows the layout of the logic part of the gate driver chip, and Figure 10 shows the layout of the high-voltage (45-V) output stage of the gate driver chip. Two negative channel MOSs (NMOSs) in the output stage are made large enough (total W = 24,000 µm) to provide enough load current to get acceptable rise and fall times. Each of these NMOSs comprises six hundred 45-V NMOSs (W = 40 µm)

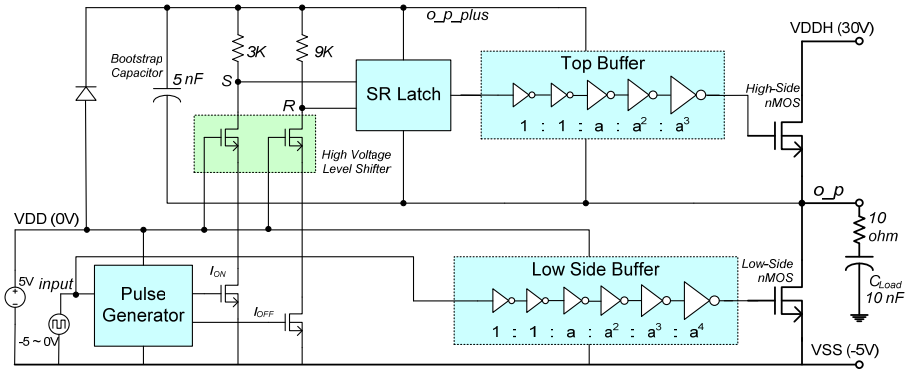


Figure 7. Schematic of the gate driver circuit.

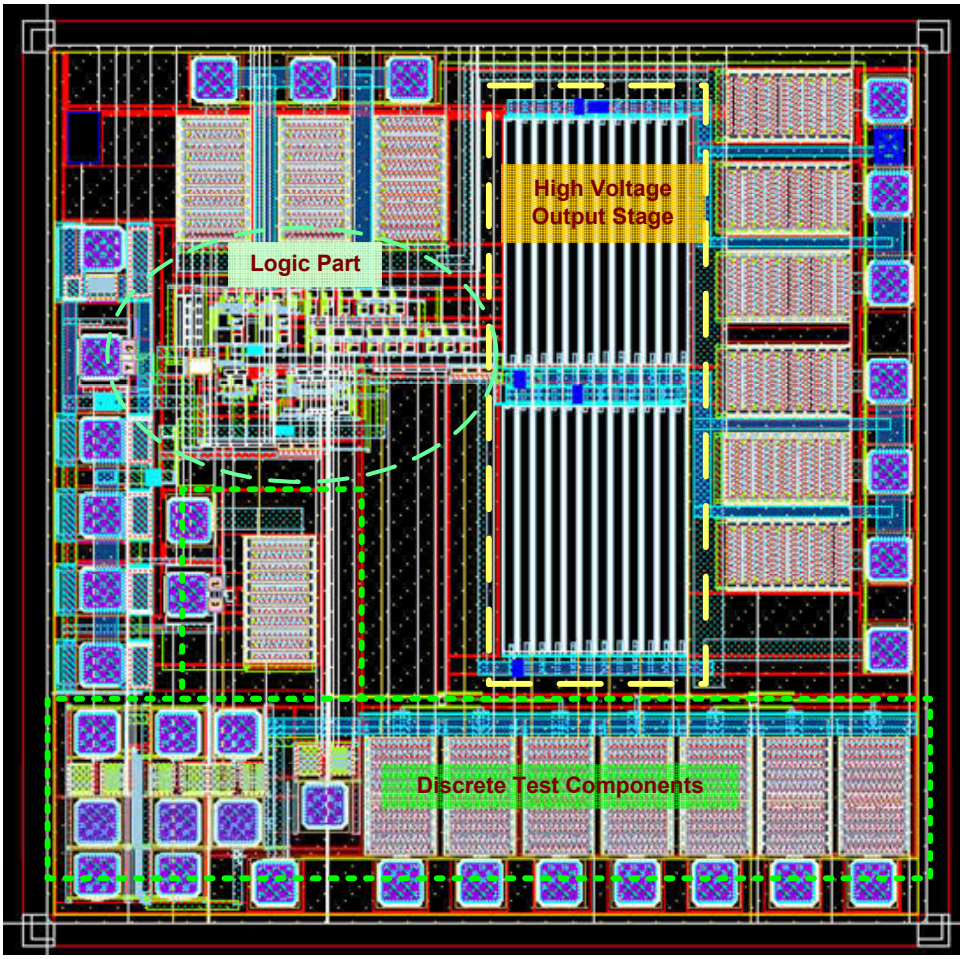


Figure 8. Complete layout of the gate driver chip.

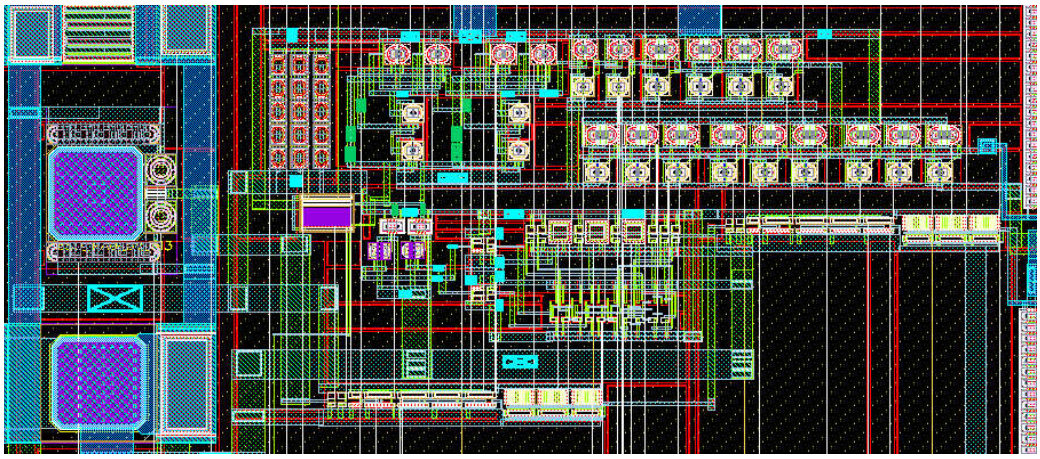


Figure 9. Layout of the logic part of the gate driver chip.

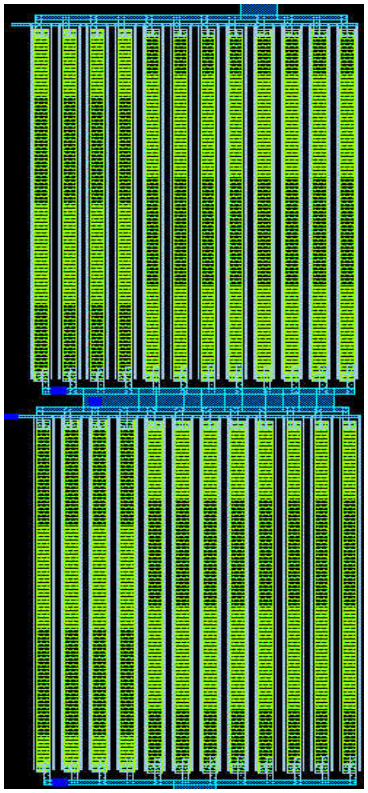


Figure 10. Layout of the high-voltage output stage.

connected in parallel. In the layout, the high-voltage output stage and low-voltage logic sections are carefully laid separately for the safety of the chip. Gate and power supply protections are also ensured in the pad frame. Post-layout simulations were performed to check the functionality of the layout.

Other than the gate driver circuit, some discrete components [45-V NMOS, 5-V NMOS and positive-channel MOS (PMOS), 25 NMOS and PMOS] are also added in the layout for testing and characterization at high temperature so that after these are characterized, we will know if these can be used in future chips.

Fabrication of the gate drive chip by Atmel will occur during the last 3 months of 2006 (first quarter of FY 2007). High-temperature printed circuit boards will be evaluated for use with the gate drive chip.

High-Temperature Capacitors

Penn State contacted a number of capacitor companies and procured samples from several sources. A list of capacitors is shown in Table 1.

Table 1. U.S. capacitor industry products for high-temperature capacitors

Company	Capacitance value (μF)	Temperature range (°C)	Voltage rating (V)	Comments	Size W × H × T (cm)
Johansen Dielectric	0.22	Up to 200	100	NPO type	1.2 × 1.27 × 0.38
	2.70		100	X7R type	
Kemet	0.033	Up to 200	100	NPO type X7R type	0.78 × 0.78 × 0.38
	1.0		100		
Wright Capacitors	0.082	Up to 200	500	NPO type	1.57 × 1.68 × 0.64
	2.75		500	X7R type	
Dearborn Electronics	1.0	Up to 125	50	Metallized film	1.8(h) × 0.625 (diam)
	1.0		250		2.5(h) × 1.5 (diam)
Electronic Concepts	150	Up to 100	500	Metallized film	4.0(h) × 8.3 (diam)
K Systems	<1.0	Up to 300	50	Diamondlike	Not specified
TRS Technologies	1	Up to 300	500	Almost X7R	1.6 × 1.6 × 0.7
	50	Up to 600	2000	Almost NPO	

The largest multilayer ceramic capacitors (MLCCs) are 1 μF, and they need to be stacked in parallel to achieve the total capacitance that is required by the power converter. The highest-temperature polymer film capacitors were found to be 125°C, and MLCCs have substantially higher temperature capability (600°C).

In addition to ac characterization of commercial capacitors, the dc performance was evaluated for commercial capacitors and prototype capacitors made at TRS Technologies and Penn State. An "*RC* figure-of-merit" which combines capacitance and dc resistance results was established. High dc resistance is important for component reliability, and high capacitance is important for volume-efficient inverters. The "figure-of-merit" was derived from the following:

$$R = \frac{\rho d}{A} \quad , \tag{1}$$

$$C = \frac{\varepsilon_r \varepsilon_o A}{d} \quad , \tag{2}$$

$$RC = \rho \varepsilon_o \varepsilon_r \quad , \tag{3}$$

where A is the capacitor area, d is the capacitor thickness, ε_o is the permittivity of free space, ρ and ε_r are the resistivity and relative permittivity (same as dielectric constant) of the dielectric material, respectively. Note that the "*RC*" value only contains material parameters and that the capacitor geometry is factored out of Equation (3). The "*RC*" value shown in Equation (3) is not the standard "time constant" for capacitor discharge, but a figure-of-merit related to capacitor reliability and volumetric efficiency. Low leakage current in a material represents a high R-value and is important for capacitor reliability. A high C-value is important for shrinking capacitor size. Penn State surveyed more than 50 materials, including polymer film and ceramic, and the *RC* values ranged from 10^{-4} to 100 at 200°C. Table 2 shows that the best material was found to be $BaZrO_3$.

Table 2. Summary of high-temperature materials survey (taken from a study of more than 50 materials)

Material	*RC* at 200°C	*RC* at 300°C	*RC* at 400°C
Polypropylene	0.000081	Too low to measure	Too low to measure
$BaZrO_3$	103	59	0.33
JDI NPO	90	Bad terminations	Bad terminations
Average PLZT	280	13	0.04

The *RC* value is very low at 200°C for commercial polypropylene, which is used in film capacitors for pulsed-power applications. As temperature is increased, the resistance "*R*" drops for all dielectric materials. Therefore the *RC* product also decreases for all dielectric materials as temperature is increased. A commercial high-temperature capacitor material, JDI NPO, has a high *RC* value at 200°C; however, we were unable to measure the electrical properties at higher temperatures. The terminations of this commercial capacitor did not work at 300°C.

Experimental materials PLZT and $BaZrO_3$ were explored, and both have excellent *RC* values at 200°C. $BaZrO_3$ is the best overall dielectric material at higher temperatures. The capacitance and loss of a prototype $BaZrO_3$ capacitor is shown in Figure 11. Penn State and TRS Technologies have been collaborating on high-temperature capacitor development, and the results show that $BaZrO_3$ has low losses up to 350°C, well above the DOE FreedomCAR specification of 140°C.

Researchers from Penn State University and TRS Technologies visited Wright Patterson Air Force Base to deliver high-temperature capacitors to its power electronic group. Jim Scofield and coworkers have assembled an all-SiC converter, operating at 2 kW, 200 V, and 200°C. They are presently using commercial Y5V 4.7-μF multilayer ceramic capacitors for the dc bus capacitors. These capacitors are only rated to 125°C and 50 V, but they perform well above these specifications. However, these capacitors were only operated for a short time at these elevated temperature and voltage ratings, and it is expected that the lifetime of the capacitor would be significantly reduced. A summary of commercial capacitor temperature specifications for consumer electronics is shown in Table 3.

Figure 12 shows a typical response for commercial Y5V multilayer ceramic capacitors, and the industry specifications are shown in Table 3 for common capacitor types. Typically NPO capacitors are used for high-temperature operation. Figure 13 shows the dielectric response of the commercial Kemet capacitors under a 200-V bias (which is four times the voltage rating). The capacitance has a peak value of 0.35 μF at 200°C, which is the operating temperature of the SiC converter at Wright Patterson Air Force Base.

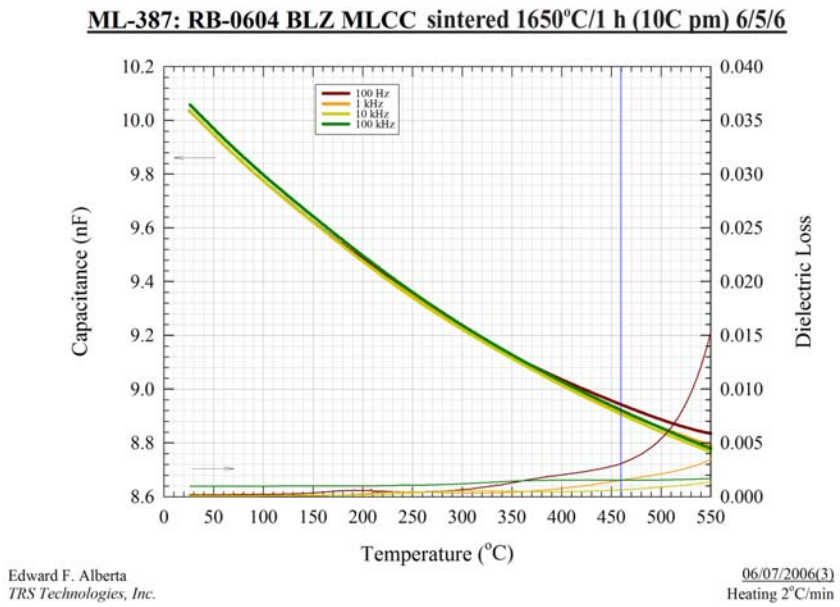


Figure 11. Capacitance and loss for a $BaZrO_3$ prototype capacitor manufactured at TRS Technologies. Note that the capacitance changes approximately 10% from room temperature to 550°C. The loss value at 100 Hz exceeds the DOE FreedomCAR specification at 350°C. High dielectric loss at low frequency suggests that dc conduction is an important factor at high temperature.

Table 3. General commercial capacitor classes (Note the trade-off between dielectric constant and temperature dependence of dielectric constant)

Capacitor specification	Y5V	X7R	NPO
Dielectric constant	6000	2000	60
Temperature range °C	10 to 85	–55 to 125	–55 to 125
Δ°C over temperature range	80%	30%	30 ppm

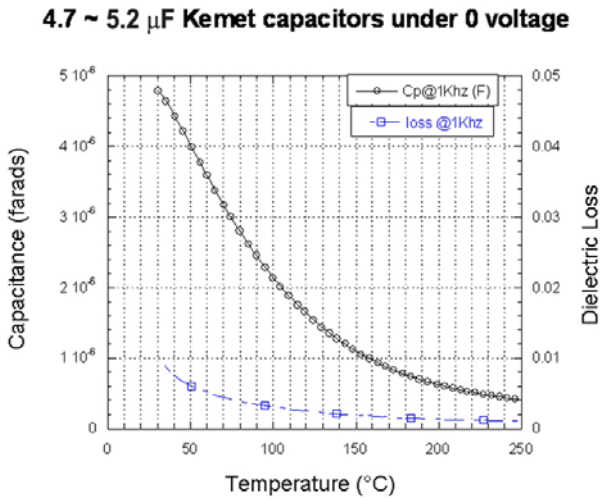


Figure 12. Temperature dependence of capacitance and loss for a commercial multilayer ceramic capacitor. The capacitor is "Y5V" specified and is designed to have a maximum capacitance at room temperature.

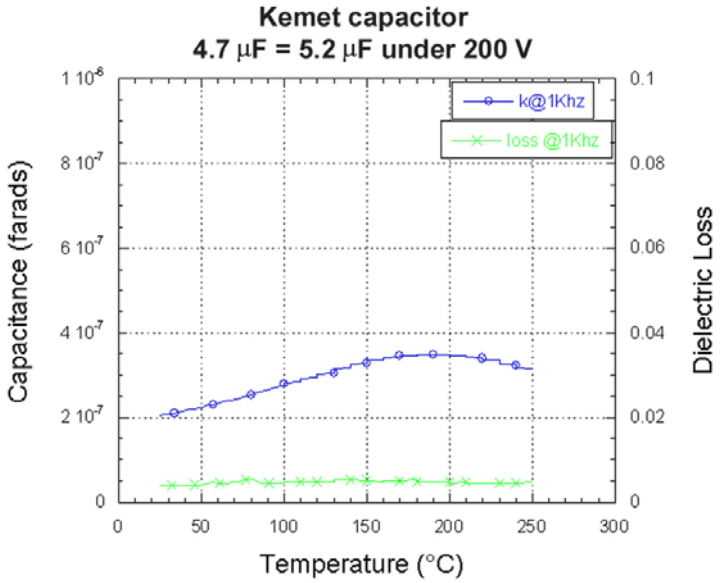


Figure 13. Temperature dependence of capacitance and loss for a commercial multilayer Y5V ceramic capacitor under an applied dc voltage of 200 V.

Both ac and dc tests of commercial and experimental capacitors were carried out as a collaborative effort between Penn State, ORNL, and industrial partners. It was found that high-temperature polymer film capacitors had very low dielectric loss up to temperatures of 120°C. The ac properties of commercial MLCCs were characterized up to 180°C, and the dielectric properties improved continuously as temperature was increased. dc tests were also performed and an RC figure-of-merit was used to compare capacitors. A new dielectric $BaZrO_3$, developed in collaboration with TRS Technologies, was found to have the best high-temperature properties. dc bus capacitors in an all-SiC power inverter which operates at 200°C, are presently being explored at Wright Patterson Air Force Base. Presently, an array of commercial 5-µF MLCCs is employed in a parallel array for the dc bus capacitor. Penn State characterized the high- temperature and high-voltage dielectric properties of these capacitors.

Conclusion

This challenging project involves the development and demonstration of several novel technologies to achieve a converter that can operate at high ambient temperatures. Novel magnetic-less dc-dc converter topologies will result in reduced volume and weight compared with conventional topologies. The multilevel design of these converters will also allow segregation of the battery pack into multiple modules. This will allow only a portion of the battery pack to be replaced if there is a failure. It may also result in an increase in reliability and availability of the battery power, as the converter designs will allow for a damaged or failed battery module or power electronics module to be bypassed.

A high-temperature gate drive has been designed and will be tested in the upcoming year. High-temperature packaging of SiC-based power electronics will transition from diodes to controllable switches in the upcoming year as another step toward a complete high-temperature module. Gains made from this project will likely impact other power electronics projects that need high-temperature packaging, gate drives, or modular conceptual designs.

Future Direction

During FY 2007, detailed design, fabrication, and testing will be conducted of two different magnetic-less dc-dc converters to demonstrate the feasibility of the topologies. These will have conventional packaging and heat transfer technology. The development of converter control will be done during FY 2007 of the necessary algorithms to control power flow in both directions while regulating the voltage at the receiving end of the converter.

In addition, a high-temperature gate drive fabricated in SOI that was submitted for fabrication in September 2006 will be manufactured by Atmel during the first quarter of FY 2007 and then tested to determine its characteristics over a wide temperature range (–50 to 200ºC). Based upon the results of the testing, a revised gate drive design will be done and submitted for fabrication.

A high-temperature power module will be designed and fabricated that leverages some of the high-temperature packaging techniques that were used in the Wide Bandgap Semiconductor project at ORNL. This module will likely consist of several SiC junction field effect transistors, SiC Schottky diodes, and high-temperature capacitors. The module will be a building block of one of the two dc-dc converter topologies that are being tested during FY 2007. The selection of the topology will be based on availability of components (SiC switches and high-temperature capacitors) and which converter looks most promising in terms of meeting FreedomCAR goals after testing.

Upon successful testing of these power modules and gate drives, these will then be ready for a system assembly using five of these units to complete the fabrication of a dc-dc converter capable of bidirectional power transfer. The complete converter assembly and testing will be done during FY 2008.

Publications

F. H. Khan and L. M. Tolbert, “A Multilevel Modular Capacitor Clamped DC-DC Converter,” *IEEE Industry Applications Society Annual Meeting*, *Tampa, Florida*, October 8–12, 2006.

L. M. Tolbert, H. Zhang, M. Chinthavali, and B. Ozpineci, "SiC-based Power Converters for High Temperature Applications," *European Conference on Silicon Carbide and Related Materials (ECSCRM)*, *Newcastle, United Kingdom*, September 3–7, 2006.

H. Zhang, M. Chinthavali, B. Ozpineci, and L. M. Tolbert, "System Modeling and Characterization of SiC Schottky Power Diodes," *IEEE Workshop on Computers in Power Electronics*, Troy, New York, July 16–19, 2006.

F. H. Khan, L. M. Tolbert, and F. Z. Peng, "Deriving New Topologies of DC-DC Converters Featuring Switching Cells," *IEEE Workshop on Computers in Power Electronics*, Troy, New York, July 16–19, 2006.

M. Chinthavali, L. M. Tolbert, B. Ozpineci, and H. Zhang, "High Temperature Power Electronics—Application Issues of SiC Devices," *IMAPS International Conference on High Temperature Electronics*, *Santa Fe, New Mexico*, May 15–18, 2006.

References

1. Z. Pan, F. Zhang, and F. Z. Peng, "Power Losses and Efficiency Analysis of Multilevel DC-DC Converters," pp. 1393–1298 in *IEEE Applied Power Electronics Conference*, March 2005.
2. F. Zhang, F. Z. Peng, and Z. Qian, "Study of Multilevel Converters in DC-DC Application," pp. 1702–1706, in *IEEE Power Electronics Specialists Conference*, June 2004.
3. F. Z. Peng, F. Zhang, and Z. Qian, "A Novel Compact DC-DC Converter for 42V Systems," pp. 33–38, in *IEEE Power Electronics Specialists Conference*, June 2003.
4. K. D. T. Ngo and R. Webster, "Steady-State Analysis and Design of a Switched-Capacitor DC-DC Converter," *IEEE Transactions on Aero. and Elec. Systems*, **30**(1), 92–101 (Jan. 1994).
5. W. Harris and K. Ngo, "Power Switched-Capacitor DC-DC Converter, Analysis and Design," *IEEE Transactions on Aero. and Elec. Systems*, **33**(2), 386–395 (April 1997).
6. S. V. Cheong, H. Chung, and A. Ioinovici, "Inductorless DC-to-DC Converter with High Power Density," *IEEE Transactions on Industrial Electronics*, **41**(2), 208–215 (April 1994).
7. O. Mak, Y. Wong, and A. Ioinovici, "Step-up DC Power Supply Based on a Switched-Capacitor Circuit," *IEEE Transactions on Industrial Electronics*, **42**(1), 90–97 (February 1994).
8. C. K. Tse, S.C. Wong, and M. H. L. Chow, "On Lossless Switched-Capacitor Power Converters," *IEEE Transactions on Power Electronics*, **10**(3), 286–291 (May 1995).
9. E. Bayer, "Optimized Control of the 'Flying'-Capacitor Operating Voltage in 'Gear-Box'–Charge Pumps—The Key Factor for a Smooth Operation," pp. 610–615, in *IEEE Power Electronics Specialists Conference*, June 2003.
10. R. D. Middlebrook, "Transformerless DC-to-DC Converters with Large Conversion Ratios," *IEEE Transactions on Power Electronics*, **3**(4), 484–488 (October 1988).
11. L. Cheng, I. Sankin, J. N. Merrett, V. Bondarenko, R. Kelley, S. Purohit, Y. Koshka, J. R. B. Casady, J. B. Casady, and M. S. Mazzola, "Cryogenic and High Temperature Performance of 4H-SiC Vertical Junction Field Effect Transistors (VJFETs) for Space Applications," *International Symposium on Power Semiconductor Devices & ICs, May 23–26, 2005*.
12. D. C. Hopkins, D. W. Kellerman, R. A. Wunderlich, C. Basaran, and J. Gomez, "High-temperature, High-density Packaging of a 60-kW Converter for >200ºC Embedded Operation," pp. 871–877 in *IEEE Applied Power Electronics Conference*, *Dallas, March 19–23, 2006.*
13. D. Katsis, B. Geil, T. Griffin, G. Koebke, S. Kaplan, G. Ovrebo, and S. Bayne, "Silicon Carbide Power Semiconductor Module Development for a High Temperature 10-kW ac Drive," pp. 399–403 in *IEEE Industry Application Society Annual Meeting*, *Hong Kong, China*, *October 2–6, 2005*.
14. T. Funaki, J. C. Balda, J. Junghans, A. S. Kashyap, F. D. Barlow, H. A. Mantooth, T. Kimoto, and T. Hikihara, "Power Conversion with SiC Devices at Extremely High Ambient Temperatures," pp. 2030–2035 in *IEEE Power Electronics Specialists Conference*, *Recife, Brazil, June 12–16, 2005*.

15. S. Mounce, B. McPherson, R. Schupbach, and A. B. Lostetter, “Ultra-lightweight, High Efficiency SiC Based Power Electronic Converters for Extreme Environments,” *IEEE Aerospace Conference*, March 4–11, 2006.
16. M. Chinthavali, B. Ozpineci, and L. M. Tolbert, “High Temperature and High Frequency Performance Evaluation of 4H-SiC VJFET and Schottky Diodes,” pp. 322–328in *IEEE Applied Power Electronics Conference*, *Austin, Texas*, *March 6–10, 2005.*

4.5 dc/dc Converter for Fuel Cell and Hybrid Vehicle

Principal Investigator: Lizhi Zhu
Ballard Power Systems
15001 Commerce Drive North
Dearborn, MI 48120
Voice: 313-354-5973; Fax: 313-583-5990; E-mail: lizhi.zhu@ballard.com

DOE Technology Development Manager: Susan A. Rogers
Voice: 202-586-8997; Fax: 202-586-1600; E-mail: Susan.Rogers@ee.doe.gov

ORNL Program Manager: Mitch Olszewski
Voice: 865-946-1350; Fax: 865-946-1262; E-mail: olszewskim@ornl.gov

---

Objectives

The goal of this project is to develop and fabricate a 5-kW dc/dc converter with a baseline 14-V output capability for fuel cell and hybrid vehicles. The major objectives for this dc/dc converter technology are to provide

- higher efficiency (92%)
- high coolant temperature capability (105°C)
- high reliability (15 years/150,000 miles)
- smaller volume (5 L)
- lower weight (6 kg)
- lower cost ($75/kW)

Approach

The key technical challenge for this converter is the 105°C coolant temperature. The power switches and magnetics must be designed to sustain higher operating temperatures reliably, without a large cost/mass/volume penalty. The following key technologies are proposed to break through technical barriers to achieve a high-temperature, high-power-density, and lower-cost design.

1. Converter topology

A novel interleaved dc/dc converter topology is proposed as shown in Figure 1. The key merits of the converter are

- lower rms current stresses on components due to interleaving
- reduced ripple current on capacitors due to interleaving
- lower power losses due to low Rds_on and soft-switching
- smaller magnetics due to high switching frequency
- low EMI due to integrated power devices and magnetics

2. Integrated module-based dc/dc converter

Power module-based integration technology has been employed in this design. The thermal requirements are a challenge. The coolant temperature is 105°C. To meet the junction temperature 125°C design criteria, the thermal impedance has to be very small. Power module integration simplifies thermal stack-up layers, obtaining smaller thermal resistance. Furthermore, the customized power module optimizes the high-current interconnection path, reducing conduction losses. By using wirebonds in the

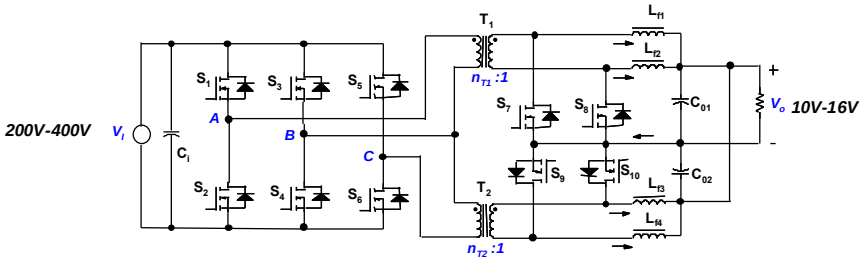


Figure 1. The novel interleaved dc/dc converter topology.

transformer design, rather than the traditional bolts and busbars, the reliability is also improved. The major advantages of the power module based dc/dc converters are

- enhanced thermal performance
- reduced number of devices
- increased reliability
- higher level of integration

3. Planar magnetics with enhanced cooling

This converter has also been designed using planar magnetics, a technology that Ballard thinks is critical for reliable and cost-effective high-volume production of such products. The benefits from this technology are

- lower leakage inductance due to shorter winding termination and smaller circuit paths
- elimination of discrete contacts' Ohmic loss
- reduction of Ohmic loss due to shorter conduction paths
- lower ac loss due to flat winding structure
- higher core window utilization ratio
- smaller core volume and weight
- higher surface to volume ratio for improved heat conduction
- direct cooling of core by direct contact to heat sink
- higher power density

Major Accomplishments of FY 2006

In FY 2006, Ballard focused on the production Beta design to address differences between the DOE goals and the Alpha design results. The major achievement in FY 2006 was the design and verification of the final Beta unit to meet the targets. Tasks included

- electrical improvements over the Alpha design
- cost reduction
- volume reduction
- weight reduction
- thermal design improvement
- manufacturing process improvements

The project timing consisted of four phases: Phase I: Key technologies prove-out; Phase II: Full function Alpha design and test; Phase III: Final Beta prototype design; Phase IV: Final build, DV test, delivery, and report. In FY 2005, we have finished Phase I and part of Phase II. The results have been reported as shown in Table 1.

Table 1. The percentage of goals achieved as of FY 2005 through Alpha design

	Alpha Design	DOE Goal	% Target
Output Power	5.1kW	5kW	102%
Efficiency	93%	92%	101%
Cost Estimation	$545	$375 total, ($75/kW)	69%
Coolant Temperature	90 Deg C	105 Deg C	86%
Volume	6.5 Liter	5 Liter	77%
Weight	7.6kg	6kg	79%
Coolant Pressure Drop	2.3 PSI	0.73PSI (5kPa)	32%

In FY 2006, we continued working on the Alpha prototype testing work, completed the Beta design and part purchasing, and developed the manufacturing process to produce the final prototype. The major tasks follow:

1. Continued electrical evaluation testing on Alpha prototype:

Figure 2 shows the test implementation for the Alpha prototype. At the end of FY 2005, we had finished the efficiency tests at Vi = 200 V, 300 V, 350 V up to 5 kW, and achieved the 92% efficiency target. The remaining issue was when the input voltage reached ~400 V, the efficiency dropped substantially, and excessive switching noise appeared in the synchronized rectifier switches. This problem prevented the dc/dc converter from delivering full power at 400 V.

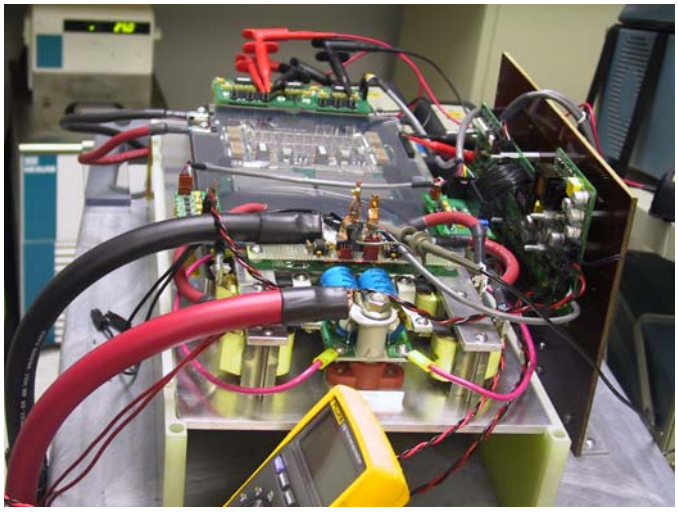


Figure 2. Alpha dc/dc converter under test.

Troubleshooting of the noise problem had been done in early FY 2006 to solve the switching noise problem. It turned out to be that a higher Qrr loss occurred under hot coolant test conditions. When coolant was raised to 90°C, the ambient temperature surrounding the die and gate drive circuit rose. It

caused a small change in signal delay. However, the delay was big enough to cause a higher reverse recovery current in the rectifier turn on/off transitions, leading to excessive Qrr losses on the rectifiers. An improvement was made in the gate drive circuit to compensate the delay due the high-temperature operation. The dc/dc passed the full-input voltage (Vi = 400 V) and full-power (Po = 5 kW) operation with 90°C coolant. The overall efficiency kept above 92%, as shown in the final test results in Figure 3.

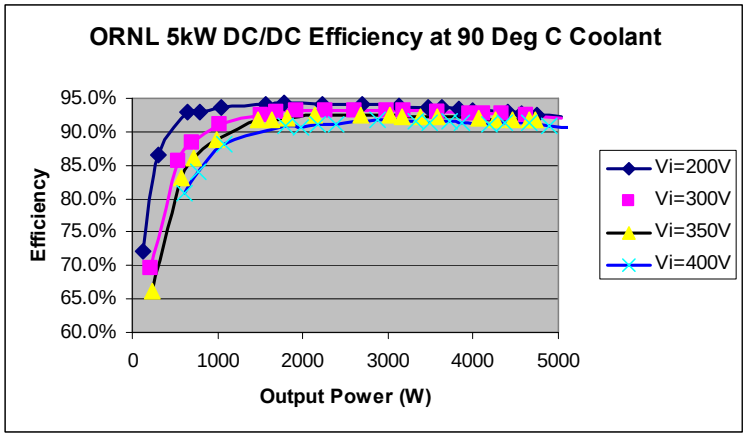
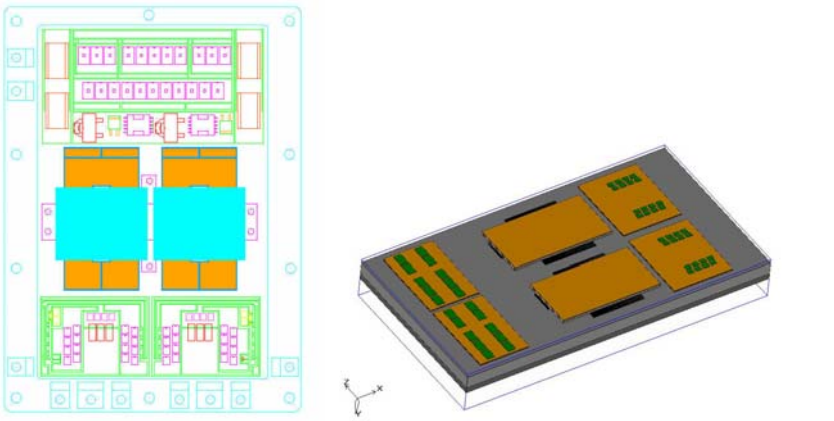


Figure 3. Efficiency test results at Vi = 200 V, 300 V, 350 V, and 400 V.

2. Cost reduction—Beta design

The cost of the customized power module is a major portion of the dc/dc converter costs, making up more than 50% of the total. In the Beta design, a new lead frame design concept was adopted to eliminate signal pin inserts. As a result, the power module baseplate width was reduced by 33 mm. Figure 4 depicts the Alpha and Beta power module design. The reduction of the power module width reduces the power module cost by 7%. The improved lead frame design also saves in the tooling costs. The high-volume cost estimation based on the Beta design is $458 at high volume; this is 82% of the DOE goal.



a) Alpha (203 X 315 mm) **b) Beta (170 X 315 mm)**

Figure 4. Alpha and Beta power module layout.

3. Volume and weight reduction

The 33-mm saving in power module width dimension also contributes to volume and weight reduction in the final packaging. To pass the environmental requirements, an aluminum cast housing was designed for the Beta prototype. The total volume was reduced to 5.1 L in the Beta design, down from the 6.5-L Alpha prototype design. Figure 5 shows the final Beta dc/dc converter packaging without cover.

The adoption of the final power module design greatly simplified the interconnection of the dc/dc converter. The part count was reduced to a total of 42 parts, including 2 wire harnesses and 11 types of fasteners. Table 2 lists the bill of materials of the Beta design and the weight estimation. The total weight is 7.4 kg. Although the aluminum housing is included, the total weight is 0.2 kg less than the Alpha prototype.

Figure 6 illustrates the bottom view of the Beta packaging. It shows the interfaces between the dc/dc converter and the end-user. The high-voltage connector connects the high-voltage input (200–400 V) to the dc/dc converter; the LV studs are the 12-V output to deliver the low-voltage power to the 12-V battery and loads in a vehicle. The coolant in/outlet ports bring a circulating coolant into the unit to remove the heat generated in the dc/dc converter. The signal connector is the control path between the dc/dc converter and vehicle controller. It includes the voltage command and enable signals through a controller area network interface.

4. Thermal design improvement

Two major design improvements have been made in the Beta design: the lead frame material and baseplate material.

To meet 105°C coolant operation requirements, AMODEL A-4133 L had been selected for the high-temperature plastic lead frame. It has high heat resistance, high strength and stiffness over a broad temperature range, low moisture absorption, excellent chemical resistance, and excellent electrical properties. It has been advantageously used for many automotive electrical and electronics applications. Its heat deflection temperature is as high as 300°C. An injection mold was required to manufacture the plastic lead frame. It added a substantial tooling cost for the Beta prototype development.

To design for a 15-year reliability requirement, aluminum silicon carbide (AlSiC) had been selected for the power module baseplate material. The AlSiC composite materials are designed to have a high thermal conductivity and a controlled thermal expansion (CTE) behavior that provides better CTE matching between the substrate and baseplate. A baseplate and substrate assembly was built to perform the thermal cycle test. It passed the thermal shock tests (–40ºC to +125ºC) 100 times without delaminating.

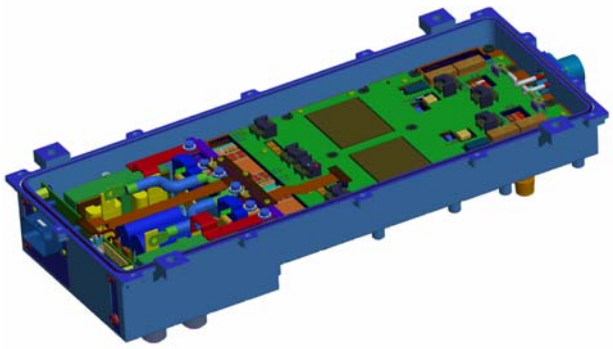


Figure 5. The Beta version of dc/dc converter (5.1 L).

Table 2. The BOM and weight of Beta design

	Part Description/Remarks	Ballard Part No.	Drawing No.	Qty /Per M	Weight (kG)
1	Fasteners, M4X8, (Inductor Bracket to Housing)	5109167		10	0.001
2	Fasteners, M3X10, (HV connector to Housing)	5109391		4	0.002
3	Fasteners, M5X12 , (Cover to Housing)	5109393		17	0.002
4	Sealing Washer, Fastener to Housing	5109394		8	
5	Inductor, 4.5uH, 125A, 100Vpk, 100KHz Ripple	5109397		4	0.295
6	Pad, Silicon Gel Gasket, Inductor Bracket, ORNL	5109605	DRW5106205	2	
7	Fasteners, M5x8, (Control BRD to Stand-off)	5110338		4	0.001
8	Fastener, Hi-Low, Gate DRV to Plastic Bracket,	5110602		13	0.001
9	Fasteners, M4X12, (LV Positive Busbar to PCB Capacitor ASY)	100330-PAA		4	0.002
10	Connector, 2Pin, 1 Row	101666-PAA		1	
11	Fastener, Hi-Low, Control Board to Housing	102264-PAA		4	0.005
12	Capacitor, Ceramic, 200V, 0.01uF, 10%, Radial	5106357-s		2	
13	Fasteners, M5X14, (LV Connections to Power Module)	5108401-s		6	0.003
14	Fasteners, M5X10, (Inductor Cables to Inductor)	5108404-s		2	0.002
15	Capacitor, Ceramic, 200V, 0.15uF, 10%, Radial	5106359-s		1	
16	Gasket, HV Connector to Housing	5109392		1	0.005
17	Fasteners, M6X16, (AC Connector, Negative)	5109511-s		2	0.005
18	Brass Hose Fitting, Barb X Male Pipe for 3/4" Hose Id, 3/4" Pipe	5110760		2	0
19	HEX Nut, M5, (Inductor Cable to Inductor)	5110481-S		6	0.005
20	LV Positive Busbar Cable, Inductor(3&4) to Power Module, ORNL	5109603	DRW5106203	2	0.01
21	Connector, High Voltage, ITT Cannon ORNL	5111030		1	0.07
22	O-ring, Inside coolant channal, ORNL	5110400	DRW5106911	1	0.005
23	O-ring, Outside, Cooling Channel, ORNL	5110407	DRW5106911	1	0.005
24	O-Ring, Electronic Housing, ORNL	5110528	DRW5106911	1	0.005
25	O-Ring Seal, Divider Coolant, ORNL	5110550	DRW5106913	1	0.005
26	Harness, 2-Pin, Control BRD to Capacitor BRD	5109387	DRW5105907	1	0.005
27	Current Sensor	5109144		2	0.023
28	Electronic Box Cover - Oakridge	5109098	DRW5105707	1	0.76
29	Capacitor, Electrolytic, 8200uF, 25V, 150Deg C	5109637		2	
30	Busbar Assembly, LV Positive	5109105	DRW5105712	1	0.09
31	LV Positive Busbar, Inductor(1) to Power Module, ORNL	5109600	DRW5106199	1	0.025
32	LV Positive Busbar, Inductor(2) to Power Module, ORNL	5109601	DRW5106200	1	0.025
33	Busbar Assembly, LV Negative	5109102	DRW5105709	1	0.023
34	HSG - ELEC BOX	5109101	DRW5105708	1	2.295
35	AC Connector, LV Positive	5109808-s		2	0.145
36	Inductor Bracket, ORNL	5109104	DRW5105711	2	0.01
37	Stand-off, Female-Female, 15mm Body, M5 thread	5109604	DRW5106204	4	0.005
38	Fastener, M5X30, (Power Module to Housing)	5108406-s		15	0.006
39	Flex Circuit, Gate Drive Board to Control Board, ORNL	5109141	DRW5105742	1	0.05
40	PCB Bare Board, LV Capacitors, ORNL	5109650		1	0.1
41	Power Module			1	1.535
42	PCB Assembly, Control Board, ORNL	5109173	DRW5105735	1	0.55

Weight (kg)	7.378
DOE Target (kg)	6
% of Target	81%

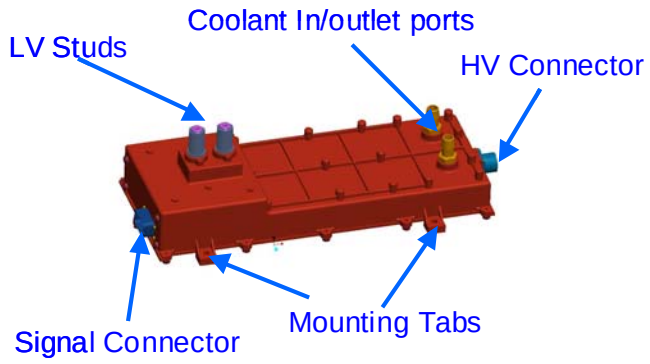


Figure 6. Beta dc/dc converter interfaces.

5. Coolant channel final design

The 105°C coolant operation requirement poses a significant challenge to the thermal design. The junction temperature is targeted at 125°C to allow metal oxide semiconductor field effect transistor switches to operate at a higher efficiency. There is only 20°C of temperature rise budgeted from die to coolant. In the Alpha design, a pin-fin pattern was designed in the coolant channel to achieve lower thermal impedance, as shown in Figure 7.

The pin-fin structure increases the surface area of the baseplate and increases the velocity of fluid in the coolant channel. As a result, the thermal resistance can be very low. However, the test result for the Alpha baseplate design revealed that the pressure drop with the pin-fin design was as high as 2.3 psi at 7 L/min, which is three times higher than the DOE goal (0.73 psi). In the Beta design, a decision was made to eliminate all pin-fins to meet the pressure drop target. The baseplate was redesigned as shown in Figure 8. A sample plate was made to test the pressure drop. The test result verified that the pressure drop in the baseplate coolant channel drops to 0.25 psi at 25ºC with a 7-L/min coolant flow rate. This meets the DOE target of 0.73 psi.

The location of inlet and outlet ports was also adjusted accordingly to minimize the turbulence of the coolant inside the channel. A 15-mm chamfer was added to the inlet/outlet chamber. The simulation result of the fluid field is shown in Figure 9.



Figure 7. Alpha baseplate pin-fin design with pin-fin.

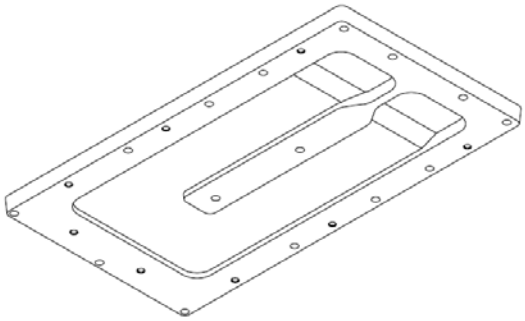


Figure 8. Beta baseplate design without pin-fin.

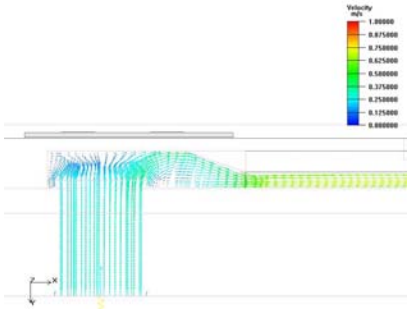


Figure 9. Coolant channel fluid simulation.

Thermal simulations were also performed using ICE pack to verify the junction temperature was within the 125 °C limit. The maximum junction temperature is 122.4°C for the worst case, as shown in Figure 10.

6. Solving practical issues

Given the coolant temperature range of –40ºC to +105ºC, a coolant pressure peak was detected as high as 60 psi. It broke the O-ring seal of the baseplate and caused leaking of coolant. Figure 11 illustrates

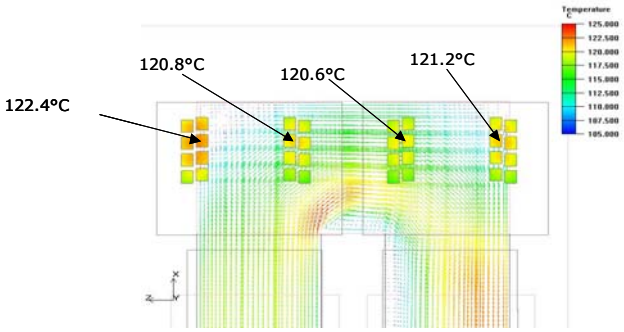


Figure 10. The thermal simulation results.



Figure 11. Baseplate leak test setup.

the baseplate coolant leak test setup. Figure 12 demonstrates the initial seal design leaked at –18ºC. After a few iterations, the seal design was improved and passed the leakage test over the entire range of –40ºC to +105ºC.



Figure 12. Baseplate leaks with initial seal design.

Technical Discussion

In FY 2006, the Beta version of dc/dc converter design has been completed. Several improvements have been made to meet DOE targets; however, there are still some gaps existing in the weight and cost goals.

1. Weight target—6 kg

The Beta design is 7.4 kg, which is 1.4 kg over the target. There are two opportunities to meet the weight target. The first opportunity is in housing weight reduction. Currently, we use sand casting for the Beta housing design to reduce the development costs. The housing itself occupies 3.1 kg. Using die casting in high-volume production instead of sand casting, we will be able to reduce the wall thickness from 4 mm to 2.5 mm, resulting in 30% weight reduction. The second opportunity is in power module baseplate weight reduction. The power module baseplate is 1.2 kg. Because the pin-fin is removed from the coolant channel, we can move the coolant channel into the molded housing, allowing us to make a thinner flat baseplate. This change will gain 45% weight reduction in the baseplate. The above two improvements will potentially lead to a 1.47-kg weight saving, which will eventually meet the DOE 6-kg target in high-volume production.

2. Cost target—$375 for the 5-kW dc/dc converter

The Beta design result reached 82% of the DOE target. The use of two expensive materials in this design can be revisited to reduce the cost. They are (1) AlSiC power module baseplate and (2) silicon nitride planar transformer windings. The opportunities are to (1) improve the material utilization factor and (2) work with the suppler to identify the major cost driver and improve the yield.

Conclusion

In the FY 2006, the testing of the Alpha prototype was completed. Based on the Alpha test results, we have implemented dramatic improvements in the design of the production Beta design. The status summary of the Beta design is presented in Table 3.

Table-3. Status summary from the Beta design during FY 2006

	DOE Goal	Beta Design Results (7/25/06)	Beta Design % Target
Output Power	5kW	5.1kW	102%
Efficiency	92%	93%	101%
Cost Estimation	$375 total, ($75/kW)	$458	82%
Coolant Temperature	105 Deg C	105 Deg C	100%
Volume	5 Liter	5.1 Liter	98%
Weight	6kg	7.4kg	81%
Coolant Pressure Drop	0.73PSI (5kPa)	0.25 PSI	292%

Publications and Presentations

Presentation on U.S. Council for Automotive Research meeting, Southfield, Michigan, March 30, 2006.

Presentation on 2006 DOE FreedomCAR APEEM Annual Review, Pollard Technology Conference Center, Oak Ridge, Tennessee, August 16, 2006.

Presentation on Industrial Power Converter Products and Services Session in IEEE IAS 2006, Tampa, Florida, October 12, 2006.

Patents

"An Interleaved High Power DC/DC Converter," PAT0589-01US, filed on June 4, 2004.

"Integration of Planar Magnetics Transformer and Power Switching Devices in a Liquid-cooled High Power DC/DC Converter," PAT0588-02US, filed on October 12, 2004.

4.6 High Temperature Film Capacitors

Principal Investigator: Bruce Tuttle
Sandia National Laboratories
P.O. Box 5800, MS 1411
Albuquerque, NM 87185-1411
Voice : (505) 845-8026, Fax: (505) 844-9781; E-mail: batuttl@sandia.gov

DOE Technology Development Manager: Susan A. Rogers
Voice: 202-586-8997; Fax: 202-586-1600; E-mail: Susan.Rogers@ee.doe.gov

Contractor: Sandia National Laboratories, Albuquerque, New Mexico
Prime Contract No.: 04-94AL85000

Objectives

Develop high operating temperature (150 ^{o}C) polymer film and nanoceramic capacitor technologies for dc bus capacitors used for FreedomCAR fuel cell/electric hybrid vehicles

Develop nanoceramic dielectrics for two different material families: 1) high dielectric constant PLZT and 2) high breakdown field, low dielectric constant TiO_2 dielectrics

Develop a high-temperature polymer dielectric film technology that has dielectric properties technically superior to the best commercial polymer film capacitors and will result in comparable or smaller size.

Perform extensive high temperature testing of nanoceramic and polymer film dielectrics

Scale up cost-competitive polymer film and nanoceramic dielectric technologies.

Fabricate prototype capacitors.

Approach

Contact DOE program managers, automobile design and component engineers, dielectric powder and polymer film suppliers, and capacitor manufacturers to determine state-of-the-art capabilities and to define market-enabling technical goals.

Develop a project plan with DOE Program Managers, automobile manufacturers and large and small capacitor companies to fabricate polymer dielectric sheets suitable for FreedomCAR capacitor manufacturing.

Synthesize unique norbornene chemical solution precursors that result in dielectric films with low dissipation factors (DFs) and excellent high-temperature dielectric properties.

Develop norbornene polymer film dielectric processes and technologies that will lower costs to permit competitive high-volume capacitor manufacturing.

Develop chemically prepared nanoceramic powders and high density layers of two classes of dielectrics: 1) High K PLZT materials and 2) lower K, High breakdown field TiO_2 materials

Fabricate capacitors to be tested at high temperatures for ripple current voltages.

Interact with Oak Ridge National Laboratory (ORNL) with regard to mechanical characterization and ripple current measurements of dielectric films.

Major Accomplishments

Invented chemical synthesis procedures for three different polymer film families: (1) low cost polyphenylated polyethylene dielectrics, (2) polyaryl ether dielectrics, and (3) Norbornene based purified product.

Developed a chemical synthesis route that resulted in lower cost polyphenylated polyphenylene product that should reduce cost of these polymer films by more than a factor of ten compared to previous synthesis routes.

Demonstrated excellent high temperature electrical performance for low cost polyphenylated polyphenylene polymer dielectrics spin deposited on Al Coated Si wafers (dissipation factor less than 0.01 at 150^{o}C).

Performed mechanical property characterization of the low cost polyphenylated polyethylene dielectrics and polyaryl ethers - these materials were too brittle to be wound into capacitors.

Invented chemical synthesis procedures for Norbornene purified product, this material has high glass transition temperature, good high temperature electrical performance and is potentially mechanically flexible.

Synthesized three different types of nanoceramic powders: 1) relaxor PLZT, 2) field enforced Antiferroelectric to Ferroelectric (AFE – FE) PLZT, and 3) second generation TiO_2 powders.

Fabricated high quality chem-prep nanoceramic dielectric layers of 50 micrometer thickness using our direct write aerosol spray deposition (ASD) process to evaluate these three types of dielectric materials

Using ASD, we down selected to a PLZT composition that exhibited a dielectric constant of 2000 and a dissipation factor of 0.003 at 150^{o}C, this will result in a factor of two reduction in volume compared to state of the art barium titanate capacitors.

Collaborated with Honeywell to develop the technology for tape casting 20 layer chem-prep multilayer PLZT capacitors.

Improved the capacitance of the chem-prep PLZT multilayer capacitors by a factor of three in development efforts over the last 9 months.

Collaborated with ORNL (Andy Wereszczak) to mechanically characterize both polymer film dielectrics and PLZT nanoceramic thick film layers.

Technical Discussion

Strategy and Interactions

SNL has interacted with DOE program managers, representatives from the automobile industry and industrial representatives from industry to obtain their perspective on what is needed for capacitors for 2010 automobiles. There is no clear consensus as to whether polymer film or ceramic multilayer capacitors are better for FreedomCAR capacitor applications. Because of the interest in both technologies and Sandia's long standing expertise in chemical preparation of electronic ceramic materials and components, in FY 2006, SNL increased the portion of its development efforts of nanoceramic capacitors. Development of high operating temperature polymer film dielectrics was also continued. DOE and EE tech team members have retained their position that soft breakdown dielectric film technology is highly

desired. Soft breakdown is a phenomenon that large volume manufactured polymer film capacitors inherently possess. Sandia, for the present, is relying on the developments of Mike Lanagan and coworkers at Penn State for benign breakdown technology for ceramic capacitors. Our interactions with DOE program managers, experts from the capacitor industry and automobile manufacturers led us to the conclusion that the most viable technology for improvement of DC bus capacitor performance by 2010 is either multilayer polymer film or multilayer ceramic capacitors. Reducing the size of the polymer capacitors was most often cited by automobile design engineers and capacitor manufacturers as a needed technology-enabling breakthrough. In addition, it is necessary to improve high-temperature (150^{o}C) performance while keeping the technology cost-competitive. Further, high temperature nanoceramic multilayer capacitors may result in an overall decrease in system cost, since cooling loops could be eliminated. Thus SNL is pursuing development of both polyfilm and nanoceramic MLC technologies in FY07. There is a decision point to continue development of polymer film capacitors at the end of FY07.

Sandia scientists have continued our efforts to interact with industry and automobile manufacturers. In FY06, SNL began an extensive collaboration with Honeywell in Kansas City to develop procedures for chem-prep PLZT multilayer capacitor fabrication. At the end of FY06, 0.2 μF, 20 layer chem-prep PLZT MLCs were fabricated. Based on initial electrical measurements of these capacitors, a design for a 138 μF replacement PLZT capacitor for the Prius capacitors was developed. The chem-prep PLZT MLC would consist of 85 each 5 cm by 10 cm dielectric layers of 40 microns each. These capacitors would be roughly one sixth the size of the Prius capacitors. Sandia also consulted with the Advanced Technology Vehicles Division of GM, Custom Electronics, AVX, TPL, Hydrosize, Inc., and Brady Corporation about polymer film and nanoceramic MLC technologies and future scale up operations. Hydrosize, Inc. was contacted for scale up of polymer solution synthesis processes to enable fabrication of large area polymer films suitable for fabrication of 0.2 microfarad to 200 microfarad capacitors. Sandia has worked with Brady Corporation in the past and fabricated rolls of polymer film that were 1 foot wide and 1000 feet long. Polymer films of this size can be used to fabricate either six 200 μF capacitors or sixty 20 μF capacitors for prototype testing. These capacitors would be roughly a factor of two smaller in volume compared to the polyfilm capacitors used in the 2004 Toyota Prius.

Details of the calculations for these prototype polymer film capacitors are described. An individual dielectric layer thickness of approximately 3 μm for polyfilm capacitors is projected to reduce capacitor size. These thickness values are based on operating field strengths of 2 MV/cm for the newly developed polyfilm capacitors. Based on these assumptions and on measurement of presently available commercial capacitors, size comparisons and capacitance densities were obtained for 500 μF dc bus capacitors for different technologies. The projected polymer film capacitor volume was calculated assuming that there is 40% non-active capacitor space and 200-nm thick electrodes are used. Note that the volumetric capacitance efficiency for a K = 4.5 polyfilm capacitor of 2.4 μF/cm^3 exceeds the near-term commercialization goal of 2 μF/cm^3. In order to meet the 2010 EE Tech team specification of 5μF/cm^3, a polymer with dielectric constant of 6 and operating field of 2.7 MV/cm will be required. From recent discussions, it is expected that DOE program managers and the EE Tech team will support SNL scale up of dielectric film technology that is more volumetrically efficient than present state of the art commercial technologies.

Polymer Film Dielectric Development

SNL polymer film dielectric development has been based on the request from manufacturers that the new polyfilm dielectrics have voltage and temperature stability equivalent to that of present polyphenylene sulfide (PPS) technology. Thus a structural family of polymer dielectrics has been designed and synthesized to meet two of the most stringent FreedomCAR requirements: (1) low dielectric loss and (2) extremely good temperature stability. Very low dissipation factors on the order of 0.003 were measured at 150^{o}C for these SNL fabricated films. A patent disclosure has been initiated covering

the design and synthesis techniques for this polymeric family [1] based on phenylated polyphenylene (PPP). A previous drawback to this technology was the high synthesis costs of these materials. In FY 2006, our team developed procedures that substantially lowered the cost of synthesis of scale up quantities. Lower cost was achieved by developing new procedures that eliminated two chemical synthesis steps and the identification of less expensive raw materials.

A total of three different major polymer film chemistries were developed and investigated in FY06. These three polymer film families were low cost polyphenylated polyphenylene, polyaryl ethers, and norbornene chemistries. Modifications to these major families resulted in the fabrication and characterization of over 50 different types of polymer films. Our metrics were synthesis of purified product, film fabrication, mechanical properties and electrical properties. Specifically, the structure of low cost hydroxylated phenylated polyphenylene synthesized by SNL is shown in Figure 1.

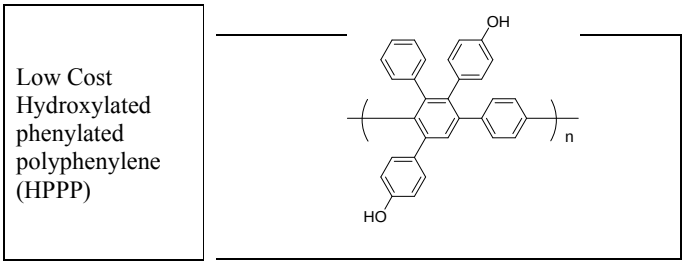


Figure 1. Structure of low cost hydroxylated phenylated polyphenylene

Excellent high temperature dielectric properties are shown in Figure 2 for the low cost (PPP) films developed by SNL in FY06. These films were spin deposited on Al coated Si wafers and were approximately 0.7 micrometers thick. Unfortunately, we were not able to spin deposit these films on Mylar due to poor adherence during processing or cracking. It is necessary to deposit polymer films on Mylar to create free standing films for mechanical evaluation. Free standing polymer films, both commercial and developed by SNL, have been sent to Andy Wereszczak at Oak Ridge National Laboratories in FY06. From this work, the metric of strain to failure rather than the strength of the film has been adopted as the primary metric for suitability for high volume winding of polymer thin films. ORNL measured a strain to failure of 25% for the polymer film in the Prius capacitors compared to 5% strain to failure for SNL high temperature polymer films. A second reason for the need to deposit polymer films on Mylar is that this substrate permits release of free standing films for subsequent capacitor manufacturing. Large area, free standing films are necessary to fabricate either wound or stacked polymer film capacitors. These capacitors are needed in order to fabricate prototype capacitors for testing by OEM and ORNL engineers for ripple current tests. The dissipation factors measured to 140^{o}C and shown in Figure 2 for the SNL low cost hydroxylated phenylated polyphenylene film were exceedingly low, on the order of 0.005, and encouragingly decreased with increasing temperature. This result is promising for high temperature inverter operation. Dielectric constants for these films are approximately 3.5 and are very insensitive to temperature. The dielectric constants of the low temperature polyphenylated polyphenylene films are almost 20% greater than those of commercial state of the art polyphenylene sulfide films.

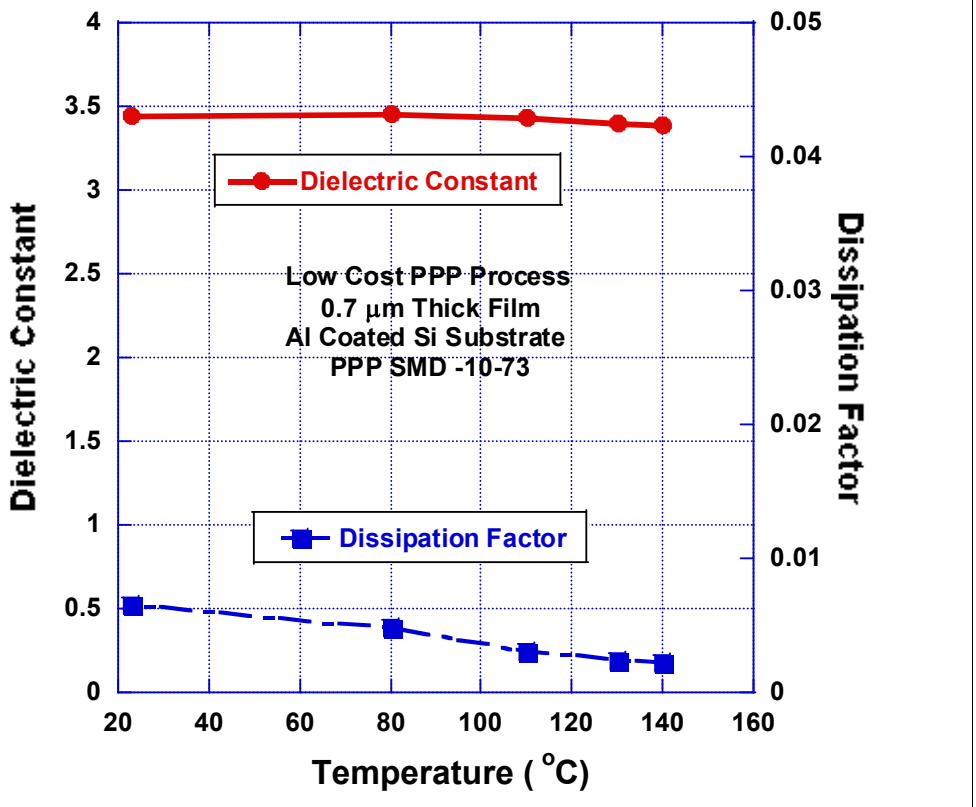


Figure 2. Dielectric Constant and Dissipation Factor Versus Temperature for Low cost PPP film

High quality nanoceramic powders of three different types of high energy density materials were fabricated in FY06 by SNL scientists. These different types of materials were: 1) low dielectric constant, high breakdown strength TiO_2, 2) relaxor ferroelectric PLZT and 3) Field enforced AFE to FE phase transition PLZT were fabricated in FYO6 by SNL scientists. The chem-prep nanopowder synthesis facility and computer controlled aerosol spray deposition apparatus are shown in Figure 3. The SNL patented process [2] consists of an acetic acid solution of Pb acetate, Zr butoxide and Ti isopropoxide precursors precipitated with oxalic acid using high shear rate mixing. Extremely homogenous, fine particles are created with a crystallite size on the order of 60 nm. Figure 3 shows the powder synthesis precipitation step and SNL lab facilities for 1.5 kg batches. Ten kilogram PZT batches can be fabricated at SNL facilities. In addition, the latest version of the SNL ASD direct write apparatus is shown. The desired substrate is rastered under the nozzle head by LabView programmed linear drive motors. Six layer multilayer PLZT capacitors have been fabricated by the direct write process [3,4] using a single fire process. Capacitors of 1 cm^2 area that are 50 μm thick can be deposited in less than a minute. We have fabricated aerosol spray deposited PLZT films of 50 micrometer thickness [5] that have breakdown strengths that exceed 200 kV/cm.

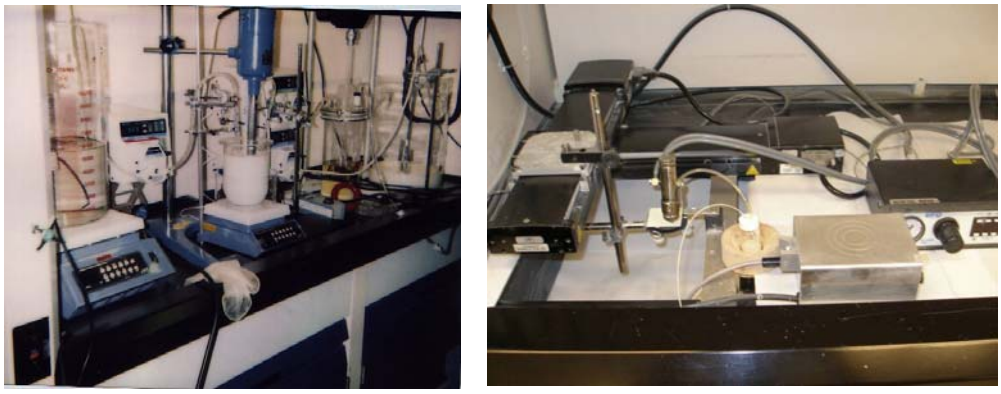


Figure 3: Chemical powder synthesis facility and aerosol spray deposition apparatus for nanoceramics.

SNL scientists used direct write ASD to fabricate high quality 50 micron thick layers of the three different types of high energy density nanoceramic dielectrics in FY06. TiO_2 was chosen as the first lower dielectric constant, higher breakdown strength dielectric to investigate. Powders of titania with less than 20 nm particle size were synthesized. These nanopowders were fabricated using a Ti-n butoxide based synthesis. The solution was pumped/sheared at 6000 RPM to create a homogeneous mixture of fine particles. In-situ densification studies were performed to determine optimum firing conditions for densification. An analogous procedure was used to fabricate PLZT powders for dielectrics with either relaxor or field enforced AFE to FE characteristics. While titania films withstood fields of 600 kV/cm or 3000 volts, the PLZT materials withstood fields in excess of 200 kV/cm. The overall energy densities of the PLZT thick films were greater than those of the titania films due to their larger dielectric constants. We down selected the PLZT relaxor composition for further development over the AFE to FE phase

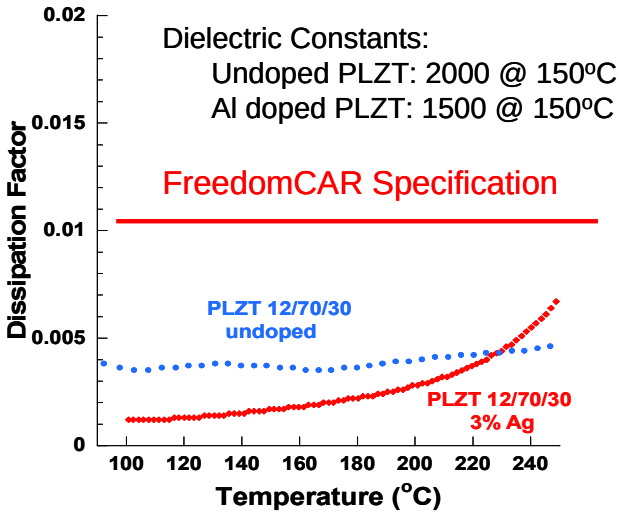


Figure 4. High Temperature Dielectric Properties of SNL ASD Chem-Prep PLZT Dielectric

transition material due to less variation in dielectric properties over the -40°C to 150°C temperature range. The excellent high temperature dielectric properties of the relaxor composition with and with out silver oxide additions are shown in Figure 4. A very low dissipation factor of 0.003 and a dielectric constant of 2000 were measured at 150°C for the undoped material. The PLZT dielectric with 3% Ag addition also exhibits very low loss at high temperature and has a dielectric constant of 1500 at 150 °C. Both materials have dissipation factors that are less than the 0.01 dissipation factor FreedomCAR requirement. Unlike SNL PLZT, state of the art barium titanate materials do not meet the FreedomCAR standards for loss with measured values in the range of 0.015. The low dissipation factors measured at high temperatures for the chem-prep PLZT thick films indicates that ripple current handling capability should be very good.

Sandia National Laboratories initiated technical efforts with Honeywell FM&T in Kansas City to fabricate multilayer chem-prep PLZT capacitors for eventual evaluation by engineers associated with the DOE FreedomCAR program. SNL and HW worked together to solve process issues for tape rheology, pyrolysis treatment, firing procedures and delamination. Multilayer chem-prep PLZT capacitors were successfully fabricated (Figure 5) that exhibited nominal 0.2 μF capacitance at low voltage (1 volt ac rms). During FY06, several technical accomplishments enabled chem-prep PLZT MLC fabrication. First, chem-prep PLZT powders were synthesized in sufficient quantities - approximately 6 kilograms – for MLC development by SNL and delivered to HWFM&T. Second, high quality tape cast rheology was developed by HWFM&T for research scale tape casting and then the rheology was modified such that high quality tapes were produced using the larger prototype development tape caster at HWFM&T.

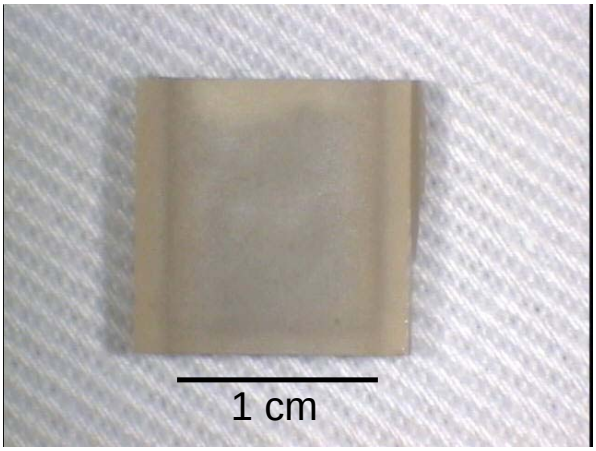


Figure 5. SNL/HW 20 Layer Chem-Prep Multilayer Capacitor

Third, pyrolysis and sintering procedures were developed and modified for chem-prep PLZT single layer tapes and multilayer capacitors. Further, proper lamination and electrode procedures were developed for these capacitors such that delamination and electrical shorting did not occur. A key development was determining the proper sintering procedures using weighted assemblies to prevent delamination of PLZT and electrode tapes during firing. SNL scientists are in the process of performing an extensive set of low voltage measurements. After these low voltage (less than 10 volt) measurements are completed, prototype capacitors will be evaluated for their high field properties. If these high voltage tests are successful, then these units will be delivered to ORNL for ripple current testing. During FY06, process improvements resulted in an increase of the low voltage measured capacitance of our chem-prep PLZT MLCs from 30% to 100% of the projected 0.2 μF capacitance value.

Conclusion

Discussions with DOE program managers, DOE consultants, automotive engineers and capacitor industry representatives in FY06 reinforced the importance of pursuing both high temperature polymer film and nanoceramic dielectric development. There is no clear consensus to date as to which technology, multilayer ceramic capacitor or multilayer polymer film capacitors, is best for achieving FreedomCAR program goals. In general, while polyfilm multilayer capacitors have advantages with regard to cost, the volumetric efficiency and the temperature handling capability of ceramic based multilayer capacitors is superior. The 2010 temperature specifications put forth by DOE and the EE TECH team of –40°C to 150°C will not be met by recently developed state of the art polyethylene dielectrics or state of the art barium titanate dielectrics. Thus development of high temperature polymer and nanoceramic dielectric materials is necessary to reduce volume and improve temperature performance of DC bus capacitor dielectrics to meet the FreedomCAR specifications. In FY06, SNL launched a multifaceted program of chemical synthesis, electrical characterization, film processing, and mechanical characterization for development of low volume, high temperature DC bus capacitors. Among the FY06 accomplishments was the development of a low cost norbornene synthesis procedure. Capacitors fabricated on aluminum coated silicon wafers exhibited low loss and had dielectric constants that exceeded that of state of the art polyphenylene sulfide. Further, SNL scientists synthesized high quality nanoceramic dielectric powders of PLZT and TiO_2. We used our recently developed direct write aerosol spray deposition process to fabricate high quality ceramic layers for the evaluation of three different nanoceramic materials. From extensive electrical testing of these materials at high temperatures, a PLZT composition was chosen for further development. Aerosol spray deposited layers of this material exhibited a dielectric constant of 2000 and a dissipation factor of 0.003 at 150°C. Unlike for $BaTiO_3$ based dielectrics, the dissipation factor at 150°C meets FreedomCAR specifications. Sandia scientists have collaborated extensively with Honeywell engineers to fabricate 20 layer multilayer chem-prep PLZT capacitors of the chosen PLZT composition. These capacitors exhibited capacitance values that were in agreement with the original engineering design values.

Future Directions

In FY 2007, we will develop the processes necessary for the development of lower sintering temperature nanoceramic dielectrics with no porosity. This development will permit integration with low temperature cofired ceramic technology and permit further reduction in capacitor size due to higher operating fields. High quality chem-prep PLZT nanoceramic multilayer capacitors will be developed for evaluation by SNL, ORNL and OEMs. For our polymer film development, we will develop synthesis procedures and fabricate Norbornene based polymer films. Further, a systematic study entailing the modification of Oxynorbornene and Norbornene polymers will be undertaken. There will be a go / no go decision for the continuation of the polymer film synthesis effort at the end of FY07. Specific tasks for our FY07 efforts are shown below.

Task 1: Chemical Synthesis: Develop new chemistry of low cost Norbornene polymer film dielectrics

Task 2: Fabricate and characterize spin deposited Norbornene films on Al coated Si and on Mylar coated Si wafers and characterize electrical and mechanical properties of these films.

If these film properties are acceptable to DOE program managers initiate scale up to 1 to 5 liter batches of solution (Hydrosize, Inc) and have polymer sheets fabricated of 500 foot length for fabricating wound polymer capacitors.

If the processing and electrical measurements of the SNL polyfilms are successful, then large-value (20 μF to 200 μF) capacitors will be fabricated by vendor(s) and evaluated by SNL, ORNL and auto manufacturers in simulated electric hybrid and fuel cell vehicle environments.

Task 3: Mechanically and Electrically Test New Polymer Films and Provide Report

Task 4: Develop Chem-Prep Nanoceramic Dielectrics with Lower Sintering Temperatures and No Porosity

Task 5: Fabricate High Quality Multilayer Capacitors for Electrical Testing (SNL, ORNL, OEMs) via Industrial Collaborations

Publications

1. Bruce Tuttle, David Williams, Jill Wheeler, Luke Brewer, Mark Rodriguez and T. Headley, "Characterization of PLZT Based Materials For High Energy Density Applications," Proceedings of the 12th Annual US-Japan Seminar, Annapolis, MD, November 8-11, 2005.

2. Duane Dimos, Nelson S. Bell, Joseph Cesarano III, Paul G. Clem, Kevin G. Ewsuk, Terry J. Garino, Bruce A. Tuttle, "Integration and Process Strategies for Ceramics in Advanced Microsystems, Proceedings First International Congress on Ceramics, Toronto, Canada, p. 385-389, June 25-29, 2006.

3. G. Samara, E. Venturini, B. Tuttle, D. Williams, M. Rodriguez, C. Frazer, R. Grubbs, L. Brewer and P. Hlava, "Ferroelectric and Antiferroelectric Properties and Behavior of La-Substituted Zr-Rich Pb($Zr_{1-x}Ti_xO_3$ (PLZT): Sandia Report SAND2-006-5002, September, 2006.

Patents

1. D. Wheeler and G. Jamison, "Novel Polymer Film Synthesis Routes of Voltage and Temperature Stable Dielectrics," October 5, 1999.
2. J. A. Voigt, D.L. Sipola, B.A. Tuttle, and M. T. Anderson, U.S. Patent No. 5,908,802, "Nonaqueous Solution Synthesis Process for Preparing Oxide Powders of Lead Zirconate Titanate and Related Materials, issued June 1, 1999.

References

1. D. Wheeler and G. Jamison, "Novel Polymer Film Synthesis Routes of Voltage and Temperature Stable Dielectrics," US Patent October 5, 1999.
2. J. A. Voigt, D.L. Sipola, B.A. Tuttle, and M. T. Anderson, U.S. Patent No. 5,908,802, "Nonaqueous Solution Synthesis Process for Preparing Oxide Powders of Lead Zirconate Titanate and Related Materials," issued June 1, 1999.
3. B. Tuttle, "Materials Aspects of High Energy Density Dielectrics," University of Arizona Materials Science Seminar Series," March 27, 2006 (Invited Presentation).
4. B. Tuttle, D. Williams, G. Brennecka, J. Voigt, and D. Moore, "High Energy Density Capacitor Development," TCGX-10 Meeting Los Alamos, NM April 12, 2006.
5. D. Williams*, B. Tuttle, J. Voigt, D. Moore, M.Niehaus, and J.Cesarano, "Fabrication of Integrated Multilayer PLZT Capacitors," IEEE International Symposium on Applications of Ferroelectrics, Sunset Beach NC, July 28 – August 2, 2006.

4.7 Embedded Capacitors for (P)HEV Power Electronic Systems

D.Y. Kaufman, B. Ma, and U. Balachandran
Energy Systems Division
Argonne National Laboratory
9700 S. Cass Ave.
Argonne, IL 60439
Voice: (630)252-4250 Fax: (630)252-3604 E-mail: balu@anl.gov

DOE Technology Development Manager: Susan A. Rogers
Voice: 202-586-8997; Fax: 202-586-1600; E-mail: Susan.Rogers@ee.doe.gov

---

Objectives

This R&D program is developing high performance and economical DC bus capacitor technologies that will achieve APEEM specifications for (P)HEV power electronic systems. Current DC bus capacitors occupy a large fraction of the volume and weight of the inverter module, cannot tolerate temperatures >120°C, suffer from poor packaging and reliability, and deleterious failure modes. Traditional capacitor architectures with conventional dielectrics cannot adequately meet all of the performance goals for capacitance density, weight, volume, and cos. This requires a high permittivity, high temperature rated dielectric packaged in a high volumetric efficiency architecture with benign failure features.

Approach

Argonne National Laboratory's (Argonne) capacitor R&D program addresses the technology gap in an innovative manner. We are developing high performance, low cost capacitors embedded directly into the printed wire board (PWB). In these "embedded film-on-foil capacitors" a base-metal foil (Nickel or Copper) is coated with a high permittivity ferroelectric material, $(Pb,La)(Zr,Ti)O_3$ (abbreviated as PLZT). Ferroelectrics possess high permittivity, breakdown electric fields, and insulation resistance. They can withstand high temperatures such that high ripple currents can be tolerated at under hood temperatures. Use of base-metals and solution-based deposition techniques reduces the cost. An embedded capacitors approach significantly reduces component footprint, improves device performance, provides greater design flexibility, and offers an economic advantage. This technology will achieve the highest degree of packaging volumetric efficiency with lowest weight.

Our R&D efforts focus on examining the underpinning issues of film-on-foil embedded capacitor performance, developing low cost capacitor designs, establishing robust commercially and economically viable fabrication protocols, and transferring the technology to industry for manufacturing.

Major Accomplishments

- Refined $LaNiO_3$ (LNO) buffer layers to avoid deleterious effects of a parasitic low capacitance interfacial oxide layer.
- Developed a core technology of PLZT/ LNO/ Ni capacitor foils with dielectric constants > 1150 (1.5 $\mu F/cm^2$) and loss ≤ 0.06.
- Developed PLZT/LNO/Ni capacitor foils reaching 580 V with breakdown fields ≥ 1.2 MV/cm.

- Designed electrode architectures to achieve benign failure via self-clearing. In such a mode evolving faulted areas become removed from the larger structure and the capacitor continues to operate with a nearly undetectable loss in performance. This mechanism parallels fail-safe designs hailed in metallized polymer capacitors.
- Began an alliance with a PWB manufacturer and an automotive electronics company to embed our 'film-on-foil' dielectric elements and fabricate embedded (P)HEV capacitor prototypes.

Technical Discussion

The replacement of bulky inefficient discreet capacitors with capacitors embedded within the layers of a printed wire board is an innovative solution to high capacitance density and high volumetric efficiency capacitors. Embedded capacitors can be located directly underneath the active devices, greatly reducing component footprint and improving reliability. While this technology has primarily received attention for low voltage, high frequency decoupling capacitors, it can be extended to the higher voltages of (P)HEV systems. The vision of embedded DC bus capacitors is compelling and offers US automotive companies a substantial technological advantage over their foreign counterparts. The bulky coke-can-like banks of capacitors will be replaced instead by lengths of capacitors tucked flat and neatly underneath the active components and bus structure.

The key provision is the integration of high-k ferroelectric dielectric layers within the printed wire board. Since high temperature processing (~650°C) is required to obtain crystalline ferroelectric materials, direct deposition on the polymeric printed wire board is not possible. Instead, a pre-fabricated 'film-on-foil' approach is adopted whereby the ferroelectric is first deposited via chemical solution deposition (CSD) on a thin base metal foil, crystallized at high temperatures, and the coated foil subsequently embedded within the printed wire board.

A principal concern in the fabrication of 'film-on-foil' capacitors is eliminating the deleterious effects of a low-k parasitic oxide at the metal-ferroelectric interface. This would act as a series capacitor and reduce the overall capacitance. To negate the influence of the interfacial oxide two approaches have been pursued: 1- A conductive oxide buffer layer is interposed between the ferroelectric and the metal foil. The buffer layer acts as the bottom electrode and any secondary oxide that may form below it at the metal interface is inconsequential to the parallel plate capacitor. 2- Crystallizing the ferroelectric in a controlled reduced pO_2 environment such that formation of an interfacial oxide is prevented, yet the oxide dielectric is not decomposed.

1-PLZT/LNO/Ni Capacitors

We have developed a core technology for CSD PLZT on Ni film-on-foil capacitors with $LaNiO_3$ [LNO] buffer layers. CSD solutions were synthesized at Argonne and the films deposited by spin coating. All annealing and pyrolosis were done in air and repeated to build up layers of sufficient thickness.

Even a single layer of LNO (~0.15 microns) is sufficient to obviate the parasitic influence of any interfacial NiO formation (Figure 1). LNO film metrology exerts a pronounced influence on dielectric loss and breakdown strength. Three layers of LNO are required to completely cover and ameliorate the roughness of the Ni substrate. The planarizing influence of the LNO layer is highlighted in the cross-sectional SEM image shown in Figure 2. Besides obviating any NiO formation along the Ni interface, the LNO provides a smooth interface for nucleation and growth of dense PLZT. These PLZT/LNO/Ni capacitors achieved capacitance densities of 1.5 microfarads/cm^2, nearly equivalent to that obtained using inert platinized Si substrates. The smooth interfaces and dense microstructure both contribute to high breakdown strengths.

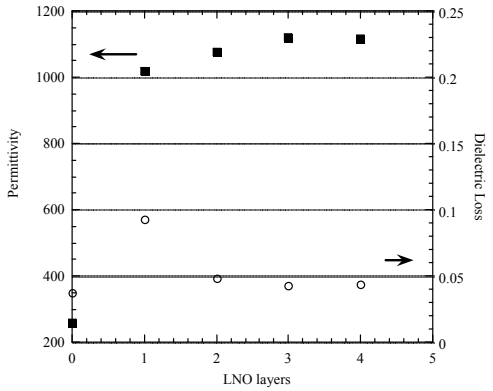


Figure 1. Dielectric properties of a PLZT film on LNO buffer layers of various number.

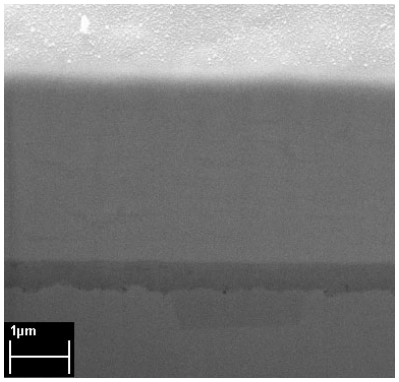


Figure 2. Cross sectional SEM micrograph of a PLZT/LNO/Ni film-on-foil heterostructure.

2-PLZT/Cu Capacitors

Cu is the primary material for PWB interconnects and metallization. We have initiated development of PLZT on bare Cu foils. Here a controlled reduced pO_2 environment is used to prevent formation of a parasitic interfacial oxide layer. The pO_2 must be low enough to prevent oxidation of the Cu-PLZT interface, yet not too low to induce decomposition of the PLZT oxide chemistry. Thermodynamic models aid in determining the appropriate pO_2 for the heating, crystallization, and cooling cycles.

Graceful Failure

We have developed film-on-foil capacitors that exhibit graceful failure – a gradual loss in capacitance upon localized breakdown events. Following a breakdown occurrence the capacitor continues to function and is only considered to have failed at such time that a defined leakage current or dielectric loss is reached.

At sufficiently high voltages, dielectric breakdown occurs at a discrete faulted area. This discharges the stored energy of the dielectric in that localized spot. In a matter of microseconds the discharge heats the immediate area, which physically "clears" away the dielectric from the defect site, and vaporizes the

metal top electrode in a small region surrounding the defect. By this process the breakdown site becomes electrically isolated and removed from the remainder of the capacitor structure. The capacitor continues to operate to even higher voltages. Self-clearing capacitors can sustain many breakdown events during their lifetime and can tolerate higher voltages. A small loss in capacitance is observed only after several breakdown/clearing events occur. Indeed, it usually takes hundred to thousands of such clearings to cause a few percent loss in capacitance. In such a manner, instead of shorting, the capacitor effectively "self-heals", and failure occurs gracefully. Such self-clearing failure modes are the same as those in metallized polymer capacitors

Prototype Development

We have demonstrated proof-of-concept film-on-foil capacitors. To proceed towards the next step of prototype embedded capacitors we have begun an alliance with Delphi Electronics and Safety, a leading automotive electronics supplier, and Diversified Systems, Inc., a PWB manufacturer. Together with these partners we will begin to develop technologies for integration of the film-on-foils into PWB fabrication. This will include embedding, imaging and etching, and interconnects and terminations. Novel PWB circuit designs will be conceived to maximize the capacitance and voltage in as small a volume. The embedded capacitors will be assembled and analyzed under (P)HEV inverter conditions.

Conclusion

We have developed a core technology for high capacitance density, high breakdown strength film-on-foil capacitors exhibiting graceful failure. PLZT film-on-foil capacitors have been fabricated with LNO buffer layers atop the Ni foils allowing the capacitors to be processed in air. Additionally, the LNO ameliorates the roughness of the Ni foil and provides a smooth interface for the PLZT films, resulting in higher breakdown strengths. Low pO_2 processing will be used to fabricate PLZT capacitor on Cu foils without the need for a buffer layer. Top electrode metallization design enables self-clearing of faults and graceful failure. This film-on-foil technology will be used to fabricate (P)HEV embedded DC bus capacitors with significant size and weight reduction, and improved performance and reliability.

Future Directions

The R&D achieved thus far sets the stage for developing prototype PWBs with embedded (P)HEV capacitors. This will require refinement of our technology and alignment with PWB fabrication routines. An ultrasonic aerosol coater will be used to fabricate PLZT dielectric films on large area Cu foil sheets. Robust processing condition will be developed to crystallize the film without formation of a parasitic interfacial capacitance. We will evaluate the high voltage and high temperature behavior of the ferroelectric film-on-foils with a perspective on reliability. We will investigate the microstructural aspects of dielectric breakdown and degradation and tailor devices based on those findings.

These film-on-foil sheets will be integrated into a PWB manufacturing process and embedded into the boards. Working with our alliance partners we will address the challenges posed by embedding, imaging the inner-layers, metallization, and circuit design. Prototype embedded capacitors will be evaluated for device performance and benchmark against APEEM goals. These initial prototypes will be evaluated by ORNL as well.

Publications

"PLZT Film-on-Foil Capacitors for Embedded Passives", D. Y. Kaufman, S. Saha, and K. Uprety, Proceedings of the 12th US-Japan Seminar on Dielectric and Piezoelectric Ceramics, November 2005, Annapolis, MD, pp. 305-308.

"Dielectric Performance of PLZT Film-on-Foil Capacitors for Embedded Passives", S. Saha and D.Y. Kaufman, in preparation.

Patents

"Ceramic Capacitor Exhibiting Graceful Failure by Self-Clearing", D.Y. Kaufman and S. Saha, U.S. Patent 7,099,141.

4.8 Glass Ceramic Dielectrics for DC Bus Capacitors

Principal Investigators: Mike Lanagan and Carlo Pantano
Researchers: Do-Kyun Kwon and Eugene Furman
280 Materials Research Laboratory
Penn State University
University Park, PA 16802
E-mail: MLanagan@psu.edu
Phone: 814-865-6992

DOE Technology Development Manager: Susan A. Rogers
Voice: 202-586-8997; Fax: 202-586-1600; E-mail: Susan.Rogers@ee.doe.gov

Objectives

Power converters play a major role by converting energy stored in electrochemical batteries and fuel cells from direct current (DC) into alternating current (AC) for electric and hybrid vehicles. The conversion from DC into AC is not ideal; however, and the operation of a typical switch mode inverter leads to alternating currents on the DC bus at harmonics associated with the switching frequency. DC bus capacitors are required to reduce ripple current. The overall goal of this program is to reduce the cost, volume, and weight of power electronic inverter modules by focusing research efforts on capacitor components and dielectric materials for capacitors

Targets

Recently, U.S. capacitor manufacturers are focusing on high voltage high power capacitors. These companies see increased demand from the medical, telecommunication, and automotive industries for high voltage capacitors. Major manufacturers include: AVX, Kemet, Taiyo Yuden, Murata, TDK and EPCOS. The comparison of Multilayer Ceramic Capacitors (MLCCs) with EE tech team specifications is shown in Figure 1.

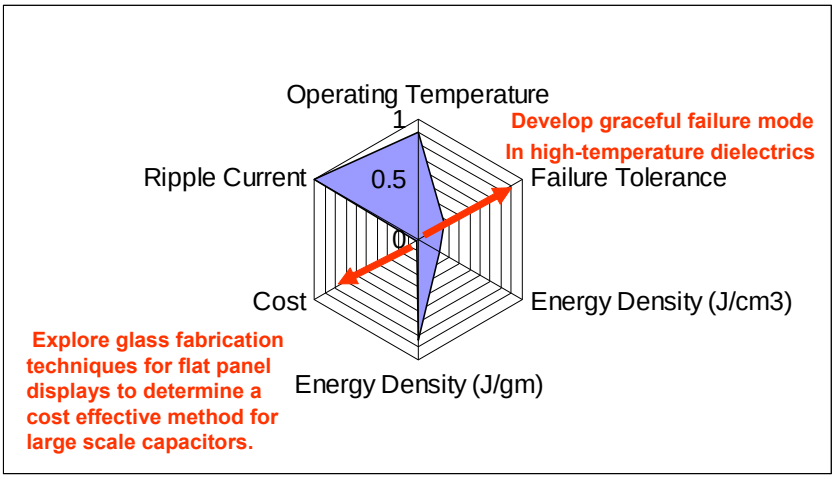


Figure 1: Comparison of MLCC Capacitor Parameters with DOE FreedomCAR specifications.

As shown in Figure 1, the ripple current and operating temperature specifications are close to meeting the Department of Energy inverter specifications; however, failure tolerance, energy density and cost targets are substantially below what is required for hybrid vehicles. The multilayer ceramic capacitor temperature specification is generally limited by the dependence of dielectric constant on temperature. One of the major drawbacks of MLCCs is the failure mode, which often results in a short circuit. Generally, the fabrication process involves deposition of thick electrode layers which melt and fuse together at high temperature. For this reason, the voltage ratings for MLCCs substantially below the failure voltage, which limits the energy density and increases cost. Future research and development activities need to focus on graceful failure mechanisms in multilayer ceramic capacitors. The ripple current capability of MLCCs, especially at high temperature, is superior to all of the other capacitor types.

Approach

In order to address the critical gaps shown in Figure 1, the major focus is on developing graceful failure mechanisms in glass capacitors and finding a large-scale manufacturing process for D.C bus capacitors. We have had several fruitful interactions with flat-panel display manufacturers, Corning and Schott, to determine if their materials are appropriate for capacitors. As shown in Figure 2, very large glass sheets can be manufactured for the high-volume low-cost consumer market.



Figure 2: Large area glass panels for flat panel displays were studied for high temperature D.C. bus capacitors for hybrid electric vehicles. This project explores the electrical properties of display glass at high temperatures.

The first task was to characterize dielectric material and capacitor performance (capacitance, loss, ESR) as a function of frequency, temperature, and voltage. These properties are directly related to reducing capacitor volume in the inverter.

Task two identified capacitor failure mechanisms in which capacitors fail in the “open mode” instead of a short circuit.

Task three focused on a low-cost glass process for manufacturing recrystallized glass capacitors which can operate at high temperatures in automotive applications. We found that recrystallized glass was difficult to synthesize in large areas and discontinued this line of research. Task three will not be discussed in this final report and there are several publications from this research (see Publications section of this report).

Prototype capacitor designs, based on flat panel display glass, are shown in Figure 3. The designs were given to Schott and Corning to determine if this geometry is feasible with current manufacturing processes. In addition, we have contacted AVX for more information on their glass capacitor manufacturing line.

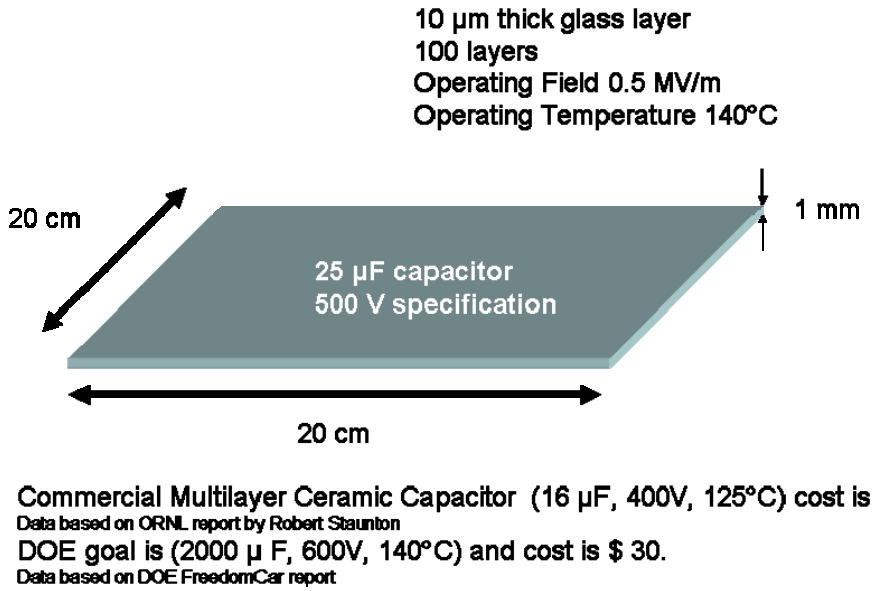


Figure 3: Prototype capacitor design based on flat panel display glass. Current commercial capacitor specifications are shown with DOE freedom car projections for capacitors in hybrid vehicles.

Major Accomplishments

In FY2005 we explored flat panel display glass from Corning. In FY2006 we evaluated flat panel display glass from Schott North America and the results are shown in Figures 4 and 5. As with the Corning glass samples, the dielectric properties of the flat panel display glass exceed the DOE freedom car goals up to temperatures of 350°C.

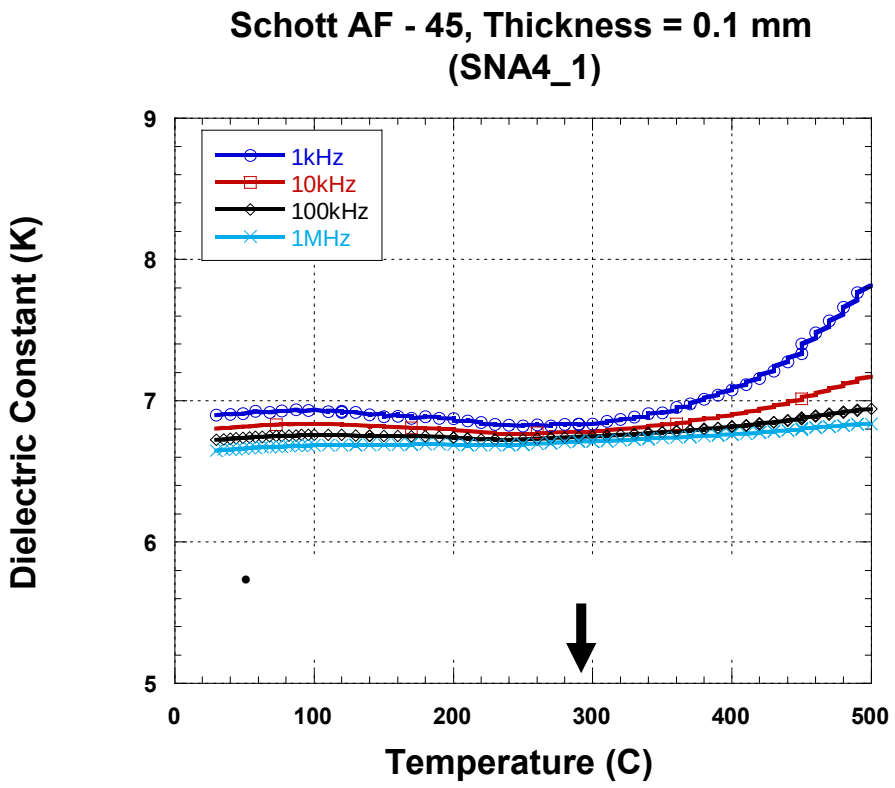


Figure 4: The dielectric constant of Schott glass as a function of temperature and frequency. The materials were characterized in the typical frequency range for a DC bus inverter (1 kHz to 1 MHz). The dielectric constant of 7 is triple that of conventional polymers, which will decrease the capacitor size by over 60%. In addition the permittivity is constant up to 400°C which far exceeds the DOE FreedomCAR goal of 140°C.

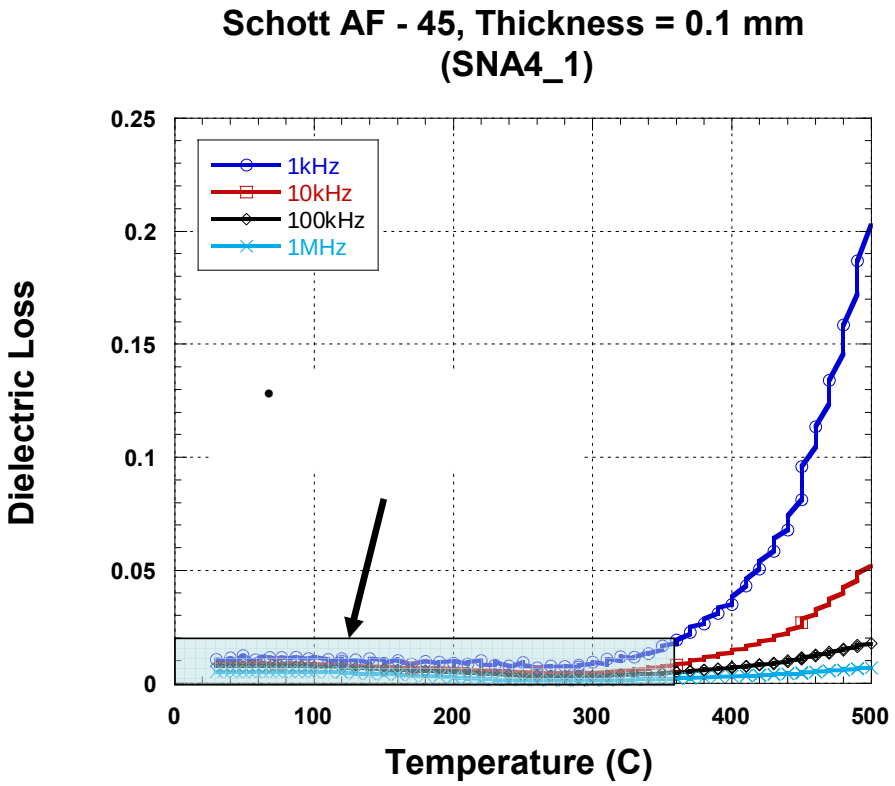


Figure 5: The dielectric loss of Schott AF glass as a function of temperature and frequency. The dielectric loss is within DOE Freedom Car specifications up to a temperature of 350°C.

Technical Discussion

Since DC bus capacitors store large amounts of energy and are positioned between the high voltage terminal and ground, the failure mechanism is a critical factor. A open circuit failure mode can be developed in capacitors with thin manganese oxide (MnO_2) electrodes. MnO_2 is semiconductor material having ~1 Ω·cm of resistivity and is commonly used in electrolytic capacitors. The benefit of using the semiconductor MnO_2 for electrode is realized because the higher temperature phase, Mn_2O_3 has a higher resitivity, an unusual property for metal oxides. If a current path occurs in the dielectric, then the current into that defect site is concentrated in a small area in MnO_2 and causes joule heating at the localized area. The MnO_2 phase is unstable at high temperature and converts to Mn_2O_3, which is an insulator (resititivity $\approx 10^5$ to 10^6 Ω·cm).

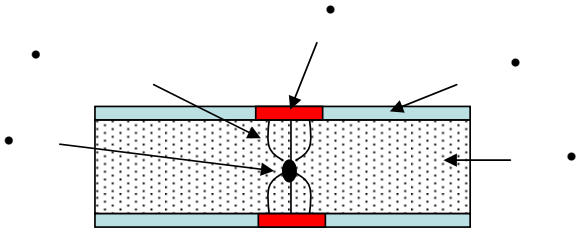


Figure 6: Open circuit formation by a phase transition of conducting MnO_2 to insulating Mn_2O_3 at a localized high temperature region.

Mn solution for spin coating on glass

Thin layers of MnO_2 were deposited on commercial flat panel display glass substrates by a sol-gel process. Two kind of precursors, manganese acetate ($Mn(C_2H_3O_2)_2{\cdot}4H_2O$) and manganese nitrate ($Mn(NO_3)_2{\cdot}xH_2O$) were dissolved in DI-water, acetic acid, 2-metoxyethanol (2MOE), and ethanol. Manganese nitrate was more soluble than manganese acetate in any of the solvent. However, the wetting of manganese nitrate solutions on glass substrates was not as good. Manganese acetate completely dissolved in acetic acid and 35% DI water mixed solution. A stable manganese solution was prepared with 0.35 M of concentration and its PH was 2.7. The solution nicely wet on glass surfaces and films were fabricated by spin coating. Film thicknesses of 300 nm were achieved. Figure 7 shows the process to deposit MnO_2 thin films on glass substrates.

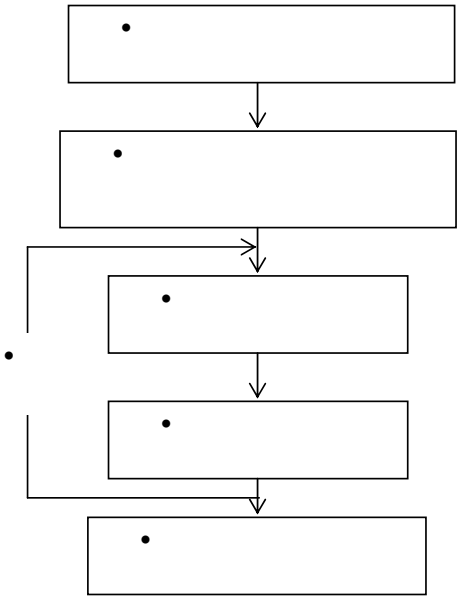


Figure 7: Processing flow chart for chemical deposition of MnO_2 thin films on glass.

Conclusion

This project has two major thrusts: 1) Explore commercial glass as a dielectric material for high temperature DC bus capacitors and 2) Synthesize electrodes that support an open failure mode. Capacitors made from glass will have the energy density, reliability, and the low-loss needed for high frequency power conditioning and filtering. This material exhibits high temperature capability (> 200°C) that will be required for next generation power converters based on silicon carbide (SiC). Thin manganese oxide electrodes were successfully deposited on commercial glass in order to establish graceful failure modes in DC bus capacitors.

Future Direction

Future research and development activities will further explore graceful failure modes in glass capacitors with thin MnO_2 electrodes. We will explore breakdown test of the glass capacitors under high voltage (up to 30kV). The failure behavior of glass capacitors with MnO_2 electrodes will be compared with that of glass capacitors with metal electrodes. Future research activities for DC bus capacitors will focus on polymer, glass, and ceramics, with high dielectric constant and high temperature operation. Current work at Sandia National Laboratories on hydroxylated polystyrene (PVOH) has demonstrated dielectric constants between 4.5 and 6 and excellent high temperature properties. Glass research at Penn State University has shown that high temperature operation can be achieved. Research at Argonne National Laboratory on $(Ba_xSr_{1-x})Ti\ O_3$ films has demonstrated the possibility of operating these films up to 150ºC. Critical Issues will be in achieving the energy density and temperature goals set forth by the EE Tech Team, and in the scale-up of the processes being developed under the current program.

Publications

M. Lanagan, J. Du, C. Wang, B. Jones, B. Rangarajan*, T. Perrotta, and T. Shrout, "Glass Ceramic Dielectrics," The 12th US-Japan Seminar on Dielectric and Piezoelectric Ceramics, Annapolis, Maryland, p. 401-404 (Nov 6-9, 2005).

Cheng CT, Lanagan M, Jones B, et al., Crystallization kinetics and phase development of PbO-BaO-SrO-Nb2O5-B2O3-SiO2-based glass-ceramics, JOURNAL OF THE AMERICAN CERAMIC SOCIETY 88 (11): 3037-3042 NOV 2005.

Du J, Jones B, Lanagan M, Preparation and characterization of dielectric glass-ceramics in Na2O-PbO-Nb2O5-SiO2 system, MATERIALS LETTERS 59 (22): 2821-2826 SEP 2005.

Cheng CT, Lanagan M, Lin JT, et al., Crystallization kinetics and dielectric properties of nanocrystalline lead strontium barium niobates, JOURNAL OF MATERIALS RESEARCH 20 (2): 438-446 FEB 2005.

Kwon DK, Lanagan MT, Shrout TR., Synthesis of BaTiTe3O9 ceramics for LTCC application and its dielectric properties, JOURNAL OF THE CERAMIC SOCIETY OF JAPAN 113 (1315): 216-219 MAR 2005.

Pan Ming-Jen, Lanagan M., Bender B., Cheng CT, High Energy Density Ferroelectric Glass Ceramics, CERAMIC TRANSACTIONS, 169, 187-193, 2005.

5. Systems Research and Technology Development

5.1 Fully Integrated HEV Traction Motor Drive Development Using Thermoelectrics and Film Capacitor Innovations

Principal Investigator: C. W. Ayers
Oak Ridge National Laboratory
National Transportation Research Center
2360 Cherahala Boulevard
Knoxville, TN 37932
Voice: 865-946-1342; Fax: 865-946-1400; E-mail: ayerscw@ornl.gov

DOE Technology Development Manager: Susan A. Rogers
Voice: 202-586-8997; Fax: 202-586-1600; E-mail: Susan.Rogers@ee.doe.gov

ORNL Program Manager: Mitch Olszewski
Voice: 865-946-1350; Fax: 865-946-1262; E-mail: olszewskim@ornl.gov

---

Objectives

The intent of this project is to produce an integrated motor and inverter with special heat transfer paths that promote and improve operation at high power density in a high-temperature environment. It is intended to apply thermoelectric (TE) device innovations to form temperature-controlled islands within the system. These temperature islands will allow high- and low-temperature devices to function side by side, for example, high-temperature silicon carbide (SiC) power electronics in close proximity with silicon electronics and film capacitors.

Silicon-based electronics need their core temperature to be controlled at or below 125ºC, and polypropylene capacitors operate best at or below 85ºC. SiC components are being tested at temperatures above 300ºC, so there is a strong application of the temperature-controlled island concept with this combination of components.

Approach

The first task was to perform literature research on TEs, evaluate what devices were commercially available, and compare different devices to see which devices would be most applicable to our intended applications. It would be important as well to evaluate what new devices are emerging on the market or under development in order to augment or redirect design ideas for an integrated motor and inverter.

Oak Ridge National Laboratory (ORNL) would then procure TE devices that best fit the design ideas, as well as film capacitors, to aid in conceptualizing an integrated motor/inverter traction drive for building and testing the following year.

Major Accomplishments

The TE research that was performed was used to produce a comparison chart of commercially available TE devices. Many manufacturers' products were evaluated, and the data have been pulled together for comparison of costs and capabilities. Informative results were obtained that provide good insight into how the available TEs perform and how some emerging TE technologies are improving performance in some helpful areas.

A motor type was chosen to provide a tangible basis for design concepts and packaging innovations. The design chosen was a commercially available General Electric 5-kW induction motor.

Physical packaging design ideas were introduced and developed. These ideas resulted in the concept of the layered SiC/TE packaging that allows silicon electronics and film capacitors to be packaged closely with the SiC. This idea utilizes TEs to keep the silicon and film capacitors cool while allowing the SiC to operate at much higher ambient temperatures.

The higher operational temperature environment enabled by this technology provides a pathway for the possibility of air cooling the entire traction drive system. The primary problems involved with air cooling a high-power system are the volume required for the system-to-ambient heat sink and the typical high air flow rate. The simplicity of air cooling is an attractive option for traction drives if the volume can be kept to a minimum, and the higher operating temperatures that can be used with SiC power devices promotes reduced volume with reasonable air flow quantities.

Technical Discussion

Thermoelectric Comparison Chart

TEs were researched extensively, looking at ongoing development, commercially available components, and emerging products or near-market technologies. The results of this research are tabulated in a spreadsheet to provide a quick means of comparing sizes, costs, heat flux, etc., for the devices. It was interesting to find that essentially all of the commercially available TE products are produced using bismuth-telluride junctions; the only differences between the products seem to be packaging shapes, thickness, bonding methods, etc. The packaging and bonding methods seem to be where the near-term innovations will be found. These parameters are the controlling factors in TE temperature limitation. Packaging and thickness seem to be the parameters that are being studied and improved to provide better efficiencies for the devices. Heat losses in TE packaging are major contributors to their low coefficient of performance (COP).

See Table 1 for an abbreviated list of manufacturers and key parameters of the TE devices. A more exhaustive list of TE devices presently available on the market is presented in Appendix A.

Emerging TE Devices

Thin film devices are an emerging technology, with products such as the MicroPelt® Peltier Coolers coming onto the market this year. The manufacturing technology for thin film TE devices, based on methods used in the semiconductor industry, produces very small and thin discrete devices. MicroPelt® device thickness is on the order of 0.4 mm. The conventional devices are thicker (such as the Advanced Thermoelectrics devices) and are built up using subcomponents with solder joints connecting the layers together, producing devices that are 2–3 mm thick. The thin film devices ORNL has evaluated are very expensive at first glance, but as a result of a much higher heat flux capability than the conventional bismuth-telluride devices, thicker, the relative price to handle a certain heat load looks much better. When cost is normalized to their ability to remove heat (i.e., dollars per unit of heat flux), the new thin-film devices are actually the cheapest devices on the market. This cost comparison is highlighted in Table 2. If the physical configuration of these can be adapted to match the application, then the thin film devices are a good cost-effective candidate for near-term development of temperature- controlled islands that can be used in our motor and inverter integration concept. With another year or two of maturity, and assuming reasonable manufacturing quantities, the cost of these devices is expected to drop much lower than the present prices.

Motor and Inverter Integration Concepts

The motor chosen earlier this fiscal year was a 5-kW induction motor (General Electric model # 5KE184AC105) that provided an easy platform for procurement, laboratory handling, and measuring/modeling. The motor model developed from this physical motor served as a productive tool for developing the SiC/TE/silicon/film capacitor layering design. It is not necessarily suggested that an induction motor is the motor of choice; this motor was simply chosen for expediency at this stage of the

Table 1. TE device manufacturer comparison data

Advanced Thermoelectrics	ST-127-1.4-6.0	25.00	40.00	40.00	4.20	3.56	71.00	8.48	150.00	$7.86
	ST-127-1.4-8.5	25.00	40.00	40.00	3.95	5.00	72.00	12.66	150.00	$5.60
ADV Engineering	A-TM-8.5-127-1.4	25.00	40.00	40.00	3.70	4.50	72.00	12.16	150.00	
ALTEC	Altec-CM-1-S-IE -127-2.0x2.0-1.15	27.00	40.00	40.00	4.70	9.38	70.00	19.95	150.00	
BHCE	TEC1-16115T125	27.00	40.00	40.00	3.00	11.78	60.00	39.25	150.00	
Custom Thermoelectric	12711-4L31-09RI	50.00	40.00	40.00	3.80	4.69	68.00	12.35	150.00	
Fandis	TM1-1274085	25.00	40.00	40.00	3.40	4.50	71.00	13.24	150.00	
Ferrotec (Thin Film)	9502/065/018MP		11.20	12.10	1.79	5.31	66.00	29.68	135.00	
INB Products	inbDT-1.2	27.00	40.00	40.00	3.60	7.19	69.00	19.97	150.00	$3.90
	inbDT-1.15	27.00	40.00	40.00	3.40	7.50	69.00	22.06	150.00	$3.73
	inbDT-1.05	27.00	40.00	40.00	3.30	8.19	69.00	24.81	150.00	$3.42
	inbDT-0.8	27.00	40.00	40.00	3.20	10.75	69.00	33.59	150.00	$2.60
INTERM	TECB-32-110-(24.7-25-400)-62-69	25.00	62.00	62.00	4.80	10.41	69.00	21.68		
Marlow	DT12-6	27.00	40.00	40.00	4.01	3.38	66.00	8.42	150.00	UA
	DT12-8	27.00	40.00	40.00	3.53	4.44	66.00	12.57	150.00	UA
Melcor	HT8-12-40	25.00	44.00	40.00	3.30	4.09	63.00	12.40	225.00	$5.68
	CP 2-127-10L	25.00	62.00	62.00	5.60	2.01	68.00	3.58	80.00	$20.79
	CP 2-127-06L	25.00	62.00	62.00	4.60	3.12	67.00	6.79	80.00	$12.65
	CP 5-31-06L	25.00	55.00	55.00	4.90	4.13	67.00	8.43	80.00	UA
Micropelt (Thin Film)	MPC-D301-M44	25.00	0.72	0.72	0.43	42.05	22.80	982.53	85.00	$0.88
	MPC-D901-M44	25.00	4.80	4.80	0.43	62.93	21.90	1463.58		
TE Technologies	HT-199-1.4-0.8	27.00	40.00	40.00	3.20	10.75	67.00	33.59	150.00	$2.95
	HT-199-1.4-1.15	27.00	40.00	40.00	3.40	7.50	69.00	22.06	150.00	$3.63
	HT-199-1.4-1.5	27.00	40.00	40.00	3.90	5.88	70.00	15.06	150.00	$4.26
	HP-199-1.4-1.15	25.00	40.00	40.00	3.60	7.50	69.00	20.83	80.00	$2.85
	HP-199-1.4-1.05	25.00	40.00	40.00	3.50	8.19	69.00	23.39	80.00	$3.00

Table 2. TE comparisons showing normalized cost per unit of heat flux

Manufacturer	Qmax W/cm^2	Delta Tmax C	Price/cm^2	Price/(W/cm^2)
Advanced Thermoelectrics	5.00	72.00	$1.24	$5.60
INB Products	10.75	69.00	$1.75	$2.60
Marlow	4.44	66.00	UA	UA
Melcor - (high temperature series)	4.09	63.00	$1.32	$5.68
Micropelt (Thin Film)	60.00	31.90	$3,495.84	$0.62
TE Technologies (high temperature series)	10.75	67.00	$1.98	$2.95
Tellurex	4.09	79.00	$1.22	$5.26

conceptual development (better availability, easier handling and testing, etc.). Permanent magnet motors are an equally acceptable candidate for this concept and are typically the preferred traction motor in most HEV developments. Scalability of the concept is not expected to be an issue when designing for larger motors (50- to 100-kW capacity).

The primary concept was developed based on the motor platform, film capacitor shaping, and TE in an attempt to provide very tight integration of the inverter into the motor. Figure 1 shows a cutaway isometric view of the motor concept. This motor concept is based on SiC power electronics and an air-

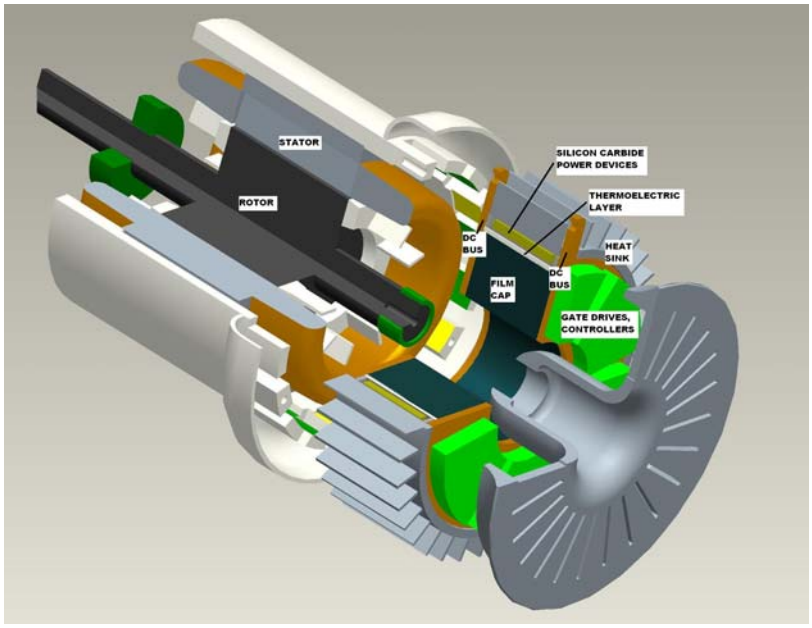


Figure 1. Cutaway view of integrated motor and inverter utilizing silicon carbide power electronics, thermoelectric temperature boundaries, silicon electronics and film capacitors.

cooled motor and inverter housing. The inverter is attached to the end of the motor casing. Although packaging the inverter into the end of the motor is not necessarily a new idea, the TE application enables much tighter packaging than before and promotes air cooling through the use of high-temperature SiC.

Figure 2 shows a view of the power electronics section of the motor concept design. This proposed arrangement shows heat flow paths from the various components in the system, in which the components that need to remain cooler are embedded in and surrounded by the warmer motor environment. The white band wrapped around the lower side of the SiC power electronics (yellow) represents the TE temperature control boundary that protects the silicon and film capacitor from the very hot SiC. The lower perimeter of these components is protected from the warmer motor environment using passive insulation techniques. The reason that passive insulation is not used on the top perimeter of these components is the need to promote heat flow up and out of their core (i.e., the "cool zone"); in other words, the capacitor and control electronics produce some minimal heat. The heat removal for the capacitor and controls can only be accomplished with a heat pumping action (TEs) to draw the heat from this area and remove it through the hotter zone.

There can be several arrangements of electronics in this situation, and this is one embodiment of the concept. The main point to be made is that as integration increases, there is an increased likelihood that components with incompatible heat capacities will be adjacent to each other. This method of integration requires a small amount of power, but it can potentially greatly increase the power density of the traction drive while simultaneously enabling air cooling for the whole system.

The simplicity of air cooling is a desirable characteristic for vehicle traction drive cooling because it offers a continuously available low-temperature source, no problem with leaks, and no need for pumps or piping (probably only a fan and some ducting would be required). Although heat sink volume will continue to be the critical issue, an air-cooling method would allow simplification of the system and reduction of active components and weight.

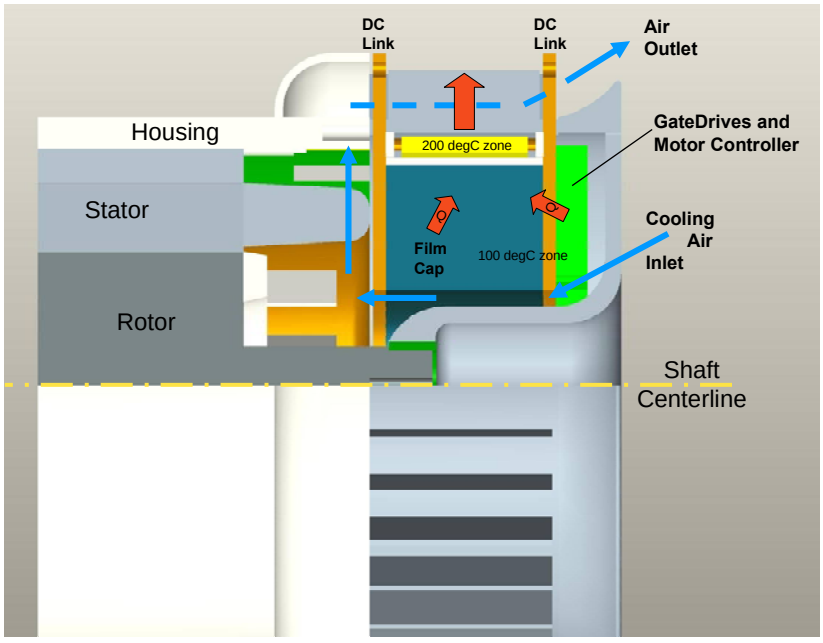


Figure 2. Motor concept section view showing detail of component arrangement and proposed heat flow path.

Thermal Mechanical Modeling of the Concept

ORNL has performed some basic thermal modeling to validate several ideas:

- show air-cooling viability for the integrated package
- show feasibility of use of TEs in relation to system COP
- evaluate temperature profiles throughout the layers to indicate if the packaging/layering concept allows reasonable temperatures in the cold zone and at the TE interfaces

Mechanical models developed with ProEngineer Wildfire software have been thermally analyzed using ProEngineer Mechanica finite element software. Figure 3 shows the mechanical model produced in Wildfire, exploded and labeled to show the subcomponents of the assembly. The primary subcomponents, starting at the bottom of the assembly, are (1) the cold-zone components (silicon-based gate drivers, digital signal processor controller, and film capacitor), (2) the thermoelectric device layer, and (3) the SiC power electronics devices. This design was modeled using the specific material properties for each layer or component, and the heat generated in each section was calculated and input into the software. Using data acquired from research on the TE devices, power consumption for the TE boundary layer was calculated and used as input into the thermal model (i.e., the losses that are incurred in the TE devices as a result of their inefficiencies). Also, based on TE research, it was established that the TE boundary layer can maintain certain temperature differences at corresponding heat flux values. Based on these findings, temperature boundary constraints were established for the upper and lower surfaces of the TE boundary. The TE device itself was not modeled in detail but is basically assumed to control upper and lower surface temperature, generate a certain amount of internal heat, and provide a conduit for the heat flux coming from the lower components.

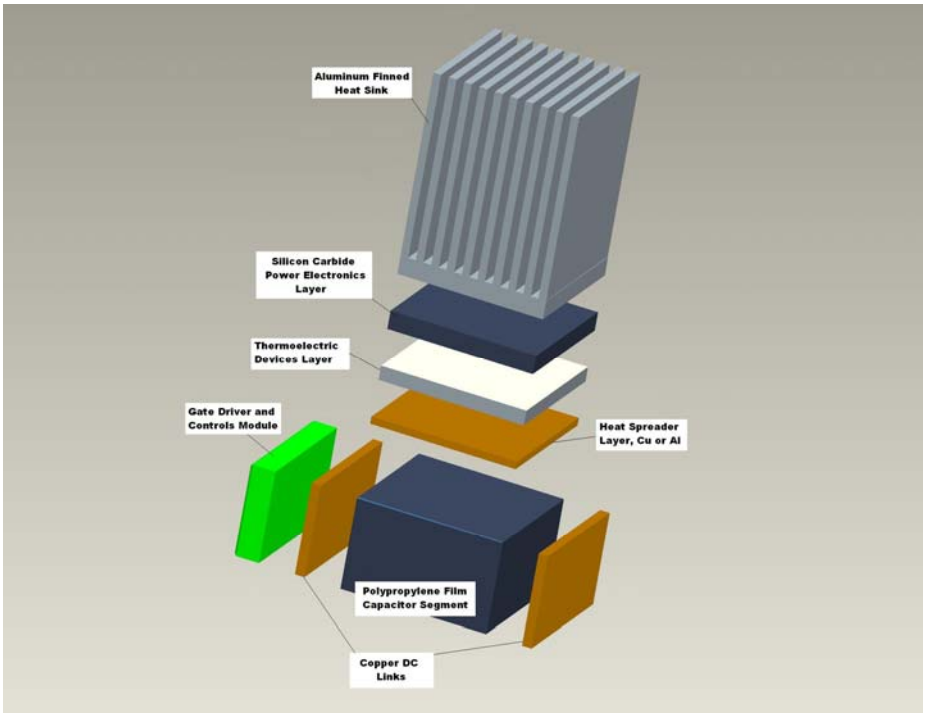


Figure 3. Exploded view of ProEngineer mechanical model used to analyze the thermal performance of the ORNL SiC-TE motor/inverter integration concept.

The model constraints and assumptions are listed in Table 3. Volumetric heat generation values were calculated for potted-module style components such as gate drivers, digital signal processors, and SiC power sections, based on estimated heat losses and their approximate sizes and shapes. The modeling was performed in three stages with two simplified models of upper and lower sections and a third model as an entire cross-section of the concept. This was done to provide a validation of how the TE device interacts with the system without having to actually model the internal conditions of the TE itself—in other words, to treat the TE as a black box.

Table 3. Thermal model calculations and assumptions

Subcomponent description	Constraint	Material
Gate drive and controller module	280,000 W/m^3	Thermal potting mixture
Film capacitor	5,000 W/m^3	Polypropylene
Silicon carbide power electronics	750,000 W/m^3	Thermal potting mixture
TE boundary layer	5.2 W	Ceramic (approximation)
TE cold surface	100°C	—
TE hot surface	200°C	—
Ambient temperature	120°C	—
Heat transfer coefficient	100 W/m^{2}K	—
DC links	—	Copper

The first thermal model (shown in Figure 4) is made up of the cold zone components, configured in the way the laboratory model was designed, and is used to evaluate heat flows and temperature distribution in the lower section. The copper dc links for the inverter design make up two sides of the model, sandwiching the film capacitor block in between. This design places the electronics, that is, digital

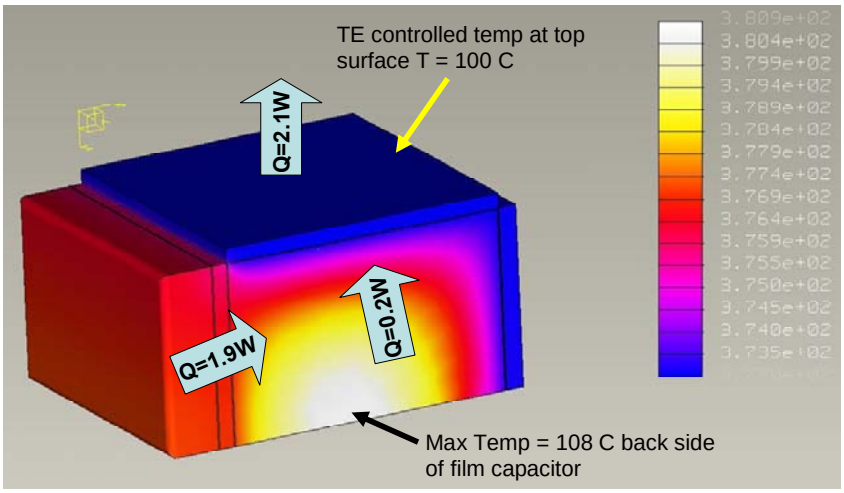


Figure 4. First model analyzed showing the "cold zone" heat flows—the top layer (just a copper heat spreader) interfaces with the rest of the system through the TE layer (not in this model). The silicon electronics are shown on the lower left and the film capacitor cross-section is the major component in the lower middle portion. This model shows temperature distribution for these estimated heat flows.

signal processor controller and gate drivers, on the outside of one of the dc links (left side). Heat in this zone is generated in the silicon electronics section (about 1.9 W) and in the film capacitor (lower middle, about 0.2 W). The constraints in this model consist of insulation all around the unit, except on the top surface, which removes a total heat flux of 2.1 W (up through the TE "black box" device, next layer). The specifications for these subcomponents can be found in Table 3. The TE device is not needed in this model and is omitted to keep the analysis simple.

The second model seen in Figure 5 was developed to look at heat flow and temperature for the upper or "hot zone" components. This unit includes the SiC power device module and a finned heat sink to transfer heat to the ambient air. The constraints for this model consist of (1) heat flux entering the bottom surface (lower section's heat plus TE device losses) of 7.3 W, (2) SiC module losses of 7.1 W, and (3) insulation all around except for the finned heat sink surfaces. The heat sink surfaces are given a heat transfer coefficient of 100 W/m^{2}K; for a fourth condition, the ambient air temperature is set at 120°C for these analyses. The TE device is not included in this model segment for simplicity.

The third model (Figure 6) represents the entire cross-section of the SiC/silicon/film cap layering concept. The TE device is included in this model, but is represented by a "black box" with boundary constraints. Except for the addition of the TE device, this model is basically made up of Model 1 and Model 2. The boundary constraints for these two models are included as required with the addition of the TE device. The results from this thermal model closely match the results from the first two models, in temperature distribution and maximum temperatures seen at critical parts of the system, and these results provide good validation for the total system model. In future work, this model can be used to perform "what-if" cases for different designs or other concepts.

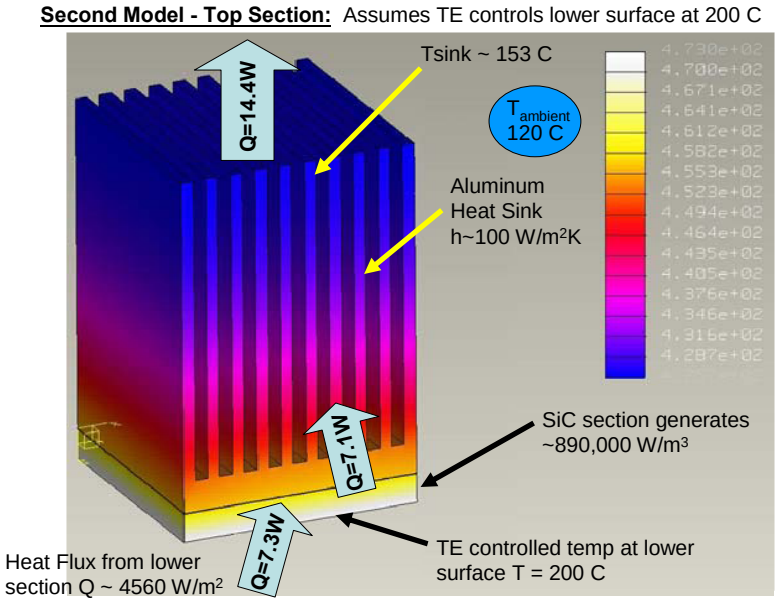


Figure 5. Second model showing the "hot zone" heat flows. The lower surface (SiC section) rests on top of the TE device. The heat from the SiC and the lower section moves upward to the heat sink and then to ambient. This model shows the temperature distribution for the upper section using the heat generated in the SiC and the heat flux from the lower section (Model 1).

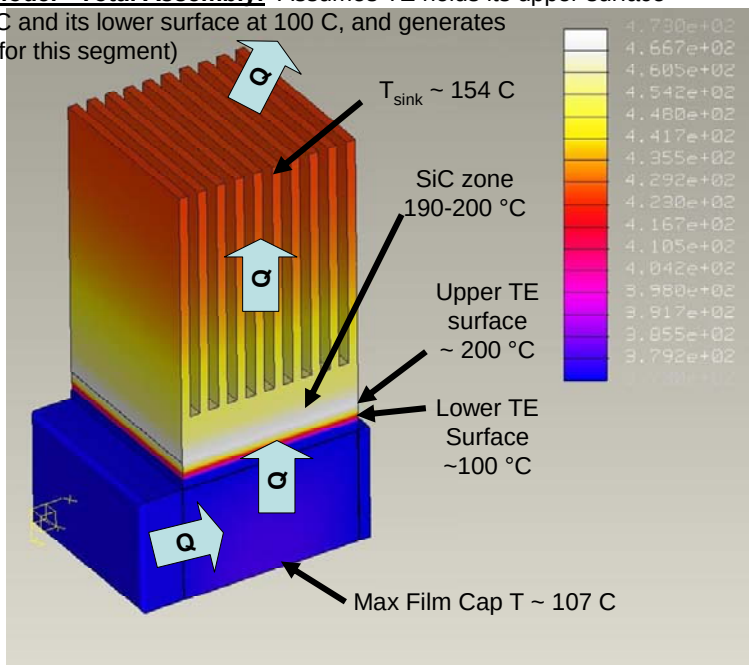


Figure 6. This third model shows the whole assembly where Model 1 and Model 2 structures are basically joined together using the TE boundary layer. This more complex model (with assumptions about the TE boundary layer) is validated by observing the temperature profile and seeing a close match with the system temperatures in Models 1 and 2.

TEs in general are found to have a relatively low heat flux carrying capability and in single layers have a limited temperature rise/drop capability across their boundaries. The low heat flux (i.e., ~5–10 W/cm^2) capability makes them unsuitable for use directly to remove heat from conventional power electronics, which require on the order of 50–100 W/cm^2 in conventional inverter designs. It was originally desired to produce a concept where power electronics were cooled directly as needed in a high-integration design, but the heat flux numbers proved to be too small for this idea. Thin film TE devices are rapidly approaching the required heat flux numbers, however, and in the near future may be suitable to be incorporated into various applications of direct power electronics high flux cooling with reasonable efficiencies.

This understanding of TE heat flux limitations influenced the design ideas that were evaluated during this project The main result of that has been the development of the concept of temperature-controlled islands that allow silicon electronics and film capacitors to be used in close proximity with SiC power electronics. In this design scenario, the SiC power electronics can be allowed to operate at much higher than conventional temperatures (>200ºC), which makes the use of air cooling much more viable (reasonable heat sink size would then be possible). What limits the use of high-temperature SiC in a tightly integrated motor drive is the relatively low-temperature environment required for the silicon control electronics and dc filtering capacitors. These devices need an environment much closer to 80–90ºC. Figure 7 depicts a basic layout of the integration concept and shows how the TE layers provide a lower-temperature island to protect the silicon and film capacitor. This lower-temperature island allows

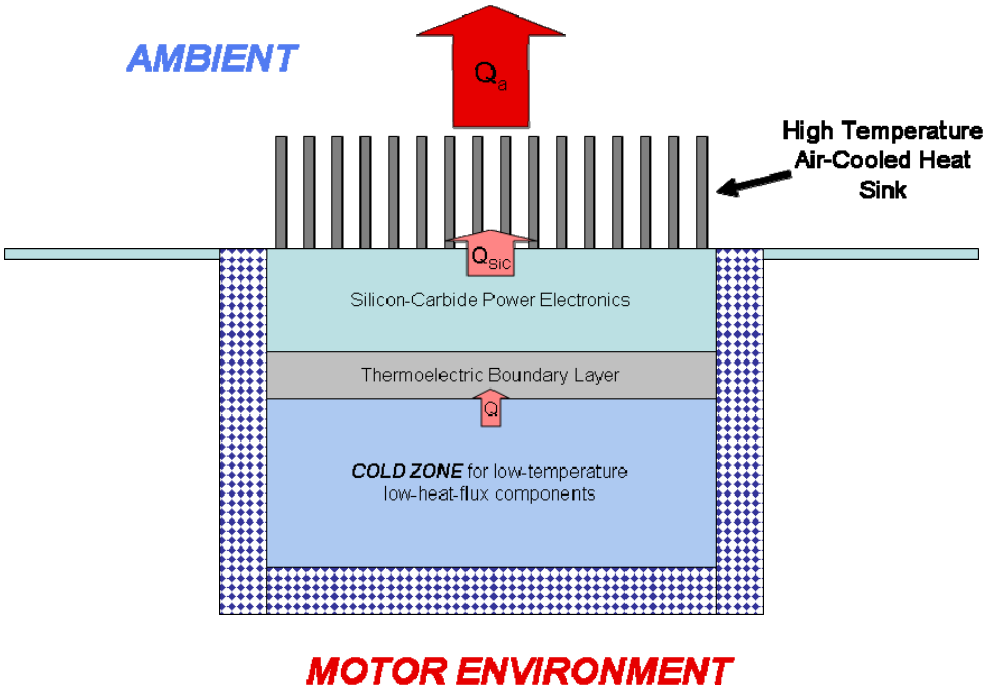


Figure 7. Cold zone produced by TE layer. Cold zone components are protected from high-temperature SiC and motor zones by the heat pumping action of the TEs.

for improved reliability, better utilization of the silicon and much reduced volume/weight for the film capacitor.

Although the heat flux is low, the internal heat must be removed from the silicon electronics and film capacitor(s). Otherwise, the internal temperature of these components will rise to excessive levels and result in failure. This packaging concept requires that this heat energy be transferred out to the ambient zone by traveling through a higher-temperature zone. Because this is against the natural flow of heat, the TEs are used to provide a heat pumping action to remove the energy from the cold zone (80–90°C) out through the hot zone (>200°C).

Thermoelectric Performance and Multilayer Benefits Modeling:

Because of the high heat flux capabilities of the Micropelt TE devices and the project initiative to perform analysis on the most advanced thermoelectric technology, a model of this device was constructed using Matlab. The model is based on data provided by the manufacturer specifications and consists of analysis of the cooling capability of the device in relation to temperature and input current. This provides a COP relationship to temperature and cooling capability per TE device.

The requirements to maintain the silicon control devices and dc filtering capacitors at or below 100ºC and to allow the SiC to reach temperatures exceeding 150ºC produce temperature gradients in excess of 50ºC. This condition necessitated the use of a multilayer strategy as seen in Figure 8. Using the model developed in Matlab and combining the concept of layering, the maximum obtainable COP was determined for each load based on a particular temperature difference and a number of layers.

The analysis conducted with the Matlab model revealed that an increase in the maximum temperature difference and COP could be obtained with increased layers as seen in Figure 9. There seems to be a

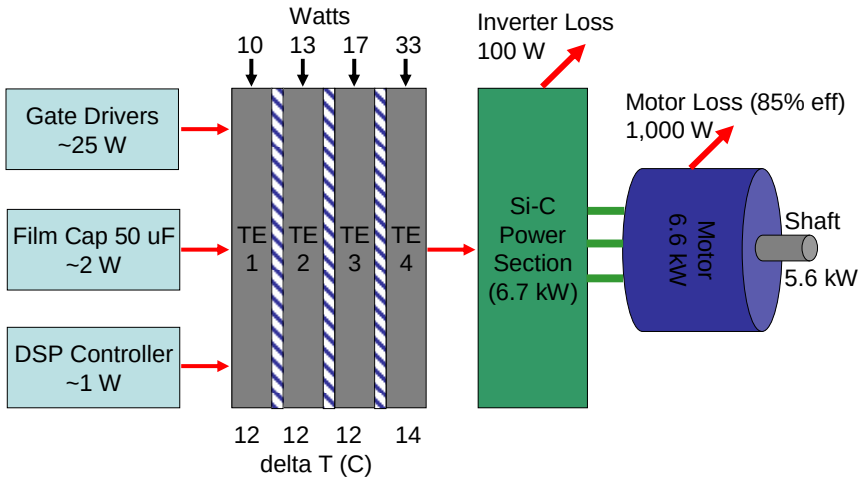


Figure 8. Power flow schematic in the SiC/TE/silicon/film capacitor integration concept.

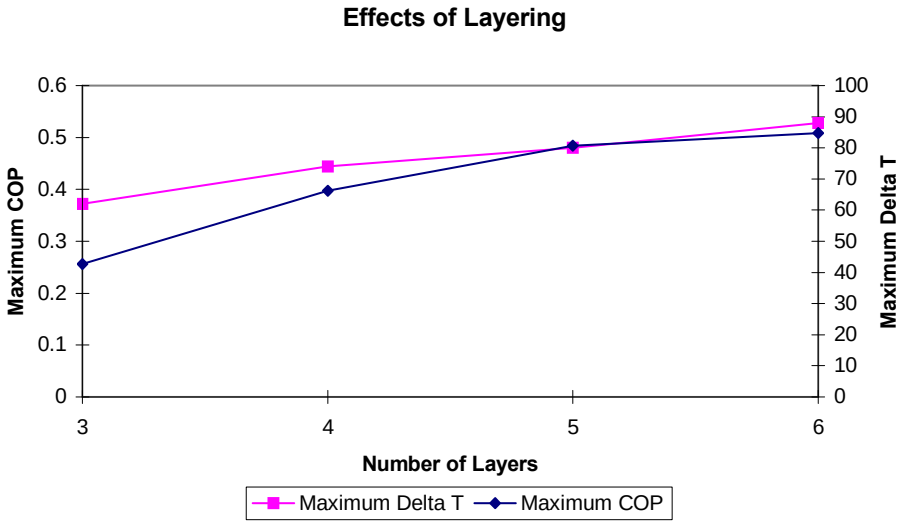


Figure 9. The effect of layering on maximum temperature difference.

diminishing return on increasing the number of layers, as seen in Figure 9, but we have limited data at this point. Continued research must be done to fully understand this phenomenon. If this is a real phenomenon, it would be of great interest to determine what part of the system causes this drop in COP/layer as the number of layers increases. Understanding this effect could direct future research and development for TE devices.

To make use of this data, a value for the heat load was necessary. For the motor assembly developed, the heat load stems from the gate drivers, dc filter capacitor, and digital signal processor controller. The gate drivers were estimated to produce a maximum of 4 W each or a total of 24 W. The DSP controller from manufacturer specifications produces a maximum of approximately 1W. The capacitor heat load is a more difficult estimate and was determined through a voltage-power factor matrix provided in Table 4. For this matrix, a 6.6-kW motor is assumed, and the inverter is expected to be operating in full-over modulation. The capacitor expected to be used in the motor assembly has a capacitance of 500 μF and an ESR of 0.0031 at 10 kHz. From this table, the maximum heat load is approximately 2 W.

From these calculations, the final heat flux is expected to be extremely low with less than 1-W/cm^2 cooling requirements. Using this heat flux number and varying the temperature gradient, Table 5 was created. This table demonstrates the COP in terms of the number of layers and temperature difference.

Table 4. Capacitor power dissipation (W) due to voltage and power factor effects

	PF								
Voltage	**0.6**	**0.65**	**0.7**	**0.75**	**0.8**	**0.85**	**0.9**	**0.95**	**1**
130	0.193	0.296	0.685	0.998	1.254	1.466	1.644	1.795	1.923
150	0.145	0.223	0.514	0.749	0.942	1.101	1.235	1.348	1.445
170	0.113	0.173	0.400	0.583	0.733	0.857	0.961	1.050	1.125
190	0.090	0.139	0.320	0.467	0.587	0.686	0.770	0.840	0.900
210	0.074	0.114	0.262	0.382	0.481	0.562	0.630	0.688	0.737
230	0.062	0.095	0.219	0.319	0.401	0.468	0.525	0.573	0.614
250	0.052	0.080	0.185	0.270	0.339	0.396	0.445	0.485	0.520
270	0.045	0.069	0.159	0.231	0.291	0.340	0.381	0.416	0.446
290	0.039	0.060	0.138	0.200	0.252	0.295	0.330	0.361	0.387
310	0.034	0.052	0.120	0.175	0.221	0.258	0.289	0.316	0.338
330	0.030	0.046	0.106	0.155	0.195	0.228	0.255	0.279	0.298
350	0.027	0.041	0.094	0.138	0.173	0.202	0.227	0.248	0.265
370	0.024	0.037	0.085	0.123	0.155	0.181	0.203	0.222	0.237
390	0.021	0.033	0.076	0.111	0.139	0.163	0.183	0.199	0.214
410	0.019	0.030	0.069	0.100	0.126	0.147	0.165	0.180	0.193
430	0.018	0.027	0.063	0.091	0.115	0.134	0.150	0.164	0.176
450	0.016	0.025	0.057	0.083	0.105	0.122	0.137	0.150	0.161
470	0.015	0.023	0.052	0.076	0.096	0.112	0.126	0.137	0.147
490	0.014	0.021	0.048	0.070	0.088	0.103	0.116	0.126	0.135
510	0.013	0.019	0.044	0.065	0.081	0.095	0.107	0.117	0.125
530	0.012	0.018	0.041	0.060	0.075	0.088	0.099	0.108	0.116
550	0.011	0.017	0.038	0.056	0.070	0.082	0.092	0.100	0.107
570	0.010	0.015	0.036	0.052	0.065	0.076	0.086	0.093	0.100
590	0.009	0.014	0.033	0.048	0.061	0.071	0.080	0.087	0.093
610	0.009	0.013	0.031	0.045	0.057	0.067	0.075	0.082	0.087

Table 5. COP in terms of number of layers and temperature gradient

		Layers		
Temperature	3 layers	4 layers	5 layers	6 layers
50	0.049	0.075		0.111
60	0.023	0.043		0.07
70	X	0.022		0.044
80	X	X		
88	X	X	X	0.0154

Conclusions

Tighter integration of conventional electronics into a SiC based motor/traction drive, which creates thermal compatibility problems, can be aided by embedding TE layers strategically into the package. Combining SiC power electronics with conventional silicon controls and polypropylene film dc link capacitors, utilizing TE thermal control "islands," enables air cooling of the entire traction drive. The viability of air cooling is further enhanced when this concept is used in combination with higher temperature motor windings and advanced magnets.

Research indicates presently available TE maximum temperature rating/gradient and maximum heat flux are a little low. Emerging devices show great promise to make this concept highly attractive, so the project has been put on hold for the following year to evaluate these devices as they become available. Thin film Te cost on the surface appears very high, but their ability to produce high heat flux at a reasonable delta T brings the relative cost down lower than conventional TEs that do not perform as well.

Future Direction

When the project resumes, prototype models need to be built to validate the information that is being seen in the models. Further modeling needs to be performed to evaluate the entire traction drive heat removal system. Data from these models will indicate viability of air cooling of the whole system including motor/gears, SiC power electronics, silicon controls, and the dc link film capacitor.

When the technology of thin film TEs matures to a greater degree, ORNL will pursue further development of this or similar system concepts, possibly in partnership with a company such as MicroPelt®. Their work in the area of thin film devices looks very promising for the next year.

The need is to produce a geometry suitable for integration into the SiC/TE/silicon/film capacitor, using an array of devices in a flexible/conformable substrate. Multiple layering of the devices can be achieved by a coiled TE layer wrapped around the capacitor and electronics core, which can be made with a flexible circuit board containing thin film TE devices.

Three Areas of Particular Interest as TEs Mature

1. Maximum temperature limitations presently are approximately 80–150ºC. This temperature needs to approach 200ºC and higher to make this concept most feasible.
2. Heat flux numbers with good delta T need to improve above the present ~10 W/cm^2 at a few degrees C delta T. The multiple layering concept helps mitigate the problem with limited delta T, but higher numbers are still needed such that a maximum of 2–3 layers can produce a total delta T of ~150–200ºC.
3. Efficiency of the devices needs to improve. Thin film technology appears to be improving the COP of the TE device. This is definitely of interest and will benefit this concept, but it is not a critical path for this type of motor/inverter integration.

Publications

M. Starke, "Thermoelectrics for Cooling Power Electronics," Masters Thesis, University of Tennessee, August 2006

Patents

"Motor and Inverter Drive Design Concept Integrating Silicon Carbide Power Devices with Silicon Controls and Capacitors Utilizing Thermoelectrics," provisional patent filed July 8, 2006, with the U.S. Patent and Trademark Office.

References

1. J. Vandersande and J. Fleurial, "Thermal Management of Power Electronics using Thermoelectric Coolers," pp. 253–255 in *15th International Thermoelectrics Conference, March 1996*.
2. D. M. Rowe, *CRC Handbook of Thermoelectrics*, G. S. Nolas, J. Sharp, H. J. Goldsmid, *Thermoelectrics: Basic Principles and New Materials Developments*, Springer-Verlag Berlin Heidelberg, 2001.
3. G. W. Sutton, *Direct Energy Conversion*, McGraw-Hill, 1966.
4. D. T. Morelli, "Potential Applications of Advanced Thermoelectrics in the Automobile Industry," pp. 383–386 in *15th International Conference on Thermoelectrics, March 1996*.
5. G. Min, D. M. Rowe, and F. Volklein, "Integrated Thin Film Thermoelectric Cooler," *Electronics Letters*, **34**, p. 222–223 (January 1998).
6. H. Bottner, "Micropelt Miniaturized Thermoelectric Devices: Small Size, High Cooling Power Densities, Short Response Time," pp. 1–8 in *24th International Conference on Thermoelectrics, June 2005*.
7. H. Bottner, J. Nurnus, M. Braun, J. Wollenstein, F. Volkert, and A. Schubert, "Micropelt: State of the Art, Road Map and Applications," Infineon Technologies AG, München, Germany, 2004.
8. http://www.illinoiscapacitor.com/techcenter/lifecalculators.asp, Illinois Capacitor, Inc., 2006.
9. A. M. Hava, R. J. Kerkman, and T. A. Lipo, "Simple Analytical and Graphical Methods for Carrier-Based PWM-VSI Drives," *IEEE Transactions on Power Electronics*, **14**(1), 49–61 (January 1999).

Appendix A. Thermoelectric Device Manufacturer Comparison Data

MANUFACTURERS

Manufacturer	Product	Operating Th C	Dimensions L mm	W mm	H mm	Qmax W/cm^2	Delta Tmax C	Power Density kW/L	Max Operating Th	Price/W/cm^2
3 Stone Company	TES1-0401A	25.00	3.40	1.80	2.40	3.59	67.00	14.98		$2.23
(Hong Kong)	TES1-0801A	25.00	3.40	3.40	2.40	3.72	67.00	15.50		$2.29
	TES1-1201A	25.00	5.00	3.40	2.40	3.82	67.00	15.93		$2.35
	TES1-1801A	25.00	5.00	5.00	2.40	3.88	67.00	16.17		$2.84
	TES1-3201A	25.00	6.60	6.60	2.40	3.95	67.00	16.45		$3.04
	TES1-0401B	25.00	4.20	2.20	2.70	3.46	67.00	12.83		$2.31
	TES1-0801B	25.00	4.20	4.20	2.70	3.68	67.00	13.65		$2.31
	TES1-1201B	25.00	6.20	4.20	2.70	3.73	67.00	13.80		$2.42
	TES1-1801B	25.00	6.20	6.20	2.70	3.80	67.00	14.07		$2.90
	TES1-3201B	25.00	8.30	8.30	2.70	3.76	67.00	13.92		$3.19
	TES1-0401C	25.00	2.20	4.20	2.40	4.33	67.00	18.04		$1.85
	TES1-0801C	25.00	4.20	4.20	2.40	4.59	67.00	19.13		$1.85
	TES1-1201C	25.00	4.20	6.20	2.40	4.65	67.00	19.36		$1.94
	TES1-1801C	25.00	6.20	6.20	2.40	4.73	67.00	19.73		$2.32
	TES1-3201C	25.00	8.30	8.30	2.40	4.69	67.00	19.54		$2.56
	TES1-0402D	25.00	2.20	4.20	2.20	5.84	67.00	26.56		$1.37
	TES1-0802D	25.00	4.23	4.20	2.20	6.08	67.00	27.63		$1.40
	TES1-1202D	25.00	4.20	6.20	2.20	6.18	67.00	28.10		$1.46
	TES1-1802D	25.00	6.20	6.20	2.20	6.32	67.00	28.73		$1.74
	TES1-3202D	25.00	8.30	8.30	2.20	6.27	67.00	28.50		$1.91
	TES1-0401E	25.00	1.80	3.40	2.40	3.59	67.00	14.98		$2.23
	TES1-0801E	25.00	3.40	3.40	2.40	3.72	67.00	15.50		$2.29
	TES1-1201E	25.00	3.40	5.00	2.40	3.82	67.00	15.93		$2.35
	TES1-1801E	25.00	5.00	5.00	2.40	3.88	67.00	16.17		$2.84
	TES1-3201E	25.00	6.60	6.60	2.40	3.95	67.00	16.45		$3.04
	TES1-0401F	25.00	2.20	4.20	2.70	3.46	67.00	12.83		$2.31
	TES1-0801F	25.00	4.20	4.20	2.70	3.68	67.00	13.65		$2.31
	TES1-1201F	25.00	4.20	6.20	2.70	3.73	67.00	13.80		$2.42
	TES1-1801F	25.00	6.20	6.20	2.70	3.80	67.00	14.07		$2.90
	TES1-3201F	25.00	8.30	8.30	2.70	3.76	67.00	13.92		$3.19
	TES1-0401G	25.00	2.20	4.20	2.40	4.33	67.00	18.04		$1.85
	TES1-0801G	25.00	4.20	4.20	2.40	4.59	67.00	19.13		$1.85
	TES1-1201G	25.00	4.20	6.20	2.40	4.65	67.00	19.36		$1.94
	TES1-1801G	25.00	6.20	6.20	2.40	4.73	67.00	19.73		$2.32
	TES1-3201G	25.00	8.30	8.30	2.40	4.69	67.00	19.54		$2.56
	TES1-0402H	25.00	2.20	4.20	2.20	5.84	67.00	26.56		$1.37
	TES1-0802H	25.00	4.20	4.20	2.20	6.12	67.00	27.83		$1.39
	TES1-1202H	25.00	4.20	6.20	2.20	6.18	67.00	28.10		$1.46
	TES1-1802H	25.00	6.20	6.20	2.20	6.32	67.00	28.73		$1.74
	TES1-3202H	25.00	8.30	8.30	2.20	6.27	67.00	28.50		$1.91
	TES1-3602H	25.00	6.60	13.20	2.20	4.13	67.00	18.78		
	TES1-0701I	25.00	1.80	3.40	2.40	6.21	67.00	25.87		$1.37
	TES1-1101I	25.00	3.40	5.00	2.40	3.53	67.00	14.71		$2.55
	TES1-1701I	25.00	3.40	5.00	2.40	5.41	67.00	22.55		$2.03
	TES1-3101I	25.00	5.00	6.60	2.40	5.06	67.00	21.09		$2.37
	TES1-0701J	25.00	4.20	4.20	2.40	3.23	67.00	13.46		$2.63
	TES1-1101J	25.00	4.20	6.20	2.70	3.42	67.00	12.66		$2.63
	TES1-1701J	25.00	6.20	6.20	2.70	3.56	67.00	13.20		$3.09
	TES1-3101J	25.00	8.30	8.30	2.70	3.64	67.00	13.49		$3.29
	TES1-0701K	25.00	4.20	4.20	2.70	4.02	67.00	14.91		$2.11
	TES1-1101K	25.00	4.20	6.20	2.70	4.26	67.00	15.79		$2.11
	TES1-1701K	25.00	6.20	6.20	2.40	4.47	67.00	18.64		$2.46
	TES1-3101K	25.00	8.30	8.30	2.40	4.54	67.00	18.93		$2.64
	TES1-0702L	25.00	4.20	4.20	2.20	5.39	67.00	24.48		$1.58
	TES1-1102L	25.00	6.20	6.20	2.20	3.88	67.00	17.62		$2.32
	TES1-1702L	25.00	6.20	6.20	2.20	5.98	67.00	27.20		$1.84
	TES1-1702L	25.00	6.60	6.60	2.20	5.99	67.00	27.24		$1.84
	TES1-3102L	25.00	8.30	8.30	2.20	6.07	67.00	27.58		$1.98
	TES1-0702M	25.00	6.00	6.00	3.40	2.78	67.00	8.17		$2.34
	TES1-1702M	25.00	12.00	9.00	3.40	2.22	67.00	6.54		$3.60
	TES1-3102M	25.00	12.00	12.00	3.40	3.06	67.00	8.99		$2.78
	TES1-6302M	25.00	18.00	25.00	3.40	2.00	67.00	5.88		$5.00
	TES1-7102M	25.00	8.00	18.00	3.40	7.01	67.00	20.63		$1.43

	TES1-0702N	25.00	12.00	8.00	4.00	1.25	67.00	3.13		$4.80
	TES1-1702N	25.00	15.00	12.00	4.00	1.61	67.00	4.03		$4.03
	TES1-3102N	25.00	20.00	15.00	4.00	1.77	67.00	4.42		$3.68
	TES1-4902N	25.00	20.00	20.00	4.00	1.98	67.00	4.94		$4.05
Advanced Thermoelectric	ST-71-1.0-3.0	25.00	22.40	22.40	3.20	3.14	71.00	9.81	150.00	$5.22
	ST-127-1.0-3.0	25.00	30.00	30.00	3.95	3.11	71.00	7.88	150.00	$5.32
	ST-71-1.0-4.0	25.00	22.40	22.40	4.20	3.85	71.00	9.16	150.00	$4.32
	ST-127-1.0-4.0	25.00	30.00	30.00	3.95	4.22	72.00	10.69	150.00	$3.97
	ST-127-1.4-4.0	25.00	40.00	40.00	4.20	2.38	72.00	5.65	150.00	$7.63
	ST-71-1.4-6.0	25.00	30.00	30.00	4.20	3.56	72.00	8.47	150.00	$4.73
	ST-127-1.4-6.0	25.00	40.00	40.00	4.20	3.56	71.00	8.48	150.00	$5.26
	ST-71-1.4-8.5	25.00	30.00	30.00	3.95	5.00	72.00	12.66	150.00	$3.52
	ST-127-1.4-8.5	25.00	40.00	40.00	3.95	5.00	72.00	12.66	150.00	$3.96
ADV Engineering	A-TM 8.5-127-1.4		40.00	40.00	3.70	4.50	72.00	12.16	150.00	
(Russia)	A-TM 6.0-127-1.4		40.00	40.00	4.20	3.31	72.00	7.89	150.00	
	A-TM 3.9-127-1.4		40.00	40.00	5.10	3.31	73.00	6.50	150.00	
	A-TM 3.9-127-1.0		30.00	30.00	3.90	3.78	71.00	9.69	150.00	
	A-TM 37.5-49-3.0		40.00	40.00	4.30	8.13	71.00	18.90	150.00	
	A-TM 6.0-31-1.4		20.00	20.00	4.20	3.13	72.00	7.44	150.00	
Altec	Altec-CM-1-S-SQ-7-0.8x0.8-2.5		6.00	6.00	4.40	1.67	72.00	3.79	200.00	
(Ukraine)	Altec-CM-1-S-SQ-17-0.8x0.8-2.5		9.00	9.00	44.00	1.85	72.00	0.42	200.00	
	Altec-CM-1-S-SQ-31-0.8x0.8-2.5		12.00	12.00	4.40	1.88	72.00	4.26	200.00	
	Altec-CM-1-S-SQ-63-0.8x0.8-2.5		12.00	24.00	4.40	1.88	72.00	4.26	200.00	
	Altec-CM-1-S-SQ-71-0.8x0.8-2.5		18.00	18.00	4.40	1.88	72.00	4.28	200.00	
	Altec-CM-1-S-SQ-127-0.8x0.8-2.5		24.00	24.00	4.40	1.91	72.00	4.34	200.00	
	Altec-CM-1-S-SQ-7-0.8x0.8-2.0		6.00	6.00	3.90	1.94	71.00	4.99	200.00	
	Altec-CM-1-S-SQ-17-0.8x0.8-2.0		9.00	9.00	3.90	2.22	71.00	5.70	200.00	
	Altec-CM-1-S-SQ-31-0.8x0.8-2.0		12.00	12.00	3.90	2.29	71.00	5.88	200.00	
	Altec-CM-1-S-SQ-63-0.8x0.8-2.0		12.00	24.00	3.90	2.33	71.00	5.97	200.00	
	Altec-CM-1-S-SQ-71-0.8x0.8-2.0		18.00	18.00	3.90	2.35	71.00	6.01	200.00	
	Altec-CM-1-S-SQ-127-0.8x0.8-2.0		24.00	24.00	3.90	2.34	71.00	6.01	200.00	
	Altec-CM-1-S-SQ-7-0.8x0.8-1.5		6.00	6.00	3.40	2.78	70.00	8.17	200.00	
	Altec-CM-1-S-SQ-17-0.8x0.8-1.5		9.00	9.00	3.40	2.96	70.00	8.71	200.00	
	Altec-CM-1-S-SQ-31-0.8x0.8-1.5		12.00	12.00	3.40	2.99	70.00	8.78	200.00	
	Altec-CM-1-S-SQ-63-0.8x0.8-1.5		12.00	24.00	3.40	3.06	70.00	8.99	200.00	
	Altec-CM-1-S-SQ-71-0.8x0.8-1.5		18.00	48.00	3.40	1.16	70.00	3.40	200.00	
	Altec-CM-1-S-SQ-127-0.8x0.8-1.5		24.00	24.00	3.40	3.09	70.00	9.09	200.00	
	Altec-CM-1-S-SQ-7-0.8x0.8-1.3		6.00	6.00	3.20	3.06	69.00	9.55	200.00	
	Altec-CM-1-S-SQ-17-0.8x0.8-1.3		9.00	9.00	3.20	3.33	69.00	10.42	200.00	
	Altec-CM-1-S-SQ-31-0.8x0.8-1.3		12.00	12.00	3.20	3.40	69.00	10.63	200.00	
	Altec-CM-1-S-SQ-63-0.8x0.8-1.3		12.00	24.00	3.20	3.47	69.00	10.85	200.00	
	Altec-CM-1-S-SQ-71-0.8x0.8-1.3		18.00	18.00	3.20	3.49	69.00	10.90	200.00	
	Altec-CM-1-S-SQ-127-0.8x0.8-1.3		24.00	24.00	3.20	3.51	69.00	10.96	200.00	
	Altec-CM-1-S-SQ-7-0.8x0.8-1.15		6.00	6.00	3.10	3.61	68.00	11.65	200.00	
	Altec-CM-1-S-SQ-17-0.8x0.8-1.15		9.00	9.00	3.10	3.70	68.00	11.95	200.00	
	Altec-CM-1-S-SQ-31-0.8x0.8-1.15		12.00	12.00	3.10	3.82	68.00	12.32	200.00	
	Altec-CM-1-S-SQ-63-0.8x0.8-1.15		12.00	24.00	3.10	3.89	68.00	12.54	200.00	
	Altec-CM-1-S-SQ-71-0.8x0.8-1.15		18.00	18.00	3.10	3.89	68.00	12.54	200.00	
	Altec-CM-1-S-SQ-127-0.8x0.8-1.15		24.00	24.00	3.10	3.91	68.00	12.60	200.00	
	Altec-CM-1-S-SQ-7-1.0x1.0-2.5		8.00	8.00	4.50	1.41	72.00	3.13	200.00	
	Altec-CM-1-S-SQ-17-1.0x1.0-2.5		12.00	12.00	4.50	1.53	72.00	3.40	200.00	
	Altec-CM-1-S-SQ-31-1.0x1.0-2.5		15.00	15.00	4.50	1.78	72.00	3.95	200.00	
	Altec-CM-1-S-SQ-63-1.0x1.0-2.5		15.00	30.00	4.50	1.82	72.00	4.05	200.00	
	Altec-CM-1-S-SQ-71-1.0x1.0-2.5		23.00	23.00	4.50	1.74	72.00	3.86	200.00	
	Altec-CM-1-S-SQ-127-1.0x1.0-2.5		30.00	30.00	4.50	1.83	72.00	4.07	200.00	
	Altec-CM-1-S-SQ-7-1.0x1.0-2.0		8.00	8.00	4.00	1.72	71.00	4.30	200.00	
	Altec-CM-1-S-SQ-17-1.0x1.0-2.0		12.00	12.00	4.00	1.88	71.00	4.69	200.00	
	Altec-CM-1-S-SQ-31-1.0x1.0-2.0		15.00	15.00	4.00	2.22	71.00	5.56	200.00	
	Altec-CM-1-S-SQ-63-1.0x1.0-2.0		15.00	30.00	4.00	2.24	71.00	5.61	200.00	
	Altec-CM-1-S-SQ-71-1.0x1.0-2.0		23.00	23.00	4.00	2.16	71.00	5.39	200.00	
	Altec-CM-1-S-SQ-127-1.0x1.0-2.0		30.00	30.00	4.00	2.27	71.00	5.67	200.00	
	Altec-CM-1-S-SQ-7-1.0x1.0-1.5		8.00	8.00	3.50	2.34	70.00	6.70	200.00	
	Altec-CM-1-S-SQ-17-1.0x1.0-1.5		12.00	12.00	3.50	2.50	70.00	7.14	200.00	
	Altec-CM-1-S-SQ-31-1.0x1.0-1.5		15.00	15.00	3.50	2.89	70.00	8.25	200.00	
	Altec-CM-1-S-SQ-63-1.0x1.0-1.5		15.00	30.00	3.50	2.96	70.00	8.44	200.00	

Altec-CM-1-S-SQ-71-1.0x1.0-1.5	23.00	23.00	3.50	2.84	70.00	8.10	200.00
Altec-CM-1-S-SQ-127-1.0x1.0-1.5	30.00	30.00	3.50	2.98	70.00	8.51	200.00
Altec-CM-1-S-SQ-7-1.0x1.0-1.3	8.00	8.00	3.30	2.66	69.00	8.05	200.00
Altec-CM-1-S-SQ-17-1.0x1.0-1.3	12.00	12.00	3.30	2.85	69.00	8.63	200.00
Altec-CM-1-S-SQ-31-1.0x1.0-1.3	15.00	15.00	3.30	3.33	69.00	10.10	200.00
Altec-CM-1-S-SQ-63-1.0x1.0-1.3	15.00	30.00	3.30	3.40	69.00	10.30	200.00
Altec-CM-1-S-SQ-71-1.0x1.0-1.3	23.00	23.00	3.30	3.25	69.00	9.85	200.00
Altec-CM-1-S-SQ-127-1.0x1.0-1.3	30.00	30.00	3.30	3.42	69.00	10.37	200.00
Altec-CM-1-S-SQ-7-1.0x1.0-1.15	8.00	8.00	3.20	2.97	68.00	9.28	200.00
Altec-CM-1-S-SQ-17-1.0x1.0-1.15	12.00	12.00	3.20	3.13	68.00	9.77	200.00
Altec-CM-1-S-SQ-31-1.0x1.0-1.15	15.00	15.00	3.20	3.64	68.00	11.39	200.00
Altec-CM-1-S-SQ-63-1.0x1.0-1.15	15.00	30.00	3.20	3.73	68.00	11.67	200.00
Altec-CM-1-S-SQ-71-1.0x1.0-1.15	23.00	23.00	3.20	3.57	68.00	11.16	200.00
Altec-CM-1-S-SQ-127-1.0x1.0-1.15	30.00	30.00	3.20	3.76	68.00	11.74	200.00
Altec-CM-1-S-SQ-7-1.0x1.0-2.5	8.00	8.00	4.50	1.41	72.00	3.13	200.00
Altec-CM-1-S-SQ-17-1.0x1.0-2.5	12.00	12.00	4.50	1.53	72.00	3.40	200.00
Altec-CM-1-S-SQ-31-1.0x1.0-2.5	15.00	15.00	4.50	1.78	72.00	3.95	200.00
Altec-CM-1-S-SQ-63-1.0x1.0-2.5	15.00	30.00	4.50	1.82	72.00	4.05	200.00
Altec-CM-1-S-SQ-71-1.0x1.0-2.5	23.00	23.00	4.50	1.74	72.00	3.86	200.00
Altec-CM-1-S-SQ-127-1.0x1.0-2.5	30.00	30.00	4.50	1.83	72.00	4.07	200.00
Altec-CM-1-S-SQ-7-1.0x1.0-2.0	8.00	8.00	4.00	1.72	71.00	4.30	200.00
Altec-CM-1-S-SQ-17-1.0x1.0-2.0	12.00	12.00	4.00	1.88	71.00	4.69	200.00
Altec-CM-1-S-SQ-31-1.0x1.0-2.0	15.00	15.00	4.00	2.22	71.00	5.56	200.00
Altec-CM-1-S-SQ-63-1.0x1.0-2.0	15.00	30.00	4.00	2.24	71.00	5.61	200.00
Altec-CM-1-S-SQ-71-1.0x1.0-2.0	23.00	23.00	4.00	2.16	71.00	5.39	200.00
Altec-CM-1-S-SQ-127-1.0x1.0-2.0	30.00	30.00	4.00	2.27	71.00	5.67	200.00
Altec-CM-1-S-SQ-7-1.0x1.0-1.5	8.00	8.00	3.50	2.34	70.00	6.70	200.00
Altec-CM-1-S-SQ-17-1.0x1.0-1.5	12.00	12.00	3.50	2.50	70.00	7.14	200.00
Altec-CM-1-S-SQ-31-1.0x1.0-1.5	15.00	15.00	3.50	2.89	70.00	8.25	200.00
Altec-CM-1-S-SQ-63-1.0x1.0-1.5	15.00	30.00	3.50	2.96	70.00	8.44	200.00
Altec-CM-1-S-SQ-71-1.0x1.0-1.5	23.00	23.00	3.50	2.84	70.00	8.10	200.00
Altec-CM-1-S-SQ-127-1.0x1.0-1.5	30.00	30.00	3.50	2.98	70.00	8.51	200.00
Altec-CM-1-S-SQ-7-1.0x1.0-1.3	8.00	8.00	3.30	2.66	69.00	8.05	200.00
Altec-CM-1-S-SQ-17-1.0x1.0-1.3	12.00	12.00	3.30	2.85	69.00	8.63	200.00
Altec-CM-1-S-SQ-31-1.0x1.0-1.3	15.00	15.00	3.30	3.33	69.00	10.10	200.00
Altec-CM-1-S-SQ-63-1.0x1.0-1.3	15.00	30.00	3.30	3.40	69.00	10.30	200.00
Altec-CM-1-S-SQ-71-1.0x1.0-1.3	23.00	23.00	3.30	3.25	69.00	9.85	200.00
Altec-CM-1-S-SQ-127-1.0x1.0-1.3	30.00	30.00	3.30	3.42	69.00	10.37	200.00
Altec-CM-1-S-SQ-7-1.0x1.0-1.15	8.00	8.00	3.20	2.97	68.00	9.28	200.00
Altec-CM-1-S-SQ-17-1.0x1.0-1.15	12.00	12.00	3.20	3.13	68.00	9.77	200.00
Altec-CM-1-S-SQ-31-1.0x1.0-1.15	15.00	15.00	3.20	3.64	68.00	11.39	200.00
Altec-CM-1-S-SQ-63-1.0x1.0-1.15	15.00	30.00	3.20	3.73	68.00	11.67	200.00
Altec-CM-1-S-SQ-71-1.0x1.0-1.15	23.00	23.00	3.20	3.57	68.00	11.16	200.00
Altec-CM-1-S-SQ-127-1.0x1.0-1.15	30.00	30.00	3.20	3.76	68.00	11.74	200.00
Altec-CM-1-S-SQ-7-1.2x1.2-2.5	8.00	8.00	4.90	2.03	72.00	4.15	200.00
Altec-CM-1-S-SQ-17-1.2x1.2-2.5	12.00	12.00	4.90	2.22	72.00	4.54	200.00
Altec-CM-1-S-SQ-31-1.2x1.2-2.5	15.00	15.00	4.90	2.58	72.00	5.26	200.00
Altec-CM-1-S-SQ-63-1.2x1.2-2.5	15.00	30.00	4.90	2.62	72.00	5.35	200.00
Altec-CM-1-S-SQ-71-1.2x1.2-2.5	23.00	23.00	4.90	2.51	72.00	5.13	200.00
Altec-CM-1-S-SQ-127-1.2x1.2-2.5	30.00	30.00	4.90	2.64	72.00	5.40	200.00
Altec-CM-1-S-SQ-7-1.2x1.2-2.0	8.00	8.00	4.40	2.50	71.00	5.68	200.00
Altec-CM-1-S-SQ-17-1.2x1.2-2.0	12.00	12.00	4.40	2.78	71.00	6.31	200.00
Altec-CM-1-S-SQ-31-1.2x1.2-2.0	15.00	15.00	4.40	3.16	71.00	7.17	200.00
Altec-CM-1-S-SQ-63-1.2x1.2-2.0	15.00	30.00	4.40	3.29	71.00	7.47	200.00
Altec-CM-1-S-SQ-71-1.2x1.2-2.0	23.00	23.00	4.40	3.16	71.00	7.17	200.00
Altec-CM-1-S-SQ-127-1.2x1.2-2.0	30.00	30.00	4.40	3.31	71.00	7.53	200.00
Altec-CM-1-S-SQ-7-1.2x1.2-1.5	8.00	8.00	3.90	3.44	70.00	8.81	200.00
Altec-CM-1-S-SQ-17-1.2x1.2-1.5	12.00	12.00	3.90	3.61	70.00	9.26	200.00
Altec-CM-1-S-SQ-31-1.2x1.2-1.5	15.00	15.00	3.90	4.27	70.00	10.94	200.00
Altec-CM-1-S-SQ-63-1.2x1.2-1.5	15.00	30.00	3.90	4.31	70.00	11.05	200.00
Altec-CM-1-S-SQ-71-1.2x1.2-1.5	23.00	23.00	3.90	4.14	70.00	10.62	200.00
Altec-CM-1-S-SQ-127-1.2x1.2-1.5	30.00	30.00	3.90	4.36	70.00	11.17	200.00
Altec-CM-1-S-SQ-7-1.2x1.2-1.3	8.00	8.00	3.70	3.91	69.00	10.56	200.00
Altec-CM-1-S-SQ-17-1.2x1.2-1.3	12.00	12.00	3.70	4.17	69.00	11.26	200.00
Altec-CM-1-S-SQ-31-1.2x1.2-1.3	15.00	15.00	3.70	4.84	69.00	13.09	200.00
Altec-CM-1-S-SQ-63-1.2x1.2-1.3	15.00	30.00	3.70	4.93	69.00	13.33	200.00
Altec-CM-1-S-SQ-71-1.2x1.2-1.3	23.00	23.00	3.70	4.74	69.00	12.82	200.00
Altec-CM-1-S-SQ-127-1.2x1.2-1.3	30.00	30.00	3.70	4.98	69.00	13.45	200.00

	Altec-CM-1-S-SQ-7-1.2x1.2-1.15	8.00	8.00	3.50	4.22	68.00	12.05	200.00
	Altec-CM-1-S-SQ-17-1.2x1.2-1.15	12.00	12.00	3.50	4.58	68.00	13.10	200.00
	Altec-CM-1-S-SQ-31-1.2x1.2-1.15	15.00	15.00	3.50	5.33	68.00	15.24	200.00
	Altec-CM-1-S-SQ-63-1.2x1.2-1.15	15.00	30.00	3.50	5.44	68.00	15.56	200.00
	Altec-CM-1-S-SQ-71-1.2x1.2-1.15	23.00	23.00	3.50	5.22	68.00	14.91	200.00
	Altec-CM-1-S-SQ-127-1.2x1.2-1.15	30.00	30.00	3.50	5.48	68.00	15.65	200.00
	Altec-CM-1-S-SQ-7-1.4x1.4-2.5	10.00	10.00	4.90	1.80	72.00	3.67	200.00
	Altec-CM-1-S-SQ-17-1.4x1.4-2.5	15.00	15.00	4.90	1.96	72.00	3.99	200.00
	Altec-CM-1-S-SQ-31-1.4x1.4-2.5	20.00	20.00	4.90	2.03	72.00	4.13	200.00
	Altec-CM-1-S-SQ-63-1.4x1.4-2.5	20.00	40.00	4.90	2.05	72.00	4.18	200.00
	Altec-CM-1-S-SQ-71-1.4x1.4-2.5	30.00	30.00	4.90	2.06	72.00	4.20	200.00
	Altec-CM-1-S-SQ-127-1.4x1.4-2.5	40.00	40.00	4.90	2.06	72.00	4.21	200.00
	Altec-CM-1-S-SQ-7-1.4x1.4-2.0	10.00	10.00	4.40	2.30	71.00	5.23	200.00
	Altec-CM-1-S-SQ-17-1.4x1.4-2.0	15.00	15.00	4.40	2.40	71.00	5.45	200.00
	Altec-CM-1-S-SQ-31-1.4x1.4-2.0	20.00	20.00	4.40	2.48	71.00	5.63	200.00
	Altec-CM-1-S-SQ-63-1.4x1.4-2.0	20.00	40.00	4.40	2.53	71.00	5.74	200.00
	Altec-CM-1-S-SQ-71-1.4x1.4-2.0	30.00	30.00	4.40	2.53	71.00	5.76	200.00
	Altec-CM-1-S-SQ-127-1.4x1.4-2.0	40.00	40.00	4.40	2.54	71.00	5.78	200.00
	Altec-CM-1-S-SQ-7-1.4x1.4-1.5	10.00	10.00	3.90	3.00	70.00	7.69	200.00
	Altec-CM-1-S-SQ-17-1.4x1.4-1.5	15.00	15.00	3.90	3.16	70.00	8.09	200.00
	Altec-CM-1-S-SQ-63-1.4x1.4-1.5	20.00	40.00	3.90	3.31	70.00	8.49	200.00
	Altec-CM-1-S-SQ-71-1.4x1.4-1.5	30.00	30.00	3.90	3.32	70.00	8.52	200.00
	Altec-CM-1-S-SQ-127-1.4x1.4-1.5	40.00	40.00	3.90	3.34	70.00	8.57	200.00
	Altec-CM-1-S-SQ-7-1.4x1.4-1.3	10.00	10.00	3.70	3.40	69.00	9.19	200.00
	Altec-CM-1-S-SQ-31-2.0x2.0-2.5	20.00	20.00	4.90	4.08	72.00	8.32	200.00
	Altec-CM-1-S-SQ-63-2.0x2.0-2.5	20.00	40.00	4.90	4.15	72.00	8.47	200.00
	Altec-CM-1-S-SQ-71-2.0x2.0-2.5	30.00	30.00	4.90	4.17	72.00	8.50	200.00
	Altec-CM-1-S-SQ-127-2.0x2.0-2.5	40.00	40.00	4.90	4.19	72.00	8.55	200.00
	Altec-CM-1-S-SQ-7-2.0x2.0-2.0	10.00	10.00	4.80	4.60	71.00	9.58	200.00
	Altec-CM-1-S-SQ-17-2.0x2.0-2.0	15.00	15.00	4.80	4.89	71.00	10.19	200.00
	Altec-CM-1-S-SQ-31-2.0x2.0-2.0	20.00	20.00	4.80	5.03	71.00	10.47	200.00
	Altec-CM-1-S-SQ-63-2.0x2.0-2.0	20.00	40.00	4.80	5.10	71.00	10.63	200.00
	Altec-CM-1-S-SQ-71-2.0x2.0-2.0	30.00	30.00	4.80	5.11	71.00	10.65	200.00
	Altec-CM-1-S-SQ-127-2.0x2.0-2.0	40.00	40.00	4.80	5.14	71.00	10.72	200.00
	Altec-CM-1-S-SQ-7-2.0x2.0-1.5	10.00	10.00	4.60	6.00	70.00	13.04	200.00
	Altec-CM-1-S-SQ-17-2.0x2.0-1.5	15.00	15.00	4.60	6.44	70.00	14.01	200.00
	Altec-CM-1-S-SQ-31-2.0x2.0-1.5	20.00	20.00	4.60	6.63	70.00	14.40	200.00
	Altec-CM-1-S-SQ-63-2.0x2.0-1.5	20.00	40.00	4.60	6.74	70.00	14.65	200.00
	Altec-CM-1-S-SQ-71-2.0x2.0-1.5	30.00	30.00	4.60	6.77	70.00	14.71	200.00
	Altec-CM-1-S-SQ-127-2.0x2.0-1.5	40.00	40.00	4.60	6.80	70.00	14.78	200.00
	Altec-CM-1-S-SQ-7-2.0x2.0-1.3	10.00	10.00	4.70	6.90	69.00	14.68	200.00
	Altec-CM-1-S-SQ-17-2.0x2.0-1.3	15.00	15.00	4.70	7.33	69.00	15.60	200.00
	Altec-CM-1-S-SQ-31-2.0x2.0-1.3	20.00	20.00	4.70	7.55	69.00	16.06	200.00
	Altec-CM-1-S-SQ-63-2.0x2.0-1.3	20.00	40.00	4.70	7.68	69.00	16.33	200.00
	Altec-CM-1-S-SQ-71-2.0x2.0-1.3	30.00	30.00	4.70	7.70	69.00	16.38	200.00
	Altec-CM-1-S-SQ-127-2.0x2.0-1.3	40.00	40.00	4.70	7.74	69.00	16.48	200.00
	Altec-CM-1-S-SQ-7-2.0x2.0-1.15	10.00	10.00	4.70	8.10	68.00	17.23	200.00
	Altec-CM-1-S-SQ-17-2.0x2.0-1.15	15.00	15.00	4.70	8.62	68.00	18.35	200.00
	Altec-CM-1-S-SQ-31-2.0x2.0-1.15	20.00	20.00	4.70	8.90	68.00	18.94	200.00
	Altec-CM-1-S-SQ-63-2.0x2.0-1.15	20.00	40.00	4.70	9.03	68.00	19.20	200.00
	Altec-CM-1-S-SQ-71-2.0x2.0-1.15	30.00	30.00	4.70	9.07	68.00	19.29	200.00
	Altec-CM-1-S-SQ-127-2.0x2.0-1.15	40.00	40.00	4.70	9.11	68.00	19.39	200.00
Custom Thermoelectric	00901-9G30-11D	5.99	4.00	2.92	2.71	68.00	9.29	225.00
	01801-9G30-11B	8.13	6.10	2.92	2.62	68.00	8.98	225.00
	03601-9G30-11B	13.46	10.16	2.92	1.90	68.00	6.51	225.00
	00901-9G30-15D	5.99	4.00	2.46	3.67	68.00	14.93	225.00
	03601-9G30-15B	13.46	10.16	2.46	2.59	68.00	10.52	225.00
	00901-9G30-18D	5.99	4.00	2.24	4.17	68.00	18.63	225.00
	01801-9G30-18B	8.13	6.10	2.24	4.23	68.00	18.90	225.00
	03601-9G30-18B	13.46	10.16	2.24	3.14	68.00	14.04	225.00
	04101-9G30-20B	19.05	12.19	3.94	2.33	68.00	5.90	225.00
	04101-9G30-27B	19.05	12.19	3.43	3.14	68.00	9.16	225.00
	00901-9L31-04B	19.05	15.75	5.28	0.79	68.00	1.49	225.00
	01701-9L31-04B	23.11	23.11	5.28	0.86	68.00	1.62	225.00
	03101-9L31-04B	31.75	31.75	5.28	0.81	68.00	1.53	225.00
	04901-9L31-04B	38.10	38.10	5.28	0.89	68.00	1.68	225.00
	0711-9L31-04B	29.72	29.72	4.57	2.10	68.00	4.60	225.00

	12601-9L31-04B		49.78	49.78	5.28	1.34	68.00	2.53	225.00
	12701-9L31-04B		42.67	42.67	5.28	1.83	68.00	3.47	225.00
	12701-9L31-04C		50.80	50.80	5.28	1.29	68.00	2.45	225.00
	00901-9L31-06B		19.05	15.75	4.70	1.18	68.00	2.52	225.00
	01701-9L31-06B		23.11	23.11	4.70	1.25	68.00	2.67	225.00
	03101-9L31-06B		31.75	31.75	4.70	1.21	68.00	2.57	225.00
	04901-9L31-06B		38.10	38.10	4.70	1.33	68.00	2.83	225.00
	0711-9L31-06B		29.72	29.72	4.06	3.17	68.00	7.81	225.00
	12601-9L31-06B		49.78	49.78	4.70	2.00	68.00	4.26	225.00
	12701-9L31-06B		42.67	42.67	4.70	2.75	68.00	5.84	225.00
	12701-9L31-06C		50.80	50.80	4.70	1.94	68.00	4.12	225.00
	00901-9L31-09B		19.05	15.75	5.28	1.77	68.00	3.36	225.00
	01701-9L31-09B		23.11	23.11	5.28	1.89	68.00	3.58	225.00
	03101-9L31-09B		31.75	31.75	5.28	1.82	68.00	3.44	225.00
	04901-9L31-09B		38.10	38.10	5.28	2.00	68.00	3.78	225.00
	0711-9L31-09B		29.72	29.72	3.56	4.76	68.00	13.36	225.00
	12601-9L31-09B		49.78	49.78	5.28	3.01	68.00	5.69	225.00
	12701-9L31-09B		42.67	42.67	5.28	4.12	68.00	7.81	225.00
	12701-9L31-09C		50.80	50.80	5.28	2.91	68.00	5.51	225.00
	00901-9L31-14B		19.05	15.75	4.70	2.77	68.00	5.89	225.00
	01701-9L31-14B		23.11	23.11	4.70	2.92	68.00	6.21	225.00
	03101-9L31-14B		31.75	31.75	4.70	2.83	68.00	6.02	225.00
	04901-9L31-14B		38.10	38.10	4.70	3.11	68.00	6.61	225.00
	12601-9L31-14B		49.78	49.78	4.70	4.67	68.00	9.94	225.00
	12701-9L31-14C		50.80	50.80	4.70	4.53	68.00	9.63	225.00
Huimao	TEC1-007106T150	27.00	30.00	30.00	3.90	3.51	65.00	9.00	150.00
(Beijing)	TEC1-007110T150	27.00	30.00	30.00	3.30	5.86	62.00	17.74	150.00
	TEC1-007112T150	27.00	38.00	38.00	3.90	4.38	63.00	11.22	150.00
	TEC1-007118T150	27.00	38.00	38.00	3.40	6.57	60.00	19.31	150.00
	TEC1-007106T200	27.00	30.00	30.00	3.90	3.51	65.00	9.00	200.00
	TEC1-007110T200	27.00	30.00	30.00	3.30	5.86	62.00	17.74	200.00
	TEC1-007112T200	27.00	38.00	38.00	3.90	4.38	63.00	11.22	200.00
	TEC1-007118T200	27.00	38.00	38.00	3.40	6.57	60.00	19.31	200.00
	TEC1-007106T250	27.00	30.00	30.00	3.90	3.51	65.00	9.00	250.00
	TEC1-007110T250	27.00	30.00	30.00	3.30	5.86	62.00	17.74	250.00
	TEC1-007112T250	27.00	38.00	38.00	3.90	4.38	63.00	11.22	250.00
	TEC1-007118T250	27.00	38.00	38.00	3.40	6.57	60.00	19.31	250.00
	TEC1-12706T150	27.00	40.00	40.00	3.90	3.53	65.00	9.05	150.00
	TEC1-12710T150	27.00	40.00	40.00	3.30	5.89	62.00	17.84	150.00
	TEC1-12712T150	27.00	50.00	50.00	3.90	4.52	63.00	11.59	150.00
	TEC1-12718T150	27.00	50.00	50.00	3.40	6.78	60.00	19.95	150.00
	TEC1-12706T200	27.00	40.00	40.00	3.90	3.53	65.00	9.05	200.00
	TEC1-12710T200	27.00	40.00	40.00	3.30	5.89	62.00	17.84	200.00
	TEC1-12712T200	27.00	50.00	50.00	3.90	4.52	63.00	11.59	200.00
	TEC1-12718T200	27.00	50.00	50.00	3.40	6.78	60.00	19.95	200.00
	TEC1-12706T250	27.00	40.00	40.00	3.90	3.53	65.00	9.05	250.00
	TEC1-12710T250	27.00	40.00	40.00	3.30	5.89	62.00	17.84	250.00
	TEC1-12712T250	27.00	50.00	50.00	3.90	4.52	63.00	11.59	250.00
	TEC1-12718T250	27.00	50.00	50.00	3.40	6.78	60.00	19.95	250.00
	TEC1-03140T150	27.00	40.00	40.00	5.00	5.34	63.00	10.69	150.00
	TEC1-03140T200	27.00	40.00	40.00	5.00	5.34	63.00	10.69	200.00
	TEC1-03140T250	27.00	40.00	40.00	5.00	5.34	63.00	10.69	250.00
Fandis	TM1-1273030-NX	25.00	30.00	30.00	3.80	2.94	71.00	7.75	150.00
(Italy)	TM1-1273039-NX	25.00	30.00	30.00	3.60	3.78	71.00	10.49	150.00
	TM1-1274039-NX	25.00	40.00	40.00	4.70	2.13	69.00	4.52	150.00
	TM1-1274060-NX	25.00	40.00	40.00	3.80	3.31	71.00	8.72	150.00
	TM1-1274085-NX	25.00	40.00	40.00	3.40	4.50	71.00	13.24	150.00
	TM2-1274050-N	25.00	40.00	40.00	11.70	1.06	95.00	0.91	150.00
	TM2-1274065-N	25.00	40.00	40.00	7.50	2.19	86.00	2.92	150.00
Ferrotec	9500/018/012 M P		6.05	6.05	2.09	3.55	66.00	16.99	135.00
	9502/031/012 M P		7.97	7.97	2.09	3.62	66.00	17.32	135.00
	9502/065/012 M P		12.10	11.20	2.09	3.54	66.00	16.95	135.00
	9500/018/018 M P		6.05	6.05	1.79	5.19	66.00	29.00	135.00
	9502/031/018 M P		7.97	7.97	1.79	5.35	66.00	29.90	135.00
	9502/065/018 M P		12.10	11.20	1.79	5.31	66.00	29.68	135.00

	9501/128/030 B		29.70	29.70	3.94	3.29	72.00	8.34	135.00	
	9501/127/030 B		29.70	29.70	3.94	3.29	72.00	8.34	135.00	
	9501/071/030 B		22.40	22.40	3.18	3.19	72.00	10.03	135.00	
	9501/031/030 B		15.10	15.10	3.18	3.07	72.00	9.65	135.00	
	9501/023/030 B		7.39	22.40	3.18	3.14	72.00	9.88	135.00	
	9501/017/030 B		11.50	11.50	3.18	2.87	72.00	9.04	135.00	
	9501/128/040 B		29.70	29.70	3.94	4.31	72.00	10.93	135.00	
	9500/128/040 B		39.70	39.70	4.16	2.41	72.00	5.80	135.00	
	9501/127/040 B		29.70	29.70	3.94	4.31	72.00	10.93	135.00	
	9500/127/040 B		39.70	39.70	4.16	2.41	72.00	5.80	135.00	
	9501/071/040 B		22.40	22.40	3.18	4.19	72.00	13.16	135.00	
	9500/071/040 B		29.80	29.80	4.16	2.36	72.00	5.68	135.00	
	9501/063/040 B		21.10	39.70	4.16	2.15	72.00	5.17	135.00	
	9500/035/040 B		15.10	29.80	4.16	2.22	72.00	5.34	135.00	
	9501/031/040 B		15.10	15.10	3.18	4.08	72.00	12.83	135.00	
	9500/031/040 B		20.00	20.00	4.16	2.33	72.00	5.59	135.00	
	9501/023/040 B		7.39	22.40	3.18	4.17	72.00	13.11	135.00	
	9501/017/040 B		11.50	11.50	3.18	3.86	72.00	12.13	135.00	
	9500/017/040 B		15.01	15.10	4.16	2.25	72.00	5.41	135.00	
	9500/035/060 B		15.10	29.80	4.16	3.56	72.00	8.55	135.00	
	9500/031/060 B		20.00	20.00	4.16	3.50	72.00	8.41	135.00	
	9500/017/060 B		15.10	15.10	4.16	3.33	72.00	8.01	135.00	
	9500/071/060 B		29.80	29.80	4.16	3.60	72.00	8.66	135.00	
	9500/127/060 B		39.70	39.70	4.16	3.62	72.00	8.69	135.00	
	9501/127/060 B		29.70	29.70	3.61	6.46	72.00	17.90	135.00	
	9500/128/060 B		39.70	39.70	4.16	3.62	72.00	8.69	135.00	
	9500/017/085 B		15.10	15.10	3.94	4.82	72.00	12.24	135.00	
	9500/031/085 B		20.00	20.00	3.94	5.00	72.00	12.69	135.00	
	9500/035/085 B		15.10	29.80	3.94	4.89	72.00	12.41	135.00	
	9500/063/085 B		39.70	39.70	3.94	2.54	72.00	6.44	135.00	
	9500/071/085 B		29.80	29.80	3.94	5.07	72.00	12.86	135.00	
	9500/127/085 B		39.70	39.70	3.94	5.08	72.00	12.88	135.00	
	9500/128/085 B		39.70	39.70	3.94	5.08	72.00	12.88	135.00	
	9500/031/090 B		29.80	29.80	4.60	2.48	72.00	5.39	135.00	
	9500/071/090 B		29.80	29.80	3.94	5.29	72.00	13.43	135.00	
	9500/097/090 B		29.80	29.80	3.55	7.32	72.00	20.62	135.00	
	9501/063/100 B		20.10	39.70	3.64	5.89	72.00	16.18	135.00	
	9500/127/100 B		39.70	39.70	3.64	6.03	72.00	16.56	135.00	
	9504/071/120 B		40.10	40.10	4.65	3.92	72.00	8.43	135.00	
	9504/017/150 B		22.00	22.00	4.65	3.93	72.00	8.44	135.00	
	9500/031/150 B		29.80	29.80	4.60	3.94	72.00	8.57	135.00	
	9504/071/150 B		40.10	40.10	4.65	4.91	72.00	10.57	135.00	
	9504/031/240 B		39.70	39.70	4.62	3.49	72.00	7.55	135.00	
	9504/031/400 B		55.00	55.00	4.85	3.04	72.00	6.27	135.00	
HB	TEC1-07103HTS		30.00	30.00	4.90	1.33	65.00	2.72	225.00	$3.74
	TEC1-07108HT		30.00	30.00	3.80	4.22	65.00	11.11	225.00	$1.13
	TEC1-12703HT		40.00	40.00	4.70	1.59	65.00	3.39	225.00	$3.76
	TEC1-12703HTS		40.00	40.00	4.70	1.34	65.00	2.86	225.00	$4.65
	TEC1-12705HT		40.00	40.00	4.20	2.69	65.00	6.40	225.00	$2.04
	TEC1-12706HTS		40.00	40.00	3.80	2.63	65.00	6.91	225.00	$2.19
	TEC1-12707HT		40.00	40.00	3.70	3.69	65.00	9.97	225.00	$1.62
	TEC1-12707HTS		40.00	40.00	3.70	3.16	65.00	8.53	225.00	$1.98
	TEC1-12708HTS		40.00	40.00	3.50	3.56	65.00	10.18	225.00	$1.75
	TEC1-12710HT		40.00	40.00	3.30	5.28	65.00	16.00	225.00	$1.19
	TEC1-12710HTS		40.00	40.00	3.30	4.44	65.00	13.45	225.00	$1.47
	TEC1-12715HT		50.00	50.00	4.30	5.12	65.00	11.91	225.00	$3.75
	TEC1-12715HTS		50.00	50.00	4.30	4.32	65.00	10.05	225.00	$4.61
	TEC-12730HT		62.00	62.00	4.80	6.61	65.00	13.77	225.00	$2.71
	TEC-12730HTS		62.00	62.00	4.80	5.54	65.00	11.54	225.00	$3.34
Hitech	QTEC 2-017.03	27.00	15.00	15.00	4.90	1.73	65.00	3.54	200.00	
	QTEC 2-031.03	27.00	20.00	20.00	4.90	1.80	65.00	3.67	200.00	
	QTEC 2-035.03	27.00	30.00	15.00	4.90	1.81	65.00	3.70	200.00	
	QTEC 2-049.03	27.00	25.00	25.00	4.90	1.81	65.00	3.69	200.00	
	QTEC 2-063.03	27.00	40.00	20.00	4.90	1.81	65.00	3.70	200.00	
	QTEC 2-071.03	27.00	30.00	30.00	4.90	1.82	65.00	3.72	200.00	
	QTEC 2-127.03	27.00	40.00	40.00	4.90	1.83	65.00	3.74	200.00	

	QTEC 2-017.04	27.00	15.00	15.00	4.70	2.00	65.00	4.26	200.00
	QTEC 2-031.04	27.00	20.00	20.00	4.70	2.05	65.00	4.36	200.00
	QTEC 2-035.04	27.00	30.00	15.00	4.70	2.04	65.00	4.35	200.00
	QTEC 2-049.04	27.00	25.00	25.00	4.70	2.06	65.00	4.39	200.00
	QTEC 2-063.04	27.00	40.00	20.00	4.70	2.06	65.00	4.39	200.00
	QTEC 2-071.04	27.00	30.00	30.00	4.70	2.08	65.00	4.42	200.00
	QTEC 2-127.04	27.00	40.00	40.00	4.70	2.09	65.00	4.44	200.00
	QTEC 2-017.05	27.00	15.00	15.00	4.00	2.44	65.00	6.11	200.00
	QTEC 2-031.05	27.00	20.00	20.00	4.00	2.50	65.00	6.25	200.00
	QTEC 2-035.05	27.00	30.00	15.00	4.00	2.51	65.00	6.28	200.00
	QTEC 2-049.05	27.00	25.00	25.00	4.00	2.53	65.00	6.32	200.00
	QTEC 2-063.05	27.00	40.00	20.00	4.00	2.53	65.00	6.31	200.00
	QTEC 2-071.05	27.00	30.00	30.00	4.00	2.53	65.00	6.33	200.00
	QTEC 2-127.05	27.00	40.00	40.00	4.00	2.56	65.00	6.41	200.00
	QTEC 2-017.06	27.00	15.00	15.00	3.80	3.07	65.00	8.07	200.00
	QTEC 2-031.06	27.00	20.00	20.00	3.80	3.13	65.00	8.22	200.00
	QTEC 2-035.06	27.00	30.00	15.00	3.80	3.16	65.00	8.30	200.00
	QTEC 2-049.06	27.00	25.00	25.00	3.80	3.20	65.00	8.42	200.00
	QTEC 2-063.06	27.00	40.00	20.00	3.80	3.19	65.00	8.39	200.00
	QTEC 2-071.06	27.00	30.00	30.00	3.80	3.19	65.00	8.39	200.00
	QTEC 2-127.06	27.00	40.00	40.00	3.80	3.21	65.00	8.45	200.00
	QTEC 2-017.08	27.00	15.00	15.00	3.30	4.09	65.00	12.39	200.00
	QTEC 2-031.08	27.00	20.00	20.00	3.30	4.20	65.00	12.73	200.00
	QTEC 2-035.08	27.00	30.00	15.00	3.30	4.22	65.00	12.79	200.00
	QTEC 2-049.08	27.00	25.00	25.00	3.30	4.24	65.00	12.85	200.00
	QTEC 2-063.08	27.00	40.00	20.00	3.30	4.28	65.00	12.95	200.00
	QTEC 2-071.08	27.00	30.00	30.00	3.30	4.28	65.00	12.96	200.00
	QTEC 2-127.08	27.00	40.00	40.00	3.30	4.30	65.00	13.03	200.00
	QTEC 2-031.09	27.00	30.00	30.00	5.60	1.17	65.00	2.08	200.00
	QTEC 2-049.09	27.00	36.00	36.00	5.60	2.28	65.00	4.06	200.00
	QTEC 2-071.09	27.00	44.00	44.00	5.60	2.23	65.00	3.98	200.00
	QTEC 2-127.09	27.00	62.00	62.00	5.60	2.02	65.00	3.60	200.00
	QTEC 2-031.14	27.00	30.00	30.00	4.60	3.28	65.00	7.13	200.00
	QTEC 2-049.14	27.00	36.00	36.00	4.60	3.56	65.00	7.73	200.00
	QTEC 2-071.14	27.00	44.00	44.00	4.60	3.47	65.00	7.55	200.00
	QTEC 2-127.14	27.00	62.00	62.00	4.60	3.13	65.00	6.81	200.00
INB Products	inbC2-040-065-31-17	27.00	11.50	11.50	6.60	2.34	85.00	3.55	200.00
	inbC2-055-065-31-17	27.00	15.00	15.00	7.20	2.69	85.00	3.73	200.00
	inbC2-055-065-71-31	27.00	20.00	20.00	7.20	3.16	85.00	4.39	200.00
	inbC2-040-050-127-63	27.00	30.00	30.00	7.10	1.79	85.00	2.52	200.00
	inbC2-055-045-127-63	27.00	40.00	40.00	7.50	2.16	85.00	2.88	200.00
	inbC1-017.03	27.00	15.00	15.00	4.90	1.73	65.00	3.54	150.00
	inbC1-031.03	27.00	20.00	20.00	4.90	1.80	65.00	3.67	150.00
	inbC1-035.03	27.00	30.00	15.00	4.90	1.81	65.00	3.70	150.00
	inbC1-049.03	27.00	25.00	25.00	4.90	1.81	65.00	3.69	150.00
	inbC1-063.03	27.00	40.00	20.00	4.90	1.81	65.00	3.70	150.00
	inbC1-071.03	27.00	30.00	30.00	4.90	1.82	65.00	3.72	150.00
	inbC1-127.03	27.00	40.00	40.00	4.90	1.83	65.00	3.74	150.00
	inbC1-017.04	27.00	15.00	15.00	4.70	2.00	65.00	4.26	150.00
	inbC1-031.04	27.00	20.00	20.00	4.70	2.05	65.00	4.36	150.00
	inbC1-035.04	27.00	30.00	15.00	4.70	2.04	65.00	4.35	150.00
	inbC1-049.04	27.00	25.00	25.00	4.70	2.06	65.00	4.39	150.00
	inbC1-063.04	27.00	40.00	20.00	4.70	2.06	65.00	4.39	150.00
	inbC1-071.04	27.00	30.00	30.00	4.70	2.08	65.00	4.42	150.00
	inbC1-127.04	27.00	40.00	40.00	4.70	2.09	65.00	4.44	150.00
	inbC1-017.05	27.00	15.00	15.00	4.00	2.44	65.00	6.11	150.00
	inbC1-031.05	27.00	20.00	20.00	4.00	2.50	65.00	6.25	150.00
	inbC1-035.05	27.00	30.00	15.00	4.00	2.51	65.00	6.28	150.00
	inbC1-049.05	27.00	25.00	25.00	4.00	2.53	65.00	6.32	150.00
	inbC1-063.05	27.00	40.00	20.00	4.00	2.53	65.00	6.31	150.00
	inbC1-071.05	27.00	30.00	30.00	4.00	2.53	65.00	6.33	150.00
	inbC1-127.05	27.00	40.00	40.00	4.00	2.56	65.00	6.41	150.00
	inbC1-017.06	27.00	15.00	15.00	3.80	3.07	65.00	8.07	150.00
	inbC1-035.06	27.00	30.00	15.00	3.80	3.16	65.00	8.30	150.00
	inbC1-049.06	27.00	25.00	25.00	3.80	3.20	65.00	8.42	150.00
	inbC1-063.06	27.00	40.00	20.00	3.80	3.19	65.00	8.39	150.00
	inbC1-071.06	27.00	30.00	30.00	3.80	3.19	65.00	8.39	150.00

	inbC1-127.06	27.00	40.00	40.00	3.80	3.21	65.00	8.45	150.00
	inbC1-017.08	27.00	15.00	15.00	3.30	4.09	65.00	12.39	150.00
	inbC1-031.08	27.00	20.00	20.00	3.30	4.20	65.00	12.73	150.00
	inbC1-035.08	27.00	30.00	15.00	3.30	4.22	65.00	12.79	150.00
	inbC1-049.08	27.00	25.00	25.00	3.30	4.24	65.00	12.85	150.00
	inbC1-063.08	27.00	40.00	20.00	3.30	4.28	65.00	12.95	150.00
	inbC1-071.08	27.00	30.00	30.00	3.30	4.28	65.00	12.96	150.00
	inbC1-127.08	27.00	40.00	40.00	3.30	4.30	65.00	13.03	150.00
	inbC1-031.09	27.00	30.00	30.00	5.60	2.09	65.00	3.73	150.00
	inbC1-049.09	27.00	36.00	36.00	5.60	2.28	65.00	4.06	150.00
	inbC1-071.09	27.00	44.00	44.00	5.60	2.23	65.00	3.98	150.00
	inbC1-127.09	27.00	62.00	62.00	5.60	2.02	65.00	3.60	150.00
	inbC1-031.14	27.00	30.00	30.00	4.60	3.28	65.00	7.13	150.00
	inbC1-049.14	27.00	36.00	36.00	4.60	3.56	65.00	7.73	150.00
	inbC1-071.14	27.00	44.00	44.00	4.60	3.47	65.00	7.55	150.00
	inbC1-127.14	27.00	62.00	62.00	4.60	3.13	65.00	6.81	150.00
	inbC1-127.14-50	27.00	50.00	50.00	4.70	4.82	65.00	10.26	150.00
Interm	TECB-1-1-(15.4-6.0-51.4)-40-71	25.00	40.00	40.00	3.60	3.21	71.00	8.92	250.00
	TECB-1-3-(15.4-8.5-68.8)-40-69	25.00	40.00	40.00	3.30	4.30	69.00	13.03	250.00
	TECB-1-14-(15.4-3.9-33.4)-40-72	25.00	40.00	40.00	4.70	2.09	72.00	4.44	250.00
	TECB-1-29-(15.4-10-86)-40-71	25.00	40.00	40.00	3.50	5.38	71.00	15.36	250.00
	TECB-1-33-(15.4-1.0-8.6)-40-72	25.00	40.00	40.00	4.80	0.54	72.00	1.12	250.00
	TECB-1-34-(15.4-11.4-97)-40-70	25.00	40.00	40.00	3.30	6.09	70.00	18.47	250.00
	TECB-2-2-(15.4-3.9-33.4)-30-71	25.00	30.00	30.00	3.20	3.71	71.00	11.60	250.00
	TECB-2-43-(15.4-4.8-41.0)-30-69	25.00	30.00	30.00	3.00	4.56	69.00	15.19	250.00
	TECB-2-44-(15.4-3.5-30.2)-30-70	25.00	30.00	30.00	3.40	3.36	70.00	9.87	250.00
	TECB-2-45-(15.4-2.4-20.7)-30-71	25.00	30.00	30.00	4.10	2.30	71.00	5.61	250.00
	TECB-13-13-(8.6-3.9-18.7)-30-72	25.00	30.00	30.00	4.60	2.08	72.00	4.52	250.00
	TECB-13-46-(8.6-4.2-21.0)-30-72	25.00	30.00	30.00	4.40	2.33	72.00	5.30	250.00
	TECB-13-47-(8.6-4.7-23.0)-30-71	25.00	30.00	30.00	4.20	2.56	71.00	6.08	250.00
	TECB-13-48-(8.6-5.1-25.2)-30-70	25.00	30.00	30.00	4.00	2.80	70.00	7.00	250.00
	TECB-13-49-(8.6-6.0-29.6)-30-70	25.00	30.00	30.00	3.70	3.29	70.00	8.89	250.00
	TECB-14-88-(12-6-40)-40-71	25.00	40.00	40.00	3.50	2.50	71.00	7.14	250.00
	TECB-14-91-(12-6.5-44)-40-71	25.00	40.00	40.00	3.40	2.75	71.00	8.09	250.00
	TECB-14-92-(12-7-47)-40-71	25.00	40.00	40.00	3.30	2.94	71.00	8.90	250.00
	TECB-15-15-(24.7-11.4-173)-40-69	25.00	40.00	40.00	3.00	10.81	69.00	36.04	250.00
	TECB-15-16-(24.7-7.9-120)-40-69	25.00	40.00	40.00	3.40	7.50	69.00	22.06	250.00
	TECB-15-26-(24.0-3.9-52)-40-71	25.00	40.00	40.00	4.20	3.25	71.00	7.74	250.00
	TECB-15-50-(24.7-9.5-130)-40-69	25.00	40.00	40.00	3.30	8.13	69.00	24.62	250.00
	TECB-15-101-(24.7-14.5-220)-40-69	25.00	40.00	40.00	2.90	13.75	69.00	47.41	250.00
	TECB-16-89-(24.2-7-100)-30-70	25.00	30.00	30.00	3.10	11.11	70.00	35.84	250.00
	TECB-16-93-(24.2-6.3-90)-30-70	25.00	30.00	30.00	3.20	10.00	70.00	31.25	250.00
	TECB-16-94-(24.2-5.7-81)-30-70	25.00	30.00	30.00	3.30	9.00	70.00	27.27	250.00
	TECB-17-17-(15.4-14.0-120)-62-71	25.00	62.00	62.00	5.00	3.12	71.00	6.24	250.00
	TECB-17-21-(15.4-8.3-72)-62-71	25.00	62.00	62.00	5.90	1.87	71.00	3.17	250.00
	TECB-17-51-(15.4-9.3-81)-62-71	25.00	62.00	62.00	5.70	2.11	71.00	3.70	250.00
	TECB-17-52-(15.4-11.1-94.4)-62-71	25.00	62.00	62.00	5.50	2.46	71.00	4.47	250.00
	TECB-17-53-(15.4-12.6-107)-62-70	25.00	62.00	62.00	5.30	2.78	70.00	5.25	250.00
	TECB-18-18-(8.6-2.5-12)-23-71	25.00	23.00	23.00	3.60	2.27	71.00	6.30	250.00
	TECB-18-54-(8.6-2.1-9.9)-23-72	25.00	23.00	23.00	4.00	1.87	72.00	4.68	250.00
	TECB-18-55-(8.6-2.3-10.6)-23-71	25.00	23.00	23.00	3.80	2.00	71.00	5.27	250.00
	TECB-18-56-(8.6-3.3-15.0)-23-71	25.00	23.00	23.00	3.40	2.84	71.00	8.34	250.00
	TECB-18-57-(8.6-3.9-18.1)-23-71	25.00	23.00	23.00	3.20	3.42	71.00	10.69	250.00
	TECB-18-87-(8.2-3.7-20)-23-71	25.00	28.00	23.50	3.30	3.04	71.00	9.21	250.00
	TECB-21-102-(42-12-300)-55-69	25.00	55.00	55.00	4.00	9.92	69.00	24.79	250.00
	TECB-21-103-(42-15-330)-50-69	25.00	55.00	55.00	4.00	10.91	69.00	27.27	250.00
	TECB-21-104-(42-16.7-350)-50-69	25.00	55.00	55.00	3.80	11.57	69.00	30.45	250.00
	TECB-21-105-(42-20-400)-50-68	25.00	55.00	55.00	3.50	13.22	68.00	37.78	250.00
	TECB-22-22-(17.4-6.0-57)-40-71	25.00	40.00	40.00	3.80	3.56	71.00	9.38	250.00
	TECB-22-58-(17.4-4.0-39)-40-71	25.00	40.00	40.00	4.30	2.44	71.00	5.67	250.00
	TECB-22-59-(17.4-4.8-45.5)-40-71	25.00	40.00	40.00	4.10	2.84	71.00	6.94	250.00
	TECB-22-60-(17.4-5.5-52.2)-40-70	25.00	40.00	40.00	3.90	3.26	70.00	8.37	250.00
	TECB-22-61-(17.4-7.3-70.0)-40-70	25.00	40.00	40.00	3.50	4.38	70.00	12.50	250.00
	TECB-22-62-(17.4-8.1-77.4)-40-70	25.00	40.00	40.00	3.30	4.84	70.00	14.66	250.00
	TECB-25-25-(15.4-8.5-72)-70-71	25.00	70.00	70.00	5.70	1.47	71.00	2.58	250.00
	TECB-25-30-(15.4-11.4-100)-70-70	25.00	70.00	70.00	5.50	2.04	70.00	3.71	250.00
	TECB-25-35-(15.4-14-125)-70-70	25.00	70.00	70.00	5.00	2.55	70.00	5.10	250.00

	TECB-25-63-(15.4-17-150)-70-70	25.00	70.00	70.00	4.00	3.06	70.00	7.65	250.00	
	TECB-25-64-(15.4-10.2-88)-70-71	25.00	70.00	70.00	5.70	1.80	71.00	3.15	250.00	
	TECB-26-90-(30-19-300)-70-69	25.00	70.00	70.00	5.70	6.12	71.00	10.74	250.00	
	TECB-26-95-(30-17.5-275)-70-69	25.00	70.00	70.00	5.80	5.61	71.00	9.68	250.00	
	TECB-26-96-(30-16.4-260)-70-69	25.00	70.00	70.00	5.90	5.31	71.00	8.99	250.00	
	TECB-27-27-(19-14-147)-40-70	25.00	40.00	40.00	3.10	9.19	70.00	29.64	250.00	
	TECB-27-65-(19-11.6-123)-40-70	25.00	40.00	40.00	3.30	7.50	70.00	22.73	250.00	
	TECB-27-66-(19-9.8-106)-40-70	25.00	40.00	40.00	3.50	6.63	70.00	18.93	250.00	
	TECB-27-67-(19-8.6-93.3)-40-71	25.00	40.00	40.00	3.70	5.83	71.00	15.76	250.00	
	TECB-27-68-(19-7.6-83.0)-40-71	25.00	40.00	40.00	3.90	5.19	71.00	13.30	250.00	
	TECB-28-28-(2.5-3.9-5.4)-20-72	25.00	20.00	20.00	4.70	1.35	72.00	2.87	250.00	
	TECB-28-69-(2.5-4.4-6.0)-20-71	25.00	20.00	20.00	4.50	1.50	71.00	3.33	250.00	
	TECB-28-70-(2.5-5.0-6.9)-20-71	25.00	20.00	20.00	4.30	1.73	71.00	4.01	250.00	
	TECB-28-71-(2.5-5.4-7.5)-20-71	25.00	20.00	20.00	4.10	1.88	71.00	4.57	250.00	
	TECB-29-109-(24.7-11.5-175)-50-69	25.00	50.00	50.00	4.00	7.00	69.00	17.50	250.00	
	TECB-32-32-(24.7-19.0-300)-62-69	25.00	62.00	62.00	5.10	7.80	69.00	15.30	250.00	
	TECB-32-72-(24.7-17.0-270)-62-69	25.00	62.00	62.00	5.30	7.02	69.00	13.25	250.00	
	TECB-32-73-(24.7-15.0-240)-62-69	25.00	62.00	62.00	5.50	6.24	69.00	11.35	250.00	
	TECB-32-74-(24.7-13.0-200)-62-70	25.00	62.00	62.00	5.70	5.20	70.00	9.13	250.00	
	TECB-32-110-(24.7-25.0-400)-62-69	25.00	62.00	62.00	4.80	10.41	69.00	21.68	250.00	
	TECB-39-97-(30-15.2-270)-50-69	25.00	50.00	50.00	5.50	10.80	69.00	19.64	250.00	
	TECB-39-98-(30-14.0-255)-50-69	25.00	50.00	50.00	5.60	10.20	69.00	18.21	250.00	
	TECB-39-99-(30-12.7-240)-50-69	25.00	50.00	50.00	5.70	9.60	69.00	16.84	250.00	
	TECB-39-100-(30-12.7-240)-50-69	25.00	50.00	50.00	6.10	4.40	70.00	7.21	250.00	
	TECB-40-40-(17.4-6.0-58)-50-71	25.00	50.00	50.00	4.00	2.32	71.00	5.80	250.00	
	TECB-40-75-(17.4-4.0-38)-50-71	25.00	50.00	50.00	4.60	1.52	71.00	3.30	250.00	
	TECB-40-76-(17.4-4.6-45.2)-50-71	25.00	50.00	50.00	4.40	1.81	71.00	4.11	250.00	
	TECB-40-77-(17.4-5.5-52.3)-50-71	25.00	50.00	50.00	4.20	2.09	71.00	4.98	250.00	
	TECB-40-78-(17.4-6.9-66.0)-50-70	25.00	50.00	50.00	3.80	2.64	70.00	6.95	250.00	
	TECB-41-41-(30-3.0-50)-40-71	25.00	40.00	40.00	3.20	3.13	71.00	9.77	250.00	
	TECB-41-79-(30-2.7-45)-40-71	25.00	40.00	40.00	3.40	2.81	71.00	8.27	250.00	
	TECB-41-80-(30-2.5-42.3)-40-71	25.00	40.00	40.00	3.60	2.64	71.00	7.34	250.00	
	TECB-41-81-(30-2.3-37.8)-40-72	25.00	40.00	40.00	3.80	2.36	72.00	6.22	250.00	
	TECB-41-82-(30-2.1-34.5)-40-72	25.00	40.00	40.00	4.00	2.16	72.00	5.39	250.00	
Kryotherm	TB-7-1,0-2,5		8.00	8.00	4.80	1.56	70.00	3.26	150.00	$5.82
	TB-17-1,0-2,5		11.50	11.50	4.80	1.89	70.00	3.94	150.00	$5.21
	TB-31-1,0-2,5		14.80	14.80	4.80	2.05	70.00	4.28	150.00	$5.66
	TB-63-1,0-2,5		15.00	15.00	4.80	4.04	70.00	8.43	150.00	$3.14
	TB-71-1,0-2,5		23.00	23.00	4.80	1.93	70.00	4.02	150.00	$6.72
	TB-83-1,0-2,5		22.00	19.00	4.80	2.87	70.00	5.98	150.00	$4.70
	TB-127-1,0-2,5		30.00	30.00	4.80	2.03	70.00	4.24	150.00	$6.98
	TB-7-1,0-2,0		8.00	8.00	4.30	2.03	70.00	4.72	150.00	$3.15
	TB-17-1,0-2,0		11.50	11.50	4.30	2.34	70.00	5.45	150.00	$3.58
	TB-31-1,0-2,0		14.80	14.80	4.30	2.56	70.00	5.95	150.00	$3.99
	TB-63-1,0-2,0		15.00	30.00	4.30	2.53	70.00	5.89	150.00	$4.42
	TB-71-1,0-2,0		23.00	23.00	4.30	2.42	70.00	5.63	150.00	$4.96
	TB-83-1,0-2,0		22.00	19.00	4.30	3.56	70.00	8.29	150.00	$3.65
	TB-127-1,0-2,0		30.00	30.00	4.30	2.54	70.00	5.92	150.00	$5.34
	TB-71-1,4-3,175		30.00	30.00	5.60	1.83	72.00	3.27	150.00	$9.88
	TB-7-1,0-1,5		8.00	8.00	3.80	2.66	69.00	6.99	150.00	$2.35
	TB-17-1,0-1,5		11.50	11.50	3.80	3.02	69.00	7.96	150.00	$2.71
	TB-31-1,0-1,5		14.80	14.80	3.80	3.33	69.00	8.77	150.00	$3.00
	TB-63-1,0-1,5		15.00	30.00	3.80	3.29	69.00	8.65	150.00	$3.28
	TB-71-1,0-1,5		23.00	23.00	3.80	3.16	69.00	8.31	150.00	$3.64
	TB-83-1,0-1,5		22.00	19.00	3.80	4.67	69.00	12.28	150.00	$2.63
	TB-127-1,0-1,5		30.00	30.00	3.80	3.32	69.00	8.74	150.00	$4.06
	TB-7-1,0-1,3		8.00	8.00	3.60	2.97	69.00	8.25	150.00	$2.11
	TB-17-1,0-1,3		11.50	11.50	3.60	3.48	69.00	9.66	150.00	$2.36
	TB-23-1,0-1,3		30.00	5.00	3.60	4.13	69.00	11.48	150.00	$2.36
	TB-31-1,0-1,3		14.80	14.80	3.60	3.83	69.00	10.65	150.00	$2.82
	TB-63-1,0-1,3		15.00	30.00	3.60	3.80	69.00	10.56	150.00	$3.09
	TB-71-1,0-1,3		23.00	23.00	3.60	3.65	69.00	10.13	150.00	$3.15
	TB-83-1,0-1,3		22.00	19.00	3.60	5.38	69.00	14.95	150.00	$2.23
	TB-127-1,0-1,3		30.00	30.00	3.60	3.83	69.00	10.65	150.00	$3.29
	TB-32-1,0-0,8		40.00	6.00	3.10	5.88	69.00	18.95	150.00	$1.91
	TB-127-1,0-0,8		30.00	30.00	3.10	6.22	69.00	20.07	150.00	$2.31
	TB-195-1,0-0,8		50.00	25.00	3.10	6.88	69.00	22.19	150.00	$4.62

	TB-7-1,4-2,5		10.00	10.00	4.90	2.10	72.00	4.29	150.00	$4.12
	TB-17-1,4-2,5		15.00	15.00	4.90	2.22	72.00	4.54	150.00	$4.77
	TB-31-1,4-2,5		20.00	20.00	4.90	2.28	72.00	4.64	150.00	$5.45
	TB-63-1,4-2,5		20.00	40.00	4.90	2.33	72.00	4.74	150.00	$5.85
	TB-71-1,4-2,5		30.00	30.00	4.90	2.32	72.00	4.74	150.00	$6.24
	TB-127-1,4-2,5		40.00	40.00	4.80	2.34	72.00	4.87	150.00	$6.31
	TB-71-1,4-1,8		30.00	30.00	4.20	3.10	70.00	7.38	150.00	$4.65
	TB-7-1,4-1,5		10.00	10.00	4.00	3.30	70.00	8.25	150.00	$2.48
	TB-17-1,4-1,5		15.00	15.00	4.00	3.56	70.00	8.89	150.00	$2.87
	TB-31-1,4-1,5		20.00	20.00	4.00	3.65	70.00	9.13	150.00	$3.12
	TB-63-1,4-1,5		20.00	40.00	4.00	3.71	70.00	9.28	150.00	$3.39
	TB-71-1,4-1,5		30.00	30.00	4.00	3.71	70.00	9.28	150.00	$3.72
	TB-127-1,4-1,5		40.00	40.00	3.90	3.75	70.00	9.62	150.00	$4.48
	TB-127-1,4-1,2		40.00	40.00	3.60	4.69	70.00	13.02	150.00	$3.71
	TB-7-1,4-1,15		10.00	10.00	3.60	4.20	69.00	11.67	150.00	$2.06
	TB-17-1,4-1,15		15.00	15.00	3.60	4.53	69.00	12.59	150.00	$2.54
	TB-31-1,4-1,15		20.00	20.00	3.60	4.65	69.00	12.92	150.00	$2.89
	TB-63-1,4-1,15		20.00	40.00	3.60	4.74	69.00	13.16	150.00	$2.91
	TB-71-1,4-1,15		30.00	30.00	3.60	4.78	69.00	13.27	150.00	$3.14
	TB-127-1,4-1,15		40.00	40.00	3.40	4.75	69.00	13.97	150.00	$4.06
	TB-127-1.4-1.05		40.00	40.00	3.30	5.25	69.00	15.91	150.00	$4.11
	TB-7-2,0-2,5		14.80	14.80	4.80	1.92	72.00	3.99	150.00	$4.69
	TB-17-2,0-2,5		22.00	22.00	4.80	2.11	72.00	4.39	150.00	$5.74
	TB-31-2,0-2,5		30.00	30.00	4.80	2.08	72.00	4.33	150.00	$6.59
	TB-71-2,0-2,5		40.00	40.00	4.80	2.69	72.00	5.60	150.00	$11.39
	TB-127-2,0-2,5		48.00	48.00	4.80	3.30	72.00	6.87	150.00	$14.85
	TB-127-2,0-2,5		55.00	55.00	4.80	2.51	72.00	5.23	150.00	$19.50
	TB-127-2,0-2,5		62.00	62.00	4.80	1.98	72.00	4.12	150.00	$24.78
	TB-127-2,0-1,65		48.00	48.00	4.00	4.82	70.00	12.04	150.00	$9.91
	TB-7-2,0-1,5		14.80	14.80	3.80	3.06	70.00	8.05	150.00	$4.12
	TB-17-2,0-1,5		22.00	22.00	3.80	3.37	70.00	8.86	150.00	$4.16
	TB-31-2,0-1,5		30.00	30.00	3.80	3.31	70.00	8.71	150.00	$4.32
	TB-71-2,0-1,5		40.00	40.00	3.80	4.25	70.00	11.18	150.00	$6.92
	TB-127-2,0-1,5		48.00	48.00	3.80	5.30	70.00	13.93	150.00	$9.29
	TB-127-2,0-1,5		55.00	55.00	4.80	4.03	70.00	8.40	150.00	$12.20
	TB-127-2,0-1,5		62.00	62.00	3.90	3.17	70.00	8.14	150.00	$15.50
	TB-127-2,0-1,15		48.00	48.00	3.40	6.77	69.00	19.91	150.00	$6.76
	TB-32-2,8-1,5		40.00	40.00	4.00	3.75	70.00	9.38	150.00	$5.15
	TB-31-5,0-2,5		55.00	55.00	6.00	3.70	70.00	6.17	150.00	$10.16
	TB-31-5,0-1,5		55.00	55.00	5.00	6.15	70.00	12.30	150.00	$5.81
Marlow	DT12-2.5	27.00	30.00	30.00	4.04	2.56	66.00	6.33	150.00	
	DT12-2.5-01L	27.00	30.00	30.00	4.04	2.56	66.00	6.33	150.00	
	DT12-4	27.00	30.00	30.00	3.43	4.00	66.00	11.66	150.00	
	DT12-4-01	27.00	30.00	30.00	3.43	4.00	66.00	11.66	150.00	
	DT12-4-01L	27.00	30.00	30.00	3.43	4.00	66.00	11.66	150.00	
	DT12-4-01S	27.00	30.00	30.00	3.43	4.00	66.00	11.66	150.00	
	DT12-4-06LS	27.00	30.00	30.00	3.43	4.00	66.00	11.66	150.00	
	DT12-6	27.00	40.01	40.01	4.01	3.37	66.00	8.41	150.00	
	DT12-6-01L	27.00	40.01	40.01	4.01	3.37	66.00	8.41	150.00	
	DT12-6-01LS	27.00	40.01	40.01	4.01	3.37	66.00	8.41	150.00	
	DT12-6-01S	27.00	40.01	40.01	4.01	3.37	66.00	8.41	150.00	
	DT12-6-05	27.00	40.01	40.01	4.01	3.37	66.00	8.41	150.00	
	DT12-8	27.00	40.01	40.01	3.53	4.44	66.00	12.56	150.00	
	DT12-8-01L	27.00	40.01	40.01	3.53	4.44	66.00	12.56	150.00	
	DT3-2.5	27.00	16.00	16.00	4.04	2.34	65.00	5.80	150.00	
	DT3-2.5-01	27.00	16.00	16.00	4.04	2.34	65.00	5.80	150.00	
	DT3-4	27.00	16.00	16.00	3.43	3.52	65.00	10.25	150.00	
	DT3-4-01L	27.00	16.00	16.00	3.43	3.52	65.00	10.25	150.00	
	DT3-6	27.00	19.99	19.99	4.01	3.25	65.00	8.11	150.00	
	DT3-6-01	27.00	19.99	19.99	4.01	3.25	65.00	8.11	150.00	
	DT3-6-01LS	27.00	19.99	19.99	4.01	3.25	65.00	8.11	150.00	
	DT3-6-01S	27.00	19.99	19.99	4.01	3.25	65.00	8.11	150.00	
	DT3-8	27.00	19.99	19.99	3.63	4.25	65.00	11.72	150.00	
	DT6-2.5	27.00	23.50	23.50	4.04	2.35	65.00	5.83	150.00	
	DT6-2.5-01L	27.00	23.50	23.50	4.04	2.35	65.00	5.83	150.00	
	DT6-2.5-01LS	27.00	23.50	23.50	4.04	2.35	65.00	5.83	150.00	
	DT6-4	27.00	23.50	23.50	3.43	3.62	65.00	10.56	150.00	

	DT6-4-01	27.00	23.50	23.50	3.43	3.62	65.00	10.56	150.00
	DT6-4-01L	27.00	23.50	23.50	3.43	3.62	65.00	10.56	150.00
	DT6-4-01LS	27.00	23.50	23.50	3.43	3.62	65.00	10.56	150.00
	DT6-6	27.00	30.00	30.00	4.01	3.33	65.00	8.31	150.00
	DT6-6-01L	27.00	30.00	30.00	4.01	3.33	65.00	8.31	150.00
	DT6-8	27.00	30.00	30.00	3.63	4.33	65.00	11.94	150.00
	DT6-8-01L	27.00	30.00	30.00	3.63	4.33	65.00	11.94	150.00
	MI1010T	27.00	3.96	3.96	2.41	3.00	61.00	12.44	150.00
	MI1011T	27.00	6.60	6.60	2.41	2.30	61.00	9.53	150.00
	MI1012T	27.00	8.79	8.79	2.41	2.72	61.00	11.28	150.00
	MI1012T-01AC	27.00	8.79	8.79	2.41	2.72	61.00	11.28	150.00
	MI1013T	27.00	13.16	13.16	2.41	2.77	61.00	11.50	150.00
	MI1015T	27.00	8.79	10.97	2.39	2.70	61.00	11.28	150.00
	MI1020T	27.00	3.91	3.91	2.16	5.89	64.00	27.25	150.00
	MI1020T-02AC	27.00	3.91	3.91	2.16	5.89	64.00	27.25	150.00
	MI1021T	27.00	6.60	6.60	2.16	5.05	64.00	23.38	150.00
	MI1021T-02AC	27.00	6.60	6.60	2.16	5.05	64.00	23.38	150.00
	MI1022T	27.00	8.79	8.79	2.16	5.18	64.00	23.97	150.00
	MI1023T	27.00	13.16	13.16	2.16	5.31	64.00	24.59	150.00
	MI1023T-02AC	27.00	13.16	13.16	2.16	5.31	64.00	24.59	150.00
	MI1025T	27.00	8.79	10.97	2.16	5.39	64.00	24.97	150.00
	NL1010T	27.00	3.96	3.96	2.41	3.00	61.00	12.44	150.00
	NL1011T	27.00	6.60	6.60	2.41	2.30	61.00	9.53	150.00
	NL1012T	27.00	8.79	8.79	2.41	2.72	61.00	11.28	150.00
	NL1013T	27.00	13.16	13.16	2.41	2.77	61.00	11.50	150.00
	NL1015T	27.00	8.79	10.97	2.39	2.70	61.00	11.28	150.00
	NL1020T	27.00	3.96	3.96	2.16	5.74	64.00	26.57	150.00
	NL1021T	27.00	6.60	6.60	2.16	5.05	64.00	23.38	150.00
	NL1022T	27.00	8.79	8.79	2.16	5.18	64.00	23.97	150.00
	NL1023T	27.00	13.16	13.16	2.16	5.31	64.00	24.59	150.00
	NL1025T	27.00	8.79	10.97	2.16	5.39	64.00	24.97	150.00
	RC12-2.5	27.00	30.00	30.00	4.04	2.56	66.00	6.33	150.00
	RC12-4	27.00	30.00	30.00	3.43	4.00	66.00	11.66	150.00
	RC12-6	27.00	40.13	40.13	4.01	3.35	66.00	8.36	150.00
	RC12-8	27.00	40.13	40.13	3.63	4.41	66.00	12.15	150.00
	RC3-2.5	27.00	16.00	16.00	4.04	2.34	65.00	5.80	150.00
	RC3-4	27.00	16.00	16.00	3.43	3.52	65.00	10.25	150.00
	RC3-6	27.00	19.99	19.99	4.01	3.25	65.00	8.11	150.00
	RC3-8	27.00	19.99	19.99	3.63	4.25	65.00	11.72	150.00
	RC6-2.5	27.00	23.50	23.50	4.04	2.35	65.00	5.83	150.00
	RC6-4	27.00	23.50	23.50	3.43	3.62	65.00	10.56	150.00
	RC6-6	27.00	30.00	30.00	4.01	3.33	66.00	8.31	150.00
	RC6-8	27.00	30.00	30.00	3.63	4.33	65.00	11.94	150.00
	SP1507	27.00	11.28	11.28	2.44	4.24	64.00	17.39	150.00
	SP1848	27.00	25.40	25.40	4.88	3.26	62.00	6.67	150.00
	SP1848-03AC	27.00	25.40	25.40	4.88	3.26	62.00	6.67	150.00
	SP5025	27.00	5.97	6.22	2.51	5.12	64.00	20.39	150.00
	SP5162	27.00	5.99	6.15	1.65	6.24	68.00	37.84	150.00
	SP5255	27.00	6.02	8.18	1.65	6.70	68.00	40.61	150.00
	SP5446	27.00	5.99	12.19	1.65	6.85	68.00	41.50	150.00
Melcor	H OT 1.2-18-F2A	25.00	7.20	6.00	2.70	3.38	64.00	12.52	225.00
	H OT 1.2-24-F2A	25.00	10.80	6.60	2.50	2.76	64.00	11.05	225.00
	H OT 1.2-30-F2A	25.00	12.30	6.20	2.40	3.19	64.00	13.28	225.00
	H OT 1.2-31-F2A	25.00	11.00	8.80	2.70	2.59	64.00	9.60	225.00
	H OT 1.2-65-F2A	25.00	13.20	13.20	2.70	3.06	64.00	11.35	225.00
	H OT 1.5-30-F2A	25.00	12.30	6.20	2.20	3.97	64.00	18.06	225.00
	H OT 1.5-31-F2A	25.00	11.00	8.80	2.40	3.23	64.00	13.47	225.00
	H OT 1.5-65-F2A	25.00	13.20	12.10	2.40	4.11	64.00	17.14	225.00
	H OT 2.0-30-F2A	25.00	12.30	10.30	1.80	3.19	64.00	17.72	225.00
	H OT 2.0-65-F2A	25.00	13.20	13.20	2.20	5.03	64.00	22.85	225.00
	HT2-12-30	25.00	34.00	30.00	3.60	1.96	63.00	5.45	225.00
	HT3-12-30	25.00	34.00	30.00	3.20	2.35	63.00	7.35	225.00
	HT4-12-40	25.00	34.00	30.00	3.20	3.24	63.00	10.11	225.00
	HT6-12-40	25.00	34.00	30.00	3.80	2.84	63.00	7.48	225.00
	HT8-7-30	25.00	44.00	40.00	3.60	2.90	63.00	8.05	225.00
	HT8-12-40	25.00	44.00	40.00	3.30	4.09	63.00	12.40	225.00
	HT9-3-25	25.00	29.00	25.00	4.90	2.76	66.00	5.63	225.00

MicropeIt	MPC-D301-M44	25.00	0.72	0.72	0.43	42.05	22.80	982.53	85.00	$0.88
(Thin Film)	MPC-D901-M44	25.00	4.80	4.80	0.43	62.93	21.90	1463.58		
TE Technologies	VT-127-1.0-1.3-71	27.00	30.00	30.00	3.60	4.00	71.00	11.11	200.00	
	VT-127-1.4-1.15-71	27.00	40.00	40.00	3.40	5.00	71.00	14.71	200.00	
	VT-127-1.4-1.5-72	27.00	40.00	40.00	3.90	3.88	72.00	9.94	200.00	
	VT-199-1.4-0.8	27.00	40.00	40.00	3.20	10.75	67.00	33.59	200.00	
	VT-199-1.4-1.15	27.00	40.00	40.00	3.40	7.50	69.00	22.06	200.00	
	VT-199-1.4-1.5	27.00	40.00	40.00	3.90	5.88	70.00	15.06	200.00	
Tellurex	CZ-1.0-127-1.27	50.00	34.00	31.00	3.20	3.67	79.00	11.47	100.00	
	CZ-1.4-127-1.65	50.00	40.00	40.00	3.70	3.50	79.00	9.46	100.00	
	CZ1-1.4-127-1.14	50.00	44.00	40.00	3.20	4.58	79.00	14.31	100.00	
	CZ1-1.4-219-1.14	50.00	54.00	54.00	3.20	4.77	79.00	14.90	100.00	
Thermion	1MC04-004-03		1.60	3.20	1.70	14.65	70.00	86.17	175.00	
	1MC04-008-03		3.20	3.20	1.70	14.65	70.00	86.17	175.00	
	1MC04-012-03		3.20	4.80	1.70	14.97	70.00	88.08	175.00	
	1MC04-018-03		4.80	4.80	1.70	14.76	70.00	86.81	175.00	
	1MC04-032-03		6.40	6.40	1.70	14.65	70.00	86.17	175.00	
	1MC04-064-03		9.60	8.00	1.70	14.32	70.00	84.25	175.00	
	1MC04-004-02		3.20	1.60	1.60	21.48	68.00	134.28	175.00	
	1MC04-008-02		3.20	3.20	1.60	21.48	68.00	134.28	175.00	
	1MC04-012-02		4.80	3.20	1.60	21.48	68.00	134.28	175.00	
	1MC04-018-02		4.80	4.80	1.60	21.70	68.00	135.63	175.00	
	1MC04-032-02		6.40	6.40	1.60	21.48	68.00	134.28	175.00	
	1MC04-060-02		9.60	8.00	1.60	20.83	68.00	130.21	175.00	

5.2 Studies of Competitive Products

5.2.1 Benchmarking of Competitive Technologies

Principal Investigator: Robert Staunton
Oak Ridge National Laboratory
National Transportation Research Center
2360 Cherahala Boulevard
Knoxville, TN 37932
Voice: 865-946-1351; Fax: 865-946-1262; E-mail:stauntonrh@ornl.gov

DOE Technology Development Manager: Susan A. Rogers
Voice: 202-586-8997; Fax: 202-586-1600; E-mail: Susan.Rogers@ee.doe.gov

ORNL Program Manager: Mitch Olszewski
Voice: 865-946-1350; Fax: 865-946-1262; E-mail: olszewskim@ornl.gov

---

Objectives

The Benchmarking of Competitive Technologies project is intended to conduct electrical and mechanical studies of hybrid electric vehicle (HEV) and plug-in hybrid electric vehicle (PHEV) systems as new system innovations are developed and introduced into the automotive market. The testing produces valuable data on efficiency, torque, speed, and voltage-current relationships that cannot be obtained from other open-literature sources. The full inspection and characterization of the electric motors and inverters also defines their thermal system performance in terms of temperature and corresponding sustainable power levels. Testing of these systems helps to rapidly advance the domestic technology base of electric traction drive systems suitable for HEV/PHEV applications.

The Oak Ridge National Laboratory (ORNL) testing program documents how the systems are manufactured and packaged and what performance limitations exist. These data are obtained by (1) thorough design inspections/assessments, (2) instrumenting the motor/inverter system, and (3) conducting locked-rotor, back-electromotive force (back-emf), thermal, and performance tests over the entire design envelope. These data permit ORNL to determine mechanical and electrical losses and map the inverter and/or motor efficiencies over the entire torque-speed domain.

Approach

Benchmarking of HEV traction drive systems provides detailed electrical and mechanical data from known permanent magnet synchronous motors (PMSMs) and inverters and yields information concerning their thermal performance. The overall approach of this project is to thoroughly define the systems and then perform a detailed evaluation of their performance in a controlled laboratory environment. This approach has proved to be technically sound and quite successful.

During the year, the efficiency mapping tests of the Prius were completed using a test plan developed in the prior year. This same methodology was duplicated for the evaluation of Accord subsystems. Accord activities included preparing the motor with a new rotor shaft design and motor end plates; preparing the inverter through analysis of the circuit and the construction of an auxiliary circuit; and tests that included back-emf, locked rotor, and efficiency mapping.

The technical approach for performing benchmarking evaluations during the year included the following tasks:

- Complete Prius subsystem testing, share detailed test data, and fully document the benchmarking activities. (Completed: May 2006)

- Test the performance of the Accord motor, inverter, and components in the laboratory to generate baseline performance data. (Completed: July 2006)
- Provide the auto company partners with a consistent, open-literature source for complete characterization of Accord technology recently introduced in the marketplace. (Completed: September 2006)
- Query DOE and industry partners regarding emerging technology issues and which competitive technologies hold the greatest technical interest. (Completion: duration of project)
- Based on resources, complete additional limited benchmark assessments of emerging hybrid technology selected by the FCVT program and/or FCVT technical partners. (Completed: September 2006)
- Continue to apply benchmarking information to assist in program planning efforts, developing and executing specific projects, and to support the partnership with the original equipment manufacturers at U.S. Council for Automotive Research. (Completion: duration of project)
- Confirm the realism of performance goals for the technologies and components and identify technology gaps. (Completion: duration of project)
- Use benchmarking data to validate/refine multiproject R&D modeling efforts so that they may be better used in developing new prototype designs to support research. (Successfully completed by some reseachers—ongoing as new results are published)
- Use results to confirm the validity of the project technology thrust and avoid duplication of existing efforts. (Completion: duration of project)
- Provide technical insights that can be used to guide research efforts. (Completion: corresponds to presentation and report dates)

Major Accomplishments

The FY 2006 accomplishments have made it possible to combine test data with design, packaging, and fabrication assessments to enable analysts to determine how various commercial HEV traction systems, such as the Accord and the Prius, compare with system and program technology targets (peak-power-to-weight and -volume ratios). ORNL and other researchers have used data from the benchmarking project in motor models such as Motorsoft SPEEDCAD, Flux2D (FEA), and PSAT (ORNL/Sentech). Other researchers at ORNL have used the data to (1) perform fabrication and cost analyses for the Prius motor and (2) conduct thermal control studies using ORNL's HEATING 7.3, a general-purpose, finite-difference conduction heat transfer model. Ongoing work on another model, developed as part of the benchmarking project, is described in "Future Direction."

The following summarize other major accomplishments of the project during the year:

- The efficiency mapping tests of the Prius PMSM and inverter were completed in a specially prepared test cell using an ORNL controller system developed for this project.
- The benchmarking design and packaging evaluation were completed for the Accord subsystems.
- The Accord motor was prepared with a new rotor shaft design and motor end plates, and the inverter was prepared through analysis of the circuit and the construction of auxiliary circuitry.
- Tests were completed on the Accord subsystems that included back-emf, locked rotor, and efficiency mapping.
- Prius and Accord technical evaluations and test results were documented, and technical reports were issued for both during the year.
- Special by-request benchmarking evaluations were also completed and are documented in this report (see Technical Discussion).

Technical Discussion

The 2005 hybrid Accord is an example of how the automotive industry is introducing hybrid technology to preexisting vehicle models. This Accord design is considered to be a "mild hybrid" because

of the small power rating of the integrated motor assist (IMA) and the fact that it is used only for acceleration assist to the engine. The PMSM/inverter system is not used for acceleration without engine power as in the case of a "strong hybrid." After the vehicle reaches highway speeds, the IMA is used to contribute torque during moderate or strong accelerations.

In contrast, the Prius was designed from the beginning to be a hybrid vehicle and is considered to be a "strong hybrid." Many of the significant Accord vs Prius design differences are summarized in Table 1.

The Accord PMSM casing is very narrow (68 mm) to allow it to be inserted between the engine and torque converter. Consequently, the motor was designed without a full casing (ends are missing), and the rotor was designed without a shaft and bearings. In preparation for motor operation in the ORNL laboratory, a shaft was designed and installed in the rotor, and end plates with bearings were designed and installed. The completed, stand-alone motor assembly is shown in Figure 1. The completed test stand is shown in Figure 2.

Locked Rotor Test

A series of locked rotor tests were performed to determine the torque-producing behavior of the PMSM motor. A motorized mechanical-gear mechanism was used to precisely position and lock the rotor based on readings from the absolute position sensor in the motor.

A motor-driven gear mechanism was used to rotate the motor incrementally every 5 electrical degrees, and the fixture remained rigidly locked each time a set level of dc current was applied. Torque values were obtained from an in-line shaft torque sensor when the motor windings were energized. The resulting Accord and Prius data were used to produce torque-vs-shaft-angle plots, which are shown in Figure 3 for various current levels and more than one-half an electrical cycle. The levels of torque that were produced reflect the absolute maximum torque obtainable from the motor for each current (magnetic

Table 1. Differences between the hybrid Accord and the Prius

Design feature	Hybrid Accord	Prius
Motor peak power rating, kW	12.4 @ 840 rpm	50 @ 1200–1540 rpm
Motor peak torque rating, Nm	136	400
Separate generator	No	Yes (although the motor also serves as a generator)
PMSM used for initial acceleration	Engine assist	Exclusively
Source of power to PMSM	Battery	Generator and battery
Purpose of the hybrid system	Primarily performance	Primarily improved fuel economy
PMSM rotor design	Interior permanent magnets embedded near the rotor surface	Interior permanent magnets with "V" configuration at each pole
Number of rotor poles	16	8
Boost converter used	No	Yes
Inverter bus voltage	144	200–500
PMSM cooling	Passive cooling	Water/glycol loop
Inverter cooling	Forced air convection	Water/glycol loop
Location of inverter	Behind rear seat in passenger compartment	Engine compartment
Physical integration of the PMSM	Flat (68-mm) motor-only assembly located between engine and torque converter; the rotor shaft is replaced by dual rotor hubs with bolt flanges	PMSM is included in an engine-mounted casing ("axle assembly") that contains the generator and planetary gear/reduction gear assemblies

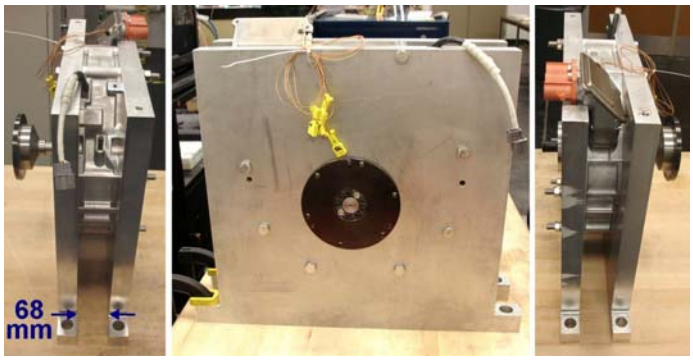


Figure 1. Accord motor with custom-designed end plates and shaft.

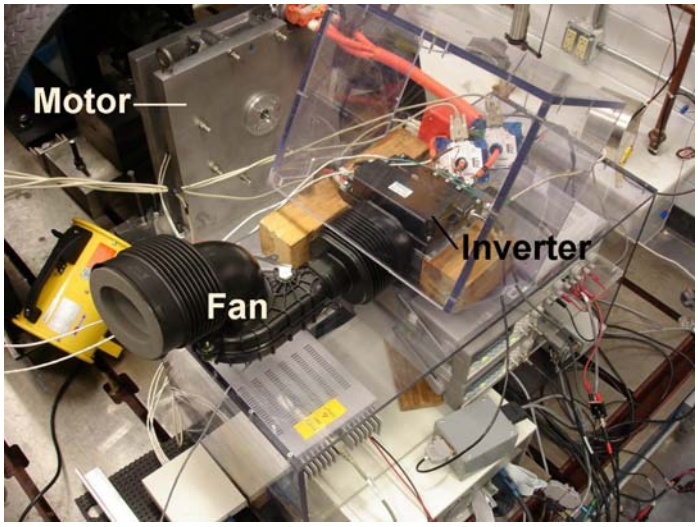


Figure 2. Preparation of test cell for Accord performance testing.

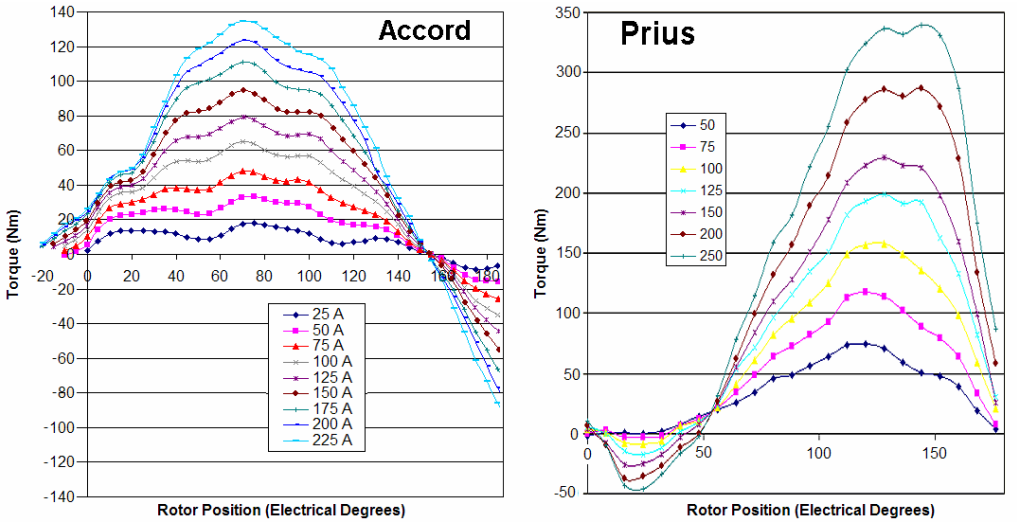


Figure 3. Accord/Prius locked-rotor torque vs electrical position at varying levels of stator current.

torque and reluctance torque). In contrast to an operating motor, there are no eddy current core losses, losses due to windage, and bearing friction.

Prius testing did not continue to the full torque specification of 400 Nm because of rapidly escalating stator winding temperatures. To collect several sets of data for averaging, it was necessary to remain at each speed-torque combination for about 20 s.

Accord/Prius Efficiency Mapping Data

Figures 4 through 6 show comparisons of the Accord and Prius Efficiency contour maps for the motor, inverter, and motor plus inverter, respectively. In each case, the bottom plot is for the Prius, and it shows comments pertaining to how the Prius efficiency compares with Accord efficiency for the designated area of the map. These comments are "broad-brush" comparisons and should not be taken in a precise, mathematical sense. For instance, very narrow contour regions of the map may be disregarded in the interest of placing emphasis on the larger, more significant areas.

The most important conclusion to be drawn from these figures is the fact that, in terms of efficiency, the Prius inverter excels, the Accord motor excels (except in the high-speed, low-torque region), and the combined HEV system efficiency is essentially the same except at the low-speed (<1000 rpm), high-torque region* where the Accord efficiency excels and the high-speed range where the Prius excels.

*Expressions such as "low-speed, high torque" for the Accord and Prius systems simply refer to corresponding areas or domains in the speed-load maps, even though the actual torque values may be quite different.

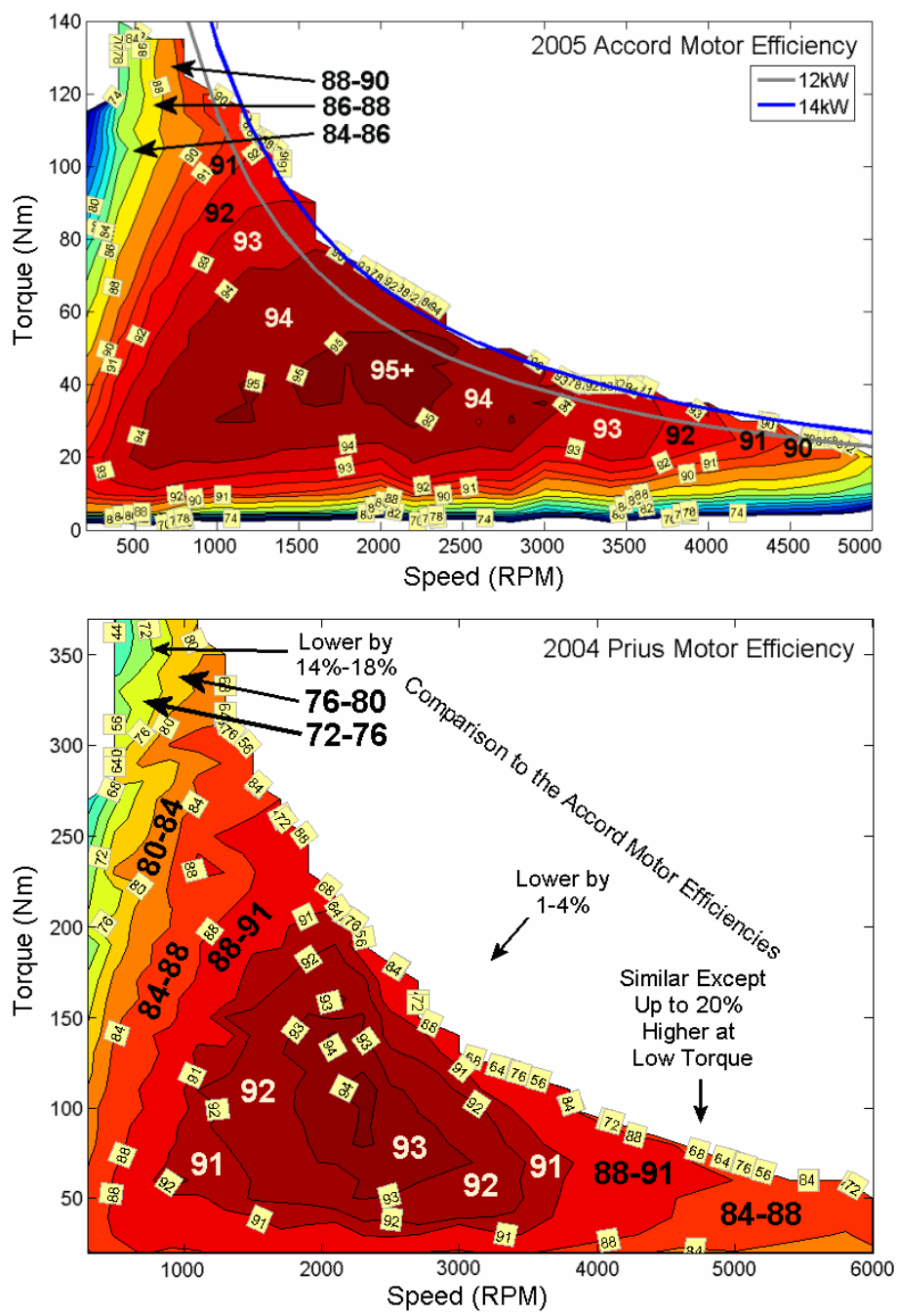


Figure 4. Comparison of Accord and Prius motor efficiency contour maps.

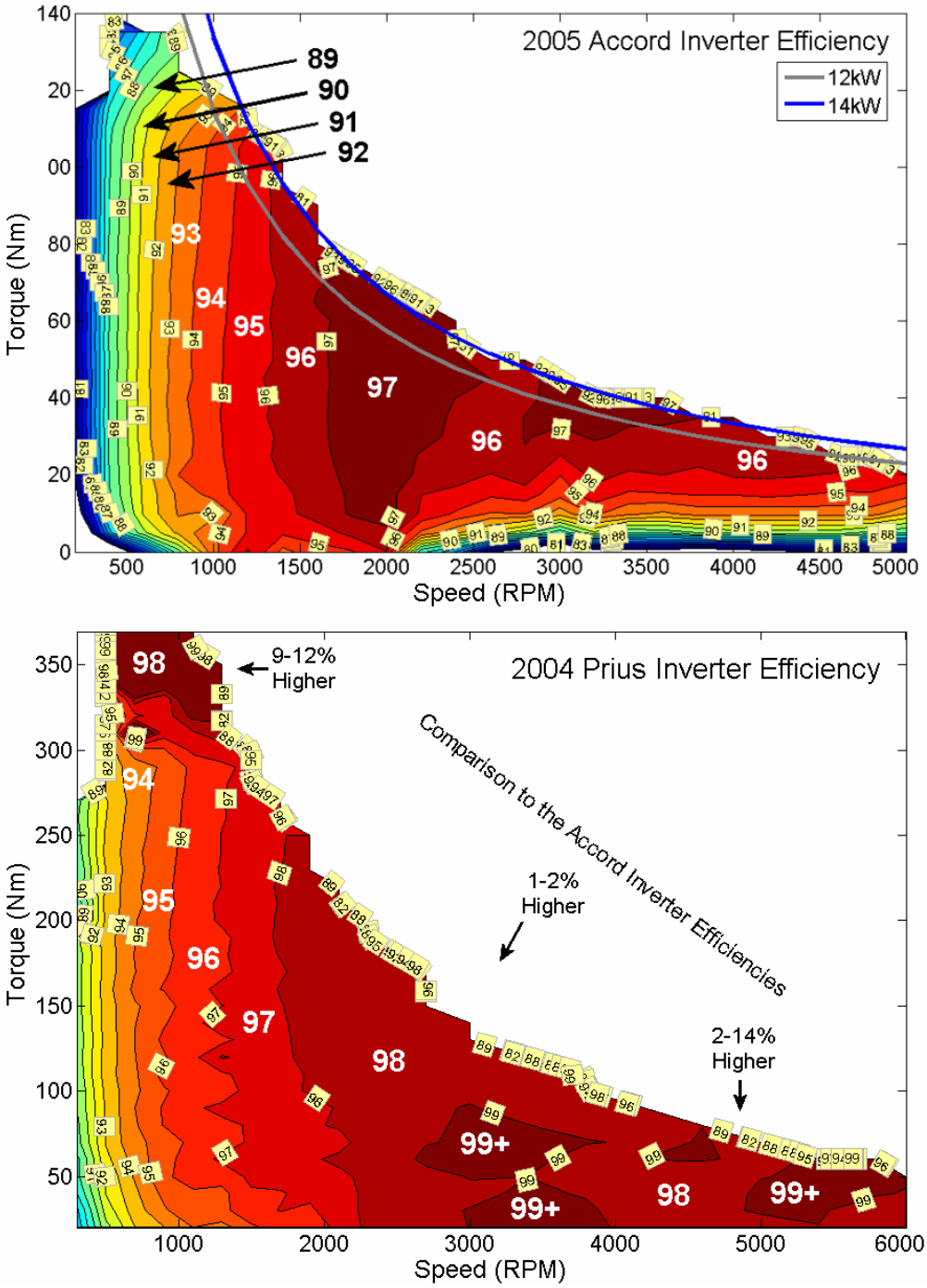


Figure 5. Comparison of Accord and Prius inverter efficiency contour maps.

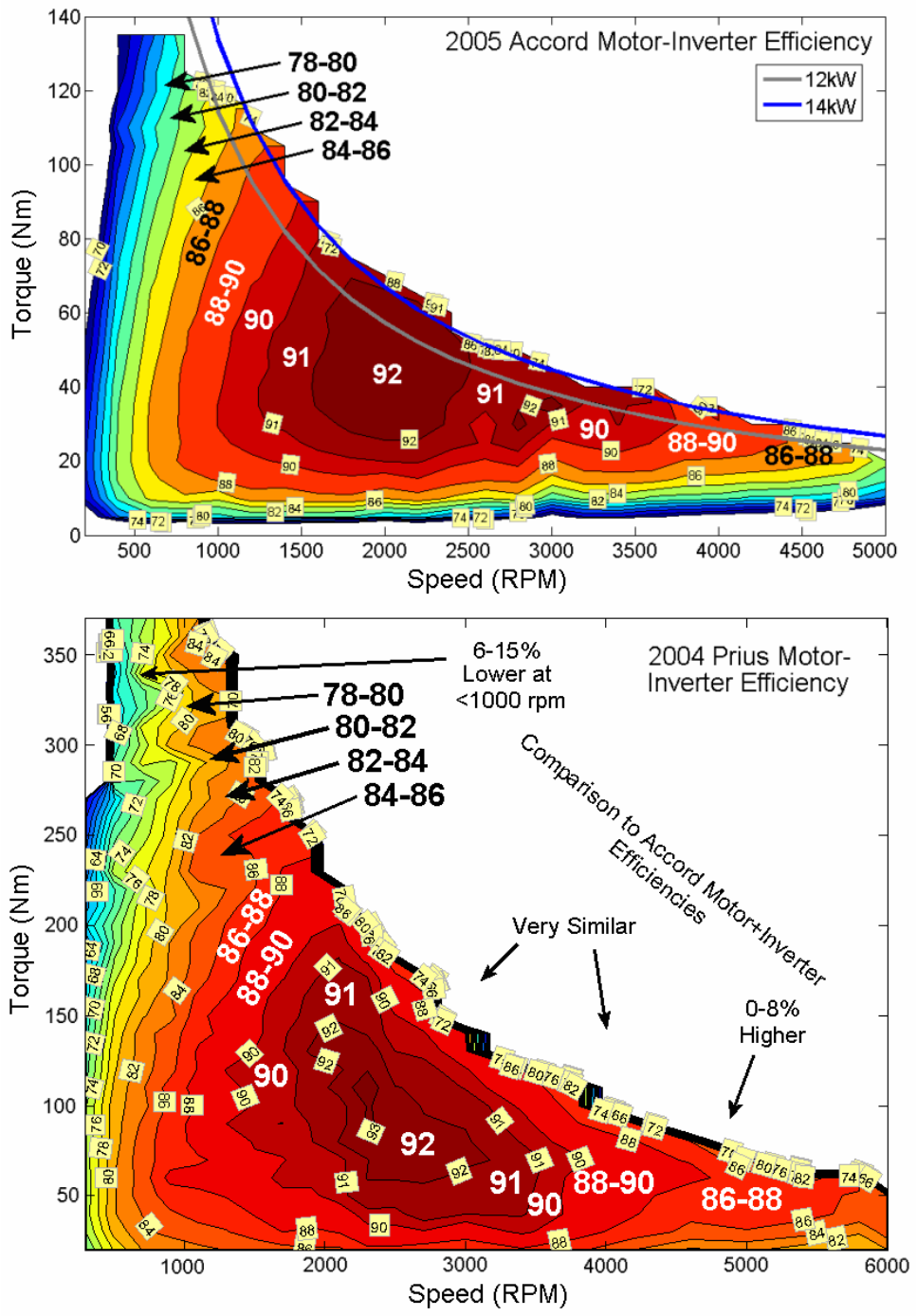


Figure 6. Comparison of Accord and Prius motor plus inverter efficiency contour maps.

Design Parameters for Prius/Accord

Table 2 summarizes the motor design and inverter insulated gate bipolar transistor (IGBT) ratings for the original Prius, the 2004 Prius, and the 2005 hybrid Accord designs. Included in the table are several design parameters describing each PMSM stator and rotor assembly and the PM volume and mass. Figure 7 provides clarification regarding the PM configurations used in each of the vehicle designs.

Table 2. Comparison of design parameters for Prius and Accord

Parameter	Prius I	Prius II	Accord	Comments
Stator OD, mm	269	269	315.5	
Stator ID, mm	162	162	232	
Rotor OD, mm	160	160	230	
Rotor ID, mm	115.6	111	188	
Rotor stack length, mm	90.7	83.6	41.2	Lamination only
Stator stack length, mm	89	84	40.1	Lamination only
Air gap, mm	1	1	1	
Lamination thickness, mm	0.356	0.33	0.343	
End-turn length, mm	83	80	35	Approx middle line
End-turn length (phase lead side), mm	83	80	35	Approx middle line
End turn arc extension, mm	31.8	30.5	~6.5–10	
Stator turns per coil	9	9	52	
Parallel circuit per phase	2	0	8	
Turns in series per phase	4	8	0	
Number of poles	8	8	16	
Number of stator slots	48	48	24	
Number of wires in parallel	13	13	0	
Wire diameter	Awg 19	Awg 19	1.55 mm	
Slot depth, mm	33.5	33.5	30.6	
Slot opening, mm	1.93	1.93	4.75	
Slot area, mm	–	–	307	
Phase resistance at 21°C, ohm	0.017	0.069	0.0097	
Stator winding mass, kg	7.48	6.8	3.01	
Stator core mass, kg	19.7	19.05	7.704	Laminations only
Rotor mass, kg	10.2	10.2	8.02	Prius I/II included bearings; Accord without bearings
Magnet width, mm	34.8	18.9	18.45	Individual magnets or bonded pairs as applicable
Magnet thickness, mm	6.15	6.5	4.46	Individual magnets or bonded pairs as applicable
Magnet length, mm	90.3	83.1	40.4	Individual magnets or bonded pairs as applicable
Magnet volume, mm	19330	10210	3320	For a pole, double Prius II and Accord volumes
Magnet mass, g	144	76	25	For a pole, double Prius II and Accord masses
IGBT current rating, A	Not tested	~195	~175	Max i during tests (per phase or IGBT pair)
IGBT voltage rating, V	600	1200	300 or 600	Assumed rating based on peak V

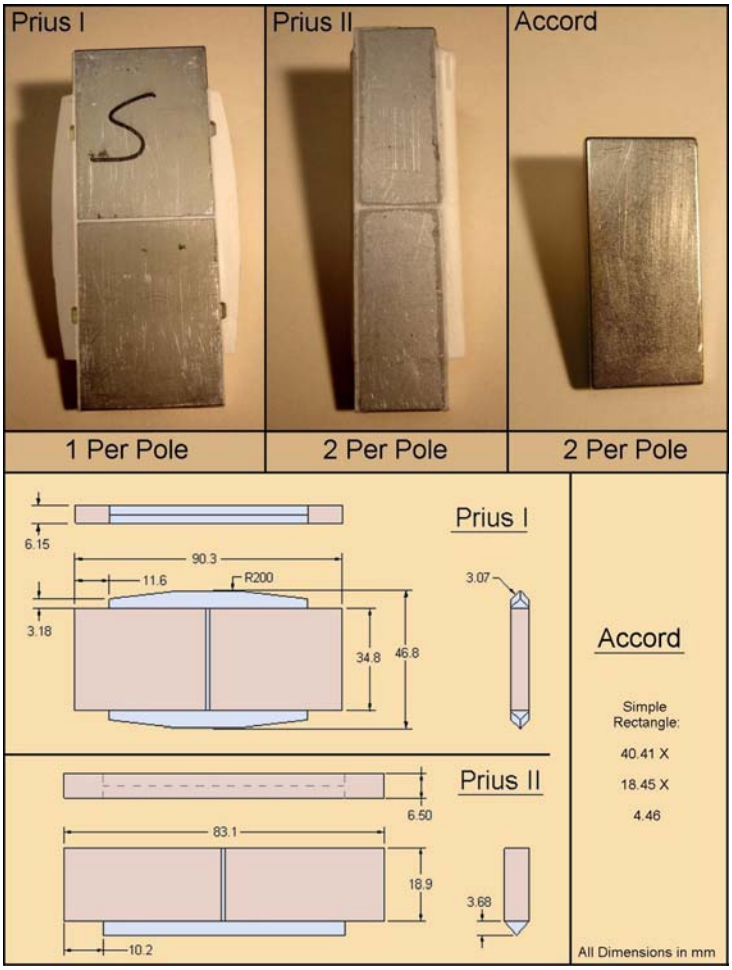


Figure 7. PM configurations and dimensions for three hybrid rotor designs.

Prius Inverter-only Mass and Volume Estimates

This section derives the inverter and casing mass and volume estimates for the Prius as if the buck/boost converter and generator-related circuitry did not exist. This has not been previously documented in any benchmarking report. The total volume of the Prius inverter/converter casing is 17.8 L as depicted in Figure 8.

The total volume of the Prius "inverter *only"* with resized casing is 9.9 L and is derived as follows:

- The midsection volume is reduced by 55% to account for the exclusion of the converter components, the generator portion of the inverter board (a 1/2 reduction), the generator portion of the power module (a 1/3 reduction), and the corresponding portion of the cold plate (a 60% reduction). See the change in the size of the cold plate in Figure 9 as a visualization aid.
- The casing is also reduced by the deletion of the bottom compartment (unrelated circuitry).
- The "cap" volume (or lid and capacitor volume) is retained in full.

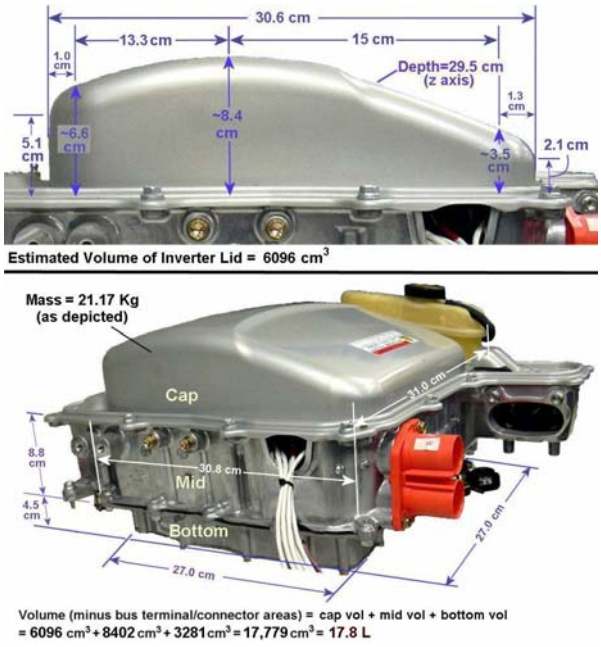


Figure 8. Volume of entire Prius inverter/converter assembly.

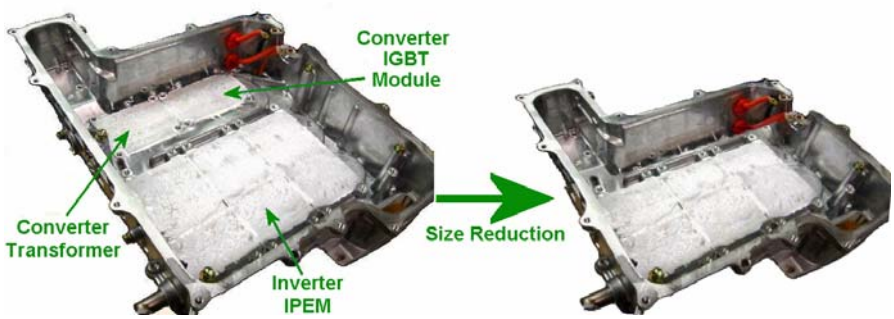


Figure 9. Conceptual change to inverter/converter casing for excluding the buck/boost converter.

The total mass of inverter/converter casing as depicted in Figure 8 is 21.2 kg.

The total mass of the "inverter *only*" is 9.4 kg and is derived in a similar manner to the volume (100% of cap mass, 45% of midsection mass, and 0% of bottom section mass). To be more precise, the mass of the converter transformer and converter power module were first fully excluded before the 45% was applied to the remainder of the midsection. This is quite significant considering that the converter transformer has a mass of 2.57 kg.

Prius Planetary Gear Packaging

The 2004 Prius has a planetary gear assembly that is integral to the motor/generator casing, and it is linked to reduction gears and a differential. Figure 10 shows the gear assembly with number-of-teeth

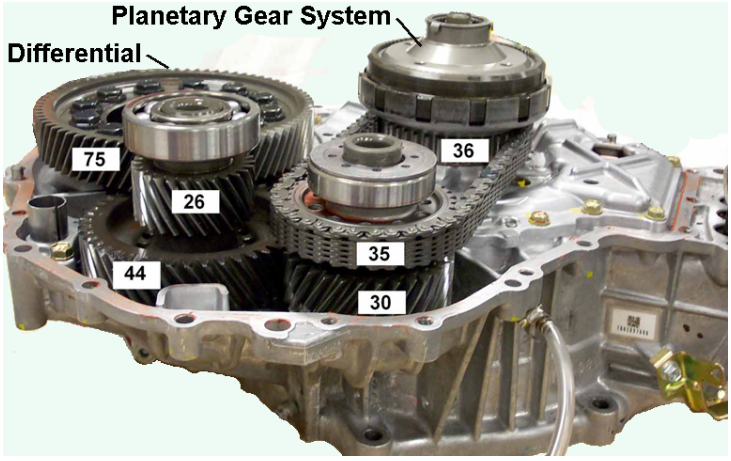


Figure 10. 2004 Prius gear assembly in an open casing.

labels on each gear. The planetary gear system uses the chain depicted in the figure to drive a series of reduction gears that power the differential and the axles. Because of the integral design, certain assumptions and estimates must be made to determine approximate mass and volume of the planetary gear system. The information provided in this section will include certain details on discrete components.

Figure 11 lays out the same gearing components as shown in Figure 10 and supplies masses associated with each. The fasteners represent an approximation because they were not fully inventoried.

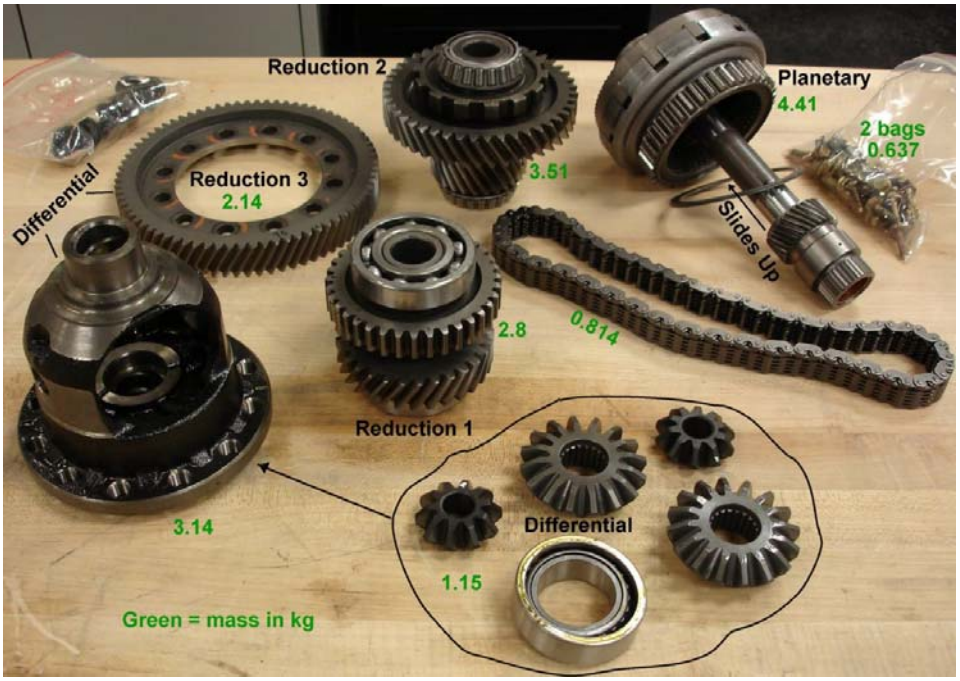


Figure 11. Components making up the Prius gear box.

The casing for the assembly is not shown, and because of the two-piece design that is shared with the generator and motor, mass and volume estimates are difficult to produce with precision. Nevertheless, it is estimated from mass measurements of selected and modified Prius gear/motor casing parts that the entire gear assembly could be housed in an ~8-kg casing with a 17-L volume [also see Figure 12(a)].

A close-up of the partially disassembled planetary gear assembly with the top and bottom plates removed is shown in Figure 12(b).

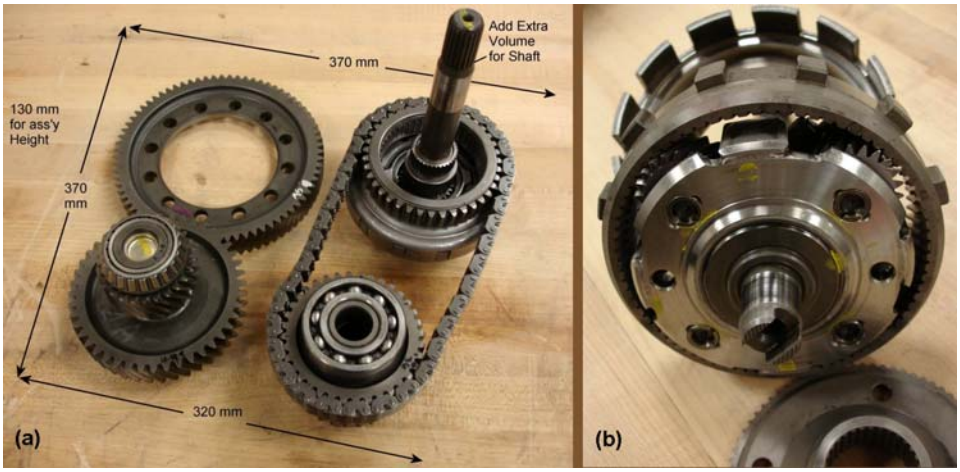


Figure 12. Approximate volume estimation and planetary gear assembly.

Additional information regarding dimensions for both components and the assembly are given in Figure 13.

Core loss tests

The core losses can be determined from energized spin tests where the motor shaft is uncoupled. Figure 14 provides the ac electrical power vs speed plot for the Accord PMSM.



Figure 13. Dimensions for planetary gear, the first reducer gear, and extension.

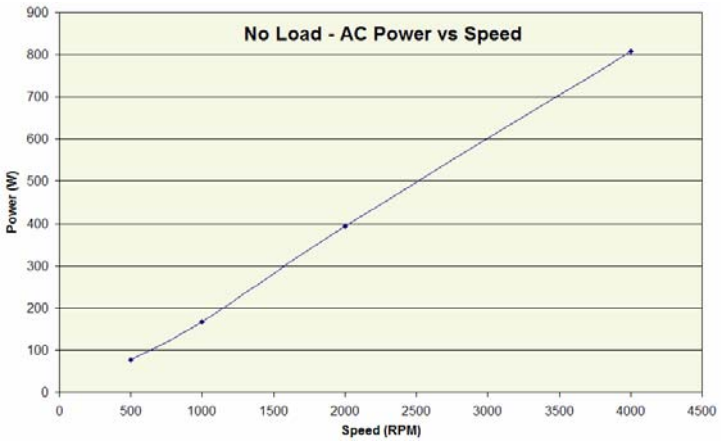


Figure 14. Uncoupled, energized spin test of the Accord motor to assess core losses.

Conclusion

The benchmarking project has been very successful in assessing the Prius and Accord designs and completing a full range of tests, including back-emf, locked-rotor, and efficiency mapping tests. The sets of data obtained from these tests have (1) helped to provide a technical basis for the FCVT management to determine program targets/direction and (2) enabled researchers to improve/refine their analytical models so that greater accuracy is obtained for high-power density PMSMs.

Future Direction

The FY 2007 goal of the benchmarking project is to complete testing of various traction drive subsystems that would be useful to the FCVT program integration/management. The design, packaging, and fabrication assessments will be combined with comprehensive performance mapping test results to enable analysts to determine how each HEV/PHEV traction drive subsystem compares with the other and with program technology targets (thermal efficiency, peak power density, and peak specific power goals). The project will focus on inverters, converters, and PMSMs. Since FY 2006, the impact of the collective data obtained from each vehicle has impacted the broader program, including program planning. This is expected to continue in FY 2007.

One specific test planned for FY 2007 is an assessment and performance evaluation of a high-speed PMSM such as used in the Toyota Highlander and the Lexus GS450 and RX400h. High-speed operation, up to 12,500 rpm, is clearly the most recent hybrid technology that has been successfully introduced into the market.

The Benchmarking project will continue its efforts to improve the accuracy of a PMSM model using data obtained from no-load and back-emf tests. Because the empirical approaches used in the performance tests ensure optimal operation, high-quality data are obtained that are well suited for this purpose. The model will effectively incorporate effects of saturation and the impact of variance in other parameters such as stator resistance and inductance, all of which fluctuate with speed, current, or temperature. The efforts to improve the motor model will aid in understanding the operational behavior of the 2006 Accord motor and other interior PM motors of similar design.

If capital funding is obtained in FY 2007, the project will upgrade the test cell with a larger dynamometer to permit the testing of high-power motors. The need for this can be underscored by considering that if the Prius motor had actually been capable of providing 400 Nm without rapid thermal

escalation beyond short-term limits, the ORNL dynamometer would have proved to be inadequate to support thorough testing.

Limited evaluation of state-of-the-art capacitors and magnetic materials will be performed to ascertain their applicability for use in high-power, high-temperature FreedomCAR automotive applications.

Publications

R. H. Staunton, C. W. Ayers, J. Chiasson, T. A. Burress, and L. D. Marlino, *Evaluation of 2004 Toyota Prius Hybrid Electric Drive System*, ORNL/TM-2006-423, Oak Ridge National Laboratory, May 16, 2006.

R. H. Staunton, T. A. Burress, and L. D. Marlino, *Evaluation of 2005 Honda Accord Hybrid Electric Drive System*, ORNL/TM-2006-535, Oak Ridge National Laboratory, UT-Battelle, LLC, September 2006.

5.2.2 Component Characterization

Principal Investigator: Larry Seiber
Oak Ridge National Laboratory
National Transportation Research Center
2360 Cherahala Boulevard
Knoxville, TN 37932
Voice: 865-946-1334; Fax: 865-946-1400; E-mail: seiberle@ornl.gov

DOE Technology Development Manager: Susan A. Rogers
Voice: 202-586-8997; Fax: 202-586-1600; E-mail: Susan.Rogers@ee.doe.gov

ORNL Program Manager: Mitch Olszewski
Voice: 865-946-1350; Fax: 865-946-1262; E-mail: olszewskim@ornl.gov

---

Objective

As capacitor and magnet technologies mature, it is important to ascertain the limitations of these new technologies by subjecting the components to testing that will evaluate their capabilities and limitations. The object of this project is to test and characterize new capacitor and magnet components to determine their ability to provide improvements in power electronics and motor designs to meet the FreedomCAR goals.

Approach

- Capacitor performance data were acquired by testing over temperature in both static and dynamic modes of operation. A data acquisition system (DAQ) was developed and used to log the test results for the capacitor parameter evaluations.
- A full four-quadrant hysteresis graph was used to evaluate the new magnet technologies over an expanded temperature range.

Major Accomplishments

- Commercial film and ceramic capacitor benchmarks were defined and characterized.
  Capacitor test samples were tested in two modes, statically and dynamically. Capacitor testing in the static mode requires a thermal cycling process that must continue uninterrupted for extended periods of time. Capacitor testing in the dynamic mode requires testing at thermal extremes and requires ripple current and bias voltage input from the operator.
- Magnet benchmarks for bonded and sintered magnets were defined and characterized.
- Magnet test samples were tested over a temperature range from 20 to 235ºC.
- The development of a DAQ using LABView was completed to control the environmental chamber and log data from the measuring instruments for capacitor evaluations.

Technical Discussion

Data Acquisition System

The DAQ consists of a Dell Precision 380 Workstation running LABView 7.1. In the static mode the instruments used are an Espec environmental chamber and an Agilent 4284 LCR meter. Figure 1 shows the input screen for the static test.

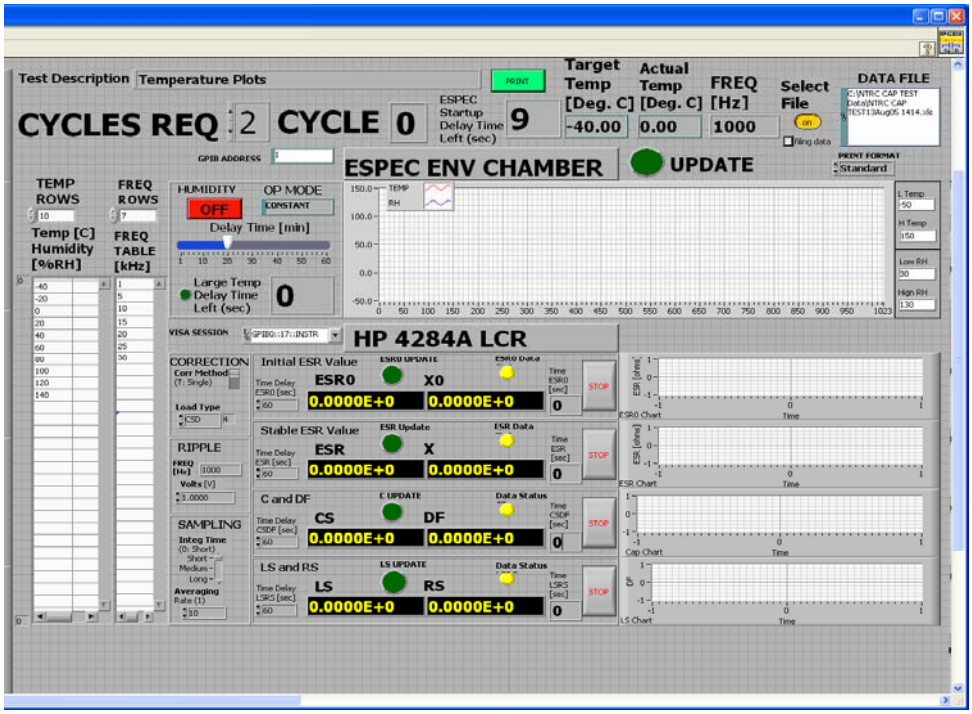


Figure 1. Static test input screen.

At the beginning of the static thermal cycling test, temperature steps and test frequencies are entered in the tables on the left of the screen. A test description is entered at the top of the screen, and the number of cycles requested is also entered. A delay time is set using the slider bar in the large temperature delay time window. This preprogrammed delay is to ensure that the temperature of the dielectric has equalized once the target temperature of the environmental chamber has been reached. When the temperature difference between the ambient temperature of the chamber and the target temperature of the chamber is 40ºC or greater, the preprogrammed delay is invoked after the target temperature is reached. The amount of delay is determined by the operator and is based on the size of the capacitor. A larger capacitor will require a larger delay to ensure that the temperature of the dielectric is uniform.

Once data have been entered, the program turns on the environmental chamber and commands a target temperature to the chamber. After the target temperature is reached and the preprogrammed delay time is met, the program sends a command to the LCR meter to output the first test frequency and then begin to monitor the equivalent series resistance (ESR) from the capacitor under test. When that value is stable, the ESR is recorded, and the next parameter is measured and recorded. After the ESR, the dissipation factor (DF), and capacitance value are recorded at the first test frequency, the command is given to the LCR meter to output the next test frequency and the monitoring and recording process is repeated. After all data are recorded at all test frequencies, the next temperature step is commanded to the environmental chamber, and the process is repeated.

Capacitor testing in the dynamic mode also uses the DAQ. Figure 2 shows the dynamic test input screen.

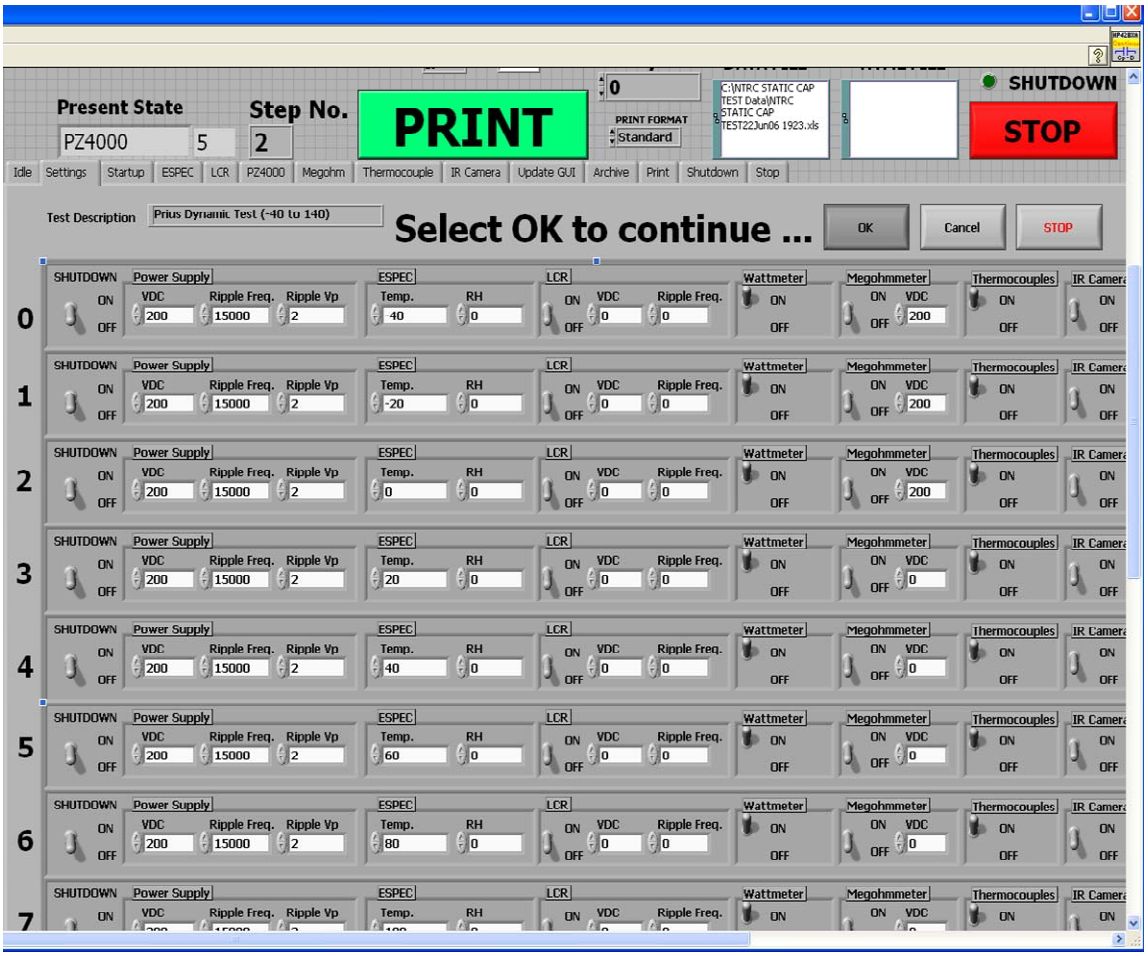


Figure 2. Dynamic test input screen.

Capacitor testing in the dynamic mode requires a dc bias voltage to be applied to the capacitor under test along with a ripple current. The maximum bias voltage value is 75% of the maximum rated dc voltage of the capacitor. The dc bias voltage is applied in series with the secondary of a transformer and across the capacitor under test. The primary of the transformer is connected to the output of an ac amplifier, and a signal generator is connected to the ac amplifier. This configuration will provide a ripple current that is at a dc level similar to what would be seen in an inverter. The signal generator also allows the ripple current frequency to be adjusted. The ripple current value in amps can be adjusted by adjusting the gain of the ac amplifier.

Thermocouples are attached at three different locations on the capacitor, one on each end and one in the middle to monitor temperature rise as ripple current values increase.

After the bias voltage and ripple current have been adjusted, the DAQ dynamic mode is activated, and temperature limits and steps are entered. Ripple current amplitude and frequency can be changed along with the dc bias voltage at each temperature step if needed. Different measuring instruments can also be selected or turned off at each temperature step. Instruments can be selected or deselected by clicking on the toggle switch located on the front panel of the dynamic test input screen in Figure 2.

After all temperature step values, dc voltage values, and test frequencies have been entered, the program turns on the environmental chamber, commands a target temperature, and begins monitoring the chamber temperature. When the target temperature is reached, the program waits for operator input before logging ripple current, chamber temperature, and thermocouple data. The next temperature step will then be commanded.

Static Testing

Single Prius film capacitor

A single 140-µF 600-Vdc film capacitor was extracted from the 2004 Prius capacitor module to use as a benchmark for film capacitor evaluations. The module was taken to a materials lab to be x-rayed to identify the layout of the ten capacitors in the module. The film was brought back to the Power Electronics on Electric Machines Research Center lab, and several single capacitors were extracted for testing. Figure 3 shows the test configuration used to evaluate the single Prius capacitor, in the static and dynamic mode, inside the environmental chamber.

The capacitor was placed in a vise with copper strips on each end bent to allow connection to a cable capable of carrying high ripple currents. Electrically insulating material was added between the vise and the copper strips. This material also provided some thermal insulation in an effort to keep the vise from becoming a heat sink during the ripple current vs temperature evaluation.

Figure 4 shows the results of the static test on the single Prius film capacitor.

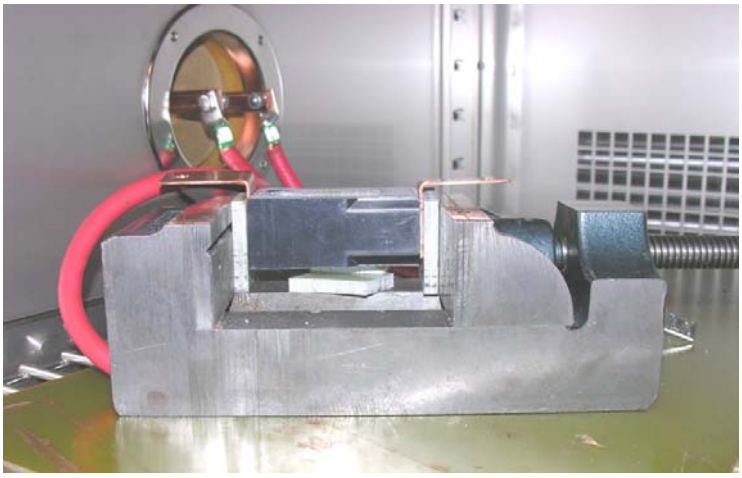


Figure 3. Single Prius film capacitor test set up.

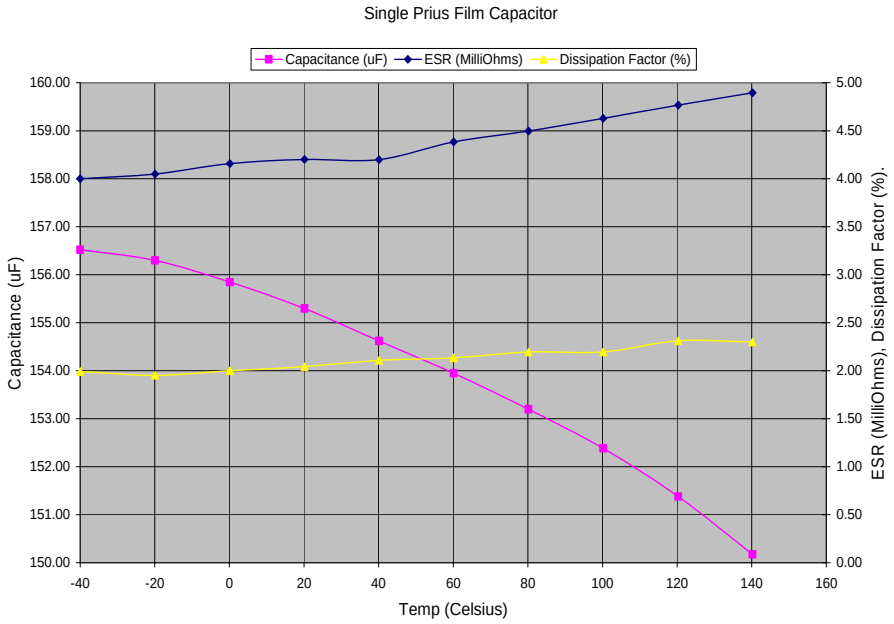


Figure 4. Single Prius film capacitor tested in the static mode at 5 kHz.

When tested at 5 kHz, the DF increased less than 0.5% over the entire temperature test range of –40ºC to 140ºC. The capacitance value decreased less than 5%, and the ESR increased less than 1 mΩ.

The ESR, DF, and capacitance values of the single Prius capacitor were evaluated at frequencies of 1 kHz, 2 kHz, 5 kHz, 10 kHz, and 15 kHz at three different temperatures: –40ºC, 20ºC, and 120ºC. Figures 5–7 show these results.

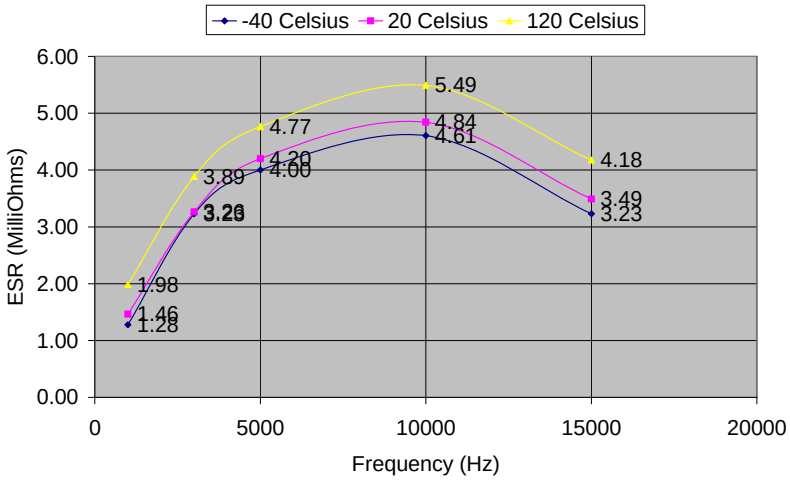


Figure 5. Single Prius film capacitor ESR frequency response.

The ESR peaked at 10 kHz at all temperatures and increased from an average of 1.57 mΩ at 1 kHz to an average of 4.98 mΩ at 10 kHz. The average at 5 kHz was 4.32 mΩ.

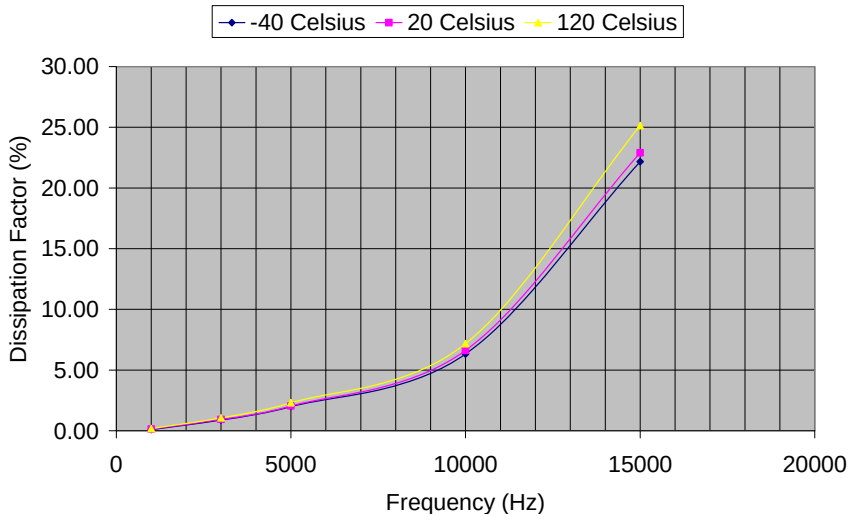


Figure 6. Single Prius film capacitor DF frequency response.

The DF increased from a value of 0.14% at 1 kHz to a value of 2.04% at 5 kHz. At 10 kHz, the average value was 6.7%. The increase was substantial above 10 kHz.

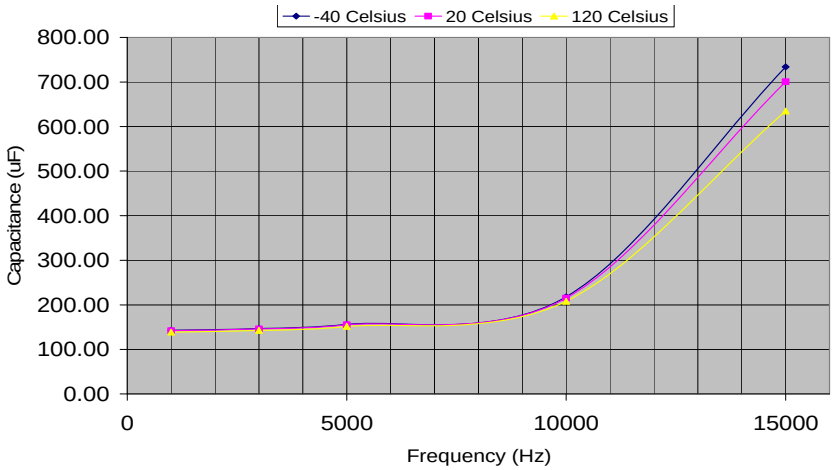


Figure 7. Single Prius film capacitor frequency response.

The capacitance value increased 9% from 1 kHz to 5 kHz at all three temperatures. Above 10 kHz, there was a very substantial increase in capacitance that was evident up to 15 kHz.

Kemet ceramic capacitor

A Kemet 1-µF 500-Vdc ceramic capacitor was tested in the static mode as a ceramic benchmark. The capacitor is rated at 200ºC. Figure 8 shows ESR, DF, and capacitance values over the temperature range of –40ºC to 180ºC.

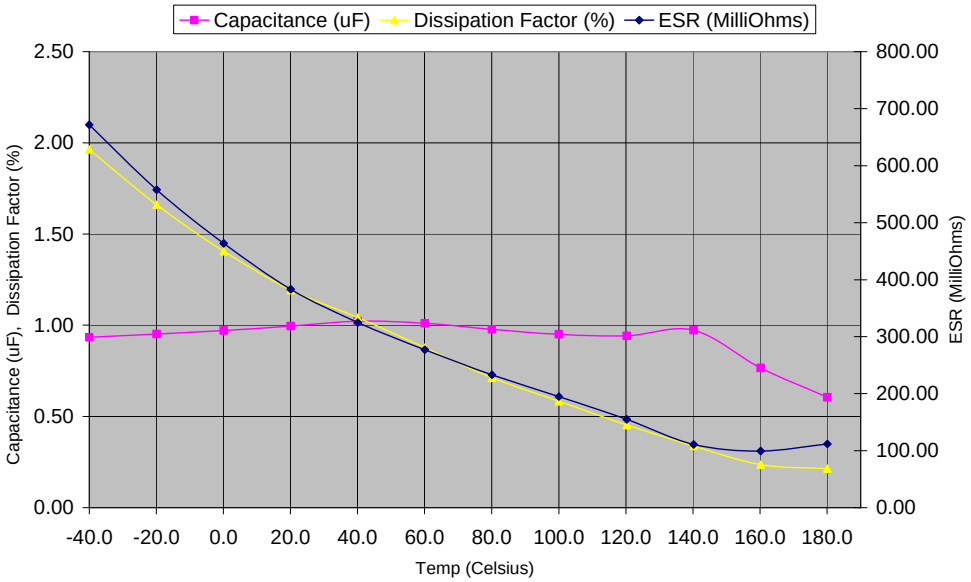


Figure 8. Kemet ceramic capacitor static test at 5 kHz.

The Kemet 1-µF ceramic capacitor was tested over the temperature range of –40ºC to 180ºC. The DF decreased from 1.96% to 0.21%, and the ESR changed from 671 mΩ to 111 mΩ. The capacitance value was basically flat up to 140ºC; at that point it changed from 0.93 µF to 0.61 µF at 180ºC.

Penn State multilayer ceramic capacitor

Pennsylvania State University (Penn State) supplied a 90-nF 500-Vdc high-temperature prototype multilayer ceramic capacitor for evaluation. The capacitor is rated at 300ºC. The static test of this capacitor at 5 kHz is shown in Figure 9.

The Penn State 300ºC prototype multilayer ceramic capacitor was tested in the static mode at 5 kHz over the temperature range of –40ºC to 180ºC. The DF decreased from 6.39% to 1.8%, and the ESR decreased from 144 Ω to 8.68 Ω. The capacitance value increased from 14.1 nF to 66.5 nF.

This capacitor did not function well at lower temperatures, but as the temperature increased it continued to improve. The capacitor was rated at 300ºC, but the evaluation was made to 180ºC because of the limitations of the environmental chamber.

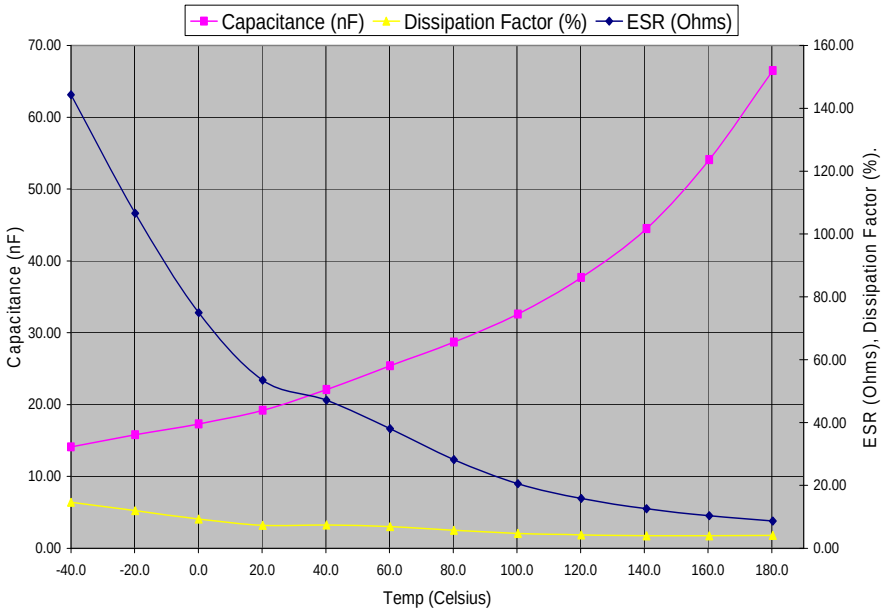


Figure 9. Penn State ceramic high-temperature static test at 5 kHz.

Dynamic Testing

The single film capacitors extracted from the Prius capacitor module were also tested in the dynamic mode. The bias voltage was 250 Vdc. Maximum ripple current was determined at several different ambient temperatures; leakage current and effective series inductance (ESL) were also measured. No prototype film capacitors were supplied to Oak Ridge National Laboratory for dynamic tests during this reporting period.

Because of the size and the fact that they will not be used as a dc bus filtering capacitors, the smaller value ceramic capacitors were not tested in the dynamic mode.

Single Prius film capacitor ripple current

Figure 10 shows the results of a single 140-µF Prius film capacitor's ripple current test. This capacitor was extracted from the Prius capacitor module and was tested by increasing the ripple current and measuring the temperature rise above an ambient temperature of 22ºC. The test was repeated at an ambient temperature of 100ºC.

The maximum ripple current was determined by increasing the current in 5-A steps until the capacitor failed. After each increase, the temperature on the surface of the capacitor was allowed to stabilize before increasing the ripple current to the next value. At 100ºC ambient, the capacitor failed after 20 min at 70 A of ripple current. The ambient temperature was raised to 140ºC, and another single film capacitor was tested from the Prius module. This capacitor failed at 20 A ripple current after 30 min. The ambient temperature was decreased to –40ºC, and another single film capacitor was tested from the Prius module. This capacitor failed at 100 A of ripple current after 35 min. Table 1 lists these ripple current limits. All tests were done at 5 kHz. The capacitors failed when their film melted and thus shorted.

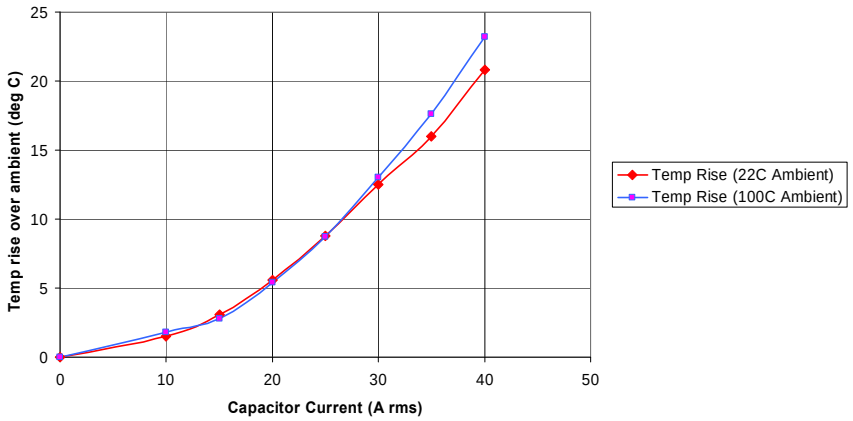


Figure 10. Temperature rise over ambient at 5 kHz.

Table 1. Maximum ripple current for the single Prius film capacitor

Ambient temperature	20 A	70 A	100 A
–40ºC			Failure after 35 min
100ºC		Failure after 20 min	
140ºC	Failure after 30 min		

Single Prius film capacitor leakage current

Leakage current test results measured on a single Prius film capacitor using a Danbridge 621 megohmmeter are listed in Figure 11. The capacitor was placed in the environmental chamber, and leakage current was measured at five different temperatures: 25ºC, 40ºC, 60ºC, 80ºC, and 100ºC.

Leakage current increased through the single Prius film capacitor from 16 nA to 16 µA over the test range of 25ºC to 100ºC.

Single Prius film capacitor ESL

ESL was measured on the single Prius film capacitor using a method and circuit configuration offered by Electronic Concepts, Inc. This circuit is shown in Figure 12.

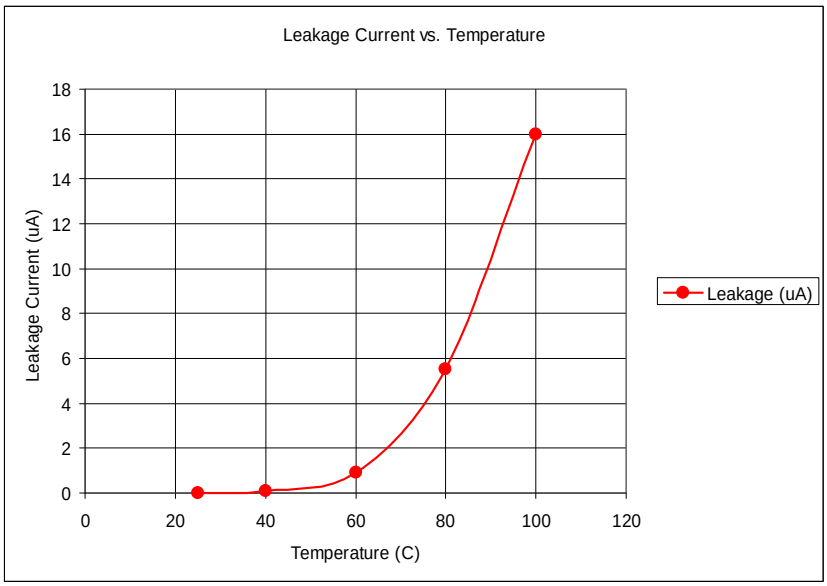


Figure 11. Single Prius film capacitor leakage current vs temperature.

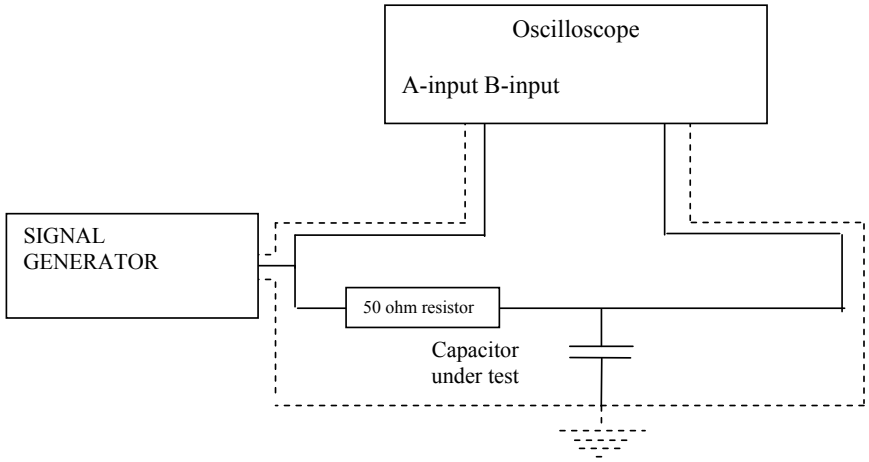


Figure 12. Circuit used to calculate ESL.

After the resonant frequency was found using the circuit in Figure 12, the ESL was derived as a function of the inductive reactance (X_L) and the capacitive reactance (X_C). At resonant frequency, the two are equal so that $X_L = X_C$; therefore, $2\pi fL = 1/(2\pi fC)$, and from this the equation for inductance is ESL = $L = 1/(4\pi^2 f^2 c)$. The ESL of the single Prius film capacitor was found to be 147 nH at an ambient temperature of 22ºC.

Magnet Evaluation

Magnet samples were evaluated using a Walker Scientific AMH-40 automatic hysteresisgraph. This computer-controlled system is used for testing, analyzing, and evaluating the hysteresis properties of magnetic materials. The system consists of a PC-based control console, two computer-interfaced integrating flux meters, a gauss meter, B and B-H coil sets, two 7-in.-diam variable-gap water-cooled electromagnets with cobalt-iron tipped poles, and a 5-kW 50-A programmable power supply. The 1200-lb electromagnets are capable of generating demagnetizing forces up to 30,000 Oersteds. This system allows the operator to perform five different types of tests: (1) manual H-Field sweep, (2) second-quadrant demagnetization curves, (3) complete four-quadrant full hysteresis loops, (4) recoil minor loops after saturation in the first quadrant, and (5) first-quadrant saturation or demagnetization of the samples. Also complementing the system is a pulse charger capable of saturating very hard magnetic materials and a Model TCS2 temperature-controlled, water-cooled fixture for testing materials at temperatures ranging from –100 to +300ºC. This fixture is used with a compatible, high-temperature coil set with integral thermocouples.

The basic magnetic properties measured using the AMH-40 automatic hysteresisgraph are residual induction (Br), coercive force (Hc), intrinsic coercivity (Hci), and energy product (BHmax).

Sintered magnets

A Prius magnet was evaluated as the sintered magnet benchmark using the AMH-40 Hysteresisgraph, four-quadrant full hysteresis loop. Two other sintered magnets were evaluated against the Prius benchmark using the same four-quadrant full hysteresis loop: Shin-Etsu's N43TS and a magnet developed at Argonne National Laboratory (ANL).

Table 2 shows that the Hci value for the Shin-Etsu N43TS sintered magnet is 30% less than the Prius benchmark magnet at 183ºC. The intrinsic coercivity (Hci) parameter, is used as an indication of a magnet's resistance to demagnetization. The hysteresis plot of the N43TS will show the knee of the demagnetization curve in the second quadrant. If the operating point of the magnet falls below the knee of this curve, the magnet will have an irreversible loss of magnetization. The Prius magnet had better resistance to demagnetization at elevated temperatures than other sintered magnets tested. The maximum energy product (BHmax) of the N43TS magnet is 12% better than the Prius at 183ºC, and the residual induction (Br) of the N43TS is 6% better than the Prius.

The magnet developed at ANL was not tested beyond 175ºC because it falls far below the Prius benchmark in all areas except Br. In this area, the ANL magnet is 3% better than the benchmark.

Figures 13–15 show the full four-quadrant hysteresis graph of the Prius sintered magnet, the Shin-Etsu N43TS sintered magnet, and the ANL sintered magnet at elevated temperatures.

Table 2. Sintered magnet test results

Magnet type	Residual induction (Br) (kG)	Coercivity (Hc) (kOe)	Intrinsic coercivity (Hci) (kOe)	Energy product (BHmax) (MGOe)
Prius (sintered) [a]	**12.55 (ambient)**	**12.18 (ambient)**	**>24 (ambient)**	**38.19 (ambient)**
	10.42 (183ºC)	**9.13 (183ºC)**	**9.87 (183ºC)**	**26.17 (183ºC)**
	9.37 (235ºC)	**5.44 (235ºC)**	**5.63 (235ºC)**	**20.83 (235ºC)**
Shin-Etsu	13.33 (ambient)	12.92 (ambient)	>24 (ambient)	42.95 (ambient)
N43TS (sintered)	11.09 (182ºC)	6.79 (182ºC)	6.87 (182ºC)	29.43 (182ºC)
ANL (sintered)	12.91 (ambient)	11.85 (ambient)	15.01 (ambient)	38.68 (ambient)
	10.75 (175ºC)	3.05 (175ºC)	3.07 (175ºC)	19.6 (175ºC)

[a] Bold indicates benchmark magnet.

Br = 10.42 kG
Hc = 9.13 kOe
Hci = 9.87 kOe
BHmax = 26.17 MGOe

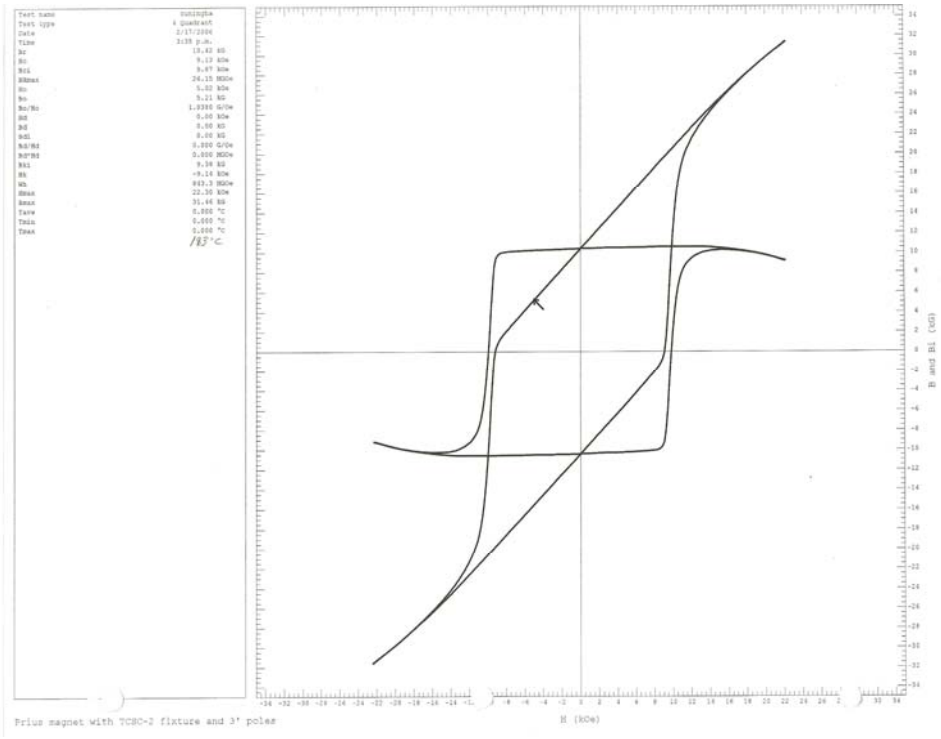


Figure 13. Hysteresis plot of the Prius sintered benchmark magnet at 183ºC.

Br = 11.09 kG
Hc = 6.79 kOe
Hci = 6.87 kOe
BHmax = 29.43 MGOe

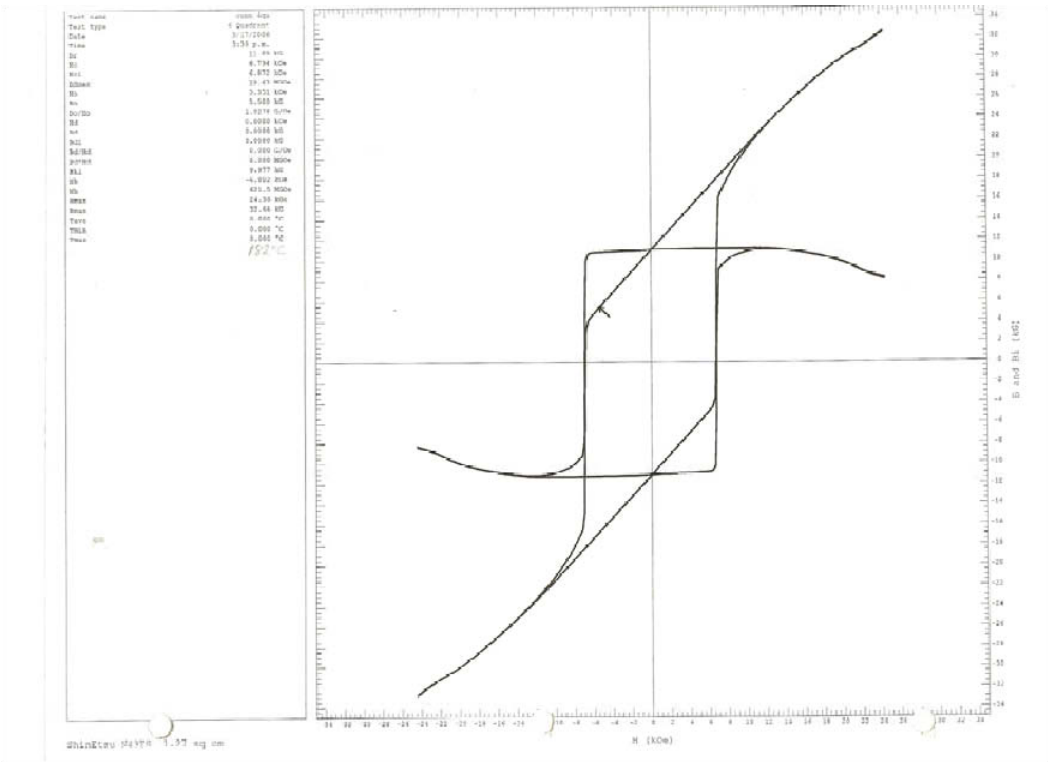


Figure 14. Hysteresis plot of the Shin-Etsu N43TS sintered magnet at 182ºC.

Br = 10.75 kG
Hc = 3.05 kOe
Hci = 3.07 kOe
BHmax = 19.60 MGOe

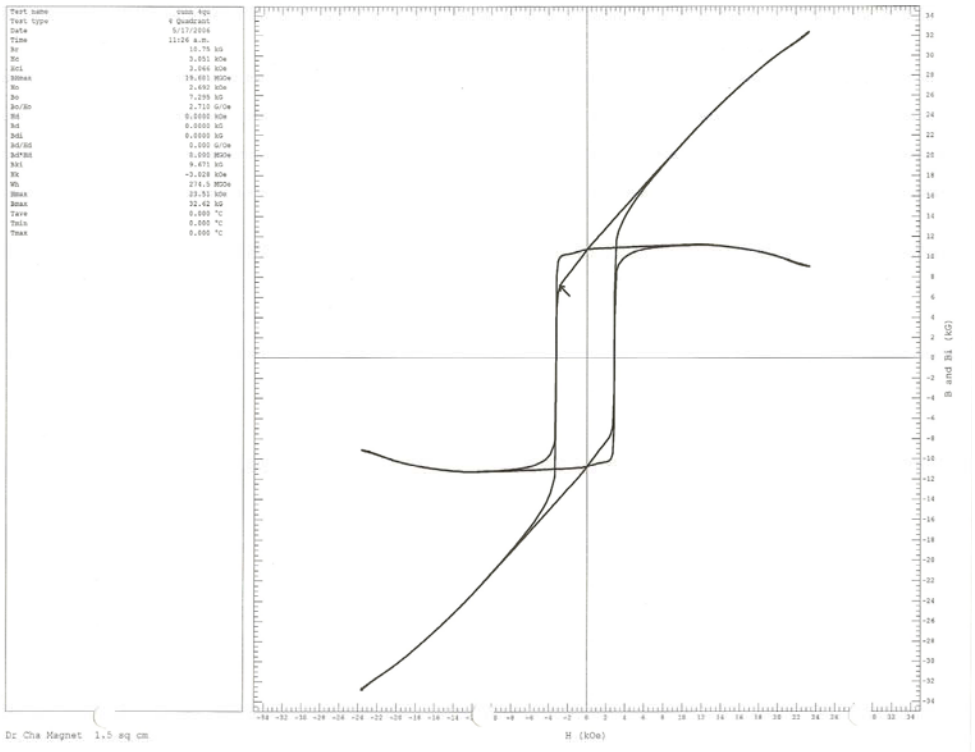


Figure 15. Hysteresis plot of the ANL sintered magnet at 175ºC.

Bonded magnets

Arnold Magnetics Plastiform 2205 was evaluated as the bonded magnet benchmark using the AMH-40 Hysteresisgraph, four-quadrant full hysteresis loop. Two other bonded magnets were evaluated against the Arnold Magnetics benchmark using the same four-quadrant full hysteresis loop: Ames Laboratory (Ames) MQP-11HTP and Ames MQP-O. The Ames MQP-O bonded magnet was made from the same alloy powder used to make the plastiform 2205 benchmark magnet. However, this magnet was fabricated using a hot-pressured process instead of being extruded. The Ames MQP-11 HTP magnet was fabricated with the same process, but it used an alloy powder developed by Iver Anderson at the Ames Lab. Table 3 lists the test results.

Table 3. Bonded magnet test results

Magnet type	Residual induction (Br) (kG)	Coercivity (Hc) (kOe)	Intrinsic coercivity (Hci) (kOe)	Energy product (BHmax) (MGOe)
Arnold Magnetics Plastiform 2205 (bonded)[a]	**5.03 (ambient) 3.70 (200ºC)**	**4.24 (ambient) 2.85 (200ºC)**	**11.49 (ambient) 5.10 (200ºC)**	**5.29 (ambient) 2.68 (200ºC)**
Ames MQP-11HTP (bonded)	3.93 (ambient) 3.41 (200ºC)	3.56 (ambient) 2.89 (200ºC)	11.87 (ambient) 5.72 (200ºC)	3.49 (ambient) 2.51 (200ºC)
Ames MQP-O (bonded)	4.46 (ambient) 3.15 (200ºC)	4.03 (ambient) 2.55 (200ºC)	12.23 (ambient) 5.25 (200ºC)	4.53 (ambient) 2.03 (200ºC)

[a]Bold indicates benchmark magnet.

At 200ºC, the Ames MQP-11 HTP magnet has a 12% higher Hci than the benchmark, indicating a superior resistance to demagnetization at elevated temperatures. The BHmax of the MQP-11 HTP is 6% less than the benchmark at 200ºC. The Br of the MQP-11 HTP is just under 8% less than the benchmark at 200ºC.

At 200ºC, the Ames MQP-O magnet has a 3% higher Hci than the benchmark, indicating a slightly better ability to resist demagnetization at elevated temperatures. The BHmax of the MQP-O magnet is 24% less than that of the benchmark at 200ºC. The Br of the MQP-O magnet is 15% less than that of the benchmark at 200ºC.

Figures 16–18 show the full four-quadrant hysteresis graph of the Arnold Magnetics Plastiform 2205 bonded benchmark magnet, the Ames MQP-11 HTP bonded magnet, and the Ames MQP-O bonded magnet at 200ºC.

Br = 3.70 kG
Hc = 2.85 kOe
Hci = 5.10 kOe
BHmax = 2.68 MGOe

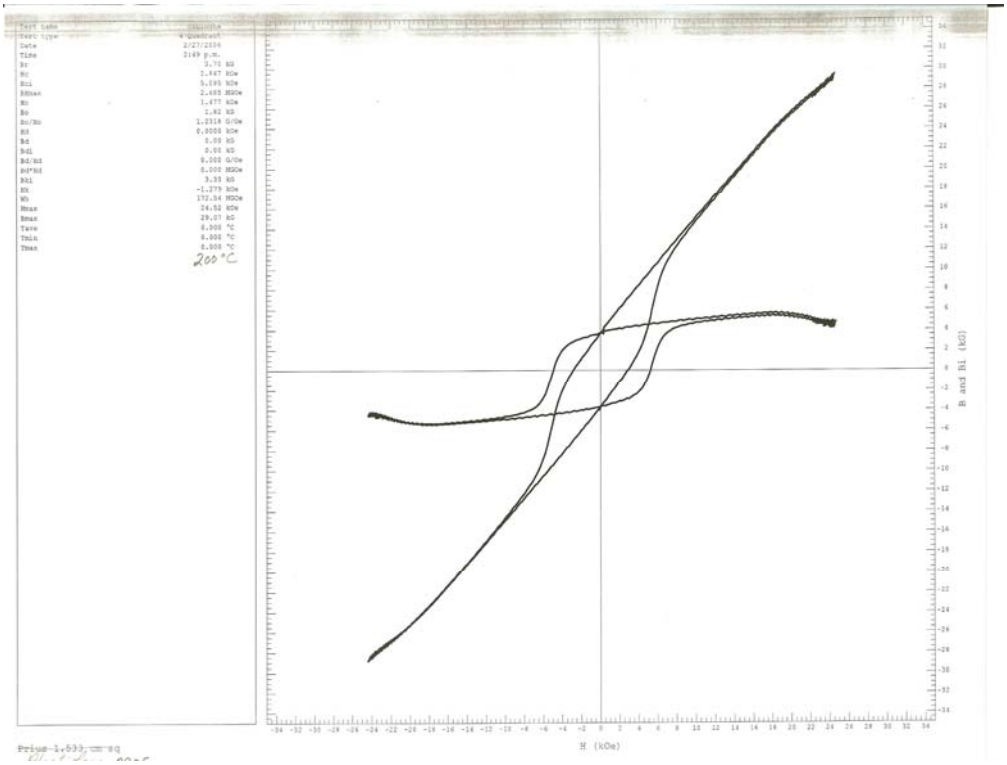


Figure 16. Hysteresis plot of Arnold Magnetics Plastiform 2205 bonded benchmark magnet at 200ºC.

Br = 3.41 kG
Hc = 2.89 kOe
Hci = 5.72 kOe
BHmax = 2.51 MGOe

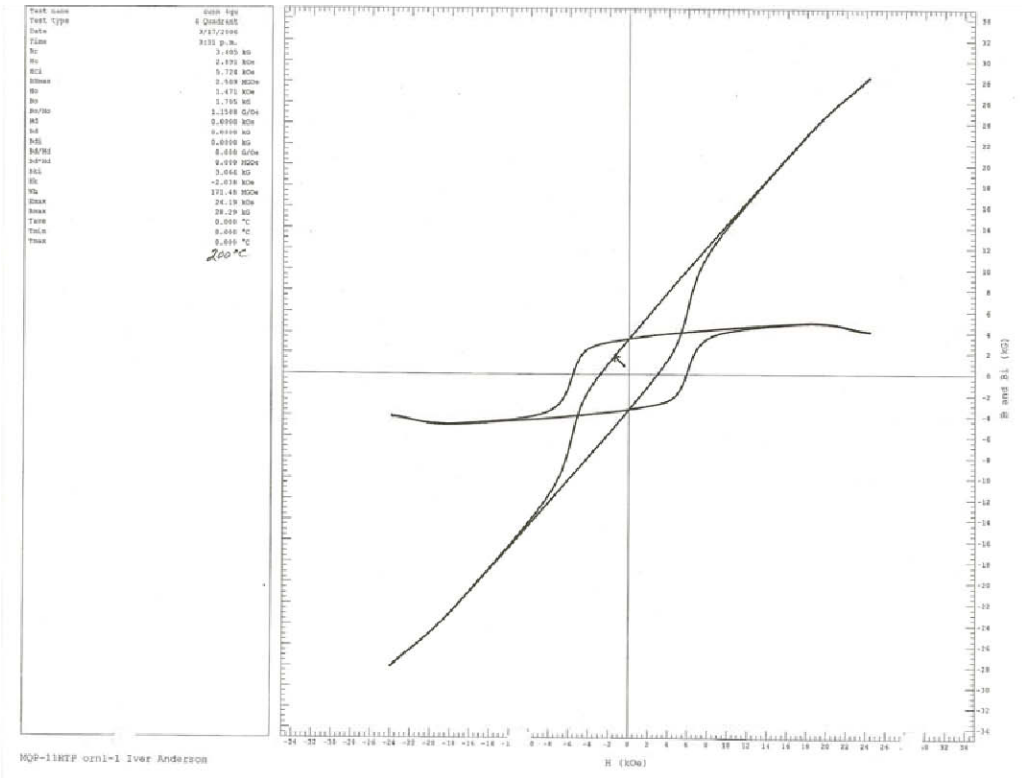


Figure 17. Hysteresis plot of the Ames MQP-11 HTP magnet at 200ºC.

Br = 3.15 kG
Hc = 2.55 kOe
Hci = 5.25 kOe
BHmax = 2.03 MGOe

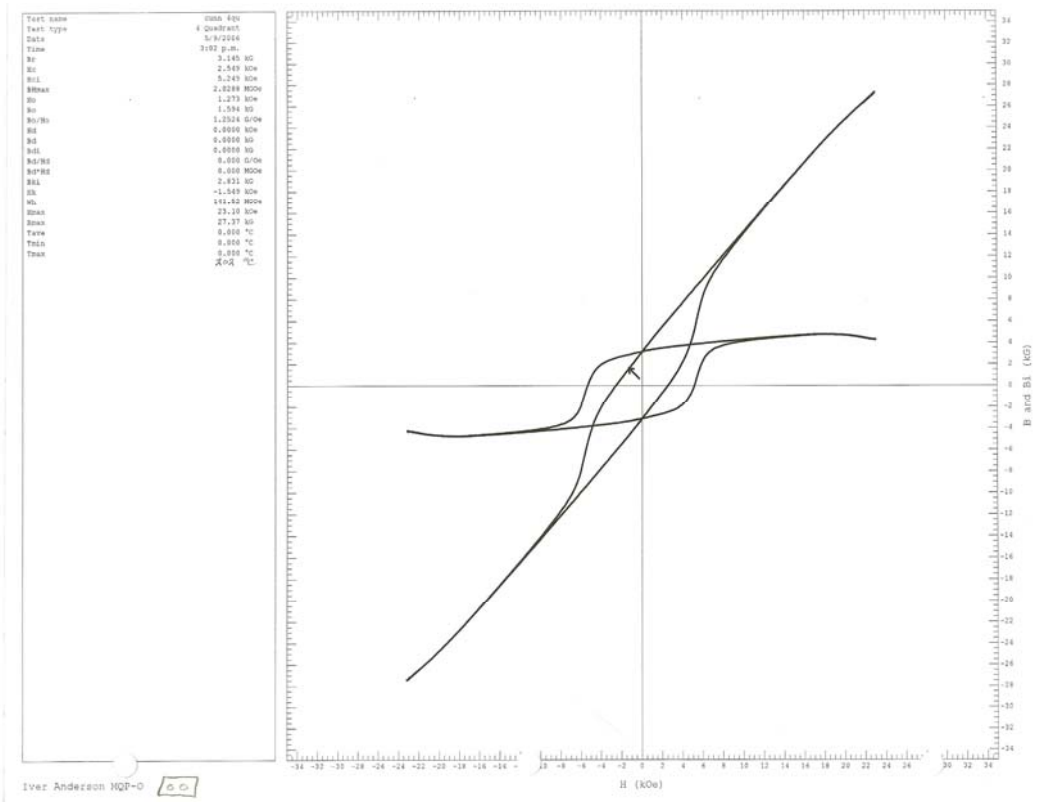


Figure 18. Hysteresis plot of the Ames MQP-O bonded magnet at 202ºC.

Conclusion

The evaluation and characterization of capacitor and magnet technologies was accomplished through the testing of these components at elevated temperatures and in simulated operating conditions. All components that were received were evaluated. No prototype film capacitors were received for evaluation during this reporting period.

The film capacitor evaluated as the benchmark was taken from the Prius HEV capacitor module. The Prius capacitor module contains ten film capacitors in parallel. Several of these were extracted and used in the evaluation process.

A Kemet 1-µF 500-Vdc ceramic capacitor was evaluated as the ceramic benchmark. Penn State supplied a prototype 90-nF 500-Vdc ceramic capacitor for evaluation. No other prototype ceramic capacitors were received from developers for evaluation during this reporting period.

The Kemet capacitor performed worse in the area of capacitance value and ESR as the temperature approached its rated value. The Penn State capacitor started out poorly in both of those areas at lower

temperatures, but as the temperature increased the ESR improved by over 70%, and the capacitance value improved by over 370%.

Benchmark characterizations of anisotropic sintered and isotropic bonded rare earth magnets were performed to determine the basic properties of these very hard magnetic materials. Magnets taken from the Prius motor were used as the sintered benchmark, and commercial Arnold Plastiform bonded magnets were used as the bonded magnet benchmark.

Tests included pulse charging the magnetic samples to saturation and performing second quadrant demagnetization curves. Sintered magnets from Shin-Etsu as well as bonded magnets from Ames Laboratory were tested. Several samples of both types of magnets were evaluated and compared with the benchmarks. The performance of all the magnets varied with temperature and was unique for each sample. The actual performance of any magnet in a magnetic circuit depends on the geometric design and operating conditions such as temperature and demagnetizing fields. The basic properties of the Shin-Etsu magnet indicate it could possibly be used with good results if the temperature can be kept low.

Future Direction

Evaluation of prototype components will be done on a case-by-case basis as the need arises.

This document highlights work sponsored by agencies of the U.S. Government. Neither the U.S. Government nor any agency thereof, nor any of their employees, makes any warranty, express or implied, or assumes any legal liability or responsibility for the accuracy, completeness, or usefulness of any information, apparatus, product, or process disclosed, or represents that its use would not infringe privately owned rights. Reference herein to any specific commercial product, process, or service by trade name, trademark, manufacturer, or otherwise does not necessarily constitute or imply its endorsement, recommendation, or favoring by the U.S. Government or any agency thereof. The views and opinions of authors expressed herein do not necessarily state or reflect those of the U.S. Government or any agency thereof.



Printed on
recycled
paper

A Strong Energy Portfolio for a Strong America

Energy efficiency and clean, renewable energy will mean a stronger economy, a cleaner environment, and greater energy independence for America. Working with a wide array of state, community, industry, and university partners, the U.S. Department of Energy's Office of Energy Efficiency and Renewable Energy invests in a diverse portfolio of energy technologies.

For more information contact:
EERE Information Center
1-877-EERE-INF (1-877-337-3463)
www.eere.energy.gov